MULTIPHOTON IONIZATION STUDIES OF METAL ATOM-SOLVENT INTERACTIONS FROM THE VAN DER WAALS DIMER TO THE MESOSCOPIC SCALE

Thesis by

James Michael Spotts

In Partial Fulfillment of the Requirements

for the Degree of

Doctor of Philosophy

California Institute of Technology

Pasadena, CA

1998

(Submitted May 29, 1998)

© 1998

James Michael Spotts

All rights reserved.

This thesis is dedicated to my parents,

Clyde E. Spotts, Jr. and Alice M. Spotts,

for all of their support throughout the years.

ACKNOWLEDGMENTS

Similar to the cultural phenomenon of Christian pilgrimages across the Western Europe throughout the medieval era, graduate school represents an indefinite journey of faith dedicated to surpassing the limits of common human experience to achieve some fundamental insight into the otherwise abstract nature of truth. Unfortunately, unlike the medieval pilgrimages converging on Santiago de Compostela where each step of the journey was delineated by a series of churches replete with holy relics to guide the spiritual journey, the modern pursuit of scientific truths is fraught with ambiguity, often lacking definitive benchmarks or even a specific goal from which some indicator of definitive progress can be extrapolated. While the completion of a thesis may symbolize the denouement of some portion of this journey, it is nevertheless difficult to acquire the proper perspective upon the accomplishment in light of the apparent incompleteness of the pursuit - the experiments that did not get done, the results that obstinately defied a proper theoretical treatment, the fastidiously designed experimental systems that inexplicably failed to perform as expected. In the end, one is left with the realization that the basic essence of the time spent in graduate school is the imperfect experience itself, not some permanent record destined to gather dust on some shelf. In particular, the intrinsic value of graduate study manifests itself as the accumulated experiences and knowledge acquired through the extensive network of interpersonal relationships between those we encounter during the course of the journey.

Throughout my years at Caltech, I feel fortunate to have had the opportunity to

interact with an extraordinary array of teachers and mentors who have significantly influenced me both on a scientific as well as personal level. Foremost, I would like to thank my graduate advisor, Mitchio Okumura, for his support, advice, and encouragement over the course of my graduate career. Most importantly, Mitchio has always given me the sense that he valued and respected my judgment throughout my years in the group. As a result, I have been fortunate to have been able to work in an atmosphere where the open exchange of ideas has been both appreciated and encouraged. Likewise, his faith in me and my abilities even in instances where I had personal doubts is gratefully acknowledged. This overall sense of trust has greatly assisted in the development an increasing sense of confidence in my own abilities that is critical to the growth of any scientist, convincingly demonstrating to me that lack of expertise need not necessarily serve as a barrier to scientific pursuit. Mitchio is an exceedingly gifted scientist whose keen insights and extensive scientific acumen were invaluable resources during my years in the group, and will be missed as I move on to the next stage of my career.

I have been also fortunate to have had the opportunity to interact with a host of talented scientists that have been members of the Okumura group either as graduate students or postdoctoral fellows. Foremost, I would like to express my appreciation to Matt Johnson who perhaps more than anyone else in the group had the greatest influence on my practical laboratory training during my early formative years. The innumerable skills that Matt taught me - electronic design and repair, machining, design and construction principles for scientific instruments - have served as the foundation for the successful implementation of the experimental work presented in this thesis. I would also

like to acknowledge the great friendship that Matt has demonstrated over the years despite the significant geographical separation since his graduation. Some of my fondest memories of graduate school revolve around the late nights we would often spend working together in the lab blasting loud, raucous tunes from our favorite bands.

In a similar light, I would like to thank Yibin Cao and Jong-Ho Choi for the innumerable skills that they taught me during my early years in the group. Their perseverance in the face of both great pressure and experimental difficulties, their ingenuity, and their commitment to achieving the highest standards of perfection in their work set a standard that I both admired and sought to emulate throughout my own thesis work.

I would also like to acknowledge the assistance of Alex Wong with whom I have had the pleasure of working over the course of my later years in the group. It has been a rewarding experience to watch Alex develop into a committed and successful experimental scientist from his original background in theory. While it is difficult to finally relinquish control of the experimental apparatus whose design and construction has been central to my life during these past years and to which I have a strong emotional attachment, I have complete confidence that Alex will successfully utilize the machine to explore new and exciting issues related to the microscopic description of condensed phase behavior. I wish him the best of luck and continued success during the remainder of his graduate career.

The experimental work presented in Chapters 3, 4, and 5 of this thesis has benefited greatly from theoretical calculations that have been performed by Jerry Boatz and Jeff Sheehy at the Phillips Laboratory, Edwards Air Force Base, as a result of an

ongoing collaborative effort. I thank Jeff for the perseverance he has shown towards deriving accurate ground and excited state *ab initio* potentials for the Al•Ar diatomic molecule, and Jerry for the dedication he has demonstrated towards generating accurate simulations of the $Al•Ar_n$ cluster spectra presented in Chapter 5. Over the years, Jerry and Jeff have provided invaluable insights into the fundamental physical nature of the observed experimental spectral behavior, greatly assisting in the dissemination of the experimental results as well as indicating potentially interesting issues for future experimental inquiry.

A particular note of appreciation should be extended to one of our first year students, Hern Paik. Hern went beyond the call of duty during the time I was writing this thesis to perform the BCONT simulations that are presented in Chapter 4 of this thesis. His assistance was invaluable during a period of extreme time pressure, and I am grateful for all the help he provided. I wish Hern the very best of luck as he embarks on his own graduate project.

I would like to thank all past Okumura group members - Thomas Schindler, Teresa Moore, Christine Nelson, Keith Kuwata, Chun-Cheng Tsao, Bernd-Michael Haas, Ted Dibble, Xu Zhang, and Todd Fuelberth - for all of their advice, assistance and friendship over the years. I would also like to particularly thank Thomas Schindler who, during his time as a postdoctoral fellow in the group, was extremely helpful in passing along technological advances and practical knowledge attained during his graduate career in Vladimir Bondybey's group at the Techniche Universität München. Likewise, I would like to thank the other Bondybey graduates and group members, in particular Christian Berg and Martin Beyer, for all of their advice towards the development and

implementation of a new piezoelectric pulsed valve originally designed during the course of Christian's thesis work.

Three summer students deserve recognition for their help that they provided during their brief tenure in the group. Gary Olsen and Prakash Jothee, both SURF students during the summers of 1992 and 1995 respectively, were helpful in advancing the progress of the project. In addition, Ju Guo, a pre-first year graduate student during the summer of 1995 warrants credit for the assistance he provided in helping to design the time-of-flight mass spectrometer.

With respect to the other present members of the Okumura group, namely Julio Lobo, Lance Christensen, and Eva Garland, I wish them success with all of their future endeavors here at Caltech. I would also especially like to thank Julio for introducing me to the pleasure of top-down LA freeway driving in his Cabriolet convertible during a number of Okumura group outings.

It has been an honor and a privilege to have had the opportunity to work with the exceedingly talented technical support staff without whom my progress would have been undoubtedly less facile. Guy Duremberg, Ray Garcia, and Mike Roy in the chemistry shop are extraordinary craftsmen who consistently brought whatever design I presented to them to complete functional fruition. I also admire them all as paragons of patience and cheerful helpfulness, and their friendship over the years is gratefully acknowledged. Similarly, Tom Dunn in the electrical shop deserves a heartfelt word of thanks for all of the assistance that he has provided during my graduate career. Whether I sought specific information or to borrow some component or piece of equipment, Tom always went out

of his way to accommodate all questions or requests. The fact that Tom would come to the lab at 7 PM on a Friday night to ensure that certain problems were successfully solved is a testament to the helpful dedication he has demonstrated over the years.

A special word of thanks is extended to those who are truly responsible for keeping the day-to-day operations running smoothly, namely those in the secretarial staff. In particular, I would like to thank Dian Buchness who has always done her best to ensure that I always had submitted all the proper forms, obtained all the proper signatures etc., over my graduate career. I admire the sincere compassion with which Dian approaches her daily interactions with the chemistry graduate students, and I appreciate her cheerful support over the years. In addition, I would like to thank Lena Lenore for all the help that she has extended to me during my time in the Okumura group. Finally, I am grateful to Mo Renta for welcoming me as an honorary Barton group member, as well as running one of the best coffee pools in which a graduate student could hope to partake.

During the summer of 1997, I was fortunate to have been accepted to attend the embryology summer course at the Marine Biological Laboratory that was directed by Marianne Bronner-Fraser and Scott Fraser. This experience ranks as one of the most enjoyable educational experiences in which I have participated throughout my many years of academic training, and has been a major motivation towards my decision to change my academic course to pursue a postdoctoral position in the field of developmental biology. I owe a deep debt of gratitude to Marianne and Scott, both for giving me the opportunity to attend the embryology course, as well as for all the support they have provided to obtain a postdoctoral position in such a dramatically different field. I would also like to thank

Mary Dickinson who has been an insightful sage in advising me during this transitional period of my career. It was Mary who originally encouraged me to apply for the embryology course, and I greatly appreciate all the advice that she has provided over the past months.

For financial support, I would like to thank both the National Science Foundation and the W. R. Grace Company for pre-doctoral fellowships. I would also like to acknowledge the financial support of the Air Force Office of Scientific Research for funding the both construction of the new experimental apparatus presented in Chapter 2 as well as the experiments that compose this thesis.

On a more personal note, I would like to thank my past roommates with whom I have shared many of the trials and tribulations of my graduate school career. Bryan Hathorn has had the dubious pleasure of living with me over the past few months during which time I was little more than a concentrated mass of anxiety and stress. While the friendship that he has extended to me may not have been properly acknowledged as the thesis deadline drew near, I would like him to know that all of his assistance was greatly appreciated. I owe Bryan a great many washed dishes while he is busy writing his thesis over the summer. Glenn Soberman was also a good friend and roommate during my early years, and I wish him continued success in his post graduate school career.

I have dedicated this thesis to my parents who were my first and most influential teachers in my life. While I realize that they may have been somewhat puzzled by the path my graduate career has taken during the course of the past seven years, I thank them for their continuing unconditional and unwavering support while I discovered my primary

scientific interests.

It would be an understatement to say that this thesis would not have been possible without the love, support, and friendship of Ai Ching Lim during the past five years. Our relationship has become inextricably linked to both of our graduate careers here at Caltech, during which time we have shared successes, disappointments, as well as the omnipresent daily tedium inherent to research. I am particularly indebted to Ai Ching for all the help she provided over the past seven weeks that I was writing this thesis, from assembling and typing references, to making figures, to proofreading the entire text. Ai Ching is one of the most compassionate, generous, and kind people I have ever known, and it brings me unfathomable happiness to know that she will become my wife in just two short weeks. To merely thank her seems somewhat inadequate, but I hope that I will have the ability to reciprocate all the joy that she has brought into my life over the course of our lifetime together.

ABSTRACT

A unified molecular-level description of solute-solvent interactions within condensed-phase systems has remained elusive despite recent advances towards the detailed understanding of the fundamental electrostatic interactions between the atomic and/or molecular moieties that compose a bulk system. Through the use of simplified cluster model systems such as those employing metal atoms solvated by a rare gas solvent, however, microscopic details pertaining to the intrinsic composite nature of the atomic orbital interactions can be effectively dissected away from the complexity inherent to condensed-phase systems.

This thesis work presents a systematic spectroscopic investigation of $Al{\bullet}Ar_n$ ($n \leq 60$) clusters generated by standard laser ablation techniques using $1'_{UV} + 1_{vis}$ two-color and $2_{vis} + 1_{vis}$ single-color resonance-enhanced multiphoton ionization (REMPI) in the vicinity of the Al($3d$) $\leftarrow$ Al($3p$) atomic transitions. UV absorption spectra were collected for $Al{\bullet}Ar_n$ cluster sizes corresponding to solvation within the first icosahedral solvation shell ($1 \leq n \leq 12$) as well as the second icosahedral solvation shell ($13 \leq n \leq 54$). These spectra exhibited significant red-shifted absorption features whose absolute peak positions were noted to be highly sensitive to the degree of solvation. Such behavior was strongly suggestive of an aluminum atom surface binding site. Nevertheless, classical Monte Carlo simulations failed to reproduce the observed magnitude of the spectral shifts. Consequently, the underlying origin of this anomalous spectral behavior was believed to derive from electronic state mixing interactions between those states originating from the

Al(3*d*) and Al(4*p*) electronic manifolds.

Evidence for such a coupling was sought at the level of the diatomic Al•Ar molecule using both $1'_{UV} + 1_{vis}$ and $2_{vis} + 1_{vis}$ REMPI to characterize all electronic states arising from the Al(3*d*)•Ar and Al(4*p*)•Ar asymptotes. Strong evidence for state mixing was observed among the $^2\Pi(4p)$, $^2\Pi(3d)$, and $^2\Sigma^+_{1/2}(3d)$ diatomic electronic states. With increasing solvation, this coupling was believed to result in the formation of aluminum 3*d*/4*p* hybrid orbitals that permitted aluminum electron density to be drawn away from the cluster surface. The concomitant introduction of partial ionic character directly adjacent to the cluster surface provided a net stabilizing effect that increased upon further solvation.

TABLE OF CONTENTS

		page
DEDICATION		iii
ACKNOWLEDGMENTS		iv
ABSTRACT		xii
TABLE OF CONTENTS		xiv
LIST OF TABLES		xix
LIST OF FIGURES		xxi
Chapter 1.	**Introduction**	1
1.1.	Introduction	2
1.2.	References	9
Chapter 2.	**Design and Construction of the Experimental Apparatus**	11
2.1.	Introduction	12
2.2.	Experimental Apparatus	12
2.2.1.	Source Vacuum Chamber	13
2.2.2.	General Source Design: Mounting and Alignment	21
2.2.3.	The Pulsed Valve Design	28
2.2.3.1.	The Original Piezoelectric Pulsed Valve Design	31
2.2.3.2.	Modified Design	36
2.2.3.2.	Modified Design for Use with Helium Carrier Gas - Christian Berg Piezoelectric Valve Design	41
2.2.4.	Laser Vaporization Source Design	46
2.2.4.1.	First Generation Laser Vaporization Source	48
2.2.4.2.	Second Generation Laser Vaporization Sources	61
2.2.4.3.	Third Generation Laser Vaporization Source	71

2.2.5. The MPI Region 84

2.2.5.1. Chamber Components 86

2.2.5.2. Time-of-Flight (TOF) Ion Optics 92

2.2.5.3. Microchannel Plate Detector Flange and Mass Gate Components 99

2.3. Experimental Methodology Overview 105

2.3.1. The Gas Inlet System 107

2.3.2. The Laser Systems 109

2.3.2.1. Laser Vaporization Laser 110

2.3.2.2. MPI Laser System 114

2.3.3. Electronics and Data Acquisition 120

2.4. Conclusion 126

2.5. References

Chapter 3: Multiphoton Ionization Studies of the Al(3*d*)•Ar and Al(4*p*)•Ar Electronic Manifolds using both Single-Photon and Two-Photon Excitation Probes 239

3.1. Introduction 240

3.1.1. Bonding Interactions in Metal-Rare Gas Systems 240

3.1.2. State Mixing in Metal-Rare Gas Systems 244

3.2. Background on the Al•Ar Molecule 248

3.3. Background on the Al(3*d*)•Ar and Al(4*p*)•Ar States 250

3.4. Experimental 254

3.5. Results 258

3.5.1. $2_{vis} + 1_{vis}$ and $1_{UV} + 1'_{vis}$ REMPI Spectra of Al•Ar and Al Fragments Above the Al(3*d*)•Ar Dissociation Limit 258

3.5.1.1. $2_{vis} + 1_{vis}$ REMPI Spectra Above the Al(3*d*)•Ar Dissociation Limit 258

3.5.1.2. $1_{UV} + 1'_{vis}$ REMPI Spectra Above the Al($3d$)•Ar Dissociation Limit 262

3.5.2. $2_{vis} + 1_{vis}$ and $1_{UV} + 1'_{vis}$ REMPI Spectra of Al•Ar and Al Fragments Below the Al($3d$)•Ar Dissociation Limit 265

3.5.2.1. $^2\Pi_{1/2}(3d)$, $^2\Pi_{3/2}(3d)$, $^2\Pi_{1/2}(4p)$, $^2\Pi_{3/2}(4p)$ States 265

3.5.2.2. $^2\Delta(3d)$ States 274

3.5.3. Preliminary *ab initio* Results on the Al($3d$)•Ar and Al($4p$)•Ar Electronic Manifolds 276

3.6. Discussion 281

3.6.1. Electronic States Originating Above the Al($3d$)•Ar Dissociation Limit 281

3.6.1.1. $^2\Pi_{1/2}(4p)$, $^2\Pi_{3/2}(4p)$, $^2\Sigma^+_{1/2}(3d)$ Electronic States 281

3.6.2. Spectroscopic Region Below the Al($3d$)•Ar Dissociation Limit 291

3.6.2.1. $^2\Pi_{1/2}(3d)$, $^2\Pi_{3/2}(3d)$, $^2\Delta(3d)$ Electronic States 291

3.7. Conclusion 302

3.8. References 303

3.9 Figure Captions 313

Chapter 4: Characterization of a Direct Two-Photon Bound→ Continuum Transition Between the X_1 $^2\Pi_{1/2}(3p)$ Ground State and the $^2\Sigma^+_{1/2}(4p)$ Excited State of Al•Ar 332

4.1. Introduction 333

4.2. Experimental 340

4.3. Results and Discussion 342

4.3.1. Experimental Spectra 342

4.3.1.1. $2_{vis} + 1_{vis}$ Spectra 342

4.3.1.2. $1'_{UV} + 1_{vis}$ Spectra 344

4.3.1.3. $1'_{UV} + 1'_{UV}$ Spectra 346

4.3.2. Simulation of the $1'_{UV} + 1_{vis}$ Single-Photon Excitation Spectrum 348

4.4. Conclusion 353

4.5. References 354

Chapter 5: The Observation of Novel Spectroscopic Behavior in Al•Ar_n Clusters ($n \leq 60$) in the Vicinity of the Al($3d$) ← Al($3p$) Atomic Transition 371

5.1. Introduction 372

5.2 Experimental 378

5.3. Results 379

5.3.1. Experimental Spectra 379

5.3.1.1. Solvation Trends up to Al•Ar_6 382

5.3.1.2. Solvation Trends up from Al•Ar_6 to Al•Ar_{12} 383

5.3.1.3. Solvation Behavior Within the Second Solvation Shell: Al•Ar_{12} to Al•Ar_{47} 385

5.3.1.4. The Second Icosahedral Solvation Shell Closing at Al•Ar_{54}: Comparisons with the Al•Ar_6 and Al•Ar_{12} Clusters as well as the Bulk Matrix Spectrum 387

5.3.1.5. $2_{vis} + 1_{vis}$ Single-Color Multiphoton Ionization of Al•Ar_6 and Al•Ar_{12} 388

5.3.2. Balling and Wright Model Simulations of Al•Ar_n Cluster Structure and Electronic Spectrum 390

5.4. Discussion 393

5.5. Conclusion 397

5.6.	References	398
Chapter 6:	**Design of a Disk Target Laser Vaporization Source for the Production of van der Waals Complexes between Alkali Metal Atoms and Polyatomic Solvents**	426
6.1.	Introduction	427
6.2	Design of the Disk Target Laser Vaporization Source	432
6.3.	Conclusion	441
6.4.	References	443
Appendix 1:	Drawings for the Disk Target Laser Vaporization Source	A-1
Appendix 2:	Drawings for the Original Piezoelectric Pulsed Valve Based on the Design of Trickl and Proch	A-30
Appendix 3:	Drawings for the Modified Piezoelectric Pulsed Valve Based on the Design of Christian Berg	A-49
Appendix 4:	Drawings for the Third Generation Laser Vaporization Source	A-62

LIST OF TABLES

Chapter 2: page

2-1. Polarizations of Laser Beams at Various Stages of Frequency Generation: Surelite I Nd:YAG and HG-4B Harmonic Generation Unit. 129

2-2. Polarizations of Laser Beams at Various Stages of Frequency Generation: NY-61 Nd:YAG Laser, TDL-51 Dye Laser, and UVX Mixing and Doubling System. 130

Chapter 3:

3-1. Summary of the $^2\Pi_{1/2}(4p) \leftarrow X_1{}^2\Pi_{1/2}(3p)$ and $^2\Pi_{3/2}(4p) \leftarrow X_1{}^2\Pi_{3/2}(3p)$ Vibronic Features Observed Above the Al(3*d*)•Ar Dissociation Limit Using $2_{vis} + 1_{vis}$ Two-Photon Excitation. 306

3-2. Summary of the $^2\Pi_{3/2}(4p)$ - $^2\Pi_{1/2}(4p)$ Spin-Orbit Splittings to the Blue of the Perturbed Region Above the Al(3*d*)•Ar Dissociation Limit. 307

3-3. Predicted $^2\Pi_{1/2}(4p)$ Vibronic Bands Above and Below the Al(3*d*)•Ar Dissociation Limit. 308

3-4. Predicted $^2\Pi_{3/2}(4p)$ Vibronic Bands Above and Below the Al(3*d*)•Ar Dissociation Limit. 309

3-5. Summary of the $^2\Pi_{1/2}(3d) \leftarrow X_1{}^2\Pi_{1/2}(3p)$ Vibronic Features Observed up to the Al(3*d*)•Ar Dissociation Limit. 310

3-6. Summary of the $^2\Pi_{3/2}(3d) \leftarrow X_1{}^2\Pi_{1/2}(3p)$ Vibronic Features Observed up to the Al(3*d*)•Ar Dissociation Limit. 311

3-7. Summary of the the $^2\Pi_{1/2}(3d)$ - $^2\Pi_{3/2}(3d)$ Spin-Orbit Splitting. 312

Chapter 4:

4-1. Input Parameters for the BCONT 1.4 Calculations of Absorption Coefficients for Al•Ar$^2\Sigma_{1/2}(4p) \leftarrow X_1{}^2\Pi_{1/2}(3p)$; Part 1. 356

4-2. Input Parameters for the BCONT 1.4 Calculations of Absorption Coefficients for Al•Ar$^2\Sigma_{1/2}(4p) \leftarrow X_1{}^2\Pi_{1/2}(3p)$; Part 2. 357

LIST OF FIGURES

Chapter 2:		page
Figure 2-1	Labels for the individual experimental components shown in the schematic of the newly-constructed experimental apparatus presented in Figure 2-2.	138
Figure 2-2	Schematic showing the individual components of the newly-constructed experimental apparatus.	139
Figure 2-3	The source cross chamber. (a) Front view. (b) Side view. (c) Top view.	140
Figure 2-4	Drawing of the source cross chamber - front view.	141
Figure 2-5	Drawing of the source cross chamber - back view.	142
Figure 2-6	Drawing of the source cross chamber - left side view.	143
Figure 2-7	Drawing of the source cross chamber - top view.	144
Figure 2-8	Drawing of the source cross chamber - bottom view.	145
Figure 2-9	Drawing of custom ASA-10 blankoff flange for the top ASA-10 flange of the source cross chamber.	146
Figure 2-10	Drawing of the source tee chamber - side view.	147
Figure 2-11	Drawing of the source tee chamber - top view.	148
Figure 2-12	Drawing of the source tee chamber - bottom view.	149
Figure 2-13	The source mount design. (a) Simplified schematic showing the source mount design as well as the mounted source components. (b) Simplified cutaway schematic of the source.	150
Figure 2-14	Drawing of the skimmer flange - front view facing the source chamber.	151
Figure 2-15	Drawing of the skimmer flange - back view facing the REMPI chamber.	152

Figure 2-16	Drawing of the skimmer flange - sectional views A-A and B-B.	153
Figure 2-17	Assembly Drawing showing the manner in which the molecular beam skimmer was mounted to the skimmer flange.	154
Figure 2-18	Drawing of the skimmer mount adapter flange between the skimmer flange and the skimmer mount.	155
Figure 2-19	Drawing of skimmer mount base.	156
Figure 2-20	Drawing of skimmer mount clamp.	157
Figure 2-21	Drawing of collars used to mount the source rails to the skimmer flange.	158
Figure 2-22	Drawing of the source rails.	159
Figure 2-23	Schematic showing the basic design of the rigid back mount frame used to support the free-hanging end of the source rails.	160
Figure 2-24	Drawing of collars used for rigid back mount frame.	161
Figure 2-25	Drawing of end caps bolted to the back of the collars used for rigid back mount frame.	162
Figure 2-26	Drawing of the cross-support pieces used to couple the collars of the rigid back mount frame.	163
Figure 2-27	Drawing of the Y-plate.	164
Figure 2-28	Drawing of x-y translator blocks that were mounted to the Y-plate to provide fine control of the pulsed valve housing position.	165
Figure 2-29	Drawing showing the modification made to the original Y-plate design.	166
Figure 2-30	Drawing of right angle brackets mounted onto the Y-plate.	167
Figure 2-31	Assembly drawing of the original piezoelectric pulsed valve based on the design of Trickl and Proch.	168

Figure 2-32	Drawing of original adapter piece used to couple the laser vaporization source to the faceplate of the piezoelectric pulsed valve.	169
Figure 2-33	Assembly drawing of the piezoelectric pulsed with the original laser vaporization adapter piece installed.	170
Figure 2-34	Assembly drawing of the piezoelectric pulsed valve showing the modifications made to the original design.	171
Figure 2-35	Assembly drawing of the piezoelectric pulsed valve showing the modifications made to the original design.	172
Figure 2-36	Drawing of the extended pulsed valve o-ring poppet tip.	173
Figure 2-37	Drawing of the extended pulsed valve Vespel-SP1 poppet tip.	174
Figure 2-38	Drawing of Vespel-SP1 poppet tip that was installed into the end of the new extended poppet design.	175
Figure 2-39	Drawing of the modified laser vaporization adapter piece.	176
Figure 2-40	Assembly drawing of the new piezoelectric pulsed valve based on the original design of Christian Berg.	177
Figure 2-41	Assembly drawing of the new piezoelectric pulsed valve based on the original design of Christian Berg.	178
Figure 2-42	Parts list for the individual components of the first generation laser vaporization source assembly (page 1 of 2).	179
Figure 2-43	Continuation of the parts list for the individual components of the first generation laser vaporization source assembly (page 2 of 2).	180
Figure 2-44	Drawing of the first generation laser vaporization source - exterior view.	181
Figure 2-45	Drawing of the first generation laser vaporization source - cross-sectional views.	182

Figure 2-46	Drawing of the first generation laser vaporization source - auxiliary view A.	183
Figure 2-47	Drawing of the first generation laser vaporization source - auxiliary view B.	184
Figure 2-48	Assembly drawing showing the components of the laser vaporization source screw drive assembly.	185
Figure 2-49	Drawing of the drive screw for the screw drive assembly.	186
Figure 2-50	Drawing of the screw drive housing for the screw drive assembly.	187
Figure 2-51	Drawing of the rotating screw drive housing for the screw drive assembly.	188
Figure 2-52	Drawing of the screw drive housing clamp for the screw drive assembly.	189
Figure 2-53	Drawing of the original gear table that was used with the first generation laser vaporization source.	190
Figure 2-54	Drawing of the second generation laser vaporization source (version 2) - exterior view.	191
Figure 2-55	Drawing of the second generation laser vaporization source (version 2) - back exterior view.	192
Figure 2-56	Drawing of the second generation laser vaporization source (version 2) - cross-sectional views A-A and B-B.	193
Figure 2-57	Drawing of the second generation laser vaporization source (version 2) - auxiliary view A.	194
Figure 2-58	Drawing of the second generation laser vaporization source (version 2) - cross-sectional view showing modifications made to the original design.	195

Figure 2-59	Schematic showing the second generation laser vaporization source (version 2) mounted to the piezoelectric pulsed valve via the original laser vaporization source adapter.	196
Figure 2-60	Drawing of the second generation laser vaporization source (version 3) - exterior view.	197
Figure 2-61	Drawing of the second generation laser vaporization source (version 3) - cross-sectional view.	198
Figure 2-62	Drawing of the second generation laser vaporization source (version 3) - back exterior view.	199
Figure 2-63	Drawing of the modified gear table that was used with the second generation laser vaporization sources.	200
Figure 2-64	Assembly drawing showing the design of the third generation laser vaporization source.	201
Figure 2-65	Magnified schematic detailing the assembled target rod cart with a target rod installed.	202
Figure 2-66	Schematic showing the placement of the aluminum target rod adjacent to the straight-channel nozzle piece that was used in conjunction with the third generation laser vaporization source.	203
Figure 2-67	Drawing of the REMPI chamber - side view.	204
Figure 2-68	Drawing of the REMPI chamber - front view facing the skimmer flange.	205
Figure 2-69	Drawing of the REMPI chamber - bottom view.	206
Figure 2-70	Drawing of the REMPI chamber - auxiliary side view showing the placement of the 2-3/4" ConFlat ports.	207
Figure 2-71	Drawing of the REMPI chamber - auxiliary side view showing the placement of the 3/4" compression port.	208

Figure 2-72	Drawing of the time-of-flight asymmetric double nipple - bottom view facing the REMPI chamber.	209
Figure 2-73	Drawing of the time-of-flight asymmetric double nipple - sectional view A-A.	210
Figure 2-74	Drawing of the time-of-flight asymmetric double nipple - sectional view B-B.	211
Figure 2-75	Drawing of the time-of-flight asymmetric double nipple - sectional view C-C.	212
Figure 2-76	Drawing of time-of-flight ion optic grounding pins.	213
Figure 2-77	Drawing of time-of-flight flight tube - view 1 of 2.	214
Figure 2-78	Drawing of time-of-flight flight tube - view 2 of 2.	215
Figure 2-79	Schematic showing the placement of the time-of-flight ion optics when mounted to the time-of-flight asymmetric double nipple and subsequently installed into the REMPI chamber.	216
Figure 2-80	Assembly drawing of the time-of-flight ion optics.	217
Figure 2-81	Drawing of the top mounting plate of the time-of-flight ion optics frame.	218
Figure 2-82	Drawing of the middle mounting plate of the time-of-flight ion optics frame.	219
Figure 2-83	Drawing of the bottom mounting plate of the time-of-flight ion optics frame.	220
Figure 2-84	Drawing of support posts placed between the middle and bottom mounting plates of the time-of-flight ion optics frame.	221
Figure 2-85	Drawing of support posts placed between the middle and top mounting plates of the time-of-flight ion optics frame.	222
Figure 2-86	Drawing of the deflector plate mount.	223

Figure 2-87	Drawing of the right angle bracket used to couple the deflector plate mount to the deflector plate.	224
Figure 2-88	Drawing of the deflector plate.	225
Figure 2-89	Assembly drawing showing the position and alignment of the time-of-flight deflector assembly within the upper ion optics frame.	226
Figure 2-90	Top view schematic of the time-of-flight deflector assembly showing the alternating orientation of each deflector as well as the separation between each adjacent deflector plates.	227
Figure 2-91	Drawing of the detector flange showing the placement of the various electrical feedthoughs.	228
Figure 2-92	Drawing of the detector flange - sectional view A-A.	229
Figure 2-93	Drawing of the modifications made to the original detector flange design to permit the mounting of posts.	230
Figure 2-94	Drawing of the front plate of the mass gate assembly.	231
Figure 2-95	Drawing of the rear plate of the mass gate assembly.	232
Figure 2-96	Drawing of the mass gate deflectors.	233
Figure 2-97	Drawing of the support posts that mounted the front plate of the mass gate assembly to the posts supporting the ground plate above the MCP cathode.	234
Figure 2-98	Drawing of the support posts that mounted the ground plate above the MCP cathode to the detector flange.	235
Figure 2-99	Drawing of the centering ring used to maintain the axial alignment of the MCP detector assembly.	236
Figure 2-100	Schematic overview of the experimental methodology.	237
Figure 2-101	A typical time-of-flight mass spectrum showing the size distribution of $Al \cdot Ar_n$ clusters that were observed.	238

Chapter 3:

Figure 3-1	Resonant multiphoton excitation schemes employed during the course of the experiment.	316
Figure 3-2	$2_{vis} + 1_{vis}$ single-color multiphoton ionization (MPI) spectra obtained above the Al($3d$)•Ar dissociation limit at 32557.8 cm^{-1}.	317
Figure 3-3	$1'_{UV} + 1_{vis}$ two-color multiphoton ionization (MPI) spectra obtained above the Al($3d$)•Ar dissociation limit at 32557.8 cm^{-1}.	318
Figure 3-4	$1'_{UV} + 1_{vis}$ two-color multiphoton ionization (MPI) spectrum obtained above the Al($3d$)•Ar dissociation limit at 32557.8 cm^{-1}.	319
Figure 3-5	Comparison of the $2_{vis} + 1_{vis}$ single-color multiphoton ionization (MPI) spectrum and $1'_{UV} + 1_{vis}$ two-color MPI spectrum obtained below the Al($3d$)•Ar dissociation limit at 32557.8 cm^{-1}.	320
Figure 3-6	$1'_{UV} + 1_{vis}$ two-color multiphoton ionization (MPI) spectra obtained below the Al($3d$)•Ar dissociation limit at 32557.8 cm^{-1}.	321
Figure 3-7	$2_{vis} + 1_{vis}$ single-color multiphoton ionization (MPI) spectra obtained below the Al($3d$)•Ar dissociation limit at 32557.8 cm^{-1}.	322
Figure 3-8	Birge-Sponer plot of the vibronic progression arising from the $^2\Pi_{1/2}(3d) \leftarrow X_1\ ^2\Pi_{1/2}(3p)$ transitions.	323
Figure 3-9	Birge-Sponer plot of the lowest four vibronic transitions between the $^2\Pi_{1/2}(3p)$ ground state and the $^2\Pi_{1/2}(3d)$ electronic state below the presumptive $^2\Pi_{1/2}(3d)$ / $^2\Pi_{1/2}(4p)$ curve crossing region.	324

Figure 3-10	Birge-Sponer plot of the upper vibronic transitions between the $^2\Pi_{1/2}(3p)$ ground state and the $^2\Pi_{1/2}(3d)$ electronic state above the presumptive $^2\Pi_{1/2}(3d)$ / $^2\Pi_{1/2}(4p)$ curve crossing region.	325
Figure 3-11	Comparison of the peak contours for both $^2\Pi_{1/2}(4p)$ vibronic levels assigned below the Al($3d$)•Ar dissociation limit.	326
Figure 3-12	New vibronic levels attributed to the $^2\Delta(3d)$ electronic state to the red of the previously assigned 0-0 $^2\Delta(3d)$ vibronic level by Morse and co-workers.	327
Figure 3-13	Birge-Sponer plot for the $^2\Delta(3d)$ electronic state including the newly discovered 0-0 and 0-1 vibronic bands together with those previously reported by Morse and co-workers.	328
Figure 3-14	The Al•Ar ground state $^2\Pi(3p)$ and $^2\Sigma^+(3p)$ potential energy curves derived from calculations by Jeff Sheehy.	329
Figure 3-15	The Al•Ar first excited state $B\,^2\Sigma^+(4s)$ potential energy curve derived from calculations by Jeff Sheehy.	330
Figure 3-16	Potential energy curves arising from the Al($3d$)•Ar and Al($4p$)•Ar electronic manifolds from calculations by Jeff Sheehy.	331

Chapter 4:

Figure 4-1	Low-power $2_{vis} + 1_{vis}$ single-color multiphoton ionization (MPI) spectrum of the bound→continuum transition between the $^2\Pi_{1/2}(3p)$ ground state and the excited $^2\Sigma^+_{1/2}(4p)$ electronic state on the Al^+ fragment signal channel.	360
Figure 4-2	Low-power $2_{vis} + 1_{vis}$ single-color multiphoton ionization (MPI) spectrum of the bound→continuum transition between the $^2\Pi_{1/2}(3p)$ ground state and the excited $^2\Sigma^+_{1/2}(4p)$ electronic state on the Al•Ar^+ channel.	361

Figure 4-3	High-power $2_{vis} + 1_{vis}$ single-color multiphoton ionization (MPI) spectrum of the bound→continuum transition between the $^2\Pi_{1/2}(3p)$ ground state and the excited $^2\Sigma^+_{1/2}(4p)$ electronic state on the Al^+ fragment signal channel.	362
Figure 4-4	Low UV power $1'_{UV} + 1_{vis}$ two-color multiphoton ionization (MPI) spectrum of the bound→continuum transition between the $^2\Pi_{1/2}(3p)$ ground state and the excited $^2\Sigma^+_{1/2}(4p)$ electronic state on the Al^+ fragment signal channel.	363
Figure 4-5	High UV power $1'_{UV} + 1_{vis}$ two-color multiphoton ionization (MPI) spectrum of the bound→continuum transition between the $^2\Pi_{1/2}(3p)$ ground state and the excited $^2\Sigma^+_{1/2}(4p)$ electronic state on the Al^+ fragment signal channel.	364
Figure 4-6	Low UV power $1'_{UV} + 1'_{UV}$ single-color multiphoton ionization (MPI) spectrum of the bound→continuum transition between the $^2\Pi_{1/2}(3p)$ ground state and the excited $^2\Sigma^+_{1/2}(4p)$ electronic state on the Al^+ fragment signal channel.	365
Figure 4-7	High UV power $1'_{UV} + 1'_{UV}$ single-color multiphoton ionization (MPI) spectrum of the bound→continuum transition between the $^2\Pi_{1/2}(3p)$ ground state and the excited $^2\Sigma^+_{1/2}(4p)$ electronic state on the Al^+ fragment signal channel.	366
Figure 4-8	Potential energy curves arising from the Al(4*p*)•Ar electronic manifold from the calculations by Jeff Sheehy.	367
Figure 4-9	BCONT 1.4 simulation of the single-photon $^2\Sigma^+(4p) \leftarrow {}^2\Pi(3p)$ continuum←bound transition using the calculated potential energy curves provided by Jeff Sheehy.[5]	368
Figure 4-10	Comparison of the simulated dissociative $^2\Sigma^+(4p)$ peak profile generated from the BCONT 1.4 program with the experimental low UV power$1'_{UV} + 1_{vis}$ two-color multiphoton ionization (MPI) spectrum on the Al^+ fragment signal channel.	369

Figure 4-11 Comparison of the simulated dissociative $^2\Sigma^+(4p)$ peak profile generated from the BCONT 1.4 program with the experimental low UV power $1'_{UV} + 1_{UV}$ single-color MPI spectrum on the Al^+ fragment signal channel. 370

Chapter 5:

Figure 5-1 Schematic showing the $1'_{UV} + 1_{vis}$ multiphoton ionization (MPI) methodology used for the majority of the experimental work presented in Chapter 5. 404

Figure 5-2 $1'_{UV} + 1_{vis}$ multiphoton ionization (MPI) spectrum of $Al{\bullet}Ar_3$ taken about the Al($3d$) ← Al($3p$) atomic transitions. 405

Figure 5-3 $1'_{UV} + 1_{vis}$ multiphoton ionization (MPI) spectrum of $Al{\bullet}Ar_5$ taken about the Al($3d$) ← Al($3p$) atomic transitions. 406

Figure 5-4 $1'_{UV} + 1_{vis}$ multiphoton ionization (MPI) spectrum of $Al{\bullet}Ar_6$ taken about the Al($3d$) ← Al($3p$) atomic transitions. 407

Figure 5-5 $1'_{UV} + 1_{vis}$ multiphoton ionization (MPI) spectrum of $Al{\bullet}Ar_7$ taken about the Al($3d$) ← Al($3p$) atomic transitions. 408

Figure 5-6 $1'_{UV} + 1_{vis}$ multiphoton ionization (MPI) spectrum of $Al{\bullet}Ar_{12}$ taken about the Al($3d$) ← Al($3p$) atomic transitions. 409

Figure 5-7 $1'_{UV} + 1_{vis}$ multiphoton ionization (MPI) spectrum of $Al{\bullet}Ar_{18}$ taken about the Al($3d$) ← Al($3p$) atomic transitions. 410

Figure 5-8 $1'_{UV} + 1_{vis}$ multiphoton ionization (MPI) spectrum of $Al{\bullet}Ar_{25}$ taken about the Al($3d$) ← Al($3p$) atomic transitions. 411

Figure 5-9 $1'_{UV} + 1_{vis}$ multiphoton ionization (MPI) spectrum of $Al{\bullet}Ar_{34}$ taken about the Al($3d$) ← Al($3p$) atomic transitions. 412

Figure 5-10 $1'_{UV} + 1_{vis}$ multiphoton ionization (MPI) spectrum of $Al{\bullet}Ar_{40}$ taken about the Al($3d$) ← Al($3p$) atomic transitions. 413

Figure 5-11 $1'_{UV} + 1_{vis}$ multiphoton ionization (MPI) spectrum of $Al{\bullet}Ar_{47}$ taken about the Al($3d$) ← Al($3p$) atomic transitions. 414

Figure 5-12	$1'_{UV} + 1_{vis}$ multiphoton ionization (MPI) spectrum of $Al{\bullet}Ar_{54}$ taken about the Al($3d$) ← Al($3p$) atomic transitions.	415
Figure 5-13	Comparison of the UV absorption spectra obtained for the $Al{\bullet}Ar_3$, $Al{\bullet}Ar_5$, and $Al{\bullet}Ar_6$ clusters taken about the Al($3d$) ← Al($3p$) atomic transitions.	416
Figure 5-14	Comparison of the UV absorption spectra obtained for the $Al{\bullet}Ar_6$, $Al{\bullet}Ar_7$, and $Al{\bullet}Ar_{12}$ clusters taken about the Al($3d$) ← Al($3p$) atomic transitions.	417
Figure 5-15	Comparison of the UV absorption spectra obtained for the $Al{\bullet}Ar_{12}$, $Al{\bullet}Ar_{18}$, $Al{\bullet}Ar_{25}$, $Al{\bullet}Ar_{34}$, and $Al{\bullet}Ar_{47}$ clusters taken about the Al($3d$) ← Al($3p$) atomic transitions.	418
Figure 5-16	The UV absorption spectrum obtained for the $Al{\bullet}Ar_{54}$ cluster representing the completion of the second icosahedral solvation shell.	419
Figure 5-17	$2_{vis} + 1_{vis}$ single-color multiphoton ionization (MPI) spectrum of $Al{\bullet}Ar_6$ and $Al{\bullet}Ar_6$ taken to the red of the Al($3d$) ← Al($3p$) atomic transitions.	420
Figure 5-18	Comparison of the $2_{vis} + 1_{vis}$ single-color spectra collected to the red of the Al($3d$) ← Al($3p$) atomic transitions with the UV absorption spectra obtained using $1'_{UV} + 1_{vis}$ two-color excitation. (a) $Al{\bullet}Ar_6$. (b) $Al{\bullet}Ar_{12}$.	421
Figure 5-19	Balling and Wright calculated minimum energy structures for the $Al{\bullet}Ar_6$ and $Al{\bullet}Ar_{12}$ clusters generated by classical Monte Carlo simulations.	422
Figure 5-20	Balling and Wright calculated minimum energy structures for the $Al{\bullet}Ar_{54}$ cluster generated by classical Monte Carlo simulations.	423

Figure 5-21 Predicted UV absorption spectra for the Al•Ar_6, Al•Ar_{12}, and Al•Ar_{54} cluster sizes using the Balling and Wright model. 424

Figure 5-22 Schematic showing how electronic state mixing between the Al(3*d*) and Al(4*p*) atomic states can influence the nature of the electronic interaction between a surface-solvated aluminum atom and a rare gas cluster. 425

CHAPTER 1

Introduction

1.1. Introduction

The enormous complexity intrinsic to liquids and condensed-phase solids represents a formidable challenge to those who seek a microscopic understanding of the weak bonding and/or non-bonding interactions that govern the physical properties of the bulk phase. An accurate dynamical model of condensed phase systems requires a molecular level description of the N-body potential that determines the interaction of a single molecule with all surrounding neighbors, which in turn must be correlated to all motions in all degrees of freedom present within the sample. In practice, acquiring such knowledge at an appreciable level of detail is exceedingly challenging, both due to the sheer number of binding interactions that must be characterized as well as the complications inherent in accurately describing the simple pair-wise potentials from which many-body potentials may eventually be constructed. In effect, the unique electronic structure of each chemical species necessitates a distinct dissection of the complex ensemble of attractive and/or repulsive electrostatic physical forces (due to both the presence of charges and/or dipole and higher multipole moments) that underlie bulk phase behavior for each condensed phase sample, thus rendering a comprehensive, unified model elusive.

In order to simplify an otherwise intractable problem, approximate model systems have been sought that serve to reduce the enormity of the problem while still retaining the fundamental physical properties of the bulk. Such an approach has been the domain of cluster chemistry, a field dedicated to the use of small molecular aggregates as models for the condensed phase. The advantage to studying such small systems is that a reasonably

precise description of the pair-wise and many-body potentials between a small, finite number of atomic or molecular species that comprise the model system can be achieved. Because solvent atoms or molecules can be added to a particular solute in a sequential manner, a microscopic model of the dopant surrounded by the initial few solvation shells representative of a liquid or solid can begin to emerge, providing a core model from which the properties of the bulk may eventually be successfully extrapolated.

One particular model system that has been extensively exploited over the years as a means to extract detailed information related to the electrostatic nature of weak solute-solvent interactions are metal atom-rare gas van der Waals complexes.[1] While somewhat idealized in comparison to more complicated polyatomic solvent molecules, rare gas atoms nonetheless offer the unique advantage of providing a uniform, spherically-symmetric polarizable medium devoid of complications arising from the presence of charges, dipoles, or higher multipole moments. The simplicity offered by the use of rare gas atoms provides a framework by which the metal atom contribution to the bonding or non-bonding van der Waals interaction can be effectively isolated. Since to a first approximation the role of the rare gas atom can be adequately characterized as a benign binding partner, the bonding character of specific electronic orbital orientations on the metal atom itself can be explored in great detail, providing an exquisitely sensitive means of probing how various subtle variations in the metal atomic orbital character affect the nature of the weak van der Waals bond. Likewise, by incrementally varying the degree of polarizability on the rare gas moiety by substituting constituents from different rows on the periodic table, precise information regarding how the van der Waals bonding character

of a specific electronic configuration on the metal atom varies with polarizability can be accurately assessed.

Concomitant with the interest in metal atom-rare gas van der Waals systems has been the development of highly efficient means to both generate rare gas van der Waals clusters containing refractory elements as well as to ascertain the fundamental details of the interaction potentials by highly sensitive spectroscopic methods. Developed by Smalley and co-workers in the early 1980's, laser vaporization techniques have revolutionized the process by which samples of refractory elements ranging from single atoms to large clusters can be produced.[2-6] By coupling the laser vaporization technology to the powerful intramolecular and intermolecular cooling mechanisms offered by supersonic pulsed beam expansion methods, mixed refractory atom-solvent van der Waals molecules and clusters are now routinely produced, providing a facile and efficient means to probe the intricacies of the weak bonding behavior on a microscopic scale.[7]

While a number of spectroscopic approaches have been implemented to probe the fundamental nature of the van der Waals interaction on scales ranging from the diatomic species to clusters containing tens of thousands of atoms or molecules, multiphoton ionization (MPI) methods have been among the most extensively implemented. One reason underlying the popularity of the MPI methodology is the fact that the signal arises from an ionic species formed by resonant excitation via some excited intermediate state within the species under investigation. Therefore, the MPI method affords the possibility for mass selection when combined with either time-of-flight (TOF) or quadrupole mass spectrometry. This fundamental property is extremely useful for the study of the

electronic as well as vibrational structure present within a cluster system, since the spectroscopic character of a specific cluster size can be effectively isolated from those of all other cluster species present within the region of the molecular beam irradiated by the MPI laser pulse(s).

The majority of this thesis is dedicated to the characterization of the electronic interactions between an aluminum atom and an argon rare gas solvent from the van der Waals dimer to the mesoscopic scale. While a great deal of spectroscopic characterization has been already performed on this system at the diatomic,[8-11] cluster,[12-15] as well as bulk matrix level,[16-17] several outstanding questions remain. In particular, the nature of the electronic states arising from the energetically similar Al($3d$) + Ar and Al($4p$) + Ar asymptotes which correlate to the second and third excited states of this metal-rare gas system has defied definitive characterization. The close energetic proximity of these two asymptotes suggests that electronic state mixing may play an important role in determining the nature of the van der Waals bond - a theme that will recur repeatedly throughout this thesis.

During the course of this thesis work, the pair-wise interactions arising from these two electronic manifolds have been intensively investigated at the level of the van der Waals dimer. In addition, studies on Al•Ar_n ($n \leq 60$) clusters have been performed to explore how the spectroscopic behavior of these two manifolds evolves with sequential solvation within the first two icosahedral solvation shells. To carry out these studies, a new experimental apparatus was constructed whose design is extensively detailed in Chapter 2. The new machine was designed to utilize laser vaporization techniques to

generate the Al•Ar_n species of interest, combined with MPI/TOF mass spectrometric detection. In addition, Chapter 2 provides a overview of the experimental methodologies used during the course of this thesis work.

The following two chapters present the comprehensive characterization of the spectroscopic behavior of Al(3*d*)•Ar and Al(4*p*)•Ar electronic manifolds exclusively in the van der Waals dimer. This work extended the previous work by Morse and co-workers by employing both $2_{vis} + 1_{vis}$ two-photon excitation to probe the Al(3*d*)•Ar and Al(4*p*)•Ar electronic manifolds in addition to $1'_{UV} + 1_{vis}$ single-photon excitation mode as had been performed previously.[11] Chapter 3 reports the discovery of the $^2\Pi_{1/2}(4p)$ and $^2\Pi_{3/2}(4p)$ electronic states - the first such states to be directly detected by two-photon excitation in the Al•Ar molecule. Both the $^2\Pi_{1/2}(4p)$ and $^2\Pi_{3/2}(4p)$ electronic states exhibited complex spectral behavior due to state mixing interactions with the $^2\Sigma^+_{1/2}(3d)$ as well as $^2\Pi_{1/2}(3d)$ and $^2\Pi_{3/2}(3d)$ electronic states. Likewise, Chapter 3 details the reassessment of the $^2\Delta(3d)$, $^2\Pi(3d)$, and $^2\Sigma^+(3d)$ state spectral assignments arising from the Al(3*d*)•Ar electronic configuration previously proposed by Morse and co-workers.[11]

The detection of a bound→continuum transition between the $^2\Pi_{1/2}(3p)$ ground state and the $^2\Sigma^+_{1/2}(4p)$ state probed by $2_{vis} + 1_{vis}$ two-photon excitation is the subject of Chapter 4. A broad, structureless transition was observed that was energetically situated well above the Al(4*p*) + Ar dissociation limit, indicative of the fact that the $^2\Sigma^+_{1/2}(4p)$ state was purely repulsive in character. In addition, the observed dissociative profile was found to possess significant single-photon character, suggesting that state mixing interactions between nearby electronic states strongly influenced the character of the $^2\Sigma^+_{1/2}(4p)$ state

potential. Simulations of the dissociative peak contour for the single-photon excitation spectra using potential energy curves obtained from MRCI *ab initio* calculations performed in collaboration with Jeff Sheehy enabled an initial determination of the potential energy profile for the $^2\Sigma^+_{1/2}(4p)$ state to be achieved.[18]

With the electronic spectroscopy of the Al•Ar van der Waals dimer originating from the Al(3*d*)•Ar and Al(4*p*)•Ar manifolds well characterized, Chapter 5 details the spectral evolution of these states with sequential solvation. Rather than gradually evolving towards the strongly blue-shifted spectral features observed in the bulk matrix spectra, the UV absorption spectra of Al•Ar_n clusters ($n \leq 60$) near the atomic Al(3*d*) transition demonstrated a prominent red-shifted feature that shifted further to the red upon increasing solvation. While other slightly red-shifted features had been previously noted in other metal-rare gas systems bound at the surface of a rare gas cluster,[1,19] the shifts observed in the Al•Ar_n clusters were at least five to ten times larger than any previously reported. The origin of the anomalous spectral behavior is discussed within the context of novel state mixing interactions between the Al(3*d*) and Al(4*p*) states due to the localization of the aluminum atom to the surface of the cluster.

Finally, Chapter 6 marks the point of departure away from aluminum-containing metal-rare gas van der Waals systems towards those containing alkali metals complexed to polyatomic solvents. The transition towards the use of alkali metals, however, required the development of a new source that would in accommodate the complications presented by the soft nature and high reactivity towards oxidation inherent to these metals. Chapter 6 is another experimental methods chapter that details the design and construction of a

new laser vaporization source that employed an alkali metal disk target rather than the target rod sources that have been used throughout the course of the previous work. Over the course of the following months, this new source design will be implemented with an emphasis on generating both alkali metal-carbon dioxide as well as alkali metal-benzene van der Waals dimers - two systems that bear considerable relevance to biological systems. Ultimately, the new laser vaporization disk target source, in conjunction with the laser vaporization target rod sources presented in Chapter 2, will permit any material that can be obtained as (or machined into) a rod or disk target to be employed as an atom source for the generation of a wide variety of metal atom-solvent clusters.

1.2. References

1. W. H. Breckenridge, C. Jouvet, and B. Soep, in *Advances in Metal and Semiconductor Clusters*, M. A. Duncan, Ed. (JAI Press, Greenwich, 1995).
2. T. G. Dietz, M. A. Duncan, D. E. Powers, and R. E. Smalley, *J. Chem. Phys.*, **74**, 6611 (1981).
3. D. E. Powers, S. G. Hansen, M. E. Geusic, A. C. Puiu, J. B. Hopkins, T. G. Dietz, M. A. Duncan, P. R. R. Langridge-Smith, and R. E. Smalley, *J. Phys. Chem.*, **86**, 2556 (1982).
4. D. L. Michalopoulos, M. E. Geusic, S. G. Hansen, D. E. Powers, and R. E. Smalley, *J. Phys. Chem.*, **86**, 3914 (1982).
5. D. E. Powers, S. G. Hansen, M. E. Geusic, D. L. Michalopoulos, and R. E. Smalley, *J. Chem. Phys.*, **78**, 2866 (1983).
6. J. B. Hopkins, P. R. R. Langridge-Smith, M. D. Morse, and R. E. Smalley, *J. Chem. Phys.*, **78**, 1627 (1983).
7. G. Scoles, Ed., *Atomic and Molecular Beam Methods, Vol. I* (Oxford University Press, New York, 1988).
8. J. M. Gardner and M. I. Lester, *Chem. Phys. Lett.*, **137**, 301 (1987).
9. C. L. Callender, S. A. Mitchell, and P. A. Hackett, *J. Chem. Phys.*, **90**, 5252 (1989).
10. M. J. McQuaid, J. L. Gole, and M. C. Heaven, *J. Chem. Phys.*, **92**, 2733 (1990).
11. S. A. Heidecke, Z. Fu, J. R. Colt, and M. D. Morse, *J. Chem. Phys.*, **97**, 1692 (1992).
12. K. E. Schriver, M. Y. Hahn, J. L. Persson, M. E. LaVilla, and R. L. Whetten, *J. Phys. Chem.*, **93**, 2869 (1989).
13. R. L. Whetten. K. E. Schriver, J. L. Persson, and M. Y. Hahn, *J. Chem. Soc. Farad. Trans.*, **86**, 2375 (1990).
14. X. Li., M. Y. Hahn, M. S. El-Shall, and R. L. Whetten, *J. Phys. Chem.* **95**, 8524 (1991).
15. D. A. Estrin, L. Liu, and S. J. Singer, *J. Am. Chem. Soc.*, **96**, 5325 (1992).

16. H. Abe and D. M. Kolb, *Ber. Bunsenges. Phys. Chem.* **87**, 523 (1983).

17. J. H. Ammeter and D. C. Schlosnagle, *J. Chem. Phys.*, **59**, 4784 (1973).

18. J. A. Boatz, J. A. Sheehy, and P. W. Langhoff, in *Monte Carlo Simulations of the Structures and the Optical Absorption Spectra of Al/Ar$_N$ Clusters: Applications of the Spectral Theory of Chemical Binding, Proceedings of the High Energy Density (HEDM) Conference*, June 1997 (USAF Office of Scientific Research, Bolling AFB, DC, 1997).

19. J. P. Visticott, P. de Pujo, J. M. Mestdagh, A. Lallement, J. Berlande, O. Sublemontier, P. Meynadier and J. Cuvellier, *J. Chem. Phys.*, **100**, 158 (1994).

CHAPTER 2

Design and Construction of the Experimental Apparatus Employed for the Study of Metal Atom-Solvent van der Waals Interactions Using Multiphoton Ionization Methods

2.1. Introduction

A significant portion of this thesis work has revolved around the design, construction, and optimization of a new experimental apparatus to be employed for the investigation of refractory atom interactions with solvent molecules and clusters. Two principal criteria have guided the construction of this new machine - ease of use and versatility. In particular, a critical aspect of the design was to permit several different types of experiments to be performed interchangeably on a single apparatus, both with respect to the types of systems that could be studied and the detection schemes by which these systems could be probed. Herein are outlined the details related to the construction of this apparatus for the experimental configuration used during the course of the work described in this thesis - that related to multiphoton ionization (MPI) studies of metal-solvent interactions formed by laser ablation/pulsed beam expansion methods. Specifics of the other experimental methodology pursued during the course of this thesis work, namely laser induced fluorescence of aluminum-containing molecules and clusters, will not be presented here since they appear comprehensively detailed elsewhere.[1]

2.2. Experimental Apparatus

The following sections describe the specific details related to the different components of experimental apparatus itself, as well as the laser systems employed and the data acquisition scheme. In characterizing the functional components of the newly-constructed machine itself, the experimental design can be broadly subdivided into two principal categories - those dedicated to the various constituent parts of the source region,

and those dedicated to the implementation of the multiphoton ionization/time-of-flight (MPI/TOF) detection methodology.

2.2.1. Source Vacuum Chamber

The key to producing both very weakly bound van der Waals molecules as well as large van der Waals clusters is to be able to very efficiently cool the species of interest via three-body collisions within the initial supersonic expansion. At the beginning of this work, the target systems were $Li \bullet H_2$ and $B \bullet H_2$, which in the case of the former, possesses a calculated zero point binding energy of perhaps 4 cm^{-1}.[1,2] As a result, considerable effort was expended to ensure that the optimal expansion conditions could be attained.

One key parameter in generating an efficient cooling expansion is the sheer amount of gas that can be introduced into the expansion with each duty cycle since higher number density of gas enhances the three-body collision probability. This simplifies to a mass balance problem where the number of torr-*l* released by the source with each shot must be matched by the number of torr-*l* that can be effectively pumped away in order to maintain a constant average source chamber pressure.[3] Since amount of gas introduced can be arbitrarily varied, the gas pumping system becomes the key design parameter.

Near the time when the source chamber was being designed, work out of Scole's group demonstrated that large helium clusters, with sizes ranging close to the ten thousand atom range, could be generated.[4] For this experiment, an enormous 32,000 *l*/s (He pumping rate) diffusion pump was employed. Due to both space and financial constraints, such a brute force approach was not an option. Ultimately, the optimal compromise for

this apparatus was resolved to be the use of two Varian VHS-10 diffusion pumps employed in tandem. With this approach, a total combined pumping speed of 13,200 *l*/s (He) was achieved, while at the same time permitting the beam line to lie approximately 5.5' from the floor.

As is shown in Figures 2-1 and 2-2, the source chamber was designed around the need for two large diffusion pumps. The source chamber consists of two separable sections joined by a NW-320 (i.e., 320 mm or 12.75") ISO flange to flange coupling, each pumped by a single 10" diffusion pump (Varian VHS-10). The two custom chambers are best characterized as an asymmetrical reducing six-way cross (Figures 2-3 through 2-8) and a reducing four-way cross (Figures 2-10 through 2-12) respectively. Colloquially, these two chambers are referred to as the source cross and the source tee respectively, and this vernacular will be utilized for the remainder of this chapter. Both custom chambers (built by MDC) are composed of 3/16" thick stainless steel tube.

As seen in Figure 2-3, the source cross is a standard cross in two of the three dimensions, consisting of three orthogonally-oriented tubes of different diameter. The first tube oriented along the beam line (horizontally along the plane of the page) possess a nominal outer tube diameter of 12.75", with NW-320 ISO flanges on each end. A second, vertically oriented tube has a nominal 12" outer tube diameter with ASA-10 flanges on each end. The upper ASA-10 flange on the vertical tube was designed with a female precision key (see Figure 2-7) such that exact alignment of experimental components mounted on the upper mating ASA-10 flange (shown in Figure 2-9) could be maintained in the event the mating flange was removed. Both of these tubes delineate the axes of

symmetry of this chamber, with the center lines along the horizontally-oriented tube along the beam line and the vertically-oriented tube intersecting at the center point of the chamber.

Off-axis from these other two tubes is the third tube of this six-way cross shown in Figure 2-3b. This tube possess a 10" outer tube diameter, with NW-250 ISO flanges welded onto each end. As is evident from Figure 3b, this tube is offset by a distance of 4.25" relative to the center of the chamber determined by the other two tubes. This offset is due to the fact that a completely variable source to skimmer distance was sought. With this offset, it is possible to introduce a laser vaporization laser pulse through the 10" tubes directly into the source while the source remaines within approximately 1.5" of the skimmer orifice. Such a design provides a complete range of source to skimmer distances to be accessible, greatly assisting in optimizing source expansion conditions.

In addition, six 2-3/4" ConFlat half-nipples were added, three on each side, each separated by 45° angles as shown in Figures 2-4 through 2-8. Each port has a 1.510" nominal outer tube diameter, with each 2-3/4" ConFlat flange raised 1.0" away from the main tube body. These auxiliary ports serve any number of purposes, primarily as electrical and gas feedthroughs.

The second chamber, a reducing four-way cross shown in Figures 2-10 through 2-12, is a stripped-down version of the asymmetrical reducing six-way cross described above. The horizontal tube along the beam line has, as before, a nominal outer tube diameter of 12.75", with NW-320 ISO flanges on each end. The bottom, vertically-oriented tube has a nominal 12" outer tube diameter with standard ASA-10 flange welded

on the end. An additional port was added to the top of the chamber as a potentially useful feedthrough location, although it has remained unused to date. The port consists of a 5.01" outer tube diameter half nipple with a standard ASA-4 non-rotatable flange. In addition, two 3/4" outer tube size diameter compression ports (quick disconnects in MDC nomenclature) were added, one on each side of the chamber. These compression ports are used to mount both the thermocouple gauge (DST-531, Duniway Stockroom) used for monitoring the pressure when roughing out the chamber (via a Varian 531 Analog Controller, TCG-MTR-531 from Duniway Stockroom), as well as the iridium filament ionization gauge (I-075-N, Duniway Stockroom) used to monitor the basal source chamber pressure with the diffusion pumps engaged. A Granville-Phillips Model 307 Vacuum Gauge Controller was used for all source chamber pressure measurements, as well as to monitor the VHS-10 foreline pressure for both diffusion pumps.

As shown in Figures 2-1 and 2-2, each chamber is mounted on its own pumping stack, consisting of the chamber, a 10" electro-pneumatically actuated aluminum gate valve (VRC LP Series, now owned by the Kurt J. Lesker Company), a 1" thick aluminum baseplate, a 10" diffusion pump liquid nitrogen trap (Varian 316-10 Cryotrap), and a 10" diffusion pump (Varian VHS-10). Each chamber is mounted directly to the gate valves. In turn, each gate valve is bolted to the baseplate via the upper ASA-10 flange of the diffusion pump trap. In essence, the baseplate becomes sandwiched between the trap and gate valve, with the bolts supporting the ASA-10 flange of the diffusion pump trap passing through the baseplate, and screwing directly into the tapped holes in gate valve. Each VHS-10 diffusion pump is then mounted directly to the supported diffusion pump trap.

For future reference, there exists an aluminum gasket between the baseplate and the diffusion pump trap of the source tee. This is an adapter that was required due to the fact that both the baseplate and trap possessed o-ring surfaces that needed to be joined.

A key concern when designing the source chamber was how to maximize access to the interior of the chamber, and in particular the source region. In order to solve this problem, the decision was made to treat the entire source chamber, complete stacks and all, as an exterior shell that could be peeled away from around the source at will, completely exposing the source region. To accomplish this, the stainless steel frame designed to support the apparatus was extended lengthwise by approximately 19" over what was required, and two six foot long, 0.6245/0.6240" diameter high-carbon steel ground rails (Thomson Case 60 Class PD) were mounted on the upper surface of the frame in the lengthwise direction. The rails were supported by a series of twelve (six on each side) 4.000" long low shaft supports (Thomson LSR-PD) spaced periodically along the length of the rails. In turn, on the bottom of each baseplate were mounted four open-style pillow blocks containing 5/8" working bore diameter linear ball bushings (custom order - Thomson Type SPB-10-OPN pillow block with Super Ball Bushing removed and replaced with an Open-type Series OPN 5/8" working bore diameter linear ball bushing). The pillow block were arranged two on each side of the baseplates to prevent any play in the baseplates, ultimately enabling both baseplates to be translated lengthwise along the length of the frame in a frictionless manner. Once the complete stacks were assembled onto each baseplate, the entire source chamber could be moved with ease along the length of the rails. In fact, the motion was so facile that the approximate half-ton of equipment

contained within the two stacks can be translated along the length of the frame with the force from one's index finger. As will become clear in the following section detailing the source mount design, by mounting the entire source chamber on rails, we gain complete unrestricted access to the source region simply by releasing a single NW-320 ISO flange coupling and sliding the source chamber out of the way.

The pneumatic gate valves were interlocked using a home-built circuit that monitored water flow to the 10" diffusion pump (via a Proteus Model 100C110 flow switch), the temperature of the diffusion pump (via a Varian Klixon-300 thermal overload switch), and the diffusion pump foreline pressure (via a Hastings DV-6M thermocouple gauge monitored by a Granville-Phillips 307 Vacuum Gauge Controller). The Granville-Phillips 307 controller outputs a pressure-calibrated DC voltage that was used as the pressure input for the interlock. This pressure is then subsequently compared to a preset DC voltage using a LM613 comparitor chip within the interlock. A failure signal from any of the three monitored components resulted in the gate valve being immediately closed, as well as immediate termination of power to the diffusion pump by tripping a power relay within the interlock box itself.

Both of the diffusion pump traps were cooled by a continuously circulating flow of chilled ethanol using a recirculating chiller (Model 2095, Forma Scientific) rather than using costly liquid nitrogen. Both source chamber diffusion pump traps were cooled in series, with the asymmetric six-way cross placed first in the flow circuit. Copper refrigeration tubing (1/4" diameter) was used for the flow circuit, which was extensively wrapped in refrigeration tape to reduce the heat load. In order to inject the ethanol

directly into the trap, a 1/4" stainless steel Swagelock fitting was welded opposite to one of the ends of a 1" stainless steel Swagelock elbow. The 1" Swagelock end of this elbow opposite the non-standard 1/4" Swagelock fitting was subsequently attached to the 1" diameter cryotrap fluid inlet. This way, the 1/4" copper refrigeration tubing serving as the fluid inlet line could be snaked through the 1/4" Swagelock fitting and directly into the bottom of the trap. Consequently, the cooled fluid was always introduced near the bottom surface of the trap facing the diffusion pump, insuring efficient mixing of newly injected chilled fluid with that already present in the reservoir. Fluid overflow from the continuously filling trap was allowed to flow back out around the inlet tube and back into the fluid circuit. Due to the poor cooling capacity of the recirculating chiller, an additional source of cooling was provided by an immersion chiller (Neslab CC-60) that was equipped with cold finger probe. The chilled finger probe was inserted into the ethanol reservoir of the recirculating chiller, resulting in a bath temperature of approximately -8 °C.

Two types of diffusion pump fluids were used to charge the VHS-10 diffusion pumps during the course of this work. Initially, Krytox 1625 (1*l* per pump) was utilized. Krytox 1625, which is analogous to Fomblin, is composed of chains of polyperfluoroethers whose supposed hallmark is chemical inertness to most reactive or corrosive gases. Since reactive metals such as lithium and aluminum were experimental targets, the chemical inertness of this fluid seemed an ideal choice. Nevertheless, during the course of optimizing the MPI experiments, an enormous oil fragment background was observed with the Krytox 1625 fluid that could not be effectively eliminated by low temperature trapping. Consequently, the pumps were dropped and scrubbed out, and

charged instead with Santovac 5. Santovac 5 proved far superior to the Krytox 1625 fluid with respect to producing a minimal oil fragment background, and is strongly recommended for future use. The apparent chemical instability of the Krytox 1625 is a mystery, but might be the result of degradation catalyzed by aluminum shards that inevitably drop from the laser vaporization source and into the pumps. Nevertheless, the absence of visible aluminum particles in the Krytox 1625 fluid recovered while scrubbing out the pumps tends to indicate the true origin of the degradation might lie elsewhere.

Initially, each VHS-10 was backed by a Leybold-Hereaus S30A single-stage direct drive mechanical pump rated to achieve a pumping speed of 27 cfm. The recommended backing pump speed for optimal performance of the VHS-10 diffusion pump is 30 cfm in the limit that maximal gas loads are to be introduced. During the course of this work, it became apparent that 27 cfm was insufficient since diffusion pump fluid was observed to pool in the foreline after extended periods of use. This problem was especially severe for the diffusion pump dedicated to the six-way cross chamber since this pump lay below the pulsed valve and hence bore a greater proportion of the gas load. Replacement of this Leybold-Hereaus S30A with a Leybold-Hereaus D60A (36.7 cfm) was partially effective in reducing the problem of diffusion pump fluid loss. However, the problem was ultimately solved by changing the source design that allowed the experiment to be run at significantly lower average source chamber pressures - $1x10^{-4}$ torr instead of the problematic $8.0x10^{-4}$ torr as will be outlined in Section 2.2.4.3. The source cross VHS-10 foreline is presently backed by both the Leybold-Hereaus D60A and a Welch 1397B-01 (17.7 cfm) that became necessary to add when the performance of the former deteriorated.

Presently, the base pressure achieved in the source chamber region after outgassing is typically in the high 10^{-8} torr range, $7.5x10^{-8}$ - $9.0x10^{-8}$ torr being a commonly observed benchmark. Note, however, that this base pressure has been attained only with both VHS-10 diffusion pumps pumping simultaneously. If the source is pumped by only a single diffusion pump, the base pressure is typically in the low 10^{-7} torr range.

2.2.2. General Source Design: Mounting and Alignment

As was alluded to in Section 2.2.1, a key design parameter for this apparatus was to have complete facile access to the source region. Most of this requirement was solved by placing the entire source chamber on rails as described in the previous section. The second part of the solution required mounting the source independently from the rest of the source chamber as shown in Figure 2-13. To accomplish this, a custom, multifunctional NW-320 ISO flange was used as a linker between the source region, and the second differential region housed by the REMPI chamber. This flange, colloquially referred to as the skimmer flange, is mounted onto a custom ASA flange on the REMPI chamber (see Figure 2-13 as well as Figures 2-67 through 2-71). The source chamber was mated to the skimmer flange via a NW-320 ISO flange coupling of the source cross, and was held in place by eight ISO double claw clamps. The source region, therefore, was technically an exterior component of the REMPI chamber, having neither attachment to the source chamber (outside of the NW-320 ISO flange coupling) nor the source chamber frame.

The skimmer flange, shown in Figures 2-14 through 2-16, derived from a solid

NW-320 ISO flange that had been modified for two purposes - mounting both the molecular beam skimmer and the piezoelectric pulsed valve/laser vaporization source assembly. The front side of this flange (see Figure 2-14) faced the source cross chamber, and it was from this side of the flange the source assembly had been mounted. The back side of the skimmer flange facing the REMPI chamber (see Figure 2-15) exhibited two principal features. The first was a series of six 3/8-16 UNC tapped holes on a 8.000" diameter bolt circle that served to mount the skimmer flange to the custom ASA flange of the REMPI chamber. The other main feature was a 6.000" diameter precision-keyed counterbore that served to mount the first component of the skimmer mount assembly (see Figures 2-17 and 2-18). An o-ring groove was also present to create a vacuum-tight seal between the REMPI chamber and the skimmer flange.

For the skimmer, we sought a means by which the skimmer could be installed and replaced without having to handle the skimmer itself. The solution was to build a three component clamp assembly shown in Figure 2-17. The three components, the skimmer mount, the skimmer base, and the skimmer clamp, are shown in Figure 2-17, Figure 2-18 and Figure 2-19 respectively. The key components are the skimmer base and the skimmer clamp. The skimmer base has a 1.100" diameter precision-keyed counterbore (0.010" deep) at the center of the piece that precisely matches the outer base diameter of all Beam Dynamics Model 2 skimmers. Therefore, the skimmer could be reproducibly mounted each time without the need to perform any realignment of the molecular beam. The skimmer is secured to the base by the clamp. This clamp keys directly into a groove in the base, and is secured to the base by six 4-40 UNC hex socket flat countersunk cap screws

that are flush with the molecular beam side of the skimmer assembly. The clamp also possesses a precision-keyed lip (0.015" deep) whose outer diameter exactly matches the outer base diameter of the Model 2 skimmer (ϕ1.100") and whose inner diameter (ϕ1.000") exactly matched the inner diameter of the Model 2 skimmer. This lip insures that a direct metal-to-metal contact is made between the base, skimmer, and clamp, allowing no play with respect to skimmer motion once the clamp is screwed gently into place. Hence, with the skimmer secured in the base-clamp assembly, the skimmer can be handled with ease, making installation and removal of the delicate Model 2 skimmer extremely facile.

Upon examination of Figure 2-17, the skimmer mount keyed to the back side of the skimmer flange may appear to be superfluous since the skimmer base-clamp assembly could have been keyed directly to the front side of the skimmer flange. Nevertheless, the assembly was designed in this manner for two reasons. The first was that a design was sought by which the skimmer could be mounted as close to the REMPI chamber as possible, permitting the minimal skimmer to MPI distance to be attained. The second reason for this design was that it permitted other types of experimental configurations to be installed without the need to totally redesign the skimmer mount. For example, in the event that ionic species were experimental targets, a very short skimmer to source distance would be desirable - one perhaps even less than that presently available. This mounting mechanism would permit the present skimmer mount to be removed, and another piece, perhaps a tube extension into the source cross, could be installed that also directly mounts the skimmer base-clamp assembly. Such versatility was a major impetus for this

apparently extraneous design feature. Hence, in the present configuration, the skimmer mount served as a flexible precision-keyed adapter between the skimmer flange and skimmer base-clamp assembly - one that likewise maintained the molecular beam alignment in the event disassembly was required.

The other functional purpose for the skimmer flange was to serve as a support mount for the source components. Figure 2-13a shows the principal components of the source mount as they would appear with the source chamber rolled back. Rather than attempting to present all the details of the present source configuration in a single figure, Figure 2-13a has been significantly simplified to include only the key elements upon which all other experimental components were later added.

The guiding design principle for the source mount was the desire for a mechanism whereby complete variability in the source to skimmer distance could be attained while at the same time precisely maintaining the molecular beam alignment. The optimum solution was determined to be the implementation of a precision rail/precision bearing design. One of the two essential aspects of the source mount construction was the requirement for a rigid frame consisting of precision ground rails that would exhibit two key characteristics. The first was that the frame rails must be mounted perfectly perpendicular to the skimmer flange if proper alignment of the source and skimmer were to be attained. The second criterion was that the rails must not exhibit any downward deflection due to gravity over the length of the frame shafts. Such deflections would cause the source-skimmer alignment to vary over the length of the shaft, forcing realignment of the molecular beam each time the source was moved.

The three components of the source rail assembly are shown in Figures 2-21 through 2-26. The first two parts were a set of three 304 stainless steel collars (see Figure 2-21) and three source rails consisting of 1" diameter Case 60 stainless steel precision ground shafts (Thomson Class L). The collars served as a coupling between the skimmer flange and the source rails. Each collar was slip-fitted over one end of the source rails, and was secured to the shaft by means of a completely countersunk 3/8-16 UNC socket head cap screw. Each of these three collar/shaft assemblies was then mounted to the skimmer flange by means of three 1/4-20 UNC socket head cap screws per collar. As is evident from Figure 2-14, the three collars were mounted on the skimmer flange in an equally spaced manner such the shaft centers lay precisely on a 9.000" diameter. When the skimmer flange was mounted on the REMPI chamber, the rails were arranged such that a single shaft lay precisely at the 6 o'clock position, while the other two shafts lay at the 2 o'clock and 10 o'clock positions respectively. The source rails (19.50" long) were extremely robust, with specifications indicating that deflection of the shaft fixed at one end and under a uniform gravitational load would be at most a few thousands of an inch - much less than the accuracy with which the source could be aligned.

To insure the rigidity of the frame as well as to eliminate the possibility of vibration within the shaft frame, a rigid support was designed for the free hanging end of the source rails. The components of the rigid back mount for the source rails is shown in Figures 2-23 through 2-26. The basic design is shown in Figure 2-23, which shows the back mount looking from the perspective from the back of the source cross towards the skimmer flange. Each of the source rails was capped by an aluminum collar that slip-fit

without play around the shaft. Two 0.063" deep flats separated by 120° have been machined off two of the radial surfaces of each collar. Each of these flats has had three 1/4-20 UNC tapped holes machined along the length of the shaft, that align with the slots of the support pieces (see Figure 2-26) that couple the collars together to form a rigid frame shown in Figure 2-23. Each collar also has had three 10-24 UNC tapped holes placed on the back surface that serves to mount a 1.900" diameter by 0.15" thick aluminum disk (see Figure 2-25) that served as a cap for each collar. Each of these caps possessed a central 0.404" diameter through-hole that permitted the cap-collar assembly to be screwed directly onto the source rails via a 3/8-16 UNC socket head cap screw. Each of the connecting joints was designed with some play to insure that the pieces could be easily joined with minimal tolerances, while insuring a sturdy, rigid structure once all screws were tightened down.

The source mount, therefore, provided a rigid assembly of three straight rails that were perfectly orthogonal (within a 0.001" tolerance) to the skimmer flange. The second key aspect of the source design was the construction of a specialized "cart" that would mount the piezoelectric pulsed valve/laser vaporization source assembly precisely to the rails with no play between the two. The principal component of the translating cart is a Y-shaped half-inch thick aluminum piece as shown in Figure 2-27. This piece will be referred to as the "Y-plate." The shape of this piece was due to the requirement that it serve two principal functions - that of mounting the ball bushings that couple to the Y-plate to the source rails as well as the piezoelectric pulsed valve, while maximizing gas conductance to the source tee. In effect, the Y-plate was a potential baffle for the

majority of the post-expansion gas pulse that had struck the skimmer plate and had reflected backwards. The shape is essentially a reflection of the fact that all extraneous material that might hinder the conductance has been removed.

The Y-plate was mounted to the source rails by three custom pillow blocks containing 1" shaft diameter linear bushings. These pillow blocks were chimeras of two Thomson products, namely a 1" shaft diameter Super Ball Bushing pillow block (Thomson SFB-16) and an Extra-Precision Series XA 1" shaft diameter linear ball bushing (Thomson XA-162536). The pillow block for mounting the bushing is only sold containing a self-aligning Super Ball Bushing that is designed to allow 0.5° of angular play. Consequently, a special order was made to purchase three pillow blocks that had the Super Ball Bushings removed and replaced with the Extra-Precision Series XA bushings. When installed on the Y-plate, one on each of the three "arms," these bushings permitted perfectly smooth translation of the Y-plate along the length of the rails with the Y-plate maintained perfectly orthogonal to the source rails with no detectable play. Note that the orientation of the pillow blocks relative to the Y-plate is arbitrary; they are presently oriented away from the skimmer flange.

The Y-plate was designed with a 3.375" diameter center hole that permitted clearance of the pulsed valve mount (see Part #10 of the pulsed valve shown in Appendix 2). The pulsed valve mount was designed such that its mounting flange would be bolted to the back side of the Y-plate (away from the skimmer flange) via four 10-24 UNC tapped holes that surround the central hole on a 4.14" diameter bolt circle. The central hole was oversized to permit play in the position of the source mount, enabling

precise source to skimmer alignment to be attained.

The Y-plate was also originally designed with four pairs of through holes that were separated by 1.250", each pair being offset from each of the center lines by 2.157". These holes were designed to attach blocks shown in Figure 2-28 that were to serve as x-y translators for the pulsed valve mount. These have proved largely unnecessary, and have been removed from the Y-plate in the present source configuration. They were only really needed to support the position of the pulsed valve mount during alignment, and even then they were largely disposable.

During the course of the experiments described in this thesis, two additional tapped holes were added to the Y-plate as shown in Figure 2-29. The purpose of this modification was to permit the mounting of two slotted right angle brackets (see Figure 2-30). These angle brackets were mounted such that the outer surface along the longer dimension was flush with the Y-plate horizontal flat directly above the two tapped holes. As will be described in detail below in Section 2.2.5, these brackets served the purpose of permitting a breadboard table to be mounted directly to the upper horizontal surface of the Y-plate.

2.2.3. The Pulsed Valve Design

Several types of pulsed valves have been developed over the years as a means to generate pulsed molecular beams.[5] Guiding all of these designs has been the desire to achieve very cold supersonic expansion conditions that will either cool a molecule of interest to exceeding low rotational and vibrational temperatures, or permit clustering of

some species within the jet. The ideal pulsed valve would possess two main properties essential for the generation of ultracold supersonic expansions - the ability to open at very high backing pressures and the capacity to exhibit full, unchoked flow over the shortest possible opening times. These criteria permit the maximal amount of gas to be introduced over the minimal time, a performance standard essentially all pulsed valves strive to achieve.

Each valve that has been developed to date possesses its own unique set of advantages and disadvantages that one must weigh when choosing a particular valve for a pulsed beam experiment. Perhaps the best pulsed valve in terms of satisfying the above criteria is the magnetic current loop design developed by Gentry and Giese.[6] In this design, very high opposing electric currents are pulsed between a faceplate containing the pulsed valve orifice and a 1.7 mm thick steel bar with an I-beam-shaped cross section. The two opposing currents actuate the opening of the valve by generating a very strong repulsive force between the faceplate and the steel bar, causing the bar to flex. This, in turn, transiently permits gas to flow through the valve orifice. The performance of this valve is unsurpassed to date, generating gas pulses as short as 7 μs FWHM. The disadvantage with this valve, however, is the requirement that several amperes of current must be supplied in order for proper actuation to occur. This places severe demands on the power sources used to drive the valve. This in turn limits the repetition rate at which this valve can be run, achieving optimal performance only within the 10 - 20 Hz range. The other principal drawback of this valve is that it runs very hot due to the high power dissipation within the valve. This required that the valve be externally cooled through

some heat exchanging mechanism.

A second type of pulsed valve which is widely used is based on a solenoid mechanism.[5] The solenoid valve is essentially the same technology as the fuel injectors used in automobile engines. To actuate this valve, a current is run through the solenoid, which exerts a magnetic force on the valve plunger containing a ferromagnetic core material. These valves are popular because they can be bought off the shelf from General Valve, but they have the reputation of being notoriously unreliable, requiring maintenance on the order of every few days during periods of extensive use.

The last general style of pulsed valve design is based on the use of the piezoelectric effect as a means to actuate a valve.[5,7] Piezoelectric materials possess the unique property of altering their dimensions with the application of a potential difference across the crystal. While many varieties of piezoelectric valve have been designed over the years, they all function in a similar manner. Typically, a disk of some piezoelectric material is employed with the pulsed valve plunger mounted at the center. With the application of voltage pulses, generally 500 - 1000 V, the piezoelectric disk alters its dimensions, forcing it to flex backwards. This pulls back the plunger from the sealing surface, permitting gas to flow transiently during the duration of the applied voltage pulse.

Since piezoelectric elements are essentially capacitors that require only minimal amounts of current to achieve the desired potential difference across the ceramic, they have the advantage of requiring very little power, placing minimal demands on the electronics needed to drive the valve. Consequently, these valves can be run at very high repetition rates (often in the kHz range) without significant heating. Furthermore, their

performance is at least equal to and, in general, surpasses that of the solenoid valve, especially with respect to reliability. Gas pulses as short as 100 μs FWHM have been reported with a piezoelectric actuator, but such short opening times are believed to involve partially choked flow.[7] A reasonable performance estimate for a piezoelectric valve is the capability of producing full flow, unchoked gas pulses somewhere in the range of 150 - 200 μs FWHM in duration.[7]

When originally designing the experiment, the initial desire was to use a commercially available valve based on the current loop design sold from the R. M. Jordan Company. However, the disadvantages of this valve - the need to design or purchase specialty electronic pulsers, the need to cool the valve, and the lack of flexibility with respect to mounting additional source elements such as a laser vaporization source - were ultimately deemed to outweigh the great advantage of this valve, namely performance. The pulsed valve chosen for these experiments was one based on the piezoelectric design.[7] Such a valve had been successfully employed within the lab previously.[8-9] Therefore, a great deal of practical knowledge as well was electronic resources were readily available within the lab already.

2.2.3.1. The Original Piezoelectric Pulsed Valve Design

The piezoelectric pulsed valve used for all the experiments described in this thesis derived from the original design by Trickl and Proch.[7] This valve used a circular piezoelectric bimorph disk (Physik Instrumente, University Model P-286.23) as the actuator. These disks were convenient to use because they come pre-mounted on a

0.020" thick stainless steel backing within their own stainless steel frame. These pre-packaged piezo elements also possess a convenient central hole of 0.394" diameter. This central hole is a useful feature that enabled easy mounting of retractable plunger element to be affixed to the piezo in a mechanically sturdy and reliable manner.

As shown in Figure 2-31, the pulsed valve that was constructed for these experiments was an exact replica of the Trickl and Proch design except for the faceplate. For the benefit of future users of this valve, the complete set of machine drawings for the valve as well as several useful accessory parts are reproduced in Appendix 2. For clarity, please note that the numbers in Figure 2-31 correspond to the part number for each individual part drawing compiled in Appendix 2. The faceplate piece was modified from the original design for two purposes - to readily mount an adaptor piece (see Figure 2-32) that would serve to couple the valve to the laser vaporization source (see Figure 2-33) and to permit the faceplate to be bolted directly to the pulsed valve housing (Part #10 in Figure 2-31 and Appendix 2). The drawings depicting three different views for the modified faceplate are reproduced in Appendix 2 as Part #2.

The basic mechanism of operation for this valve was simple, making it facile to use. The sealing element was a poppet (Part #7 in Figure 2-31) that was machined to a) mount a 0.042" I.D. x 0.050" thick viton o-ring (Parker #2-2002) on one end, b) possess a slot on the other end to accommodate a standard screwdriver, and c) to exhibit a 8-36 UNF threaded outer diameter along most of its length. The o-ring made a tight seal around the 1 mm (0.039") diameter valve oriface (Part #5 in Figure 2-31 or adaptor shown in Figure 2-32). The poppet was then secured to the piezoelectric element

by two pieces. The first was an aluminum adaptor (Part #5 in Figure 2-31) that was drilled and tapped through centrally for a 8-36 UNF thread. This thread mated directly to the poppet, enabling the o-ring tension between the poppet and the oriface sealing surface to be easily adjusted. The other features of the adaptor were a precision key that enabled the adaptor to mount the piezoelectric element central hole without play, as well as an exterior 5/16-40 thread that mated to an electrically insulating nut (Part #6 in Figure 2-31). This nut locked the poppet/adaptor securely to the piezoelectric disk while ensuring that no arcing would occur between it and the piezoelectric element. Another nut (Part #8 in Figure 2-31) was used to lock the poppet in place once the proper sealing tension was achieved.

The piezoelectric element itself was secured to the valve faceplate by four 3-48 UNC threaded posts (Part #4 in Figure 2-31). In the original Trickl and Proch design, these posts were welded directly into the valve body. This had the disadvantage that if one of the posts was stripped, fixing it meant machining out the post and re-welding a replacement. These removable posts circumvented the danger of stripping the threads since any of the posts can be replaced with ease. A word of caution is required, however, when adjusting the piezoelectric disk tension by tightening down on the 3-48 UNC locknuts. Since the posts are not permanently fastened to the valve faceplate, they can become very slightly undone if during the course of adjusting the locknuts one of them is turned counterclockwise. This will cause the piezoelectric disk to seat at a slight angle that may make it difficult to achieve a proper seal. If a proper seal is found to be difficult to attain, it is highly recommended to remove the piezoelectric disk and check whether any

of the posts has loosened

The piezoelectric element was seated on top of a stainless steel disk (Part #9 in Figure 2-31) that has an o-ring groove and o-ring (Parker #2-029) added to the surface facing the piezoelectric element. This o-ring was originally added as a means to assist in dampening any mechanical vibrations arising from the operational poppet driver assembly. Experience has shown that the valve functions well with the piezoelectric element clamped rather tightly but not quite completely against the steel seating disk and o-ring.

The valve body was designed in such a manner that adjustments to the valve poppet could be made without having to disrupt the source and the other experimental elements that were mounted on the faceplate. The main body of the pulsed valve consists of two parts - the faceplate (Part #2 in Figure 2-31) and the back housing (Part #1 in Figure 2-31). As was discussed above, the faceplate bolts directly into the pulsed valve housing (Part #10 in Figure 2-31) which in turn bolts directly to the Y-plate of the source mount. The back housing, however, bolts directly to the faceplate via eight 5-40 UNC tapped holes placed on a 2.450" bolt circle on the back of the faceplate. Removal of the back housing can therefore be achieved without having to remove the faceplate from the pulsed valve housing. Furthermore, since the entire piezoelectric actuator is mounted to the faceplate, complete access to the poppet was possible in the event the o-ring tension needed adjustment.

The performance of the newly constructed valve was consistent with the specifications reported by Trickl and Proch.[7] The piezoelectric disk was driven by a homebuilt high voltage pulser whose design has been previously outlined. The pulser was

capable of generating pulses typically between 200 μs and 325 μs at 350 - 800 V. Diatomic species described in this thesis could be readily formed at virtually any pulsewidth, but generation of large clusters such as those presented in Chapter 5 required rather long pulsewidths (typically 325 μs) to create a stable source. The pulsewidth of the gas pulses themselves have never been directly measured using fast ionization gauge. Nevertheless, during the early stages of the experiment when laser induced fluorescence (LIF) detection was being employed, the time delay between the pulsed valve opening and the LIF probe provided a means to indirectly measure the gas pulsewidth.[1] Such measurements provided an upper bound of a 270 μs gas pulsewidth for a minimal valve opening time, which in turn yielded an approximate 200 μs FWHM time.[1] Such performance was directly comparable to that reported by Trickl and Proch.[7] The valve also functioned over a complete range of backing pressures up to 10 atmospheres without any adjustments required in the valve poppet o-ring sealing tension, greatly facilitating source optimization.

One major disadvantage of this valve that was discovered over the course the experiments is that it was completely incompatible with helium as a carrier gas, and moderately incompatible with neon. With helium, the voltage required to maintain a constant source pressure needed to be constantly raised until ultimately the valve ceased to open. This problem was especially pronounced when high backing pressures of helium carrier gas were utilized. Under such circumstances, the piezoelectric element did not last more than about an hour before breakdown. Neon carrier gas exhibits much of the same behavior, but over the period of days rather than hours. Furthermore, the piezoelectric

disk could often be salvaged after short periods of running in neon, although requiring greater opening voltages than usually needed to be applied. According to Physik Instrumente, the manufacturer of the Model P-286.23 piezoelectric disk, helium can penetrate into the ceramic, leading to discharges within the crystal that ultimately result in mechanical failure. The inability to use helium during the course of the experiments was a major disadvantage, especially in situations where its use in varying source conditions would have been useful. A solution to this problem will be discussed in Section 2.2.3.2 where an alternate pulsed valve design has been developed, employing a new type of piezoelectric ceramic that is compatible for use with both helium and neon carrier gases.

2.2.3.2. Modified Design

One disadvantageous aspect of the early laser vaporization sources described below in Section 2.2.4 was the fact very high source chamber pressures needed to be employed in order to generate a larger $Al \bullet Ar_n$ clusters ($n > 40$). This placed exceeding high demands on the source cross diffusion pump, forcing the pump to transiently run near a regime very close or within the stalling pressure during the peak of each gas pulse. Evidence for this came from the pooling of diffusion pump fluid predominantly in the cross foreline during the large $Al \bullet Ar_n$ cluster work described in Chapter 5. The source of this problem was believed to arise from the fact that the pulsed supersonic expansion from the laser vaporization source was rather inefficient in cooling the species within the jet. Part of this was attributed to the laser vaporization source itself, and the details related to how the source itself was modified is detailed in Section 2.2.4.3.

The other cause of the problem was deemed to arise from poor functioning of the pulsed valve itself. Specifically, two features were identified as potentially problematic. The first of these was the length of the gas channel between the valve and the laser vaporization source due to the need for the adapter piece between these two elements (see Figures 2-32 and 2-33). By adding an additional 0.395" in length to the gas channel, the adapter was believed to be possibly responsible choked flow within the source, potentially leading to turbulence and ultimately limiting the efficiency of the expansion. The other potential problem that was identified was due to the o-ring seal on the poppet used to seal the valve. Work out of Vladimir Bondybey's group had found previously that the rising edge of the gas pulse can have a significant influence on the degree of clustering that can be observed with laser vaporization sources.[10] In general, a correlation between fast gas pulse rising edges and greater clustering was observed.[10] O-ring seals were found to be non-ideal since there is an intrinsic time delay between when the poppet retracts and when the gas can flow. In fact, due to its elastic nature, the o-ring can permit small leakage to occur before the o-ring can be completely pulled back from the sealing face, effectively lengthening the gas pulse.

In light of these potential problems, two principal modifications were made to the piezoelectric pulsed valve. The first was to the piezoelectric pulsed valve poppet. Instead of using an o-ring seal, a different seal that used a hard plastic poppet tip sealing against a polished metal surface was employed in the same manner as had been successfully implemented by Bondybey's group.[10-11] By changing to this new seal, there was the reasonable expectation that all gas flow would occur almost instantaneously when the

poppet was retracted, yielding gas pulses with rise times comparable to the response time of the piezoelectric disk itself.

To execute this new design, the original poppet (Part #7 in Figure 2-31) was replaced with a new poppet (see Part #7 in Figure 2-34 as well as Figure 2-37 for drawing). This new poppet was longer than the original poppet, and was designed with a 0.040" diameter by 0.100" deep central channel instead of the o-ring adapter of the old poppet. This channel was designed to accommodate a hard plastic tip shown in Figure 2-38. Two materials, Vespel-SP1 and Kel-F, were originally chosen as good candidates for the tip. Vespel-SP1 is a remarkable high-performance polyimide that was originally developed to withstand the heat of jet engines. Among its properties are high strength and low wear, as well as operating temperatures between -400° to +500° F. In addition, Vespel-SP1 machines very well, more like brass rather than typical softer plastics. Kel-F was chosen as an alternate candidate since it had been shown previously to function well as a poppet tip in a cryogenic pulsed valve developed by Continetti.[12]

To date, only the Vespel-SP1 poppet tip has been installed, but its performance has far exceeded any expectations. Once properly seated, the Vespel-SP1 poppet tip has not had to be replaced even after almost ten months of regular use. Furthermore, not a single adjustment has had to be made to the poppet to adjust for any leaks. This suggest that Vespel-SP1 will not deform even after extensive use. Another advantage to using Vespel-SP1 was determined during the process of getting the valve to seal. As was alluded to earlier, the key to getting this valve to run properly is to attain a perfect seal between the plastic tip and the polished stainless steel face. Since polishing after cutting

the plastic tip sealing face was not an option since it distorted the sealing face, a perfect smooth and flat cut had to be achieved initially. The ease with which Vespel-SP1 can be machined enabled perfectly flat and smooth surfaces to be generated directly on the lathe whereas Kel-F, due to its softer nature, had a tendency to "pull" slightly when the cutting tool was applied. This resulted in tiny radial grooves in the Kel-F tip that were not present in the Vespel-SP1 tip. For these reasons, Vespel-SP1 is *very highly recommended* for use in pulsed valve applications in the future.

As a backup poppet in the event that the Vespel-SP1-tipped poppet was unable to be implemented, a second poppet (see Part #7 in Figure 2-35 as well as Figure 2-36 for machine drawing) was also made that possesses an o-ring (Parker #2-2002) as the sealing mechanism. Due to the success with the other plastic-tipped poppet style, however, the o-ring poppet has not been installed. Nevertheless, for situations where fast gas pulse rise times are not important, this poppet will undoubtedly function quite well.

Both poppets were extended to permit the orifice sealing surface to be placed directly behind the laser vaporization source as shown in Figures 2-34 and 2-35. To minimize excess weight on the poppet as a result of this extension, both poppet types were significantly hollowed out to remove as much excess material as possible without compromising the mechanical stability of the part.

The second major modification to the pulsed valve was to change the adapter piece between the faceplate of the piezoelectric valve and laser vaporization source in order to eliminate as much of the gas channel as possible. The new adapter piece is shown in Figure 2-39, as well as in Figures 2-34 and 2-35 where it is shown sealing against the two

new poppet designs. In the event that the Vespel-SP1-tipped poppet is to be used (see Figure 2-34), it becomes imperative that the stainless steel surface to which the Vespel-SP1 tip seats be as flat and as polished as possible. Equally important is the requirement that the edge of the oriface channel be maintained at 90°, i.e., extreme care should be taken not to round these edges while polishing the sealing face. Due to the small diameter of the Vespel-SP1 poppet tip sealing face, rounding the edges of the oriface dramatically reduces the surface area upon which the poppet can contact the steel face, rendering a fully leak-tight seal dificult to attain.

As is evident from comparing Figure 2-39 with Figure 2-32, two principal changes were made with the new adapter design. The first was to machine away what used to be an extended gas channel to place the poppet sealing surface very close (within 0.055") to the laser vaporization source that mounted to the front face. This effectively reduced by almost half the distance the gas would have to travel before reaching the terminal expansion point at the end of the laser vaporzation source. The other change was to machine a constriction into the piece such that a 0.380" outer tube diameter (0.040" thick) tube joined the flange mating to the pulsed valve faceplate on one end and the laser vaporization source on the other. The purpose of this constriction was to minimize thermal conductance between the two components mounted to each end in the event that the laser vaporization source was cooled. Since the piezoelectric element only functions well at temperatures above 0 °C, heat conduction must be minimized in order to maintain proper valve function.

These modifications were a dramatic improvement over the original pulsed valve

design. With these changes as well as the implementation of the third generation laser vaporization source described in Section 2.2.4.3, identical large $Al \bullet Ar_n$ cluster distributions were obtained to those before, but at a substantially lower operational source chamber pressure - $1x10^{-4}$ rather than $8.0x10^{-4}$ torr. Consequently, the problem related to running the diffusion pumps regularly at or near their stalling regime, namely the pooling of diffusion pump fluid in the source cross foreline, was eliminated.

2.2.3.3. Modified Design for Use with Helium Carrier Gas - Christian Berg Piezoelectric Valve Design

As was alluded to earlier in Section 2.2.3.1., a major drawback of the original pulsed valve design was the unwelcome discovery that the Physik Instrumente Model P-286.23 piezoelectric disk that served as the basis for the valve was incompatible with use of helium and, to a certain degree, neon carrier gases. Fortunately, Thomas Schindler, a recent graduate from Vladimir Bondybey's group at the Techniche Universität München, brought to our attention a different type of piezoelectric valve that had been developed by his graduate co-worker, Christian Berg. This valve, based on the P-910.759 piezoelectric disk translator (Physik Instrumente) was compatible for use with helium. Fortunately, Christian Berg was willing to share his valve schematics, and it became evident that the valve constructed for these experiments could be retrofit to utilize this new design.[11] The parts that were designed as part of this retrofit are essentially identical to those originally designed by Berg. Some minor modifications, especially with respect to the mounting mechanism, were required from the original design, but nevertheless follow closely the

parts derived from the original Berg valve.

A key consideration for this retrofit was to enable both styles of piezoelectric valve, namely that from Trickl's design and Berg's design, to be readily interconverted. Ultimately, the only piece that needed to be replaced from the original Trickl design was the stainless steel seating disk for the P-286.23 piezoelectric disk (see Part #9 in Figure 2-31). The rest of the Trickl valve was able to be used unmodified.

The retrofit entailed replacing the original P-286.23 piezoelectric disk with the P-910.759 piezoelectric driver element. However, unlike the P-286.23 piezoelectric disk that comes both pre-mounted on a stainless steel backing as well as with the high voltage lead affixed to the ceramic, the P-910.759 piezoelectric disk translator can only be purchased as the ceramic itself. Therefore, to use this new ceramic, one must provide both a backing and a means to apply the high voltage to the ceramic. Most of the parts that needed to be machined were dedicated to serving both of these functions.

The new components that were fabricated to implement the Berg design are shown in Figure 2-40 and 2-41 as they would appear with use of the new Vespel-SP1-tipped poppet and o-ring poppet respectively. A complete set of machine drawings for the parts that compose the Berg piezoelectric valve design have been included in Appendix 3.

To mount the piezoelectric disk, a backing similar to that provided by Physik Instrumente for the P-286.23 was utilized. This backing (see Part #4 in Figures 2-40 and 2-41) was composed of a 0.020 thick metallic disk whose outer diameter (ϕ1.500") exactly matched the outer diameter of the P-910.759 piezoelectric element itself (see Part #3 in Figures 2-40 and 2-41). In order to insure a very stiff response time, and hence a

more impulsive opening, titanium was employed by Berg in his original design. Since a flat titanium disk was found to be too stiff, a series of radial "bumps" were machined into the surface of the titanium disk opposite to the surface at which the piezoelectric disk was affixed. These grooves serve to lower the mechanical resistance of the disk towards flexure. Stainless steel backing disks can also be employed in direct analogy to the original P-286.23 disk translator. This backing must be electrically grounded to the valve body in some manner. For the titanium disk, spot-welding a steel lead to the backing disk combined with additional reinforcement provided by the application of an electrically-conducting epoxy was employed. The stainless steel backing can be grounded by soldering an electrical lead to the back side with the aid of acid flux. This flux must be washed off thoroughly after use to prevent corrosion.

To provide the negative high-voltage required to actuate the piezoelectric translator, the P-910.759 piezoelectric element rests on a steel HV-contact ring (see Part #2 in Figures 2-40 and 2-41). The contact surface of this ring is curved such that the piezoelectric element surface has only a point contact around the circumference of the ring. Into the bottom of the ring, slots or holes can be machined to provide a location into which the high voltage lead can be soldered into place. In the present part, a slot was machined into the bottom surface that permitted a copper stranded electrical lead to be soldered in place such that the solder and lead lay below the ring surface. Note that acid flux must also be used here to make this electrical connection, and this flux must be cleaned thoroughly once soldering is complete.

The HV-contact ring is seated in a Teflon mount (see Part #1 in Figures 2-40 and

2-41) that replaced Part #9 of the original Trickl and Proch design (see Figure 2-31). This mount is designed to be multifunctional. First, this mount seats the HV-contact ring, providing an electrically insulating housing for this element. Due to the soft nature of Teflon, the mount also serves to dampen the mechanical vibrations induced when the piezoelectric driver assembly is actuated. Consequently, the o-ring present in Part #9 of the original Trickl and Proch design has been eliminated. Furthermore, this piece assumed the function of adapting the piezoelectric driver assembly to the original pulsed valve faceplate by mounting directly to the 3-48 UNC posts of the original valve. A final feature that has been designed into the mount was both a slot within the mount seating surface with the HV-contact ring, as well as a small groove placed on the outer diameter of the piece. The slot permitted access for the HV-contact ring electrical lead. Hence the slot in which this lead was mounted should be placed directly adjacent to this slot to ensure that the HV-contact ring seats flush with the mount. The groove in the outer diameter served as a useful access channel for the electrical lead between the HV feedthrough at the back of the valve and the HV-contact ring.

The last two principal components of the retrofit were related to the mechanism by which the piezoelectric disk was fastened against the HV-contact ring seated in the Teflon mount. The first of these components was a Teflon gasket (see Part #5 in Figures 2-40 and 2-41). The outer diameter of this gasket keyed to the inner counterbore of the Teflon mount accommodating the piezoelectric element. The second component was a stainless steel clamp disk (see Part #6 in Figures 2-40 and 2-41). This clamp disk mounted directly to the 3-48 UNC posts of the original pulsed valve faceplate, serving to clamp the

piezoelectric translator in place between the HV-contact ring and the Teflon gasket when the 3-48 UNC nuts that secure the assembly to the faceplate were tightened. A groove was machined on the outer diameter of the stainless steel clamp disk similar to that used in the Teflon mount to permit an electrical lead to be readily introduced to the HV-contact ring.

The other components of the Berg retrofit are identical to those designed to modify the original pulsed valve design as was discussed above in Section 2.2.3.2. These include the Vespel-SP1-tipped poppet (Part #7b and Part 7c in Figure 2-40) as well as an o-ring poppet (Part #7a in Figure 2-41). The final component is the steel adapter (Part #8 in Figures 2-40 and 2-41) coupling the pulsed valve and the laser vaporization source. As is evident by comparing Figures 2-40 and 2-41 with Figures 2-34 and 2-35, both the Berg design and the original Trickl and Proch design are completely interchangeable, enabling one to convert from one style to the other within minutes.

The main obstacle to completely implementing the new Berg design has been the inability to procure a proper epoxy adhesive with which to secure the P-910.759 piezoelectric disk to the metal backing. The problem derived from the necessity that the epoxy be electrically conducting such that a proper ground contact can be made between the piezoelectric and the backing. Berg, in his original design, was able to locate a proper epoxy (Silber-Leitkleber Epoxy 3021B Electrolit 489) from a German company called Bürklin located in Munich.[10-11] This epoxy is impregnated with tiny silver particles that render the epoxy electrically conducting. Unfortunately, Bürklin will not ship the epoxy to the United States. While a postdoctoral fellow within the group, Thomas Schindler was

able to locate a potential replacement electrically conducting epoxy, KL-325K, sold by the Kurt J. Lesker Company. This epoxy was tried, but it proved unsuitable for use with the P-910.759 piezoelectric element. The KL-325K epoxy had the unfortunate property that it dried much like a porous ceramic rather than dense polymer matrix. During use with this epoxy, blue sparks were observed to emanate from the high voltage face of the piezoelectric, indicative of poor electrical contact between the piezoelectric disk and the backing. Electrical breakdown within the porous matrix was believed to be the origin of these sparks that ultimately degraded the piezoelectric performance.

For a long time a proper electrically conducting epoxy has been sought. Recently, Martin Beyer, another graduate student from Bondybey's group, has brought to our attention another supplier of electrically conducting epoxy - Epoxy Technology, Inc., 14 Fortune Drive, Billerica, MA 01821 (1-800-227-2201).[13] If a suitable epoxy is found, this new design based on Berg's pulsed valve should be readily implemented, ultimately solving the present helium incompatibility problem with the present pulsed valve.

2.2.4. Laser Vaporization Source Design

Since its first implementation by Smalley and co-workers in the early 1980's, laser vaporization has evolved into one of the most widely utilized techniques to generate molecules and clusters containing refractory elemental materials.[14-18] One reason behind the popularity of laser ablation/pulsed beam expansion techniques derives from its simplicity. In a standard laser vaporization experimental configuration, a laser is tightly focused onto the surface of a target rod or disk containing the elemental material of

interest. The target is generally placed within the source such that the ablation point lies within or directly adjacent to the gas channel through which the expansion gas will pass. At or near the time at which the gas pulse will traverse the target region, a focused laser pulse is fired onto the target surface, ablating a small region of the surface to generate a plasma containing the refractory element of interest. These plasmas can be rather hot, exhibiting measured temperatures within the 5000 - 10,000 K range.[19] Following ablation, the plasma becomes entrained within the gas pulse within the gas channel, where it begins to cool due to collisions with the buffer gas. The majority of the cooling occurs during the supersonic expansion, which can take place immediately at the ablation region, or far downstream of extended collisional regions or "waiting rooms."[20] Expansions immediately following laser ablation have tended to function well as a means to generate mixed solvent-atom clusters with small numbers of the refractory atoms. Waiting rooms, however, tend to be more useful when large atomic clusters are sought since the turbulent mixing within these regions greatly enhances the probability of three-body collisions before the gas pulse even reaches the expansion point.[20]

Unfortunately, much of the fundamental physics behind laser ablation is utterly unknown at this point in time. Therefore, the creation of an effective laser vaporization source is often one part empirical knowledge, one part black magic. Guided only by precedent, one is often left to his or her own devices (or prejudices) to judge the best means to cool the ablated plasma and generate the species of interest.

Like most who have employed this technique over the years, a great deal of empirical evidence has been gathered during the course of this thesis work regarding both

favorable and unfavorable laser vaporization conditions. The laser vaporization sources utilized to generate aluminum-rare gas clusters ($Al•(RG)_n$) have gone through several stages of iteration that will be presented in the following three sections.

2.2.4.1. First Generation Laser Vaporization Source

During the initial stages of the laser vaporization source design, a great deal of effort was placed into trying to minimize the formation of multimeric clusters of aluminum atoms. Instead, what was sought was a means to cluster a given solvent around predominantly monomeric aluminum atoms. The initial laser vaporization source that was fabricated was derived from a source design from Costes' group that employed laser ablation of aluminum target rods.[21] This design was initially attractive because of the report that mostly monomeric aluminum was generated by the source, with only minor amount of aluminum dimer detected. Intriguingly, essentially no trimeric or higher species were observed, indicating that this design might function well as a means to generate predominantly $Al•(RG)_n$ clusters.

Past published reports from groups using laser vaporization had established that for this technique to work well, the target rod or disk had to be constantly moved with each laser shot.[14-18] Why this motion is so rigorously required is still not completely understood at a physical level, but has nevertheless been attributed to the fact that repeated shots to the same point on the target somehow anneals the surface, changing both the atomic configuration as well as the physical properties of the surface atoms. By insuring that each laser pulse strikes a clean region on the target, one can presumably

reduce this annealing process, thus ensuring a stable source with high shot-to-shot reproducibility.

For the first laser vaporization source design, both a source itself as well as a mechanical mechanism by which to drive the target were designed. The components of the first generation laser vaporization source are presented in Figures 2-42 through 2-53. Due to the ready availability of stock aluminum rods (2024 or 6160 alloy) in an enormous assortment of pre-fabricated diameters, a source that employed rods as the laser vaporization target was initially chosen.

The first two components of the first generation laser vaporization source assembly were related to the source itself, the adapter piece (Part #2) being identical to that presented earlier in Section 2.2.3.1 as part of the original pulsed valve design (see Figures 2-32 and 2-33). Following Costes' published design,[21] the source (see Figures 2-44 through 2-47) consisted of an initial 0.355" long, 1 mm diameter channel, that subsequently opened up at 45° to a 0.145" long, 0.100" diameter pre-expansion channel. The 3/16" nominal diameter target rod was placed 0.025" downstream of the beginning of the pre-expansion channel, and the target rod ablation surface was offset by 0.020" from the center line as determined by the center of the gas channel. A 0.050" diameter channel was machined through the source body perpendicular to the gas channel to permit the introduction of the laser vaporization laser directly into the source and onto the target rod surface. The 0.050" diameter channel placed behind the target rod allowed for precise alignment of the laser vaporization laser through the source once the rod was removed. No effort was made at this stage to try to reduce the efflux of gas through these channels

during each gas pulse.

Following the pre-expansion channel, the source opened up at 90° to the front surface of the source. Therefore, the end of the pre-expansion channel was reasonably assumed to represent the origin of the supersonic expansion, and hence was termed the expansion region. The cooling efficiency of the expansion from this source was not completely characterized since this design was employed for use during the initial LIF experiments detailed previously.[1] Therefore, cluster distributions such as those that can be obtained from REMPI/TOF measurements cannot be reported. Nevertheless, electronic transitions between the ground Al(3*p*)•Ar electronic manifold to both the excited Al(4*s*)•Ar and Al(3*d*)•Ar electronic manifolds were observed with LIF using this source, indicative of the fact van der Waals molecules could be produced. Evidence for higher cluster was ambiguous due to the inability to assign any spectral features definitively to species larger than Al•Ar.

One disturbing observation uncovered during the use of this source was a very asymmetric deposition of aluminum on the face of the expansion region. Specifically, a sharp pronounced deposit was only observed at the three o'clock position of the expansion region surface face as viewed looking directly at the front of the source. The fact that this residue distribution was so pronounced to the target rod side of the source was a item of some concern, perhaps indicative of unusual and/or turbulent behavior within the expansion due to the fact that the target rod projected too far into the pre-expansion region. This worrisome characteristic was one of the major motivating forces behind the development of a new laser vaporization source design when the MPI

experiments that are detailed in the thesis were implemented. The new design used for the MPI experiments will be detailed in Section 2.2.4.2.

An additional problem that became evident when the source was first being implemented was a tendency for the aluminum target rod to cold weld to the source, seizing the motion. The origin of this tendency was due to the fact that laser ablation of the target rod both produced tiny shards of ablated aluminum that would get trapped between the rod and source as well as providing a constantly clean surface between the two like surfaces. Since making the source entirely out of some other material such as stainless steel would have presented a difficult machining task, two other approaches were pursued that largely solved this problem. The first was to press fit into the source a stainless steel sleeve to house the aluminum target rod. To accomplish this, the 0.188" diameter target rod channel was enlarged, and a 0.050" wide sleeve that was pre-machined to match the interior dimensions of the source was press fit into place and sealed using Lock-tite. The use of unlike metals greatly alleviated the seizing problem, as did reducing the diameter of the target rods from a slip fit diameter to a more loosely fitting diameter of approximately 0.182" plus or minus a few thousandths of an inch. However, the use of a more loosely fitting rod precipitated an additional problem by causing the target rod to precess within the sleeve by a very small amount during a rotational period. This precessional behavior was observed to result in oscillatory source behavior that closely matched the rotational period of the rod. These issues were likewise addressed comprehensively in the second generation laser vaporization source described in the following section.

The other components of the first generation laser vaporization source were related solely to the mechanical drive mechanism for the target rod. The most efficient manner to both provide a fresh surface with each laser shot as well as utilize the maximum amount of rod surface area is to simultaneously rotate and translate the target rod. In essence, such a motion will result in a spiral thread to be ablated from the surface. Fortunately, this motion is exceedingly facile to achieve - one need only mount the target rod to the end of a screw that is constantly rotated within a fixed nut in both a clockwise, then counterclockwise manner. The remaining components of the first generation laser vaporization source listed in Figures 2-42 and 2-43, namely Part #3 through Part #13, are dedicated to performing this single, simple task.

The components of the target rod drive assembly can be seen in Figure 2-48, where the numbers refer to the part number of the component as listed in Figures 2-42 and 2-43. For the screw itself (see Figure 2-49), a non-standard 1/4-80 micrometer screw was chosen to ensure maximal ablation surface coverage on the target rod. When purchased, this screw (FAS300, Thorlabs) comes with a plastic handle that can either be machined off on a lathe, or, if in a hurry, be broken off using a vice after freezing the handle in liquid nitrogen. In addition, the screw comes with a spring loaded ball-bearing at the end that must likewise be machined away. Nevertheless, it is much more cost effective to modify this screw as opposed to fabricating this piece from scratch.

The screw threads directly into a specialized 1/4-80 brass nut (Part #4 in Figure 2-48 - Part#N80L5, Thorlabs) that can be used directly without further modification. This nut possessed an exterior 3/8-40 thread and locknut that enabled this piece to be mounted

in a keyed manner into the drive housing (Part #4 in Figure 2-48 and Figure 2-50). Besides mounting the brass nut, the drive housing was designed to slip-fit two stacked rotary ball bearings. These bearings are seated on a small 0.100" high, 0.750" inner diameter aluminum shim gasket (Part #7 on Figure 2-48) that likewise slip-fit into the housing.

The component responsible for driving the motion of the screw was the rotating screw drive housing (see Part #8 in Figure 2-48 as well as Figure 2-51). The screw drive housing slip-fit directly into the inner diameter of the stacked rotary bearings, coming to rest such that the bottom surface of the screw drive housing lay immediately adjacent to the brass nut. An external retaining ring groove machined adjacent to the bottom rotary bearing edge enabled the bearing stack to be firmly secured to the screw drive housing, enabling both components to be installed or removed from the mount simultaneously. In addition, the screw drive housing was designed with a 0.350" inner bore diameter, sufficient clearance to install this piece around the 1/4-80 screw/brass nut assembly fastened to the mount. Finally, a stainless steel clamp (see Part #9 in Figure 2-48 as well as Figure 2-52) with a precision lip designed to key into the inner diameter of the mount fastened the screw drive housing/rotary bearing assembly securely into the mount via four 4-40 UNC counterbored socket head cap screws. When tightened into place, the clamp ensured that a zero-play metal-to-metal contact was achieved between the mount and screw drive housing/rotary bearing assembly. When uncoupled from the drive screw, the screw drive housing rotated freely in a frictionless manner, without exhibiting any play along the rotational axis.

In order to drive the screw, the free rotary motion of the screw drive housing needed to be coupled to the screw itself. This was accomplished as follows. On two opposite sides of the screw drive housing were two 0.1255" wide by 2.000" long grooves that were machined completely through the piece. These grooves were designed for close clearance with the stainless steel drive pin that was installed to one end of the drive screw opposite to that end designed to couple to the target rod (see Figure 2-49). To assemble the fully functional target rod drive assembly, the drive screw without the drive pin was first carefully threaded into the brass nut that had been previously secured to the mount. The screw drive housing/rotary bearing assembly was then installed around the screw and secured to the mount by the steel clamp. Next, to couple the two components, the groove in the screw drive housing was aligned with the 0.125" diameter hole on the drive screw that accommodated the drive pin. The drive pin was then inserted into the screw, and centered such that a portion of the drive pin extended partially into both grooves on either side of the drive housing, but not beyond the outer diameter of either groove. When the drive pin was properly centered, the pin was locked into place by a 4-40 UNC set screw installed on the end of the drive screw that seated onto a 0.100" flat on the pin.

When fully operational, the screw drive assembly permitted smooth translational motion of the drive screw along the entire 2.000" groove length of the drive housing. In order to fully implement this assembly, however, two additional features were required. First, a means to mount the screw drive assembly about the laser vaporization target rod was required to be designed. This was accomplished through the use of a specialized table (see Figure 2-53) that mounted to the upper horizontal surface of the Y-plate of the

source mount (see Figure 2-27). As was discussed in Section 2.2.2, the Y-plate was modified (see Figure 2-29) to mount two right-angle brackets (see Figure 2-30). These right angle brackets served to couple the Y-plate and the table. The table rested on the flat surface provided by both the upper horizontal surface of the Y-plate and the right-angle brackets, and was secured to the brackets by two 10-32 UNF nuts and bolts.

The table possessed a 1.250" diameter through-hole surrounded by four 0.190" diameter holes places symmetrically about a 1.500" diameter bolt circle on one end of the piece. This served to mount the screw drive mount, and in turn, the screw drive assembly as a whole. When secured to the source mount, the table was designed to be positioned in such a way that the drive screw lay directly above the laser vaporization target rod. Generous clearance within the through holes in the table provided the required positional flexibility to perfectly align the screw and the target rod coaxially. The drive screw was coupled to the screw drive assembly by means of a low profile flexible spring coupling (59925K87, McMaster-Carr). A flexible coupling was required because the drive screw could not be fabricated with a straightness tolerance of less than 0.001" - 0.003" without an inordinate amount of effort on the part of the machinist. Consequently, the drive screw precessed slightly in the brass nut while rotating, especially when the screw had been fully extended in the downward direction. A rigid coupling did not accommodate for this precession, causing the drive assembly to seize when the drive screw "kicked out" of the axial alignment. The chosen coupling compensated for this precessional motion, while its short length permitted to maximal amount of target rod coaxial motion to be achieved.

With all of this equipment installed within the source, a mechanism by which the

laser vaporization target rod could be simultaneously rotated and translated was complete. Nevertheless, such motion required the screw drive housing to be rotated in both a clockwise and counterclockwise manner. This demanded the design of a robust mechanical drive mechanism by which the screw drive housing could be rotated.

Due to a number of constraints placed on the design by the LIF experimental apparatus, the drive mechanism for the screw drive housing was forced to be a bit convoluted. At the time, a suitable yet inexpensive reversible motor for use in an ultra-high vacuum environment was not known. Therefore, coupling a motor directly to the screw drive housing was not pursued as an option. Since this time, a number of groups have placed standard DC motors in vacuum without any special consideration for heat dissipation, and found that even cheap model motors can last as long as six months.[11] For future reference, the latter approach is recommended for future use since it bypasses a number of the mechanical components that were required to successfully implement the design employed for these experiments.

Rotary motion for the screw drive housing was provided by an end-mounted DC stepper motor/rotary motion feedthrough (Part #670002-03, MDC) that was driven by a homebuilt stepper motor driver (see Figures 2-1 and 2-2). To mount the motor, the top source cross ASA-10 flange (see Figure 2-9) was modified by welding into place a 2-3/4" ConFlat half nipple to the top surface of the flange 4.000" off-center. The port needed to be placed off-center in order to not interfere with the LIF light detection apparatus that was in place at the time.

In order to bring the rotary motion to the table mounted on the Y-plate, the rotary

motion produced by the end-mounted DC stepper motor/rotary motion feedthrough was first transferred to the center of the source cross ASA-10 flange. This was accomplished by mounting a gear table directly to the vacuum-surface side of the ASA-10 flange. Onto this gear table were mounted three low-profile external frames that contained coaxially-aligned rotary ball bearings seated into two separate end mounts. These bearings, in turn, slip-fit a central shaft that was secured to the rotary ball bearings through the use of external retaining rings. The central shaft possessed a flat along the length that permitted different outer diameter "No-Slip" positive drive belt pulleys (FC/FC1 Series, Pic Design) to be secured to the shaft via a set screw contained within the hub of the pulley. The frames were designed such that any diameter pulley up to 2.000" in diameter could be mounted to the shaft. One pulley housing supported a coaxial shaft extension leading directly from the motion feedthrough as well as mounting a pulley. The other two frames were devoted to gearing down the rotary motion provided by the DC stepper motor, the pulley shafts of both lying parallel to that of the motion feedthrough shaft. Of these two, one was placed such that the central shaft was placed precisely at the center of the source cross ASA-10 flange, while the other was placed at a distance intermediate between two other two pulley housings.

The means of coupling the pulleys was provided by "No-Slip" positive drive belts (FS Series, Pic Design). These belts were designed to exhibit zero-backlash upon reversal of direction when used with the aforementioned pulleys, thus ensuring that the rotary motion form the DC stepper motor was coupled to the center of the flange in a precise, zero-backlash manner. For the experiments presented in this thesis, the gear ratios of the

pulley assemblies was designed to step down the rotary motion of the DC stepper motor by a factor of eight, yielding a temporal period of approximately fifteen seconds for the shaft placed at the center of the source cross ASA-10 flange when the stepper motor driver is set to the highest speed.

From the center of the source cross ASA-10 flange, the rotary motion was brought directly down to the table mounted to the Y-plate by a coupling shaft with universal gears mounted to each end. The universal gears were used in a double-jointed configuration, hence compensating for any axial misalignment between the coupling shaft and the mating shafts on either end. The table mounted to the Y-plate possessed another pulley housing whose central shaft mated directly to the coupling shaft. This pulley housing contained a single pulley (FC-36, Pic Design). The final motion coupling was between this pulley and the screw drive housing itself. As shown in Figure 2-51, the screw drive housing was designed with an outer flange. This flange served to mount a pulley (see Part #10 in Figure 2-48 - modified FC-36, Pic Design) whose central hub was machined away to slip fit the screw drive housing inner flange diameter, as well as to possess four clearance holes for 2-56 UNC screws placed on a 0.825" diameter bolt circle. This pulley was then secured directly into the screw drive housing flange via the four 2-56 UNC tapped mating holes. A "No-Slip" positive drive belt was then used to couple the pulley mounted to the screw drive housing to the other adjacent pulley housing likewise fastened to the table. Since equal diameter pulleys were utilized for both pulleys on the table, one-to-one gearing was employed, meaning that the drive screw and hence the laser vaporization target rod were rotated at a speed one-eighth that of the DC stepper motor - the gear ratio

being determined by the upper gear table mounted to the source cross ASA-10 flange.

Control of the drive screw motion was achieved externally by means of a calibrated distance indicator coupled to the end-mounted DC stepper motor/rotary motion feedthrough. As was discussed above, the side grooves in the screw drive housing (see Figure 2-51) effectively delimited the upper and lower bounds of travel permissible for the drive screw (see Figure 2-49). Once either of these extremes was reached, further rotary motion of the screw drive housing served only to press the drive screw pin into the end of the groove, effectively halting all rotation of the screw drive housing. To ensure that the drive screw was always positioned within these two extremes, a distance indicator whose main body consisted of 13.0" x 2.0" x 0.375" long aluminum bar stock, henceforth referred to as a track, was mounted directly to one end of the DC stepper motor/rotary motion feedthrough via a homebuilt coupling. On either end of this track was placed a rotary bearing end mount containing a 0.250" inner bore diameter rotary ball bearing. A threaded brass 1/4-28 UNF threaded rod was then mounted above the track between the rotary bearings and secured to the end mount bearings by collars to prevent slippage. Pulleys were then used to couple this threaded rod to the DC stepper motor itself, such that the rotation of the stepper motor drove the rotation of this threaded rod as well as the internally mounted laser vaporization rod driver assembly.

Onto this threaded rod was mounted a 1/4-28 UNF tapped aluminum block that extended from the threaded rod into an slightly oversized channel milled along the length of the track. Rotation of the stationary threaded rod caused this block to travel along the length of the track, its rotation having been prevented by physical contact with the channel

walls. Finally, an electrical limit switch was installed onto both ends of the channel. When the aluminum block reached one extreme of the channel, the block would physically contact the limit switch and depress the switch lever. Depressing the limit switch level was the signal for the homebuilt DC stepper motor driver to switch the direction of motion, causing the block to reverse direction toward to other limit switch. Likewise, contact with the opposite limit switch caused the direction of motion to be reversed back to the original direction.

This control mechanism permitted the motion of the drive screw to be regulated as follows. The length of the brass 1/4-28 UNF threaded rod was chosen such that the number of rotations required for the aluminum block to travel the length of the channel was greater than the number of rotations required for the drive pin of the drive screw to travel to length of the 2.000" grooves in the screw drive housing. The key to the screw drive motion control was to calibrate the motion of the drive screw with that of the external aluminum block such that the aluminum block would contact a limit switch before the pin of the drive screw reached the end of the groove. Hence, the two extremes delimited by the limits switches of the external track were exactly correlated to those of the internally mounted screw drive. When the aluminum block reached one extreme, this corresponded to the analogous extreme in the screw drive assembly. Therefore, just as the drive pin was approaching the end of the groove, the aluminum block would actuate the limit switch - reversing the motion and sending the drive pin in the other direction towards the other extremum of its motion.

This control mechanism has worked reasonably well throughout the course of

these experiments. The most prominent problem arose during those times when the rod seized within the source. To protect the stepper motor in the event of seizure of the internal drive components, a miniature slip clutch (E-MSCB-4, Small Parts, Inc.) served as a coupling between the shaft of the motor feedthrough shaft itself and the shaft of the first pulley housing mounted on the source cross top ASA-10 flange. Therefore, in the event that the target rod ceased to rotate, the stepper motor continued to rotate due to the slip clutch. However, since the distance indicator was also coupled to the to the stepper motor, the calibration between the indicator and the screw drive housing was lost. After a rod seizure, care needed to be exercised to ensure that the distance indicator was re-calibrated with the screw drive housing or else there was a high probability that the drive pin would reach the extremum of the motion, again seizing the target rod drive mechanism and potentially causing damage to the drive components.

2.2.4.2. Second Generation Laser Vaporization Sources

Due to the problems with the first generation laser vaporization source discussed in the previous section, a different laser vaporization design was sought during the period when the experiment was being transitioned over from LIF to MPI/TOF-based detection of $Al{\bullet}Ar_n$ species. The new approach that was ultimately adopted was strongly influenced by a very successful laser vaporization source design developed by Michael Duncan's group for the generation of $metal{\bullet}(solvent)_n$ and $metal^+{\bullet}(solvent)_n$ clusters.[22] The basic guiding principle that grew out of this work was the observation that for the efficient generation of large distributions of mixed monomeric metal/solvent clusters the laser

ablation point should lie as close to the throat of the supersonic expansion as possible. Using this methodological principle, Duncan's group convincingly demonstrated that such an approach was equally effective for the generation of large distributions of both neutral as well as cationic clusters.[23]

Influenced by the results from Duncan's group, three different laser vaporization source designs were developed for the MPI/TOF experiment that incorporated this new postulate. Each one that was subsequently fabricated was an attempt to comprehensively characterize the effectiveness of a specific feature over another. Ultimately, two were implemented with considerable success, while a third performed poorly. In short, the results gleaned from the performance second generation of laser vaporization sources only further reinforced the axiom that simplicity of design is best.

The first source of the second generation sought to combine the insights gained from Duncan's group with the first generation design derived from Costes's work. The schematics for this source are provided in Figures 2-54 through 2-58. In addition, the complete laser vaporization source assembly as it appeared mounted to the pulsed valve can be seen in Figure 2-59.

In its original appearance, this source very closely resembles the first generation source, except that the ablation point on the target rod was moved closer to the presumptive throat of the supersonic expansion. In close analogy to the first design, an 0.315" long, 1 mm diameter channel formed an initial conduit through which the expansion gas flowed upon exiting the laser vaporization adapter (see Figures 2-32 and 2-59). This channel then opened up at 45° to a 0.145" long, 0.100" diameter pre-

expansion channel. As before, a 0.188" nominal diameter channel to accommodate the aluminum target rod was machined perpendicular to the pre-expansion channel, the ablation point on the rod being offset by 0.020" from the center line. The fundamental change was that the ablation point was moved 2 mm closer to the end of the pre-expansion channel compared to the previous design, bringing the ablation point within 1 mm of the end of the channel. Since it was believed that the throat of the expansion probably lay within the pre-expansion region to some degree due to the wide bore of the channel, this 1 mm offset was designed as an estimate of the region close to the probable throat of the expansion.

In order to maintain the pressure of the expansion gas as it passed through the laser vaporization source, the laser vaporization laser inlet/outlet channels were reduced to a 0.030" diameter as opposed to the previous 0.050" diameter. To assist aligning the laser vaporization laser through this significantly smaller hole, a 0.125" diameter, 0.240" deep counterbore reduced the effective length. Behind the laser target rod, the laser vaporization outlet channel was designed with a 5-40 UNC tapped hole that penetrated directly into the laser vaporization target channel. This was designed to accommodate a 5-40 UNC ball and spring set screw (3408A12, McMaster-Carr) that served two purposes. First, this set screw effectively plugged one of the two gas escape channels that would serve to reduce the pressure within the source. Second, the spring-loaded steel ball on the end of the set screw enabled undersized diameter target rod to be firmly pressed against the pre-expansion channel, preventing both excess gas leakage from the target rod/pre-expansion channel interface as well as preventing precession of the target rod

within the target rod channel during rotation. Furthermore, by employing reduced diameter rods, the possibility of target rod seizure was greatly reduced.

To further assist in the prevention of target rod precession, two additional 5-40 UNC tapped holes were placed 0.287" above and below the laser vaporization laser outlet channel. By providing three points of contact between the source and target rod, it was reasoned that all precession of the target rod, and hence the oscillatory source behavior, could be eliminated. In this respect, the installation of the spring-loaded set screw was a success in that precession all but disappeared. Nevertheless, use of these set screws presented an additional problem - they caused the rod to seize. The origin of this problem was that tiny shards of aluminum ablated from the surface became trapped behind the steel ball of the set screw due to the opening introduces when the ball was depressed. So much aluminum was trapped behind the ball that all spring motion was eventually lost, causing an immovable point of contact to be achieved between the target rod and the source. Any tiny shard of aluminum that got trapped between the two surfaces was then sufficient to cold weld the two components, seizing the target rod. This problem was especially severe for the central 5-40 UNC spring loaded set screw that lay directly opposite the abalation surface.

To address this problem, two approaches were employed. The first was to reduce the probability of cold welding between the aluminum target rod and the aluminum target rod channel in the source. This was accomplished by the use of a brass sleeve that was installed into the source as a lining for the target rod in an analogous manner to the first generation source. Brass was chosen as the sleeve material instead of stainless steel due

to the fact that the facile machining of brass permitted the interior dimensions of the source to be re-machined with the sleeve already inserted rather than having to pre-machine the interior dimensions into the sleeve as had to be done with the stainless steel sleeve. To perform the retrofit, the laser vaporization target channel was enlarged by 0.080" on the diameter, and into this expanded hole was press-fit a solid rod of brass. The source was then re-machined to match the original interior dimensions. The result was highly successful, with no observable discontinuities between the mating surfaces of the two materials to serve as potential sources of turbulence.

The other aspect of the solution involved modifying the spring-loaded set screw configuration within the source. Since the central 5-40 UNC spring-loaded set screw seemed especially prone to collecting aluminum shards behind the ball, the decision was made that this set screw would be slightly withdrawn away from the target rod such that no contact was made between the two components. In this manner, the central spring-loaded set screw served only to plug the laser vaporization outlet channel and prevent loss of gas during a gas pulse. The other modification was to enlarge the upper and lower 5-40 UNC tapped holes to 10-32 UNF tapped holes. The purpose of this modification was to permit the use of 10-32 UNF stainless steel spring plunger set screw (84975A27, McMaster-Carr). The advantage of a spring plunger mechanism over the previous ball and spring mechanism was that the former maintains a tight seal with the set screw body when depressed while the latter does not. Furthermore, greater spring tension was possible by employing a larger set screw, enabling very stiff tension to be attained between the target rod and the source. While the spring plungers were equipped with a nylon

locking element, the tapped holes were too shallow to permit these to become engaged. Therefore, the spring plunger threads were wrapped in Teflon tape to prevent the plungers from unscrewing during use. Ultimately, these modifications were quite successful in stopping the rod precession inherent to the first generation source while at the same time significantly reducing the occurrence of target rod seizure.

The laser vaporization source outlined above was quite successful in generating a large $Al{\bullet}Ar_n$ cluster distribution. Figure 2-101 shows a typical $Al{\bullet}Ar_n$ cluster distribution using near-resonant 315 nm plus 630 nm MPI followed by TOF detection. As is evident from inspection of Figure 2-101, clusters up to $Al{\bullet}Ar_{60}$ were clearly observable. An unusual feature about the source performance was that the maximum laser vaporization laser power (approximately 6 mJ at 355 nm) was required to generate a large cluster distribution as well as to stabalize source performance. This characteristic is counterintuitive, as one would expect that higher laser vaporization powers would result in a hotter plasma. Hotter source conditions typically generate smaller cluster distributions since additional energy must be dissipated within a given expansion environment. One possible explanation for this behavior was that perhaps the throat of the expansion was really occurring close to the beginning of the pre-expansion channel. If this were the case, the shock wave from the expansion might have served to defect aluminum atoms backwards towards the source. In this case, high laser vaporization pulse power might have permitted enhanced penetration of the plasma into the cooling region contained within the shock wave. Nevertheless, while this scenario cannot be ruled out as an explanation, the observation of an even, vertical distribution of aluminum on the source

face that was almost perfectly aligned with the vertical center line suggested that no asymmetries existed in the expansion region. If the shock wave were indeed responsible for deflecting aluminum atoms away from the expanding gas, the expectatation would be for the observation of an enhanced aluminum deposition toward the target rod side of the source. This behavior which was, in fact, observed in the first generation laser vaporization source, was clearly not evident in the new design.

The $Al•Ar_n$ cluster distributions generated by this source corresponded predominantly to solvation within the first and second icosahedral solvent shells. Previously, Whetten's group has reported a laser vaporization source design that produced $Al•Ar_n$ cluster distributions past $Al•Ar_{135}$, the cluster size at which the third icosahedral solvent shell closing occurs.[24-26] To generate such a broad size distribution, Whetten's group employed 30° nozzles with lengths varying from 0.3 to 4.0 cm long, with the ablation point positioned close to, but not at, the beginning of the nozzle.[24] In an attempt to generate cluster distributions closer to the size range obtained by Whetten's group, the laser vaporization source described above was modified slightly, taking into account some of the design philosophy of Whetten's source.

The modifications made to the source are presented in Figure 2-58. In an attempt to minimize the gas channel length prior to the pre-expansion region as well as to enhance the efficiency of the subsequent supersonic expansion, the interface between the initial 1 mm gas conduit and the pre-expansion channel was modified. In particular, the abrupt, 45° transition region between the two channels was converted to a much more gradual 10° expansion cone. This cone was machined such that the pre-expansion channel remained

the same length, while the majority of the initial gas conduit was machined away to form the cone. Unfortunately, these changes ultimately had little effect on the size distribution. Beyond a slight enhancement in shot-to-shot stability, little, if any, increase in the cluster distribution was discerned over the original design.

A second source that was developed simultaneously to that described above reflected the ultimate in simplicity. The schematics for this source design are presented in Figures 2-60 through 2-62. Stripped down to the basics, this source design consisted of a single 1 mm diameter, 0.450" long straight channel. Perpendicular to this channel, a 0.030" laser vaporization laser pulse inlet channel was machined such that the ablation point would lie precisely at the end of the gas channel. As before, two tapped holes for 10-32 UNF (see Figure 2-62) were added to mount spring plunger set screws. Likewise, a single 5-40 UNC threaded hole served as the laser vaporization pulse outlet, which was plugged with a 5-40 UNC set screw when the source was in use to prevent gas leakage.

Somewhat surprisingly, this straight channel laser vaporization source performed almost identically to the other version described above that was considerably more complicated. Cluster distributions obtained using this source were virtually indistinguishable from that presented in Figure 2-101 that was acquired using the other source. Furthermore, much of the same behavior, in particular a requirement for high laser vaporization powers to generate the larger cluster distributions, was exhibited by these two fairly distinct designs. The exact physical basis of this similarity in performance remains elusive.

One hypothesis as to why these sources appeared so similar was that if the

combined gas channel length between the laser vaporization source adapter and the laser vaporization source itself were long enough to cause choked, turbulent gas flow, then the performance might be somewhat independent of the expansion properties itself. A useful parameter when thinking about the gas flow within a straight channel is the quantity (l/d), where l represents the length of the gas channel and d represents the channel diameter.[3] As a general rule of thumb, the value of (l/d) should be minimized to ensure that maximal flow rate through the channel is achieved.

To test whether choked flow was in fact an inherent property of the source design, another laser vaporization source adapter and straight-channel laser vaporization source were created, except with a 2 mm channel diameter as opposed to the original 1 mm diameter. If, in fact, choked flow were a problem in these sources, then use of channel of twice the diameter of the original will lower the ratio of (l/d) by a factor of two, presumably resulting in a marked improvement in source performance. Surprisingly, this was not found to be the case. The straight 2 mm diameter channel source yielded extremely poor cluster distributions, generating $Al{\bullet}Ar_n$ clusters no greater in size than $Al{\bullet}Ar_{12}$ in a stable manner. In the end, there remained a number of unanswered questions regarding the fundamental basis for the source performance. Nevertheless, these sources proved quite effective for general use, generating most of the $Al{\bullet}Ar_n$ cluster data presented in Chapter 5, as well as many of the early spectra in the Al•Ar systems discussed in Chapters 3 and 4.

As mentioned earlier, the use of the second generation sources occurred concurrently with the implementation of the MPI/TOF detection scheme. A few minor

modifications were required, therefore, to make the laser vaporization target rod drive compatible with the need to accommodate varying nozzle-to-skimmer distances. The primary modification that was required was to replace the original table mounted to the Y-plate of the source mount (see Figure 2-53). This table had been designed assuming that the source would never move, which was in fact the case for the LIF experiments. In order to permit effective coupling between the gear table mounted to the top of the source cross ASA-10 flange and the screw drive housing (see Figure 2-51), a new table was designed that would accommodate different source placements (see Figure 2-63). This new table was mounted to the Y-plate an the exact manner as the original, as discussed in Section 2.2.4.1.

Implementation of this new table required that the drive pulley system on the new table be reset each time the source was moved. The requirement arose from the need to maintain one pulley housing directly below the center of the top source cross ASA-10 flange to ensure facile coupling of the rotory motion. The extended length of this new table reflected this necessity. Rather than having to make a specific diameter "No-Slip" positive drive belt to couple the screw drive housing to the pulley mounted in this housing, a second pulley housing was added to the new table to serve as an intermediary coupling. This new pulley housing contained two pulleys of the same diameter as those employed previously, directly transmitting the driven motion of other pulley connected to the drive mechanism to the screw drive housing. By placing this pulley housing in between the original two, a number of different combinations of two standard "No-Slip" positive drive belts were able to be used. Any slack in the belts was compensated for by displacing the

new pulley housing off-center from the line between the other two pulley components.

As before, the new table mounted the screw drive housing at one end of the piece. This was likewise designed such that the screw drive housing would lie directly above the laser vaporization target rod once the table was bolted to the Y-plate. The pulley housings were affixed to the table using standard laser table clamps. The series of channels machined through the table allowed for a great deal of play with respect to the mounting of the central pulley housing.

2.2.4.3. Third Generation Laser Vaporization Source

Not all materials that can potentially serve as laser vaporization targets have the advantageous physical properties of aluminum. Successful implementation of the previous source designs in the first and second generation laser vaporization sources described in the previous two sections were all highly dependent upon the high physical strength of the refractory target material. Nevertheless, there are large classes of softer materials such as the alkali or alkaline earth metals where target rods (if available) would not exhibit the physical strength to endure being translated up and down through the source supported at only one end. Since alkali metal-solvent clusters were the original target systems for this thesis, a new source design was developed that would be, for lack of a better word, universal. In effect, the ultimate goal of this new source design was to permit the use of *any* laser vaporization target material that could be obtained or somehow rendered into the form of either a rod or a disk (which encompasses almost all materials). This section outlines the design of the rod source, while the design of the disk source (which still needs

to be implemented) is presented in Chapter 6. These separate designs, while distinct in their mechanical components, are nevertheless completely interchangeable, enabling the rod source and the disk source to be readily exchanged with one another within minutes.

Previous experience with the second generation laser vaporization sources had demonstrated that placing the ablation target at the throat of the supersonic expansion was a fruitful means to generate large cluster distributions of metal•(solvent)$_n$ clusters. This fortuitous parameter eliminated one of the key obstacles in designing this source, namely how to translate a malleable material through a hard-walled channel within the laser vaporization source. Instead, placement of the ablation target at the throat of the expansion permitted the target rod to be placed outside of the source where no physical contact would occur with the nozzle. This adaptation, however, required that the target rod now be supported at both ends since there no longer would exist the target rod channel within the source to maintain a constant, steady position.

The new third generation laser vaporization assembly is shown in Figure 2-64. The numbers in Figure 2-64 correspond to the individual part numbers of the various components. A complete set of machine drawings for each of the individual components of this source is compiled in Appendix 4.

While initially appearing quite complicated, the entire design is based around the requirement to provide a reproducible means to rotate and translate a target rod outside the confines of the gas nozzle. The core component of the new source is the target rod support mechanism presented in detail in Figure 2-65, hereafter referred to as "the cart." As shown in Figure 2-65, the cart served the purpose of mounting the target rod, as well

as providing the mechanical means to rotate and translate the target rod. The target rod was mounted between two unique rod holders (Part #12 and Parts #'s 11a and 11b in Figure 2-65) designed to accommodate 0.250" diameter target rods or any target rod support assembly. Besides mounting the target rod, the upper rod holder (Part #12) coupled the cart to the screw drive as shown in Figure 2-64.

The lower rod holder components (Part #11a and Part #11b in Figure 2-65) were designed such that the target rod could be mounted using a spring-loaded mechanism. As is shown in the drawings for these components in Appendix 4, a rod holder mount (Part #11a) was machined to slip fit into the lower rod holder (Part #11b). Furthermore, the mount possessed a 0.125" wide, 0.355" long slot machined through two sides that served to fit without play a drive pin (see machine drawing for Part #11b in Appendix 4) that was installed in the lower rod holder. Care was taken to prevent the ends of the drive pin from extending beyond the outer diameter of the mount. This drive pin was secured to the lower rod holder with a 2-56 UNC set screw that seated onto a flat on the pin. This set screw was able to access the drive pin via a 2-56 UNC tapped hole extending from the bottom of the rod holder shaft to the drive pin channel. When these components were assembled with an exterior spring placed between the upper flange of the mount and the lower surface of the rod holder, spring actuated motion was achieved. To assist in withdrawing the bottom collar to release the target rod, a brass thumbscrew (see machine drawing for Part #11b in Appendix 4) was attached to the bottom of the lower rod holder using the 2-56 UNC tapped hole into which the pin-locking set screw had already been seated.

Supporting the spring-loaded target rod mounting mechanism was the top (see Part #10a in Figure 2-64) and bottom (see Part #10b in Figure 2-64) components of the cart. On one end of both the cart top and cart bottom pieces, a through-hole was machined into which were press-fit rotary ball bearings. For the cart top, a single flanged miniature precision ball bearing (57155K131, McMaster-Carr) was press-fit into the lower surface. This bearing slip-fit the shaft of the upper rod holder (Part #12 in Figure 2-65) which was subsequently secured to the bearing by an exterior retaining ring. Due to the extended length of the lower target holder mount, two flanged miniature precision rotary ball bearings (57155K137, McMaster-Carr) were used in the cart bottom, one bearing press-fit into either the upper or lower surface. This rotary bearing stack slip-fit the lower target holder mount (Part #12 in Figure 2-65), which was likewise secured to the bearing stack by an external retaining ring.

On the opposite side of both the cart top and cart bottom were a set of four drill bushings that were press-fit into each piece. Functionally, these four drill bushings were divided into two pairs. The pair of bushings spaced farthest away from the rotary bearings were designed to serve as the side supports for the cart. One of the concerns in designing the cart was how to make it flexible enough such that any target rod length could be accommodated without having to machine a new side piece each time the rod length was altered. To solve this problem, two 0.250" outer diameter stainless steel shafts were employed as the side supports. These shafts were then secured to the top and bottom cart pieces by the use of custom collars (see Part #3b in Figure 2-65) that were tightened onto the shafts at the upper and lower surfaces of both the top and bottom cart pieces. Using

such an approach, the separation between the top and bottom cart pieces is completely adjustable along the length of the steel shafts, thus compensating for almost any length of target one should desire to use.

Ultimately, when the top and bottom pieces of the cart are secured into place, they created a perfectly rigid frame that served to place the upper and lower rod holders perfectly coaxial to one another. By setting the separation between the top and bottom cart pieces such that spring tension was maintained on the target rod when the lower rod holder was released, the target rod was seated in a manner that was likewise aligned coaxially with the upper and lower target rod holders. In addition, the rod was capable of rotating freely within the cart since both target rod holders were seated into rotary bearings. This rotation was highly symmetrical, exhibiting no visible signs of wobble or precession. Therefore this cart provided a means to bring the target rod adjacent to the source nozzle while maintaining a reproducibly fixed distance between the ablation point and the throat of the expansion. The absence of any wobbling or precession of the target rod adjacent to the throat of the expansion maximized the probability that non-oscillatory and stable shot-to-shot behavior would be observed from the source.

The other pair of drill bushings that were spaced closer to the rotary bearings were designed to slide over a pair of vertical guide shafts along which the cart could be translated upwards and downwards (see Figure 2-64). The rest of the third generation laser vaporization source design merely amounts to a mechanical means to mount these two vertical shafts along which the cart could be translated. In order to accomplish this, a frame needed to be designed that was mechanically sturdy, while at the same time

permitting the positioning of the vertical rails in an adjustable manner so that the target rod could be brought directly adjacent the source nozzle.

Two-dimensional positioning of the cart both parallel and perpendicular to the molecular beam axis was achieved by mounting the cart within essentially two nested frames, each controlling the positioning of the cart in one of the two orthogonal directions. To begin, an external frame was constructed that mounted directly to the source rails of the source mount as discussed previously in Section 2.2.2. As seen in Figure 2-64, this external frame consisted of Part #7, Part #8a, Part #8b, and Part #9. Part 8a was a custom designed aluminum collar that was mounted on two of the three source rails that were on the far side of the source from the perspective of the laser vaporization pulse direction of propagation. Both of these collars were designed with an approximate 0.650" wide flat onto which were tapped two holes for a 8-32 UNC thread along the centerline. The flats of each collar were designed to mount the bottom (see Part #8b in Figure 2-64) and side (see Part #9 in Figure 2-64) supports of the external frame. A right angle block (see Part #7 in Figure 2-64) connected the bottom and side external frame supports where the two components met. This block guaranteed the rigidity of the frame as well as maintaining a perfectly perpendicular orientation between the two pieces.

When assembled onto the source rails, this external frame could be translated along the length of the rails as long as the collars that secured to frame to the rails were not tightened down. Hence, the external frame provided the mechanism by which the target rod could be positioned in the direction parallel to the molecular beam axis. When properly positioned, the collar screws were then tightened, firmly securing the external

frame and all attached components to the source rails.

In order to enable precise positioning of the target rod perpendicular to the molecular beam axis, a second internal frame was constructed. This internal frame can be considered the intermediate frame between the external frame and the laser vaporization target rod cart. In essence, the internal frame served two key functions as shown in Figure 2-64. First, the ability to mount the vertical shafts along which the laser vaporization target rod cart translated was provided by this frame. Second, positioning of the target rod perpendicular to the molecular beam was achieved by the construction of a second cart system that completely contained within it the entire laser vaporization target rod cart assembly.

The fundamental design of the internal frame was as follows. Two separate rails systems, each consisting of a pair of 0.125" diameter stainless steel shafts, were mounted above and below the source oriented perpendicular to the molecular beam axis. The upper shaft support assembly for the internal frame included Part #4a and Part #4b (see Figure 2-64). Part #4a was a pair of end blocks through which were mounted two parallel 0.125" diameter shafts separated by a 1.250" center-to-center distance. Each of these end blocks was subsequently attached to each end of a pair of overhead supports (see Part #4b in Figure 2-64). These supports served to couple to upper shaft support assembly of the interior frame to the side support of the exterior frame.

An analogous lower shaft support assembly in the interior frame was likewise fabricated. A pair of lower end blocks (Part #6 in Figure 2-64) mounted another pair of 0.125" diameter stainless steel shafts that were separated by the same 1.250" center-to-

center distance. These end blocks were subsequently attached directly to the upper surface of the bottom support of the external frame (see Part #8b in Figure 2-64). Both sets of rails are prevented from sliding out of the housing by the use of stainless steel collars that mount to the inner surface of the outer end block.

With the upper and lower shaft support assemblies in place, there existed two sets of rails placed above and below the source that were oriented perpendicular to the molecular beam axis. By design, these were envisioned as serving as a platform upon which precise positioning of the laser vaporization target rod along this axis could be accomplished. In order to achieve this final design element, two distinct carts were designed that would slide along the length of the shaft assemblies. The cart designed to ride on the upper shaft support assembly is shown as Part #3a in Figure 2-64, while that designated for the bottom shaft assembly is labeled as Part #6 in Figure 2-64. Both carts possess a channel that runs along the length of the cart, the center-to-center distance of which exactly matched the center-to-center distance separating the upper and lower shaft assemblies. All ends of these channels were capped with drill bushings that were press-fit into place to permit the cart to couple to the shafts in a zero-play manner.

As is evident from examination of the machine drawings for Part #3a and Part #6 compiled in Appendix 4, both carts were equipped with a pair of 0.250" diameter, 0.750" long drill bushings that were press-fit into place. These served the purpose of mounting the vertical rails upon which the laser vaporization target rod cart would be guided. The 0.440" separation between these drill bushings exactly matches the separation between the pair of drill bushings press-fit into the cart top and bottom components. This ensured that

the motion of the laser vaporization target rod cart would be exceedingly precise and smooth, exhibiting no deviations in motion as it traveled along the length of the vertical shaft - a design that was in fact realized when the source was assembled and placed into general use. To prevent the vertical rails from being pulled out of the lower cart of the internal frame, a custom collar (see Part #3b in Figure 2-64) was installed around the vertical rails at a point adjacent to the bottom surface of the upper cart.

A particularly convenient aspect of this design is the ease with which the entire laser vaporization target rod cart can be installed or removed. In order to mount the laser vaporization target rod cart, one need only loosen the single collar securing the vertical shafts, and pull the two shafts out of the bottom cart drill bushings. To complete the installation, the free end of the two shafts need only be inserted through the drill bushings of the laser vaporization target rod cart and then reinserted back into the bottom cart drill bushings. Likewise, the complete assembly containing the laser vaporization target rod cart mounted on the vertical rails spanning the upper and lower carts of the internal frame can be removed from the 0.125" diameter shafts. This was accomplished by simply loosening the steel collars securing each 0.125" diameter shaft to the outer shaft end support (Parts #4a and #6 in Figure 2-64), and withdrawing each of the 0.125" diameter shafts from the mounts. Clearly, rapid assembly/disassembly was extremely facile with this new design.

The upper cart of the internal frame also mounted the entire screw drive assembly that served to rotate the target rod within the laser vaporization target rod cart while simultaneously translating the entire laser vaporization target rod cart up and down along

the vertical rails. Fortunately, essentially all of the previously designed components developed for the first generation laser vaporization source (see Figures 2-48 through 2-52 as well as description in Section 2.2.4.1) were able to be reused without any further modification.

The single exception was the original screw drive mount (see Figure 2-50) which needed to be redesigned to fit within the space constraints presented by the new source design. The new screw drive housing (see Part #2 in Figure 2-64 as well as machine drawing in Appendix 4) was fabricated to mount inside of a 0.250" deep counterbore machined into the upper surface of the upper cart of the interior housing. Four 2-56 UNC tapped holes in the bottom surface of the new screw drive mount permitted this piece to be securely attached to the upper cart. In addition, the distance between the center of the new screw drive mount and the vertical rails of the upper interior frame cart was set to be equidistant to the distance between the upper laser vaporization target rod holder and the vertical rails of the laser vaporization target rod cart, thus ensuring that the screw drive would lay precisely over the target rod. In order to connect these two components, a rigid coupling was used to join the drive screw seated within the screw drive assembly to the upper laser vaporization target rod holder.

To reiterate, complete positioning and motion control of the target rod was attained with this entire assembly in place. Both the external and internal frames provided the means by which the target rod position could be adjusted parallel and perpendicular to the molecular beam line respectively. The internal frame served to mount the laser vaporization target rod cart along vertical rails along which the latter could travel, as well

as to fasten the screw drive assembly that controlled the vertical motion of the cart. By coupling the screw drive assembly to the upper laser vaporization target rod holder, a mechanism was implemented whereby the target rod could be rotated as well as moved vertically by drawing the cart vertically up and down the guide rails of the internal frame. Ultimately, target rod motion was achieved that was exactly analogous to that employed in the first and second generation sources, except with considerably better control over eliminating any form of axial precession.

To complete the design, two different nozzle pieces (see Part #1a and Part #1b in Appendix 4) were developed that would mount directly to the modified laser vaporization source adapter (see Figure 2-39). Both of the nozzles were of comparable dimensions except in the nozzle angles - one possessed nozzle cone angle of 10° while the other was designed with a 5° cone angle. The rationale behind employing nozzles rather than any pre-expansion chambers was derived from Whetten's success in generating large cluster distributions up $AlAr_{135}$ using a similar source configuration (see discussion in previous section). The principal difference between Whetten's design and the one employed here was that Whetten's source placed the target within the source nozzle, where our approach sought to place the abalation point at the end of the nozzle. Such a configuration was similar to a "pickup-type" strategy that has proven rather successful in binding atoms or molecules to large solvent clusters.[4,27-28]

To ensure that the channel length would remain as short as possible, two nozzles were machined with only a 1 mm long straight section. This distance, combined with the use of the modified laser vaporization source adaptor, brought the total distance through

which the expansion gas passed before reaching the nozzle to less than 0.100" in total length. Such a short distance was believed to all but eliminate the possibility of choking the expansion gas prior to the expansion, providing the best possible conditions for generating the coldest possible expansion.

Unfortunately, the performance of both the 10° and 5° nozzles was disappointing. Very little clustering was observed from use of either of these nozzles. In fact, it proved quite difficult to achieve any clustering higher than Al•Ar itself. Presumably, the failure of this configuation derived from the fact that the ablation point was placed far away (roughly 0.400") from the beginning of the nozzle. In effect, if the throat of the expansion occured close to the beginning of the nozzle, then the shock wave of the supersonic expansion would be well developed at the ablation point. The failure to achieve pickup of aluminum atoms onto Ar_n clusters was probably due to the fact that the ablation point lay very close to the shock front, thus hindering efficient penetration of the ablated atoms into the central "zone of silence" where pickup could occur.

In the face of failure, the principle of simplicity of design often comes to the rescue. In addition to the two nozzle pieces, a third straight nozzle piece was created (see Part #1c in Appendix 4). However, the original purpose of this piece was not to serve as a nozzle *per se*, but rather as a laser vaporization laser alignment jig. The bore of this piece, nominally 0.060" in diameter, was designed to mount a standard melting tube capillary that would serve as a target for aligning the laser vaporization laser. While cognizant of the fact that the differing diameters between the capillary jig and the laser vaporization source adapter created a discontinuity in the gas channel, this capillary mount

was nevertheless pressed into service as a straight channel nozzle. In order to permit the target rod to lay directly adjacent to the channel, the far side of the jig (from the perspective of the laser vaporization laser direction of propagation) was machined close to the channel bore diameter. A schematic showing the placement of the target rod against the modified straight channel jig is shown in Figure 2-66.

Despite some initial concerns regarding the channel diameter mismatch mentioned earlier as well as the somewhat long length (0.450") of the gas channel, this straight channel configuration worked quite well, generating large cluster distributions comparable to those observed with the second generation laser vaporization source (see Figure 2-101). The single great advantage of this new experimental configuration, coupled to the improvements to the pulsed valve discussed in Section 2.2.3.2, was that the experiment was able to be run at significantly lower source chamber pressures. As was alluded to earlier, the first and second generation laser vaporization sources only produced large $Al \bullet Ar_n$ cluster distributions when the source pressure was close or at the stalling pressure of the diffusion pumps, specifically 8.0×10^{-4} torr. The potential for stalling may have even been further accentuated by the fact that the peak pressure produced with each gas pulse was undoubtedly significantly higher than this measured average pressure, albeit for a transient period. The disconcerting observation of diffusion pump fluid pooling in the foreline tubes after extended periods of use tended to reinforce this worry. Since the time the new source was installed, however, the machine has been able to be run at a significantly lower average pressure, 1×10^{-4} torr, while generating mostly identical cluster distributions to those produced by the previous designs. Equally satisfying, this new

experimental configuration solved the problem of diffusion pump fluid being swept into the foreline.

Due to the outstanding performance of this source, the third generation laser vaporization source has become the workhorse for the machine. The only fundamental change that might be envisioned would be to play with the straight nozzle piece, in particular, the bore diameter, to see whether this has any effect on source performance. For experiments where moderate cluster sizes (metal•(solvent)$_n$, $n \leq 60$) are required, this new source design has nonetheless proven very effective in its present configuration.

2.2.5. The MPI Region

Everything that has been discussed up to this point has concerned the details of the source chamber and the mechanical details/components of the source itself. The other half of the machine that remains to be discussed was dedicated to detection of the species generated in the source. The methodology chosen to study the species presented in this thesis was multiphoton ionization (MPI). In and of itself, the acronym MPI is rather non-informative since it encompasses an expansive array of both resonant and non-resonant techniques that can be employed in linear as well as non-linear regimes. For clarification, the term MPI will be used throughout this thesis in the broadest sense, i.e., the generation of ionic species via the direct absorption of more than a single photon of light regardless whether this occurs resonantly or non-resonantly. In the case where ionization occurs via direct resonant absorption to some intermediate state by one or more photons followed by direct ionization of this excited state, the acronym REMPI (resonance-enhanced

multiphoton ionization) will be employed. This general definition is preferred over other more restrictive acronyms that exist since it allows for both single- as well as multi-color ionization schemes.

Ionization-based detection schemes possess a number of advantages over light collection-based detection schemes such as the laser induced fluorescence (LIF) that was employed in the initial experimental phase detailed previously.[1] Foremost is the possibility for mass selection, commonly achieved through the use of time-of-flight (TOF) or quadrupole mass spectrometry. This is of particular importance when one is probing an entire cluster distribution where a number of different species might possess spectral features at the same wavelength. Mass selection allows the ability to separate out the spectral intensity of each individual cluster size at a given wavelength - something that is impossible with fluorescence techniques. The second great advantage to ionization-based detection is that there is extremely low background. Unlike fluorescence, where great care must be taken to ensure all source of stray light are extensively baffled, MPI experiments can be configured such that there is almost no background beyond that derived from ions formed by the direct ionization of pump oil.

After struggling with fluorescence-based techniques for about a year and half, the decision was made to convert over to an MPI/TOF detection scheme. This required the design and construction of an entirely new section for the experimental apparatus which at that time consisted only of the source chamber. The physical components that were required in order to implement this new experimental approach are presented schematically as numbers 11 through 20 in Figures 2-1 and 2-2. The details of the design

of this new section of the machine, now referred to colloquially as the "MPI region," is the subject of the following sections.

2.2.5.1. Chamber Components

The principal components that constitute the main chamber of the MPI region are labeled by the numbers 15, 17, and 19 in Figures 2-1 and 2-2. Anchoring the entire MPI region is a reducing four-way cross (see Figures 2-67 through 2-71) referred to as the "REMPI chamber." This custom designed chamber (fabricated by MDC) was fairly simple, consisting primarily of two orthogonally-oriented tubes of differing tube diameters. The horizontal tube oriented concentric to the molecular beam axis was a nominal outer tube diameter of 6.000", with a rotatable 8" ConFlat flange welded onto one end and a custom-designed non-standard ASA flange welded to the other. The vertical tube possessed an outer tube diameter of 8.000", and was designed with a standard ASA-6 flange welded to the bottom end, while the top end of the tube was equipped with a standard NW-200 ISO flange. The tube thickness used for this piece was 0.120", the standard MDC tube thickness.

Four 2-3/4" ConFlat ports were added, two on each side of the horizontal tube, that were positioned perpendicular to the molecular beamline. Two of these ports were positioned at the intersection of the horizontal and vertical center lines on each side of the piece, while the other two were positioned 2.630" away from the surface of the custom ASA flange along the horizontal center line. These ports served as laser ports through which the MPI laser pulses could be introduced through the chamber to intersect the

molecular beam. In the present experimental configuration, only the two ports that lay along the horizontal and vertical center lines are used as MPI ports, the other two being blanked off. The laser ports consisted of a specialty 1" nominal outer diameter compression port (Laser Window C-688, R. M. Jordan Company) that was welded into the center of a standard 2-3/4 ConFlat flange. This specialty compression port is designed to accommodate a 1.200" (30 mm) diameter, 0.125" thick herasil quartz window that was transparent through most of the UV range (75% transmission efficiency at 180 nm).

In addition, a 0.750" nominal tube outer diameter compression port was added to the lower region of the vertical tube. This compression port served to mount the iridium filament ionization gauge (I-075-N, Duniway Stockroom) used to monitor the chamber pressure with the diffusion pump employed.

As is shown in Figures 2-1 and 2-2, the pumping stack for the REMPI chamber consisted of an 6" electro-pneumatically actuated aluminum gate valve (VRC LP Series, now owned by the Kurt J. Lesker Company), a 0.750" thick aluminum baseplate, a 6" diffusion pump liquid nitrogen trap, and a 6" diffusion pump (Varian VHS-6). Due to an ASA-6 size mismatch between the bottom ASA-6 flange size and the ASA-6 flange dimensions of the VRC gate valve, a thin 0.375" thick aluminum gasket needed to be installed so that a proper o-ring seating surface could be achieved between the two components. The stacks were assembled in the exact same manner as those for the source chamber discussed in Section 2.2.1. Likewise, the VHS-6 diffusion pump and 6" gate valve were interlocked in an identical manner to the VHS-10 diffusion pumps of the source chamber using a homebuilt interlock as presented in Section 2.2.1. The VHS-6

diffusion pump was backed by a Leybold-Hereaus S30A single-stage direct drive mechanical pump rated to achieve a pumping speed of 27 cfm. In the present experimental configuration, Santovac 5 (0.5 *l*) was used as the diffusion pump fluid.

As discussed earlier in Section 2.2.1, one of the key functions for the REMPI chamber was to mount the skimmer flange (see Figure 2-13) via a custom ASA flange seen in Figure 2-68. By mounting the skimmer flange, the REMPI chamber supported the entire source mount assembly. The experimental apparatus was designed such that the only opening between the source chamber and the MPI region was afforded by the 3 mm skimmer orifice (see Figure 2-13 and 2-17). Therefore, the MPI region served as the second region of differential pumping for the pulsed beam expansion. Presently, there does not exist a third differential pumping region in the apparatus. Therefore, the entire MPI region consisting of the REMPI chamber, the TOF asymmetric double nipple (labeled number 17 in Figures 2-1 and 2-2), and the TOF flight tube (labeled number 19 in Figures 2-1 and 2-2) composed the second differential pumping region since these components were contiguous in the present experimental configuration.

To reduce oil background in the experiment, liquid nitrogen was used to cool the VHS-6 cryotrap. When liquid nitrogen cooling was employed, base pressures as low as 1.0×10^{-8} to 2.0×10^{-8} torr could be achieved. With no cooling of the VHS-6 cryotrap, the MPI region could typically attain a base pressure between 6.0×10^{-8} to 8.0×10^{-8} torr once the chamber had sufficiently outgassed. During the experiment when the pulsed valve was running, the MPI chamber maintained a base pressure of 1.0×10^{-6} torr.

The MPI region was designed such that ions formed by MPI could be vertically

extracted into the TOF mass spectrometer. In general, such a configuration has the advantage that the great majority of the gas pulse is not introduced into the TOF tube with each shot. Even in the present configuration where the entire MPI region consisted of a single differential region, much of the same advantage was gained since the extracted ions formed by MPI could be mass analyzed before the jet struck the back flange of the REMPI chamber. Hence, the base pressure within the TOF mass spectrometer tube was at its minimal level during the time window at which mass analysis was occurring.

In order to implement vertical extraction of ions formed directly by MPI, the NW-200 ISO port at the top of the REMPI chamber vertical tube was used to mate to a custom designed asymmetric double nipple (see Figures 2-72 through 2-75). The primary purpose of this piece was to both mount the TOF ion optics within the REMPI chamber (see Section 2.2.5.2), as well as to provide all of the electrical feedthroughs that were required to introduce the proper potentials to each of the ion optic elements. As is evident from inspection of Figures 2-72 through 2-75, the double nipple consisted of a 6.000" long, 4" nominal outer diameter tube with a standard rotatable 6" ConFlat flange welded to one end, and an extensively modified NW-200 ISO flange welded to the other. Figure 2-72 shows the bottom surface view of the NW-200 ISO flange that mated directly to the REMPI chamber. Through the center of the NW-200 flange was a 2.000" diameter hole that served as an opening between the REMPI chamber and the TOF tube. Around the central hole was a 4.000" diameter, 0.100" deep counterbore that served to key the top mounting plate for the TOF ion optics stack (see Figures 2-79 through 2-81) whose design will be presented in the following section. The ion optics mounting plate was

attached to the bottom surface of this flange via a set of four equally-spaced 10-32 UNF tapped holes placed within the counterbore on a 3.500" diameter bolt circle.

Surrounding this central counterbore were a set of 12 equally spaced electrical feedthroughs that were welded into place. In order to accommodate any experimental configuration that might be employed in the future, three different types of electrical feedthroughs were added in excess over what was required for the experiments described in this thesis. Seven high voltage SHV electrical feed connectors, three BNC electrical feed connectors, and two 50Ω electrical feed connectors were arranged as shown in Figure 2-72. In between several of the electrical feedthroughs were tapped eight holes for 8-32 UNC thread to a 0.300" depth. These tapped holes served to attach a set of stainless steel grounding pins (see Figure 2-76) that were designed to mate directly to standard Be-Cu "Push-On" electrical pin connectors. In this manner, reliable ground connections could be made to various components of the TOF ion optics stack.

A secondary function of this double nipple was to provide an easy means to work on the TOF ion optics assembly without having to significantly dismantle the MPI region to do so. Specifically, the entire TOF components labeled by numbers 16 through 20 in Figures 2-1 and 2-2 were designed to be lifted directly out of the REMPI chamber by a half-ton pulley mounted on the ceiling of the lab directly above the TOF tube. In order to attach these components to the pulley, four lift plates designed to connect to chains suspended from the pulley were welded directly to the outer tube surface of the asymmetric double nipple as shown in Figure 2-74. These lift plates were designed to support the weight of the entire TOF assembly. This design feature made maintenance of

the TOF ion optics particularly facile. To work on the ion optics, one needed only disconnect the six ISO double claw clamps securing the asymmetric double nipple to the REMPI chamber, and lift the whole assembly out above the REMPI chamber.

The 6" rotatable ConFlat flange attached to the opposite end of the asymmetric double nipple served to mount a 6" ConFlat electro-pneumatically controlled stainless steel gate valve (Varian), labeled number 18 in Figures 2-1 and 2-2. The purpose of this gate valve was to permit the REMPI chamber to be vented without having to expose the detector (labeled number 20 in Figures 2-1 and 2-2) mounted within the TOF tube (labeled number 19 in Figures 2-1 and 2-2) to atmosphere each time - thus extending the lifetime of the detector. This gate valve was interlocked to the Granville-Phillips 307 Vacuum Gauge controller in such a manner that if the ionization gauge monitoring the pressure within the REMPI chamber ever rose higher than 8.0×10^{-6} torr, this gate valve was immediately shut. This served to protect the detector from being accidentally exposed to high gas pressures during the course of an experiment while high voltage was being applied across the detector microchannel plates.

The final structural component of the MPI region was the TOF flight tube (see Figures 2-77 and 2-78). Along the lengthwise axis of the piece, the nominal outer tube diameter of the flight tube was designed to be 4", identical to the tube diameter of the asymmetric double nipple. At the end that mated to the 6" ConFlat stainless steel gate valve, a standard rotatable 6" ConFlat flange was welded in place. The opposite end of the tube was fit with a standard non-rotatable 6" ConFlat flange that was designed to mate to the microchannel plate detector flange that will be discussed later in Section 2.2.5.3.

The length of the flight tube was chosen such that the total distance between the ionization point at the center of the REMPI chamber and the front face of the microchannel plate detector was 1 m.

A number of additional ports have been added to the flight tube, although none is presently in use. On the end closest to the 6" ConFlat gate valve, a set of four 2-3/4" ConFlat ports have been placed symmetrically about the piece. Near the other end of the tube, two nominal 4" outer diameter tubes have been added on opposite sides of the flight tube. Each of these tubes has had standard non-rotatable 6" ConFlat flanges welded to the ends. Orthogonal to the 6" ConFlat ports have been placed two additional 2-3/4" ConFlat ports.

Eventually, the goal is to mount a turbopump off one of the 6" ConFlat ports so that the TOF tube can be maintained under active vacuum when the 6" ConFlat gate valve is shut, thus prolonging the lifetime of the microchannel plates. Nevertheless, experience with the apparatus has shown that the leak rate into the TOF tube with the 6" ConFlat gate valve shut was minimal even over several days. This was inferred from the fact that opening the 6" ConFlat gate valve while the REMPI chamber was pumping out in the $1x10^{-6}$ torr range did not cause the chamber pressure to rise. In fact, opening the gate valve sometimes served to lower the chamber pressure. Therefore, the installation of a turbopump has not been a priority.

2.2.5.2. Time-of-Flight (TOF) Ion Optics

Originally reported in a classic paper by Wiley and McLaren, time-of-flight (TOF)

mass spectrometry has evolved into one of the most extensively used techniques for mass analyzing ionic species.[29] The physical principles behind TOF mass spectrometry are quite easy to understand - essentially reducing to nothing more than the principle of conservation of energy. Mass separation is achieved in a TOF experiment by suddenly placing a packet of ions within a region of high electrostatic potential. In the experiments described in this thesis, this rapid ionization was accomplished by the multiphoton ionization of neutral cluster species formed within the supersonic expansion. If, to a first approximation, all of the ionic species that are created lie at the same electrostatic potential, then all species acquire the same potential energy independent of mass. The ions will then begin to accelerate down the potential difference, converting the initial potential energy to kinetic energy. However, since all ions begin with the same potential energy, they must all acquire the same kinetic energy within the acceleration region. If we consider two masses, m_h and m_l denoting a heavier mass and a lighter mass respectively, conservation of kinetic energy requires that

$$\frac{1}{2} m_h (v_h)^2 = \frac{1}{2} m_l (v_l)^2$$

where v_h and v_l denote the steady state velocity of the heavier and lighter mass respectively upon exiting the acceleration region. If after the initial acceleration region we allow the ions to travel in a field free region for a distance, d, we can calculate the arrival times for the ions at the point, d, using the relation $v = (d/t)$. Using algebra, we obtain the following relationships for the arrival times of the two ions:

$$t_h \propto (m_h)^{1/2} \text{ and } t_l \propto (m_l)^{1/2}.$$

In other words, ions of different mass will traverse the distance, d, with an arrival time that

is proportional to the square root of the ion mass. Therefore, lighter ions will arrive before heavier ones, which is intuitive since they acquire a higher terminal velocity following the acceleration region.

Part of the popularity of this technique derives from the ease with which TOF mass analysis can be implemented. For a straight MPI experiment where the ions are formed within a confined region of space no larger than the beam diameter of the ionizing laser, the demands on the design of the electrostatic ion optics are minimal. In particular, only three primary components need to be included - an ion extraction region that serves to inject the ion formed by MPI down the TOF flight tube, an einsel lens that will focus the ions onto the detector, and a pair of x-y deflectors that serve to deflect the ion flight path towards the detector. The remainder of this section is dedicated to outlining the design of the TOF ion optics that were employed for the experiments reported in this thesis.

As was alluded to in the previous section, the ion optics were designed to mount to the bottom surface of the asymmetric double nipple where they would extend into the point at which the MPI laser pulses crossed the molecular beam. A sectional view of the ion optics mounted to the asymmetric double nipple and subsequently housed within the REMPI chamber is presented in Figure 2-79. The center lines in Figure 2-79 intersect at the exact point where the MPI laser crosses the molecular beam within the REMPI chamber.

The ion optics assembly itself can be seen in Figure 2-80. The number labels in Figure 2-80 refer to the individual part numbers for the various components that are included as machine drawings in Figures 2-81 through 2-88. To ensure both maximum

versatility and variability in the ion optic components themselves, the majority of the ion optics assembly is constructed from standard "eV parts" purchased from Kimball Physics. The salient advantage of using eV parts is that they permit an enormous variety of reliable electrostatic components to be assembled quickly and accurately.

All of the machined components numbered in Figure 2-80 with the exception of Part #6 serve as a rigid support frame upon which the eV part ion optics could be installed. As is evident from Figure 2-80, the frame has been divided into an upper and lower section. The reason for this is that the eV parts were to be mounted on a set of four alumina tubes separated by appropriate alumina spacers (all purchased from Kimball Physics). Unfortunately, Kimball Physics did not manufacture alumina tubes longer than 6.000" in length, meaning that all of the ion optics could not be mounted off of a single set of four tubes. Rather, the ion optics assembly was divided such that the lower frame would mount the ion extraction region and the einsel lenses, while the upper frame would mount the x-y deflectors.

The entire frame consists of three mounting plates (Part #1, Part #2, and Part #3 in Figure 2-80) that are separated by two sets of four stainless steel posts (Part #4 and Part #5 in Figure 2-80). The posts have been staggered in such a way that when the ion optics assembly was installed, the posts of the lower frame interfered neither with the MPI laser beam path nor the molecular beam path. Each plate has a set of four 0.124" diameter, 0.100" deep counterbores, the top and bottom plates possessing a set in one of the surface faces and the middle plate having a complete set machined into both surface faces. These counter bores were designed such that four 6" long alumina tubes (Al_2O_3-

TU-C-6000, Kimball Physics) could be mounted into the lower frame (consisting of Part #2, Part #3 and Part #4 in Figure 2-80) in a completely externally supported manner. Likewise, the upper frame served to form an externally supporting housing for four 3" long alumina tubes (Al_2O_3-TU-C-3000, Kimball Physics). All of the mounting plates possessed a 1.700" diameter central hole. Furthermore, the top mounting plate has had an additional 2.000" diameter, 0.250" deep counterbore machined into the surface that seated directly against the asymmetric double nipple. Within this counterbore has been placed four 4-40 UNC tapped holes on a 1.950" diameter bolt circle. This has been designed such that a thin plate bearing a small diameter central hole can be mounted to the top of the ion stack. While such a plate was not in place during the experiments, this can serve in the future as a means to convert the TOF tube into a third differential pumping region in the event a turbopump is ever installed near the detector region.

The ion extraction region was designed with three electrostatic plates mounted near the base of the ion optics assembly. The lowermost element, the repeller, was a solid stainless steel plate (SS-PL-C7x7-B, Kimball Physics) that slip-fit without play onto the set of four alumina tubes. During the course of the experiment, the repeller was typically maintained at a +2.0 kV potential. Offset above the repeller by 0.500" via the use of an alumina spacer(s) was the middle extraction plate. The middle extraction plate was a stainless steel plate (SS-PL-C7x7-R1000, Kimball Physics) that possessed a 1.000" diameter hole in the center. Thus hole was covered by spot-welding a thin tungsten mesh (W-KG-060/002, Kimball Physics) over the opening to prevent any curvature of the electric field lines when voltage was applied to the plate. Potentials between +1.78 kV to

+1.85 kV were generally applied to the middle extaction plate to obtain optimal TOF performance. Offset from the middle extraction plate again by 0.500", the uppermost ion extraction element was identical to the middle extraction plate, and was likewise covered with tungsten mesh. This plate was directly grounded to the asymmetric double nipple using one of the custom made steel pins (see Figure 2-76). Effectively, the uppermost ion extraction element served as the ground plane for the ion extraction stack, signifying the terminal point of the ion acceleration region and the beginning of the ion field-free flight region. The entire frame assembly was designed such that when it was installed onto the asymmetric double nipple and lowered into place within the REMPI chamber, the ionization point would lie exactly in between the repeller and middle ion extraction element at the center of both plates.

In order to optimize the focus of the extracted ion on the surface of the microchannel plate detector, an einsel lens was also installed into the lower frame of the ion optics assembly. Each individual einsel lens consisted of a 1.000" outer diameter stainless steel cylinder (SS-CY-1000/1000, Kimball Physics) with a 0.050" wall thickness and a 1.000" length. In order to mount these onto the alumina tubes of the lower frame, each of the cylinders were spot-welded directly to a stainless steel plate with a 1.000" diameter central hole (SS-PL-C7x7-R1000, Kimball Physics) via the use of stainless steel mating rings (SS-WR-1000/031, Kimball Physics). The einsel lens elements were installed into the lower frame such that the initial opening lay 0.800" above the grounded ion extraction element, and each of the einsel components was offset from other by 0.025" using an alumina spacer. The upper and lower einsel lens elements were grounded directly

to the asymmetric double nipple using one of the custom made steel pins (see Figure 2-76). The central, focusing einsel lens element was typically set between +950 V and +1.1 kV during the course of an experiment depending upon the size of the cluster distribution that was being optimized.

The purpose of the upper frame was to house a set of x-y deflectors that would permit the extracted ions to be steered accurately to the detector. No completely satisfactory deflector element was deemed feasibile using solely eV parts, so the deflector elements were custom machined (see Figures 2-86 through 2-88). The deflector assembly consisted of three simple components, of which four complete sets were fabricated. The first was a mounting block (see Figure 2-86) that permitted the deflector assembly to be mounted directly onto the set of four alumina tubes housed within the upper frame. In addition, the mounting blocks were designed with a counterbored lip onto which a stainless steel right angle bracket (see Figure 2-87) was spot-welded into place. This right angle block served to couple the the mounting block to the deflector plate itself (see Figure 2-88) such that the delector plate was oriented parallel to the alumina tubes. Each deflector plate was mounted to the deflector assembly by spot-welding each plate directly to the right angle block.

Due to the fact that each deflector mount was designed to be secured within the upper frame by two of the four alumina tubes, a staggered configuration was required to mount each of the four deflector assemblies into the upper frame (see Figures 2-89 and 2-90). To achieve this, each deflector assembly was designed such that the right angle bracket was spot-welded to the deflector plate directly at its midline. The dimensions of

the deflector mounts were subsequently chosen to ensure that each deflector assembly was symmetrical with respect to inversion about a 0.100" wide alumina spacer. In other words, one set of two deflectors controlling one dimension of ion steering were mounted right-side up on two of the alumina tubes of the upper frame. Separated by a 0.100" wide alumina spacer, the other set of two deflectors controlling the orthogonal direction of ion steering was mounted upside-down on the alumina posts, 90° relative to the other two. Due to the symmetry of the deflector mounts, this ensured that all deflector plates were alligned perfectly at the midpoint of the upper frame as well as perfectly alligned orthogonal to each other with minimal separation between adjacent deflector plates.

Before assembling the complete ion optics assembly, the surface of each spot-welded component was smoothened using a fine grit emory paper to remove any sharp edges that might result in point regions of high electric field. Once all the ion optics were smooth, each component was coated with Aquadag (an electrically-conductive graphite coating) in order to ensure that the surfaces of each electrostatic element would remain at a constant potential in the event miniscule deposits of oil or other contaminents became deposited on the surface over time.

2.2.5.3. Microchannel Plate Detector Flange and Mass Gate Components

As shown in Figures 2-1 and 2-2, a detector (labeled number 20 in Figures 2-1 and 2-2) for the mass separated ions was placed at the end of the TOF field-free flight region. The detector used for the experiments described in this thesis was a dual microchannel plate (MCP) assembly (Detection Quality Long-Life Microchannel Plate Matched Set for

Chevron Assembly, Galileo). Each MCP had the following characteristics: 25 mm active area, 12 μm center-to-center distance, 10 μm pore diameter at a 12° bias. By purchasing the plates as a matched set, the bias current within the two plates was specified to be within 10%, thus ensuring an even potential drop across the two plates. Rather than design a custom housing, a standard MCP housing assembly was purchased (TOF-2003, Galileo) that was designed with a 50Ω co-axial anode as a fundamental design feature of the detector assembly. By impedance-matching the anode, the detector could exhibit a very fast response while at the same time all but eliminating interference from pulse reflections. Another convenient design feature was that the TOF-2003 housing was designed with a built-in female BNC connector at the end of the detector, rendering mounting of the MCP detector assembly exceedingly facile.

To mount the detector as well as to supply the required operating voltages for the detector assembly, a custom 6" ConFlat flange was fabricated that was subsequently referred to as the detector flange (see Figures 2-91 through 2-93). At the center of the detector flange, a 50Ω doubled-ended BNC matched-impedance connector was welded into place. As shown in Figure 2-92, the double-ended 50Ω connector was welded to the UHV side of the 6" ConFlat flange. This provided easy access to the BNC connector to which the TOF-2003 housing was mounted. In addition, six SHV and four BNC electrical feedthrough connectors were added to the detector flange as shown in Figure 2-92. One SHV feedthrough connector was used to supply the -1.5 kV to -2.0 kV bias voltage required at the MCP cathode. Furthermore, to enhance the collection efficiency of the electrons exiting the MCP stack, the anode of the MCP stack was typically biased to

-100 V, the voltage being supplied through one of the BNC feedthrough connectors. This bias served to maintain the acceleration of the electron packets in the free space region between the anode side of the MCP stack and the metal anode of the detector.

One negative feature of the TOF-2003 detector assembly was the fact that only a single BNC connection served to fix the detector to the detector flange. As a result, the detector was somewhat wobbly when mounted to the detector flange, and had a tendency to hang slightly crooked when installed free-hanging onto the TOF tube. A less than perpendicular interface between the cathode face and the incoming ion packets will reduce the efficiency of the detector since it serves to alter the ideal 12° bias of the individual channels within the MCP. Therefore, a spring-loaded alignment collar was designed for the TOF-2003 detector shield housing that permitted perfect axial alignment to be achieved along the axis of the detector. To mount this alignment collar, three additional 8-32 UNC tapped holes were added to the UHV side of the detector flange as shown in Figure 2-93. These three tapped holes served to mount three stainless steel posts (see Figure 2-98) that were secured to the detector flange by threading the wider 0.313" diameter end of the posts into 8-32 UNC set screws previously seated into the 8-32 UNC tapped holes. Once attached to the detector flange, the smaller 0.250" diameter ends of the three posts were fitted with homemade 0.250" inner diameter springs that possessed moderate spring tension. Finally, a custom designed plate (see Figure 2-99) was fit over the 0.250" diameter ends of three posts was seated directly against the springs. The central bore of this plate was designed to fit directly against the conical shield of the TOF-2003 detector housing. Therefore, when the detector was installed onto the 50Ω BNC

connector of the detector flange, the conical shield of the detector housing lightly pressed the plate against moderate spring tension. This enabled the detector housing to be precisely aligned within the central bore of the plate, ensuring that the alignment of the detector was perfectly straight.

In addition, another thin stainless steel plate was mounted to the ends of the posts which lay within a centimeter of the surface of the MCP cathode. The purpose of this plate, besides securing the ends of the posts into a rigid assembly, was to provide a ground plane above the MCP detector to prevent any incursion of the MCP electric field lines into the field-free flight region of the ions. This plate possessed a 1.000" diameter central orifice that exposed the entire active area of the MCP. Tungsten mesh was then used to cover this orifice to ensure minimal penetration of the electric field through the hole. Furthermore, the tungsten mesh helped to maintain regular parallel field lines between the cathode of the MCP and the plate, creating an even acceleration region for the incoming ions that assisted in their efficient collection.

The final component of the machine in its present configuration was the mass gate. Little more than glorified deflectors, a typical mass gate is a pair of small parallel plates or wires that are placed within the TOF field-free flight region such that the extracted and focused ion beam passes in between these two electrostatic elements. Their purpose is to permit the selective detection of specific ion(s) to the exclusion of all others, thus greatly simplifying the observed mass spectrum as well as reducing wear on the MCP. The manner in which this is done is simple, and involves the use of narrow pulsewidth, high voltage pulses applied across the mass gate electrostatic elements. By briefly pulsing a

high voltage DC field to ground (or vice versa) across the mass gate electrostatic elements, one acquires the ability to deflect a pre-determined subset of ions away from striking the detector.

The mass gate constructed for the machine was a simple design (see Figures 2-94 through 2-97), consisting of a mounting frame and two electrostatic deflector elements. One consideration in designing the mass gate was to make the mounting frame as versatile as possible for future applications. In particular, both the front plate (see Figure 2-94) and the rear plate (see Figure 2-95) of the mounting frame have been designed with hole patterns matching those from Kimball Physics "Class C" eV parts. Consequently, the mass gate frame is well suited to serve as a platform upon which additional electrostatic elements can be readily added in the future.

Both mounting plates were machined with a 0.500" diameter central orifice that permitted the passage of the ions through the mass gate. These central holes were purposely left large so that ions formed from unfocussed MPI laser pulses could be efficiently collected without losing ions due to collisions with the front plate. The mass gate deflector elements were composed of two stainless steel bars, into which two 0.124" diameter holes were machined at a separation of 1.200" center-to-center. These dimensions match those for Kimball Physics "Class C" eV parts, enabling these two bars to be mounted directly adjacent to the central orifices of the front and back mounting plates.

To assemble the mass gate, a 1.000" long "Class C" alumina rod (Al_2O_3-RO-C-1000, Kimball Physics) was inserted through the mass gate deflectors. Next, 0.075" long

alumina spacers was added over each end of the alumina rods such that each surface of the mass gate deflectors had a single spacer positioned adjacently. The two spacer-deflector-spacer assemblies supported by the alumina rod were then sandwiched between the front and back mounting plates - the alumina rods passing through the Kimball Physics "Class C" hole pattern on both faces. The alumina rod was then held loosely in place by adding an external retaining ring around each end of the alumina rods that extended outward from the front and back plates. This served to prevent the alumina rods from sliding out. Finally, the front and back mounting plates were rigidly bolted together using four 0.500" long stainless steel 4-40 UNC standoffs that spanned four through-holes machined into both mounting plates on a 2.150" diameter bolt circle.

The entire mass gate assembly was mounted at the end of a set of three 6.075" long stainless steel posts (see Figure 2-97). The opposite end of this post was joined to the end of the stainless steel post mounting the MCP ground plate (see Figure 2-98) via set screws that were seated into the latter post. As a result, the MCP ground plate became sandwiched between the ends of the two posts. The mass gate assembly was then mounted to the other end of the 6.075" long stainless steel posts, creating a rigid frame whose total length projected almost a foot from the surface of the detector flange. The length of the posts separating the MCP ground plate and the mass gate assembly was chosen such that when a 500 V potential difference was applied across the mass gate electrostatic elements, all ions would be deflected sufficiently as to miss striking the surface of the MCP detector.

2.3. Experimental Methodology Overview

An overview of the experimental methodology as well as the hierarchical flow of control between the various experimental components is shown in Figure 2-100. Briefly, the effective time zero of the experiment was defined by the opening of the piezoelectric pulsed valve. The pulsed valve was run at a frequency of 19 Hz with a typical backing pressure of 8 - 10 atm of pure argon gas. Following injection of each gas pulse, a focused 355 nm laser pulse was fired onto the surface of an aluminum laser vaporization target rod just as the gas pulse reached the region within the source at or adjacent to the ablation point. The resultant plasma was subsequently entrained within the gas and cooled by supersonic expansion into a high vacuum environment, generating a wide distribution of $Al{\bullet}Ar_n$ van der Waals clusters.

The resultant molecular beam was then skimmed using a 3 mm orifice diameter skimmer, and allowed to drift into the region between the repeller and middle ion extraction plates that were maintained at DC voltages of +2.0 kV and approximately +1.8 kV to +1.85 kV respectively. As the molecular beam traversed over the center point of the ion extraction plates, the molecular beam was crossed with the output of the MPI pumping laser. The MPI pumping laser was a Nd:YAG pumped dye laser system that was equipped with doubling (doubled dye), mixing (dye output plus Nd:YAG fundamental), and mixing after doubling (doubled dye plus Nd:YAG fundamental) capabilities. Consequently, the MPI pumping laser was, for the most part, continuously tunable over a wavelength range spanning 844 nm to 248 nm.

Molecular species with the beam that possessed resonant spectral features at the

MPI pump wavelength were directly ionized by the absorption of two or more photons. The generated ions were then extracted into the 1 m field-free flight region of the TOF mass spectrometer after an initial acceleration region of approximate 0.750" that provided each ion with a kinetic energy of approximately 1.92 keV. During the field-free flight region, the ions became spatially separated, thus generating unique ion packets consisting of single mass species. Due to the separation in mass, each ion packet of unique mass likewise acquired a unique temporal arrival time at the detector, the lighter masses preceding the heavier ones. The ion packets were detected using a dual-microchannel plate detector to produce a mass spectrum showing the ion distribution as a function of arrival time. A characteristic TOF mass spectrum showing the $Al{\bullet}Ar_n$ cluster distributions that could be observed from the laser vaporization source is shown in Figure 2-101. Particularly noteworthy was the absence of any $Al_2{\bullet}Ar_n$ species or any other higher aluminum multimeric species bound to Ar_n clusters. TOF mass spectra obtained during the course of the experiments described in this thesis exhibited cluster distributions that commonly spanned sizes corresponding to the closing of the second icosahedral solvent shell (see Figure 2-101).

Following two stages of amplification, the signal was introduced into two separate gated integrators (SRS SR-250). These gated integrators could be used independently to gate two different masses, or in tandem - one gated integrator monitoring the signal from a specific mass while the other monitored the baseline directly preceding this mass signal. The latter approach was particularly useful when scanning larger cluster sizes since substantial ion backgrounds were typically observed that derived from the slow tails of the

preceding lower mass species. The output of each gated integrator was then sampled electronically and recorded by an A/D converter (DAS-1600, Keithley-Metrabyte). Three inputs were sent to the DAS-1600 A/D converter - two data inputs derived from the two SRS SR-250 gated integrator units and one derived from a homebuilt gated integrator that served to measure the power of the MPI laser (see Figure 2-100). Finally, the digitized data was compiled by a data aquisition program (DYEDATA) and stored in file format for subsequent analysis.

The remainder of this chapter relates the specific details of the various experimental components outside of the apparatus itself.

2.3.1. The Gas Inlet System

In order to control the gas flow to the pulsed valve, a stainless steel gas manifold was constructed using a combination of stainless steel pipe fittings, Swagelock fittings, and VCR fittings. As shown schematically in Figure 2-100, there existed two ways by which the argon carrier gas could be introduced into the pulsed valve. The first was by directly connecting the regulated output of a gas cylinder to the gas manifold. This was particularly convenient when only a single gas was to be used for the experiment since the only limitations on the backing pressure were due solely to the specifications of the gas regulator itself.

In addition, two individual mass flow controllers (825-B, Edwards) were added to the gas manifold, separated from the main body of the manifold by Nupro valves, in the event that an exact pre-set ratiometric mixture of gases was to be employed for the pulsed

beam expansion. The flow through these two mass flow controllers was determined by a two-channel flow controller (Model 1605, Edwards). Each channel internally controlled the flow through a single 825-B controller. As a result, ratiometric flow was determined by setting the relative flow rate between the two channels such that the desired gas ratio was achieved.

There were limitations, however, with the use of the mass flow controllers. Foremost was the fact that only narrow ranges of backing pressures and flow rate could be attained. This was due to the fact that the 825-B controllers can be fitted with only a specific orifice size. Since each individual orifice was expensive, only two orifices have been used. The 825-B controllers were shipped with "G1-Type" orifice (Edwards) with the following characteristics: 0.007" orifice diameter, 20 - 65 PSI upstream pressure range, and 100 scc/m flow rate. These orifices were incapable of supporting the 8 - 10 atm backing pressures typically used for the experiments, and were therefore mostly ineffective for the purposes of these experiments. During the course these experiments, the G1 -Type orifices were removed from both of the 825-B controllers and replaced with an alternate orifice, namely an "H-type" orifice (Edwards). The H-Type orifices were rated with the following characteristics: 0.004" orifice diameter, 65 - 95 PSI upstream pressure range, and 100 scc/m flow rate. While the maximum pressure that these orifices could withstand was 6.46 atm, it was nevertheless found that the flow rate through these orifices was insufficient to supply a sufficient flow of gas to the pulsed valve at the maximum pressure. In fact, one would observe that the pulsed valve pressure would drop during the course of the experiment since the flow rate of the gas released from the pulsed

valve exceeded that supplied by the 825-B controller with the H-Type orifice. Ultimately, the poor functioning of the mass flow controllers at high backing pressures combined with the helium and neon incompatibility problem with the piezoelectric element used to actuate the pulsed valve (see Section 2.2.3.1) left little need to employ the mass flow controllers.

All of the spectra presented in this thesis were taken by using pure argon expansions that were obtained by connecting the regulated flow from an argon tank directly to the gas manifold. While backing pressures of 8 - 10 atm were commonly employed, the cluster distributions obtained from the laser vaporization source appeared fairly insensitive to backing pressure. Nevertheless, slightly more stable source behavior was observed using higher backing pressure, hence motivating their use.

In order to monitor the pressure of the gas within the gas manifold, a pressure transducer (MKS Baratron capacitance manometer, 0-10,000 torr range, model 122AA-10000BB) was connected to a homebuilt circuit and LED display. Furthermore, the gas manifold was connected to a 6 cfm mechanical pump (Alcatel 2008) via a Nupro valve to evacuate the gas line when necessary, as well as a thermocouple gauge (DST-531, Duniway Stockroom) to monitor the vacuum pressure.

2.3.2. The Laser Systems

In the present experimental configuration, two separate laser system have been employed. The first system was solely dedicated to the laser vaporization source, and whose focused output was used to ablate the target material within the source. The second laser used for these experiments was a scanable system that served to generate the

tunable MPI pump pulses. The specific performance details of these systems as well as the manner in which wavelength selection was achieved is the subject of the following two sections.

2.3.2.1. Laser Vaporization Laser

Almost any laser system that can supply at least a few mJ per pulse of power can most likely be successfully utilized as a laser vaporization laser. Nevertheless, there exists a fair amount of anecdotal evidence in the chemical physics community that the beam profile of the laser ablation laser employed can have a marked effect on the source performance. For whatever reason, inhomogeneous beam profiles such as those produced by excimer laser are purported to result in poor ablation of the target surface, tearing the surface material rather than creating a clean pit from which the surface material has been completely removed. On the other hand, Nd:YAG lasers, with their highly gaussian beam profiles, have been observed to produce both effective and stable laser ablation sources. Furthermore, the surface damage produced by a Nd:YAG tends to exhibit tiny circular pits from which the material has been cleanly removed. For this reason, as well as their now very reasonable cost, Nd:YAG lasers have become one of the more popular lasers used for laser ablation.

While use of Nd:YAG lasers has become routine, there is little consensus as to which Nd:YAG harmonic yields the best laser ablation source. A great number of laboratories have successfully implemented 532 nm (Nd:YAG second harmonic) ablation. This method has a several obvious advantages, most notably eye visibility, high power,

and low cost since only a single doubling crystal needs to be purchased. However, a number of laboratories have shown a strong preference for the third harmonic (355 nm) and fourth harmonic (266 nm). One of the motivating forces behind the use of these higher harmonics is the empirical belief that use of UV ablation pulses not only efficiently remove material from the target surface, but also serves to photodissociate any resultant multimeric target atom species within the plasma via multiphoton absorption. In the end, choice of Nd:YAG harmonic remains a primarily subjective choice, dependent upon the type of source voodoo one prefers.

Drawing from the experience of others, a Nd:YAG laser (Surelite I, Continuum, 20 Hz rep. rate) was chosen as the ablation laser for these experiments. In addition, a temperature-stabilized harmonic generation crystal housing (HG4-B, Quanta-Ray) was purchased into which was installed crystals for second, third, and fourth harmonic generation. For all the experiments performed to date, the third harmonic (355 nm) has been used for the laser vaporization source. The 355 nm light was produced first by doubling the Nd:YAG fundamental to generate 532 nm light, then mixing the 532 nm light with Nd:YAG fundamental in a second crystal to generate the desired 355 nm output. The different harmonic generation crystal types as well as the resultant output powers and polarizations for each crystal are summarized in Table 2-1.

Upon exiting the harmonic crystal housing, the desired 355 nm light was strongly contaminated with residual 1064 nm and 532 nm light that exists collinear with the 355 nm output. In order to separate out the 355 nm light from the residual wavelengths, the output from the crystal housing was reflected off two high power dielectric mirror (R_{max}

355 nm, T_{max} at 1064 nm and 532 nm). Both harmonic separators serve to reflect approximately 99.5% of the 355 nm light while transmitting a high percentage of the 1064 nm and 532 nm light. After two stages of reflection off the high power dielectric mirrors, most of the residual 532 nm and 1064 nm light was successfully removed from the 355 nm beam. However, the remaining 532 nm and 1064 nm components were sufficiently diverged from the 355 nm beam at a point approximately one foot in front of the last mirror. As a result, an adjustable iris could be employed to pass the 355 nm while completely blocking the remaining 532 nm and 1064 nm components.

With the 355 nm clear of contaminating wavelengths, the laser vaporization pulse was transferred from the laser table up to a second aluminum breadboard platform that was positioned directly adjacent to the source cross of the machine. This was accomplished by the use of a periscope that consisted of two high power dielectric mirrors - the lower one mounted at level of the beam on the laser table and the upper one mounted on the breadboard at the exact height of the laser inlet channel positioned within the laser vaporization source.

Early on, the power of the laser vaporization pulse was adjusted by increasing the delay between the flashlamp firing time and the Q-switch actuation time away from the optimal timing. By doing this, however, one ran the risk of degrading the output beam profile of the Nd:YAG, resulting in inhomogeneous 355 nm beam profiles. For this reason, an alternate means to control the 355 nm power was sought that would permit the Nd:YAG to be operated at its optimal performance level. To achieve this goal, two additional optics were installed onto the breadboard platform directly following the upper

periscope mirror. The first was a multiple order quarter wave plate (QWPM-355-05-4, CVI) mounted in a rotatable housing, followed by thin film plate polarizing beam splitter (TFP-355-RW-28.6-14.3-3.2-UV, CVI) that was mounted at an angle of approximately 56° relative to the direction of beam propagation. The thin film plate polarizing beam splitter was aligned such that in the absence of the quarter wave plate, the horizontal polarization of the incident 355 nm laser vaporization pulse would be essentially completely passed to the source. Installation of the quarter wave plate prior to the thin film plate polarizing beam splitter enabled adjustable reorientation of the incident horizontal polarization to variously degrees of ellipticity. All vertically polarized light was directly reflected by the thin film plate polarizing beam splitter out of the incident beam into a beam block. In essence, by rotating the quarter wave plate, one could adjust the amount of 355 nm light that could be transmitted into the source in a continuously variable manner.

Once the amount of 355 nm light was selected, the incident laser vaporization pulse was focused into the source chamber using a 700 mm focal length suprasil lens (CVI). While optimizing the laser vaporization source, it was found that placing the focal length directly on the ablation target yielded poor source performance. Instead, the focal length was generally set such that it lay to the far side of the laser vaporization source. In general, there was a limit to how far away the laser could be focused beyond the source without a large degree of the incident pules being clipped by the inlet channel within the source itself. Nevertheless, the focal length was typically chosen to lie within a few inches of the far-side NW-250 ISO flange on the opposite side of the source cross relative to the

breadboard platform. Once passing through the focusing lens, the incident 355 nm laser vaporization pulse was transmitted into the source chamber through a 2.000" diameter, 0.250" thick uncoated suprasil window (Asco) mounted to the NW-250 ISO flange on the near-side of the source cross relative to the breadboard platform.

2.3.2.2. MPI Laser System

A multi-stage laser system was employed to generate the visible and UV laser pulses required for the MPI detection of the species within the molecular beam. The primary component was a Nd:YAG laser (NY61-20, Continuum) that served as the pump laser for the entire MPI laser system. The NY61-20 system also contained crystals for second and third harmonic generation that were mounted internally. These crystals were mounted in motor controlled housings that could be translated in and out of the 1064 nm output path at will, enabling the NY61-20 to serve as a versatile source of 532 nm and 355 nm pump energies. The resultant output powers and polarizations for the pump wavelengths attainable with the NY61-20 system are summarized in Figure 2-103. Furthermore, this laser was also equipped with an injection seeder that proved difficult to stabilize and hence was not employed during these experiments. While this did not have any effect on the ultimate resolution of the tunable MPI pulses, use of the NY61-20 in the unseeded mode would result in an approximately 10% decrease in output power.

The 532 nm output from the NY61-20 system was used to pump a dye laser system (TDL-51, Continuum/Quantel), thus providing tunability across the visible wavelength range from 844 nm to 532 nm. All of the dyes used for these experiments

were purchased from Exciton, and all were used as straight methanol solutions. To cover the visible wavelength ranges required to generate MPI pulses of the appropriate energy for these experiments, five different dyes or dye mixtures were employed - DCM, Rhodamine 640, Rhodamine 640/Rhodamine 610 (50:50 mixture), Rhodamine 610, Rhodamine 610/Rhodamine 590 (50:50 mixture), and Rhodamine 590 (Rhodamine 6G). The use of these dye permitted the following nominal dye fundamental wavelength ranges to be accessed: 676 nm - 607 nm (DCM), 630 nm - 605 nm (Rhodamine 640), 629 nm - 594 nm (50:50 Rhodamine 640/Rhodamine 610), 607 nm - 581 nm (Rhodamine 610), and 599 nm - 576 nm (50:50 Rhodamine 610/Rhodamine 590). While the quoted ranges were the dye tuning ranges reported by the specification sheets provided by Continuum, practical experience showed that the actual useable dye tuning ranges were typically much narrower, especially to the blue end of the tuning curve.

To generate the output pulses, the TDL-51 dye laser employed a Moya cavity oscillator, followed by two stages of amplification. Wavelength tunability was achieved by the use of a grating (2400 lines/mm) housed within the oscillator opposite to the output coupler. The grating was rated to provide a wavelength resolution of 0.08 cm^{-1}. The positioning of the grating was controlled by a stepper motor whose motion was controlled by a proprietary program provided by Continuum. Originally, the computer control was interfaced to the stepper motor by a card housed inside of an IBM PC-AT computer. Unfortunately, replacement parts for a PC-AT computer are almost impossible to obtain anymore, making repair difficult. For this reason, the motor driver card was installed into an IBM 486 computer. Since the original software was not compatible with the IBM 486,

a new program needed to be obtained from Continuum that was custom written for the purpose.

In order to calibrate the wavelength of the TDL-51 dye laser system, a number of approaches were used depending upon the wavelength range of the dye being used. Whenever possible, MPI detection of atomic aluminum transitions were employed as extremely accurate wavelength standards. For wavelength calibration within the DCM and Rhodamine 640 wavelength regions, the atomic Al($3d$) ← Al($3p$) transitions were employed.

$$^2D_{3/2} \leftarrow {}^2P_{1/2} \text{ at } 32435.45 \text{ cm}^{-1}$$

$$^2D_{5/2} \leftarrow {}^2P_{3/2} \text{ at } 32324.75 \text{ cm}^{-1}$$

$$^2D_{3/2} \leftarrow {}^2P_{3/2} \text{ at } 32323.41 \text{ cm}^{-1}$$

These transitions were easily saturated, so calibration scans were performed with the doubling crystal substantially detuned from the optimal doubling orientation. Even in cases where the UV was barely visible on a white card, the atomic aluminum transitions were very easily observed.

Calibration within the 50:50 Rhodamine 640/Rhodamine 610 mixture wavelength range was performed using the atomic Al($4p$) ← Al($3p$) transitions via two-photon excitation.

$$^2P_{3/2} \leftarrow {}^2P_{1/2} \text{ at } 32965.67 \text{ cm}^{-1}$$

$$^2P_{1/2} \leftarrow {}^2P_{1/2} \text{ at } 32949.84 \text{ cm}^{-1}$$

$$^2P_{3/2} \leftarrow {}^2P_{3/2} \text{ at } 32853.63 \text{ cm}^{-1}$$

$$^2P_{1/2} \leftarrow {}^2P_{3/2} \text{ at } 32837.80 \text{ cm}^{-1}$$

With high dye power, these transitions could be observed without the aid of a focusing lens. In cases when the power was sufficiently low, a 150 mm focal length lens was employed to drive the two-photon transitions.

Unfortunately, no atomic aluminum transitions were available within the wavelength range covered by the Rhodamine 610 and 50:50 Rhodamine 610/Rhodamine 590 mixture dye tuning ranges. Instead, these two dye ranges were calibrated against the transitions of the sodium D lines that were conveniently positioned (in air) at 589.5924 nm and 588.9950 nm. To accomplish this calibration, the output from a sodium lamp was focused onto the entrance slits of a Jarrell-Ash 0.5 m monochrometer. The grating was then adjusted to one of the two maximum intensity positions of the sodium D line transitions. After significant power attenuation, the straight output of the dye laser was likewise introduced into the monochrometer with the grating angle previously set by the sodium lamp. The dye laser grating was then adjusted until the output wavelength of the dye laser was coincident with one of the two sodium transitions. Conveniently, the presence of the other sodium transition provided a convenient check that the proper calibration had, in fact, been attained.

The master control over the scanning of the TDL-51 dye laser was provided by the DYEDATA program (Borland Turbo Pascal 7.0), which was a slightly modified version of the OPODATA data acquisition program written by a previous Okumura group graduate, Yi Bin Cao. This program was interfaced to the TDL-51 stepper motor program such that control of the grating was controlled by the DYEDATA program during a scan. If, however, one merely wanted to move the stepper motor to change the

dye laser output, this could be achieved independent of the DYEDATA program via the IBM PC-AT (now IBM 486). It is important to note that all calibration corrections to the stepper motor position must be entered via the stepper motor control program on the IBM PC-AT (now IBM 486). In addition, since slight deviations in the calibration were periodically observed, the calibration was checked several times during a period of scanning to ensure accurate peak positions were recorded. The exact origin of this problem remains mysterious, but probably represents an occasional malfunction in the grating stepper motor or an error in communication between the grating stepper motor and the interface card/computer controlling the motion.

In addition to the tunable visible capabilities, the TDL-51 laser was outfitted with a UV extension system (UVX-3, Continuum) that permitted almost complete access into the UV down to 248 nm. Generation of the UV light was achieved in one of three manners - straight doubling of dye fundamental (doubled dye), mixing (dye fundamental plus Nd:YAG fundamental), and mixing after doubling (doubled dye plus Nd:YAG fundamental). For the experiments presented in this thesis, straight doubling of the dye fundamental was employed using a DCC-2 (Continuum) or DCC-3 (Continuum) doubling crystal. Use of the DCC-2 crystal provided continuous wavelength coverage from the 365 nm to 295 nm range, while the DCC-3 crystal provided coverage in the 295 nm to 267 nm range. A summary of the crystals that can be presently employed with the UVX-3 system as well as the details of the output power and polarization requirements have been compiled in Table 2-2.

The crystal orientation of the UVX-3 systems was designed with an autotracking

controller that was supposed to maintain the proper crystal angle for maximum UV conversion during the course of the scan. Efforts to successfully implement the autotracker were hindered by the overall poor design of the TDL-51/UVX-3 system. In particular, the single prism that was employed to introduce a small amount of light into the tracker housing containing the photodiodes that determined the crystal positioning was mounted on a rigid stage that permitted essentially no play in the x, y, or z directions. Furthermore, due to the cramped nature of the design, a different mount could not be installed to correct for this design flaw. The best that could be done was to re-seat the prism on top of a mound of glue and hope that the proper position could be attained after the glue was set. The only problem was that if the laser alignment was at all adjusted through the UVX-3 system, this prism needed to be re-seated. Due to the troublesome nature of this aspect of the autotracker design, autotracking control of crystal orientation was abandoned in favor of manual tracking. In this manner, the crystal orientation was adjusted by hand by actuating switches that served to rotate the crystal orientation in either a clockwise or counterclockwise manner. By monitoring the power of the MPI pulse upon exiting the REMPI chamber, constant accurate adjustments to the crystal orientation could be achieved so that the maximal power was obtained.

Once the proper MPI wavelength had been attained, a periscope consisting of two suprasil, uncoated prisms (0.5" side, CVI) was employed to bring the MPI pulse from the laser table up to a second aluminum breadboard platform that had been installed adjacent to the REMPI chamber. The height and position of the upper prism of the telescope was fixed such that the incident laser pulse exited the prism exactly horizontal to the molecular

beam. The MPI pulse was then introduced through the REMPI chamber via two specialty herasil windows that were mounted on a custom designed compression port (see Section 2.2.5.1). The MPI laser was aligned such that the ionization point region within the molecular beam occurred very close to the center of the repeller and middle ion extraction plates of the TOF ion optics assembly. In the event that the MPI pulse required focusing, especially in situations where non-resonant MPI approaches were being employed, a 150 mm focal length lens was installed. The power of the MPI laser was monitored using a power meter whose output was amplified and integrated using a homebuilt gated integrator (see Figure 2-100).

2.3.3. Electronics and Data Acquisition

As is shown by the experimental schematic presented in Figure 2-100, temporal control over the various components used in the experiment was organized around three digital delay generators (DDG). The first DDG (SRS DG-535, Stanford Research Systems) labeled by the name "Master" in Figure 2-100 served to coordinate all of the timing of the experiment. The master DDG was internally set to generate the 19 Hz repetition rate that was employed in these experiment. Originally, the experiment was run at 20 Hz to match the ideal repetition rate of both laser systems. Unfortunately, by running at an even factor of the 60 Hz noise (that was quite substantial in the lab), the data acquisition system was observed to exhibit sympathetic oscillations that were in phase with the 60 Hz noise. By running the experiment (including the lasers) at 19 Hz, these oscillations were essentially eliminated due to destructive interference.

The internally generated 19 Hz repetition rate of the master DDG served to set the time zero (T_0 in Figure 2-100) for each cycle of the experiment. In addition to setting the T_0, the master DDG controlled the timing of the following components: the pulsed valve opening, the trigger of the homebuilt gated integrator that measured the power of the MPI laser, and the trigger of the A/D board of the data acquisition system. Two additional DDGs were synchronized to the T_0 generated by the master by external triggering. These two DDGs (SRS DG-535, Stanford Research Systems and Model 9650, EG&G Princeton) labeled by the term "Slave" in Figure 2-100 served to control the timing of the remaining experimental components in addition to those controlled by the master DDG.

As is evident from Figure 2-100, each of the slave DDGs were dedicated to primarily a single task. The slave SRS DG-535 DDG controlled the timing of the flashlamp firing time and the Q-switch actuation time for both the laser vaporization system and the MPI system. The other slave DDG, the EG&G model 9650, served the primary purpose of triggering the two gated integrators (SRS SR-250, Stanford Research Systems) that measured the signal amplitude from a feature derived from the TOF mass spectrum. In theory, such triggering should not be required. The SRS SR-250 units have a built-in gate delay such that one could trigger each gate with the MPI laser Q-switch that serves as the time zero for the TOF mass spectrum. This was in fact what was done for quite some time. However, during the course of optimizing the MPI experiment and in particular trying to generate a reproducible baseline signal, it was found that use of the gate delay controller inherent to the SRS SR-250 units introduced a variable DC offset that scaled with the size of the delay. The best baseline signal was obtained by using the

smallest possible delay time (1 ns) on the SRS SR-250 units, a fact that required that each be triggered separately in order to be able to selectively gate a specific feature in the mass spectrum.

In order to obtain the best possible data from the experiments, a great deal of time was invested to optimize the entire data acquisition system. During the course of this effort, two major problematic features were uncovered in the original data acquisition configuration, both of which revolved around the insufficient line-driving capabilities of the various components along the data acquisition hierarchy. The first involved using the output of the primary pre-amp directly following the MCP to drive the 50Ω inputs of the SRS SR-250 gated integrators as well as the oscilloscope input. While in theory the pre-amp was rated for such a task, this proved not to be the case. Much better performance was achieved by placing a secondary x5 pre-amp (SRS Model SR-445, Stanford Research Systems) before each of the gated integrators individually. These secondary pre-amps served the dual role of providing an additional stage of signal amplification before integration as well as serving as a line driver for the gated integrator input. The use of the secondary pre-amps coupled with triggering each gated integrator separately dramatically improved the quality of the data obtained from the gated integrators.

The second pitfall that was uncovered during the course of optimizing the data acquisition systems was the fact that the current-providing capabilities of the SRS SR-250 gated integrator outputs was lower than had been anticipated. As will be detailed below, the gated integrators were often used in a mode where the experiment was run at half the repetition rate of the gate trigger - a method that was termed "Flip-Flop Mode." By doing

this, one can take advantage of the active baseline subtraction feature of the SRS SR-250 unit that will automatically take the difference of the integrated signal between every two shots. Unfortunately, this baseline subtracted averaged output (derived from the "Average Output" BNC port) possessed only a 10 mA drive capability with which to drive the inputs of the DAS-1600 A/D board. Previously, the BNC inputs to the A/D board had been impedance-matched to 50Ω. This 50Ω impedance input, however, exerted too great of a load on the gated integrator output, causing a high degree of inconsistency in the resultant data. This was ultimately solved by changing the input impedance of the DAS-1600 A/D board to 1kΩ. The apparent impedance mismatch introduced by this modification was observed to have no noticeable negative effect on the data obtained - in fact, dramatic improvements were noted.

As was alluded to above, there were two modes in which the experiments could be run. The first was the standard mode when all experimental components were run at 19 Hz. This method had the obvious advantage that data could be collected at the maximum possible repetition rate. Less obvious, at least initially, was the fact that this method provided little discrimination between true signals and background signals when the signal one sought to detect was weak in intensity. The origin for this observation derived from the fact that even by using liquid nitrogen cryotrap cooling in the REMPI chamber, a weak background due to ionized oil fragments was always present. For strong signals, the oil background was of minimal concern. However, with a weak feature, there were often either oil features directly coincident with the desired mass, or very close in proximity. This problem was further aggravated by the fact that detection of weak signals required

higher MCP detector voltages, which in turn served to greatly amplify the oil background.

In order to deal with weak signals as well as situations where accurate baseline determination was critical, an additional powerful feature inherent to the SRS SR-250 gated integrators was exploited. Specifically, the SRS SR-250 possessed a built-in averaging capability that serves to subtract every other sample from the moving average. In order to implement this method of data acquisition, however, the frequency of the laser vaporization laser needed to be triggered at half the frequency of the MPI pump laser. In effect, this served to generate an oil background mass spectrum with every shot of the MPI laser, but a signal spectrum only on alternate shots. In this manner, the subtraction of every other sample by the SRS SR-250 gated integrator from the moving average would serve to subtract out the oil background, but at the cost of doubling the data acquisition time.

The SRS SR-250 gated integrator can be set to run in this mode by changing the average switch on the upper left of the back panel from "normal" to "toggle." Changing to toggle mode has an additional benefit as well - the SRS SR-250 has a BNC output on the back that toggles between a DC voltage of 0 V and + 2 V with each trigger. Nominally this feature serves as a convenient means to interface the unit with unipolar A/D converters. However, this feature can also be exploited as a means to generate a triggering rate at half the frequency of the triggering rate of the SRS SR-250 unit itself - a fact that proved quite useful in triggering the laser vaporization laser at half-frequency. Specifically, a "NAND" gate was designed whose two inputs were the Q-switch trigger for the laser vaporization laser and the toggle voltage from the SRS SR-250 unit. The

output of this NAND gate was positive only on alternate shots since the toggle voltage is essentially toggling between a high and low state with each trigger. By using the output from this NAND gate to trigger the Q-switch for the laser vaporization laser, an operational mode was achieved whereby the flashlamps could be run at the normal 19 Hz frequency while only the Q-switch was actuated at half frequency. This mode of operation was named "Flip-Flop Mode."

Switching between the regular 19 Hz mode of operation and flip-flop mode was simple. When in 19 Hz mode, the polarity control on the rear panel of the SRS SR-250 unit was set to normal, and the output from the gated integrators was taken from the "last sample" BNC on the front of the unit. In this case, the laser vaporization laser Q-switch trigger from the DDG was connected directly to the external triggering BNC of the laser vaporization laser, completely bypassing the NAND gate. To switch over to flip-flop mode, the polarity control on the rear panel of the SRS SR-250 unit was set to toggle, and the output of the gated integrators was taken from the "averaged output" BNC connector on the front of the unit. In order to implement the NAND gate, one BNC cable is used to connect one of the inputs to the "active baseline subtraction" BNC connector on the rear panel of the SRS SR-250 unit while the other input was connected directly to the DDG Q-switch trigger for the laser vaporization laser. The output of the NAND gate was then connected directly to the external Q-switch triggering BNC of the laser vaporization laser.

To monitor the acquired TOF mass spectra during the course of the experiment, the amplified signal from the microchannel plate detector was sent to an oscilloscope (Model TDS320, 2 Channel, 100 Mhz, 500 MS/s, Tektronix). The input signal was

typically taken in parallel from one of the inputs of one of the SRS SR-250 gated integrators. The trigger for the oscilloscope was derived from the Q-switch trigger for the MPI laser. This trigger time essentially set the time zero of the TOF mass spectrum, making calibration of the mass arrival times particularly facile to calculate.

2.4. Conclusion

This chapter has detailed the design, construction, and implementation of a new experimental apparatus for the study of weak interactions between refractory elements bound to solvent molecules and clusters. The emphasis of this chapter has focused on the methodology by which multiphoton ionization studies of the $Al{\bullet}Ar_n$ cluster systems presented in the following three chapters of this thesis was pursued. Nevertheless, the versatile design of this new machine should permit this apparatus to serve as a platform from which an almost limitless array of molecular systems can be studied, as well as providing the flexibility to implement a wide variety of different experimental techniques.

2.5. References

1. M. S. Johnson, Ph.D. Thesis, California Institute of Technology, 1996.
2. D. Scharf, G. J. Martyna, and M. L. Klein, *J. Chem. Phys.*, **99**, 8997 (1993), and references therein.
3. D. R. Miller, in *Atomic and Molecular Beam Methods, Vol. I*, G. Scoles, Ed. (Oxford University Press, New York, 1988).
4. F. Stienkemeier, W. E. Ernst, J. Higgins, and G. Scoles, *J. Chem. Phys.*, **102**, 615 (1995).
5. W. R. Gentry, in *Atomic and Molecular Beam Methods, Vol. I*, G. Scoles, Ed. (Oxford University Press, New York, 1988).
6. W. R. Gentry and C. F. Giese, *Rev. Sci. Instrum.*, **49**, 595 (1978).
7. D. Proch and T. Trickl, *Rev. Sci. Instrum.*, **60**, 713 (1989).
8. Y. Cao, Ph.D. Thesis, California Institute of Technology, 1994.
9. J.-H. Choi, Ph.D. Thesis, California Institute of Technology, 1995.
10. T. Schindler, personal communication.
11. C. Berg, personal communication.
12. R. E. Continetti, Ph.D. Thesis, University of California, Berkeley, 1989.
13. M. Beyer, personal communication.
14. T. G. Dietz, M. A. Duncan, D. E. Powers, and R. E. Smalley, *J. Chem. Phys.*, **74**, 6611 (1981).
15. D. E. Powers, S. G. Hansen, M. E. Geusic, A. C. Puiu, J. B. Hopkins, T. G. Dietz, M. A. Duncan, P. R. R. Langridge-Smith, and R. E. Smalley, *J. Phys. Chem.*, **86**, 2556 (1982).
16. D. L. Michalopoulos, M. E. Geusic, S. G. Hansen, D. E. Powers, and R. E. Smalley, *J. Phys. Chem.*, **86**, 3914 (1982).
17. D. E. Powers, S. G. Hansen, M. E. Geusic, D. L. Michalopoulos, and R. E. Smalley, *J. Chem. Phys.*, **78**, 2866 (1983).

18. J. B. Hopkins, P. R. R. Langridge-Smith, M. D. Morse, and R. E. Smalley, *J. Chem. Phys.*, **78**, 1627 (1983).
19. M. E. Fajardo, personal communication.
20. R. E. Smalley, *Laser Chemistry*, **2**, 167 (1983).
21. M. Costes, C. Naulin, G. Dorthe, G. Daleau, J. Joussot-Dubien, C. Lalaude, M. Vinckert, A. Destor, C. Vaucamps, and G. Nouchi, *J. Phys. E.: Sci. Instrum.*, **22**, 1017 (1989).
22. M. A. Duncan, personal communication.
23. L. R. Brock and M. A. Duncan, *J. Phys. Chem.*, **99**, 16571 (1995).
24. K. E. Schriver, M. Y. Hahn, J. L. Persson, M. E. LaVilla, and R. L. Whetten, *J. Phys. Chem.*, **93**, 2869 (1989).
25. R. L. Whetten. K. E. Schriver, J. L. Persson, and M. Y. Hahn, *J. Chem. Soc. Farad. Trans.*, **86**, 2375 (1990).
26. X. Li., M. Y. Hahn, M. S. El-Shall, and R. L. Whetten, *J. Phys. Chem.* **95**, 8524 (1991).
27. T. Gough, M. Mengel, P. Rowntree, and G. Scoles, *J. Chem. Phys.*, **83**, 4958 (1985).
28. J. P. Visticott, P. de Pujo, J. M. Mestdagh, A. Lallement, J. Berlande, O. Sublemontier, P. Meynadier and J Cuvellier, *J. Chem. Phys.*, **100**, 158 (1994).
29. W. C. Wiley and I. H. McLaren, *Rev. Sci. Instrum.*, **26**, 1150 (1955).

TABLE 2-1: Polarizations of Laser Beams at Various Stages of Frequency Generation: Surelite I Nd:YAG and HG-4B Harmonic Generation Unit.

Wavelength	Crystal	Power	Polarization
1.064 μM	Nd:YAG	430 mJ	Horizontal
532 nm	KD*P Type II (o + e = e)	160 mJ	Horizontal[1]
355 nm	KD*P Type I (o + o = e)	55 mJ	Vertical[1]
266 nm	KD*P Type I	40 mJ	Vertical[1]

Note:

[1] Assumes that HG-4B unit is oriented with Caltech property label on top.

TABLE 2-2: Polarizations of Laser Beams at Various Stages of Frequency Generation: NY-61 Nd:YAG Laser, TDL-51 Dye Laser, and UVX Mixing and Doubling System.

Wavelength	Medium	Power	Polarization
1.064 μM	Nd:YAG osc. and amp.	600 mJ[1]	Horizontal
532 nm	KD*P Type I	320 mJ[1]	Vertical
844 nm - 532 nm	Dye laser	60 mJ[2]	Vertical
442 nm - 369 nm	Mixing/MCC2,[3]		
	Position B, Type II	1-5 mJ	Horizontal
365 nm - 295 nm	Doubling/DCC2,[3]		
	Position B, Type I	1-5 mJ	Horizontal
295 nm - 267 nm	Doubling/DCC3,[3]		
	Position B, Type I	1-5 mJ	Horizontal
279 nm - 236 nm	Mixing after doubling:[4]		
	Doubler/DCC1&2,		
	Position A, Type I		
	Mixing/MCC2,		
	Position B, Type II	0.1-2 mJ	Horizontal

Notes:

[1] Seeder on. Subtract 10% for unseeded operation.

[2] For DCM dye at 640 nm. Power will vary for other dyes and wavelengths.

[3] Dye laser polarization rotation prism not used. If mixing and doubling is performed in position A instead of position B, the polarization rotation prism should be employed.

[4] Polarization rotation prism is necessary for mixing after doubling.

2.6. Figure Captions

Figure 2-1 Labels for the individual experimental components shown in the schematic of the newly-constructed experimental apparatus presented in Figure 2-2.

Figure 2-2 Schematic showing the individual components of the newly-constructed experimental apparatus.

Figure 2-3 The source cross chamber. (a) Front view. (b) Side view. (c) Top view.

Figure 2-4 Drawing of the source cross chamber - front view.

Figure 2-5 Drawing of the source cross chamber - back view.

Figure 2-6 Drawing of the source cross chamber - left side view.

Figure 2-7 Drawing of the source cross chamber - top view.

Figure 2-8 Drawing of the source cross chamber - bottom view.

Figure 2-9 Drawing of custom ASA-10 blankoff flange for the top ASA-10 flange of the source cross chamber.

Figure 2-10 Drawing of the source tee chamber - side view.

Figure 2-11 Drawing of the source tee chamber - top view.

Figure 2-12 Drawing of the source tee chamber - bottom view.

Figure 2-13 The source mount design. (a) Simplified schematic showing the source mount design as well as the mounted source components as it appeared with the source chamber rolled back away from the source. (b) Simplified cutaway schematic of the source chamber showing how the source mount as well as the mounted source components were housed within the source chamber with the source chamber bolted to the skimmer flange.

Figure 2-14 Drawing of the skimmer flange - front view facing the source chamber.

Figure 2-15 Drawing of the skimmer flange - back view facing the REMPI chamber.

Figure 2-16 Drawing of the skimmer flange - sectional views A-A and B-B.

Figure 2-17 Assembly Drawing showing the manner in which the molecular beam skimmer was mounted to the skimmer flange.

Figure 2-18 Drawing of the skimmer mount adapter flange between the skimmer flange and the skimmer mount.

Figure 2-19 Drawing of skimmer mount base.

Figure 2-20 Drawing of skimmer mount clamp.

Figure 2-21 Drawing of collars used to mount the source rails to the skimmer flange.

Figure 2-22 Drawing of the source rails.

Figure 2-23 Schematic showing the basic design of the rigid back mount frame used to support the free-hanging end of the source rails.

Figure 2-24 Drawing of collars used for rigid back mount frame.

Figure 2-25 Drawing of end caps bolted to the back of the collars used for rigid back mount frame.

Figure 2-26 Drawing of the cross-support pieces used to couple the collars of the rigid back mount frame.

Figure 2-27 Drawing of the Y-plate.

Figure 2-28 Drawing of x-y translator blocks that were mounted to the Y-plate to provide fine control of the pulsed valve housing position.

Figure 2-29 Drawing showing the modification made to the original Y-plate design.

Figure 2-30 Drawing of right angle brackets mounted onto the Y-plate.

Figure 2-31 Assembly drawing of the original piezoelectric pulsed valve based on the design of Trickl and Proch.

Figure 2-32 Drawing of original adapter piece used to couple the laser vaporization source to the faceplate of the piezoelectric pulsed valve.

Figure 2-33 Assembly drawing of the piezoelectric pulsed with the original laser vaporization adapter piece installed.

Figure 2-34 Assembly drawing of the piezoelectric pulsed valve showing the modifications made to the original design. Part #3 shows the modified laser vaporization adapter piece, and Part #7 shows the new extended pulsed valve poppet with the Vespel-SP1 poppet tip installed.

Figure 2-35 Assembly drawing of the piezoelectric pulsed valve showing the modifications made to the original design. Part #3 shows the modified laser vaporization adapter piece, and Part #7 shows the new extended pulsed valve poppet with the o-ring poppet tip installed.

Figure 2-36 Drawing of the extended pulsed valve o-ring poppet tip.

Figure 2-37 Drawing of the extended pulsed valve Vespel-SP1 poppet tip.

Figure 2-38 Drawing of Vespel-SP1 poppet tip that was installed into the end of the new extended poppet design.

Figure 2-39 Drawing of the modified laser vaporization adapter piece.

Figure 2-40 Assembly drawing of the new piezoelectric pulsed valve based on the original design of Christian Berg. The assembly drawing shows the appearance of the valve with both the modified laser vaporization source adapter and the extended pulsed valve Vespel-SP1 poppet tip installed.

Figure 2-41 Assembly drawing of the new piezoelectric pulsed valve based on the original design of Christian Berg. The assembly drawing shows the appearance of the valve with both the modified laser vaporization source adapter and the extended pulsed valve o-ring poppet tip installed.

Figure 2-42 Parts list for the individual components of the first generation laser vaporization source assembly (page 1 of 2).

Figure 2-43 Continuation of the parts list for the individual components of the first generation laser vaporization source assembly (page 2 of 2).

Figure 2-44 Drawing of the first generation laser vaporization source - exterior view.

Figure 2-45 Drawing of the first generation laser vaporization source - cross-sectional views.

Figure 2-46 Drawing of the first generation laser vaporization source - auxiliary view A.

Figure 2-47 Drawing of the first generation laser vaporization source - auxiliary view B.

Figure 2-48 Assembly drawing showing the components of the laser vaporization source screw drive assembly.

Figure 2-49 Drawing of the drive screw for the screw drive assembly.

Figure 2-50 Drawing of the screw drive housing for the screw drive assembly.

Figure 2-51 Drawing of the rotating screw drive housing for the screw drive assembly.

Figure 2-52 Drawing of the screw drive housing clamp for the screw drive assembly.

Figure 2-53 Drawing of the original gear table that was used with the first generation laser vaporization source.

Figure 2-54 Drawing of the second generation laser vaporization source (version 2) - exterior view.

Figure 2-55 Drawing of the second generation laser vaporization source (version 2) - back exterior view.

Figure 2-56 Drawing of the second generation laser vaporization source (version 2) - cross-sectional views A-A and B-B.

Figure 2-57 Drawing of the second generation laser vaporization source (version 2) - auxiliary view A.

Figure 2-58 Drawing of the second generation laser vaporization source (version 2) - cross-sectional view showing modifications made to the original design.

Figure 2-59 Schematic showing the second generation laser vaporization source (version 2) mounted to the piezoelectric pulsed valve via the original laser vaporization source adapter. Also shown is the mechanism by which the laser vaporization laser pulse was introduced into the source.

Figure 2-60 Drawing of the second generation laser vaporization source (version 3) - exterior view.

Figure 2-61 Drawing of the second generation laser vaporization source (version 3) - cross-sectional view.

Figure 2-62 Drawing of the second generation laser vaporization source (version 3) - back exterior view.

Figure 2-63 Drawing of the modified gear table that was used with the second generation laser vaporization sources.

Figure 2-64 Assembly drawing showing the design of the third generation laser vaporization source.

Figure 2-65 Magnified schematic detailing the assembled target rod cart with a target rod installed.

Figure 2-66 Schematic showing the placement of the aluminum target rod adjacent to the straight-channel nozzle piece that was used in conjunction with the third generation laser vaporization source. Also shown is the manner by which laser ablation of the target rod was performed.

Figure 2-67 Drawing of the REMPI chamber - side view.

Figure 2-68 Drawing of the REMPI chamber - front view facing the skimmer flange.

Figure 2-69 Drawing of the REMPI chamber - bottom view.

Figure 2-70 Drawing of the REMPI chamber - auxiliary side view showing the placement of the 2-3/4" ConFlat ports.

Figure 2-71 Drawing of the REMPI chamber - auxiliary side view showing the placement of the 3/4" compression port.

Figure 2-72 Drawing of the time-of-flight asymmetric double nipple - bottom view facing the REMPI chamber.

Figure 2-73 Drawing of the time-of-flight asymmetric double nipple - sectional view A-A.

Figure 2-74 Drawing of the time-of-flight asymmetric double nipple - sectional view B-B showing the placement of the lift plates.

Figure 2-75 Drawing of the time-of-flight asymmetric double nipple - sectional view C-C.

Figure 2-76 Drawing of time-of-flight ion optic grounding pins.

Figure 2-77 Drawing of time-of-flight flight tube - view 1 of 2.

Figure 2-78 Drawing of time-of-flight flight tube - view 2 of 2.

Figure 2-79 Schematic showing the placement of the time-of-flight ion optics when mounted to the time-of-flight assymmtric double nipple and subsequently installed into the REMPI chamber.

Figure 2-80 Assembly drawing of the time-of-flight ion optics.

Figure 2-81 Drawing of the top mounting plate of the time-of-flight ion optics frame.

Figure 2-82 Drawing of the middle mounting plate of the time-of-flight ion optics frame.

Figure 2-83 Drawing of the bottom mounting plate of the time-of-flight ion optics frame.

Figure 2-84 Drawing of support posts placed between the middle and bottom mounting plates of the time-of-flight ion optics frame.

Figure 2-85 Drawing of support posts placed between the middle and top mounting plates of the time-of-flight ion optics frame.

Figure 2-86 Drawing of the deflector plate mount.

Figure 2-87 Drawing of the right angle bracket used to couple the deflector plate mount to the deflector plate.

Figure 2-88 Drawing of the deflector plate.

Figure 2-89 Assembly drawing showing the position and alignment of the time-of-flight deflector assembly within the upper ion optics frame.

Figure 2-90 Top view schematic of the time-of-flight deflector assembly showing the alternating orientation of each deflector as well as the separation between each adjacent deflector plates.

Figure 2-91 Drawing of the detector flange showing the placement of the various electrical feedthoughs. View looks down on the UHV side of the flange.

Figure 2-92 Drawing of the detector flange - sectional view A-A.

Figure 2-93 Drawing of the modifications made to the original detector flange design to permit the mounting of the posts that supported both the ground plate above the MCP cathode as well as the mass gate assembly.

Figure 2-94 Drawing of the front plate of the mass gate assembly.

Figure 2-95 Drawing of the rear plate of the mass gate assembly.

Figure 2-96 Drawing of the mass gate deflectors.

Figure 2-97 Drawing of the support posts that mounted the front plate of the mass gate assembly to the posts supporting the ground plate above the MCP cathode.

Figure 2-98 Drawing of the support posts that mounted the ground plate above the MCP cathode to the detector flange.

Figure 2-99 Drawing of the centering ring used to maintain the axial alignment of the MCP detector assembly.

Figure 2-100 Schematic overview of the experimental methodology.

Figure 2-101 A typical time-of-flight mass spectrum showing the size distribution of $Al•Ar_n$ clusters that were observed during the course of the experiments using both the second and third generation laser vaporization sources.

1. 10" Diffusion Pump (Varian VHS-10)
2. 10" Cryotrap
3. Source Chamber Baseplate
4. Source Chamber ASA-10 Gate Valve
5. Source Tee
6. Source Cross
7. Piezoelectric Pulsed Valve
8. Laser Vaporization Source
9. DC-Stepper Motor for Laser Vaporzation Target Drive Assembly and Rotary Motion Feedthrough
10. Skimmer Flange
11. 6" Diffusion Pump (Varian VHS-6)
12. 6" Cryotrap
13. REMPI Chamber Baseplate
14. REMPI Chamber ASA-6 Gate Valve
15. REMPI Chamber
16. Time-of-Flight Ion Optics
17. Time-of-Flight Asymmetric Double Nipple
18. Time-of-Flight 6" ConFlat Gate Valve
19. Time-of-Flight Flight Tube
20. Microchannel Plate Detector

Figure 2-1

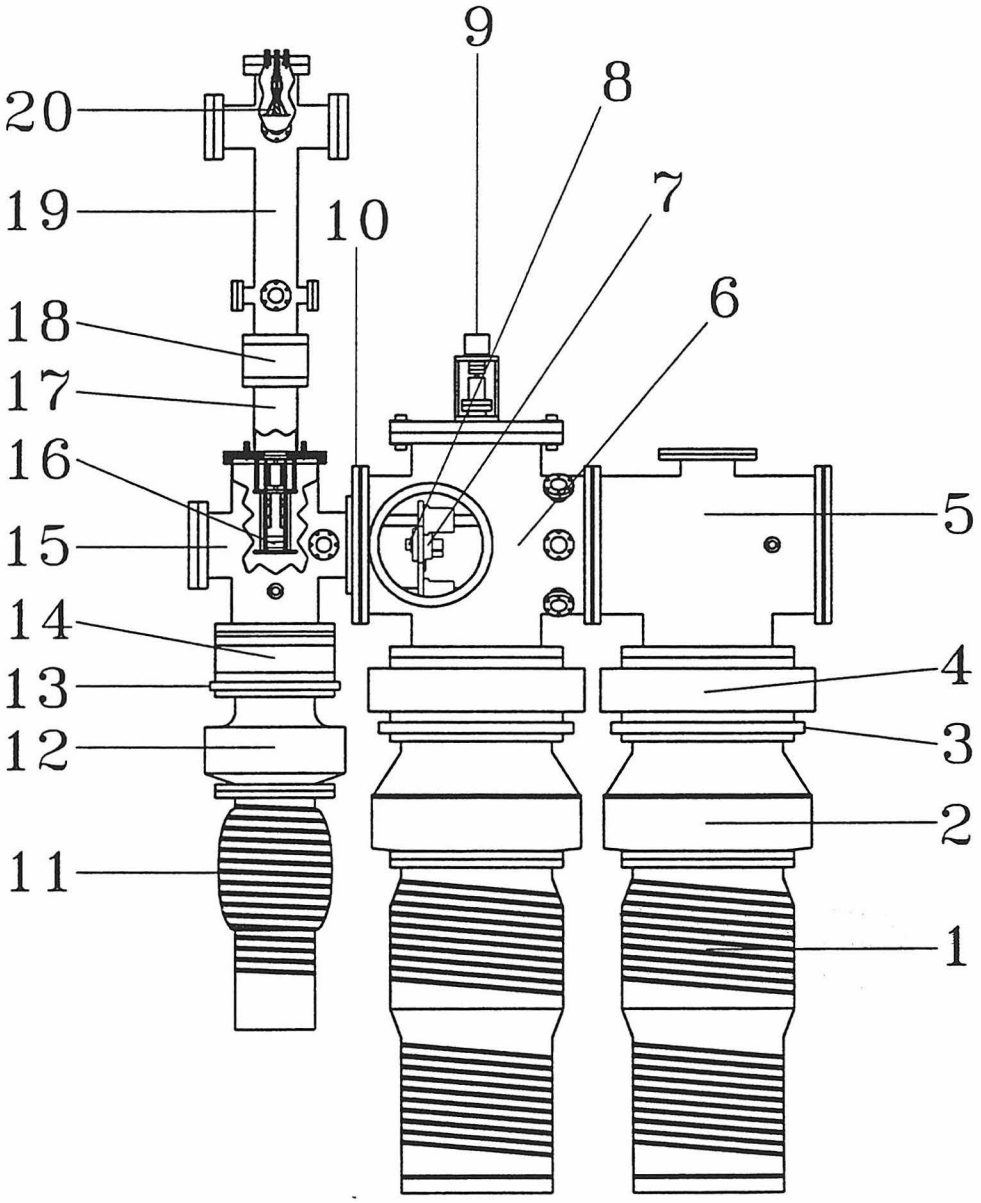
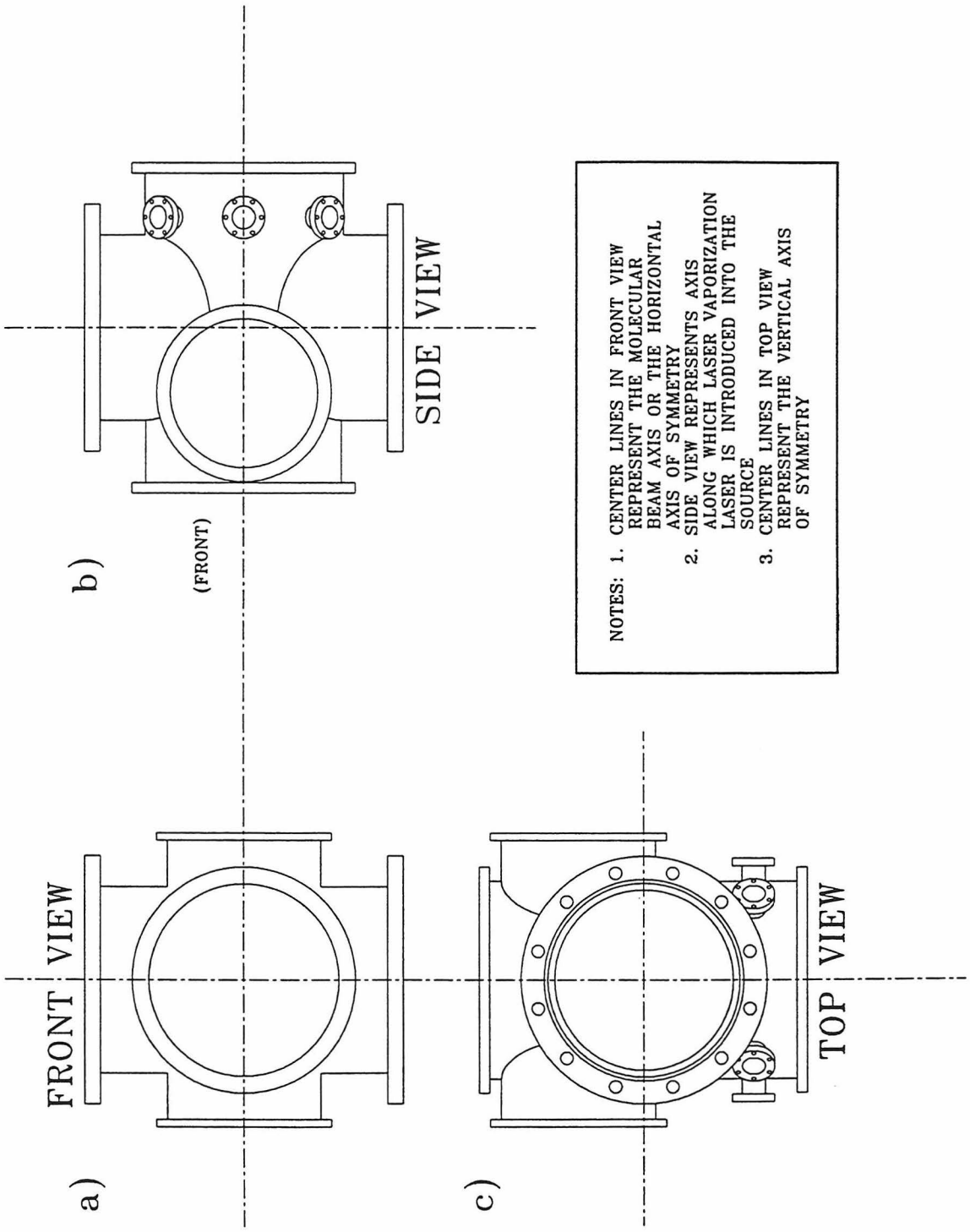


Figure 2-2



Figures 2-3a, 2-3b, and 2-3c

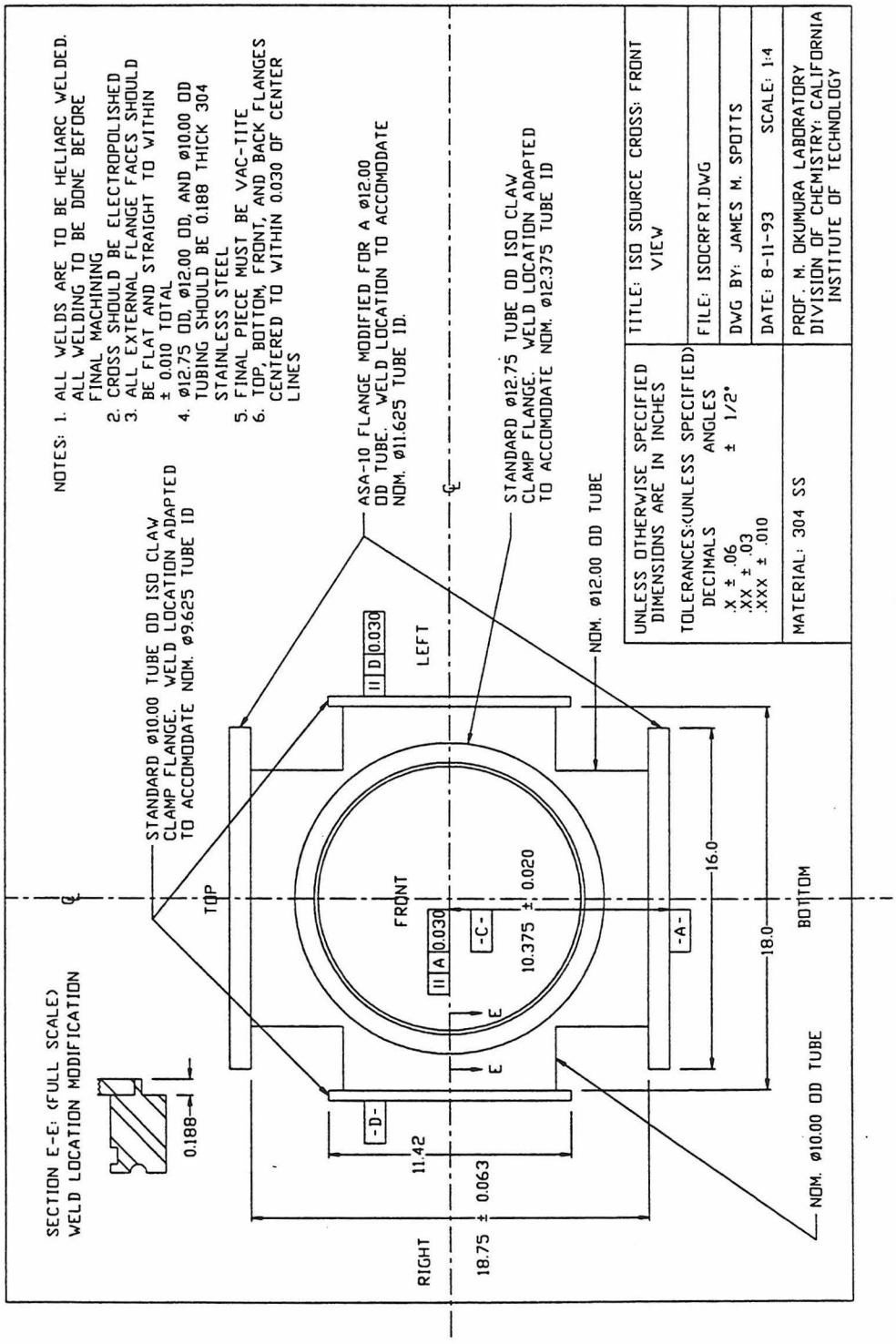

NOTES: 1. ALL WELDS ARE TO BE HELIARC WELDED. ALL WELDING TO BE DONE BEFORE FINAL MACHINING
2. CROSS SHOULD BE ELECTROPOLISHED
3. ALL EXTERNAL FLANGE FACES SHOULD BE FLAT AND STRAIGHT TO WITHIN ± 0.010 TOTAL
4. ø12.75 OD, ø12.00 OD, AND ø10.00 OD TUBING SHOULD BE 0.188 THICK 304 STAINLESS STEEL
5. FINAL PIECE MUST BE VAC-TITE
6. TOP, BOTTOM, FRONT, AND BACK FLANGES CENTERED TO WITHIN 0.030 OF CENTER LINES
STANDARD ø10.00 TUBE OD ISO CLAW CLAMP FLANGE. WELD LOCATION ADAPTED TO ACCOMODATE NOM. ø9.625 TUBE ID
ASA-10 FLANGE MODIFIED FOR A ø12.00 OD TUBE. WELD LOCATION TO ACCOMODATE NOM. ø11.625 TUBE ID.
STANDARD ø12.75 TUBE OD ISO CLAW CLAMP FLANGE. WELD LOCATION ADAPTED TO ACCOMODATE NOM. ø12.375 TUBE ID
NOM. ø12.00 OD TUBE
NOM. ø10.00 OD TUBE
TOP
BOTTOM
FRONT
LEFT
RIGHT
⌖ D 0.030
⌖ A 0.030
-A-
-C-
-D-
10.375 ± 0.020
16.0
18.0
11.42
18.75 ± 0.063
0.188
E
E
SECTION E-E: (FULL SCALE)
WELD LOCATION MODIFICATION
UNLESS OTHERWISE SPECIFIED DIMENSIONS ARE IN INCHES
TOLERANCES:(UNLESS SPECIFIED)
DECIMALS
.X ± .06
.XX ± .03
.XXX ± .010
ANGLES ± 1/2°
TITLE: ISO SOURCE CROSS: FRONT VIEW
FILE: ISOCRFRT.DWG
DWG BY: JAMES M. SPOTTS
DATE: 8-11-93
SCALE: 1:4
MATERIAL: 304 SS
PROF. M. OKUMURA LABORATORY
DIVISION OF CHEMISTRY: CALIFORNIA INSTITUTE OF TECHNOLOGY

Figure 2-4

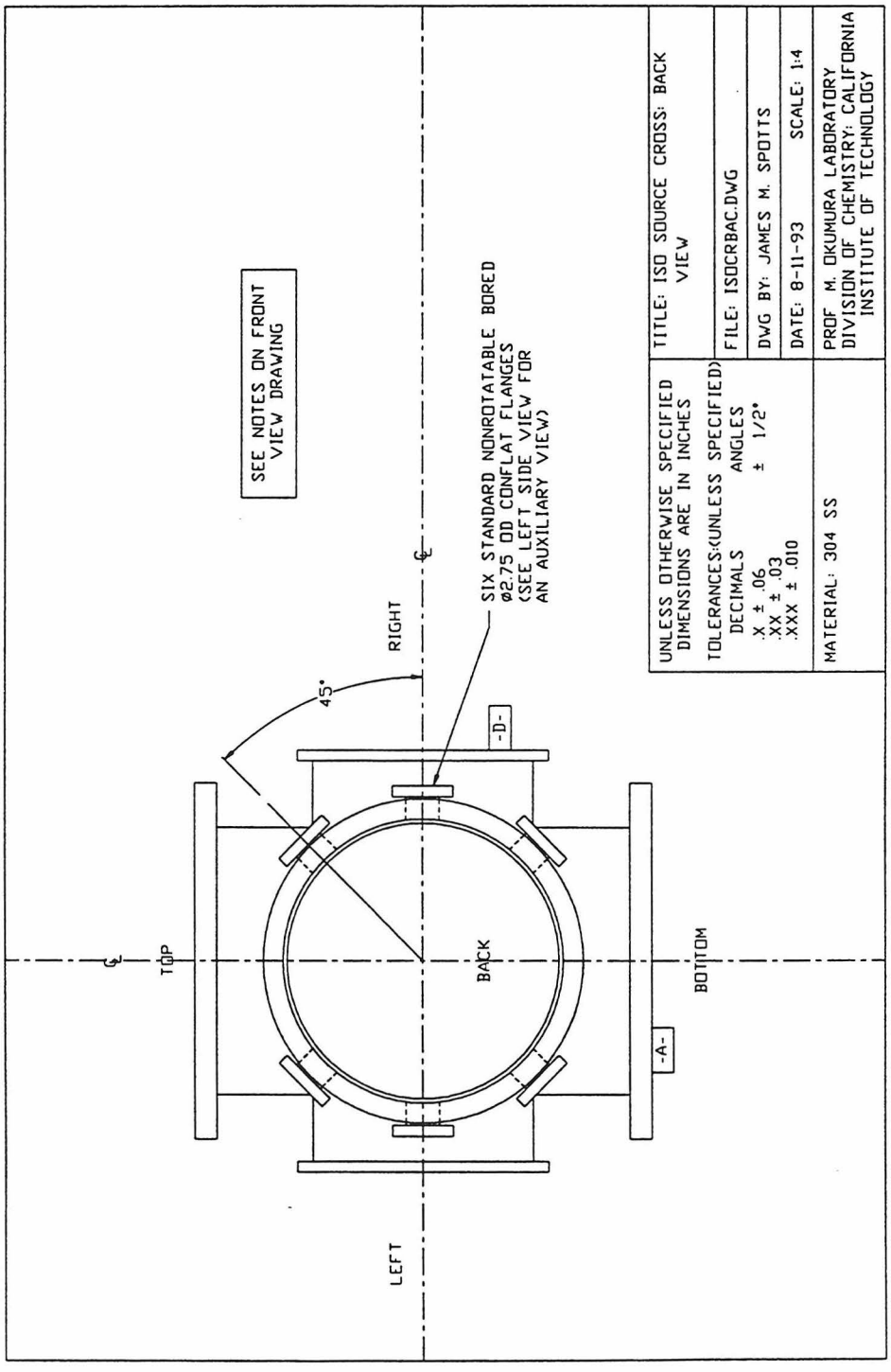

SEE NOTES ON FRONT
VIEW DRAWING
SIX STANDARD NONROTATABLE BORED
Ø2.75 OD CONFLAT FLANGES
(SEE LEFT SIDE VIEW FOR
AN AUXILIARY VIEW)
RIGHT
45°
TOP
BACK
BOTTOM
LEFT
-D-
-A-
UNLESS OTHERWISE SPECIFIED
DIMENSIONS ARE IN INCHES
TOLERANCES:(UNLESS SPECIFIED)
DECIMALS ANGLES
.X ± .06 ± 1/2°
.XX ± .03
.XXX ± .010
MATERIAL: 304 SS
TITLE: ISO SOURCE CROSS: BACK VIEW
FILE: ISOCRBAC.DWG
DWG BY: JAMES M. SPOTTS
DATE: 8-11-93 SCALE: 1:4
PROF M. OKUMURA LABORATORY
DIVISION OF CHEMISTRY: CALIFORNIA
INSTITUTE OF TECHNOLOGY

Figure 2-5

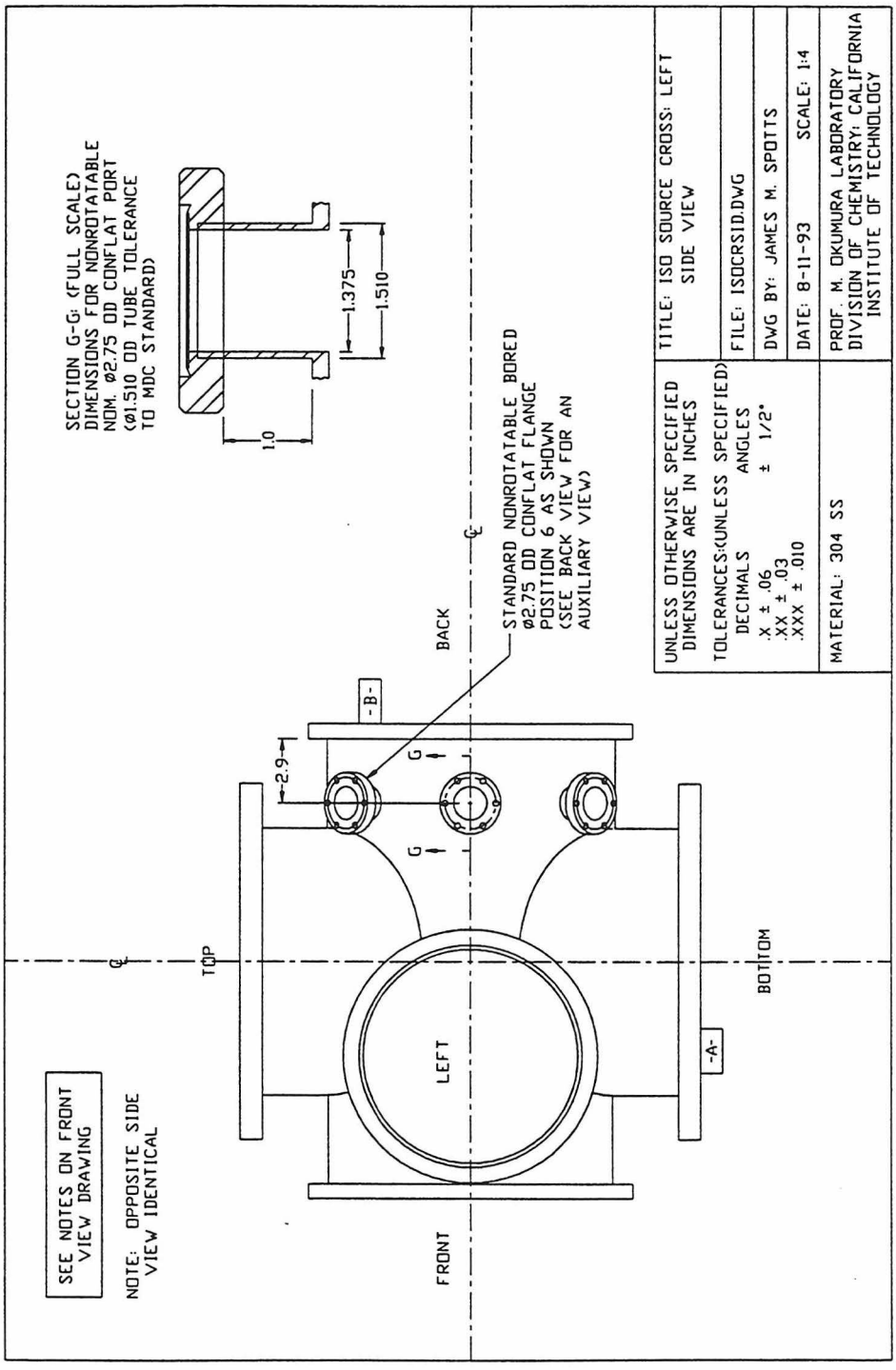

SECTION G-G: (FULL SCALE)
DIMENSIONS FOR NONROTATABLE
NOM. ø2.75 OD CONFLAT PORT
(ø1.510 OD TUBE TOLERANCE
TO MDC STANDARD)
1.0
1.375
1.510
STANDARD NONROTATABLE BORED
ø2.75 OD CONFLAT FLANGE
POSITION 6 AS SHOWN
(SEE BACK VIEW FOR AN
AUXILIARY VIEW)
BACK
-B-
2.9
G
G
TOP
BOTTOM
LEFT
-A-
FRONT
SEE NOTES ON FRONT
VIEW DRAWING
NOTE: OPPOSITE SIDE
VIEW IDENTICAL
UNLESS OTHERWISE SPECIFIED
DIMENSIONS ARE IN INCHES
TOLERANCES:(UNLESS SPECIFIED)
DECIMALS ANGLES
.X ± .06 ± 1/2°
.XX ± .03
.XXX ± .010
MATERIAL: 304 SS
TITLE: ISO SOURCE CROSS: LEFT
SIDE VIEW
FILE: ISOCRSID.DWG
DWG BY: JAMES M. SPOTTS
DATE: 8-11-93 SCALE: 1:4
PROF. M. OKUMURA LABORATORY
DIVISION OF CHEMISTRY: CALIFORNIA
INSTITUTE OF TECHNOLOGY

Figure 2-6

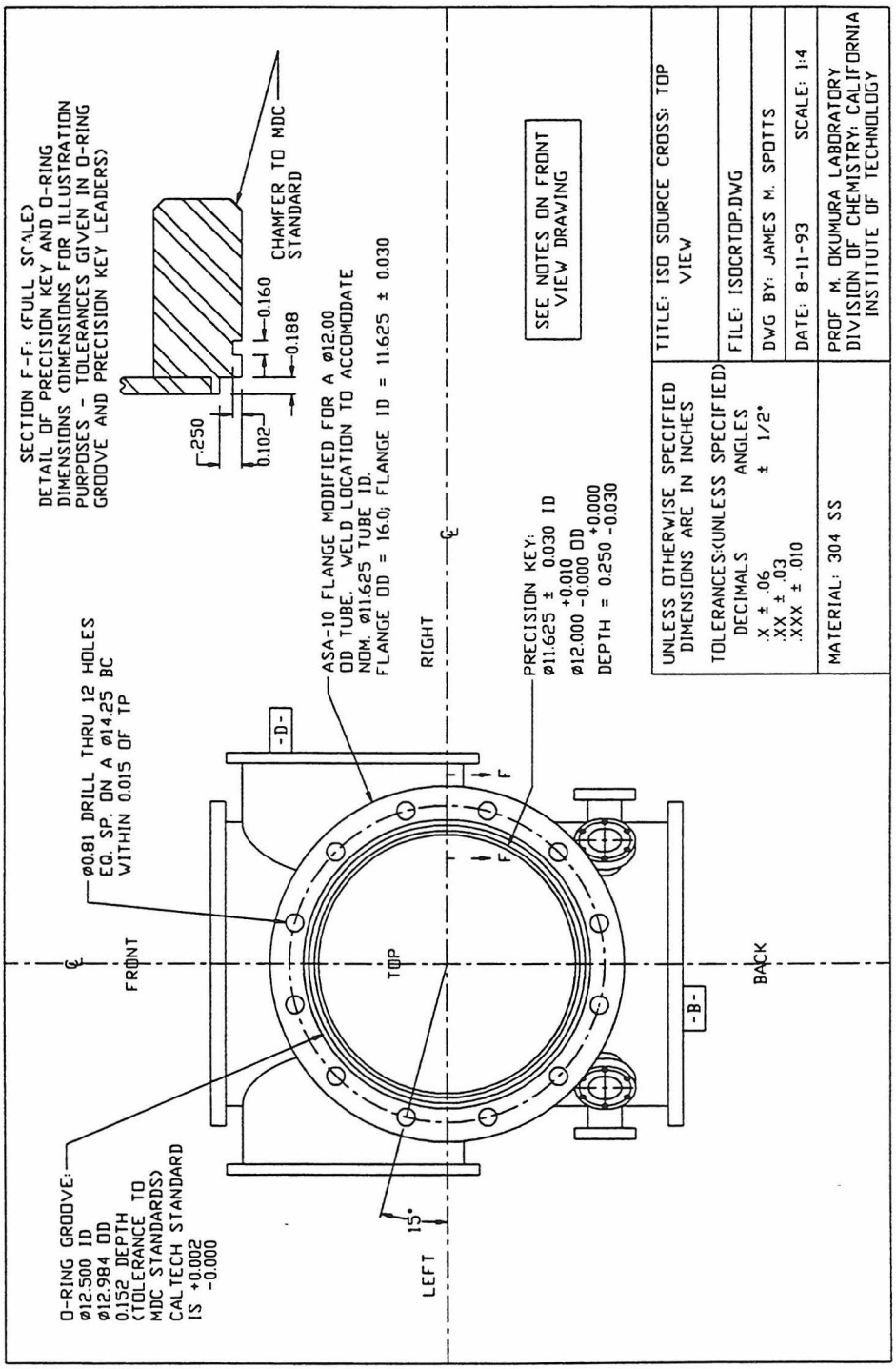

SECTION F-F: (FULL SCALE)
DETAIL OF PRECISION KEY AND O-RING
DIMENSIONS (DIMENSIONS FOR ILLUSTRATION
PURPOSES - TOLERANCES GIVEN IN O-RING
GROOVE AND PRECISION KEY LEADERS)
.250
0.102
0.160
0.188
CHAMFER TO MDC
STANDARD
ø0.81 DRILL THRU 12 HOLES
EQ. SP. ON A ø14.25 BC
WITHIN 0.015 OF TP
ASA-10 FLANGE MODIFIED FOR A ø12.00
OD TUBE. WELD LOCATION TO ACCOMODATE
NOM. ø11.625 TUBE ID.
FLANGE OD = 16.0; FLANGE ID = 11.625 ± 0.030
RIGHT
PRECISION KEY:
ø11.625 ± 0.030 ID
ø12.000 +0.010 -0.000 OD
DEPTH = 0.250 +0.000 -0.030
SEE NOTES ON FRONT
VIEW DRAWING
-D-
-B-
F
F
FRONT
TOP
BACK
LEFT
15°
O-RING GROOVE:
ø12.500 ID
ø12.984 OD
0.152 DEPTH
(TOLERANCE TO
MDC STANDARDS)
CALTECH STANDARD
IS +0.002
-0.000
UNLESS OTHERWISE SPECIFIED
DIMENSIONS ARE IN INCHES
TOLERANCES:(UNLESS SPECIFIED)
DECIMALS
.X ± .06
.XX ± .03
.XXX ± .010
ANGLES
± 1/2°
MATERIAL: 304 SS
TITLE: ISO SOURCE CROSS: TOP
VIEW
FILE: ISOCRTOP.DWG
DWG BY: JAMES M. SPOTTS
DATE: 8-11-93
SCALE: 1:4
PROF M. OKUMURA LABORATORY
DIVISION OF CHEMISTRY: CALIFORNIA
INSTITUTE OF TECHNOLOGY

Figure 2-7

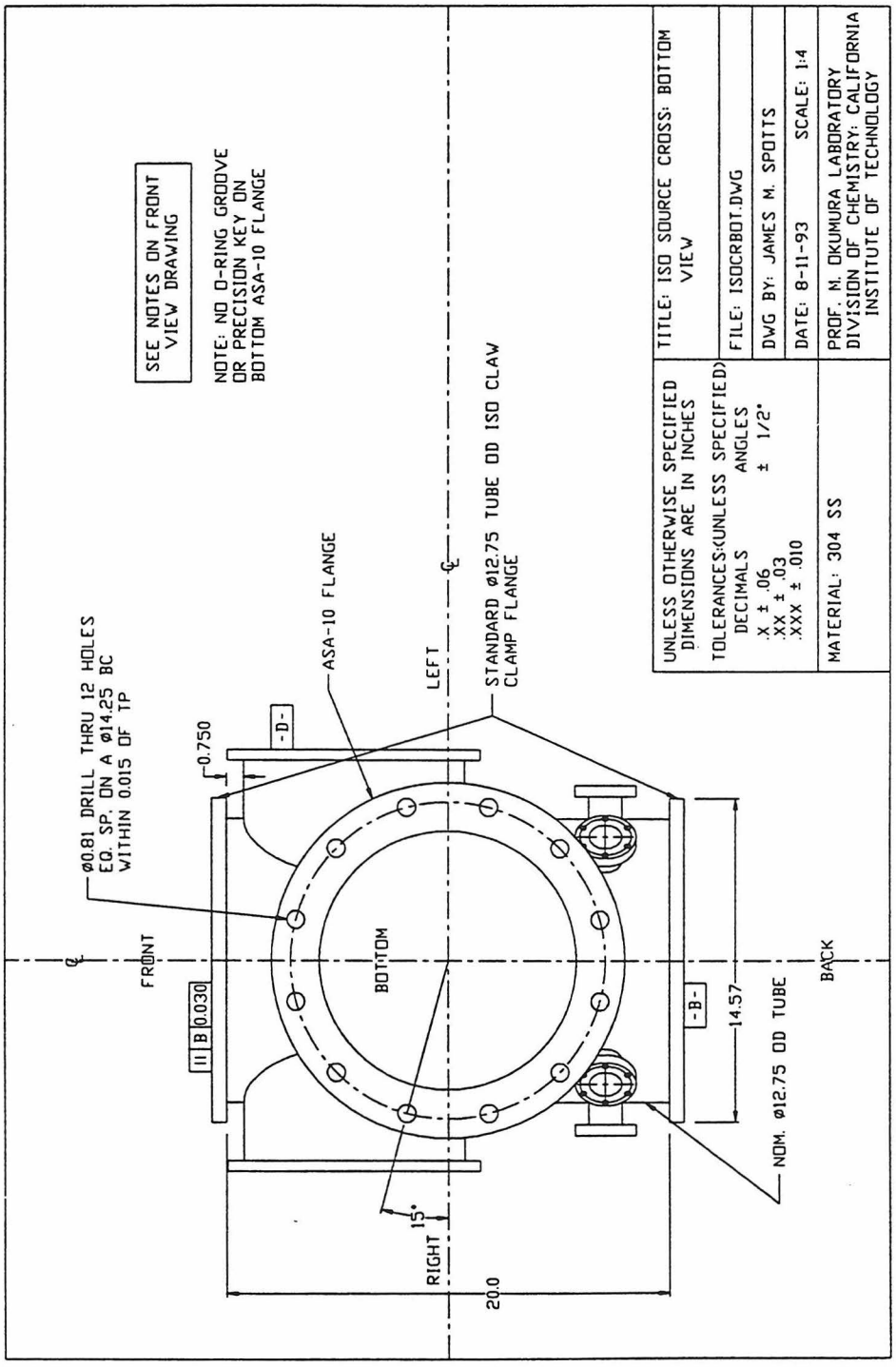

SEE NOTES ON FRONT VIEW DRAWING
NOTE: NO O-RING GROOVE OR PRECISION KEY ON BOTTOM ASA-10 FLANGE
Ø0.81 DRILL THRU 12 HOLES EQ. SP. ON A Ø14.25 BC WITHIN 0.015 OF TP
ASA-10 FLANGE
STANDARD Ø12.75 TUBE OD ISO CLAW CLAMP FLANGE
0.750
-D-
LEFT
FRONT
BOTTOM
BACK
RIGHT
15°
20.0
14.57
-B-
⊥ B 0.030
NOM. Ø12.75 OD TUBE
UNLESS OTHERWISE SPECIFIED DIMENSIONS ARE IN INCHES
TOLERANCES:(UNLESS SPECIFIED)
DECIMALS ANGLES
.X ± .06 ± 1/2°
.XX ± .03
.XXX ± .010
MATERIAL: 304 SS
TITLE: ISO SOURCE CROSS: BOTTOM VIEW
FILE: ISOCRBOT.DWG
DWG BY: JAMES M. SPOTTS
DATE: 8-11-93 SCALE: 1:4
PROF. M. OKUMURA LABORATORY
DIVISION OF CHEMISTRY: CALIFORNIA INSTITUTE OF TECHNOLOGY

Figure 2-8

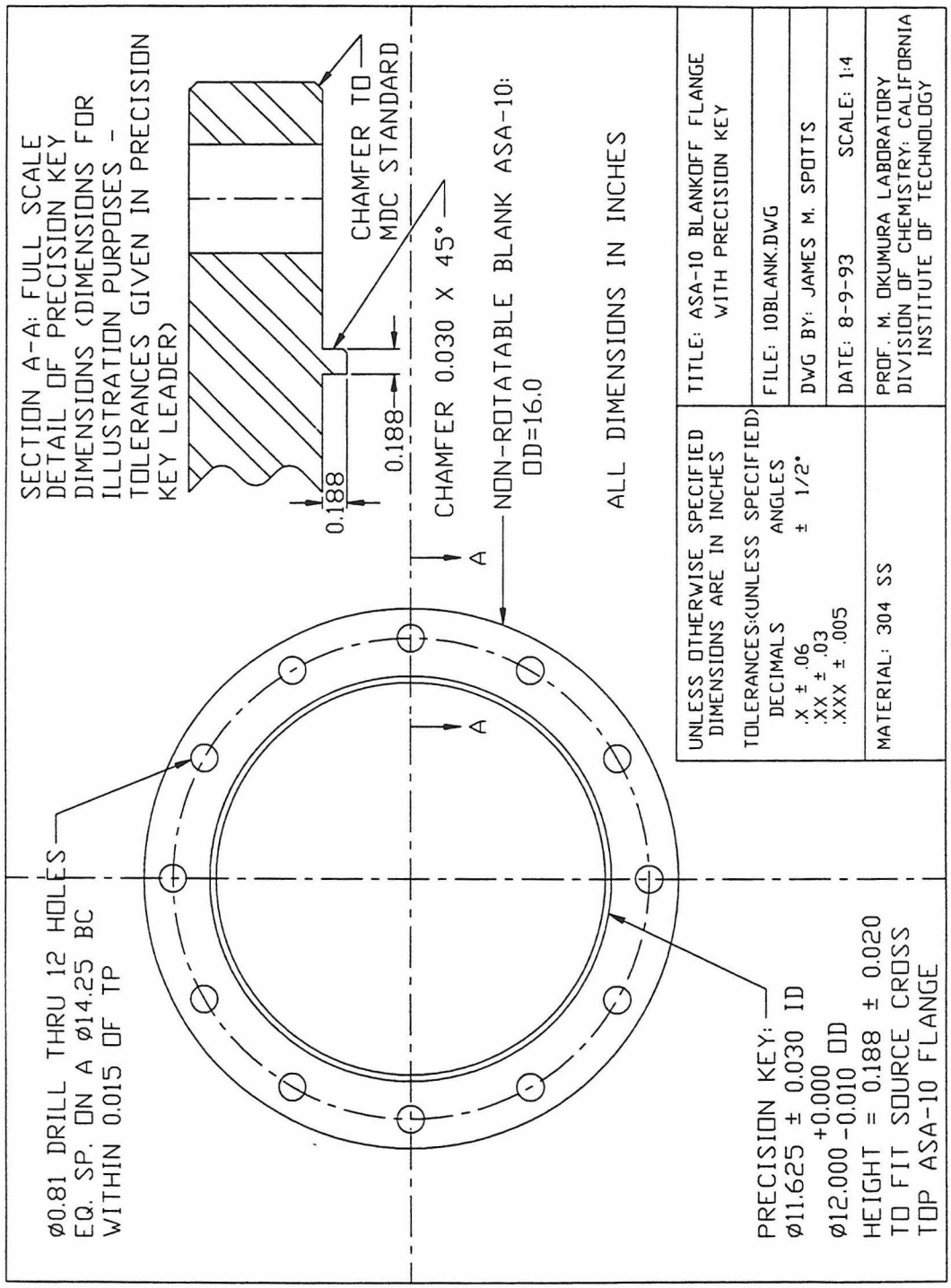

SECTION A-A: FULL SCALE
DETAIL OF PRECISION KEY
DIMENSIONS (DIMENSIONS FOR
ILLUSTRATION PURPOSES -
TOLERANCES GIVEN IN PRECISION
KEY LEADER)
0.188
0.188
CHAMFER TO
MDC STANDARD
CHAMFER 0.030 X 45°
NON-ROTATABLE BLANK ASA-10:
OD=16.0
ALL DIMENSIONS IN INCHES
A
A
ø0.81 DRILL THRU 12 HOLES
EQ. SP. ON A ø14.25 BC
WITHIN 0.015 OF TP
PRECISION KEY:
ø11.625 ± 0.030 ID
ø12.000 +0.000 -0.010 OD
HEIGHT = 0.188 ± 0.020
TO FIT SOURCE CROSS
TOP ASA-10 FLANGE
UNLESS OTHERWISE SPECIFIED
DIMENSIONS ARE IN INCHES
TOLERANCES:(UNLESS SPECIFIED)
DECIMALS ANGLES
.X ± .06 ± 1/2°
.XX ± .03
.XXX ± .005
MATERIAL: 304 SS
TITLE: ASA-10 BLANKOFF FLANGE
WITH PRECISION KEY
FILE: 10BLANK.DWG
DWG BY: JAMES M. SPOTTS
DATE: 8-9-93 SCALE: 1:4
PROF. M. OKUMURA LABORATORY
DIVISION OF CHEMISTRY: CALIFORNIA
INSTITUTE OF TECHNOLOGY

Figure 2-9

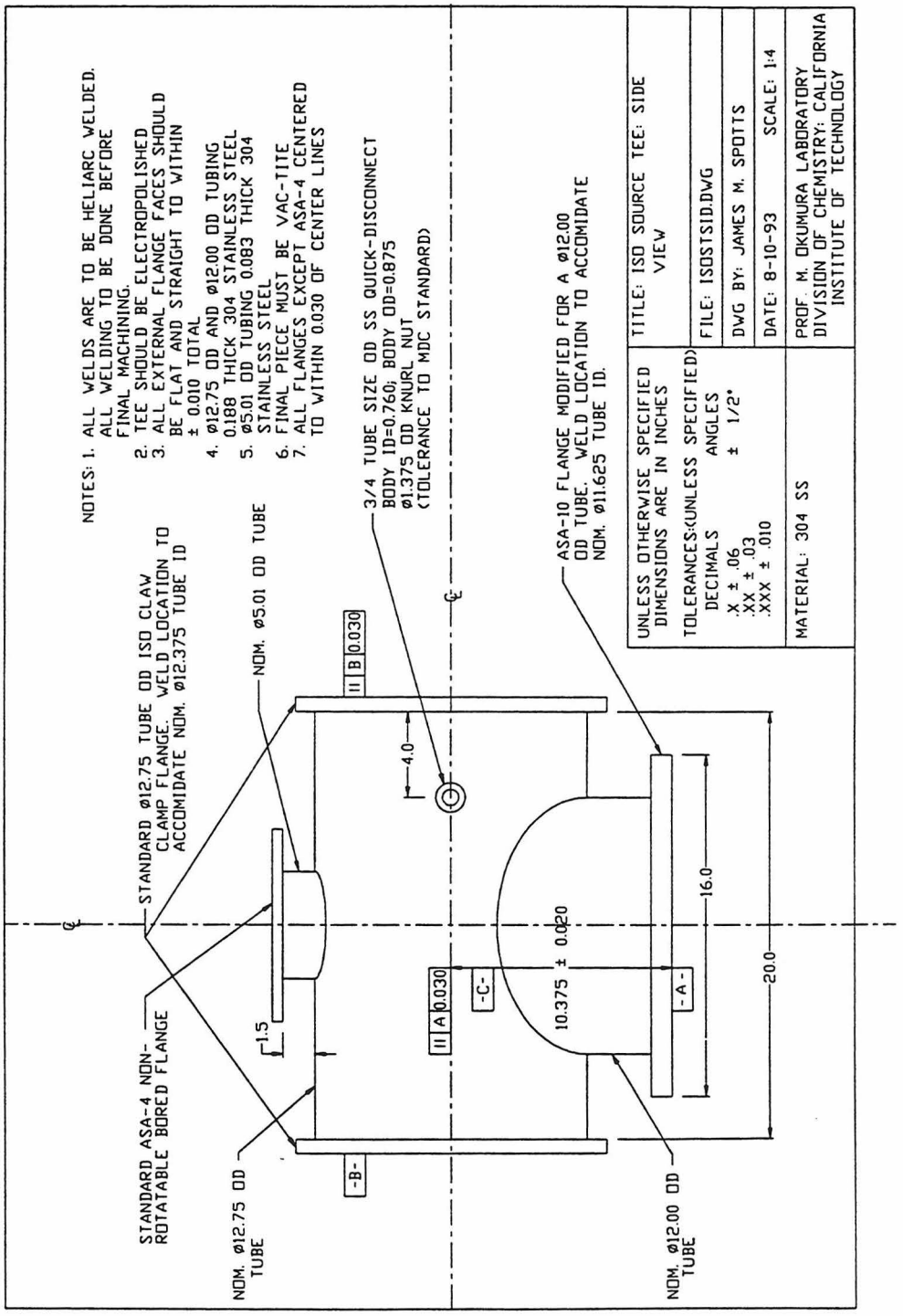

NOTES: 1. ALL WELDS ARE TO BE HELIARC WELDED. ALL WELDING TO BE DONE BEFORE FINAL MACHINING.
2. TEE SHOULD BE ELECTROPOLISHED
3. ALL EXTERNAL FLANGE FACES SHOULD BE FLAT AND STRAIGHT TO WITHIN ± 0.010 TOTAL
4. ø12.75 OD AND ø12.00 OD TUBING 0.188 THICK 304 STAINLESS STEEL
5. ø5.01 OD TUBING 0.083 THICK 304 STAINLESS STEEL
6. FINAL PIECE MUST BE VAC-TITE
7. ALL FLANGES EXCEPT ASA-4 CENTERED TO WITHIN 0.030 OF CENTER LINES
STANDARD ø12.75 TUBE OD ISO CLAW CLAMP FLANGE. WELD LOCATION TO ACCOMIDATE NOM. ø12.375 TUBE ID
NOM. ø5.01 OD TUBE
3/4 TUBE SIZE OD SS QUICK-DISCONNECT BODY ID=0.760; BODY OD=0.875 ø1.375 OD KNURL NUT (TOLERANCE TO MDC STANDARD)
ASA-10 FLANGE MODIFIED FOR A ø12.00 OD TUBE. WELD LOCATION TO ACCOMIDATE NOM. ø11.625 TUBE ID.
STANDARD ASA-4 NON-ROTATABLE BORED FLANGE
NOM. ø12.75 OD TUBE
NOM. ø12.00 OD TUBE
⌖ B 0.030
⌖ A 0.030
-A-
-B-
-C-
1.5
4.0
10.375 ± 0.020
16.0
20.0
UNLESS OTHERWISE SPECIFIED DIMENSIONS ARE IN INCHES
TOLERANCES:(UNLESS SPECIFIED)
DECIMALS ANGLES
.X ± .06 ± 1/2°
.XX ± .03
.XXX ± .010
MATERIAL: 304 SS
TITLE: ISO SOURCE TEE: SIDE VIEW
FILE: ISOSTSID.DWG
DWG BY: JAMES M. SPOTTS
DATE: 8-10-93 SCALE: 1:4
PROF. M. OKUMURA LABORATORY
DIVISION OF CHEMISTRY: CALIFORNIA INSTITUTE OF TECHNOLOGY

Figure 2-10

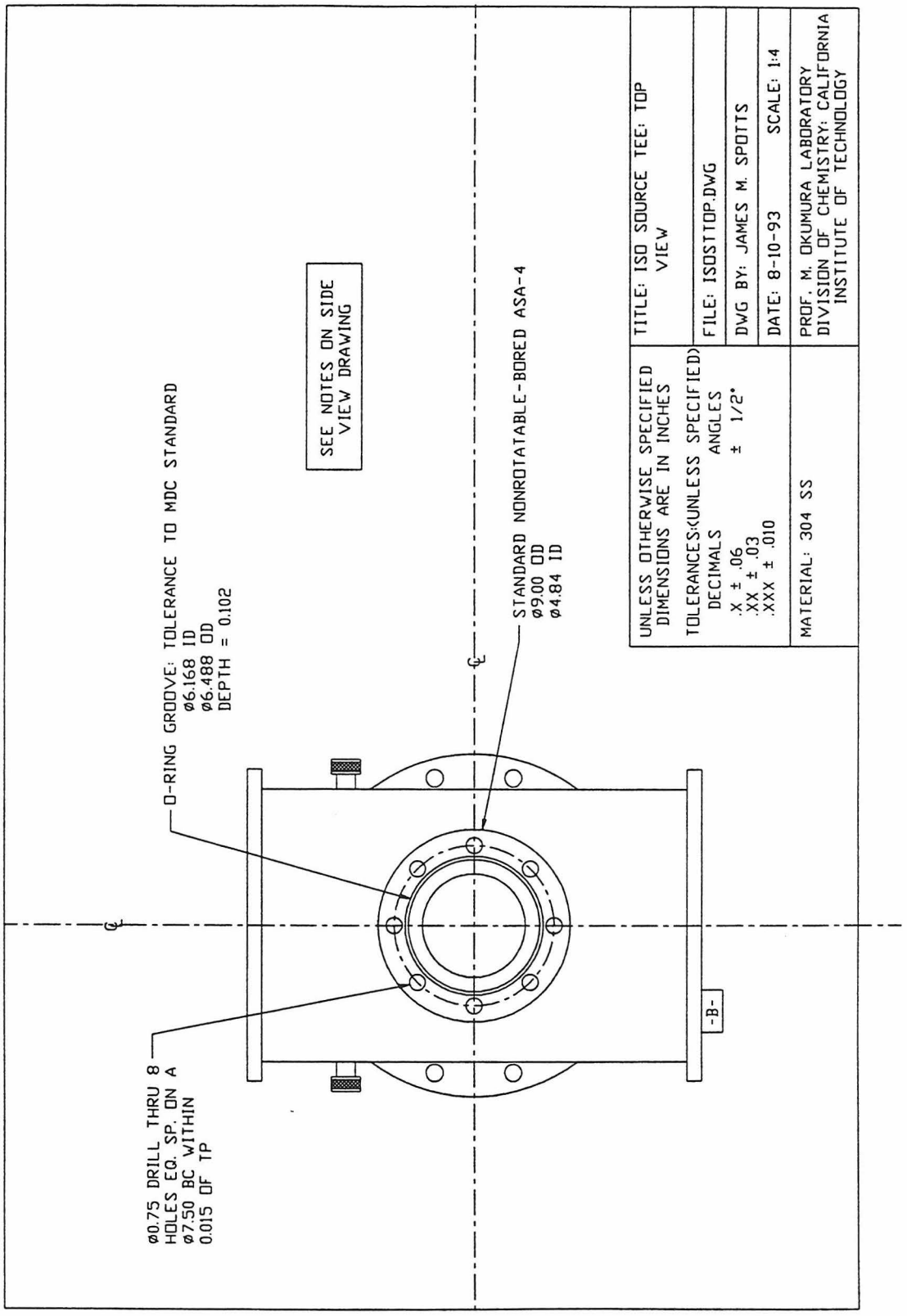

SEE NOTES ON SIDE
VIEW DRAWING
O-RING GROOVE: TOLERANCE TO MDC STANDARD
ø6.168 ID
ø6.488 OD
DEPTH = 0.102
STANDARD NONROTATABLE-BORED ASA-4
ø9.00 OD
ø4.84 ID
ø0.75 DRILL THRU 8
HOLES EQ. SP. ON A
ø7.50 BC WITHIN
0.015 OF TP
-B-
UNLESS OTHERWISE SPECIFIED
DIMENSIONS ARE IN INCHES
TOLERANCES:(UNLESS SPECIFIED)
DECIMALS ANGLES
X ± .06 ± 1/2°
.XX ± .03
.XXX ± .010
MATERIAL: 304 SS
TITLE: ISO SOURCE TEE: TOP VIEW
FILE: ISOSTTOP.DWG
DWG BY: JAMES M. SPOTTS
DATE: 8-10-93 SCALE: 1:4
PROF. M. OKUMURA LABORATORY
DIVISION OF CHEMISTRY: CALIFORNIA
INSTITUTE OF TECHNOLOGY

Figure 2-11

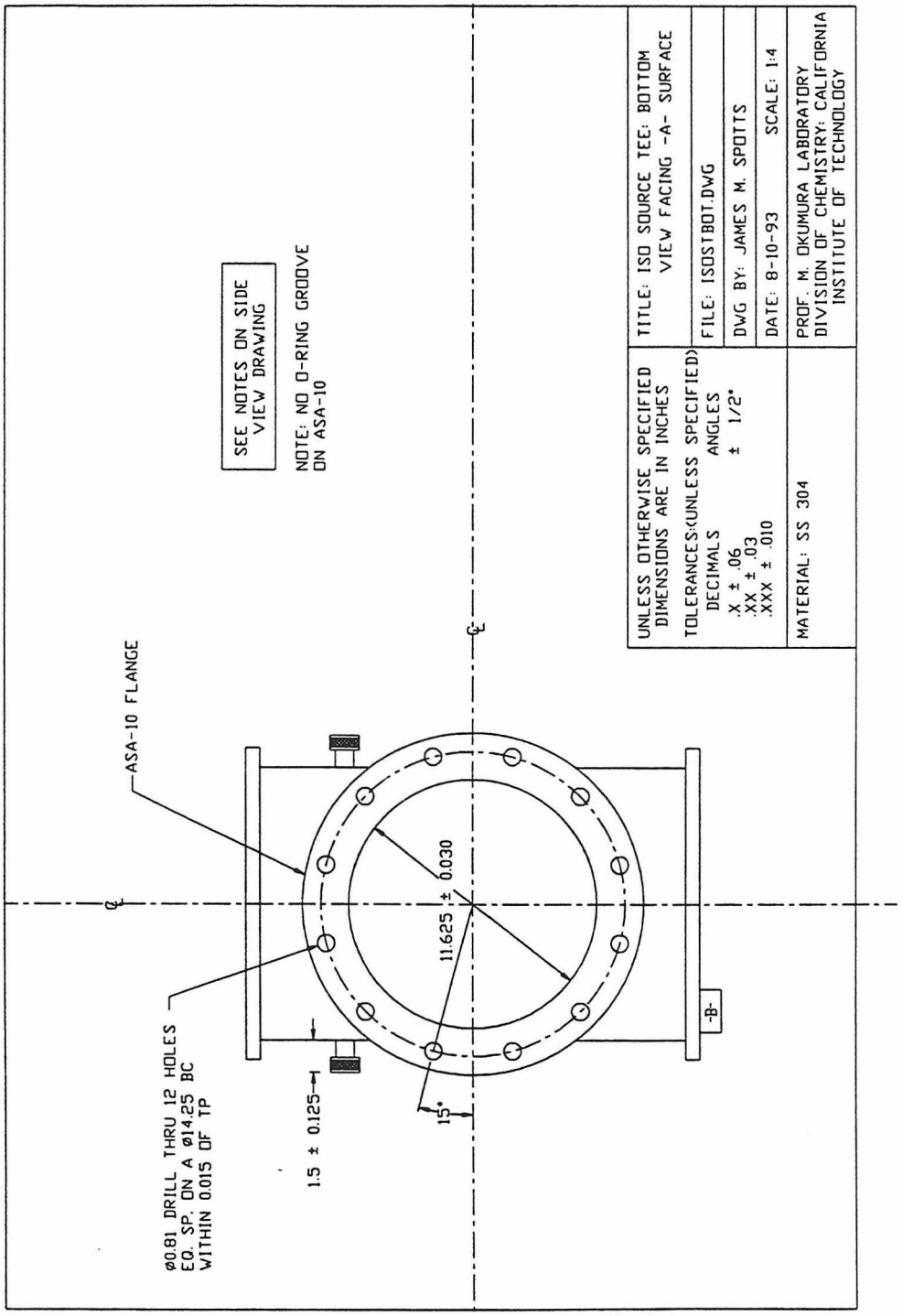
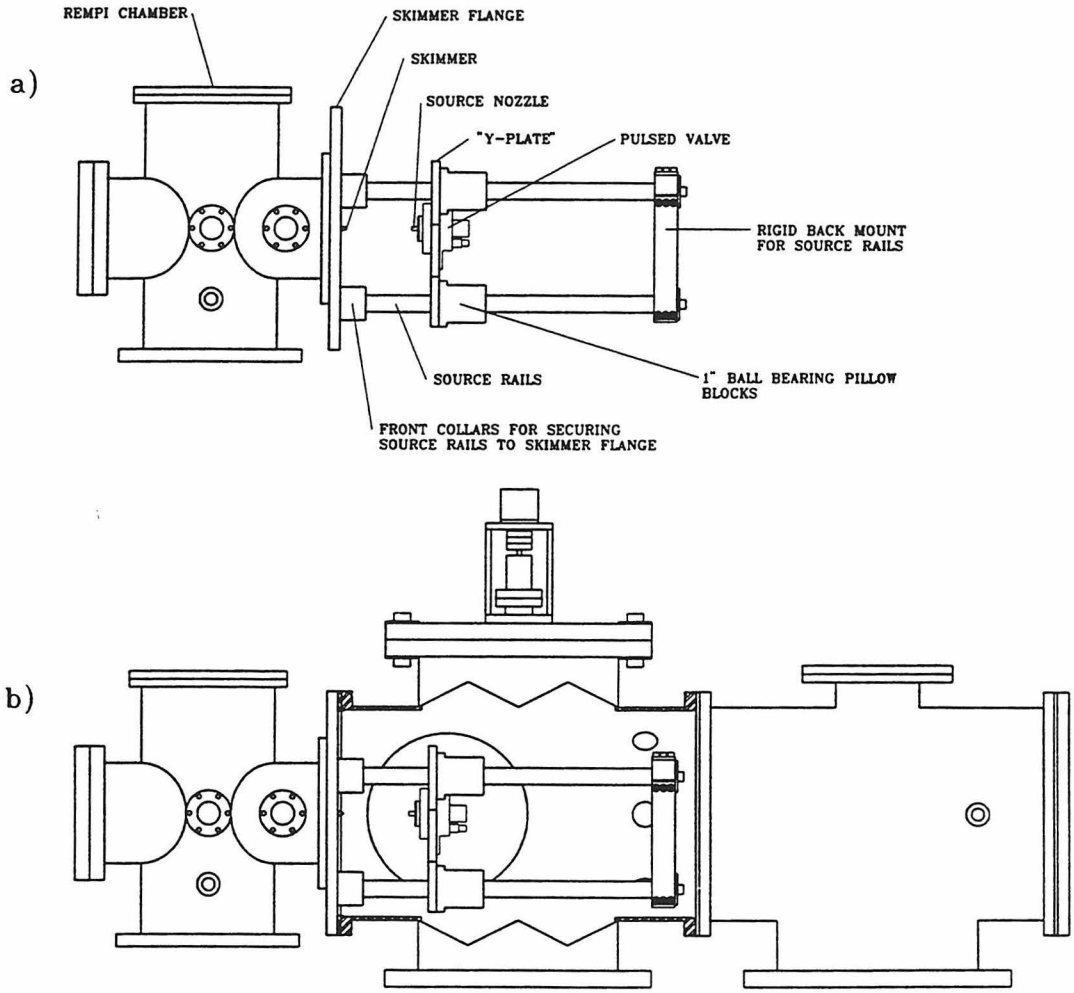

SEE NOTES ON SIDE VIEW DRAWING
NOTE: NO O-RING GROOVE ON ASA-10
ASA-10 FLANGE
ø0.81 DRILL THRU 12 HOLES EQ. SP. ON A ø14.25 BC WITHIN 0.015 OF TP
1.5 ± 0.125
11.625 ± 0.030
15°
-B-
UNLESS OTHERWISE SPECIFIED DIMENSIONS ARE IN INCHES
TOLERANCES:UNLESS SPECIFIED
DECIMALS ANGLES
.X ± .06 ± 1/2°
.XX ± .03
.XXX ± .010
MATERIAL: SS 304
TITLE: ISO SOURCE TEE: BOTTOM VIEW FACING -A- SURFACE
FILE: ISOSTBOT.DWG
DWG BY: JAMES M. SPOTTS
DATE: 8-10-93 SCALE: 1:4
PROF. M. OKUMURA LABORATORY
DIVISION OF CHEMISTRY: CALIFORNIA INSTITUTE OF TECHNOLOGY

Figure 2-12



Figures 2-13a and 2-13b

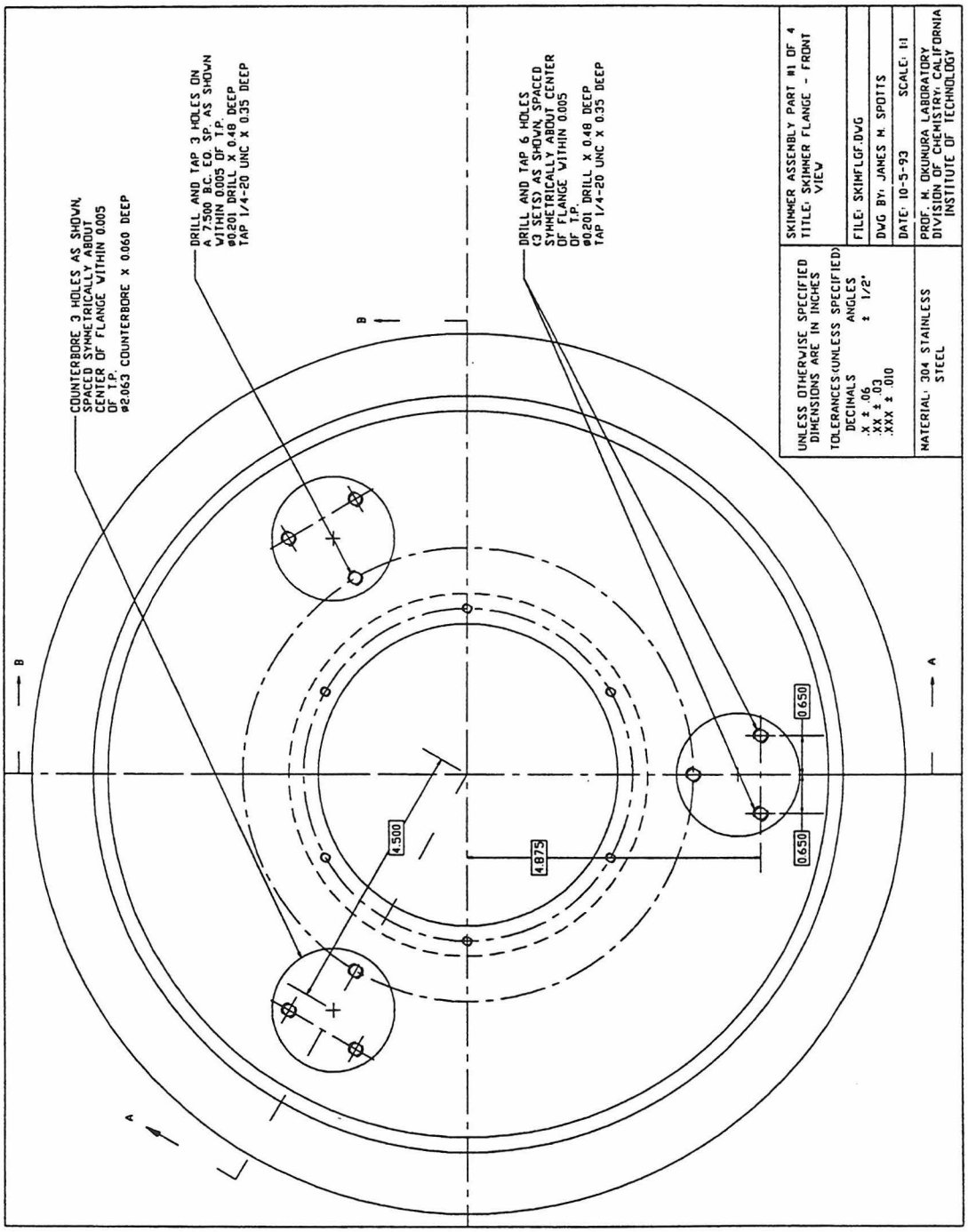

COUNTERBORE 3 HOLES AS SHOWN,
SPACED SYMMETRICALLY ABOUT
CENTER OF FLANGE WITHIN 0.005
OF T.P.
Ø2.063 COUNTERBORE x 0.060 DEEP
DRILL AND TAP 3 HOLES ON
A 7.500 B.C. EQ. SP. AS SHOWN
WITHIN 0.005 OF T.P.
Ø0.201 DRILL x 0.48 DEEP
TAP 1/4-20 UNC x 0.35 DEEP
DRILL AND TAP 6 HOLES
(3 SETS) AS SHOWN, SPACED
SYMMETRICALLY ABOUT CENTER
OF FLANGE WITHIN 0.005
OF T.P.
Ø0.201 DRILL x 0.48 DEEP
TAP 1/4-20 UNC x 0.35 DEEP
4.500
4.875
0.650
0.650
A
B
B
A
UNLESS OTHERWISE SPECIFIED
DIMENSIONS ARE IN INCHES
TOLERANCES:(UNLESS SPECIFIED)
DECIMALS
.X ± .06
.XX ± .03
.XXX ± .010
ANGLES
± 1/2°
MATERIAL: 304 STAINLESS
STEEL
SKIMMER ASSEMBLY PART #1 OF 4
TITLE: SKIMMER FLANGE - FRONT
VIEW
FILE: SKIMFLGF.DVG
DWG BY: JAMES M. SPOTTS
DATE: 10-5-93
SCALE: 1:1
PROF. M. OKUNURA LABORATORY
DIVISION OF CHEMISTRY, CALIFORNIA
INSTITUTE OF TECHNOLOGY

Figure 2-14

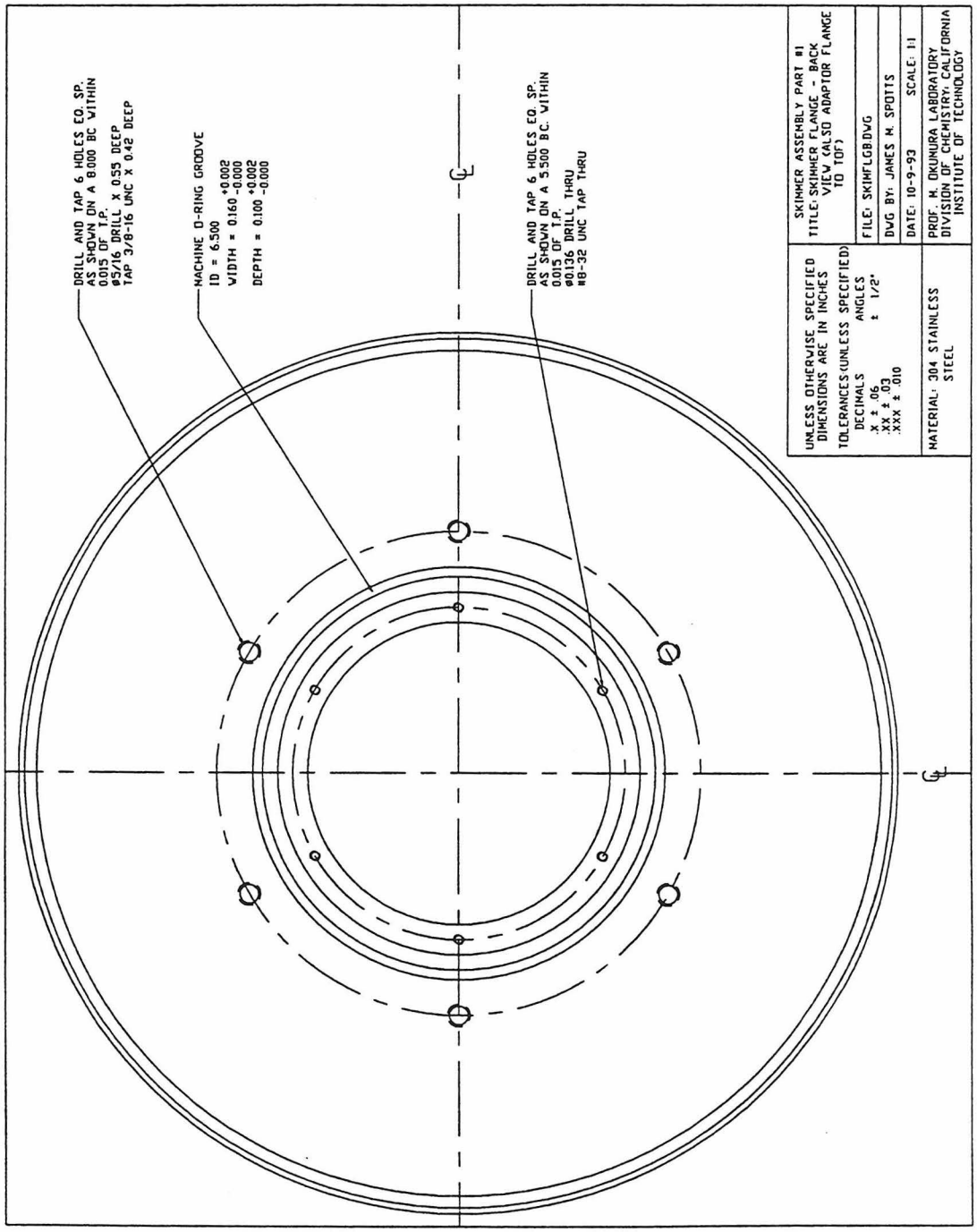

DRILL AND TAP 6 HOLES EQ. SP.
AS SHOWN ON A 8.000 BC WITHIN
0.015 OF T.P.
Ø5/16 DRILL X 0.55 DEEP
TAP 3/8-16 UNC X 0.42 DEEP
MACHINE O-RING GROOVE
ID = 6.500
WIDTH = 0.160 +0.002 -0.000
DEPTH = 0.100 +0.002 -0.000
DRILL AND TAP 6 HOLES EQ. SP.
AS SHOWN ON A 5.500 B.C. WITHIN
0.015 OF T.P.
Ø0.136 DRILL THRU
#8-32 UNC TAP THRU
SKIMMER ASSEMBLY PART #1
TITLE: SKIMMER FLANGE , BACK
VIEW (ALSO ADAPTOR FLANGE
TO TOP)
UNLESS OTHERWISE SPECIFIED
DIMENSIONS ARE IN INCHES
TOLERANCES (UNLESS SPECIFIED)
DECIMALS
ANGLES
.X ± .06
± 1/2°
.XX ± .03
.XXX ± .010
FILE: SKIMFLGB.DVG
DWG BY: JAMES M. SPOTTS
DATE: 10-9-93
SCALE: 1:1
MATERIAL: 304 STAINLESS STEEL
PROF. M. OKUNURA LABORATORY
DIVISION OF CHEMISTRY, CALIFORNIA
INSTITUTE OF TECHNOLOGY

Figure 2-15

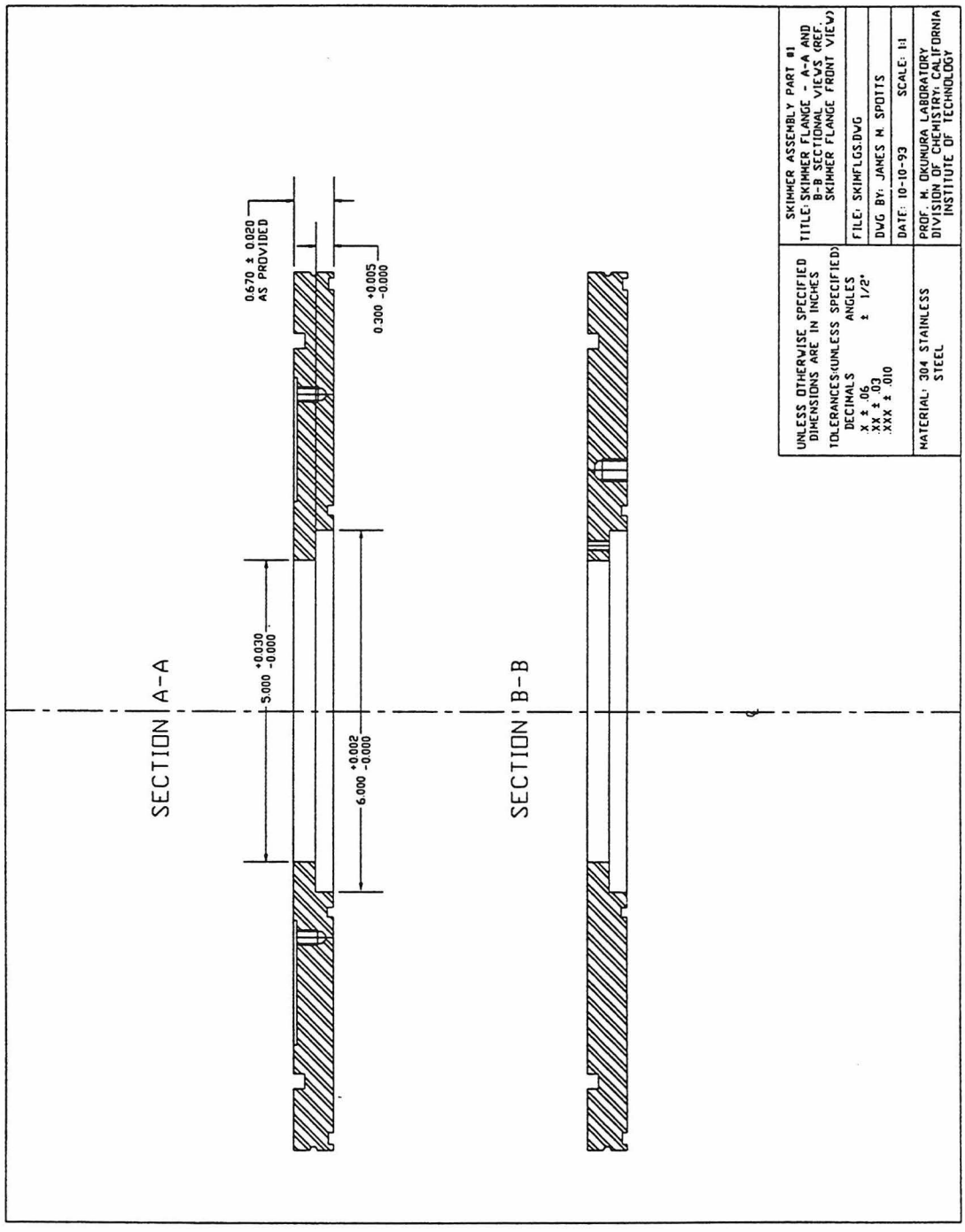

SECTION A-A
SECTION B-B
0.670 ± 0.020
AS PROVIDED
0.300 +0.005 -0.000
5.000 +0.030 -0.000
6.000 +0.002 -0.000
UNLESS OTHERWISE SPECIFIED
DIMENSIONS ARE IN INCHES
TOLERANCES:(UNLESS SPECIFIED)
DECIMALS ANGLES
.X ± .06 ± 1/2°
.XX ± .03
.XXX ± .010
SKIMMER ASSEMBLY PART #1
TITLE: SKIMMER FLANGE - A-A AND
B-B SECTIONAL VIEWS (REF.
SKIMMER FLANGE FRONT VIEW)
FILE: SKIMFLGS.DWG
DWG BY: JAMES M. SPOTTS
DATE: 10-10-93 SCALE: 1:1
MATERIAL: 304 STAINLESS
STEEL
PROF. M. OKUMURA LABORATORY
DIVISION OF CHEMISTRY: CALIFORNIA
INSTITUTE OF TECHNOLOGY

Figure 2-16

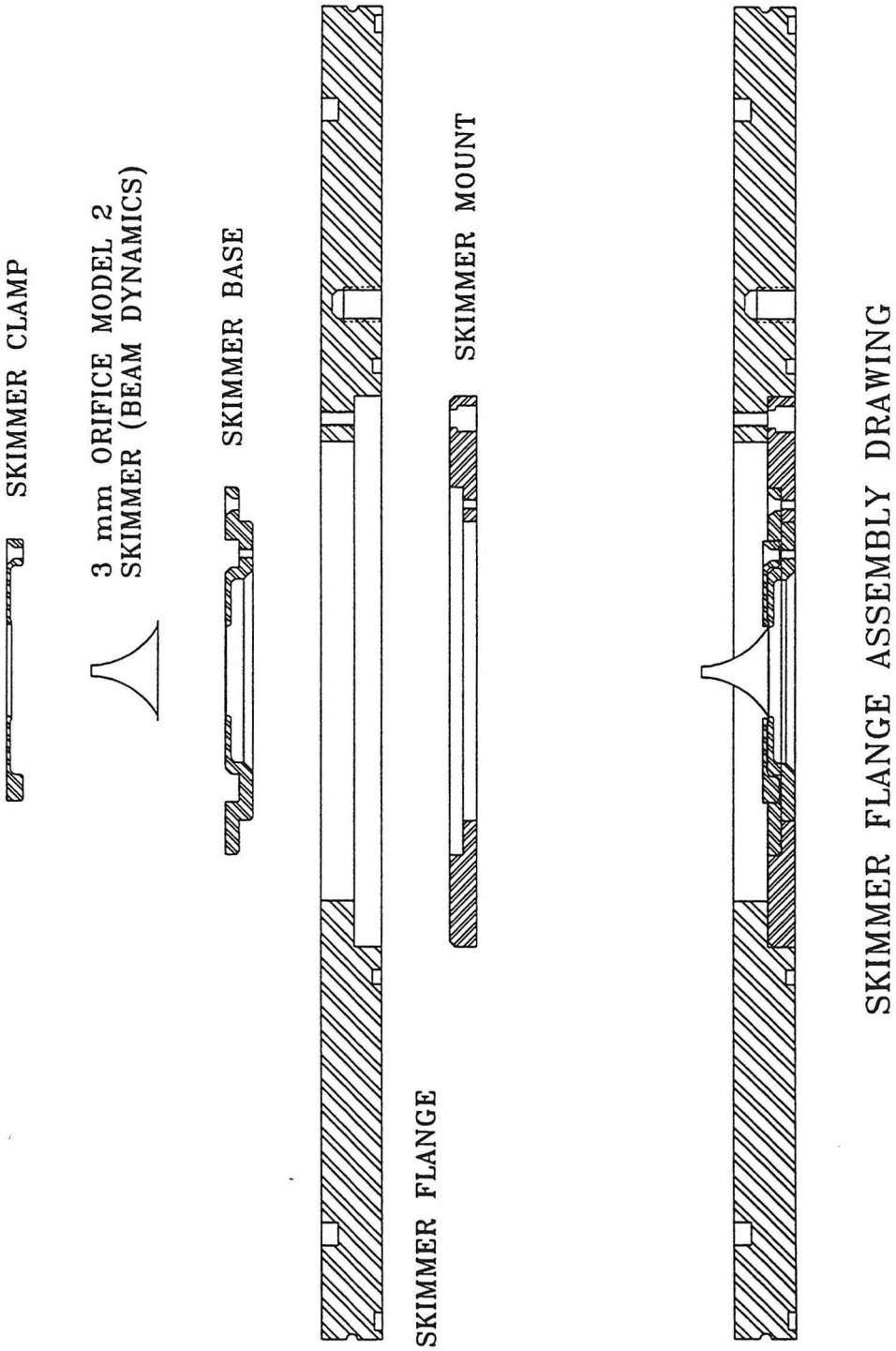

SKIMMER CLAMP
3 mm ORIFICE MODEL 2
SKIMMER (BEAM DYNAMICS)
SKIMMER BASE
SKIMMER MOUNT
SKIMMER FLANGE
SKIMMER FLANGE ASSEMBLY DRAWING

Figure 2-17

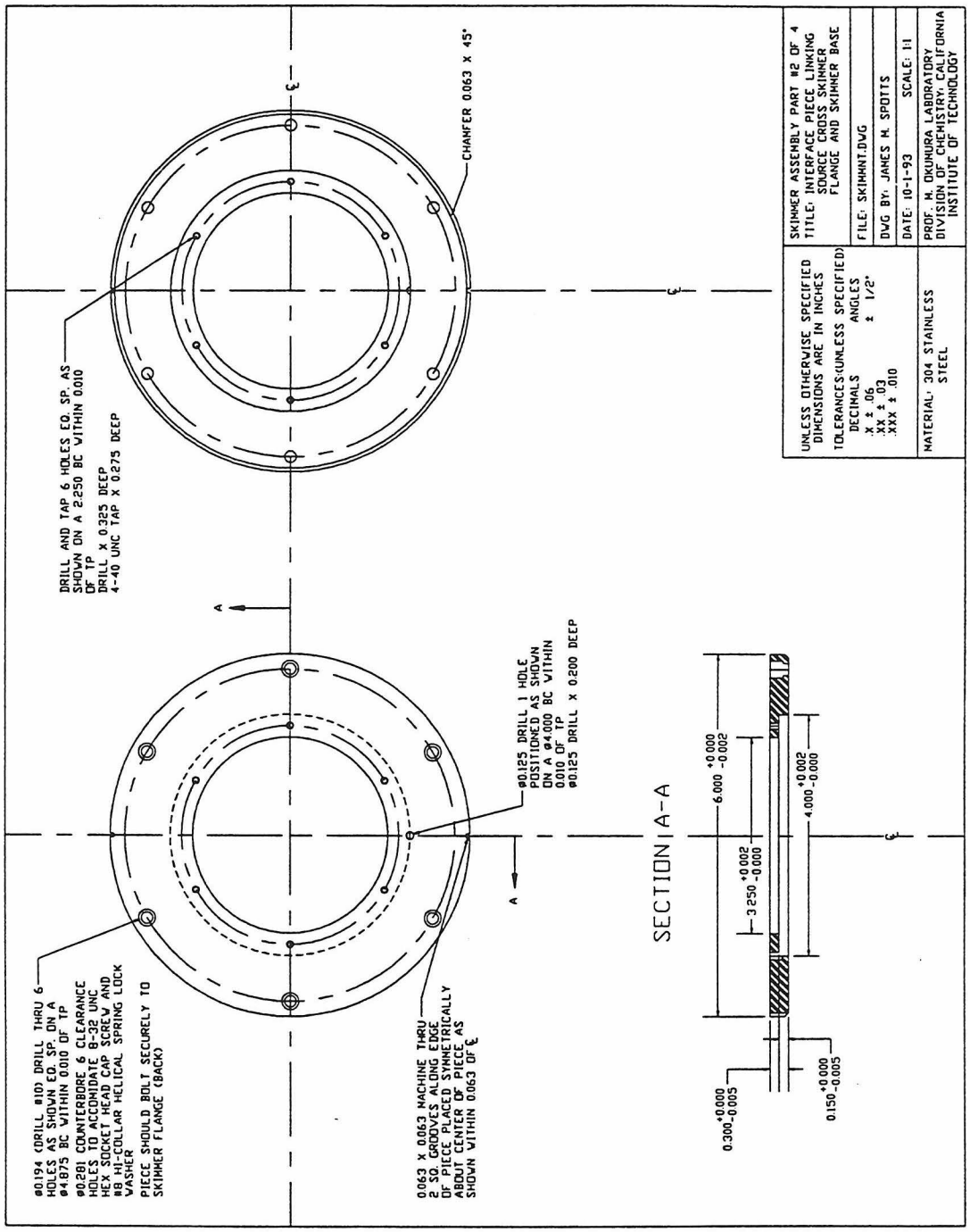

Ø.194 (DRILL #10) DRILL THRU 6 HOLES AS SHOWN EQ. SP. ON A Ø4.875 BC WITHIN 0.010 OF TP
Ø.201 COUNTERBORE 6 CLEARANCE HOLES TO ACCOMODATE 8-32 UNC HEX SOCKET HEAD CAP SCREW AND #8 HI-COLLAR HELICAL SPRING LOCK WASHER
PIECE SHOULD BOLT SECURELY TO SKIMMER FLANGE (BACK)
0.063 X 0.063 MACHINE THRU 2 SQ. GROOVES ALONG EDGE OF PIECE PLACED SYMMETRICALLY ABOUT CENTER OF PIECE AS SHOWN WITHIN 0.063 OF ℄
DRILL AND TAP 6 HOLES EQ. SP. AS SHOWN ON A 2.250 BC WITHIN 0.010 OF TP
DRILL X 0.325 DEEP
4-40 UNC TAP X 0.275 DEEP
CHAMFER 0.063 X 45°
Ø.125 DRILL 1 HOLE POSITIONED AS SHOWN ON A Ø4.000 BC WITHIN 0.010 OF TP
Ø.125 DRILL X 0.200 DEEP
SECTION A-A
6.000 +0.000 -0.002
3.250 +0.002 -0.000
4.000 +0.002 -0.000
0.300 +0.000 -0.005
0.150 +0.000 -0.005
UNLESS OTHERWISE SPECIFIED DIMENSIONS ARE IN INCHES
TOLERANCES:(UNLESS SPECIFIED)
DECIMALS
X ± .06
.XX ± .03
.XXX ± .010
ANGLES
± 1/2°
MATERIAL: 304 STAINLESS STEEL
SKIMMER ASSEMBLY PART #2 OF 4
TITLE: INTERFACE PIECE LINKING SOURCE CROSS SKIMMER FLANGE AND SKIMMER BASE
FILE: SKIMNT.DWG
DWG BY: JAMES M. SPOTTS
DATE: 10-1-93
SCALE: 1:1
PROF. M. OKUNURA LABORATORY
DIVISION OF CHEMISTRY, CALIFORNIA INSTITUTE OF TECHNOLOGY

Figure 2-18

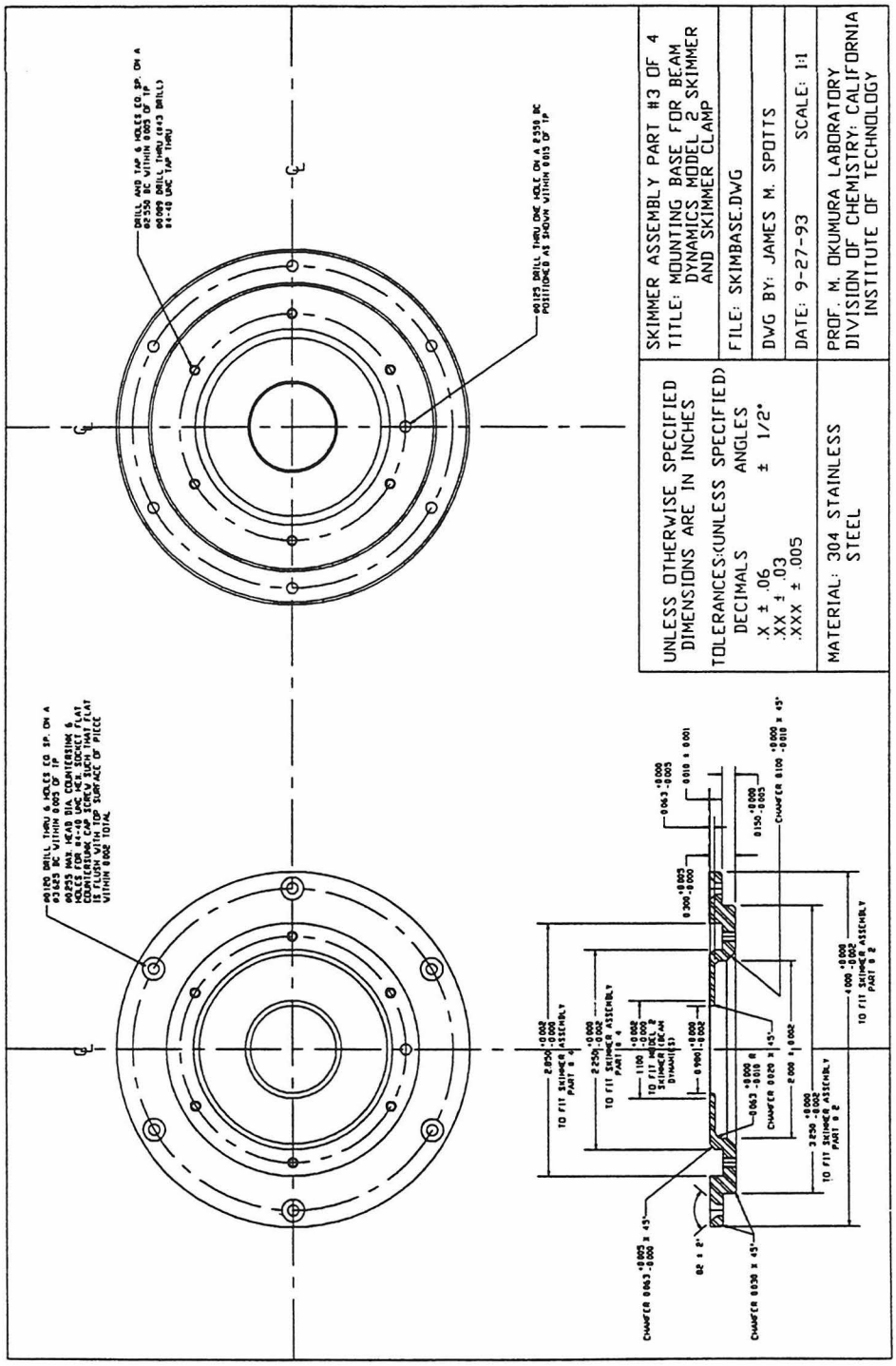

UNLESS OTHERWISE SPECIFIED
DIMENSIONS ARE IN INCHES
TOLERANCES:(UNLESS SPECIFIED)
DECIMALS
ANGLES
.X ± .06
± 1/2°
.XX ± .03
.XXX ± .005
MATERIAL: 304 STAINLESS STEEL
SKIMMER ASSEMBLY PART #3 OF 4
TITLE: MOUNTING BASE FOR BEAM DYNAMICS MODEL 2 SKIMMER AND SKIMMER CLAMP
FILE: SKIMBASE.DWG
DWG BY: JAMES M. SPOTTS
DATE: 9-27-93
SCALE: 1:1
PROF. M. OKUMURA LABORATORY
DIVISION OF CHEMISTRY: CALIFORNIA INSTITUTE OF TECHNOLOGY

Figure 2-19

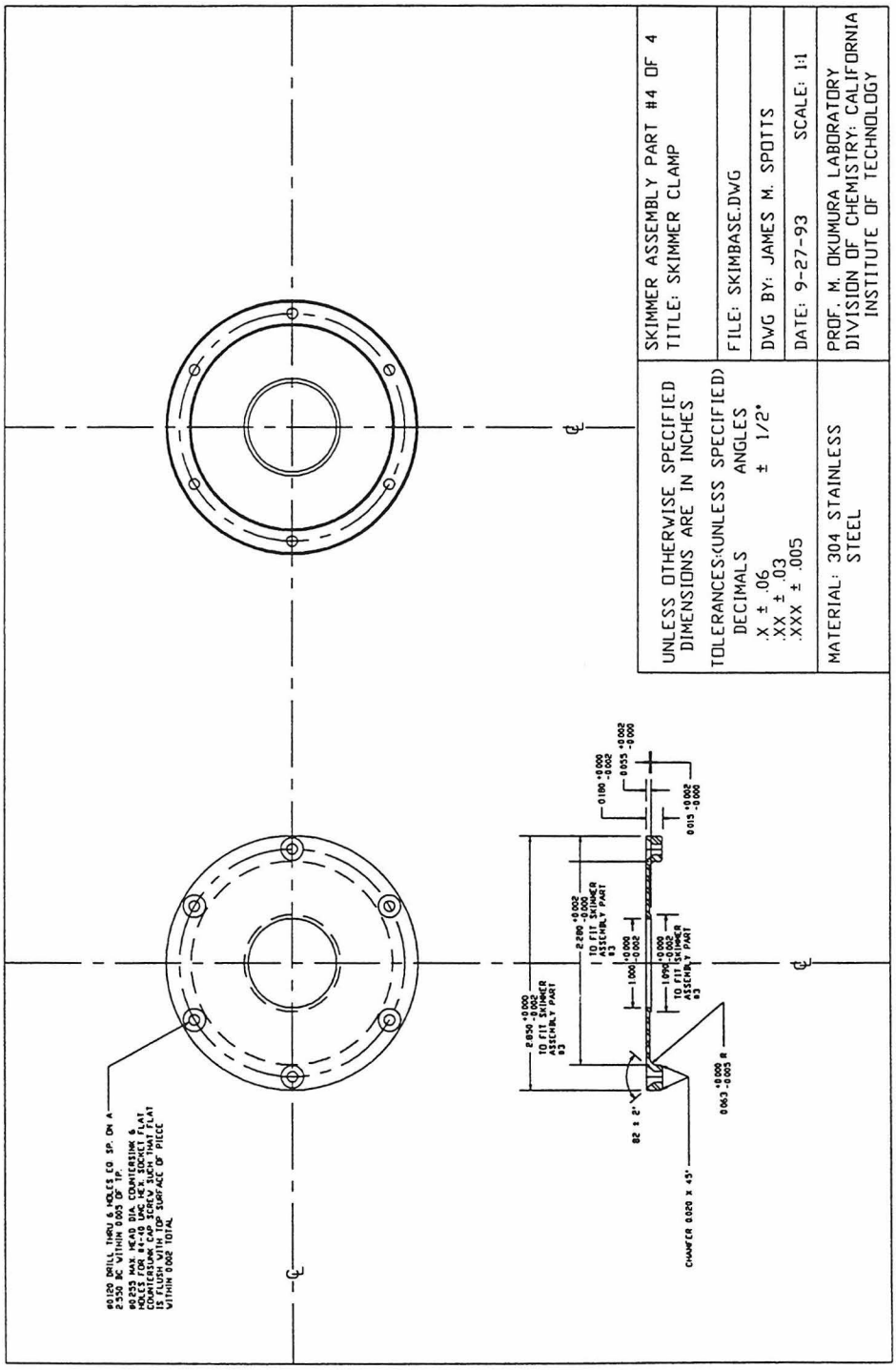

SKIMMER ASSEMBLY PART #4 OF 4
TITLE: SKIMMER CLAMP
FILE: SKIMBASE.DWG
DWG BY: JAMES M. SPOTTS
DATE: 9-27-93
SCALE: 1:1
PROF. M. OKUMURA LABORATORY
DIVISION OF CHEMISTRY: CALIFORNIA
INSTITUTE OF TECHNOLOGY
UNLESS OTHERWISE SPECIFIED
DIMENSIONS ARE IN INCHES
TOLERANCES:(UNLESS SPECIFIED)
DECIMALS
ANGLES
.X ± .06
.XX ± .03
.XXX ± .005
± 1/2°
MATERIAL: 304 STAINLESS STEEL
TO FIT SKIMMER ASSEMBLY PART #3
CHAMFER .020 x 45°

Figure 2-20

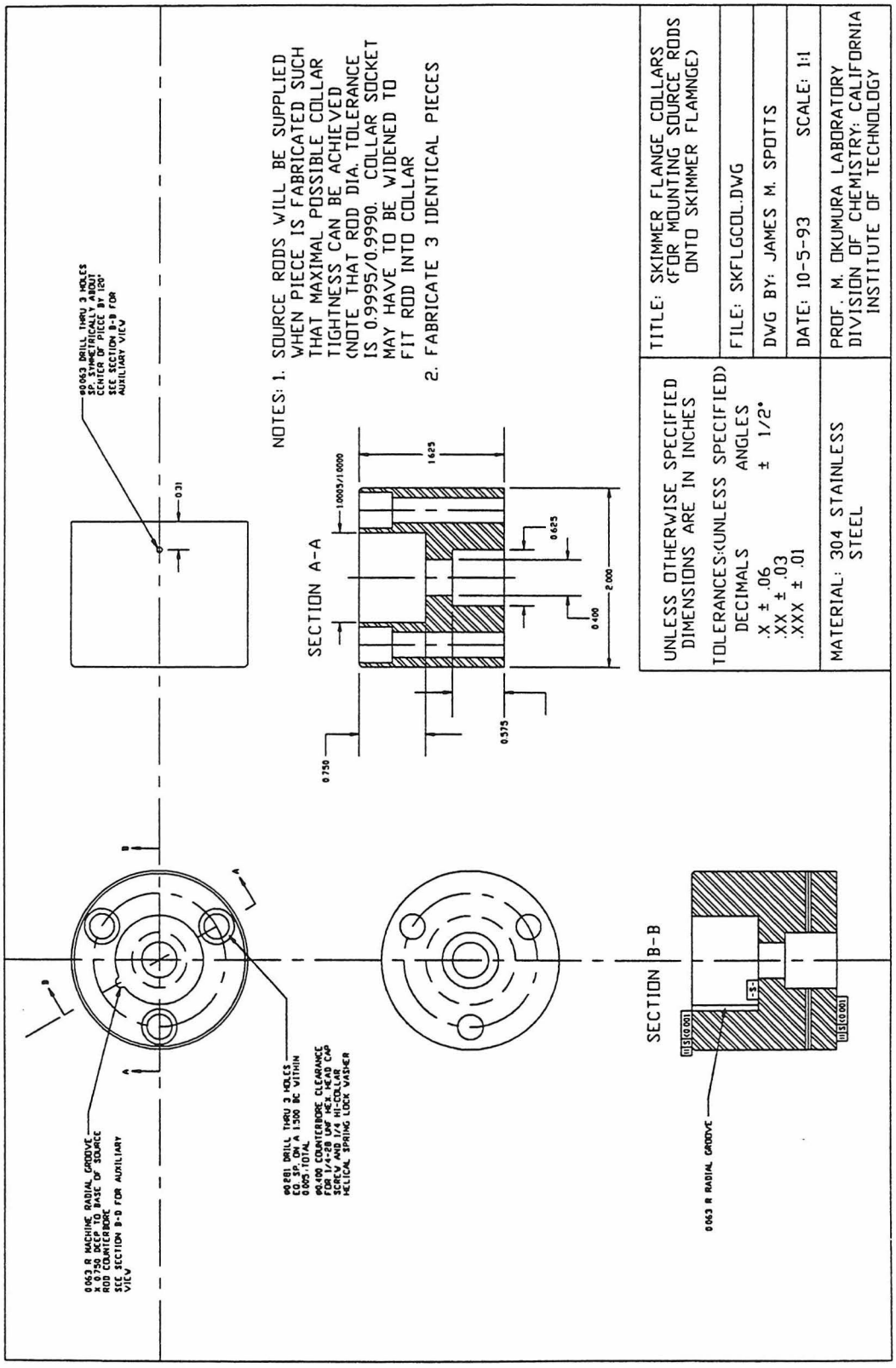

NOTES: 1. SOURCE RODS WILL BE SUPPLIED WHEN PIECE IS FABRICATED SUCH THAT MAXIMAL POSSIBLE COLLAR TIGHTNESS CAN BE ACHIEVED (NOTE THAT ROD DIA. TOLERANCE IS 0.9995/0.9990. COLLAR SOCKET MAY HAVE TO BE WIDENED TO FIT ROD INTO COLLAR
2. FABRICATE 3 IDENTICAL PIECES
SECTION A-A
SECTION B-B
TITLE: SKIMMER FLANGE COLLARS (FOR MOUNTING SOURCE RODS ONTO SKIMMER FLAMNGE)
FILE: SKFLGCOL.DWG
DWG BY: JAMES M. SPOTTS
DATE: 10-5-93
SCALE: 1:1
UNLESS OTHERWISE SPECIFIED DIMENSIONS ARE IN INCHES
TOLERANCES:(UNLESS SPECIFIED)
DECIMALS
X ± .06
.XX ± .03
.XXX ± .01
ANGLES ± 1/2°
MATERIAL: 304 STAINLESS STEEL
PROF. M. OKUMURA LABORATORY
DIVISION OF CHEMISTRY: CALIFORNIA INSTITUTE OF TECHNOLOGY

Figure 2-21

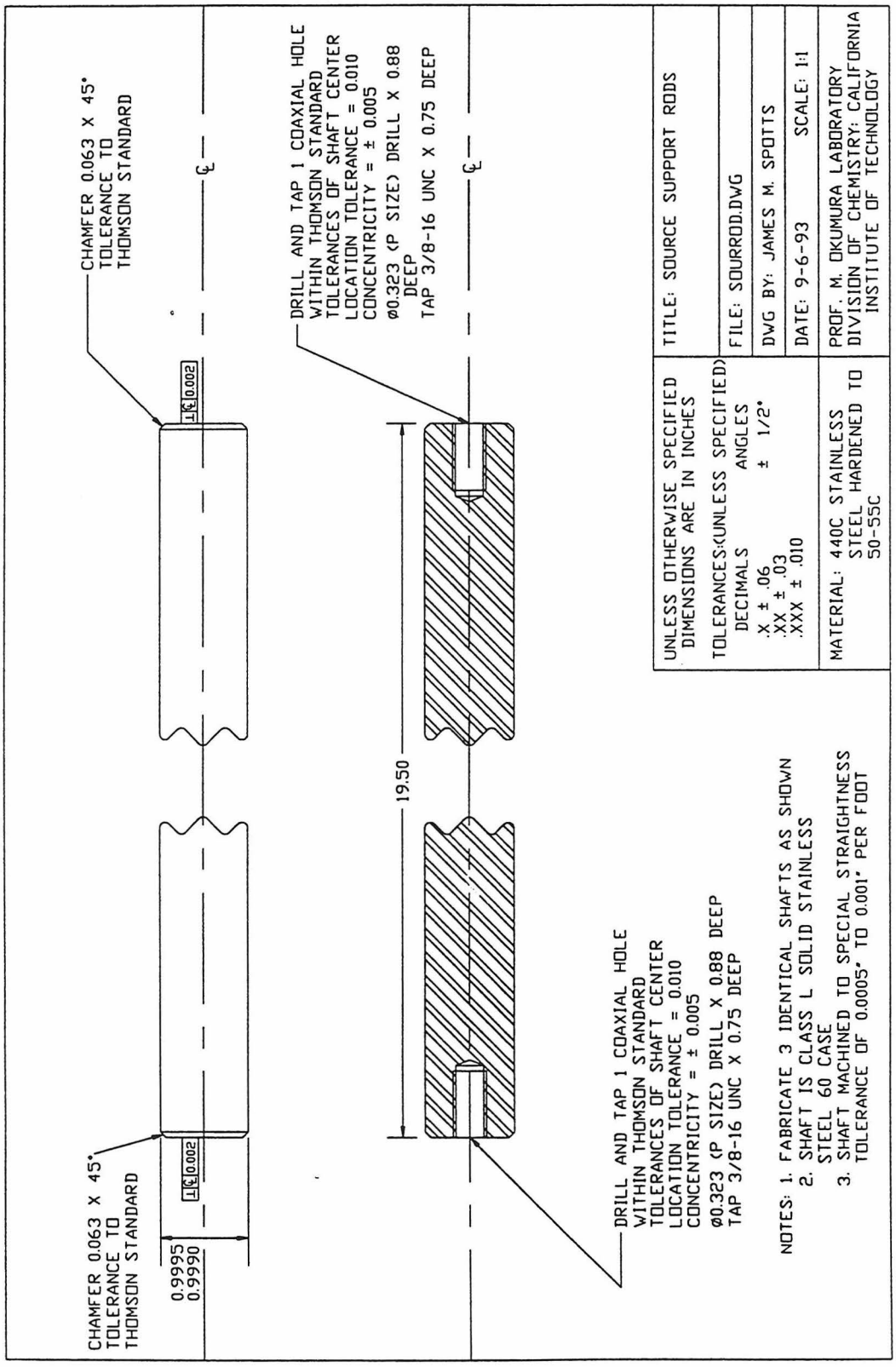

CHAMFER 0.063 X 45°
TOLERANCE TO
THOMSON STANDARD
DRILL AND TAP 1 COAXIAL HOLE
WITHIN THOMSON STANDARD
TOLERANCES OF SHAFT CENTER
LOCATION TOLERANCE = 0.010
CONCENTRICITY = ± 0.005
Ø0.323 (P SIZE) DRILL X 0.88
DEEP
TAP 3/8-16 UNC X 0.75 DEEP
1 Ⓜ 0.002
0.9995
0.9990
19.50
NOTES: 1. FABRICATE 3 IDENTICAL SHAFTS AS SHOWN
2. SHAFT IS CLASS L SOLID STAINLESS
STEEL 60 CASE
3. SHAFT MACHINED TO SPECIAL STRAIGHTNESS
TOLERANCE OF 0.0005" TO 0.001" PER FOOT
UNLESS OTHERWISE SPECIFIED
DIMENSIONS ARE IN INCHES
TOLERANCES:(UNLESS SPECIFIED)
DECIMALS ANGLES
.X ± .06 ± 1/2°
.XX ± .03
.XXX ± .010
MATERIAL: 440C STAINLESS
STEEL HARDENED TO
50-55C
TITLE: SOURCE SUPPORT RODS
FILE: SOURROD.DWG
DWG BY: JAMES M. SPOTTS
DATE: 9-6-93 SCALE: 1:1
PROF. M. OKUMURA LABORATORY
DIVISION OF CHEMISTRY: CALIFORNIA
INSTITUTE OF TECHNOLOGY

Figure 2-22

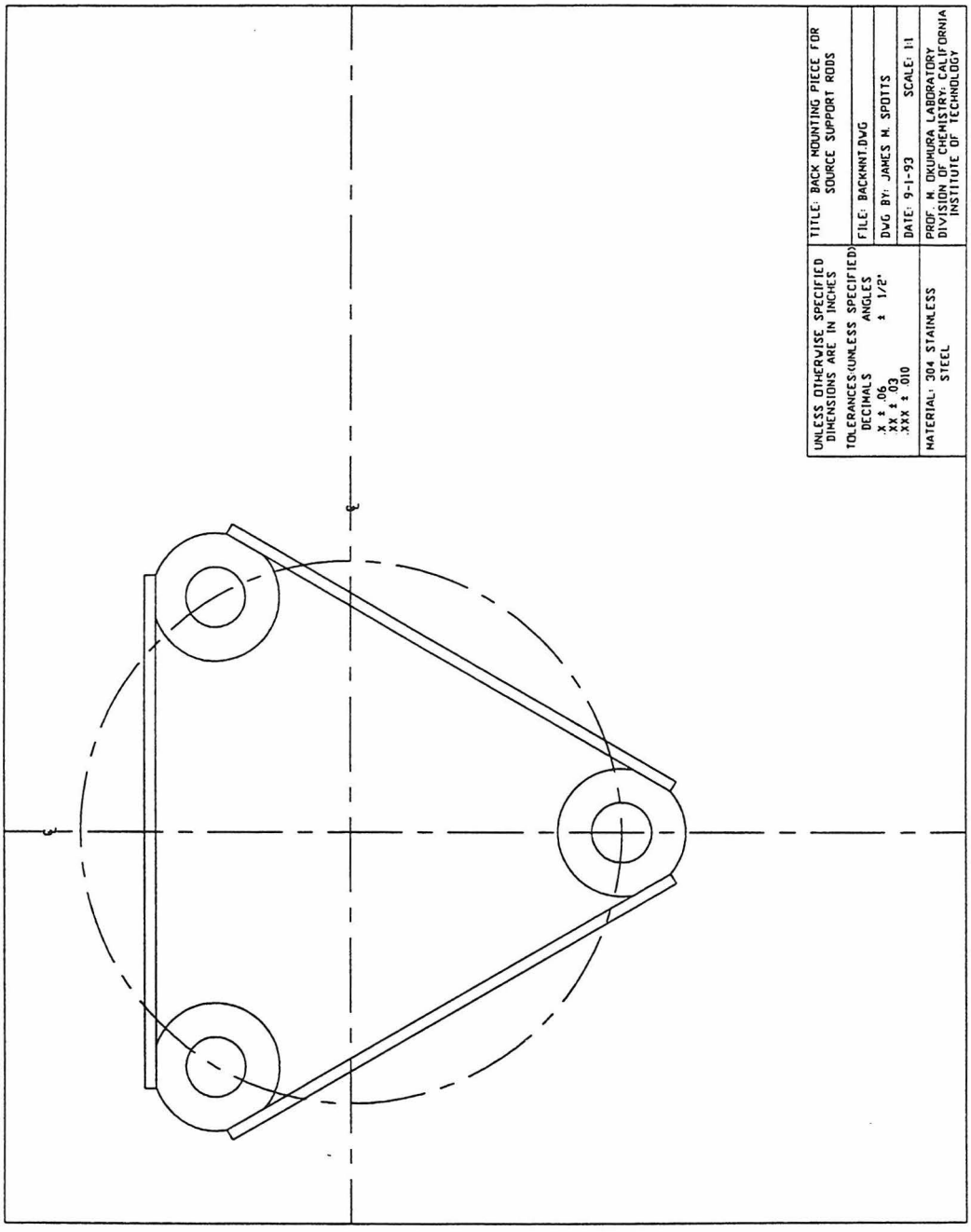

UNLESS OTHERWISE SPECIFIED DIMENSIONS ARE IN INCHES
TOLERANCES:(UNLESS SPECIFIED)
DECIMALS ANGLES
X ± .06 ± 1/2°
.XX ± .03
.XXX ± .010
MATERIAL: 304 STAINLESS STEEL
TITLE: BACK MOUNTING PIECE FOR SOURCE SUPPORT RODS
FILE: BACKMNT.DWG
DWG BY: JAMES M. SPOTTS
DATE: 9-1-93
SCALE: 1:1
PROF. M. OKUMURA LABORATORY
DIVISION OF CHEMISTRY: CALIFORNIA INSTITUTE OF TECHNOLOGY

Figure 2-23

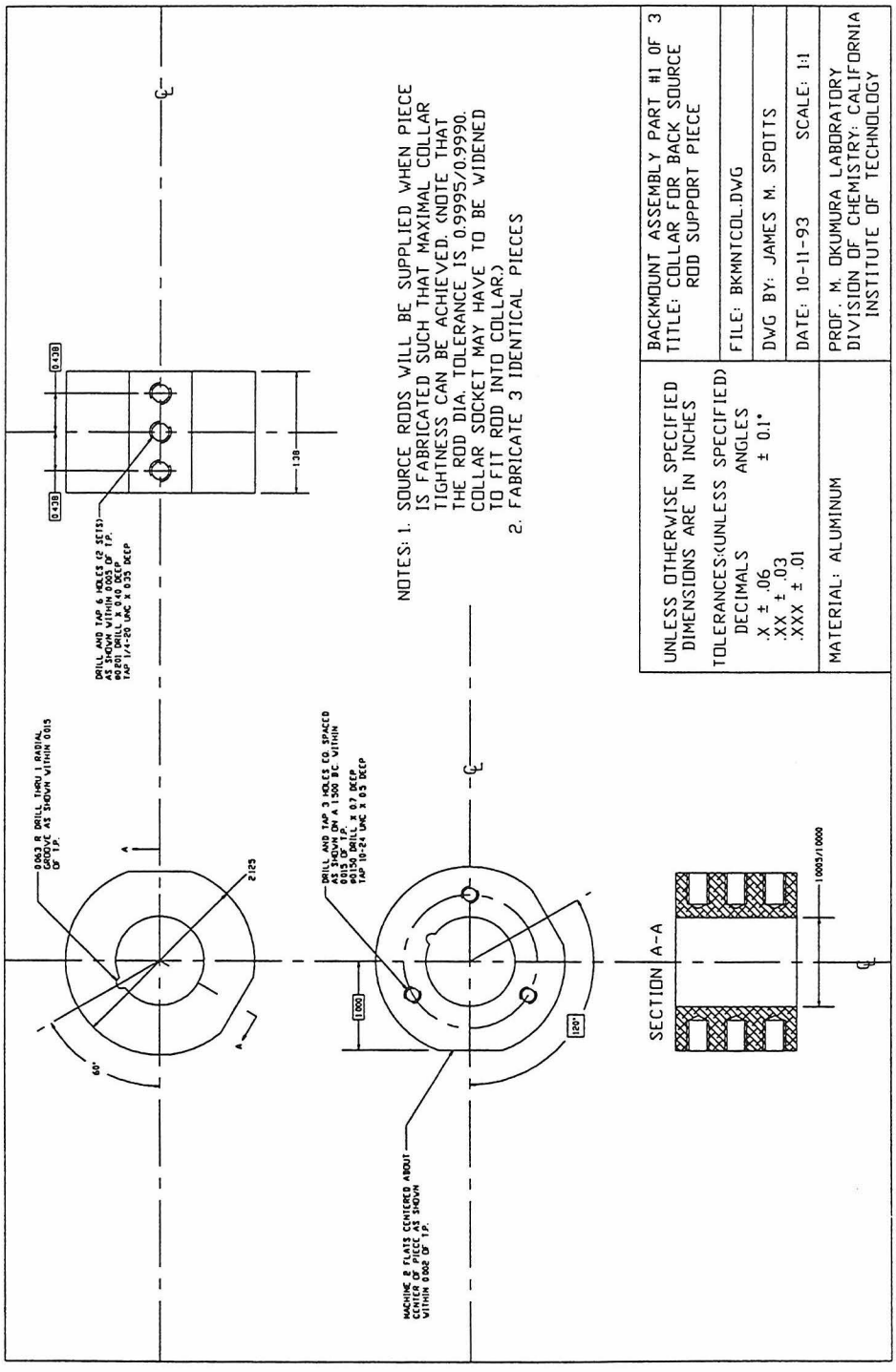

NOTES: 1. SOURCE RODS WILL BE SUPPLIED WHEN PIECE IS FABRICATED SUCH THAT MAXIMAL COLLAR TIGHTNESS CAN BE ACHIEVED. (NOTE THAT THE ROD DIA. TOLERANCE IS 0.9995/0.9990. COLLAR SOCKET MAY HAVE TO BE WIDENED TO FIT ROD INTO COLLAR.)
2. FABRICATE 3 IDENTICAL PIECES
UNLESS OTHERWISE SPECIFIED DIMENSIONS ARE IN INCHES
TOLERANCES:(UNLESS SPECIFIED)
DECIMALS
.X ± .06
.XX ± .03
.XXX ± .01
ANGLES ± 0.1°
MATERIAL: ALUMINUM
BACKMOUNT ASSEMBLY PART #1 OF 3
TITLE: COLLAR FOR BACK SOURCE ROD SUPPORT PIECE
FILE: BKMNTCOL.DWG
DWG BY: JAMES M. SPOTTS
DATE: 10-11-93
SCALE: 1:1
PROF. M. OKUMURA LABORATORY
DIVISION OF CHEMISTRY: CALIFORNIA INSTITUTE OF TECHNOLOGY
SECTION A-A
2.125
.130
.438
.438
60°
120°
1.000

Figure 2-24

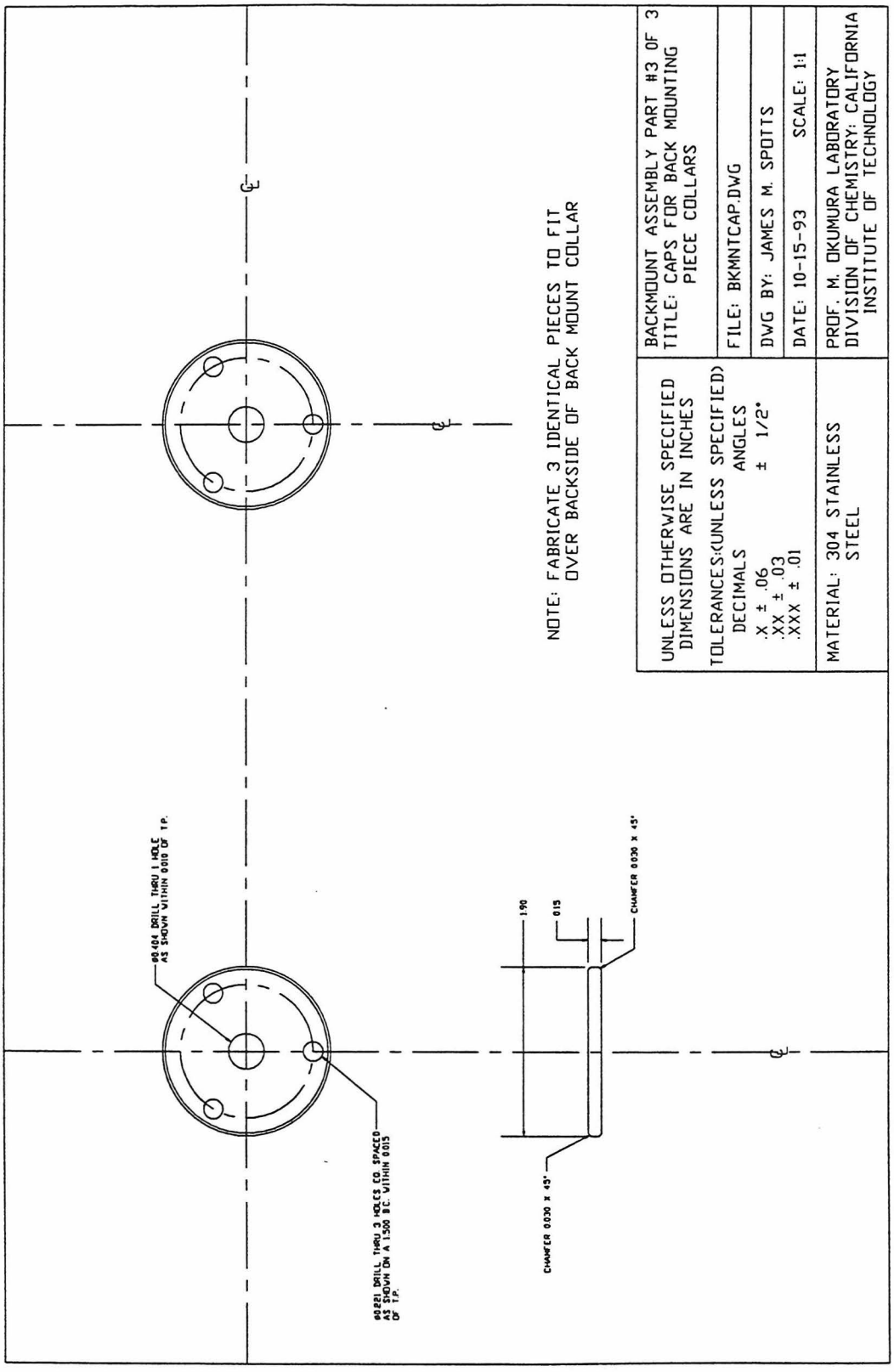

NOTE: FABRICATE 3 IDENTICAL PIECES TO FIT OVER BACKSIDE OF BACK MOUNT COLLAR
UNLESS OTHERWISE SPECIFIED DIMENSIONS ARE IN INCHES
TOLERANCES:(UNLESS SPECIFIED)
DECIMALS ANGLES
.X ± .06 ± 1/2°
.XX ± .03
.XXX ± .01
MATERIAL: 304 STAINLESS STEEL
BACKMOUNT ASSEMBLY PART #3 OF 3
TITLE: CAPS FOR BACK MOUNTING PIECE COLLARS
FILE: BKMNTCAP.DWG
DWG BY: JAMES M. SPOTTS
DATE: 10-15-93 SCALE: 1:1
PROF. M. OKUMURA LABORATORY
DIVISION OF CHEMISTRY: CALIFORNIA INSTITUTE OF TECHNOLOGY
Ø.404 DRILL THRU 1 HOLE AS SHOWN WITHIN Ø.010 OF T.P.
Ø.221 DRILL THRU 3 HOLES EQ. SPACED AS SHOWN ON A 1.500 B.C. WITHIN Ø.015 OF T.P.
CHAMFER .030 x 45°
.190
.015
CHAMFER .030 x 45°

Figure 2-25

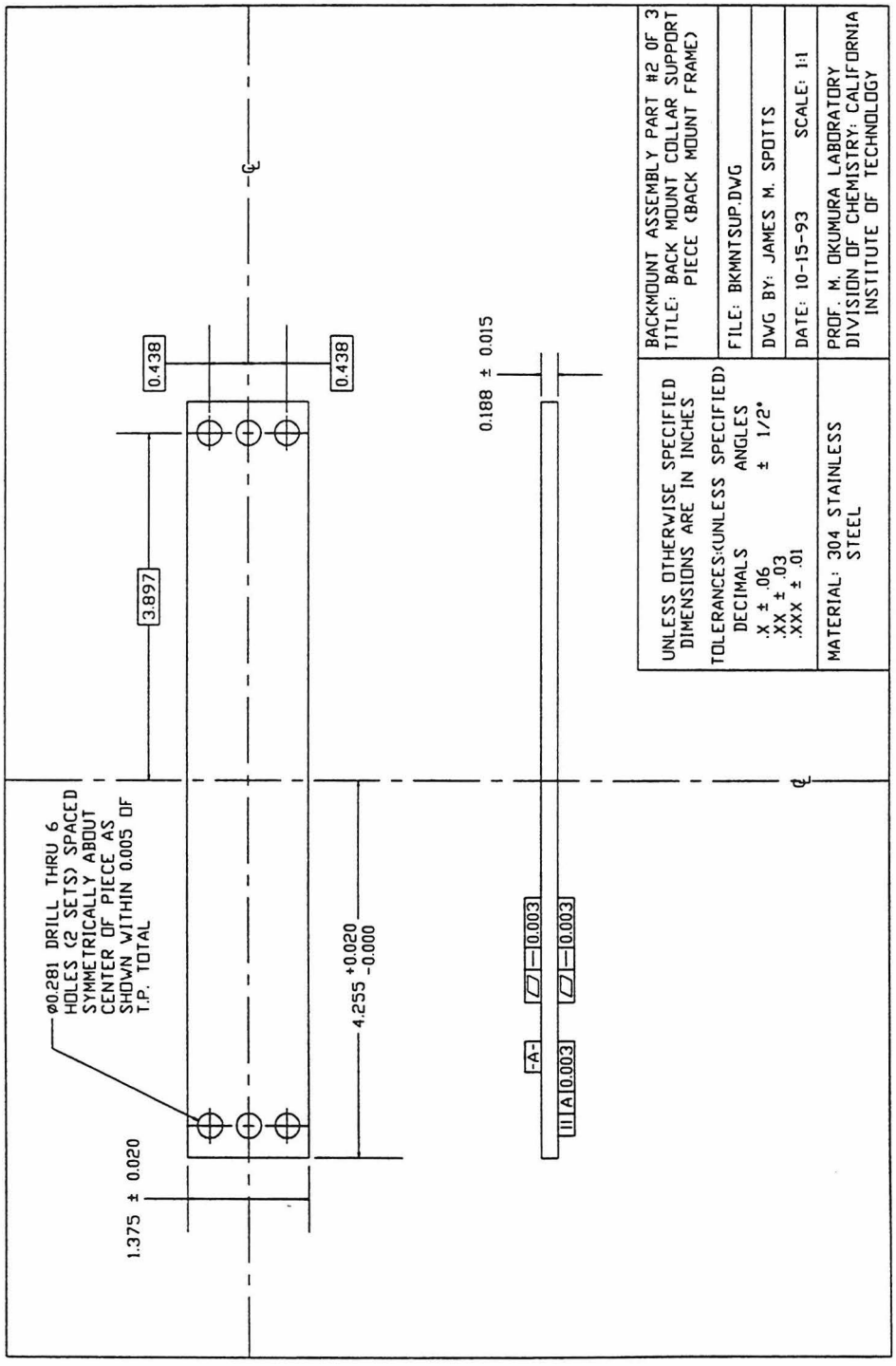

ø0.281 DRILL THRU 6
HOLES (2 SETS) SPACED
SYMMETRICALLY ABOUT
CENTER OF PIECE AS
SHOWN WITHIN 0.005 OF
T.P. TOTAL
1.375 ± 0.020
3.897
0.438
0.438
4.255 +0.020 -0.000
0.188 ± 0.015
-A-
0.003
A 0.003
UNLESS OTHERWISE SPECIFIED
DIMENSIONS ARE IN INCHES
TOLERANCES:(UNLESS SPECIFIED)
DECIMALS ANGLES
.X ± .06 ± 1/2°
.XX ± .03
.XXX ± .01
MATERIAL: 304 STAINLESS
STEEL
BACKMOUNT ASSEMBLY PART #2 OF 3
TITLE: BACK MOUNT COLLAR SUPPORT
PIECE (BACK MOUNT FRAME)
FILE: BKMNTSUP.DWG
DWG BY: JAMES M. SPOTTS
DATE: 10-15-93 SCALE: 1:1
PROF. M. OKUMURA LABORATORY
DIVISION OF CHEMISTRY: CALIFORNIA
INSTITUTE OF TECHNOLOGY

Figure 2-26

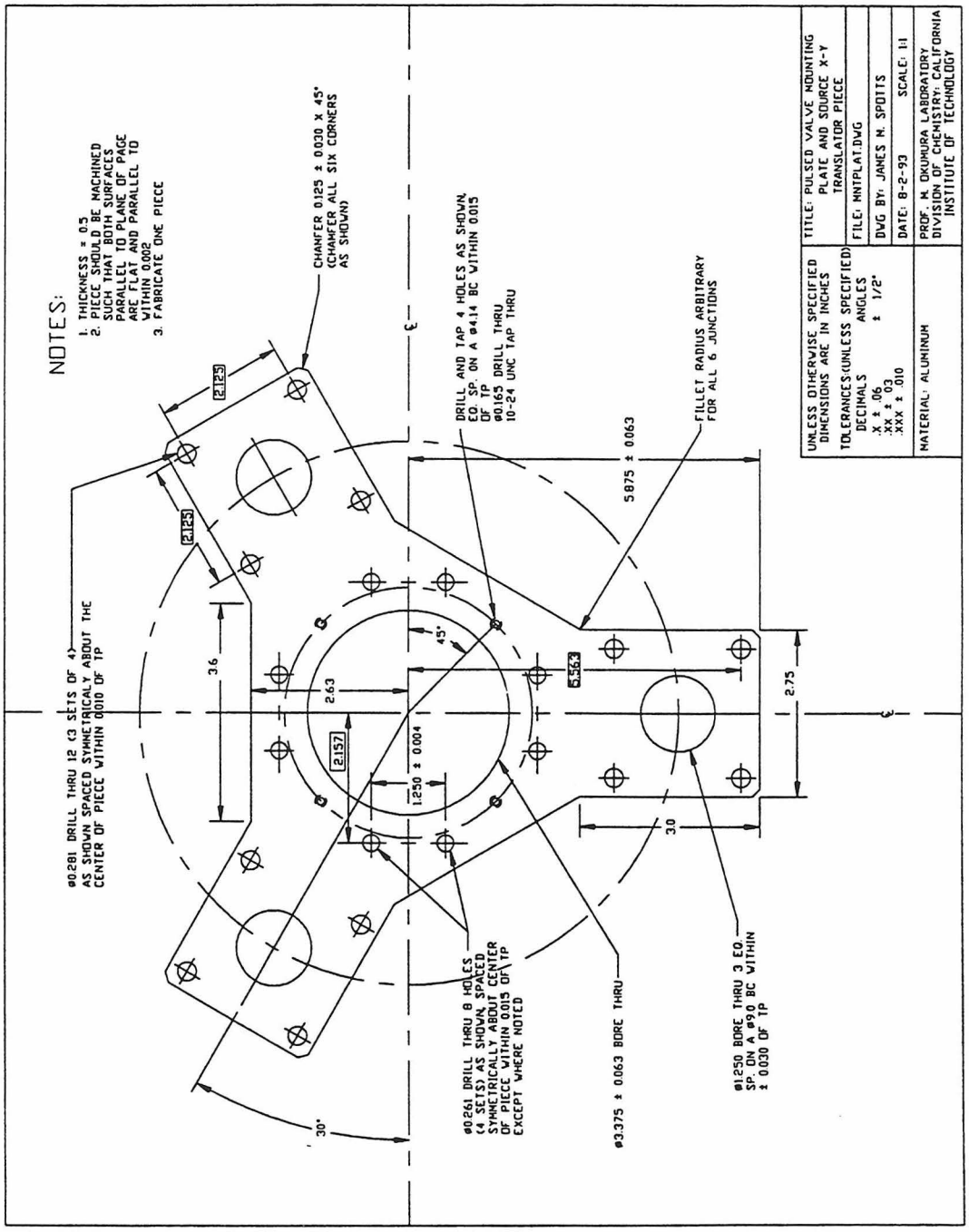

NOTES:
1. THICKNESS = 0.5
2. PIECE SHOULD BE MACHINED SUCH THAT BOTH SURFACES PARALLEL TO PLANE OF PAGE ARE FLAT AND PARALLEL TO WITHIN 0.002
3. FABRICATE ONE PIECE
CHAMFER 0.125 ± 0.030 X 45° (CHAMFER ALL SIX CORNERS AS SHOWN)
DRILL AND TAP 4 HOLES AS SHOWN EQ SP. ON A ø4.14 BC WITHIN 0.015 OF TP ø0.165 DRILL THRU 10-24 UNC TAP THRU
FILLET RADIUS ARBITRARY FOR ALL 6 JUNCTIONS
ø0.281 DRILL THRU 12 (3 SETS OF 4) AS SHOWN SPACED SYMMETRICALY ABOUT THE CENTER OF PIECE WITHIN 0.010 OF TP
ø0.261 DRILL THRU 8 HOLES (4 SETS) AS SHOWN, SPACED SYMMETRICALLY ABOUT CENTER OF PIECE WITHIN 0.015 OF TP EXCEPT WHERE NOTED
ø3.375 ± 0.063 BORE THRU
ø1.250 BORE THRU 3 EQ SP. ON A ø9.10 BC WITHIN ± 0.030 OF TP
2.125
2.125
3.6
2.63
2.157
1.250 ± 0.004
45°
30°
5.875 ± 0.063
5.563
2.75
3.0
UNLESS OTHERWISE SPECIFIED DIMENSIONS ARE IN INCHES
TOLERANCES (UNLESS SPECIFIED)
DECIMALS ANGLES
.X ± .06
.XX ± .03 ± 1/2°
.XXX ± .010
MATERIAL: ALUMINUM
TITLE: PULSED VALVE MOUNTING PLATE AND SOURCE X-Y TRANSLATOR PIECE
FILE: MNTPLAT.DWG
DWG BY: JAMES M. SPOTTS
DATE: 8-2-93
SCALE: 1:1
PROF. M. OKUMURA LABORATORY
DIVISION OF CHEMISTRY: CALIFORNIA INSTITUTE OF TECHNOLOGY

Figure 2-27

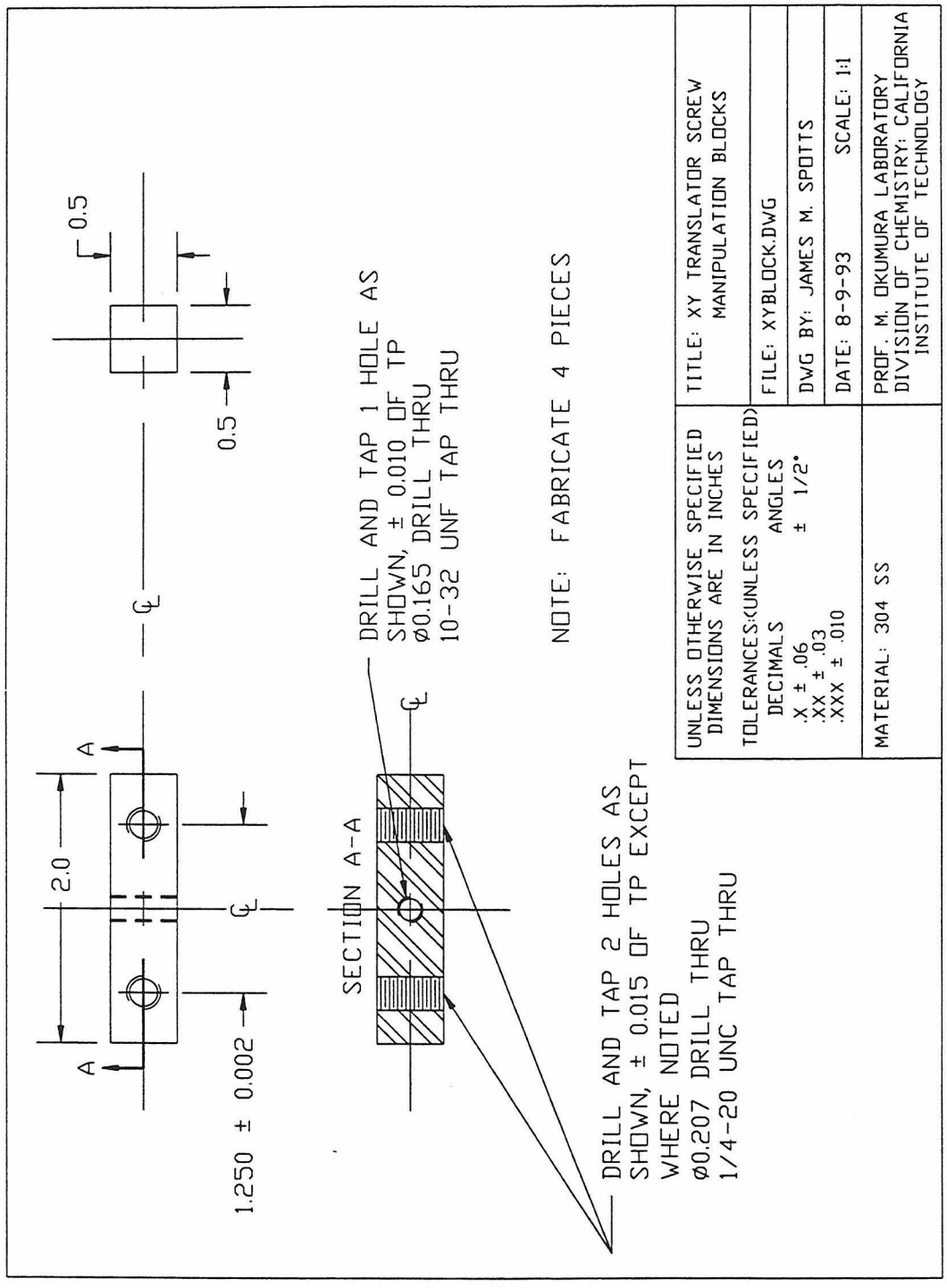

0.5
0.5
2.0
A
A
1.250 ± 0.002
SECTION A-A
DRILL AND TAP 1 HOLE AS
SHOWN, ± 0.010 OF TP
Ø0.165 DRILL THRU
10-32 UNF TAP THRU
NOTE: FABRICATE 4 PIECES
DRILL AND TAP 2 HOLES AS
SHOWN, ± 0.015 OF TP EXCEPT
WHERE NOTED
Ø0.207 DRILL THRU
1/4-20 UNC TAP THRU
UNLESS OTHERWISE SPECIFIED
DIMENSIONS ARE IN INCHES
TOLERANCES:(UNLESS SPECIFIED)
DECIMALS
.X ± .06
.XX ± .03
.XXX ± .010
ANGLES
± 1/2°
MATERIAL: 304 SS
TITLE: XY TRANSLATOR SCREW
MANIPULATION BLOCKS
FILE: XYBLOCK.DWG
DWG BY: JAMES M. SPOTTS
DATE: 8-9-93
SCALE: 1:1
PROF. M. OKUMURA LABORATORY
DIVISION OF CHEMISTRY: CALIFORNIA
INSTITUTE OF TECHNOLOGY

Figure 2-28

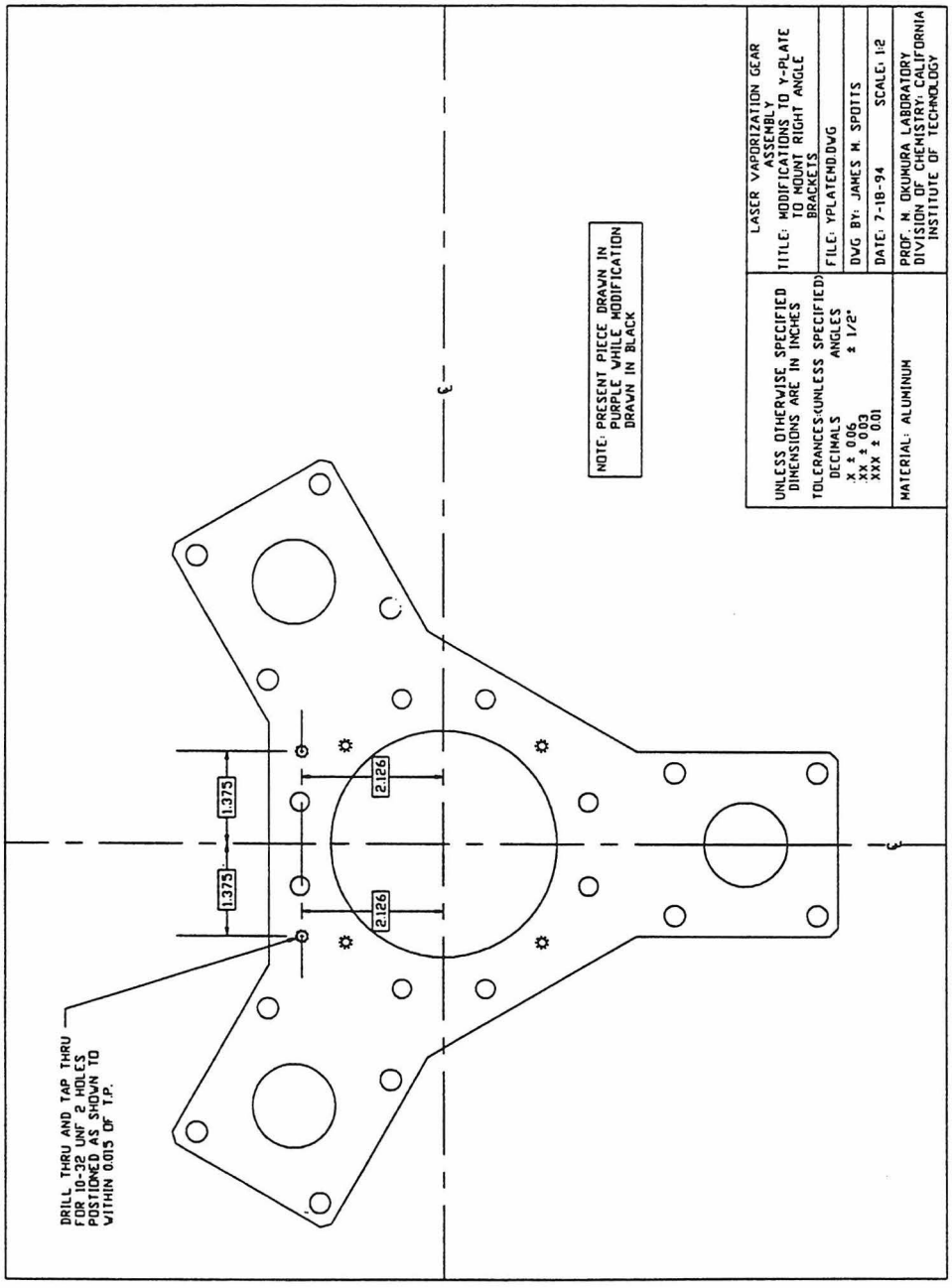

DRILL THRU AND TAP THRU
FOR 10-32 UNF 2 HOLES
POSITIONED AS SHOWN TO
WITHIN 0.015 OF T.P.
1.375
1.375
2.126
2.126
NOTE: PRESENT PIECE DRAWN IN
PURPLE WHILE MODIFICATION
DRAWN IN BLACK
UNLESS OTHERWISE SPECIFIED
DIMENSIONS ARE IN INCHES
TOLERANCES:(UNLESS SPECIFIED)
DECIMALS ANGLES
X ± 0.06 ± 1/2°
XX ± 0.03
XXX ± 0.01
MATERIAL: ALUMINUM
LASER VAPORIZATION GEAR
ASSEMBLY
TITLE: MODIFICATIONS TO Y-PLATE
TO MOUNT RIGHT ANGLE
BRACKETS
FILE: YPLATEMD.DWG
DWG BY: JAMES M. SPOTTS
DATE: 7-18-94
SCALE: 1:2
PROF. M. OKUMURA LABORATORY
DIVISION OF CHEMISTRY; CALIFORNIA
INSTITUTE OF TECHNOLOGY

Figure 2-29

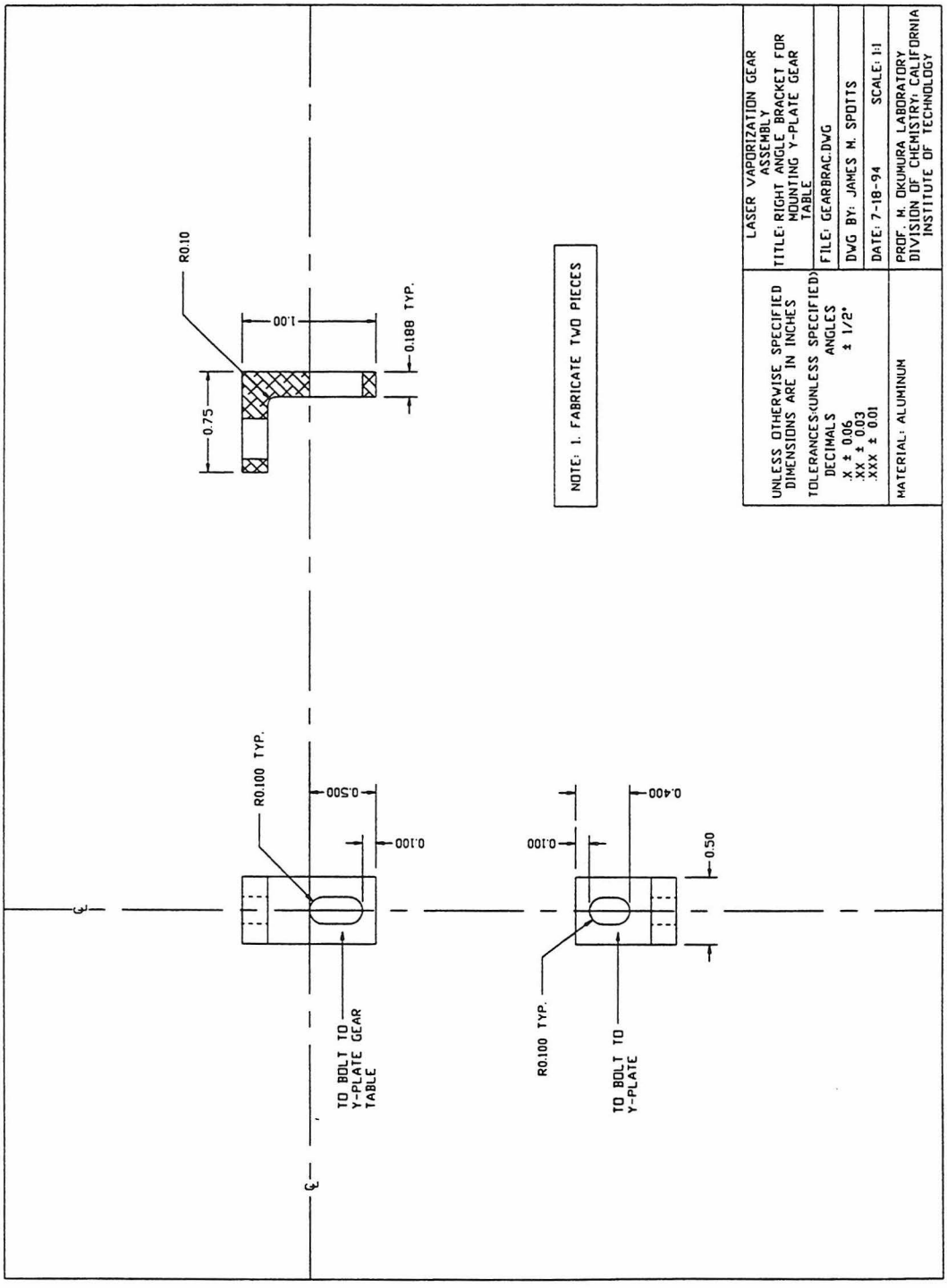

R0.10
1.00
0.188 TYP.
0.75
NOTE: 1. FABRICATE TWO PIECES
LASER VAPORIZATION GEAR ASSEMBLY
TITLE: RIGHT ANGLE BRACKET FOR MOUNTING Y-PLATE GEAR TABLE
FILE: GEARBRAC.DWG
DWG BY: JAMES M. SPOTTS
DATE: 7-18-94
SCALE: 1:1
UNLESS OTHERWISE SPECIFIED DIMENSIONS ARE IN INCHES
TOLERANCES:(UNLESS SPECIFIED)
DECIMALS
.X ± 0.06
.XX ± 0.03
.XXX ± 0.01
ANGLES
± 1/2°
MATERIAL: ALUMINUM
PROF. M. OKUMURA LABORATORY
DIVISION OF CHEMISTRY: CALIFORNIA INSTITUTE OF TECHNOLOGY
R0.100 TYP.
0.500
0.100
TO BOLT TO Y-PLATE GEAR TABLE
0.100
0.400
0.50
R0.100 TYP.
TO BOLT TO Y-PLATE

Figure 2-30

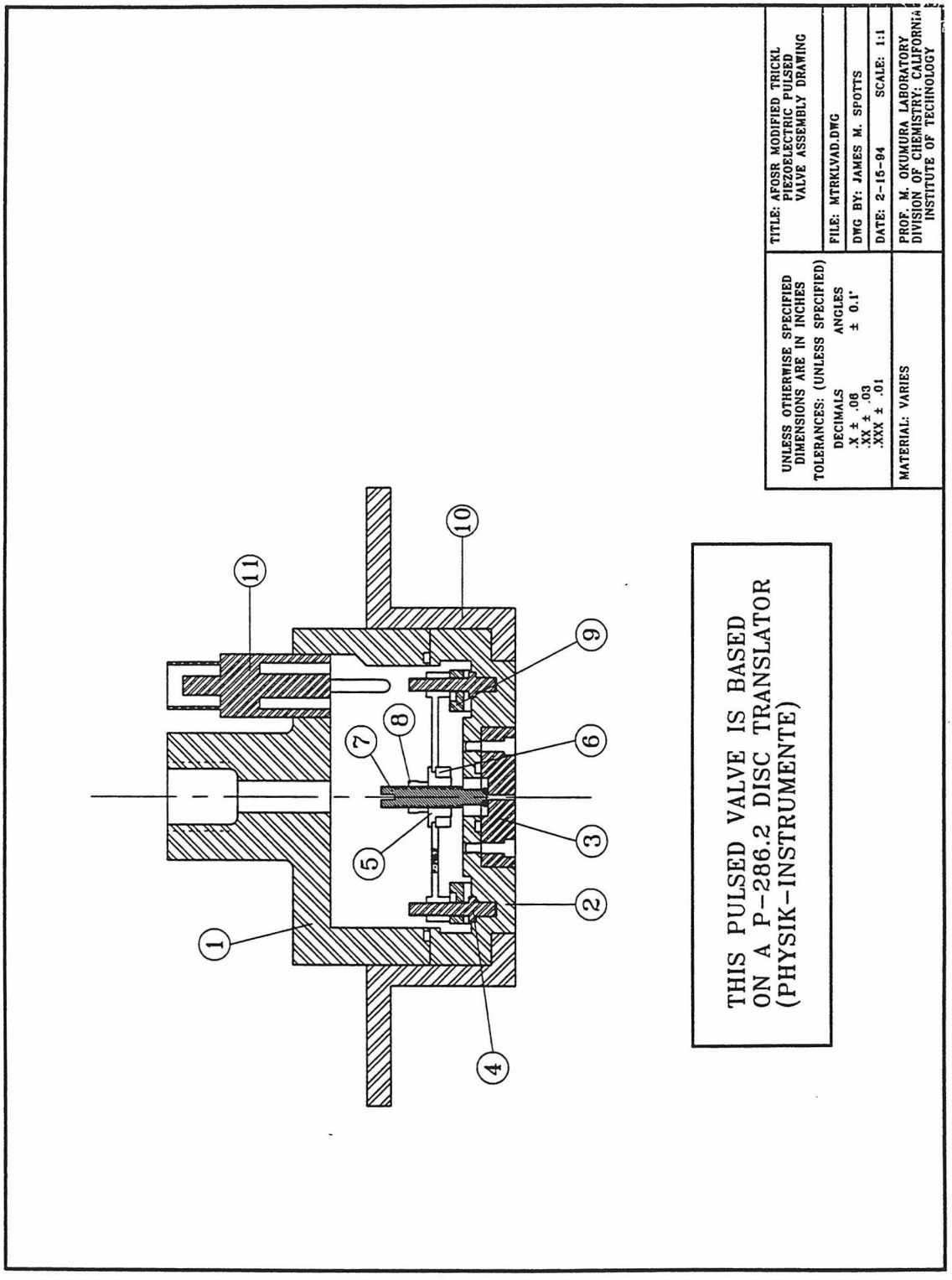

TITLE: AFOSR MODIFIED TRICKL PIEZOELECTRIC PULSED VALVE ASSEMBLY DRAWING
FILE: MTRKLVAD.DWG
DWG BY: JAMES M. SPOTTS
DATE: 2-15-94
SCALE: 1:1
PROF. M. OKUMURA LABORATORY
DIVISION OF CHEMISTRY: CALIFORNIA INSTITUTE OF TECHNOLOGY
UNLESS OTHERWISE SPECIFIED DIMENSIONS ARE IN INCHES
TOLERANCES: (UNLESS SPECIFIED)
DECIMALS
.X ± .08
.XX ± .03
.XXX ± .01
ANGLES
± 0.1°
MATERIAL: VARIES
THIS PULSED VALVE IS BASED ON A P-286.2 DISC TRANSLATOR (PHYSIK-INSTRUMENTE)
1
2
3
4
5
6
7
8
9
10
11

Figure 2-31

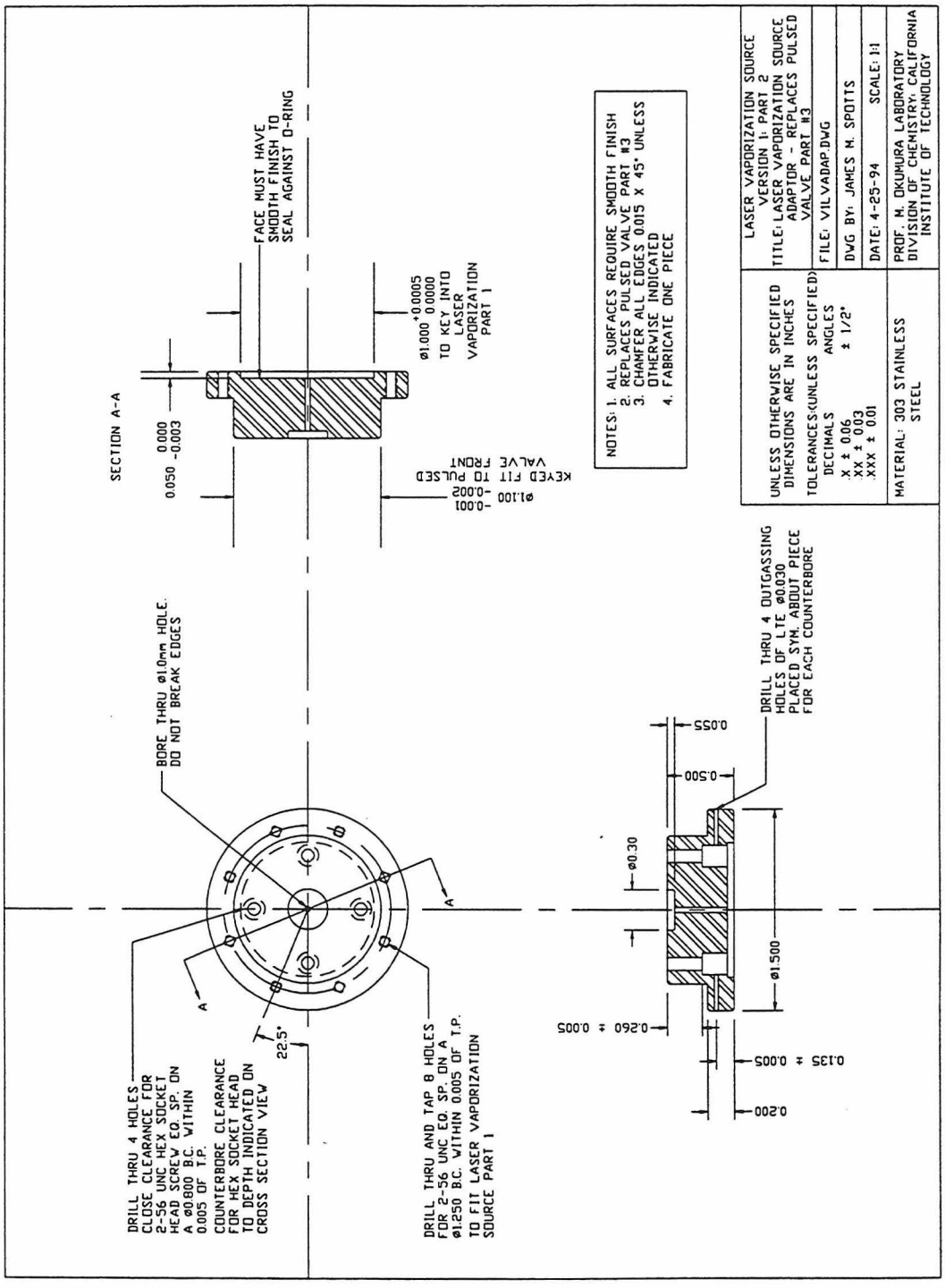

SECTION A-A
FACE MUST HAVE SMOOTH FINISH TO SEAL AGAINST O-RING
0.050 0.000 -0.003
ø1.000 +0.0005 0.0000 TO KEY INTO LASER VAPORIZATION PART 1
KEYED FIT TO PULSED VALVE FRONT
ø1.100 -0.001 -0.002
NOTES: 1. ALL SURFACES REQUIRE SMOOTH FINISH
2. REPLACES PULSED VALVE PART #3
3. CHAMFER ALL EDGES 0.015 X 45° UNLESS OTHERWISE INDICATED
4. FABRICATE ONE PIECE
UNLESS OTHERWISE SPECIFIED DIMENSIONS ARE IN INCHES
TOLERANCES: UNLESS SPECIFIED
DECIMALS ANGLES
.X ± 0.06 ± 1/2°
.XX ± 0.03
.XXX ± 0.01
MATERIAL: 303 STAINLESS STEEL
LASER VAPORIZATION SOURCE VERSION 1: PART 2
TITLE: LASER VAPORIZATION SOURCE ADAPTOR - REPLACES PULSED VALVE PART #3
FILE: VILVADAP.DWG
DWG BY: JAMES M. SPOTTS
DATE: 4-25-94 SCALE: 1:1
PROF. M. OKUMURA LABORATORY
DIVISION OF CHEMISTRY, CALIFORNIA INSTITUTE OF TECHNOLOGY
BORE THRU ø1.0mm HOLE. DO NOT BREAK EDGES
DRILL THRU 4 HOLES CLOSE CLEARANCE FOR 2-56 UNC HEX SOCKET HEAD SCREW EQ. SP. ON A ø0.800 B.C. WITHIN 0.005 OF T.P.
COUNTERBORE CLEARANCE FOR HEX SOCKET HEAD TO DEPTH INDICATED ON CROSS SECTION VIEW
22.5°
DRILL THRU AND TAP 8 HOLES FOR 2-56 UNC EQ. SP. ON A ø1.250 B.C. WITHIN 0.005 OF T.P. TO FIT LASER VAPORIZATION SOURCE PART 1
DRILL THRU 4 OUTGASSING HOLES OF LTE ø0.030 PLACED SYM. ABOUT PIECE FOR EACH COUNTERBORE
0.055
0.500
ø0.30
ø1.500
0.260 ± 0.005
0.135 ± 0.005
0.200

Figure 2-32

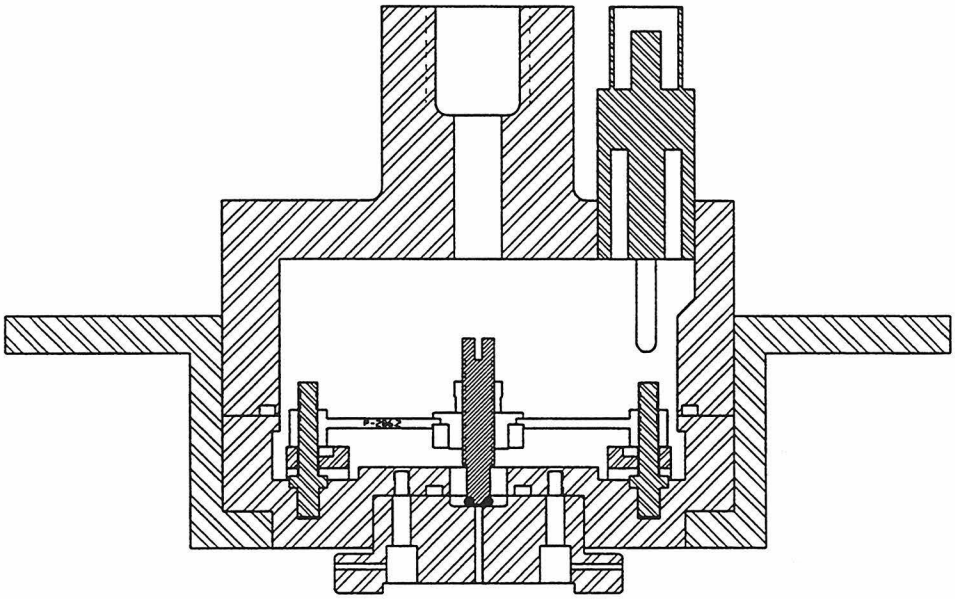


Figure 2-33

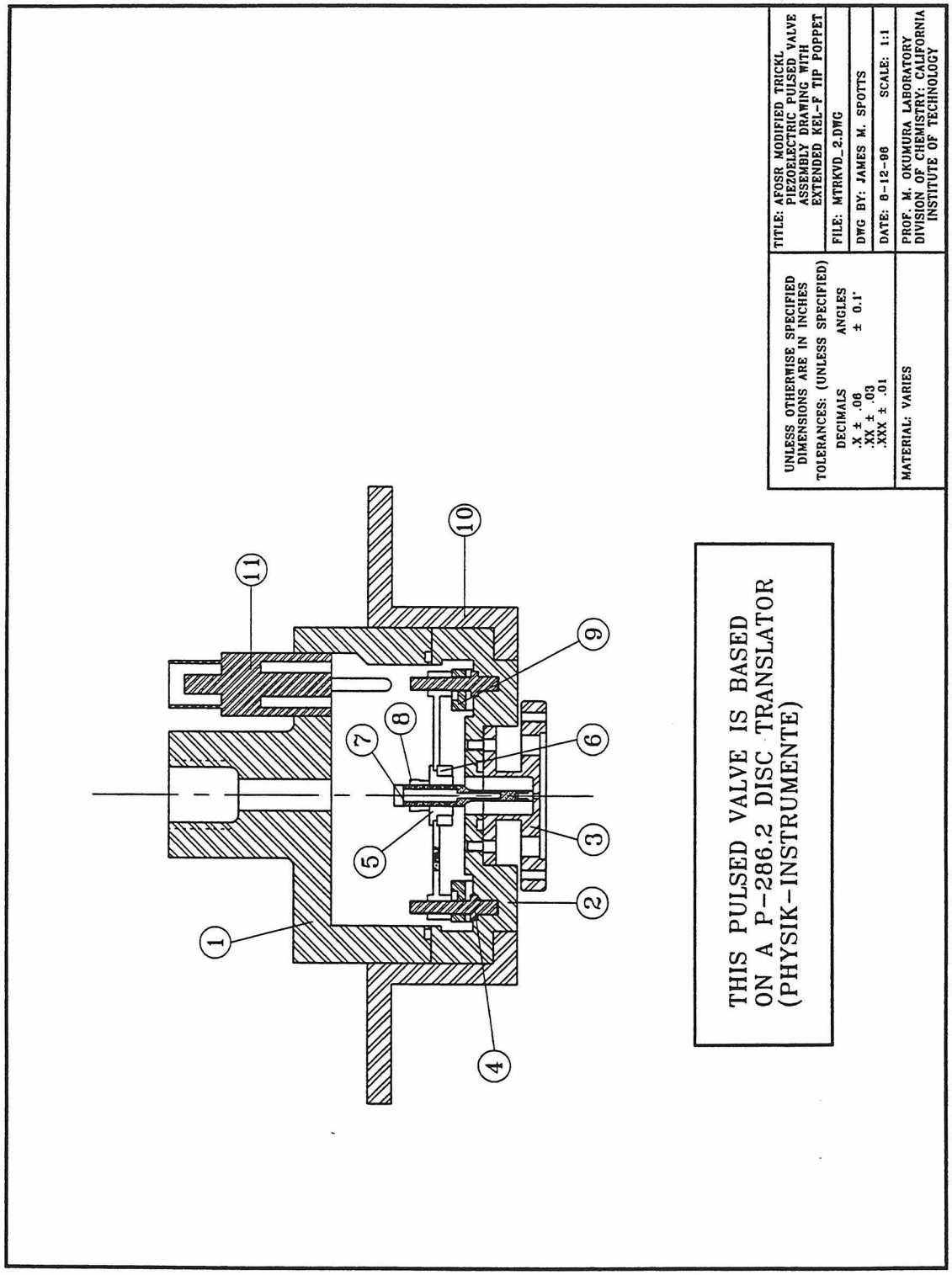

TITLE: AFOSR MODIFIED TRICKL
PIEZOELECTRIC PULSED VALVE
ASSEMBLY DRAWING WITH
EXTENDED KEL-F TIP POPPET
FILE: MTRKVD_2.DWG
DWG BY: JAMES M. SPOTTS
DATE: 8-12-96
SCALE: 1:1
PROF. M. OKUMURA LABORATORY
DIVISION OF CHEMISTRY; CALIFORNIA
INSTITUTE OF TECHNOLOGY
UNLESS OTHERWISE SPECIFIED
DIMENSIONS ARE IN INCHES
TOLERANCES: (UNLESS SPECIFIED)
DECIMALS
.X ± .06
.XX ± .03
.XXX ± .01
ANGLES
± 0.1°
MATERIAL: VARIES
THIS PULSED VALVE IS BASED
ON A P-286.2 DISC TRANSLATOR
(PHYSIK-INSTRUMENTE)
1
2
3
4
5
6
7
8
9
10
11

Figure 2-34

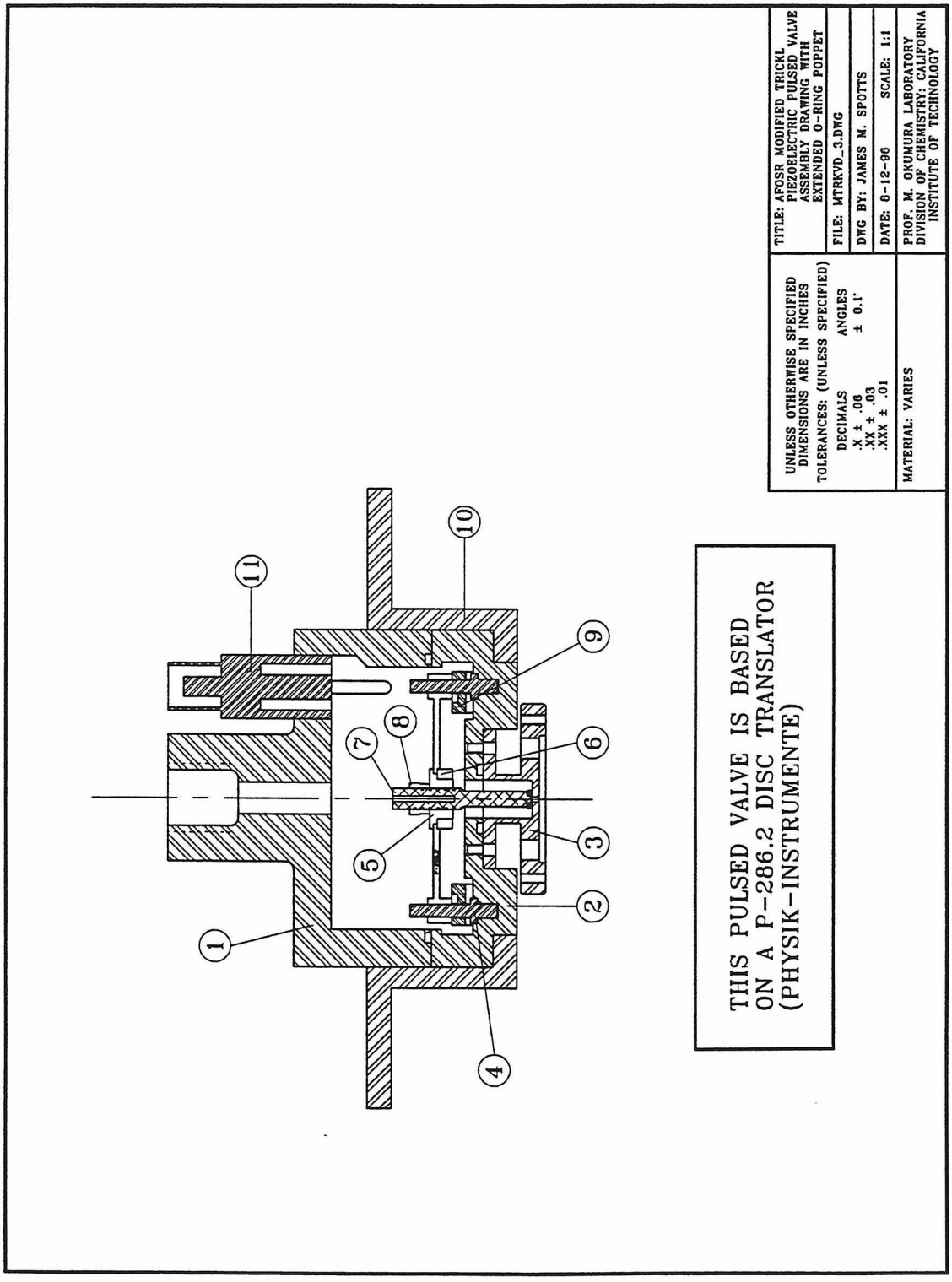

TITLE: AFOSR MODIFIED TRICKL PIEZOELECTRIC PULSED VALVE ASSEMBLY DRAWING WITH EXTENDED O-RING POPPET
FILE: MTRKVD_3.DWG
DWG BY: JAMES M. SPOTTS
DATE: 8-12-96
SCALE: 1:1
PROF. M. OKUMURA LABORATORY DIVISION OF CHEMISTRY; CALIFORNIA INSTITUTE OF TECHNOLOGY
UNLESS OTHERWISE SPECIFIED DIMENSIONS ARE IN INCHES
TOLERANCES: (UNLESS SPECIFIED)
DECIMALS
.X ± .06
.XX ± .03
.XXX ± .01
ANGLES
± 0.1°
MATERIAL: VARIES
THIS PULSED VALVE IS BASED ON A P-286.2 DISC TRANSLATOR (PHYSIK-INSTRUMENTE)
1
2
3
4
5
6
7
8
9
10
11

Figure 2-35

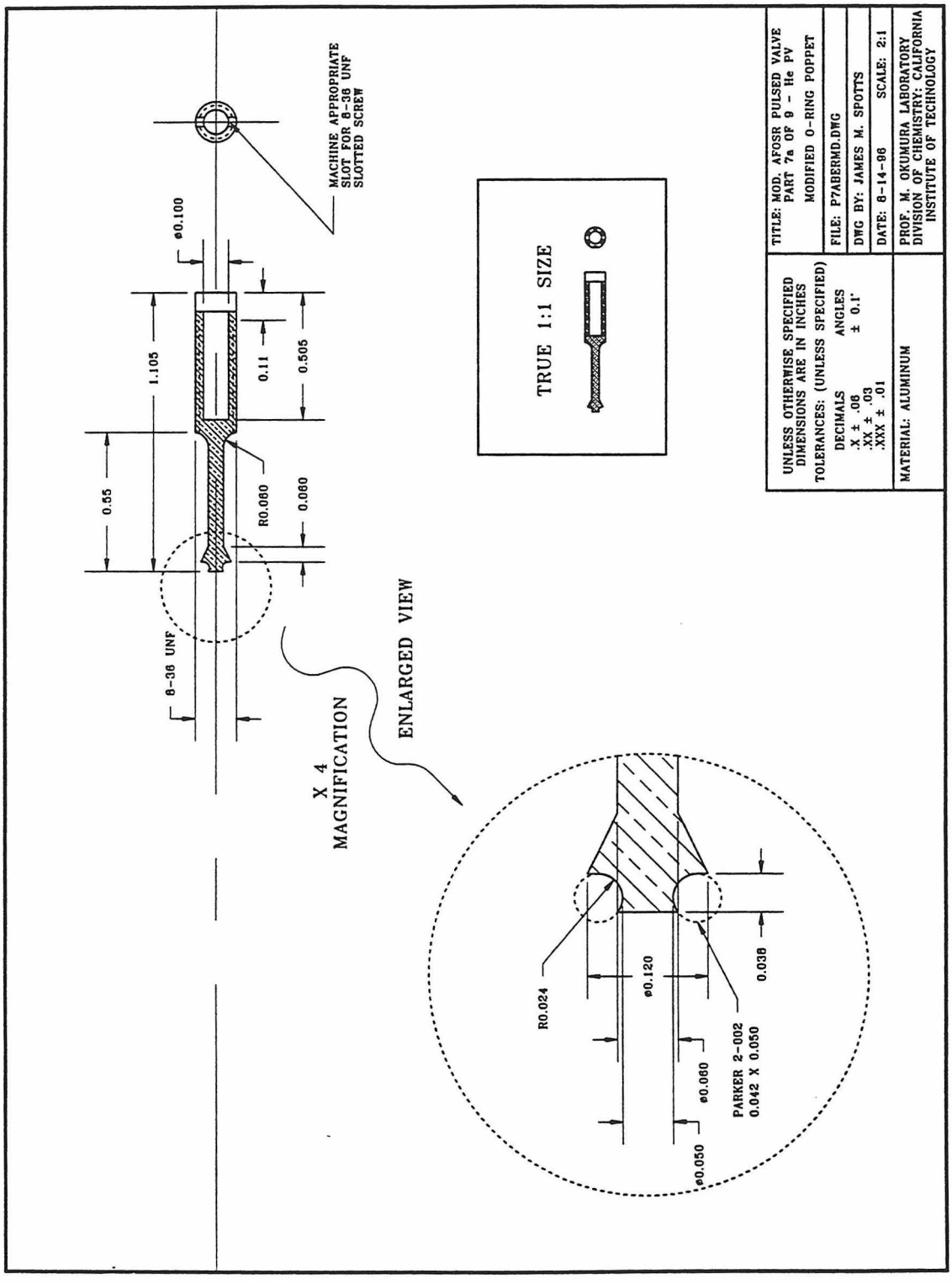

MACHINE APPROPRIATE SLOT FOR 8-36 UNF SLOTTED SCREW
ø0.100
1.105
0.11
0.505
0.55
R0.060
0.060
8-36 UNF
TRUE 1:1 SIZE
X 4 MAGNIFICATION
ENLARGED VIEW
R0.024
ø0.120
0.030
PARKER 2-002 0.042 X 0.050
ø0.060
ø0.050
UNLESS OTHERWISE SPECIFIED DIMENSIONS ARE IN INCHES
TOLERANCES: (UNLESS SPECIFIED)
DECIMALS ANGLES
.X ± .06 ± 0.1°
.XX ± .03
.XXX ± .01
MATERIAL: ALUMINUM
TITLE: MOD. AFOSR PULSED VALVE PART 7a OF 9 - He PV MODIFIED O-RING POPPET
FILE: P7ABERMD.DWG
DWG BY: JAMES M. SPOTTS
DATE: 8-14-96
SCALE: 2:1
PROF. M. OKUMURA LABORATORY
DIVISION OF CHEMISTRY: CALIFORNIA INSTITUTE OF TECHNOLOGY

Figure 2-36

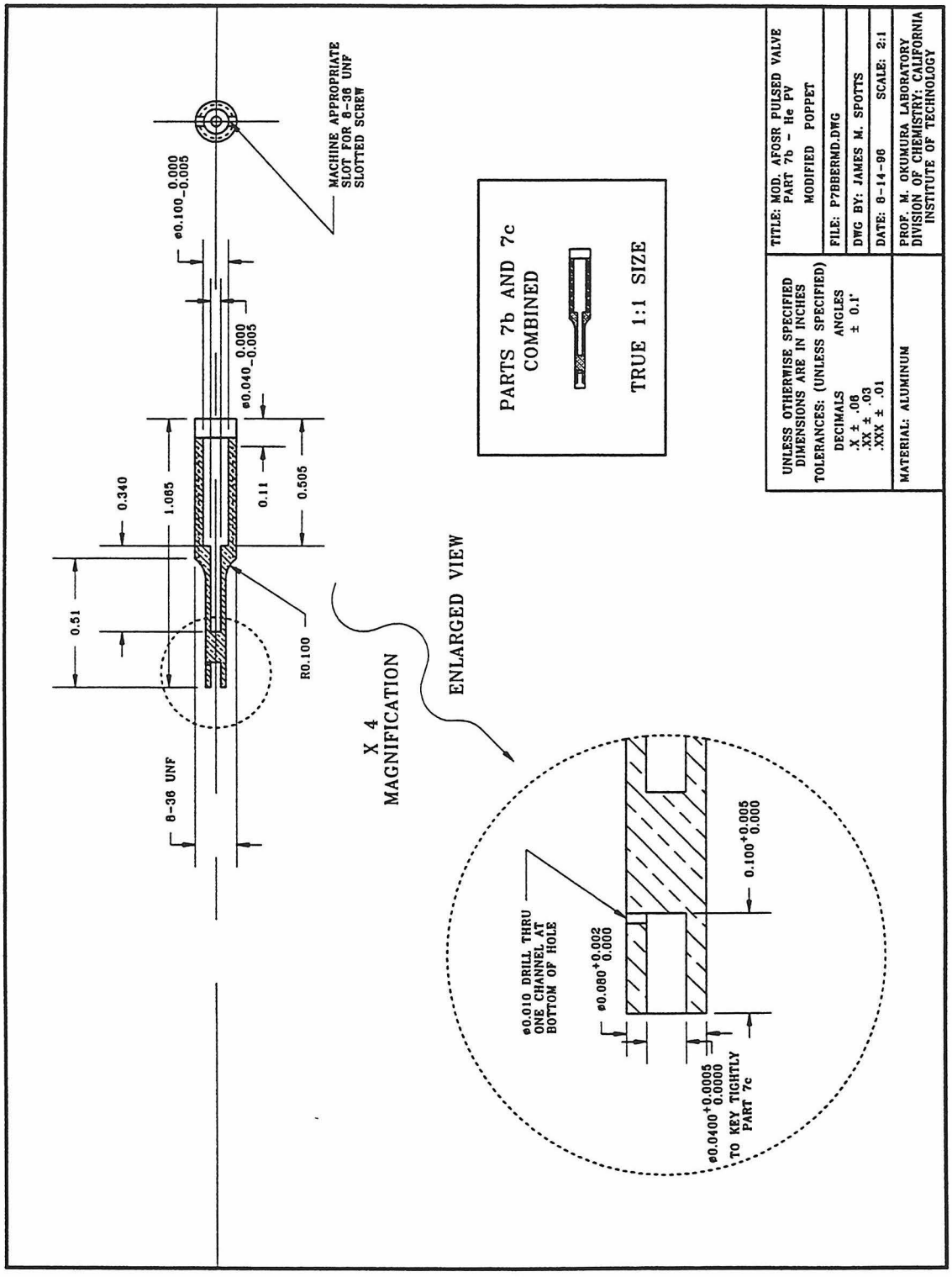

MACHINE APPROPRIATE SLOT FOR 8-36 UNF SLOTTED SCREW
ø0.100 0.000 -0.005
ø0.040 0.000 -0.005
0.340
1.065
0.11
0.505
0.51
R0.100
8-36 UNF
X 4 MAGNIFICATION
ENLARGED VIEW
ø0.010 DRILL THRU ONE CHANNEL AT BOTTOM OF HOLE
ø0.080 +0.002 0.000
0.100 +0.005 0.000
ø0.0400 +0.0005 0.0000
TO KEY TIGHTLY PART 7c
PARTS 7b AND 7c COMBINED
TRUE 1:1 SIZE
UNLESS OTHERWISE SPECIFIED DIMENSIONS ARE IN INCHES
TOLERANCES: (UNLESS SPECIFIED)
DECIMALS
.X ± .06
.XX ± .03
.XXX ± .01
ANGLES
± 0.1°
MATERIAL: ALUMINUM
TITLE: MOD. AFOSR PULSED VALVE PART 7b - He PV MODIFIED POPPET
FILE: P7BBERMD.DWG
DWG BY: JAMES M. SPOTTS
DATE: 8-14-96
SCALE: 2:1
PROF. M. OKUMURA LABORATORY DIVISION OF CHEMISTRY: CALIFORNIA INSTITUTE OF TECHNOLOGY

Figure 2-37

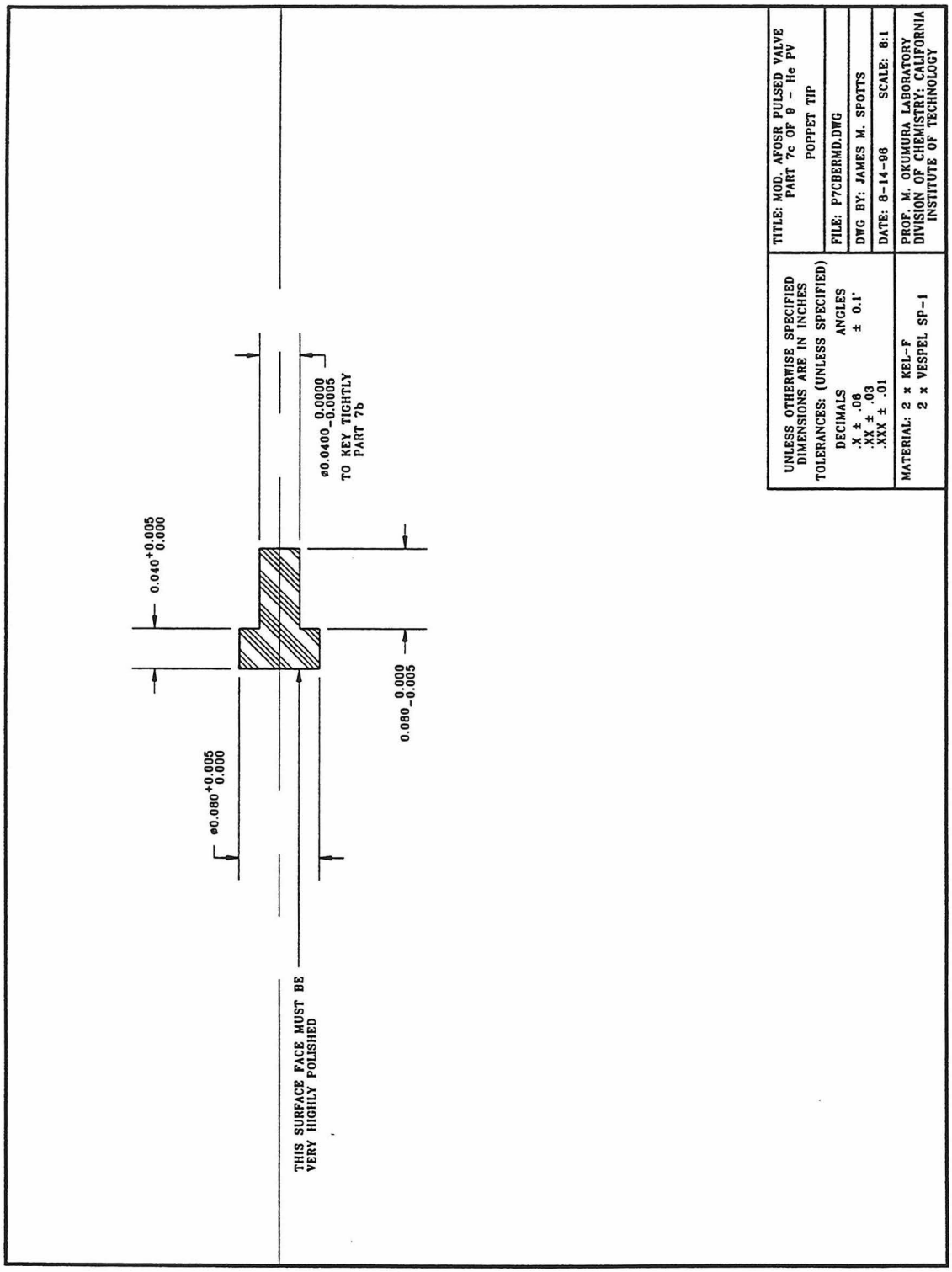

0.040 +0.005 0.000
ø0.0400 -0.0000 -0.0005
TO KEY TIGHTLY PART 7b
ø0.080 +0.005 0.000
0.080 -0.000 -0.005
THIS SURFACE FACE MUST BE VERY HIGHLY POLISHED
UNLESS OTHERWISE SPECIFIED DIMENSIONS ARE IN INCHES
TOLERANCES: (UNLESS SPECIFIED)
DECIMALS ANGLES
.X ± .06 ± 0.1°
.XX ± .03
.XXX ± .01
MATERIAL: 2 x KEL-F
2 x VESPEL SP-1
TITLE: MOD. AFOSR PULSED VALVE PART 7c OF 9 - He PV
POPPET TIP
FILE: P7CBERMD.DWG
DWG BY: JAMES M. SPOTTS
DATE: 8-14-96 SCALE: 8:1
PROF. M. OKUMURA LABORATORY
DIVISION OF CHEMISTRY: CALIFORNIA
INSTITUTE OF TECHNOLOGY

Figure 2-38

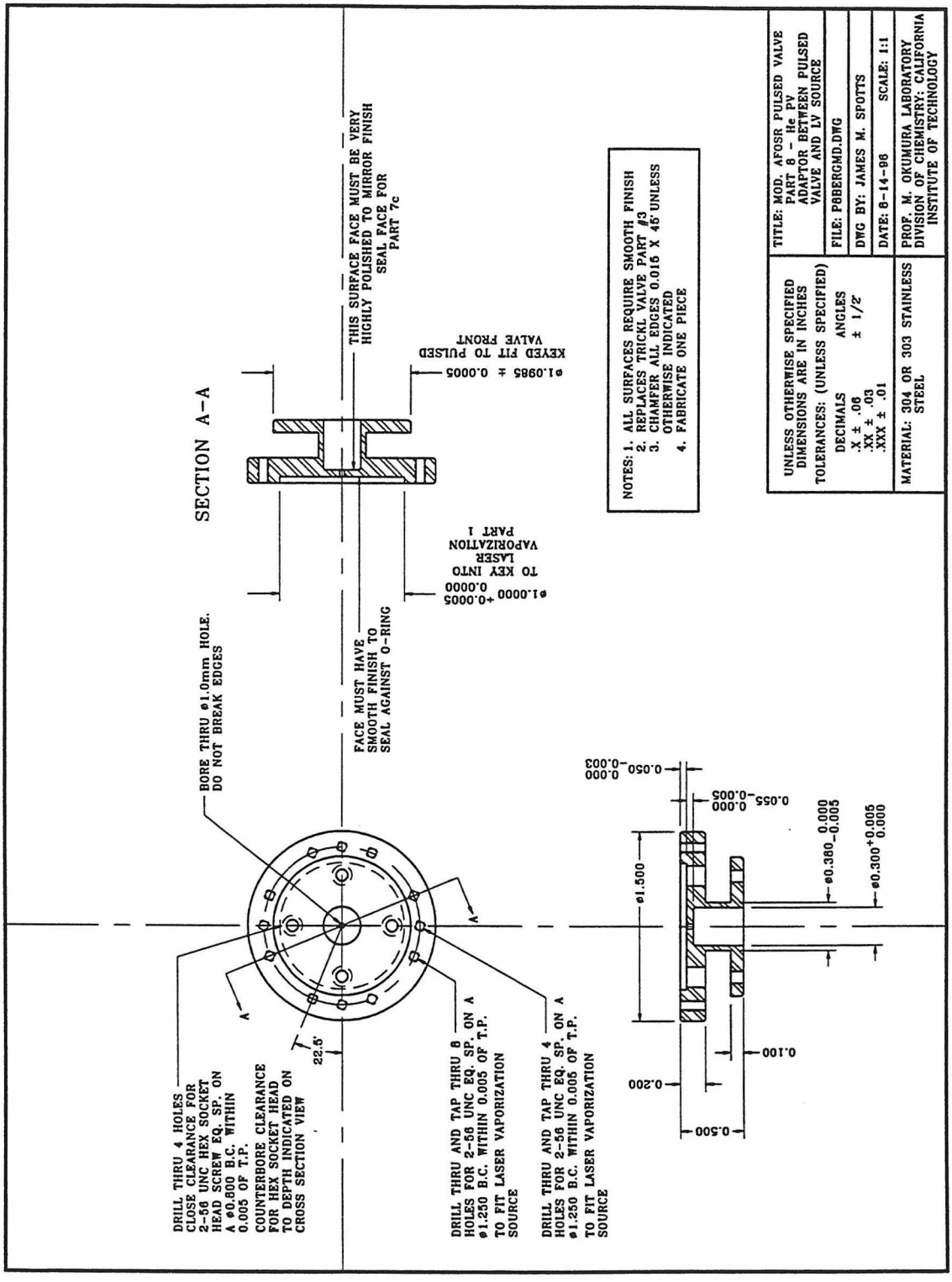

SECTION A-A
THIS SURFACE FACE MUST BE VERY HIGHLY POLISHED TO MIRROR FINISH SEAL FACE FOR PART 7c
KEYED FIT TO PULSED VALVE FRONT
ø1.0985 ± 0.0005
ø1.0000 +0.0005 0.0000
TO KEY INTO LASER VAPORIZATION PART 1
FACE MUST HAVE SMOOTH FINISH TO SEAL AGAINST O-RING
BORE THRU ø1.0mm HOLE. DO NOT BREAK EDGES
DRILL THRU 4 HOLES CLOSE CLEARANCE FOR 2-56 UNC HEX SOCKET HEAD SCREW EQ. SP. ON A ø0.800 B.C. WITHIN 0.005 OF T.P.
COUNTERBORE CLEARANCE FOR HEX SOCKET HEAD TO DEPTH INDICATED ON CROSS SECTION VIEW
22.5°
DRILL THRU AND TAP THRU 8 HOLES FOR 2-56 UNC EQ. SP. ON A ø1.250 B.C. WITHIN 0.005 OF T.P. TO FIT LASER VAPORIZATION SOURCE
DRILL THRU AND TAP THRU 4 HOLES FOR 2-56 UNC EQ. SP. ON A ø1.250 B.C. WITHIN 0.005 OF T.P. TO FIT LASER VAPORIZATION SOURCE
0.050 0.000 -0.003
0.055 0.000 -0.005
ø1.500
ø0.380 0.000 -0.005
ø0.300 +0.005 0.000
0.100
0.200
0.500
NOTES: 1. ALL SURFACES REQUIRE SMOOTH FINISH
2. REPLACES TRICKL VALVE PART #3
3. CHAMFER ALL EDGES 0.016 X 45° UNLESS OTHERWISE INDICATED
4. FABRICATE ONE PIECE
UNLESS OTHERWISE SPECIFIED DIMENSIONS ARE IN INCHES
TOLERANCES: (UNLESS SPECIFIED)
DECIMALS ANGLES
.X ± .06 ± 1/2°
.XX ± .03
.XXX ± .01
MATERIAL: 304 OR 303 STAINLESS STEEL
TITLE: MOD. APOSR PULSED VALVE PART 8 He PV ADAPTOR BETWEEN PULSED VALVE AND LV SOURCE
FILE: P8BERGMD.DWG
DWG BY: JAMES M. SPOTTS
DATE: 8-14-98
SCALE: 1:1
PROF. M. OKUMURA LABORATORY DIVISION OF CHEMISTRY; CALIFORNIA INSTITUTE OF TECHNOLOGY

Figure 2-39

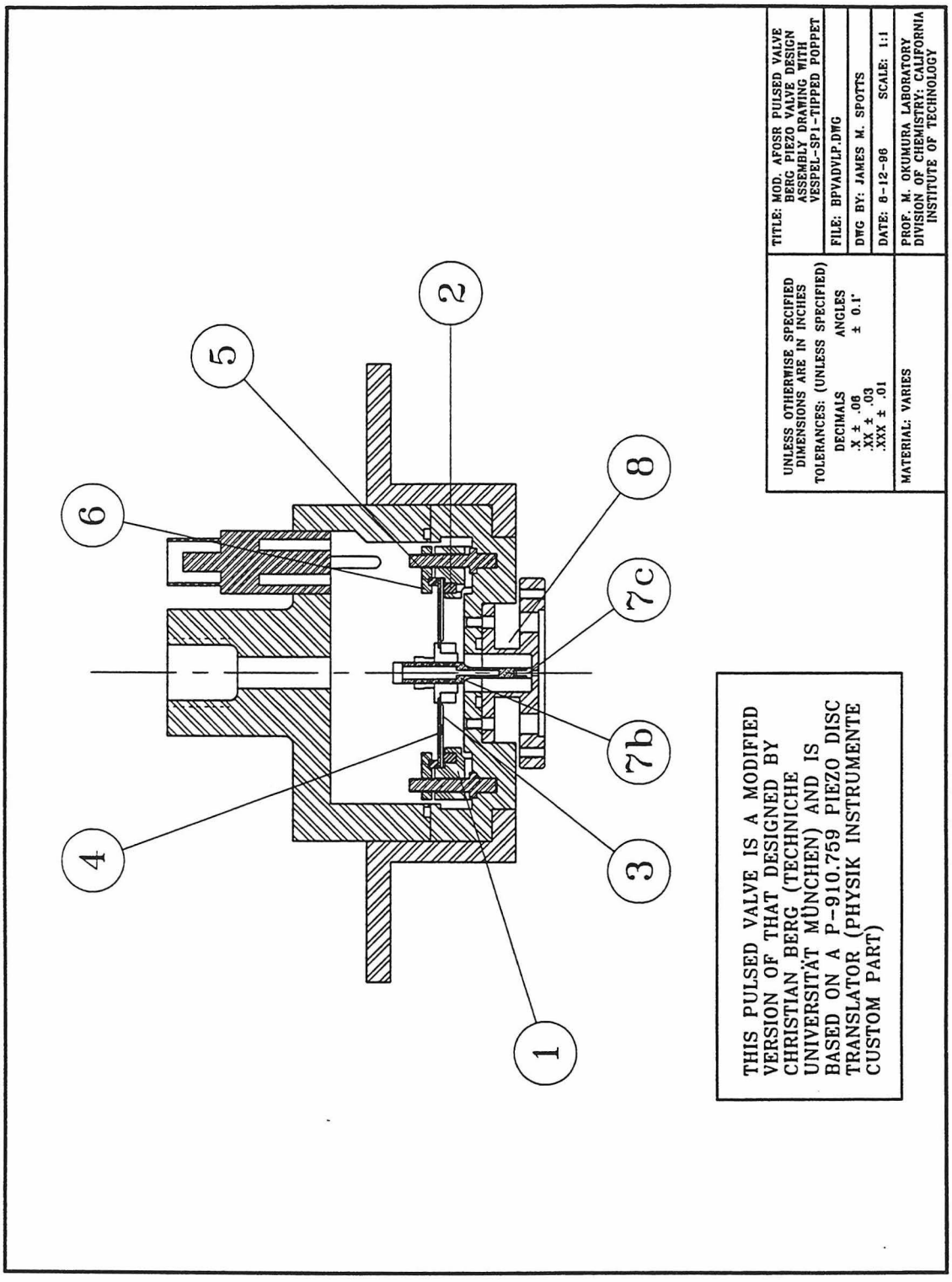

1
2
3
4
5
6
7b
7c
8
THIS PULSED VALVE IS A MODIFIED VERSION OF THAT DESIGNED BY CHRISTIAN BERG (TECHNICHE UNIVERSITÄT MÜNCHEN) AND IS BASED ON A P-910.759 PIEZO DISC TRANSLATOR (PHYSIK INSTRUMENTE CUSTOM PART)
UNLESS OTHERWISE SPECIFIED DIMENSIONS ARE IN INCHES
TOLERANCES: (UNLESS SPECIFIED)
DECIMALS
.X ± .06
.XX ± .03
.XXX ± .01
ANGLES
± 0.1°
MATERIAL: VARIES
TITLE: MOD. AFOSR PULSED VALVE BERG PIEZO VALVE DESIGN ASSEMBLY DRAWING WITH VESPEL-SP1-TIPPED POPPET
FILE: BPVADVLP.DWG
DWG BY: JAMES M. SPOTTS
DATE: 8-12-96
SCALE: 1:1
PROF. M. OKUMURA LABORATORY
DIVISION OF CHEMISTRY: CALIFORNIA INSTITUTE OF TECHNOLOGY

Figure 2-40

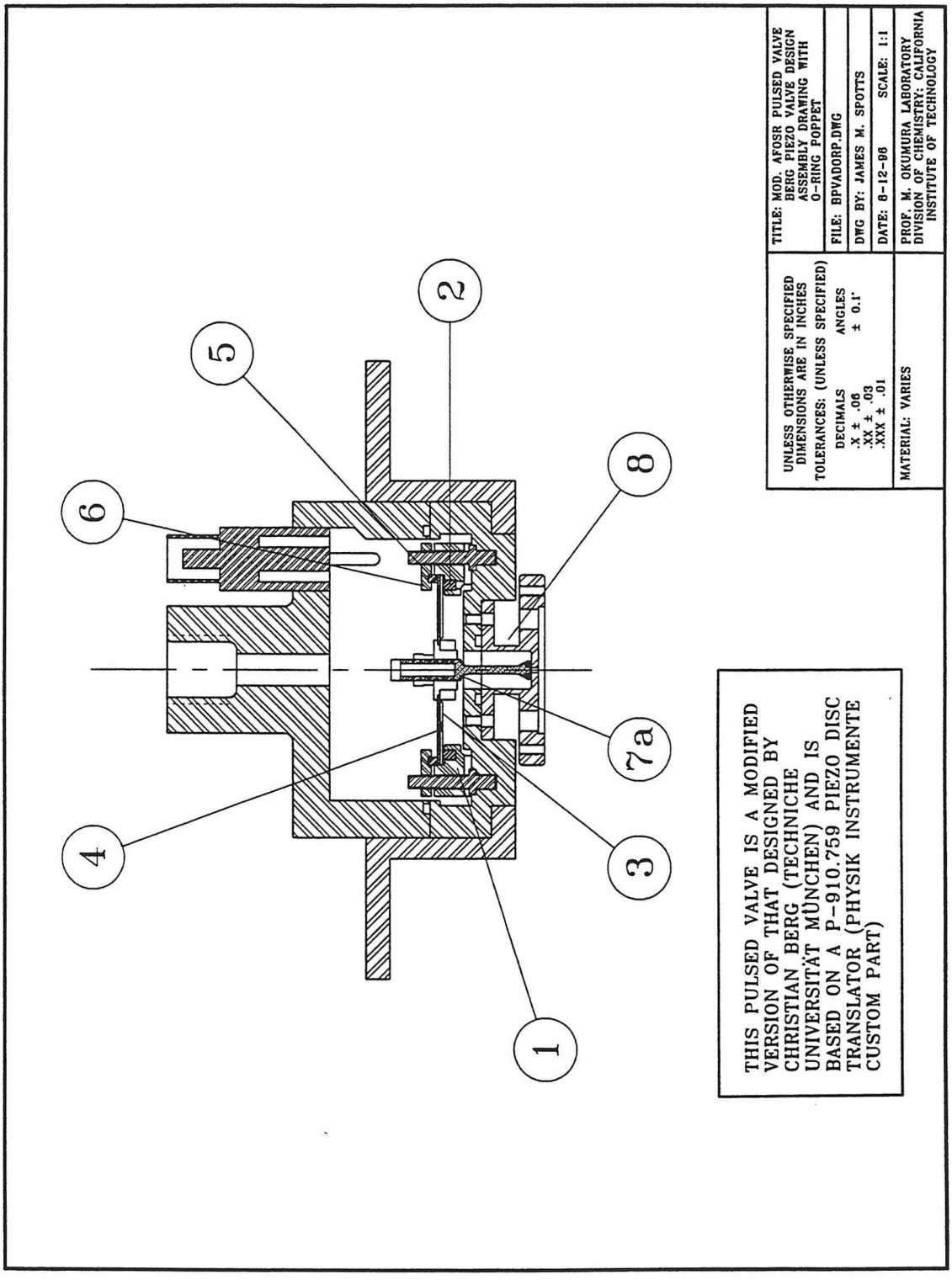

1
2
3
4
5
6
7a
8
THIS PULSED VALVE IS A MODIFIED VERSION OF THAT DESIGNED BY CHRISTIAN BERG (TECHNICHE UNIVERSITÄT MÜNCHEN) AND IS BASED ON A P-910.759 PIEZO DISC TRANSLATOR (PHYSIK INSTRUMENTE CUSTOM PART)
UNLESS OTHERWISE SPECIFIED DIMENSIONS ARE IN INCHES
TOLERANCES: (UNLESS SPECIFIED)
DECIMALS
.X ± .06
.XX ± .03
.XXX ± .01
ANGLES
± 0.1°
MATERIAL: VARIES
TITLE: MOD. AFOSR PULSED VALVE BERG PIEZO VALVE DESIGN ASSEMBLY DRAWING WITH O-RING POPPET
FILE: BPVADORP.DWG
DWG BY: JAMES M. SPOTTS
DATE: 8-12-96
SCALE: 1:1
PROF. M. OKUMURA LABORATORY
DIVISION OF CHEMISTRY; CALIFORNIA INSTITUTE OF TECHNOLOGY

Figure 2-41

LASER VAPORIZATION SOURCE ASSEMBLY PARTS LIST: VERSION 1

COMPONENT LIST

1. Mechanical Components

#	Name	Material	Quantity
1	Laser Vaporization Source	Anodized Aluminum	1
2	Pulsed Valve ⇨ Laser Vaporization Adaptor	303 Stainless Steel	1
3	1/4-80 Modified Thorlabs Screw Part #FAS300	Stainless Steel	1
4	Housing for Laser Vaporization 1/4-80 Nut and Rotory Ball Bearing	Aluminum	1
5	Thorlabs 1/4-80 Nut Part #N80L5	Brass	1
6	Rotary Ball Bearing	Standard	2
7	Shim	Aluminum	1
8	Rotating Screw Drive Housing	Bronze	1
9	Rotory Ball Bearing Clamp	303 Stainless Steel	1

Figure 2-42

10	Modified PIC No-Slip Pulley	Standard	1
11	Laser Vaporization Rod Coupling Collar: Precision Bellows-Style Flexible Coupling (McMaster-Carr Part #: 59925K87)	Nickel	1
12	Laser Vaporization Target Rod	Varies	
13	Laser Vaporization Screw Drive Assembly Base	Aluminum	1

2. O-Rings

Parker #	Size (ID X Thick)	Material	Quantity
2-012	0.364 x 0.70	Viton or Indium	1

3. Screws

Size	Type	Length	Material	Quantity
2-56 UNC	Socket Head	3/8	Stainless Steel	4
2-56 UNC	Socket Head	1/4	Stainless Steel	4
4-40 UNC	Socket Head	3/8	Stainless Steel	4

4. Set Screws

Size	Type	Length	Material	Quantity
4-40	Cup Point	1/8	Alloy Steel	1

5. Nuts

Size	Type	Material	Quantity
4-40 UNC	Hex	Stainless Steel	4

Figure 2-43

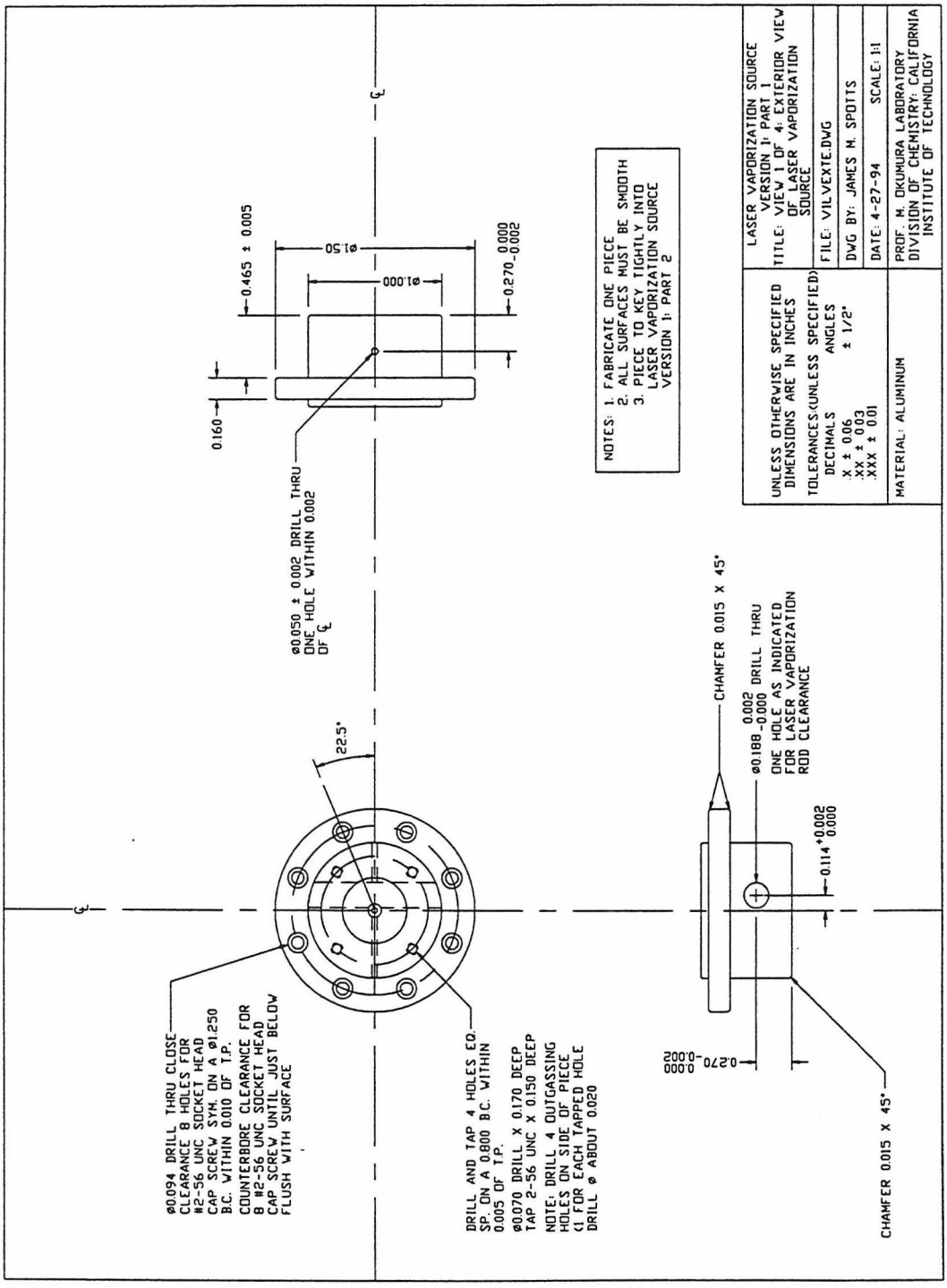

NOTES: 1. FABRICATE ONE PIECE
2. ALL SURFACES MUST BE SMOOTH
3. PIECE TO KEY TIGHTLY INTO LASER VAPORIZATION SOURCE VERSION 1: PART 2
LASER VAPORIZATION SOURCE VERSION 1: PART 1
TITLE: VIEW 1 OF 4: EXTERIOR VIEW OF LASER VAPORIZATION SOURCE
FILE: V1LVEXTE.DWG
DWG BY: JAMES M. SPOTTS
DATE: 4-27-94 SCALE: 1:1
UNLESS OTHERWISE SPECIFIED DIMENSIONS ARE IN INCHES
TOLERANCES:(UNLESS SPECIFIED)
DECIMALS ANGLES
.X ± 0.06 ± 1/2°
.XX ± 0.03
.XXX ± 0.01
MATERIAL: ALUMINUM
PROF. M. OKUMURA LABORATORY
DIVISION OF CHEMISTRY: CALIFORNIA INSTITUTE OF TECHNOLOGY
0.465 ± 0.005
ø1.50
ø1.000
0.270 0.000 -0.002
0.160
ø0.050 ± 0.002 DRILL THRU ONE HOLE WITHIN 0.002 OF ℄
22.5°
CHAMFER 0.015 X 45°
ø0.188 0.002 -0.000 DRILL THRU ONE HOLE AS INDICATED FOR LASER VAPORIZATION ROD CLEARANCE
0.114 +0.002 0.000
0.270 -0.000 -0.002
CHAMFER 0.015 X 45°
ø0.094 DRILL THRU CLOSE CLEARANCE 8 HOLES FOR #2-56 UNC SOCKET HEAD CAP SCREW SYM. ON A ø1.250 B.C. WITHIN 0.010 OF T.P.
COUNTERBORE CLEARANCE FOR 8 #2-56 UNC SOCKET HEAD CAP SCREW UNTIL JUST BELOW FLUSH WITH SURFACE
DRILL AND TAP 4 HOLES EQ. SP. ON A 0.800 B.C. WITHIN 0.005 OF T.P.
ø0.070 DRILL X 0.170 DEEP TAP 2-56 UNC X 0.150 DEEP
NOTE: DRILL 4 OUTGASSING HOLES ON SIDE OF PIECE ⟨1 FOR EACH TAPPED HOLE DRILL ø ABOUT 0.020

Figure 2-44

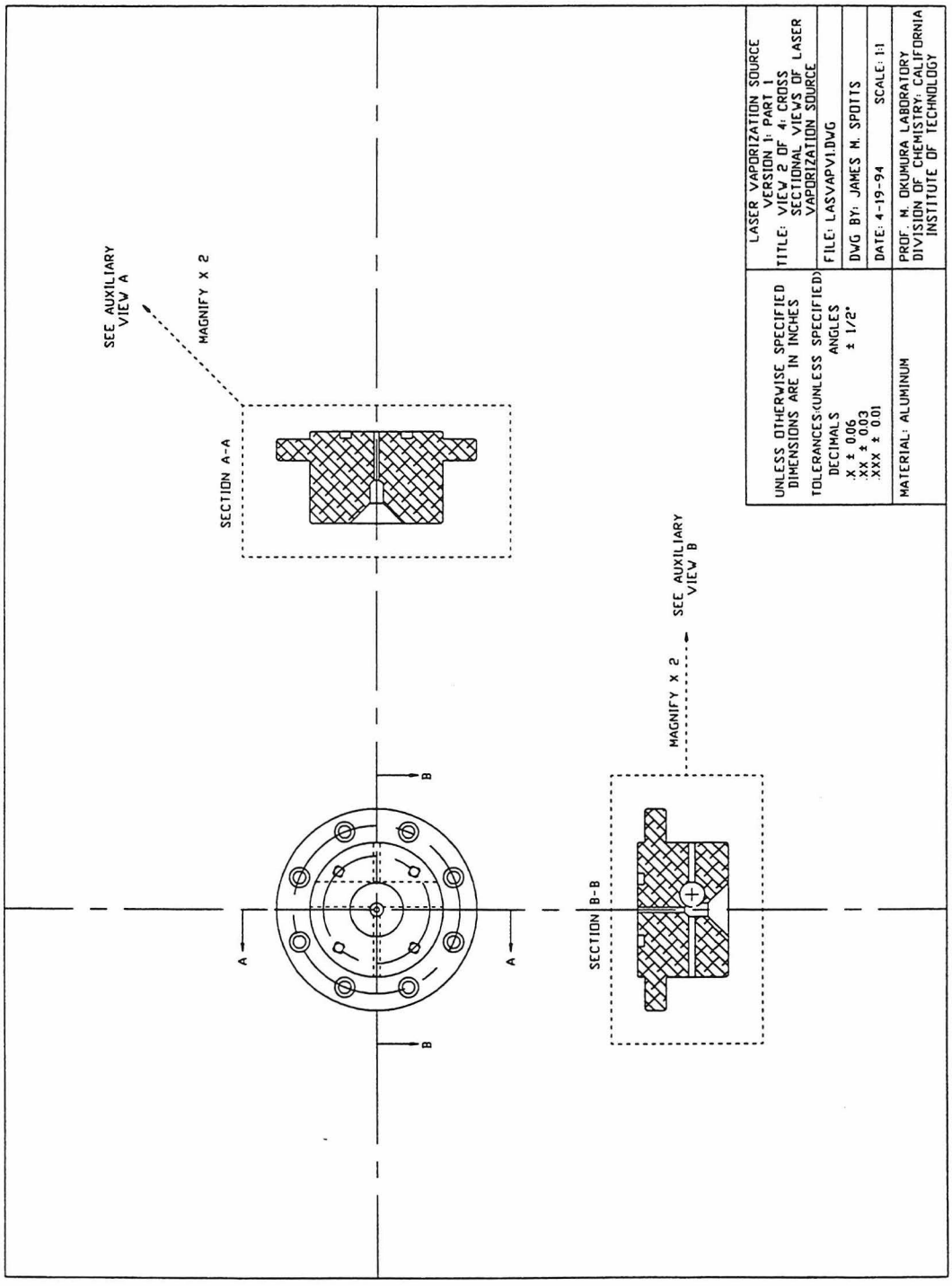

SEE AUXILIARY VIEW A
MAGNIFY X 2
SECTION A-A
SEE AUXILIARY VIEW B
MAGNIFY X 2
SECTION B-B
A
A
B
B
LASER VAPORIZATION SOURCE
VERSION 1: PART 1
TITLE: VIEW 2 OF 4: CROSS SECTIONAL VIEWS OF LASER VAPORIZATION SOURCE
FILE: LASVAPV1.DWG
DWG BY: JAMES M. SPOTTS
DATE: 4-19-94
SCALE: 1:1
UNLESS OTHERWISE SPECIFIED DIMENSIONS ARE IN INCHES
TOLERANCES:(UNLESS SPECIFIED)
DECIMALS
X ± 0.06
.XX ± 0.03
.XXX ± 0.01
ANGLES
± 1/2°
MATERIAL: ALUMINUM
PROF. M. OKUMURA LABORATORY
DIVISION OF CHEMISTRY: CALIFORNIA INSTITUTE OF TECHNOLOGY

Figure 2-45

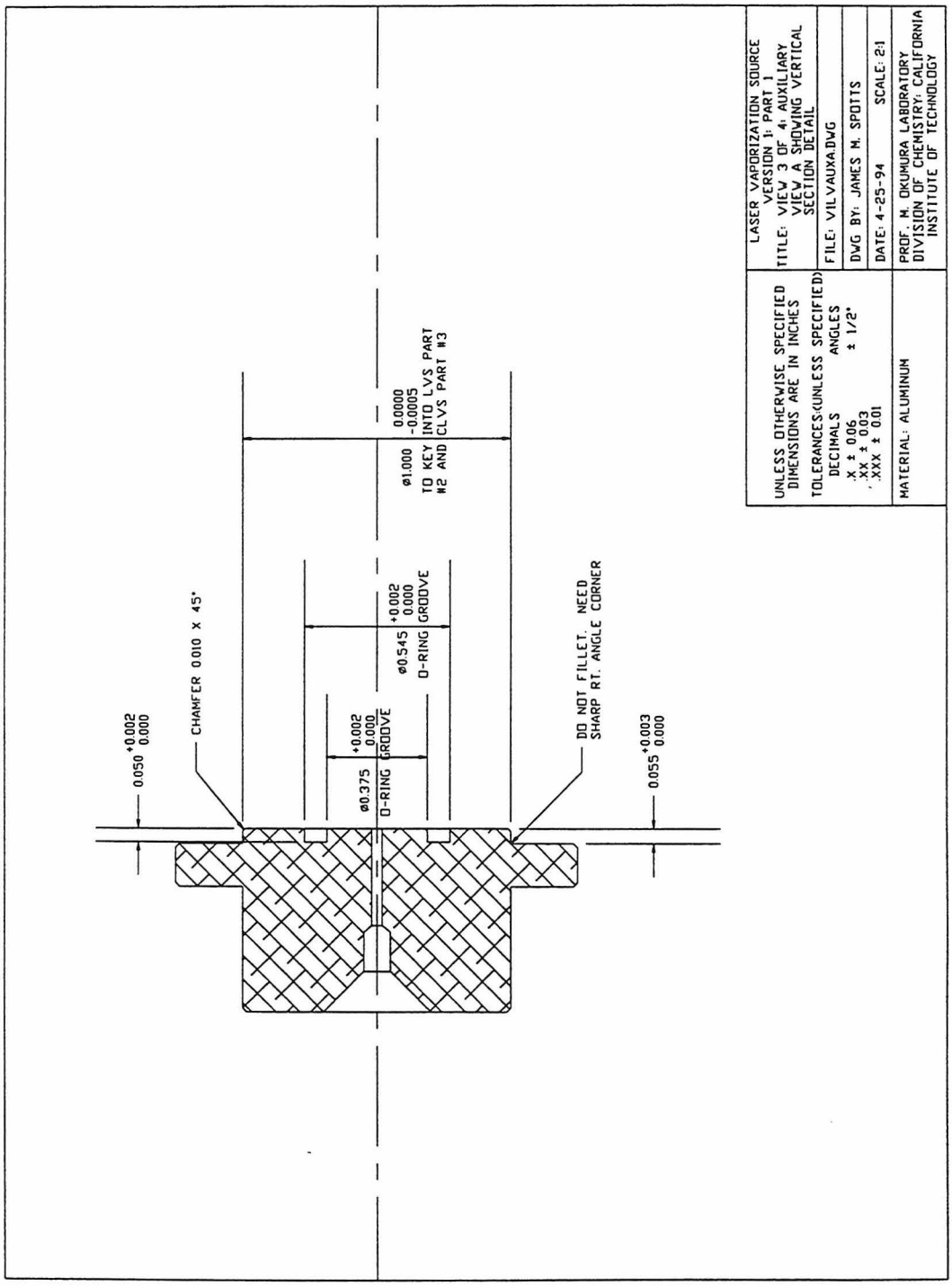

LASER VAPORIZATION SOURCE
VERSION 1: PART 1
TITLE: VIEW 3 OF 4: AUXILIARY
VIEW A SHOWING VERTICAL
SECTION DETAIL
FILE: VILVAUXA.DWG
DWG BY: JAMES M. SPOTTS
DATE: 4-25-94
SCALE: 2:1
PROF. M. OKUMURA LABORATORY
DIVISION OF CHEMISTRY: CALIFORNIA
INSTITUTE OF TECHNOLOGY
UNLESS OTHERWISE SPECIFIED
DIMENSIONS ARE IN INCHES
TOLERANCES:(UNLESS SPECIFIED)
DECIMALS
.X ± 0.06
.XX ± 0.03
.XXX ± 0.01
ANGLES
± 1/2°
MATERIAL: ALUMINUM
0.050 +0.002 0.000
CHAMFER 0.010 X 45°
ø0.375 +0.002 0.000 O-RING GROOVE
ø0.545 +0.002 0.000 O-RING GROOVE
ø1.000 0.0000 -0.0005 TO KEY INTO LVS PART #2 AND CLVS PART #3
DO NOT FILLET, NEED SHARP RT. ANGLE CORNER
0.055 +0.003 0.000

Figure 2-46

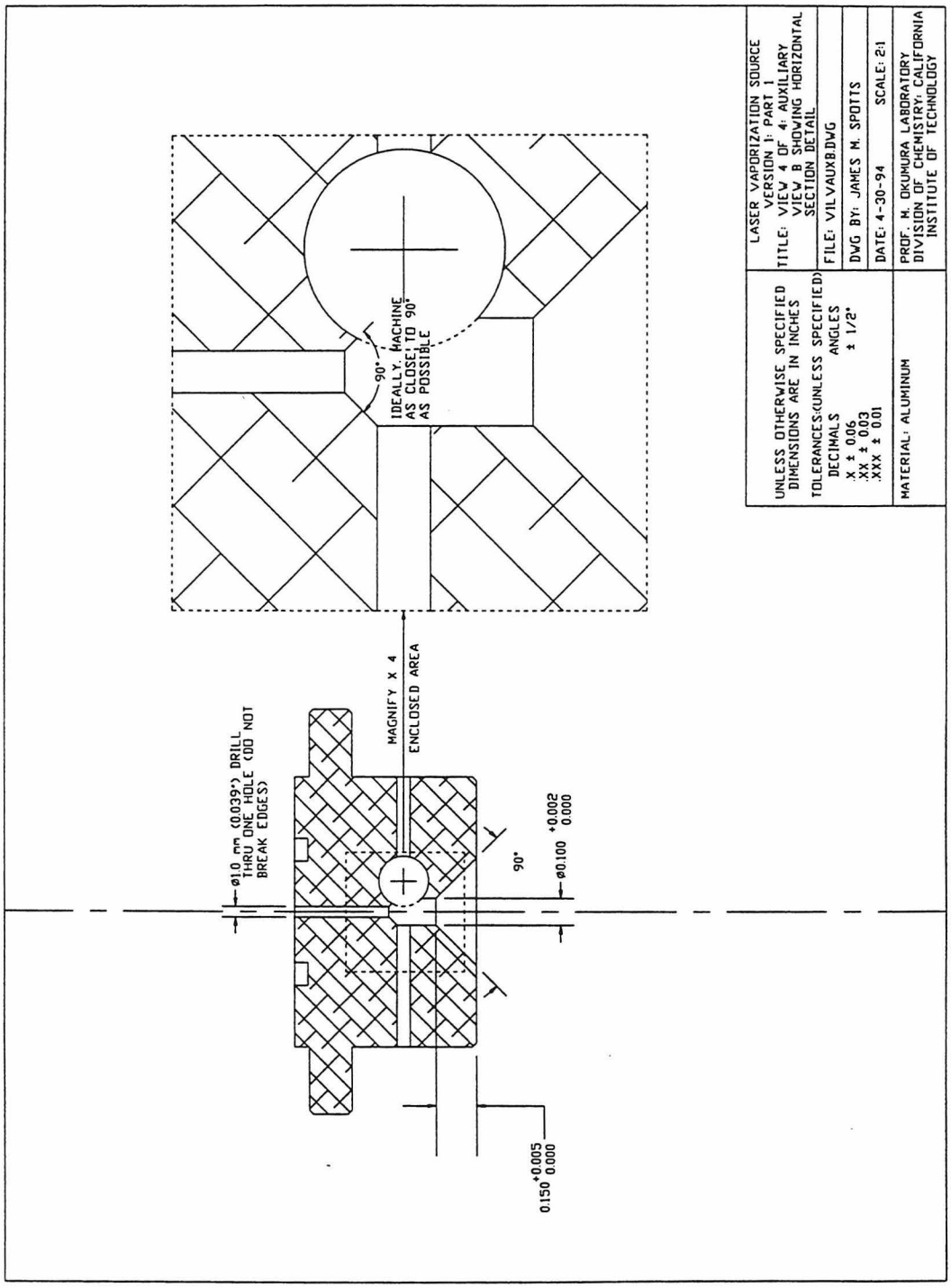

LASER VAPORIZATION SOURCE
VERSION 1: PART 1
TITLE: VIEW 4 OF 4: AUXILIARY VIEW B SHOWING HORIZONTAL SECTION DETAIL
UNLESS OTHERWISE SPECIFIED DIMENSIONS ARE IN INCHES
TOLERANCES:(UNLESS SPECIFIED)
DECIMALS
X ± 0.06
.XX ± 0.03
.XXX ± 0.01
ANGLES
± 1/2°
FILE: VILVAUXB.DWG
DWG BY: JAMES M. SPOTTS
DATE: 4-30-94
SCALE: 2:1
MATERIAL: ALUMINUM
PROF. M. OKUMURA LABORATORY
DIVISION OF CHEMISTRY: CALIFORNIA INSTITUTE OF TECHNOLOGY
90°
IDEALLY, MACHINE AS CLOSE TO 90° AS POSSIBLE
MAGNIFY X 4
ENCLOSED AREA
ø1.0 mm (.039") DRILL THRU ONE HOLE (DO NOT BREAK EDGES)
90°
ø0.100 +0.002 0.000
0.150 +0.005 0.000

Figure 2-47

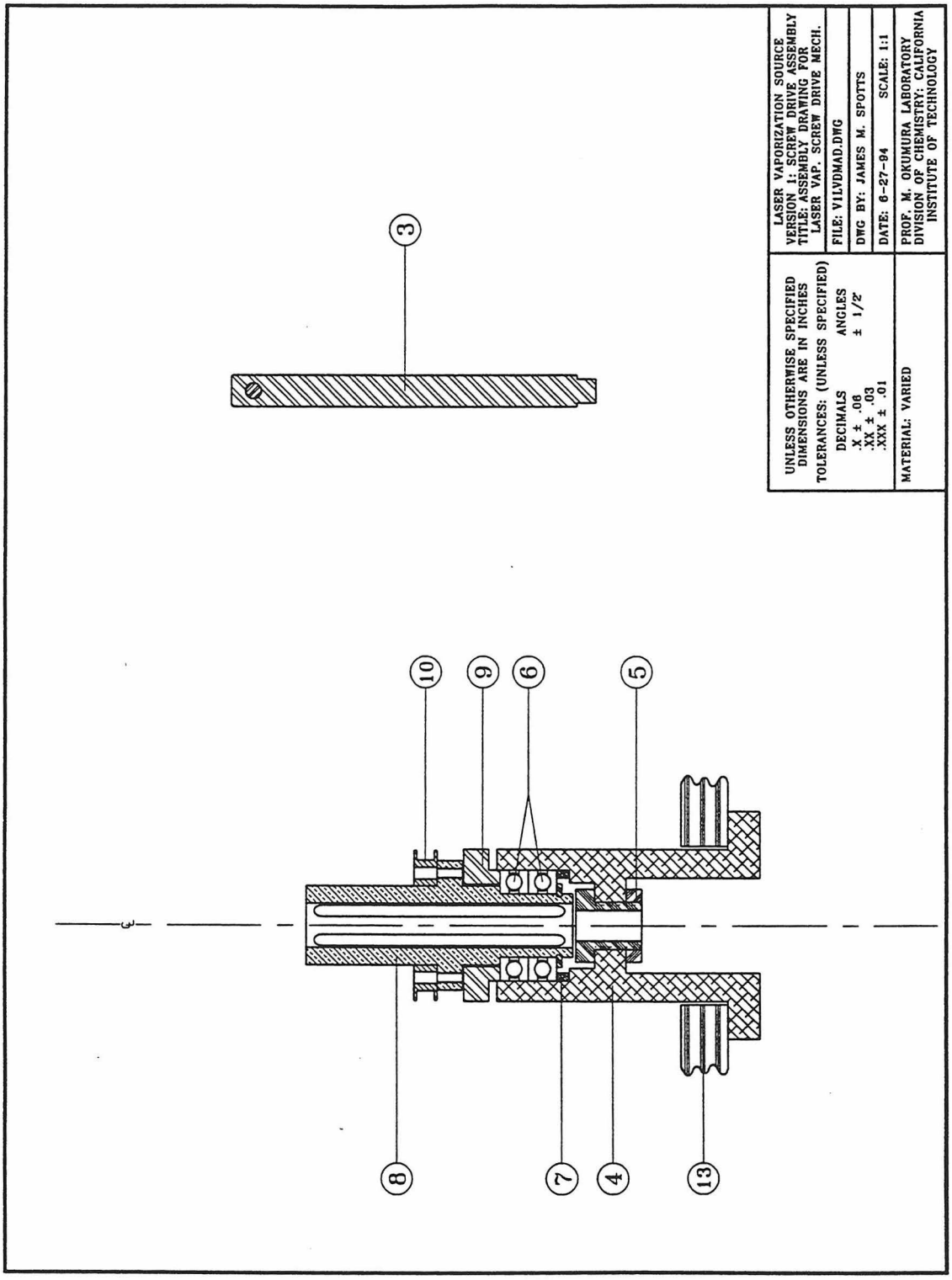

3
10
9
6
5
8
7
4
13
LASER VAPORIZATION SOURCE
VERSION 1: SCREW DRIVE ASSEMBLY
TITLE: ASSEMBLY DRAWING FOR
LASER VAP. SCREW DRIVE MECH.
FILE: V1LVDMAD.DWG
DWG BY: JAMES M. SPOTTS
DATE: 6-27-94
SCALE: 1:1
PROF. M. OKUMURA LABORATORY
DIVISION OF CHEMISTRY: CALIFORNIA
INSTITUTE OF TECHNOLOGY
UNLESS OTHERWISE SPECIFIED
DIMENSIONS ARE IN INCHES
TOLERANCES: (UNLESS SPECIFIED)
DECIMALS
X ± .06
.XX ± .03
.XXX ± .01
ANGLES
± 1/2°
MATERIAL: VARIED

Figure 2-48

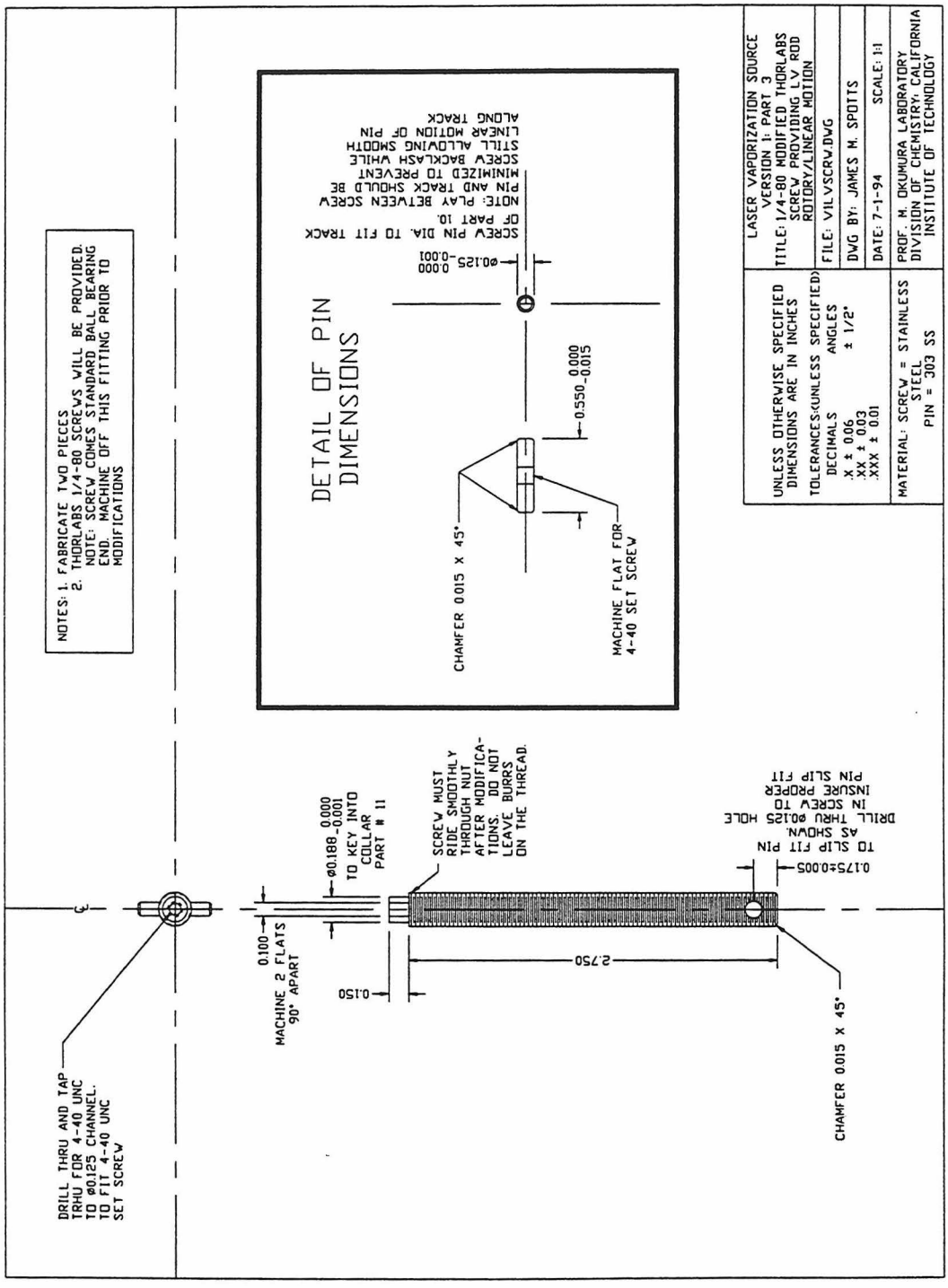

NOTES: 1. FABRICATE TWO PIECES
2. THORLABS 1/4-80 SCREWS WILL BE PROVIDED.
NOTE: SCREW COMES STANDARD BALL BEARING END. MACHINE OFF THIS FITTING PRIOR TO MODIFICATIONS
DETAIL OF PIN DIMENSIONS
SCREW PIN DIA. TO FIT TRACK OF PART 10.
NOTE: PLAY BETWEEN SCREW PIN AND TRACK SHOULD BE MINIMIZED TO PREVENT SCREW BACKLASH WHILE STILL ALLOWING SMOOTH LINEAR MOTION OF PIN ALONG TRACK
CHAMFER 0.015 X 45°
MACHINE FLAT FOR 4-40 SET SCREW
UNLESS OTHERWISE SPECIFIED DIMENSIONS ARE IN INCHES
TOLERANCES:(UNLESS SPECIFIED)
DECIMALS ANGLES
.X ± 0.06 ± 1/2°
.XX ± 0.03
.XXX ± 0.01
MATERIAL: SCREW = STAINLESS STEEL
PIN = 303 SS
LASER VAPORIZATION SOURCE
VERSION 1: PART 3
TITLE: 1/4-80 MODIFIED THORLABS SCREW PROVIDING LV ROD ROTORY/LINEAR MOTION
FILE: VILVSCRW.DWG
DWG BY: JAMES M. SPOTTS
DATE: 7-1-94
SCALE: 1:1
PROF. M. OKUMURA LABORATORY
DIVISION OF CHEMISTRY; CALIFORNIA INSTITUTE OF TECHNOLOGY
DRILL THRU AND TAP THRU FOR 4-40 UNC TO Ø0.125 CHANNEL. TO FIT 4-40 UNC SET SCREW
MACHINE 2 FLATS 90° APART
0.100
Ø0.188 0.000 -0.001
TO KEY INTO COLLAR PART # 11
SCREW MUST RIDE SMOOTHLY THROUGH NUT AFTER MODIFICATIONS. DO NOT LEAVE BURRS ON THE THREAD.
0.150
2.750
0.175±0.005
TO SLIP FIT PIN AS SHOWN.
DRILL THRU Ø0.125 HOLE IN SCREW TO INSURE PROPER PIN SLIP FIT
CHAMFER 0.015 X 45°

Figure 2-49

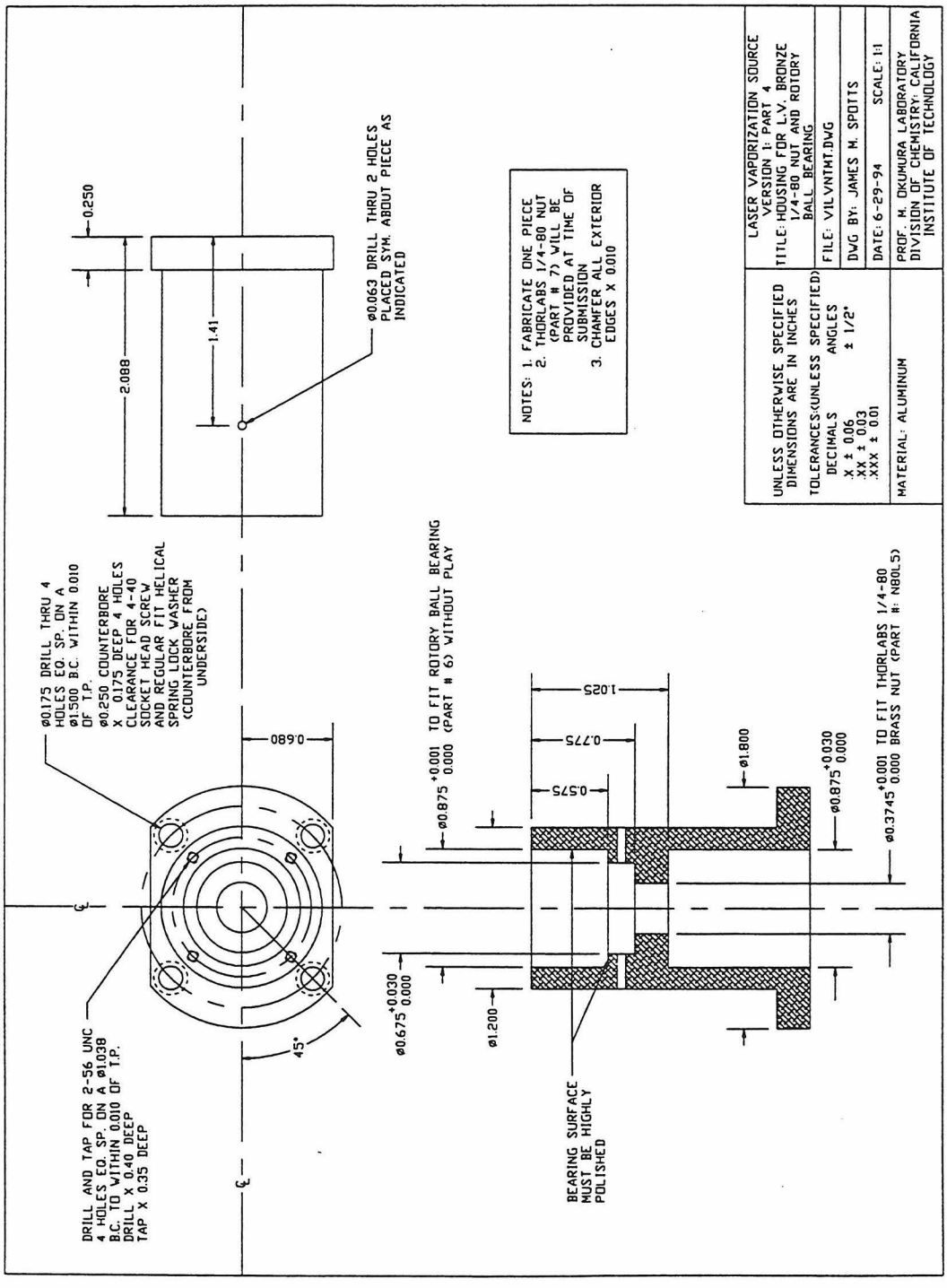

LASER VAPORIZATION SOURCE
VERSION 1: PART 4
TITLE: HOUSING FOR L.V. BRONZE
1/4-80 NUT AND ROTORY
BALL BEARING
FILE: VILVNTMT.DWG
DWG BY: JAMES M. SPOTTS
DATE: 6-29-94
SCALE: 1:1
PROF. M. OKUMURA LABORATORY
DIVISION OF CHEMISTRY: CALIFORNIA
INSTITUTE OF TECHNOLOGY
UNLESS OTHERWISE SPECIFIED
DIMENSIONS ARE IN INCHES
TOLERANCES:(UNLESS SPECIFIED)
DECIMALS ANGLES
.X ± 0.06 ± 1/2°
.XX ± 0.03
.XXX ± 0.01
MATERIAL: ALUMINUM
NOTES: 1. FABRICATE ONE PIECE
2. THORLABS 1/4-80 NUT
(PART # 7) WILL BE
PROVIDED AT TIME OF
SUBMISSION
3. CHAMFER ALL EXTERIOR
EDGES X 0.010
Ø0.063 DRILL THRU 2 HOLES
PLACED SYM. ABOUT PIECE AS
INDICATED
0.250
2.088
1.41
Ø0.175 DRILL THRU 4
HOLES EQ. SP. ON A
Ø1.500 B.C. WITHIN 0.010
OF T.P.
Ø0.250 COUNTERBORE
X 0.175 DEEP 4 HOLES
CLEARANCE FOR 4-40
SOCKET HEAD SCREW
AND REGULAR FIT HELICAL
SPRING LOCK WASHER
(COUNTERBORE FROM
UNDERSIDE)
0.680
DRILL AND TAP FOR 2-56 UNC
4 HOLES EQ. SP. ON A Ø1.038
B.C. TO WITHIN 0.010 OF T.P.
DRILL X 0.40 DEEP
TAP X 0.35 DEEP
45°
Ø0.875 +0.001 0.000 TO FIT ROTORY BALL BEARING (PART # 6) WITHOUT PLAY
Ø0.675 +0.030 0.000
Ø1.200
1.025
0.775
0.575
Ø1.800
Ø0.875 +0.030 0.000
Ø0.3745 +0.001 0.000 TO FIT THORLABS 1/4-80 BRASS NUT (PART #: N80L5)
BEARING SURFACE
MUST BE HIGHLY
POLISHED

Figure 2-50

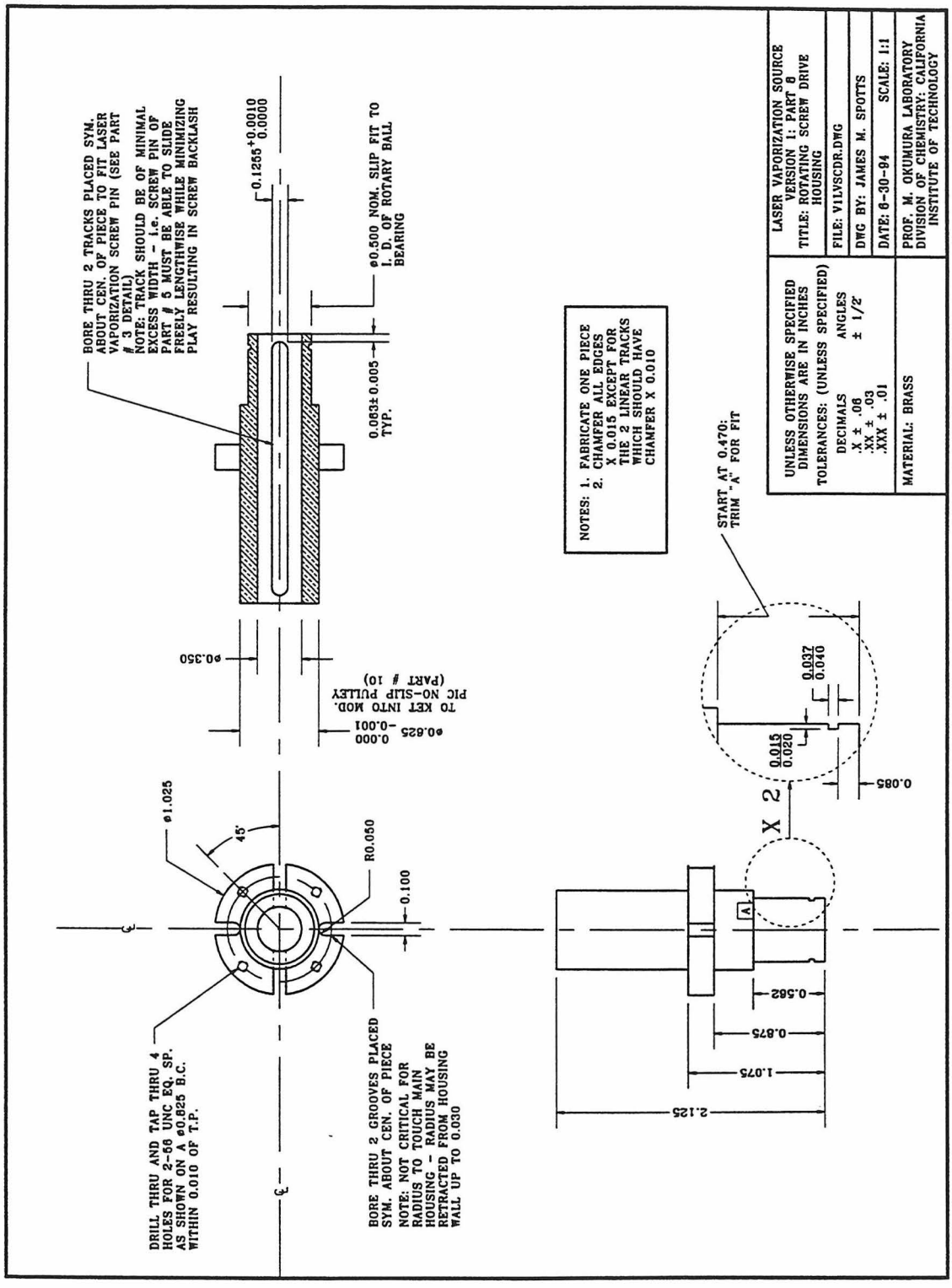

BORE THRU 2 TRACKS PLACED SYM. ABOUT CEN. OF PIECE TO FIT LASER VAPORIZATION SCREW PIN (SEE PART # 3 DETAIL)
NOTE: TRACK SHOULD BE OF MINIMAL EXCESS WIDTH - i.e. SCREW PIN OF PART # 5 MUST BE ABLE TO SLIDE FREELY LENGTHWISE WHILE MINIMIZING PLAY RESULTING IN SCREW BACKLASH
0.1255 +0.0010 0.0000
ø0.500 NOM. SLIP FIT TO I. D. OF ROTARY BALL BEARING
0.063± 0.005 TYP.
ø0.350
TO KET INTO MOD. PIC NO-SLIP PULLEY (PART # 10)
ø0.825 0.000 -0.001
ø1.025
45°
R0.050
0.100
DRILL THRU AND TAP THRU 4 HOLES FOR 2-56 UNC EQ. SP. AS SHOWN ON A ø0.825 B.C. WITHIN 0.010 OF T.P.
BORE THRU 2 GROOVES PLACED SYM. ABOUT CEN. OF PIECE
NOTE: NOT CRITICAL FOR RADIUS TO TOUCH MAIN HOUSING - RADIUS MAY BE RETRACTED FROM HOUSING WALL UP TO 0.030
NOTES: 1. FABRICATE ONE PIECE
2. CHAMFER ALL EDGES X 0.015 EXCEPT FOR THE 2 LINEAR TRACKS WHICH SHOULD HAVE CHAMFER X 0.010
START AT 0.470: TRIM "A" FOR FIT
0.015 0.020
0.037 0.040
X 2
0.085
0.562
0.875
1.075
2.125
UNLESS OTHERWISE SPECIFIED DIMENSIONS ARE IN INCHES
TOLERANCES: (UNLESS SPECIFIED)
DECIMALS ANGLES
X ± .06 ± 1/2°
.XX ± .03
.XXX ± .01
MATERIAL: BRASS
LASER VAPORIZATION SOURCE
VERSION 1: PART 8
TITLE: ROTATING SCREW DRIVE HOUSING
FILE: V1LVSCDR.DWG
DWG BY: JAMES M. SPOTTS
DATE: 6-30-94 SCALE: 1:1
PROF. M. OKUMURA LABORATORY
DIVISION OF CHEMISTRY: CALIFORNIA INSTITUTE OF TECHNOLOGY

Figure 2-51

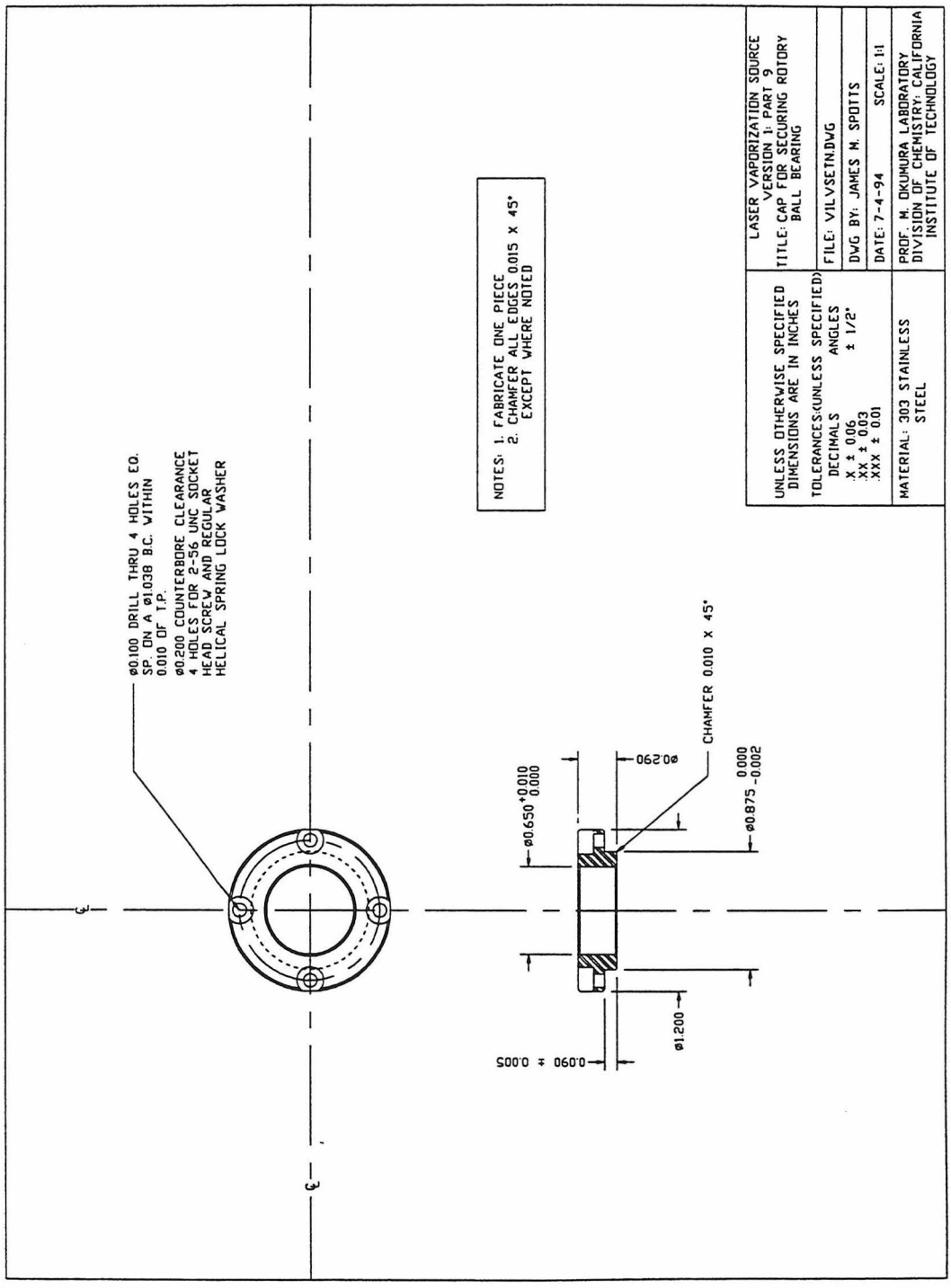

Ø0.100 DRILL THRU 4 HOLES EQ. SP. ON A Ø1.038 B.C. WITHIN 0.010 OF T.P.
Ø0.200 COUNTERBORE CLEARANCE 4 HOLES FOR 2-56 UNC SOCKET HEAD SCREW AND REGULAR HELICAL SPRING LOCK WASHER
NOTES: 1. FABRICATE ONE PIECE
2. CHAMFER ALL EDGES 0.015 X 45° EXCEPT WHERE NOTED
CHAMFER 0.010 X 45°
Ø0.650 +0.010 0.000
Ø0.290
Ø0.875 0.000 -0.002
Ø1.200
0.090 ± 0.005
UNLESS OTHERWISE SPECIFIED DIMENSIONS ARE IN INCHES
TOLERANCES:(UNLESS SPECIFIED)
DECIMALS ANGLES
X ± 0.06 ± 1/2°
XX ± 0.03
XXX ± 0.01
MATERIAL: 303 STAINLESS STEEL
LASER VAPORIZATION SOURCE VERSION 1: PART 9
TITLE: CAP FOR SECURING ROTORY BALL BEARING
FILE: VILVSETN.DWG
DWG BY: JAMES M. SPOTTS
DATE: 7-4-94
SCALE: 1:1
PROF. M. OKUMURA LABORATORY
DIVISION OF CHEMISTRY: CALIFORNIA INSTITUTE OF TECHNOLOGY

Figure 2-52

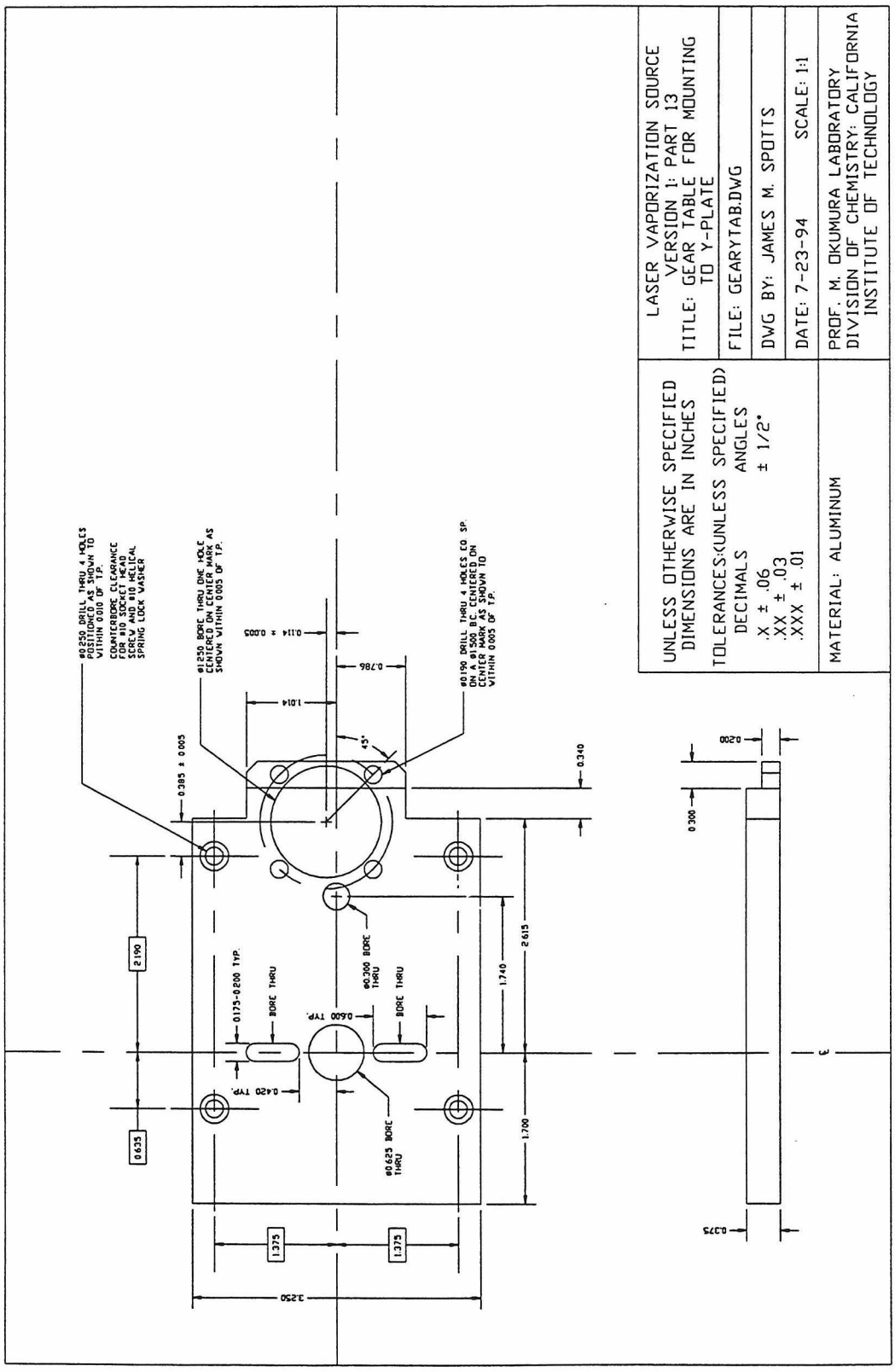

LASER VAPORIZATION SOURCE
VERSION 1: PART 13
TITLE: GEAR TABLE FOR MOUNTING TO Y-PLATE
FILE: GEARYTAB.DWG
DWG BY: JAMES M. SPOTTS
DATE: 7-23-94
SCALE: 1:1
PROF. M. OKUMURA LABORATORY
DIVISION OF CHEMISTRY: CALIFORNIA INSTITUTE OF TECHNOLOGY
UNLESS OTHERWISE SPECIFIED DIMENSIONS ARE IN INCHES
TOLERANCES:(UNLESS SPECIFIED)
DECIMALS
ANGLES
.X ± .06
± 1/2°
.XX ± .03
.XXX ± .01
MATERIAL: ALUMINUM
#0.250 DRILL THRU 4 HOLES POSITIONED AS SHOWN TO WITHIN 0.010 OF T.P.
COUNTERBORE CLEARANCE FOR #10 SOCKET HEAD SCREW AND #10 HELICAL SPRING LOCK WASHER
#1.250 BORE THRU ONE HOLE CENTERED ON CENTER MARK AS SHOWN WITHIN 0.005 OF T.P.
#0.190 DRILL THRU 4 HOLES EQ SP ON A #1.500 B.C. CENTERED ON CENTER MARK AS SHOWN TO WITHIN 0.005 OF T.P.
0.385 ± 0.005
0.114 ± 0.005
0.786
1.014
45°
0.340
0.200
0.300
2.190
0.635
0.175-0.200 TYP.
BORE THRU
0.420 TYP.
0.600 TYP.
#0.300 BORE THRU
#0.625 BORE THRU
1.740
2.615
1.700
1.375
1.375
3.250

Figure 2-53

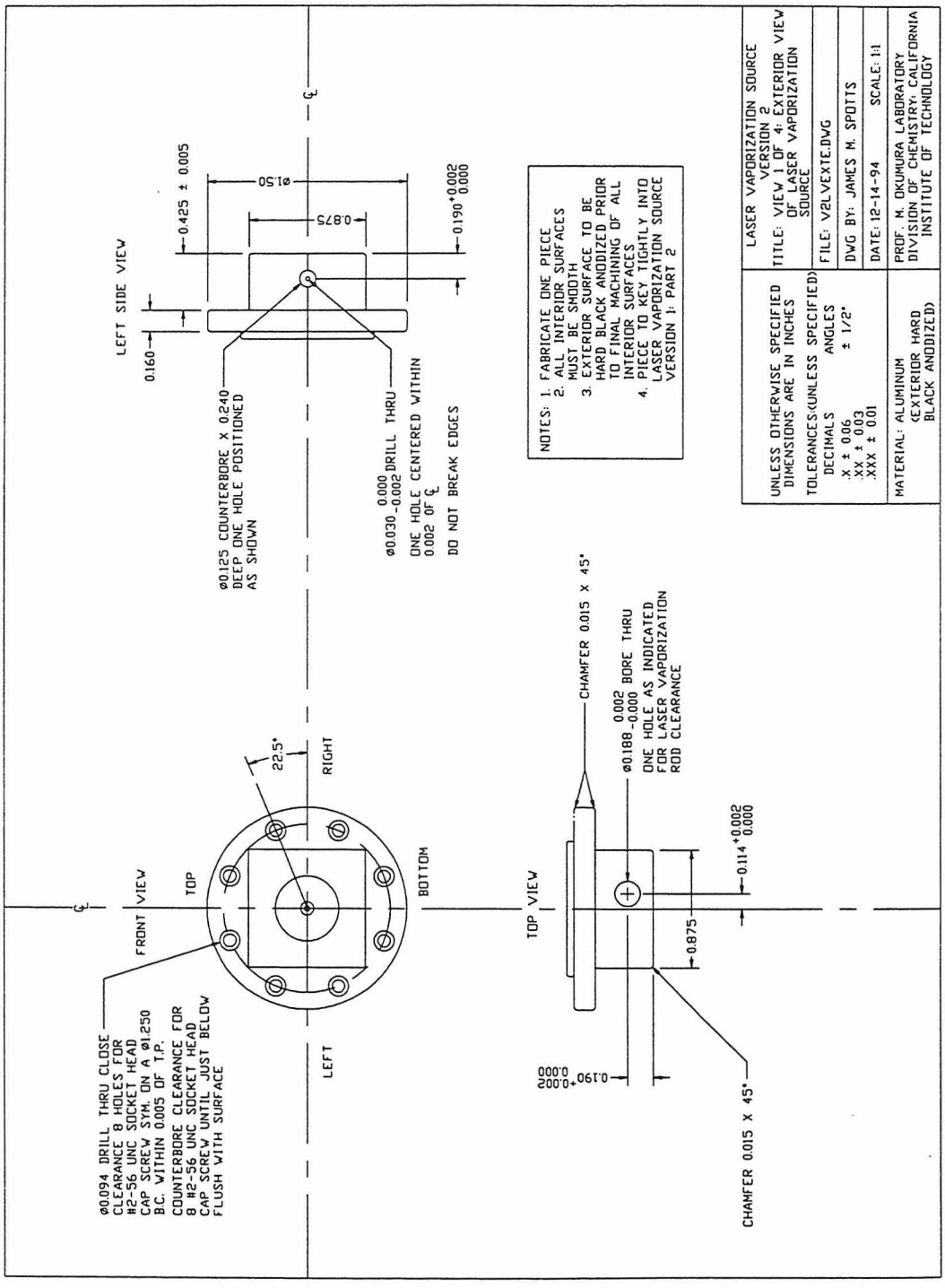

LEFT SIDE VIEW
0.425 ± 0.005
Ø1.50
0.875
0.190 +0.002 0.000
0.160
Ø0.125 COUNTERBORE X 0.240 DEEP ONE HOLE POSITIONED AS SHOWN
Ø0.030 0.000 -0.002 DRILL THRU ONE HOLE CENTERED WITHIN 0.002 OF ℄
DO NOT BREAK EDGES
NOTES: 1. FABRICATE ONE PIECE
2. ALL INTERIOR SURFACES MUST BE SMOOTH
3. EXTERIOR SURFACE TO BE HARD BLACK ANODIZED PRIOR TO FINAL MACHINING OF ALL INTERIOR SURFACES
4. PIECE TO KEY TIGHTLY INTO LASER VAPORIZATION SOURCE VERSION 1: PART 2
LASER VAPORIZATION SOURCE VERSION 2
TITLE: VIEW 1 OF 4: EXTERIOR VIEW OF LASER VAPORIZATION SOURCE
UNLESS OTHERWISE SPECIFIED DIMENSIONS ARE IN INCHES
TOLERANCES:(UNLESS SPECIFIED)
DECIMALS ANGLES
.X ± 0.06 ± 1/2°
.XX ± 0.03
.XXX ± 0.01
FILE: V2LVEXTE.DWG
DWG BY: JAMES M. SPOTTS
DATE: 12-14-94
SCALE: 1:1
MATERIAL: ALUMINUM
(EXTERIOR HARD BLACK ANODIZED)
PROF. M. OKUMURA LABORATORY
DIVISION OF CHEMISTRY: CALIFORNIA INSTITUTE OF TECHNOLOGY
℄
FRONT VIEW
TOP
22.5°
RIGHT
BOTTOM
LEFT
Ø0.094 DRILL THRU CLOSE CLEARANCE 8 HOLES FOR #2-56 UNC SOCKET HEAD CAP SCREW SYM. ON A Ø1.250 B.C. WITHIN 0.005 OF T.P.
COUNTERBORE CLEARANCE FOR 8 #2-56 UNC SOCKET HEAD CAP SCREW UNTIL JUST BELOW FLUSH WITH SURFACE
TOP VIEW
CHAMFER 0.015 X 45°
Ø0.188 0.002 -0.000 BORE THRU ONE HOLE AS INDICATED FOR LASER VAPORIZATION ROD CLEARANCE
0.114 +0.002 0.000
0.875
0.190 +0.002 0.000
CHAMFER 0.015 X 45°

Figure 2-54

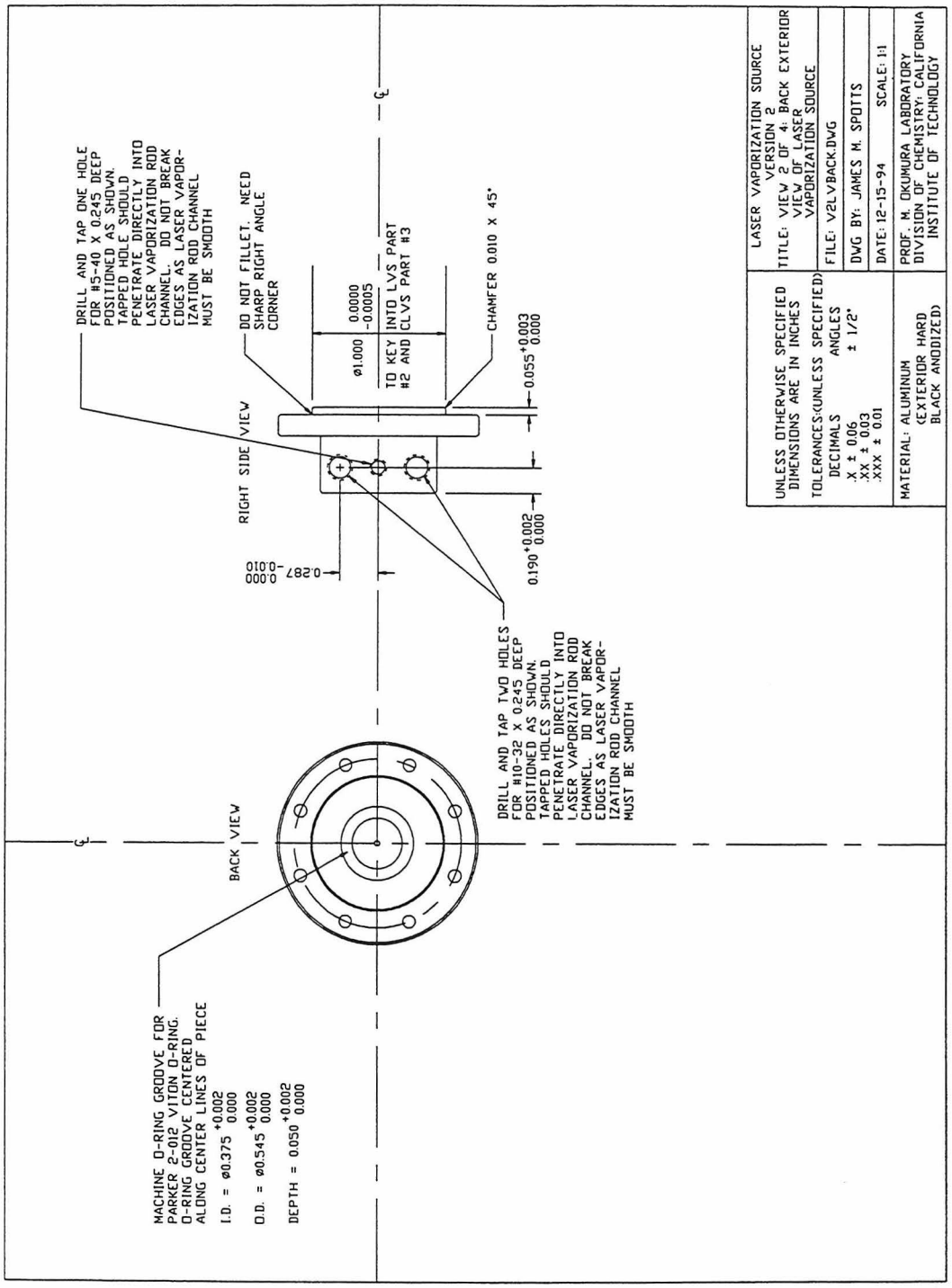

LASER VAPORIZATION SOURCE
VERSION 2
TITLE: VIEW 2 OF 4: BACK EXTERIOR
VIEW OF LASER
VAPORIZATION SOURCE
FILE: V2LVBACK.DWG
DWG BY: JAMES M. SPOTTS
DATE: 12-15-94
SCALE: 1:1
PROF. M. OKUMURA LABORATORY
DIVISION OF CHEMISTRY-CALIFORNIA
INSTITUTE OF TECHNOLOGY
UNLESS OTHERWISE SPECIFIED
DIMENSIONS ARE IN INCHES
TOLERANCES:(UNLESS SPECIFIED)
DECIMALS ANGLES
.X ± 0.06 ± 1/2°
.XX ± 0.03
.XXX ± 0.01
MATERIAL: ALUMINUM
(EXTERIOR HARD
BLACK ANODIZED)
BACK VIEW
RIGHT SIDE VIEW
DRILL AND TAP ONE HOLE FOR #5-40 X 0.245 DEEP POSITIONED AS SHOWN. TAPPED HOLE SHOULD PENETRATE DIRECTLY INTO LASER VAPORIZATION ROD CHANNEL. DO NOT BREAK EDGES AS LASER VAPORIZATION ROD CHANNEL MUST BE SMOOTH
DO NOT FILLET. NEED SHARP RIGHT ANGLE CORNER
TO KEY INTO LVS PART #2 AND LVS PART #3
CHAMFER 0.010 X 45°
DRILL AND TAP TWO HOLES FOR #10-32 X 0.245 DEEP POSITIONED AS SHOWN. TAPPED HOLES SHOULD PENETRATE DIRECTLY INTO LASER VAPORIZATION ROD CHANNEL. DO NOT BREAK EDGES AS LASER VAPORIZATION ROD CHANNEL MUST BE SMOOTH
MACHINE O-RING GROOVE FOR PARKER 2-012 VITON O-RING. O-RING GROOVE CENTERED ALONG CENTER LINES OF PIECE
I.D. = ø0.375 +0.002 0.000
O.D. = ø0.545 +0.002 0.000
DEPTH = 0.050 +0.002 0.000
ø1.000 0.0000 -0.0005
0.287 0.000 -0.010
0.190 +0.002 0.000
0.055 +0.003 0.000

Figure 2-55

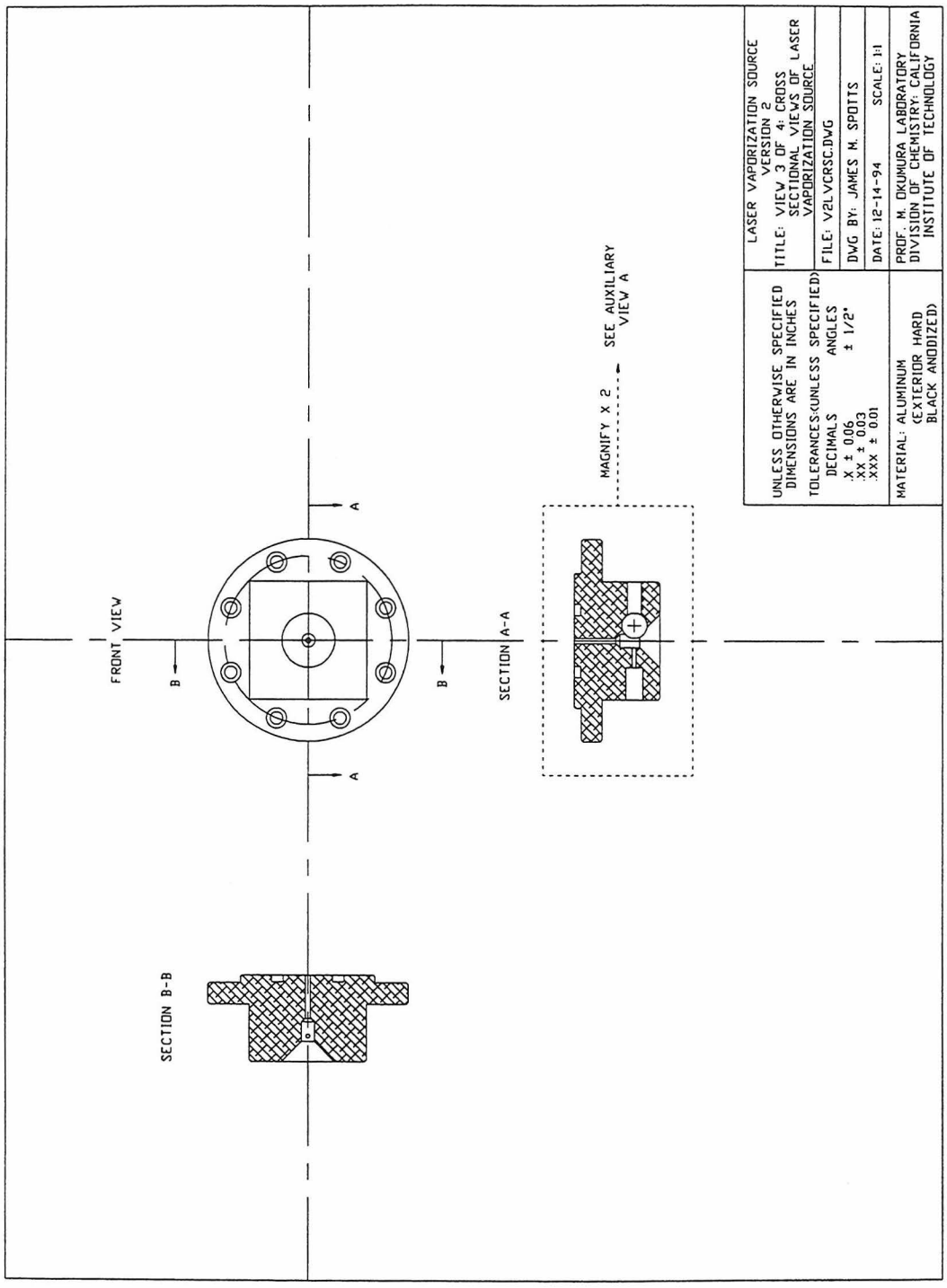

FRONT VIEW
SECTION A-A
SECTION B-B
MAGNIFY X 2
SEE AUXILIARY VIEW A
A
B
LASER VAPORIZATION SOURCE VERSION 2
TITLE: VIEW 3 OF 4: CROSS SECTIONAL VIEWS OF LASER VAPORIZATION SOURCE
FILE: V2LVCRSC.DWG
DWG BY: JAMES M. SPOTTS
DATE: 12-14-94
SCALE: 1:1
UNLESS OTHERWISE SPECIFIED DIMENSIONS ARE IN INCHES
TOLERANCES:(UNLESS SPECIFIED)
DECIMALS
.X ± 0.06
.XX ± 0.03
.XXX ± 0.01
ANGLES ± 1/2°
MATERIAL: ALUMINUM
(EXTERIOR HARD BLACK ANODIZED)
PROF. M. OKUMURA LABORATORY
DIVISION OF CHEMISTRY: CALIFORNIA INSTITUTE OF TECHNOLOGY

Figure 2-56

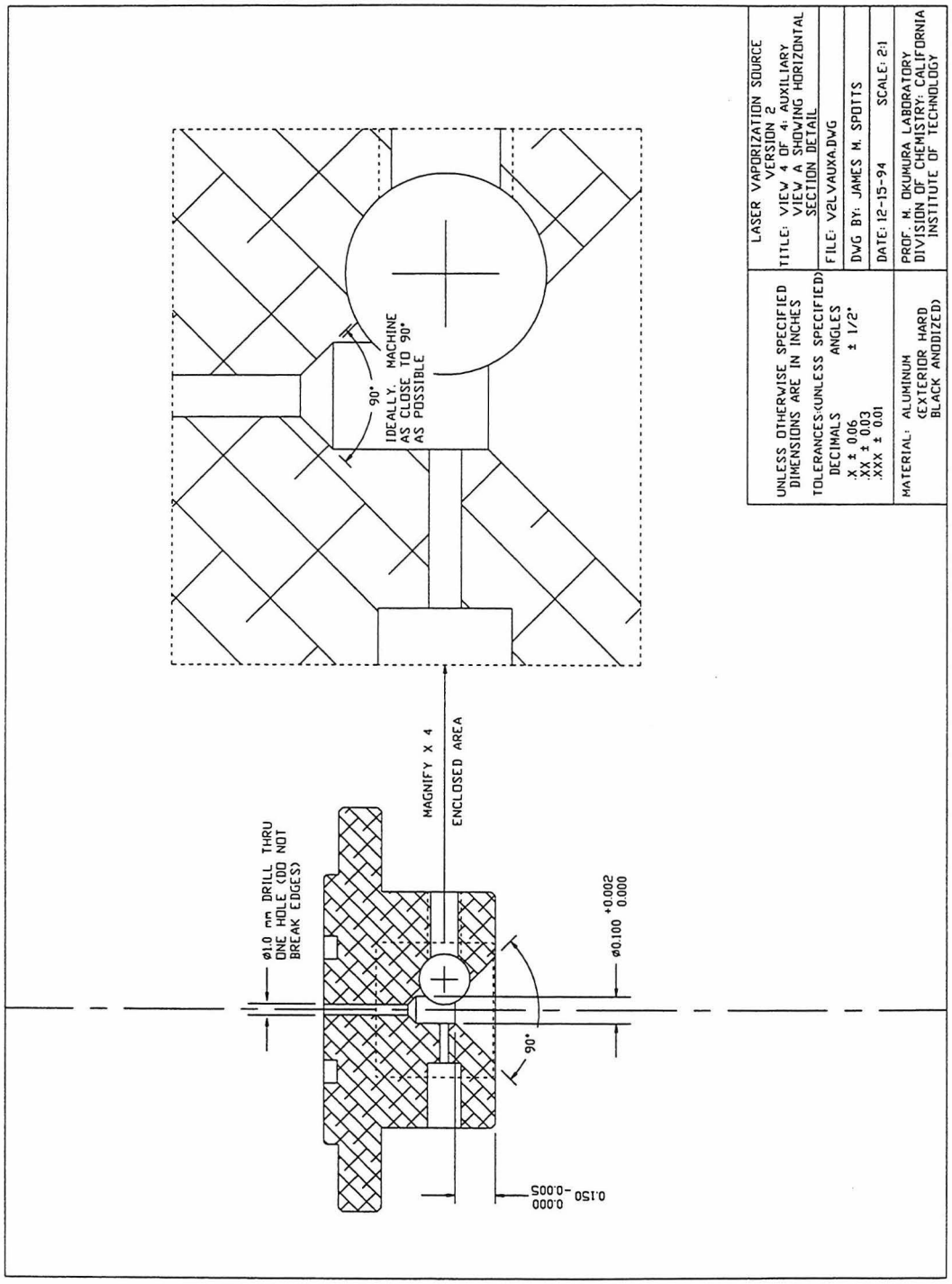

LASER VAPORIZATION SOURCE
VERSION 2
TITLE: VIEW 4 OF 4: AUXILIARY
VIEW A SHOWING HORIZONTAL
SECTION DETAIL
FILE: V2LVAUXA.DWG
DWG BY: JAMES M. SPOTTS
DATE: 12-15-94 SCALE: 2:1
PROF. M. OKUMURA LABORATORY
DIVISION OF CHEMISTRY: CALIFORNIA
INSTITUTE OF TECHNOLOGY
UNLESS OTHERWISE SPECIFIED
DIMENSIONS ARE IN INCHES
TOLERANCES:<UNLESS SPECIFIED)
DECIMALS ANGLES
.X ± 0.06 ± 1/2°
.XX ± 0.03
.XXX ± 0.01
MATERIAL: ALUMINUM
(EXTERIOR HARD
BLACK ANODIZED)
90° IDEALLY, MACHINE AS CLOSE TO 90° AS POSSIBLE
MAGNIFY X 4
ENCLOSED AREA
ø1.0 mm DRILL THRU ONE HOLE (DO NOT BREAK EDGES)
ø0.100 +0.002 0.000
90°
0.150 0.000 -0.005

Figure 2-57

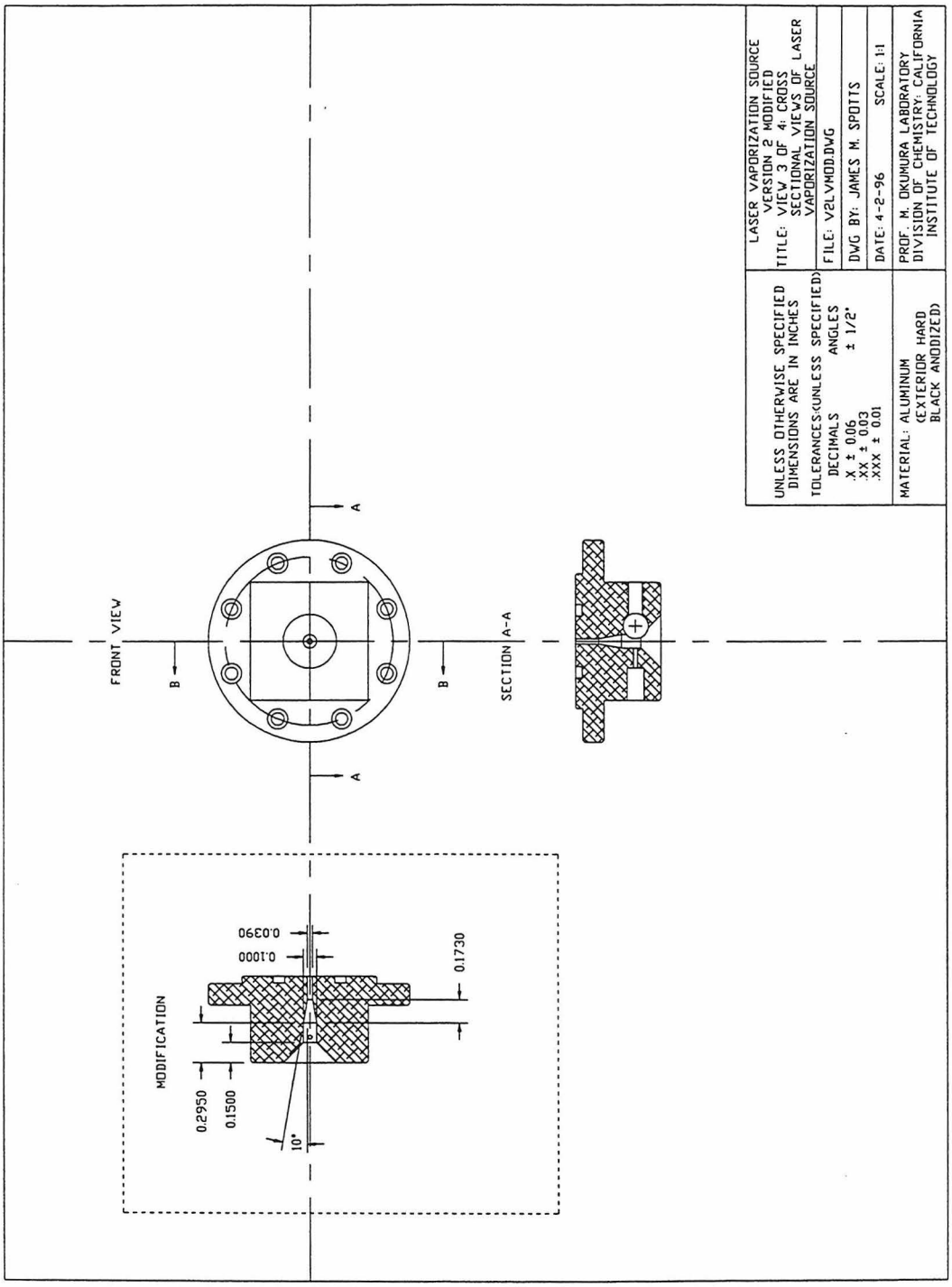

LASER VAPORIZATION SOURCE
VERSION 2 MODIFIED
TITLE: VIEW 3 OF 4: CROSS SECTIONAL VIEWS OF LASER VAPORIZATION SOURCE
FILE: V2LVMOD.DWG
DWG BY: JAMES M. SPOTTS
DATE: 4-2-96
SCALE: 1:1
PROF. M. OKUMURA LABORATORY
DIVISION OF CHEMISTRY: CALIFORNIA INSTITUTE OF TECHNOLOGY
UNLESS OTHERWISE SPECIFIED DIMENSIONS ARE IN INCHES
TOLERANCES:(UNLESS SPECIFIED)
DECIMALS
.X ± 0.06
.XX ± 0.03
.XXX ± 0.01
ANGLES
± 1/2°
MATERIAL: ALUMINUM
EXTERIOR HARD BLACK ANODIZED
FRONT VIEW
SECTION A-A
A
B
MODIFICATION
0.0390
0.1000
0.1730
0.2950
0.1500
10°

Figure 2-58

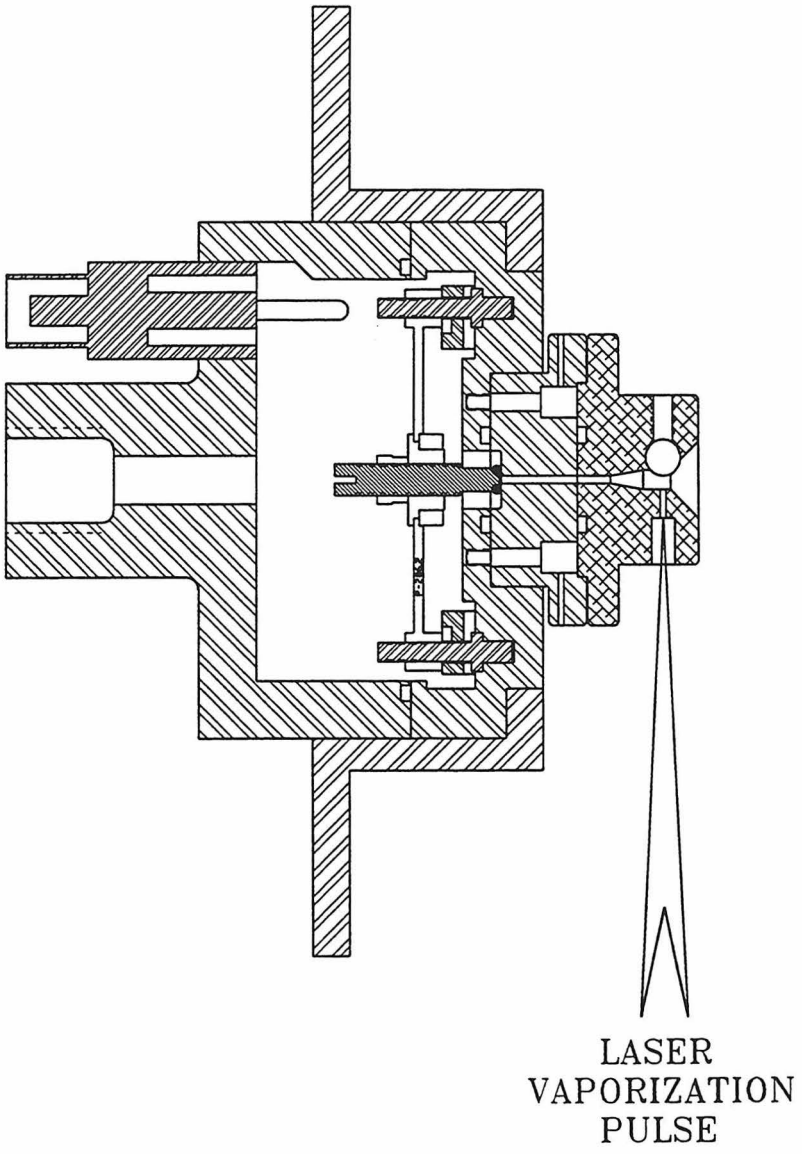


Figure 2-59

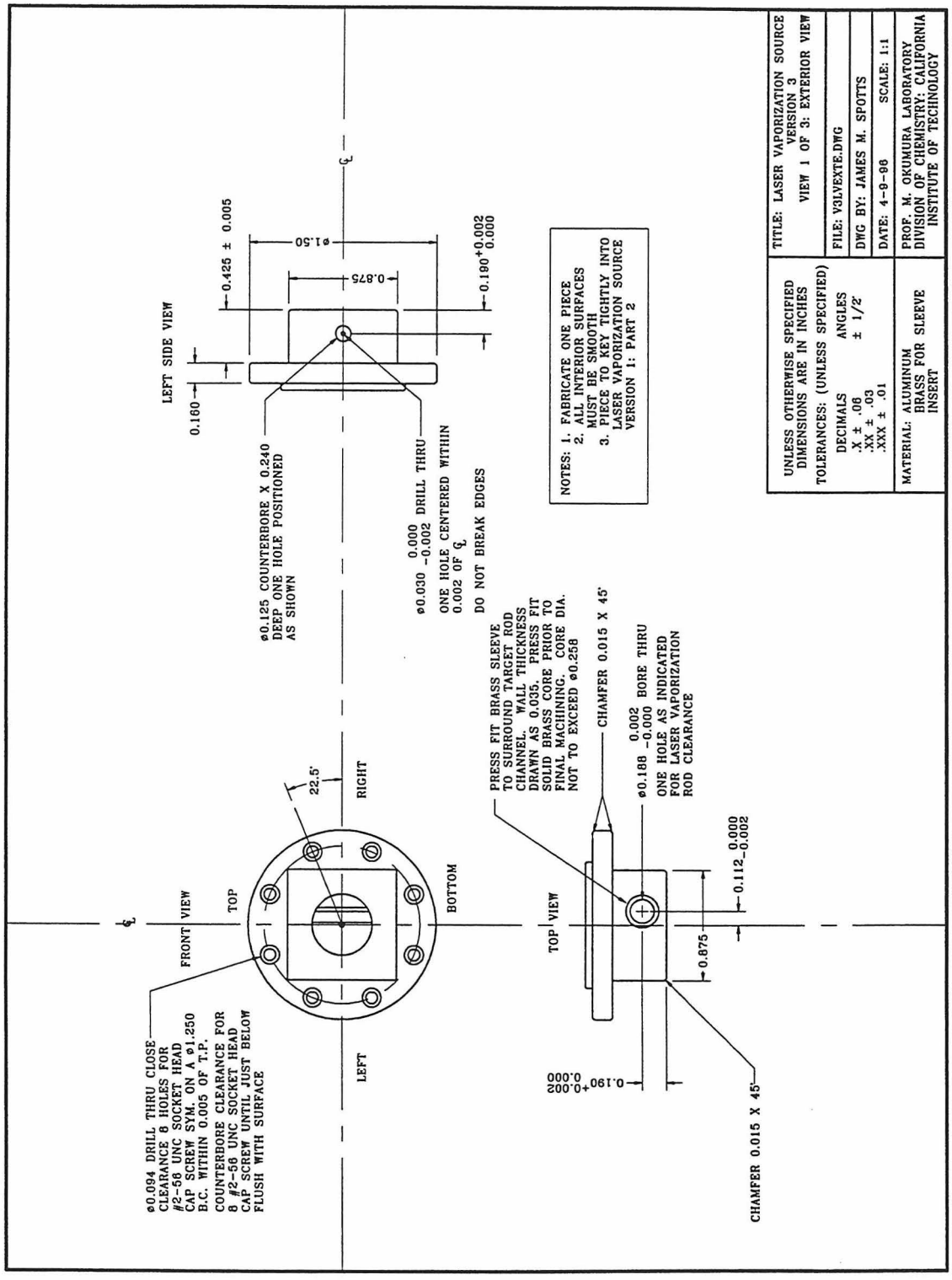

LEFT SIDE VIEW
0.160
0.425 ± 0.005
ø1.50
0.875
0.190 +0.002 0.000
ø0.125 COUNTERBORE X 0.240 DEEP ONE HOLE POSITIONED AS SHOWN
ø0.030 0.000 -0.002 DRILL THRU ONE HOLE CENTERED WITHIN 0.002 OF ℄
DO NOT BREAK EDGES
NOTES: 1. FABRICATE ONE PIECE
2. ALL INTERIOR SURFACES MUST BE SMOOTH
3. PIECE TO KEY TIGHTLY INTO LASER VAPORIZATION SOURCE VERSION 1: PART 2
UNLESS OTHERWISE SPECIFIED DIMENSIONS ARE IN INCHES
TOLERANCES: (UNLESS SPECIFIED)
DECIMALS ANGLES
.X ± .06 ± 1/2°
.XX ± .03
.XXX ± .01
TITLE: LASER VAPORIZATION SOURCE VERSION 3 VIEW 1 OF 3: EXTERIOR VIEW
FILE: V3LVEXTE.DWG
DWG BY: JAMES M. SPOTTS
DATE: 4-9-98
SCALE: 1:1
MATERIAL: ALUMINUM BRASS FOR SLEEVE INSERT
PROF. M. OKUMURA LABORATORY DIVISION OF CHEMISTRY: CALIFORNIA INSTITUTE OF TECHNOLOGY
℄
FRONT VIEW
TOP
BOTTOM
LEFT
RIGHT
22.5°
ø0.094 DRILL THRU CLOSE CLEARANCE 8 HOLES FOR #2-56 UNC SOCKET HEAD CAP SCREW SYM. ON A ø1.250 B.C. WITHIN 0.005 OF T.P.
COUNTERBORE CLEARANCE FOR 8 #2-56 UNC SOCKET HEAD CAP SCREW UNTIL JUST BELOW FLUSH WITH SURFACE
PRESS FIT BRASS SLEEVE TO SURROUND TARGET ROD CHANNEL. WALL THICKNESS DRAWN AS 0.035. PRESS FIT SOLID BRASS CORE PRIOR TO FINAL MACHINING. CORE DIA. NOT TO EXCEED ø0.258
CHAMFER 0.015 X 45°
ø0.188 0.002 -0.000 BORE THRU ONE HOLE AS INDICATED FOR LASER VAPORIZATION ROD CLEARANCE
TOP VIEW
0.112 0.000 -0.002
0.875
0.190 +0.002 0.000
CHAMFER 0.015 X 45°

Figure 2-60

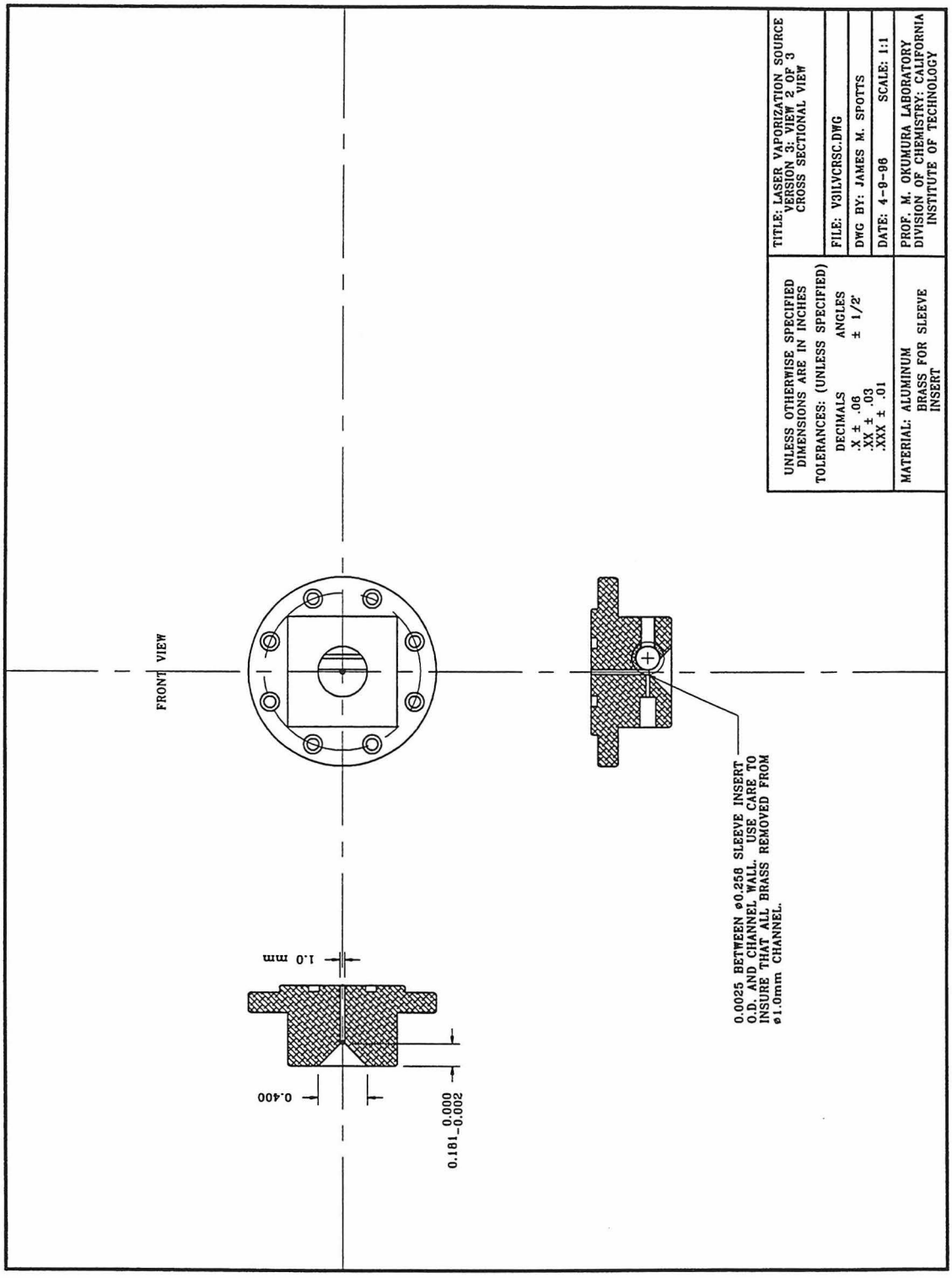

TITLE: LASER VAPORIZATION SOURCE
VERSION 3: VIEW 2 OF 3
CROSS SECTIONAL VIEW
FILE: V3ILVCRSC.DWG
DWG BY: JAMES M. SPOTTS
DATE: 4-9-96
SCALE: 1:1
PROF. M. OKUMURA LABORATORY
DIVISION OF CHEMISTRY: CALIFORNIA
INSTITUTE OF TECHNOLOGY
UNLESS OTHERWISE SPECIFIED
DIMENSIONS ARE IN INCHES
TOLERANCES: (UNLESS SPECIFIED)
DECIMALS
X ± .06
.XX ± .03
.XXX ± .01
ANGLES
± 1/2'
MATERIAL: ALUMINUM
BRASS FOR SLEEVE
INSERT
FRONT VIEW
1.0 mm
0.400
0.181 -0.000 -0.002
0.0025 BETWEEN ø0.250 SLEEVE INSERT
O.D. AND CHANNEL WALL. USE CARE TO
INSURE THAT ALL BRASS REMOVED FROM
ø1.0mm CHANNEL.

Figure 2-61

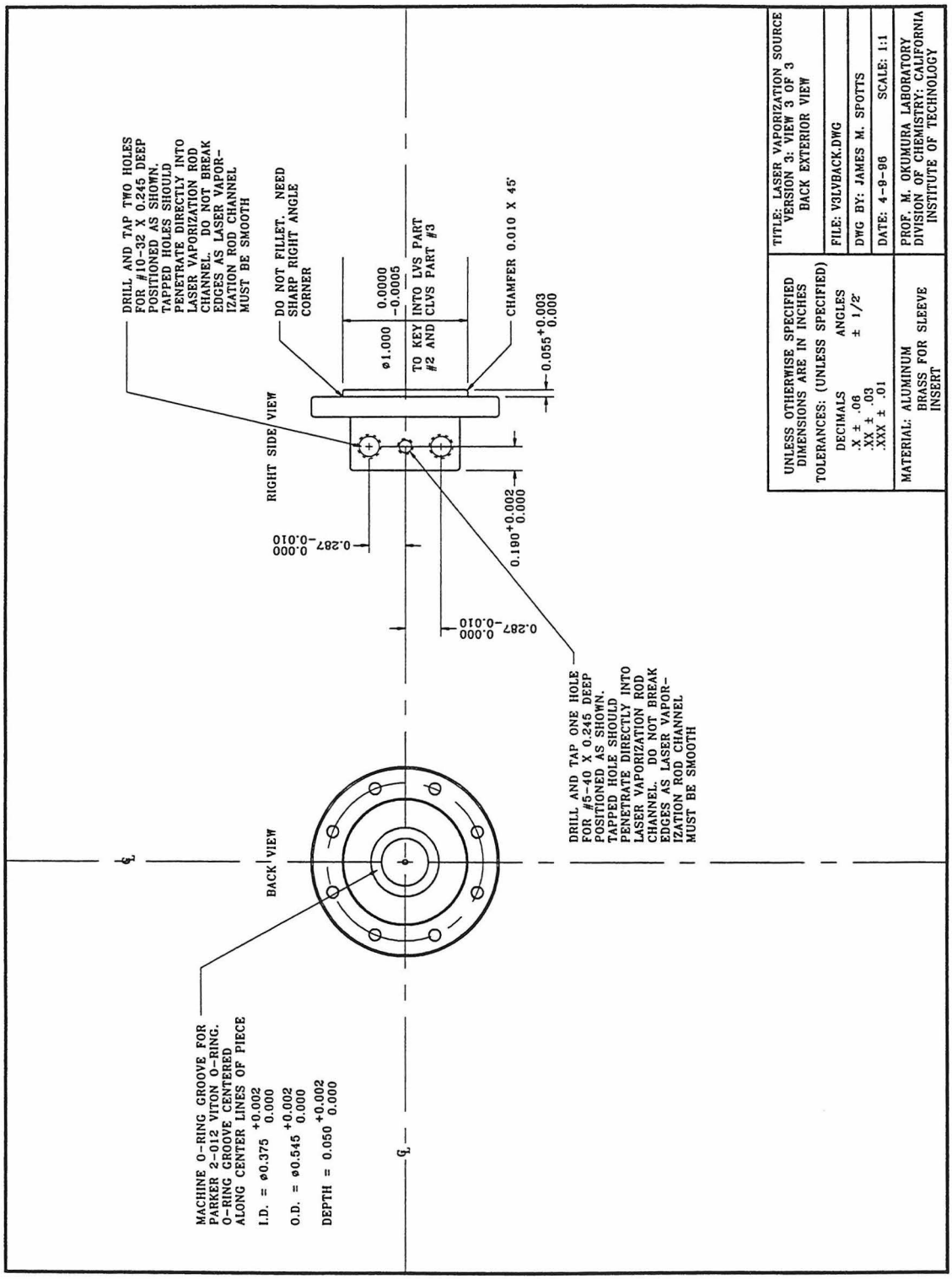

DRILL AND TAP TWO HOLES FOR #10-32 X 0.245 DEEP POSITIONED AS SHOWN. TAPPED HOLES SHOULD PENETRATE DIRECTLY INTO LASER VAPORIZATION ROD CHANNEL. DO NOT BREAK EDGES AS LASER VAPORIZATION ROD CHANNEL MUST BE SMOOTH
DO NOT FILLET. NEED SHARP RIGHT ANGLE CORNER
ø1.000 0.0000 -0.0005
TO KEY INTO LVS PART #2 AND CLVS PART #3
CHAMFER 0.010 X 45°
0.055 +0.003 0.000
RIGHT SIDE VIEW
0.287 0.000 -0.010
0.190 +0.002 0.000
0.287 0.000 -0.010
DRILL AND TAP ONE HOLE FOR #5-40 X 0.245 DEEP POSITIONED AS SHOWN. TAPPED HOLE SHOULD PENETRATE DIRECTLY INTO LASER VAPORIZATION ROD CHANNEL. DO NOT BREAK EDGES AS LASER VAPORIZATION ROD CHANNEL MUST BE SMOOTH
BACK VIEW
MACHINE O-RING GROOVE FOR PARKER 2-012 VITON O-RING. O-RING GROOVE CENTERED ALONG CENTER LINES OF PIECE
I.D. = ø0.375 +0.002 0.000
O.D. = ø0.545 +0.002 0.000
DEPTH = 0.050 +0.002 0.000
UNLESS OTHERWISE SPECIFIED DIMENSIONS ARE IN INCHES
TOLERANCES: (UNLESS SPECIFIED)
DECIMALS
.X ± .06
.XX ± .03
.XXX ± .01
ANGLES
± 1/2°
MATERIAL: ALUMINUM
BRASS FOR SLEEVE INSERT
TITLE: LASER VAPORIZATION SOURCE VERSION 3: VIEW 3 OF 3 BACK EXTERIOR VIEW
FILE: V3LVBACK.DWG
DWG BY: JAMES M. SPOTTS
DATE: 4-8-98
SCALE: 1:1
PROF. M. OKUMURA LABORATORY DIVISION OF CHEMISTRY: CALIFORNIA INSTITUTE OF TECHNOLOGY

Figure 2-62

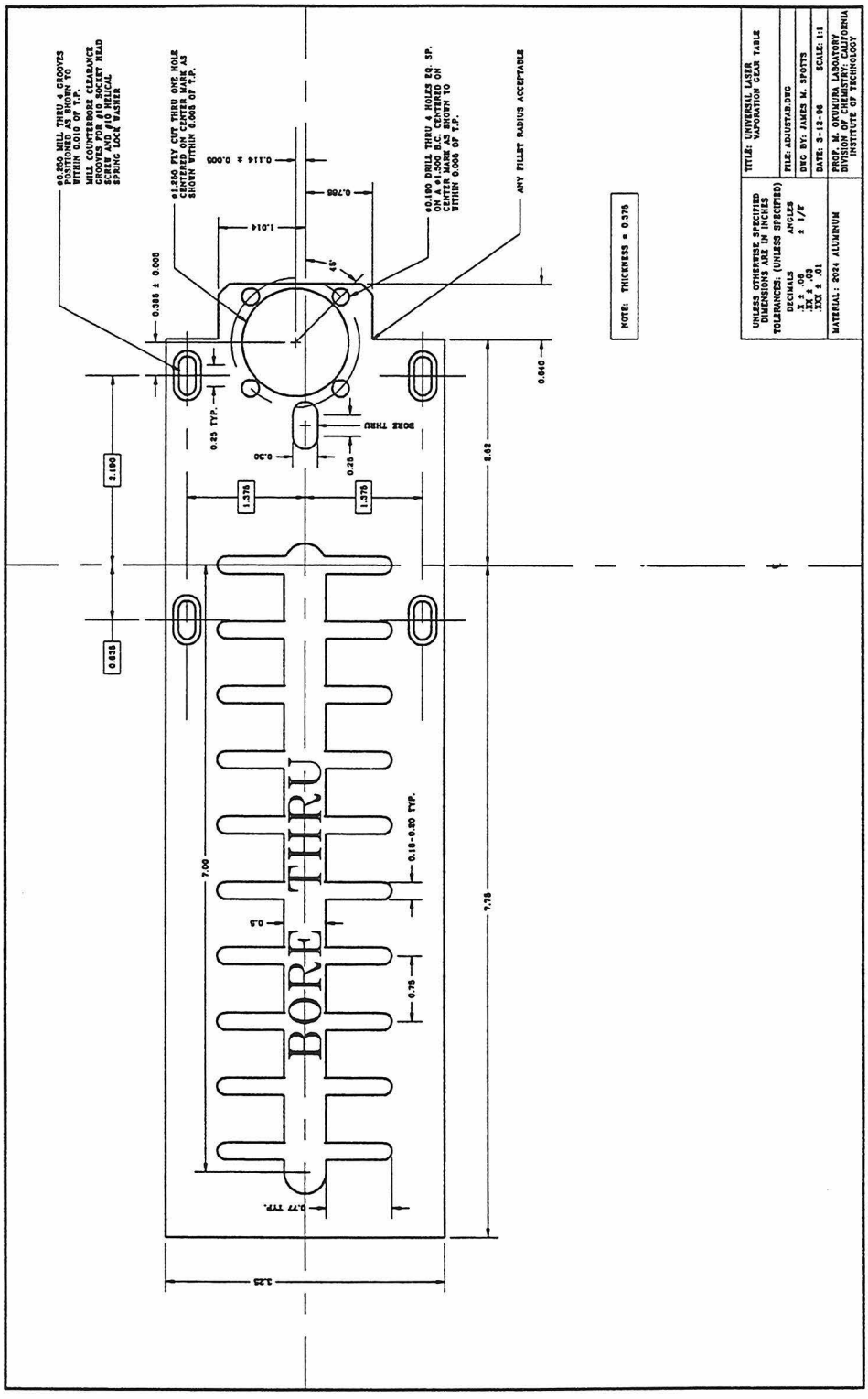

BORE THRU
NOTE: THICKNESS = 0.375
ANY FILLET RADIUS ACCEPTABLE
BORE THRU
7.00
7.75
2.100
0.635
1.375
1.375
2.62
0.640
0.25 TYP.
0.30
0.25
0.18-0.80 TYP.
0.5
0.75
0.77 TYP.
3.25
0.114 ± 0.005
0.788
1.014
45°
0.385 ± 0.005
TITLE: UNIVERSAL LASER VAPORATION GEAR TABLE
FILE: ADJUSTAB.DRG
DWG BY: JAMES M. SPOTTS
DATE: 3-12-96
SCALE: 1:1
MATERIAL: 2024 ALUMINUM
PROF. M. ORTUNURA LABORATORY
DIVISION OF CHEMISTRY, CALIFORNIA INSTITUTE OF TECHNOLOGY

Figure 2-63

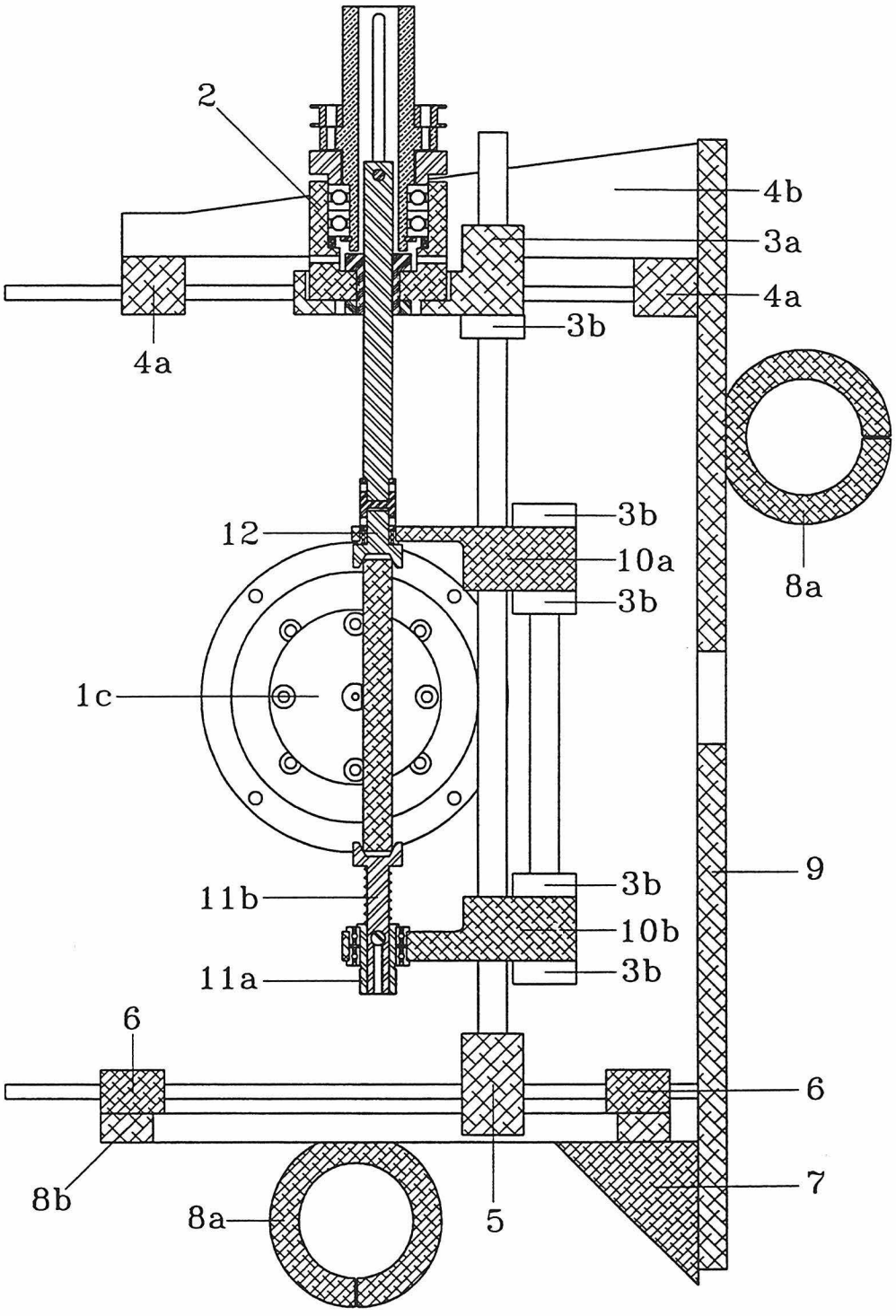


Figure 2-64

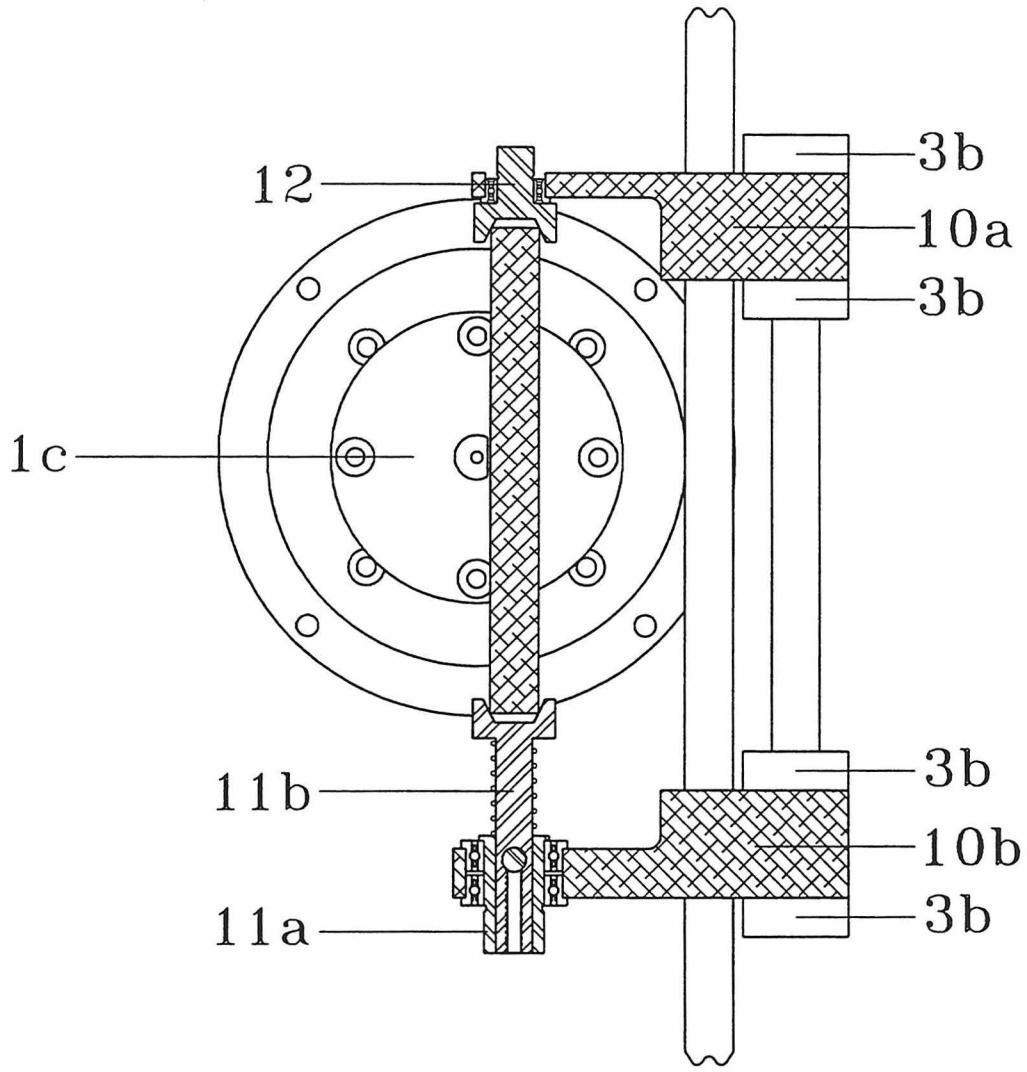


Figure 2-65

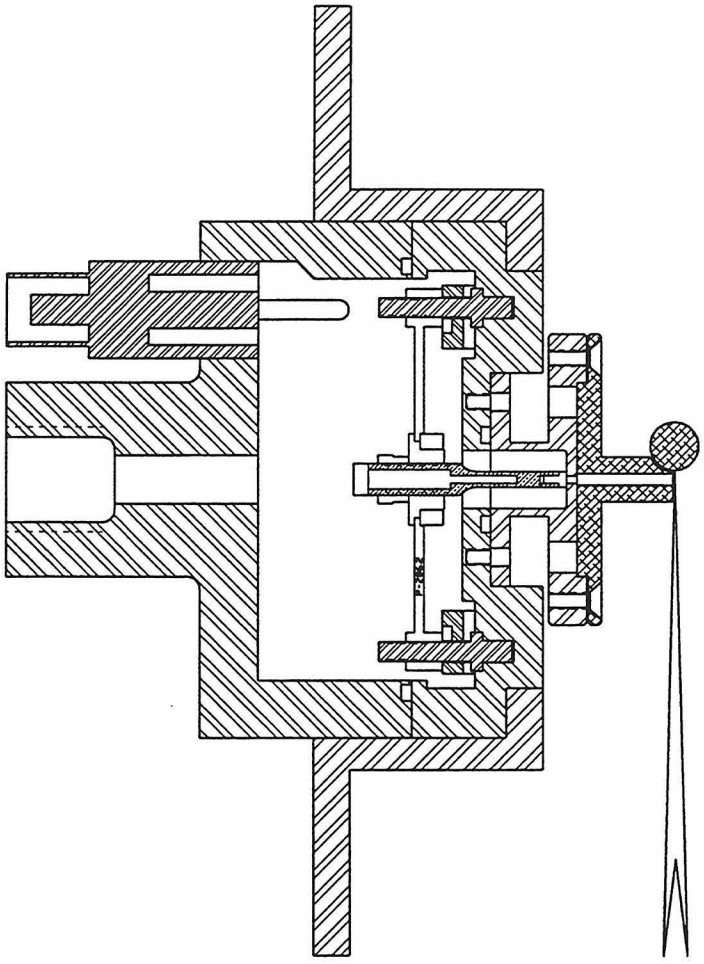


Figure 2-66

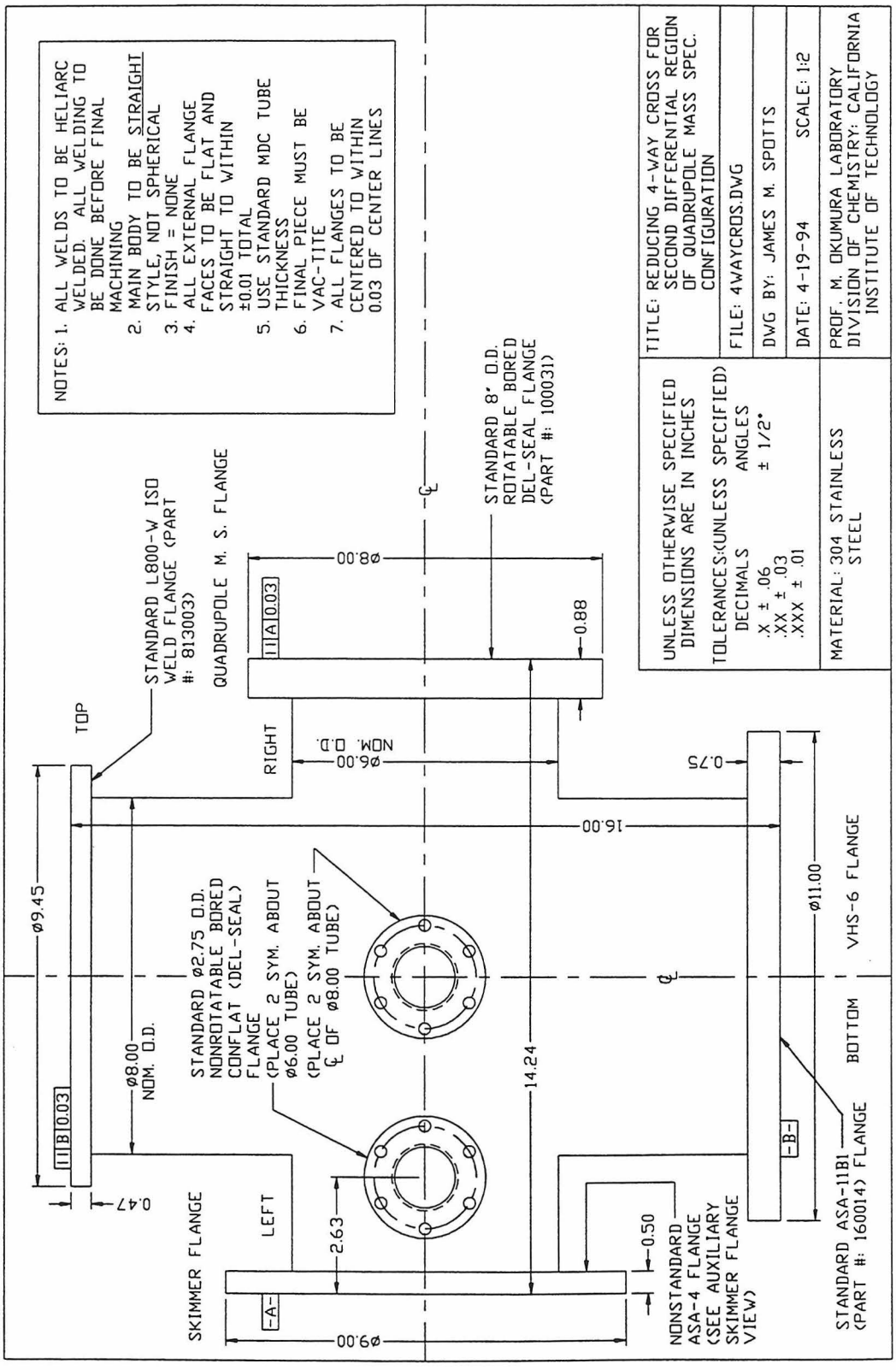

NOTES: 1. ALL WELDS TO BE HELIARC WELDED. ALL WELDING TO BE DONE BEFORE FINAL MACHINING
2. MAIN BODY TO BE STRAIGHT STYLE, NOT SPHERICAL
3. FINISH = NONE
4. ALL EXTERNAL FLANGE FACES TO BE FLAT AND STRAIGHT TO WITHIN ±0.01 TOTAL
5. USE STANDARD MDC TUBE THICKNESS
6. FINAL PIECE MUST BE VAC-TITE
7. ALL FLANGES TO BE CENTERED TO WITHIN 0.03 OF CENTER LINES
TITLE: REDUCING 4-WAY CROSS FOR SECOND DIFFERENTIAL REGION OF QUADRUPOLE MASS SPEC. CONFIGURATION
FILE: 4WAYCROS.DWG
DWG BY: JAMES M. SPOTTS
DATE: 4-19-94 SCALE: 1:2
UNLESS OTHERWISE SPECIFIED DIMENSIONS ARE IN INCHES
TOLERANCES:(UNLESS SPECIFIED)
DECIMALS ANGLES
.X ± .06 ± 1/2°
.XX ± .03
.XXX ± .01
MATERIAL: 304 STAINLESS STEEL
PROF. M. OKUMURA LABORATORY
DIVISION OF CHEMISTRY: CALIFORNIA INSTITUTE OF TECHNOLOGY
STANDARD L800-W ISO WELD FLANGE (PART #: 813003)
QUADRUPOLE M. S. FLANGE
STANDARD 8" O.D. ROTATABLE BORED DEL-SEAL FLANGE (PART #: 100031)
TOP
RIGHT
NOM. O.D.
ø6.00
ø8.00
0.88
0.75
16.00
ø9.45
ø8.00 NOM. O.D.
STANDARD ø2.75 O.D. NONROTATABLE BORED CONFLAT (DEL-SEAL) FLANGE (PLACE 2 SYM. ABOUT ø6.00 TUBE)
(PLACE 2 SYM. ABOUT ℄ OF ø8.00 TUBE)
14.24
ø11.00
VHS-6 FLANGE
0.47
2.63
0.50
SKIMMER FLANGE
LEFT
BOTTOM
NONSTANDARD ASA-4 FLANGE (SEE AUXILIARY SKIMMER FLANGE VIEW)
STANDARD ASA-11B1 (PART #: 160014) FLANGE
-A-
-B-
-℄-
0.03 B
0.03 A

Figure 2-67

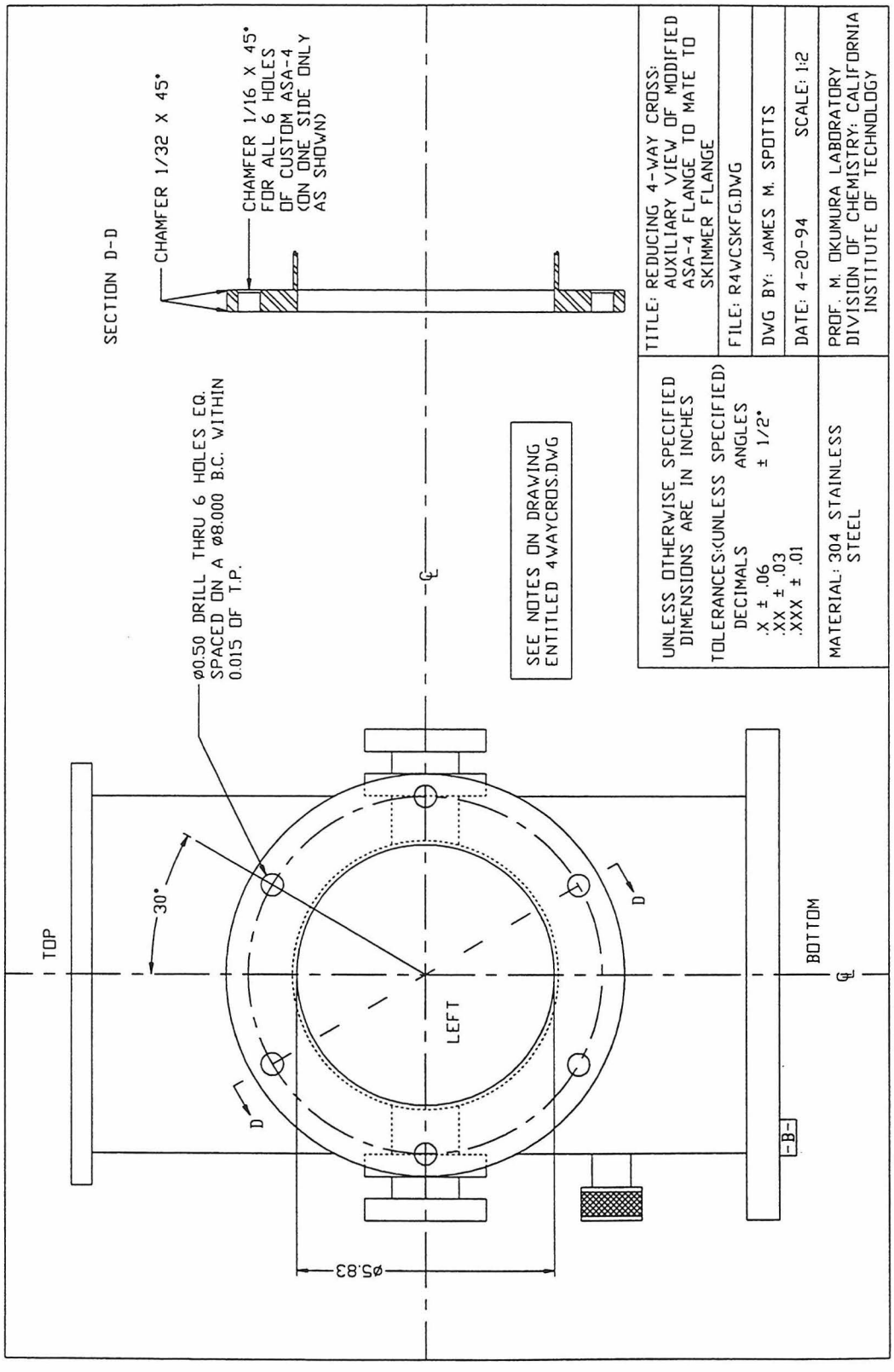

SECTION D-D
CHAMFER 1/32 X 45°
CHAMFER 1/16 X 45°
FOR ALL 6 HOLES
OF CUSTOM ASA-4
(ON ONE SIDE ONLY
AS SHOWN)
Ø0.50 DRILL THRU 6 HOLES EQ.
SPACED ON A Ø8.000 B.C. WITHIN
0.015 OF T.P.
SEE NOTES ON DRAWING
ENTITLED 4WAYCROS.DWG
TOP
BOTTOM
LEFT
30°
D
D
Ø5.83
-B-
TITLE: REDUCING 4-WAY CROSS:
AUXILIARY VIEW OF MODIFIED
ASA-4 FLANGE TO MATE TO
SKIMMER FLANGE
FILE: R4WCSKFG.DWG
DWG BY: JAMES M. SPOTTS
DATE: 4-20-94
SCALE: 1:2
UNLESS OTHERWISE SPECIFIED
DIMENSIONS ARE IN INCHES
TOLERANCES:(UNLESS SPECIFIED)
DECIMALS
.X ± .06
.XX ± .03
.XXX ± .01
ANGLES
± 1/2°
MATERIAL: 304 STAINLESS
STEEL
PROF. M. OKUMURA LABORATORY
DIVISION OF CHEMISTRY: CALIFORNIA
INSTITUTE OF TECHNOLOGY

Figure 2-68

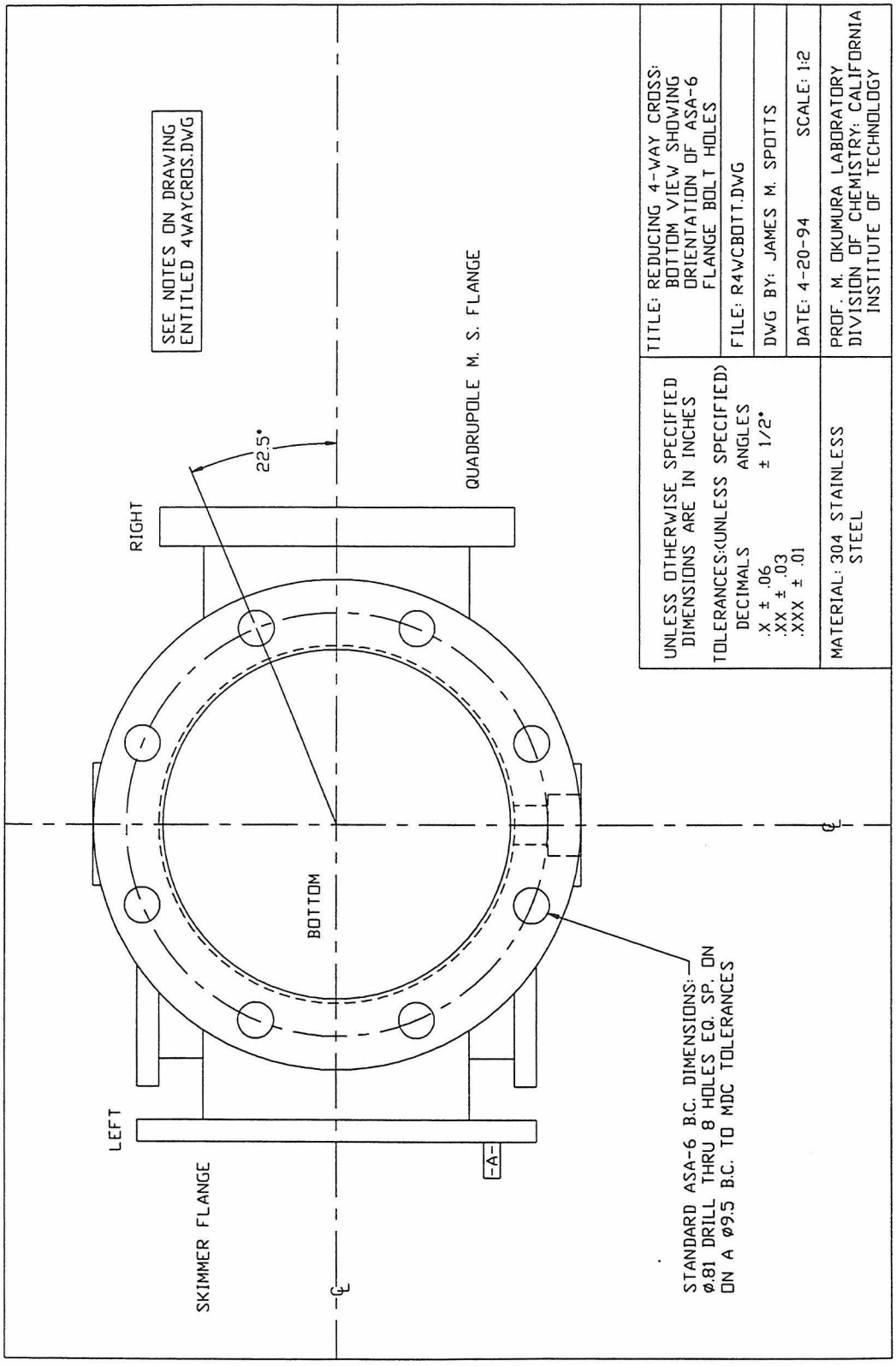

SEE NOTES ON DRAWING ENTITLED 4WAYCROS.DWG
22.5°
QUADRUPOLE M. S. FLANGE
RIGHT
BOTTOM
LEFT
SKIMMER FLANGE
-A-
STANDARD ASA-6 B.C. DIMENSIONS: ø.81 DRILL THRU 8 HOLES EQ. SP. ON ON A ø9.5 B.C. TO MDC TOLERANCES
UNLESS OTHERWISE SPECIFIED DIMENSIONS ARE IN INCHES
TOLERANCES:(UNLESS SPECIFIED) DECIMALS ANGLES
.X ± .06 ± 1/2°
.XX ± .03
.XXX ± .01
MATERIAL: 304 STAINLESS STEEL
TITLE: REDUCING 4-WAY CROSS: BOTTOM VIEW SHOWING ORIENTATION OF ASA-6 FLANGE BOLT HOLES
FILE: R4WCBOTT.DWG
DWG BY: JAMES M. SPOTTS
DATE: 4-20-94 SCALE: 1:2
PROF. M. OKUMURA LABORATORY DIVISION OF CHEMISTRY: CALIFORNIA INSTITUTE OF TECHNOLOGY

Figure 2-69

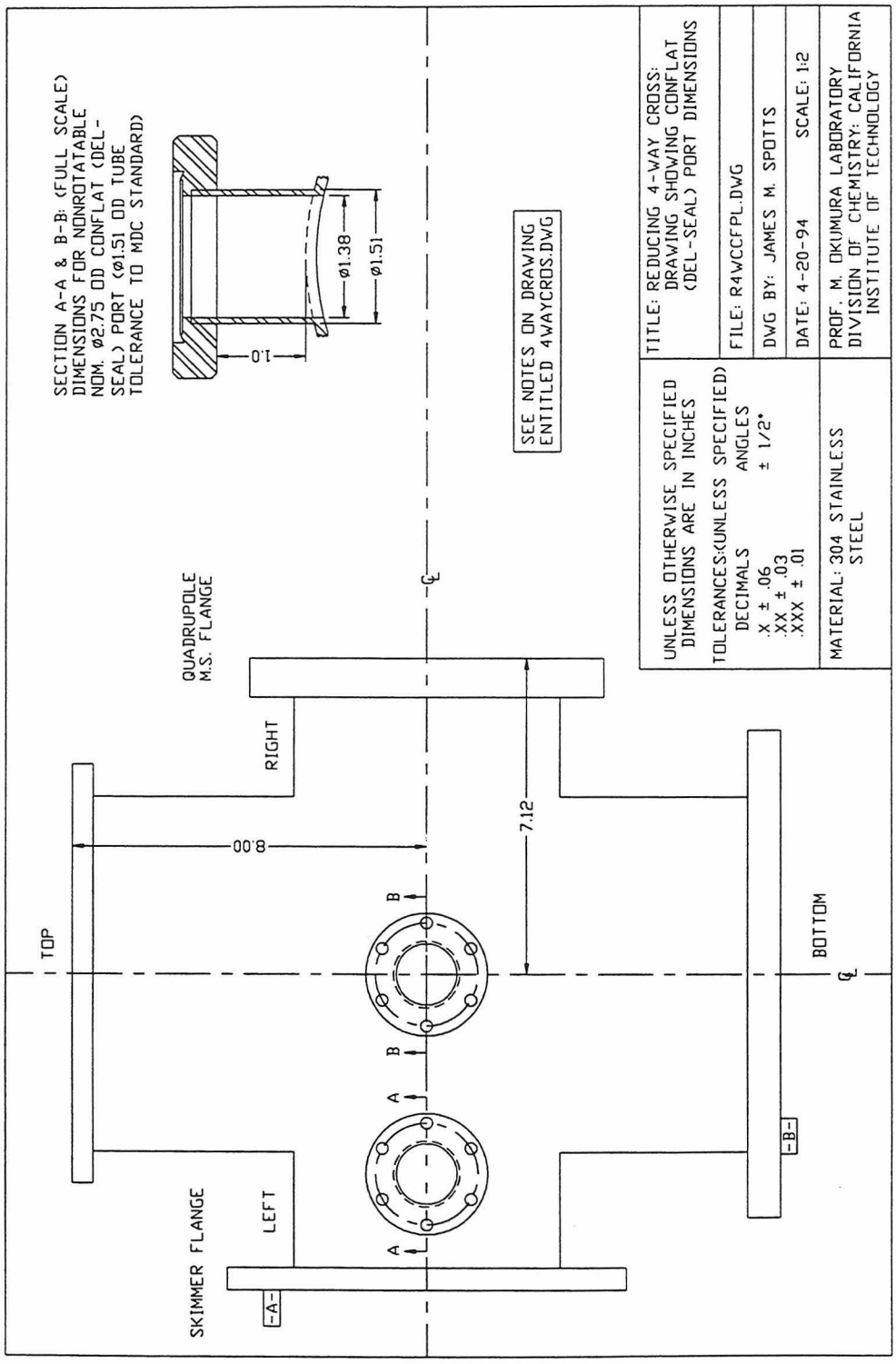

SECTION A-A & B-B: (FULL SCALE)
DIMENSIONS FOR NONROTATABLE
NOM. ø2.75 OD CONFLAT (DEL-
SEAL) PORT (ø1.51 OD TUBE
TOLERANCE TO MDC STANDARD)
1.0
ø1.38
ø1.51
SEE NOTES ON DRAWING
ENTITLED 4WAYCROS.DWG
QUADRUPOLE
M.S. FLANGE
RIGHT
8.00
7.12
TOP
BOTTOM
SKIMMER FLANGE
LEFT
-A-
-B-
A
B
UNLESS OTHERWISE SPECIFIED
DIMENSIONS ARE IN INCHES
TOLERANCES:(UNLESS SPECIFIED)
DECIMALS ANGLES
.X ± .06 ± 1/2°
.XX ± .03
.XXX ± .01
MATERIAL: 304 STAINLESS
STEEL
TITLE: REDUCING 4-WAY CROSS:
DRAWING SHOWING CONFLAT
(DEL-SEAL) PORT DIMENSIONS
FILE: R4WCCFPL.DWG
DWG BY: JAMES M. SPOTTS
DATE: 4-20-94 SCALE: 1:2
PROF. M. OKUMURA LABORATORY
DIVISION OF CHEMISTRY: CALIFORNIA
INSTITUTE OF TECHNOLOGY

Figure 2-70

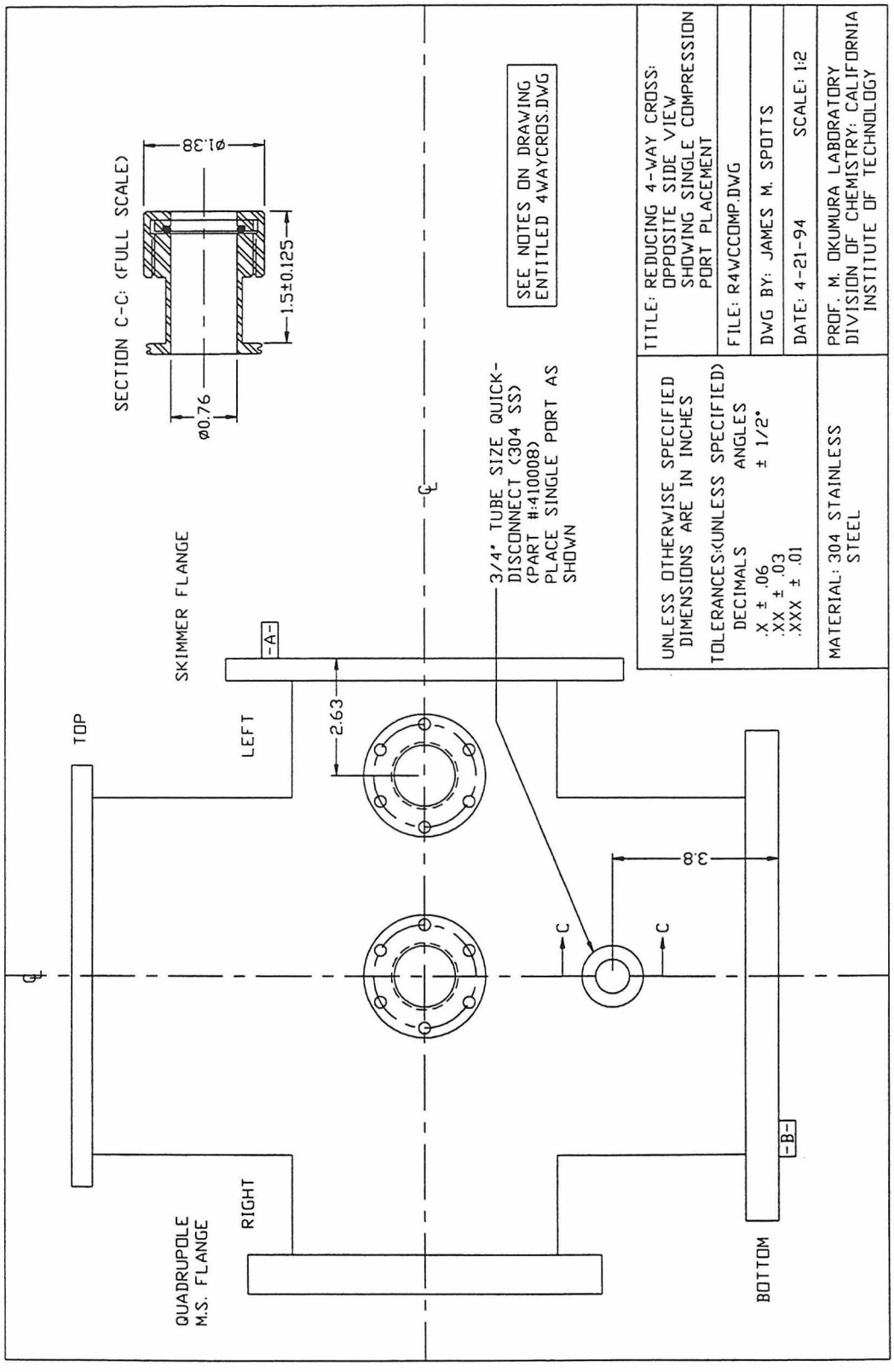

SECTION C-C: (FULL SCALE)
ø1.38
1.5±0.125
ø0.76
SEE NOTES ON DRAWING ENTITLED 4WAYCROS.DWG
3/4" TUBE SIZE QUICK-DISCONNECT (304 SS) (PART #:410008) PLACE SINGLE PORT AS SHOWN
SKIMMER FLANGE
TOP
LEFT
RIGHT
BOTTOM
QUADRUPOLE M.S. FLANGE
2.63
3.8
-A-
-B-
C
C
TITLE: REDUCING 4-WAY CROSS: OPPOSITE SIDE VIEW SHOWING SINGLE COMPRESSION PORT PLACEMENT
FILE: R4WCCOMP.DWG
DWG BY: JAMES M. SPOTTS
DATE: 4-21-94
SCALE: 1:2
UNLESS OTHERWISE SPECIFIED DIMENSIONS ARE IN INCHES
TOLERANCES:(UNLESS SPECIFIED)
DECIMALS
.X ± .06
.XX ± .03
.XXX ± .01
ANGLES
± 1/2°
MATERIAL: 304 STAINLESS STEEL
PROF. M. OKUMURA LABORATORY
DIVISION OF CHEMISTRY: CALIFORNIA INSTITUTE OF TECHNOLOGY

Figure 2-71

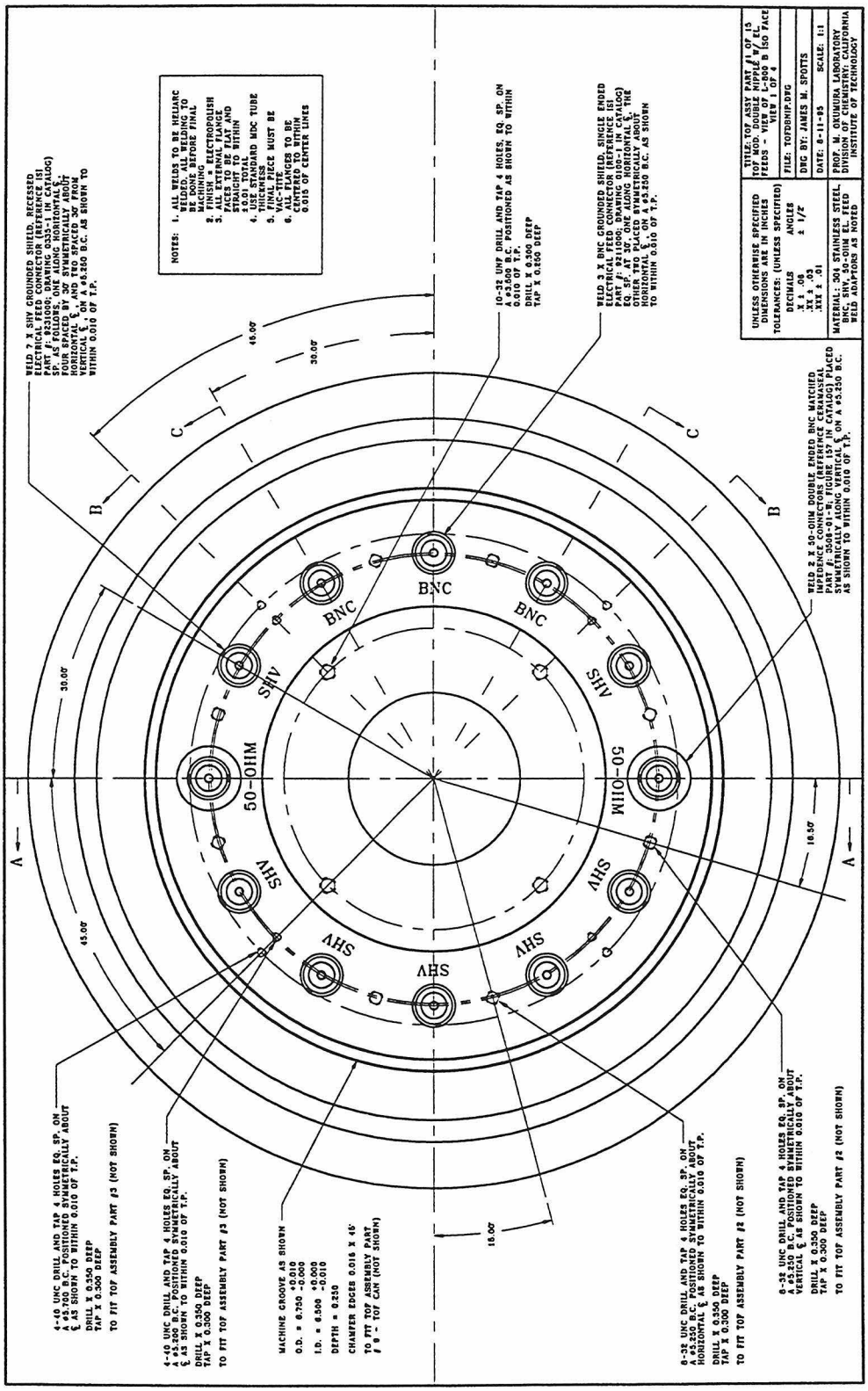

NOTES: 1. ALL WELDS TO BE HELIARC WELDED. ALL WELDING TO BE DONE BEFORE FINAL MACHINING.
2. FINISH = ELECTROPOLISH
3. ALL EXTERNAL FLANGE FACES TO BE FLAT AND PARALLEL TO WITHIN ±0.01 TOTAL
4. USE STANDARD MDC TUBE TOLERANCES
5. FINAL PIECE MUST BE VAC-TITE
6. ALL FLANGES TO BE CONCENTRIC WITHIN 0.015 OF CENTER LINES
UNLESS OTHERWISE SPECIFIED TOLERANCES ARE AS FOLLOWS: (UNLESS SPECIFIED)
DECIMALS ANGLES
X ± .05 ± 1/2°
.XX ± .03
.XXX ± .01
MATERIAL: 304 STAINLESS STEEL
TITLE: TOF ASSY PART #1 OF 15 TOF MOD. DOUBLE NIPPLE W/ F.C. FEEDS - WITH 4 LONG & 1 SHORT FACE VIEW 1 OF 4
FILE: TOFDBNIP.DFG
DRG BY: JAMES M. SPOTTS
DATE: 6-11-95 SCALE: 1:1
PROF. M. OKUMURA LABORATORY DIVISION OF CHEMISTRY: CALIFORNIA INSTITUTE OF TECHNOLOGY
BNC
SHV
50-OHM
A
B
C
30.00°
45.00°
16.50°

Figure 2-72

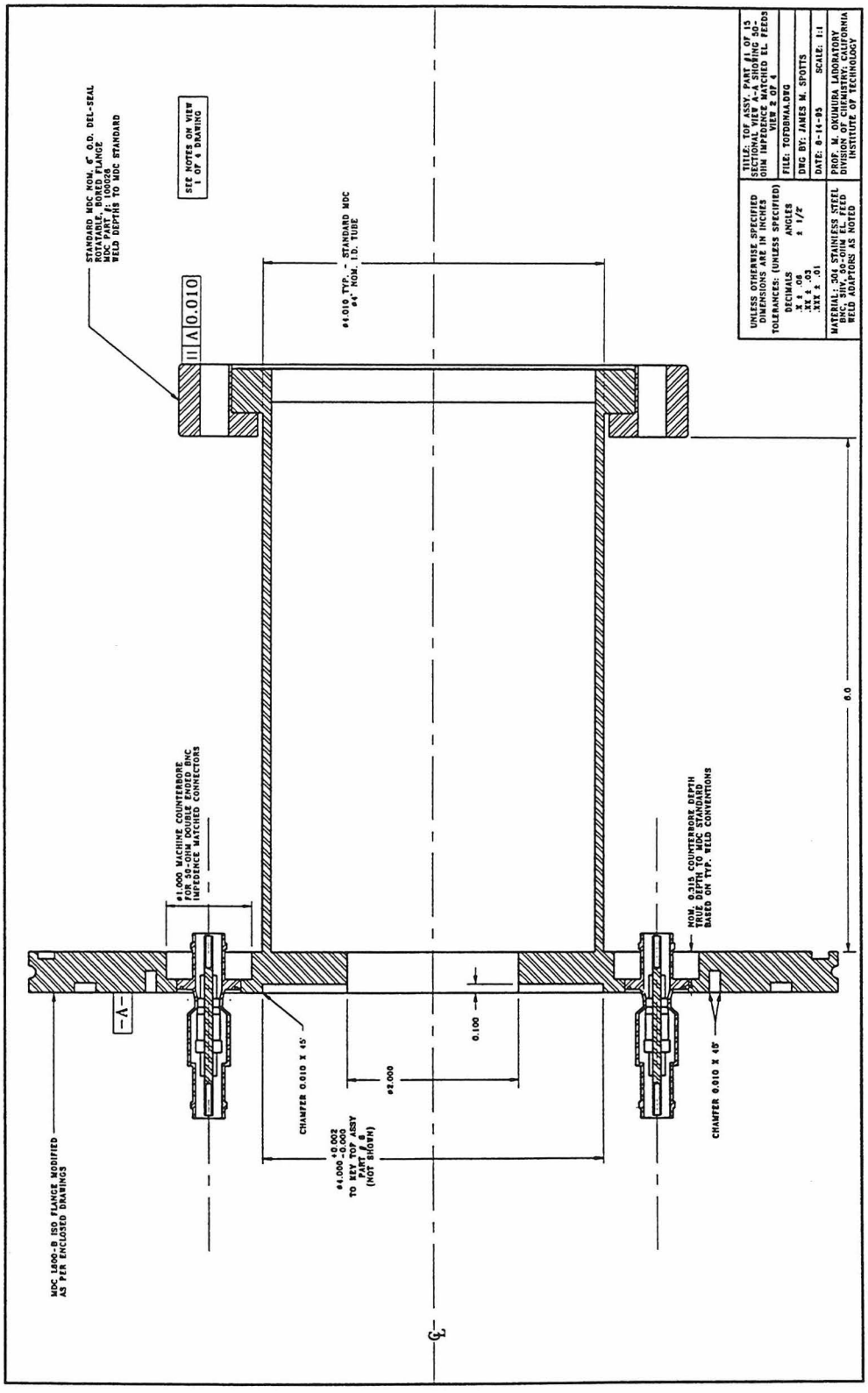

STANDARD MDC NOM. 6" O.D. DEL-SEAL ROTATABLE CONFLAT FLANGE MDC PART #: 100026 WELD DEPTHS TO MDC STANDARD
SEE NOTES ON VIEW 1 OF 4 DRAWING
⌯ A 0.010
ø1.010 TYP. - STANDARD MDC ø4" NOM. I.D. TUBE
ø1.000 MACHINE COUNTERBORE FOR 50-OHM DOUBLE ENDED BNC IMPEDANCE MATCHED CONNECTORS
CHAMFER 0.010 X 45°
ø1.000 +0.002 -0.000 TO KEY TOP ASSY PART # 8 (NOT SHOWN)
ø2.000
0.100
NOM. 0.215 COUNTERBORE DEPTH WILL DIFFER TO ACCOMMODATE WELD CONVENTIONS BASED ON TYP. WELD CONVENTIONS
CHAMFER 0.010 X 45°
6.0
MDC 1200-B ISO FLANGE MODIFIED AS PER ENCLOSED DRAWINGS
-A-
UNLESS OTHERWISE SPECIFIED DIMENSIONS ARE IN INCHES TOLERANCES: (UNLESS SPECIFIED) DECIMALS .X ± .10 .XX ± .03 .XXX ± .01 ANGLES ± 1/2°
TITLE: TOF ASSY. PART #1 OF 15 SECTIONAL VIEW A-A SHOWING 50-OHM IMPEDENCE MATCHED EL. FEEDS
SIZE B SHEET 3 OF 4
FILE: TOFDBNA.DWG
DRG BY: JAMES M. SPOTTS
DATE: 8-14-95 SCALE: 1:1
MATERIAL: 304 STAINLESS STEEL BNC, 50Ω, 50-OHM EL. FEED WELD ADAPTORS AS NOTED
PROF. M. OKUMURA LABORATORY DIVISION OF CHEMISTRY; CALIFORNIA INSTITUTE OF TECHNOLOGY
3

Figure 2-73

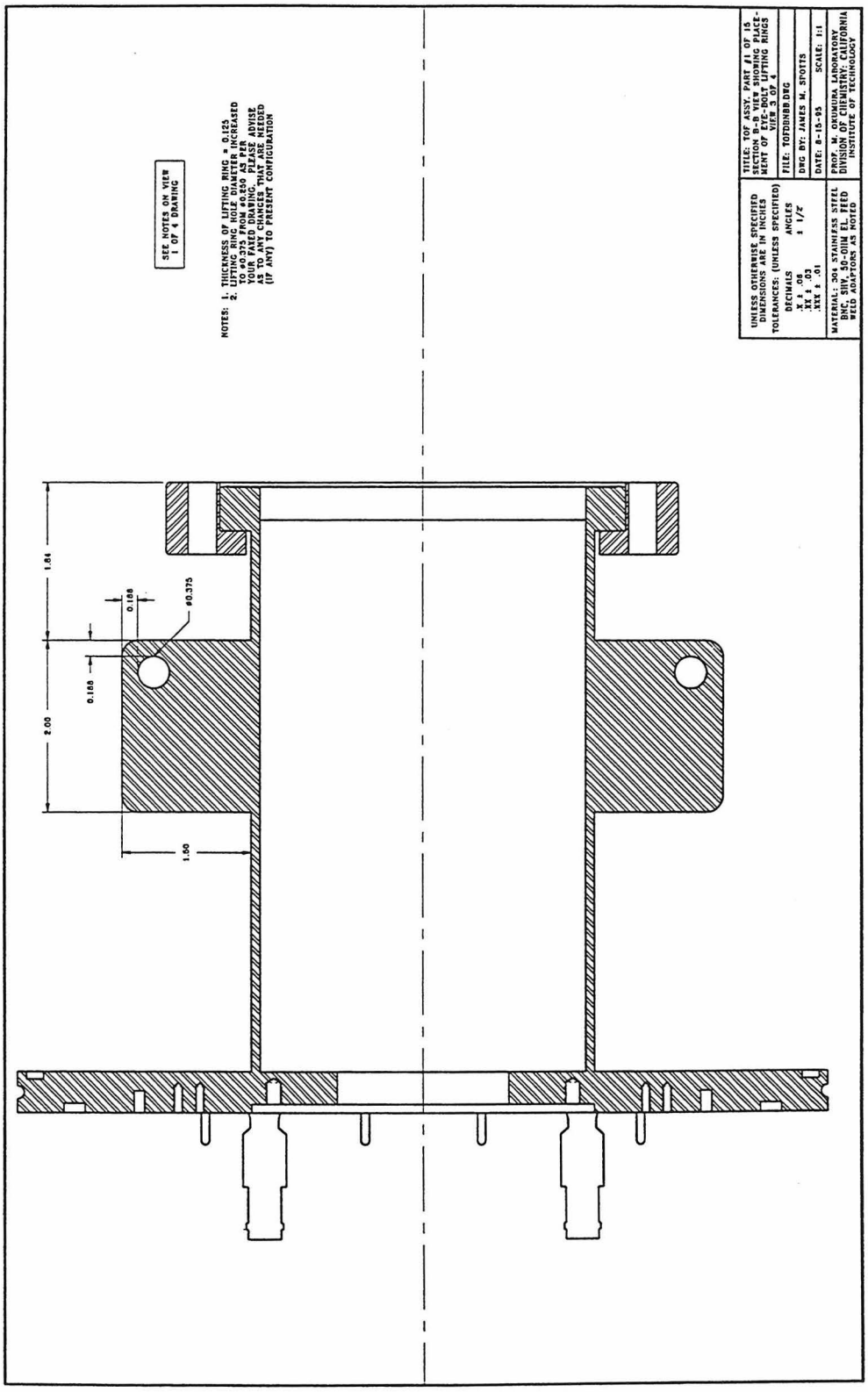

SEE NOTES ON VIEW 1 OF 4 DRAWING
NOTES: 1. THICKNESS OF LIFTING RING = 0.125
2. LIFTING RING HOLE DIAMETER INCREASED TO Ø0.375 AND 1.88 IN
YOUR FAXED DRAWING. PLEASE ADVISE AS TO ANY CHANGES THAT ARE NEEDED (IF ANY) TO PRESENT CONFIGURATION
1.84
0.188
Ø0.375
0.188
2.00
1.50
UNLESS OTHERWISE SPECIFIED DIMENSIONS ARE IN INCHES
TOLERANCES: (UNLESS SPECIFIED)
DECIMALS
ANGLES
X ± .06
± 1/2
XX ± .03
XXX ± .01
MATERIAL: 304 STAINLESS STEEL
BNC, SHV, 50-OHM FL. FEED
WELD ADAPTORS AS NOTED
TITLE: TOF ASSY. PART #1 OF 15
SECTION B-B VIEW SHOWING PLACEMENT OF EYE-BOLT LIFTING RINGS
SHEET 3 OF 4
FILE: TOFDBINBD.DRG
DRG BY: JAMES M. SPOTTS
DATE: 8-15-95
SCALE: 1:1
PROF. M. ORUMURA LABORATORY
DIVISION OF CHEMISTRY; CALIFORNIA INSTITUTE OF TECHNOLOGY

Figure 2-74

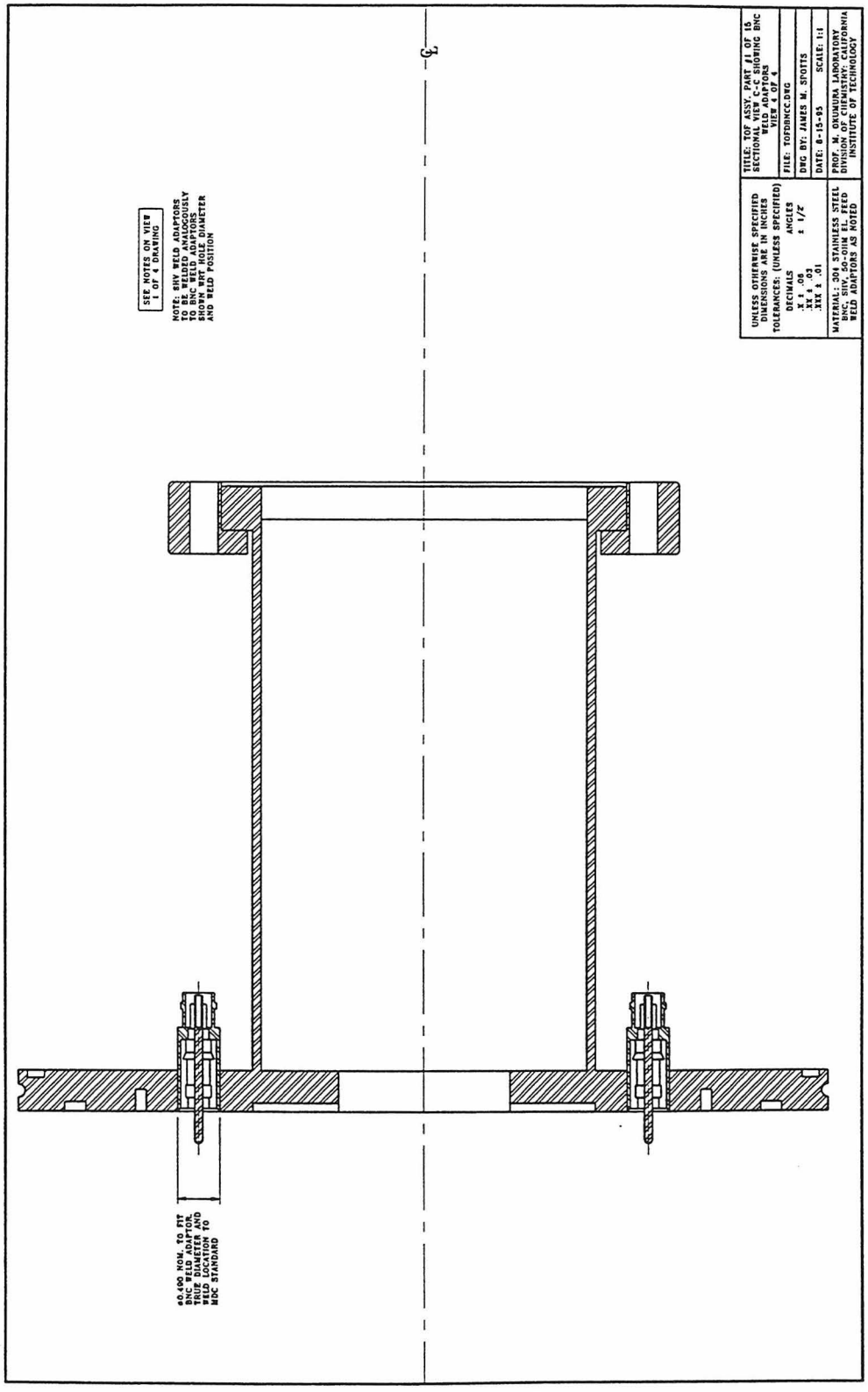

SEE NOTES ON VIEW 1 OF 4 DRAWING
NOTE: SIV WELD ADAPTORS TO BE WELDED ANALOGOUSLY TO BNC WELD ADAPTORS SHOWN WRT HOLE DIAMETER AND WELD POSITION
Ø.400 NOM. TO FIT BNC WELD ADAPTOR THRU FLANGE HOLE AND WELD LOCATION TO MDC STANDARD
UNLESS OTHERWISE SPECIFIED DIMENSIONS ARE IN INCHES
TOLERANCES: (UNLESS SPECIFIED)
DECIMALS ANGLES
X ± .05 ± 1/2°
.XX ± .03
.XXX ± .01
MATERIAL: 304 STAINLESS STEEL BNC, SIV, SO-OIM EL. FEED WELD ADAPTORS AS NOTED
TITLE: TOF ASSY. PART #1 OF 15 SECTIONAL VIEW C-C SHOWING BNC WELD ADAPTORS VIEW 1 OF 4
FILE: TOFSBNCC.DWG
DWG BY: JAMES M. SPOTTS
DATE: 8-15-95 SCALE: 1:1
PROF. M. OKUMURA LABORATORY DIVISION OF CHEMISTRY; CALIFORNIA INSTITUTE OF TECHNOLOGY

Figure 2-75

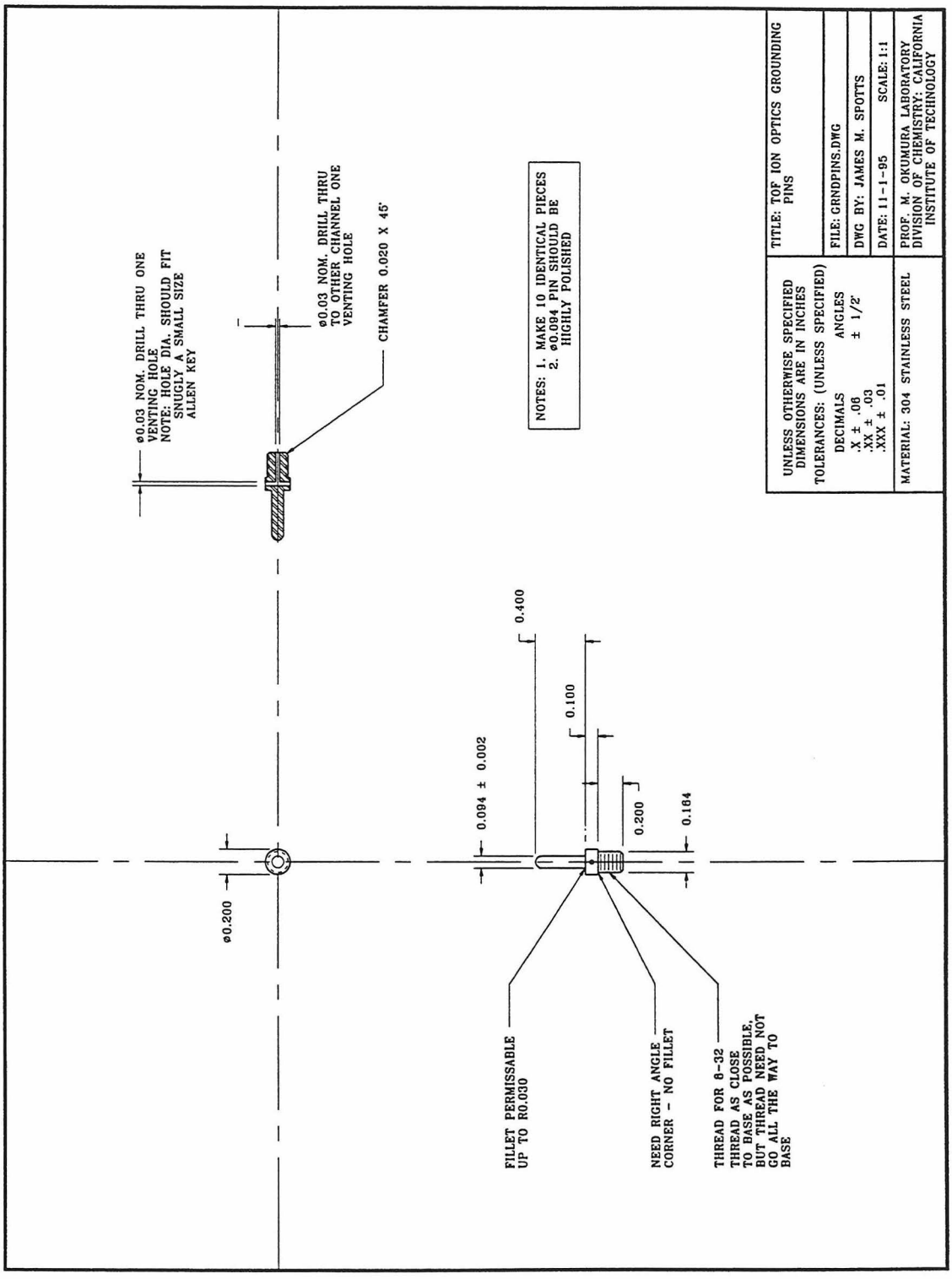

ø0.03 NOM. DRILL THRU ONE
VENTING HOLE
NOTE: HOLE DIA. SHOULD FIT
SNUGLY A SMALL SIZE
ALLEN KEY
ø0.03 NOM. DRILL THRU
TO OTHER CHANNEL ONE
VENTING HOLE
CHAMFER 0.020 X 45°
NOTES: 1. MAKE 10 IDENTICAL PIECES
2. ø0.094 PIN SHOULD BE
HIGHLY POLISHED
0.400
0.100
0.094 ± 0.002
0.200
0.164
ø0.200
FILLET PERMISSABLE
UP TO R0.030
NEED RIGHT ANGLE
CORNER - NO FILLET
THREAD FOR 8-32
THREAD AS CLOSE
TO BASE AS POSSIBLE,
BUT THREAD NEED NOT
GO ALL THE WAY TO
BASE
UNLESS OTHERWISE SPECIFIED
DIMENSIONS ARE IN INCHES
TOLERANCES: (UNLESS SPECIFIED)
DECIMALS ANGLES
.X ± .06 ± 1/2°
.XX ± .03
.XXX ± .01
MATERIAL: 304 STAINLESS STEEL
TITLE: TOF ION OPTICS GROUNDING
PINS
FILE: GRNDPINS.DWG
DWG BY: JAMES M. SPOTTS
DATE: 11-1-95 SCALE: 1:1
PROF. M. OKUMURA LABORATORY
DIVISION OF CHEMISTRY: CALIFORNIA
INSTITUTE OF TECHNOLOGY

Figure 2-76

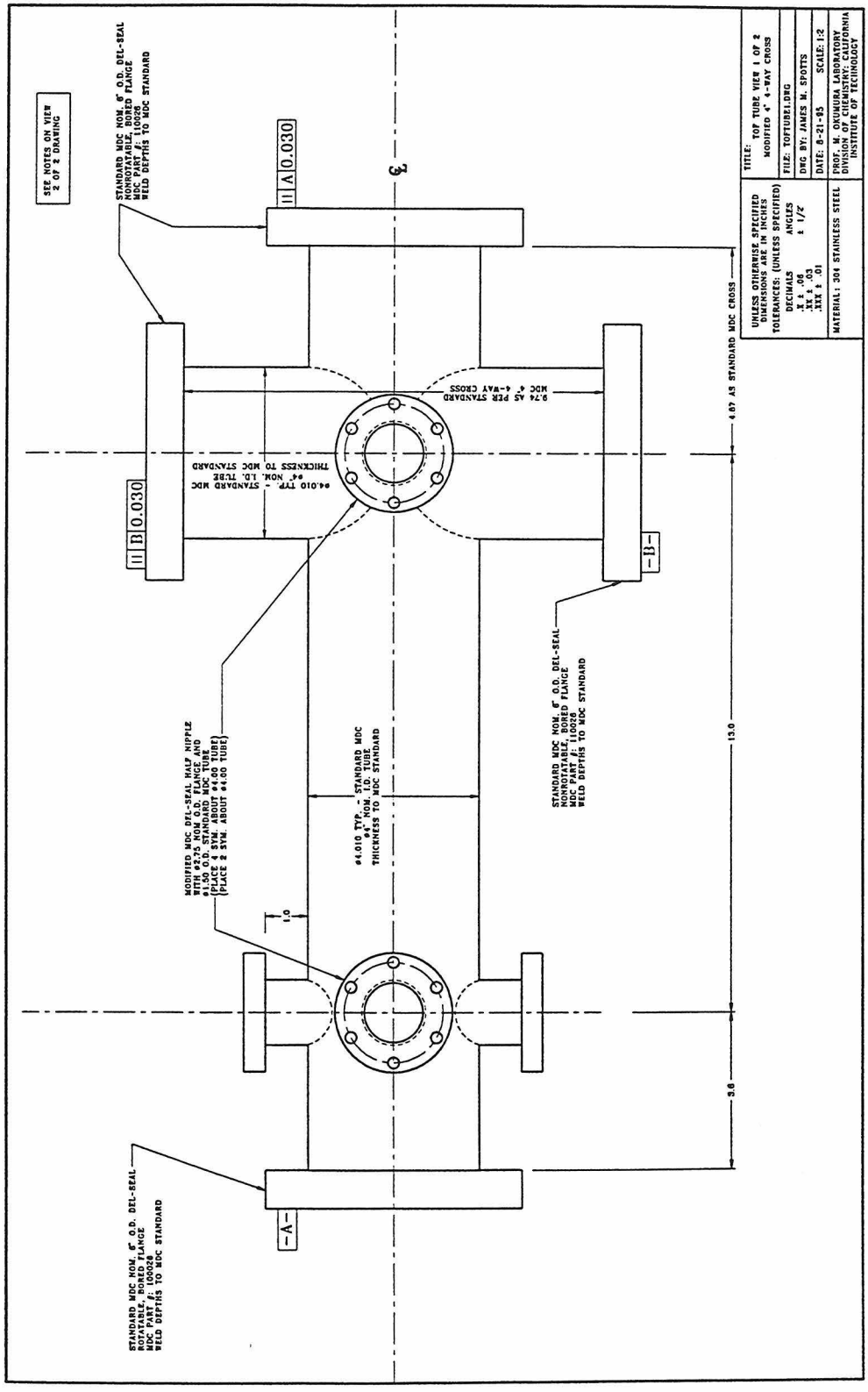

SEE NOTES ON VIEW 2 OF 2 DRAWING
STANDARD MDC NOM. 6" O.D. DEL-SEAL NONROTATABLE, BORED FLANGE MDC PART #: 110028 WELD DEPTHS TO MDC STANDARD
STANDARD MDC NOM. 6" O.D. DEL-SEAL NONROTATABLE, BORED FLANGE MDC PART #: 110028 WELD DEPTHS TO MDC STANDARD
MODIFIED MDC DEL-SEAL HALF NIPPLE WITH #2.75 NOM. O.D. FLANGE AND #1.50 O.D. STANDARD MDC TUBE (PLACE 4 SYM. ABOUT #4.00 TUBE) (PLACE 2 SYM. ABOUT #4.00 TUBE)
#4.010 TYP. - STANDARD MDC #4" NOM. I.D. TUBE THICKNESS TO MDC STANDARD
#4.010 TYP. - STANDARD MDC #4" NOM. I.D. TUBE THICKNESS TO MDC STANDARD
MDC 4" 4-WAY CROSS 9.74 AS PER STANDARD
4.87 AS STANDARD MDC CROSS
13.0
5.0
1.0
A 0.030
B 0.030
-A-
-B-
UNLESS OTHERWISE SPECIFIED DIMENSIONS ARE IN INCHES TOLERANCES: (UNLESS SPECIFIED) DECIMALS .X ± .05 .XX ± .03 .XXX ± .01 ANGLES ± 1/2
MATERIAL: 304 STAINLESS STEEL
TITLE: TOF TUBE VIEW 1 OF 2 MODIFIED 4" 4-WAY CROSS
FILE: TOFTUBE1.DRG
DWG BY: JAMES M. SPOTTS
DATE: 8-21-95
SCALE: 1:2
PROF. M. OKUMURA LABORATORY DIVISION OF CHEMISTRY; CALIFORNIA INSTITUTE OF TECHNOLOGY

Figure 2-77

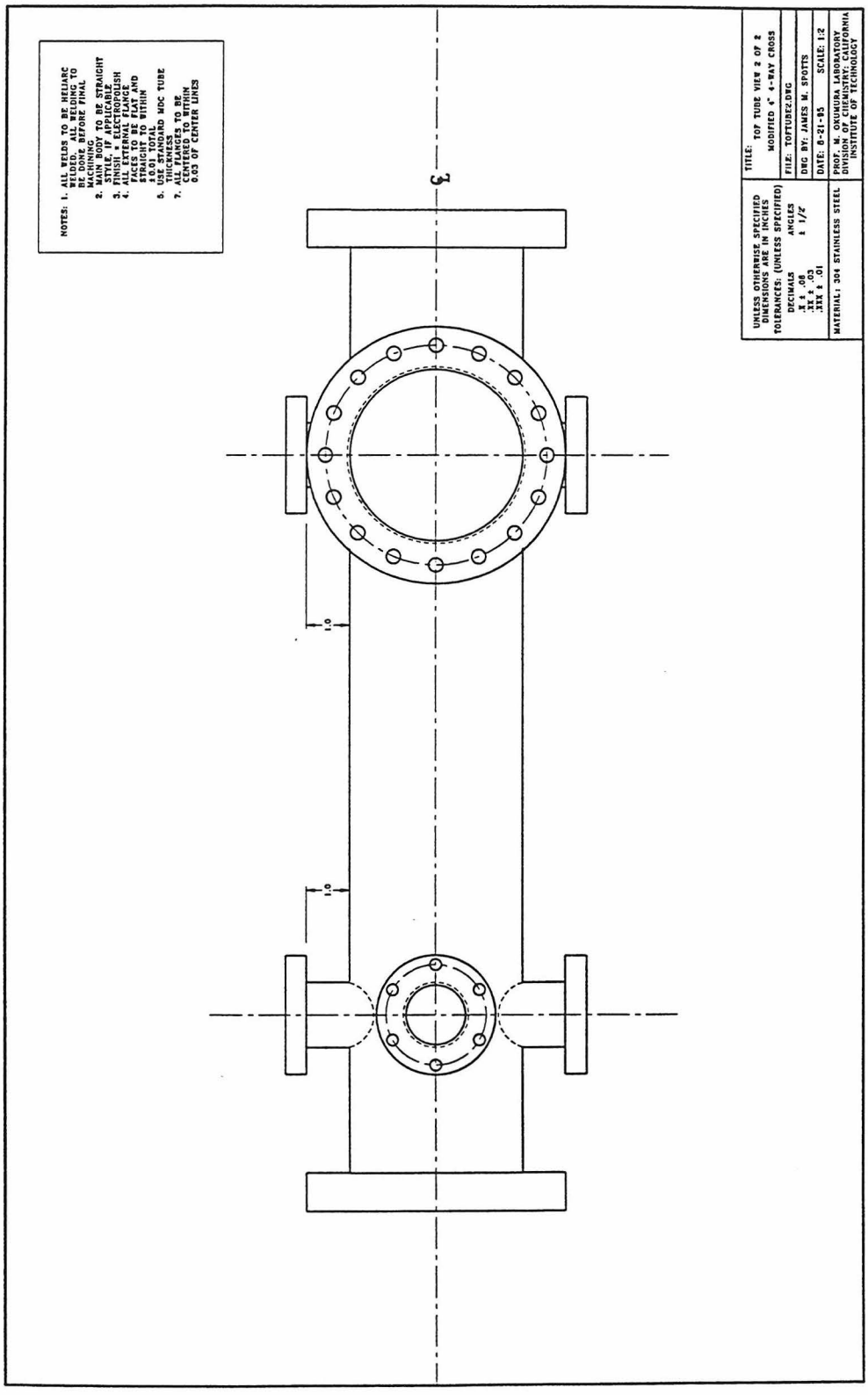

NOTES: 1. ALL WELDS TO BE HELIARC WELDED. ALL WELDING TO BE DONE BEFORE FINAL MACHINING.
2. MAIN BODY TO BE STRAIGHT STYLE, IF APPLICABLE
3. FINISH = ELECTROPOLISH
4. ALL EXTERNAL FLANGE FACES TO BE FLAT AND STRAIGHT TO WITHIN .03 TOTAL I.R.
5. USE STANDARD WOC TUBE THICKNESS
6. ALL FACES TO BE CENTERED TO WITHIN 0.03 OF CENTER LINES
UNLESS OTHERWISE SPECIFIED DIMENSIONS ARE IN INCHES
TOLERANCES: (UNLESS SPECIFIED)
DECIMALS
ANGLES
.X ± .06
± 1/2°
.XX ± .03
.XXX ± .01
MATERIAL: 304 STAINLESS STEEL
TITLE:
TOP TUBE VIEW 2 OF 2
MODIFIED 4" 4-WAY CROSS
FILE: TOPTUBE2.DWG
DRG BY: JAMES M. SPOTTS
DATE: 8-21-95
SCALE: 1:2
PROF. M. OKUMURA LABORATORY
DIVISION OF CHEMISTRY: CALIFORNIA
INSTITUTE OF TECHNOLOGY
3
1.0
1.0

Figure 2-78

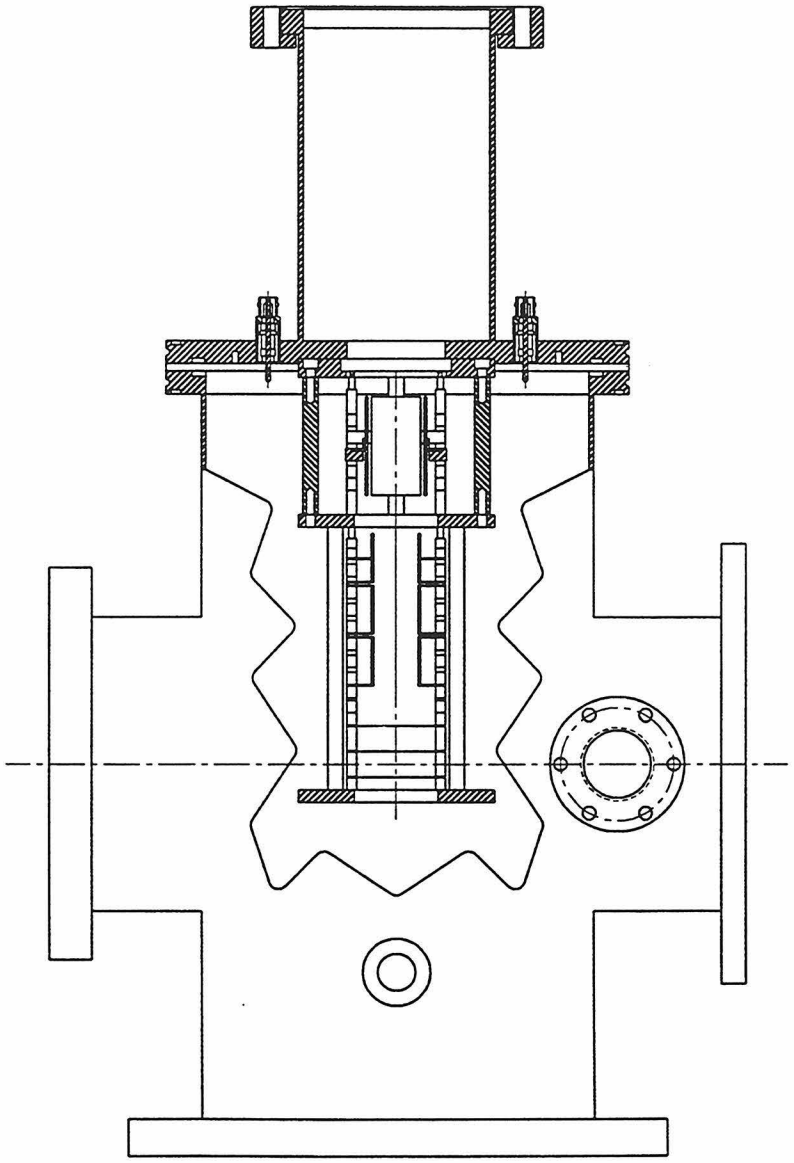


Figure 2-79

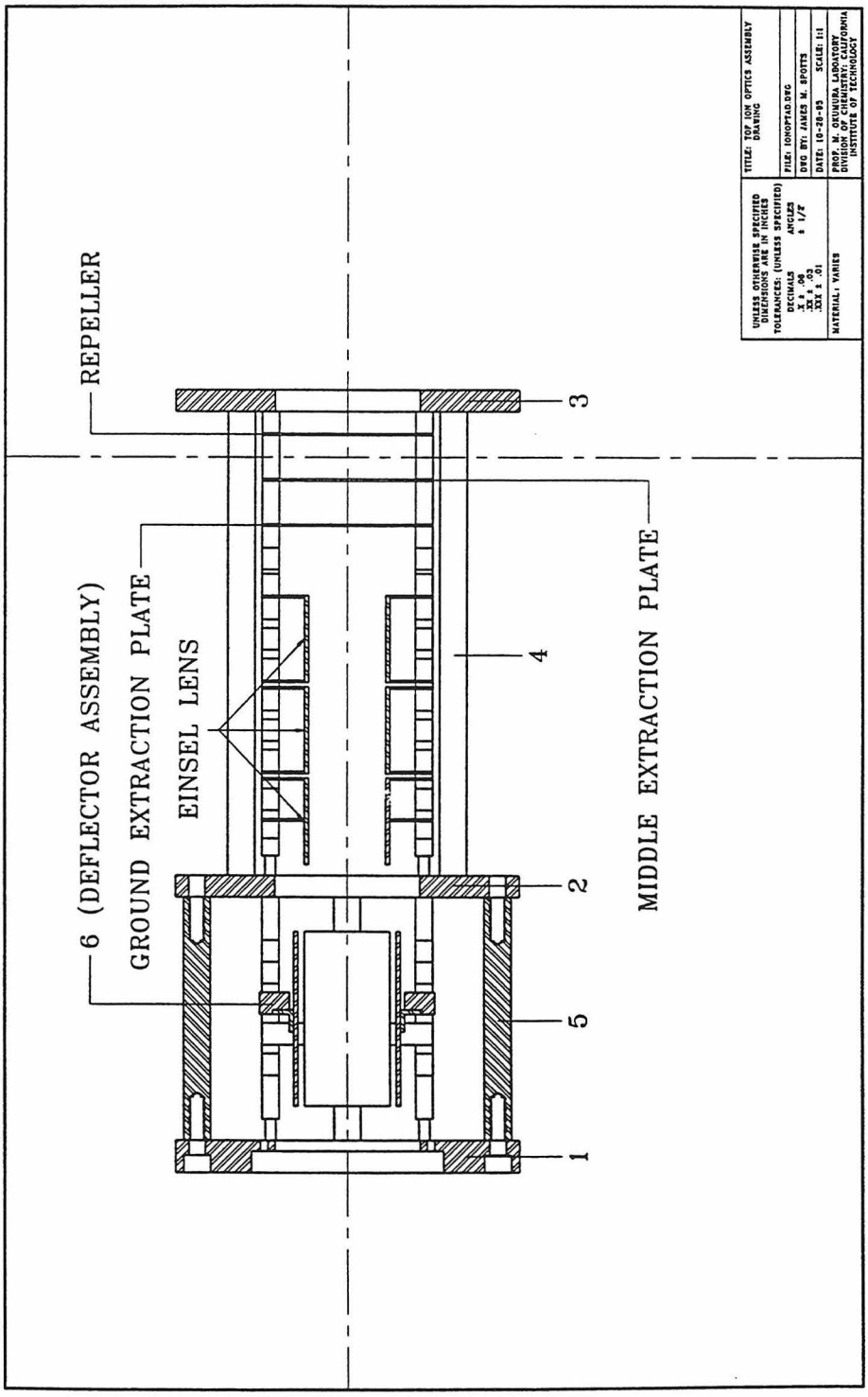

REPELLER
6 (DEFLECTOR ASSEMBLY)
GROUND EXTRACTION PLATE
EINSEL LENS
MIDDLE EXTRACTION PLATE
1
2
3
4
5
UNLESS OTHERWISE SPECIFIED DIMENSIONS ARE IN INCHES
TOLERANCES: (UNLESS SPECIFIED)
DECIMALS
ANGLES
MATERIAL: VARIES
TITLE: TOP ION OPTICS ASSEMBLY DRAWING
FILE: IONOPTAB.DRG
DWG BY: JAMES M. SPOTTS
DATE: 10-28-93
SCALE: 1:1
PROF. M. OKUMURA LABORATORY
DIVISION OF CHEMISTRY, CALIFORNIA INSTITUTE OF TECHNOLOGY

Figure 2-80

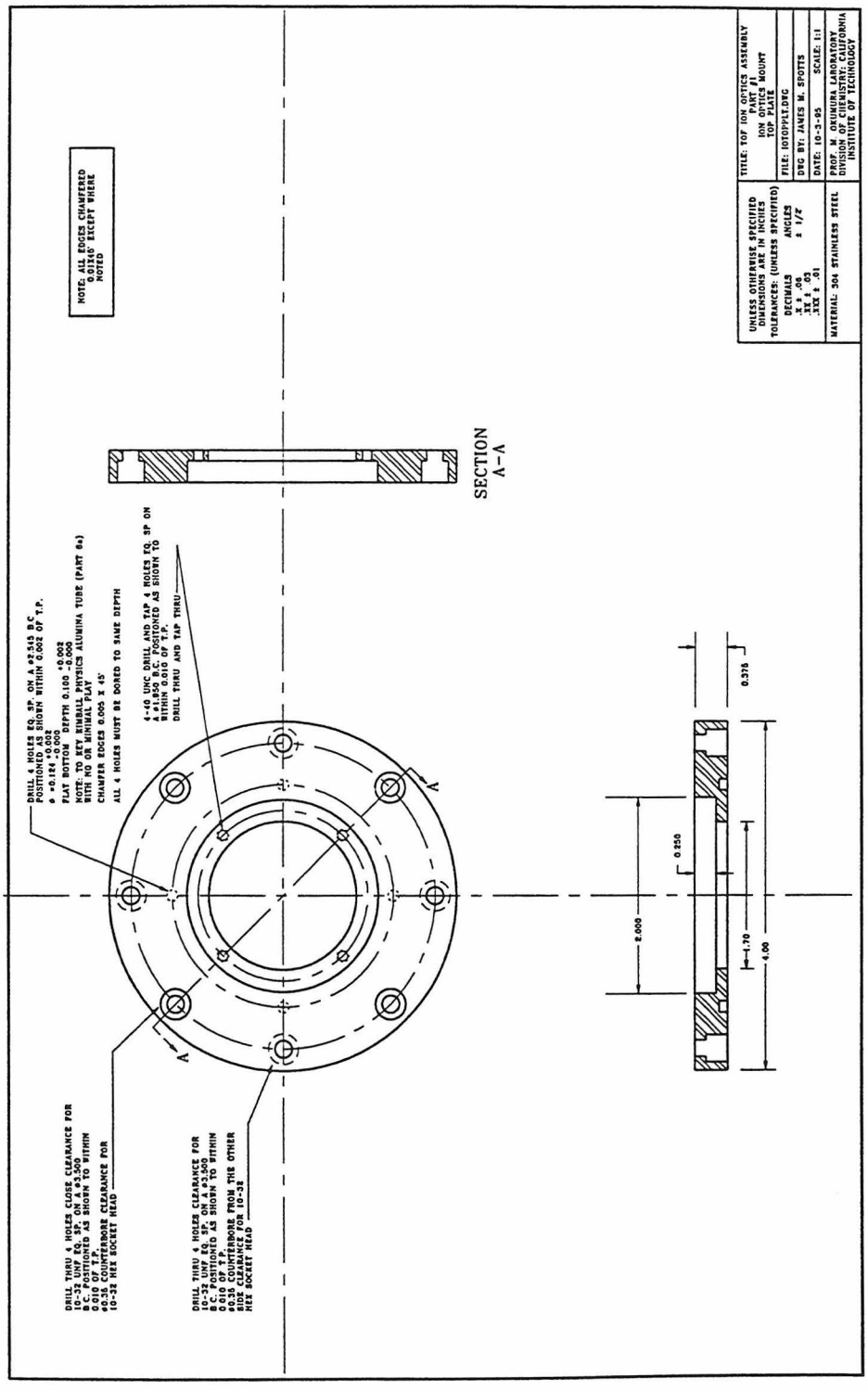

NOTE: ALL EDGES CHAMFERED 0.01X45° EXCEPT WHERE NOTED
SECTION A-A
DRILL 4 HOLES EQ. SP. ON A Ø2.510 B.C. POSITIONED AS SHOWN WITHIN 0.002 OF T.P.
Ø +0.124 -0.000 +0.000
FLAT BOTTOM DEPTH 0.100 -0.002
NOTE: TO KEY KIMBALL PHYSICS ALUMINA TUBE (PART #6) WITH NO OR MINIMAL PLAY
CHAMFER EDGES 0.005 X 45°
ALL 4 HOLES MUST BE DOWED TO SAME DEPTH
4-40 UNC DRILL AND TAP 4 HOLES EQ. SP ON A Ø1.850 B.C. POSITIONED AS SHOWN TO WITHIN 0.010 OF T.P.
DRILL THRU AND TAP THRU
DRILL THRU 4 HOLES CLOSE CLEARANCE FOR 10-32 UNF EQ. SP. ON A Ø3.500 B.C. POSITIONED AS SHOWN TO WITHIN 0.010 OF T.P.
Ø0.36 COUNTERBORE CLEARANCE FOR 10-32 HEX SOCKET HEAD
DRILL THRU 4 HOLES CLEARANCE FOR 10-32 UNF EQ. SP. ON A Ø3.500 B.C. POSITIONED AS SHOWN TO WITHIN 0.010 OF T.P.
Ø0.36 COUNTERBORE FROM THE OTHER SIDE CLEARANCE FOR 10-32 HEX SOCKET HEAD
A
A
0.250
0.375
2.000
1.70
4.00
UNLESS OTHERWISE SPECIFIED DIMENSIONS ARE IN INCHES
TOLERANCES: (UNLESS SPECIFIED)
DECIMALS
.X ± .06
.XX ± .03
.XXX ± .01
ANGLES
± 1/2
MATERIAL: 304 STAINLESS STEEL
TITLE: TOF ION OPTICS ASSEMBLY PART #1 ION OPTICS MOUNT TOP PLATE
FILE: IOTOPP1.DRG
DRG BY: JAMES W. SPOTTS
DATE: 10-3-95
SCALE: 1:1
PROF. M. OKUMURA LABORATORY
DIVISION OF CHEMISTRY; CALIFORNIA INSTITUTE OF TECHNOLOGY

Figure 2-81

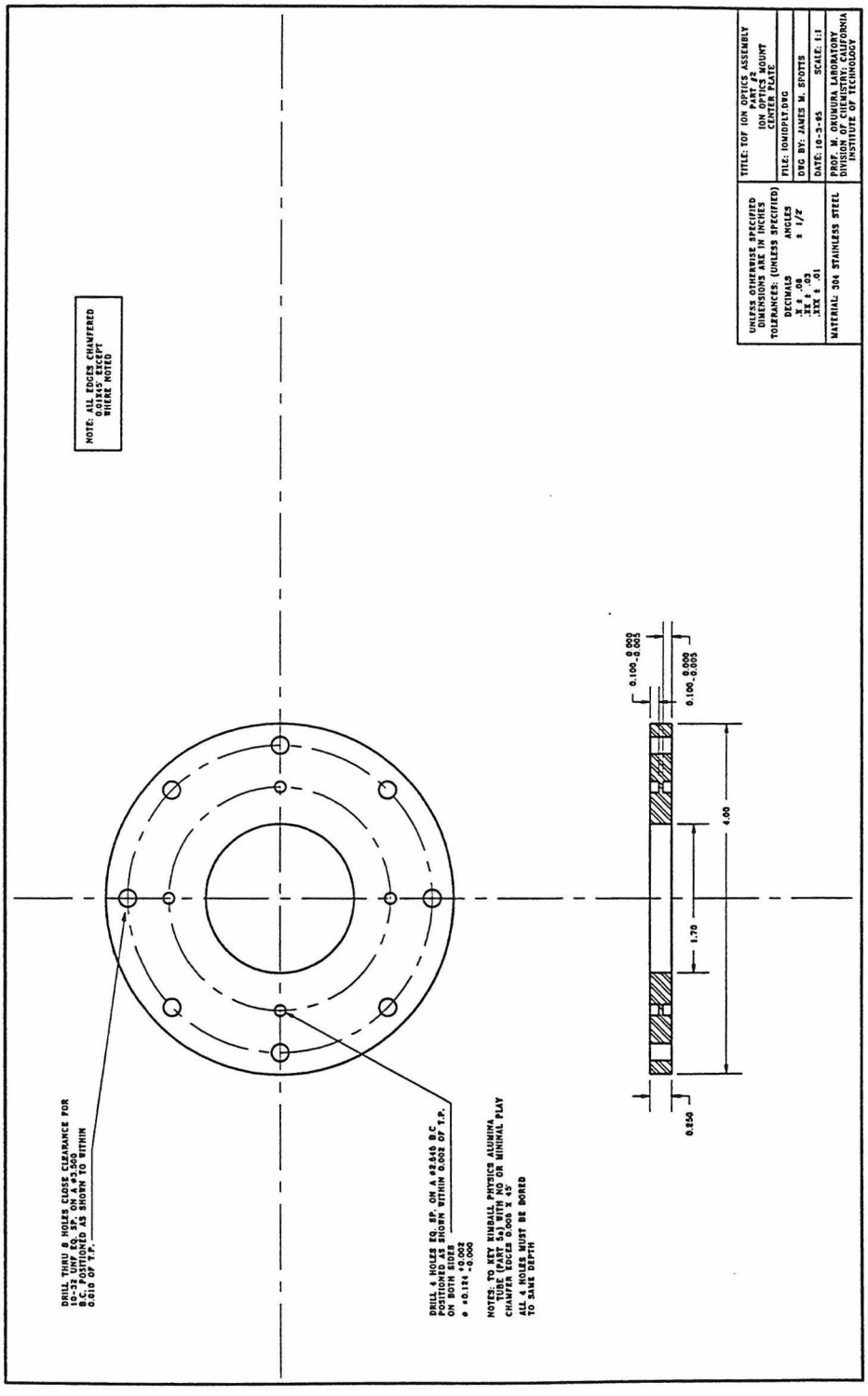

NOTE: ALL EDGES CHAMFERED 0.01X45° EXCEPT WHERE NOTED
DRILL THRU & HOLES CLOSE CLEARANCE FOR 10-32 UNF SO. ST. ON ø5.560 B.C. POSITIONED AS SHOWN TO WITHIN 0.010 OF T.P.
DRILL 4 HOLES EQ. SP. ON A ø2.840 B.C. POSITIONED AS SHOWN WITHIN 0.002 OF T.P. ON BOTH SIDES
ø +0.124 +0.002 -0.000
NOTES: TO KEY KIMBALL PHYSICS ALUMINA TUBE (PART 5a) WITH NO OR MINIMAL PLAY CHAMFER EDGES 0.005 X 45°
ALL 4 HOLES MUST BE BORED TO SAME DEPTH
0.100 +0.002 -0.005
0.100 +0.000 -0.005
4.00
1.70
0.250
UNLESS OTHERWISE SPECIFIED DIMENSIONS ARE IN INCHES
TOLERANCES: (UNLESS SPECIFIED)
DECIMALS
X ± .05
XX ± .02
XXX ± .01
ANGLES
± 1/2
MATERIAL: 304 STAINLESS STEEL
TITLE: TOF ION OPTICS ASSEMBLY PART 2 OF 2 ION OPTICS MOUNT CENTER PLATE
FILE: IONOPLT.DRG
DRG BY: JAMES M. SPOTTS
DATE: 10-3-95
SCALE: 1:1
PROF. M. GRUNTHANER LABORATORY DIVISION OF CHEMISTRY, CALIFORNIA INSTITUTE OF TECHNOLOGY

Figure 2-82

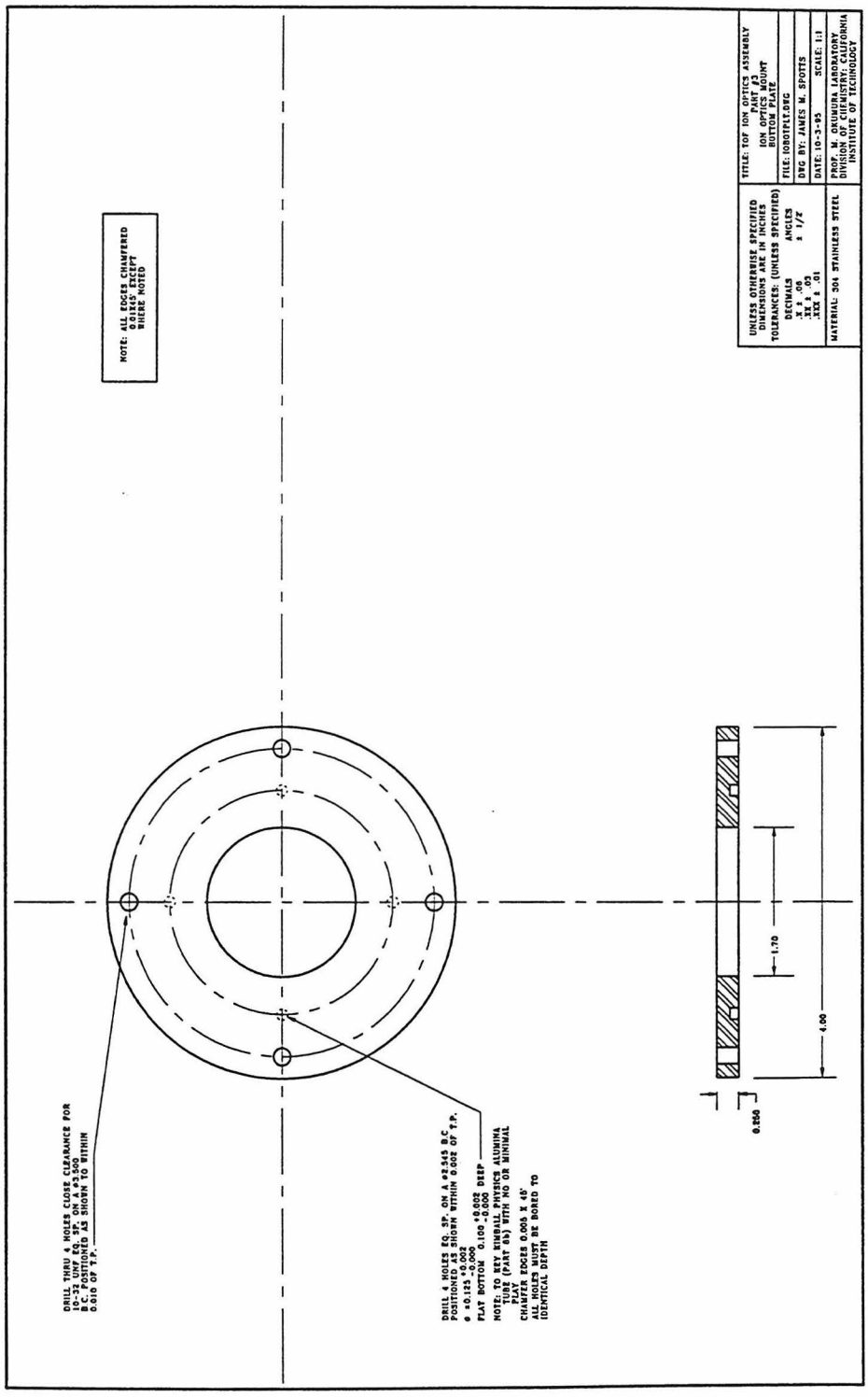

NOTE: ALL EDGES CHAMFERED
0.0185 EXCEPT
WHERE NOTED
DRILL THRU 4 HOLES CLOSE CLEARANCE FOR
10-32 UNF-2B SCREWS ON A Ø4.500
B.C. POSITIONED AS SHOWN TO WITHIN
0.010 OF T.P.
DRILL 4 HOLES EQ. SP. ON A Ø2.345 B.C.
POSITIONED AS SHOWN WITHIN 0.002 OF T.P.
Ø +0.125 -0.000
FLAT BOTTOM 0.100 +0.002 -0.000 DEEP
NOTE: TO KEY KIMBALL PHYSICS ALUMINA
TUBE (PART #6) WITH NO OR MINIMAL
PLAY.
CHAMFER EDGES 0.005 X 45°
ALL HOLES MUST BE BORED TO
IDENTICAL DEPTH
1.70
4.00
0.250
UNLESS OTHERWISE SPECIFIED
DIMENSIONS ARE IN INCHES
TOLERANCES: (UNLESS SPECIFIED)
DECIMALS
.X ± .06
.XX ± .01
.XXX ± .161
ANGLES
± 1/2
MATERIAL: 304 STAINLESS STEEL
TITLE: TOF ION OPTICS ASSEMBLY
ION OPTICS MOUNT
BOTTOM PLATE
FILE: IOBOTPLT.DFC
DRG BY: JAMES M. SPOTTS
DATE: 10-3-95
SCALE: 1:1
PROF. M. DEGUZIA LABORATORY
DIVISION OF CHEMISTRY, CALIFORNIA
INSTITUTE OF TECHNOLOGY

Figure 2-83

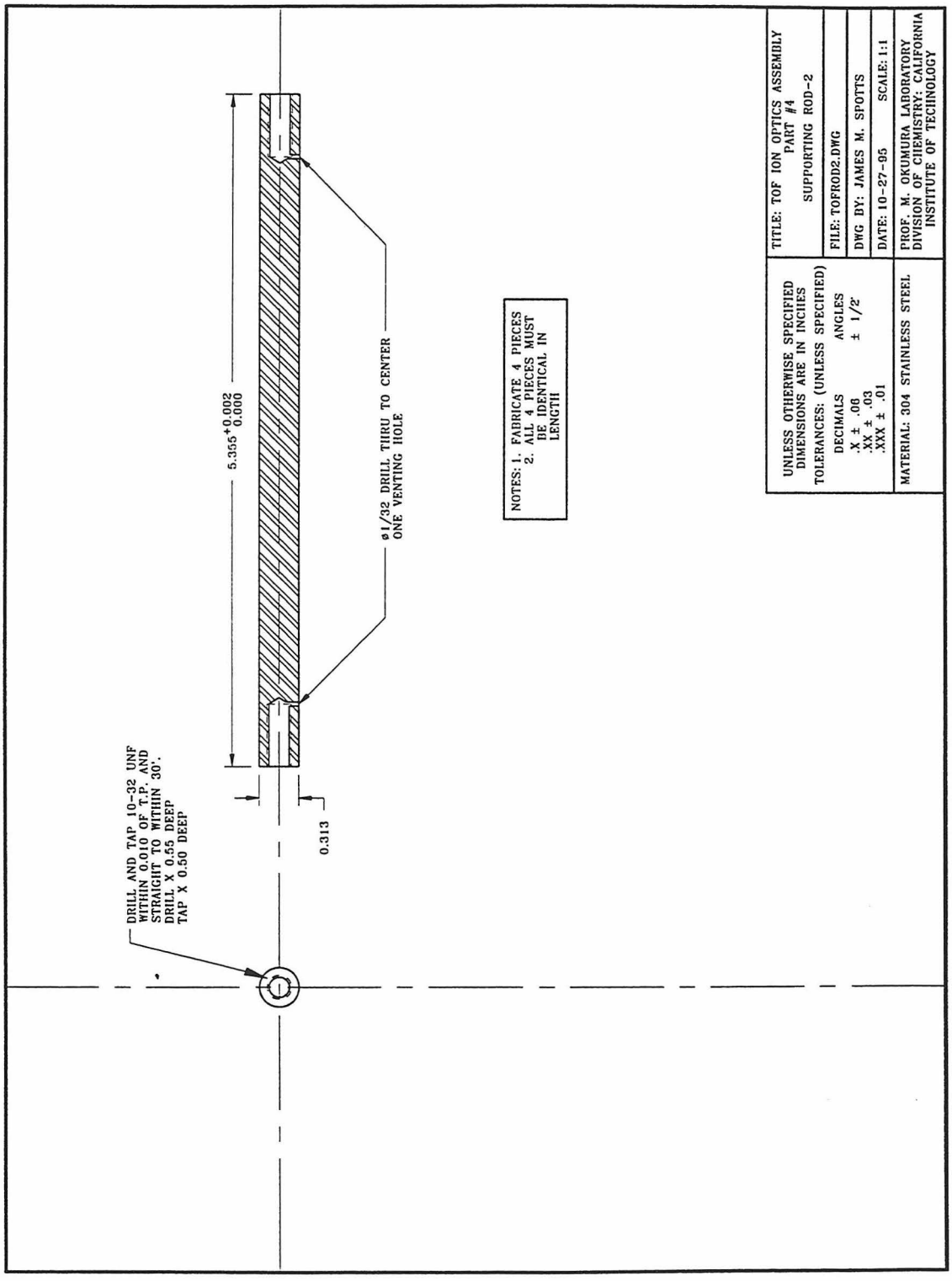

DRILL AND TAP 10-32 UNF
WITHIN 0.010 OF T.P. AND
STRAIGHT TO WITHIN 30'.
DRILL X 0.55 DEEP
TAP X 0.50 DEEP
5.355 +0.002 0.000
ø1/32 DRILL THRU TO CENTER
ONE VENTING HOLE
0.313
NOTES: 1. FABRICATE 4 PIECES
2. ALL 4 PIECES MUST
BE IDENTICAL IN
LENGTH
UNLESS OTHERWISE SPECIFIED
DIMENSIONS ARE IN INCHES
TOLERANCES: (UNLESS SPECIFIED)
DECIMALS ANGLES
.X ± .06 ± 1/2°
.XX ± .03
.XXX ± .01
TITLE: TOF ION OPTICS ASSEMBLY
PART #4
SUPPORTING ROD-2
FILE: TOFROD2.DWG
DWG BY: JAMES M. SPOTTS
DATE: 10-27-95 SCALE: 1:1
MATERIAL: 304 STAINLESS STEEL
PROF. M. OKUMURA LABORATORY
DIVISION OF CHEMISTRY: CALIFORNIA
INSTITUTE OF TECHNOLOGY

Figure 2-84

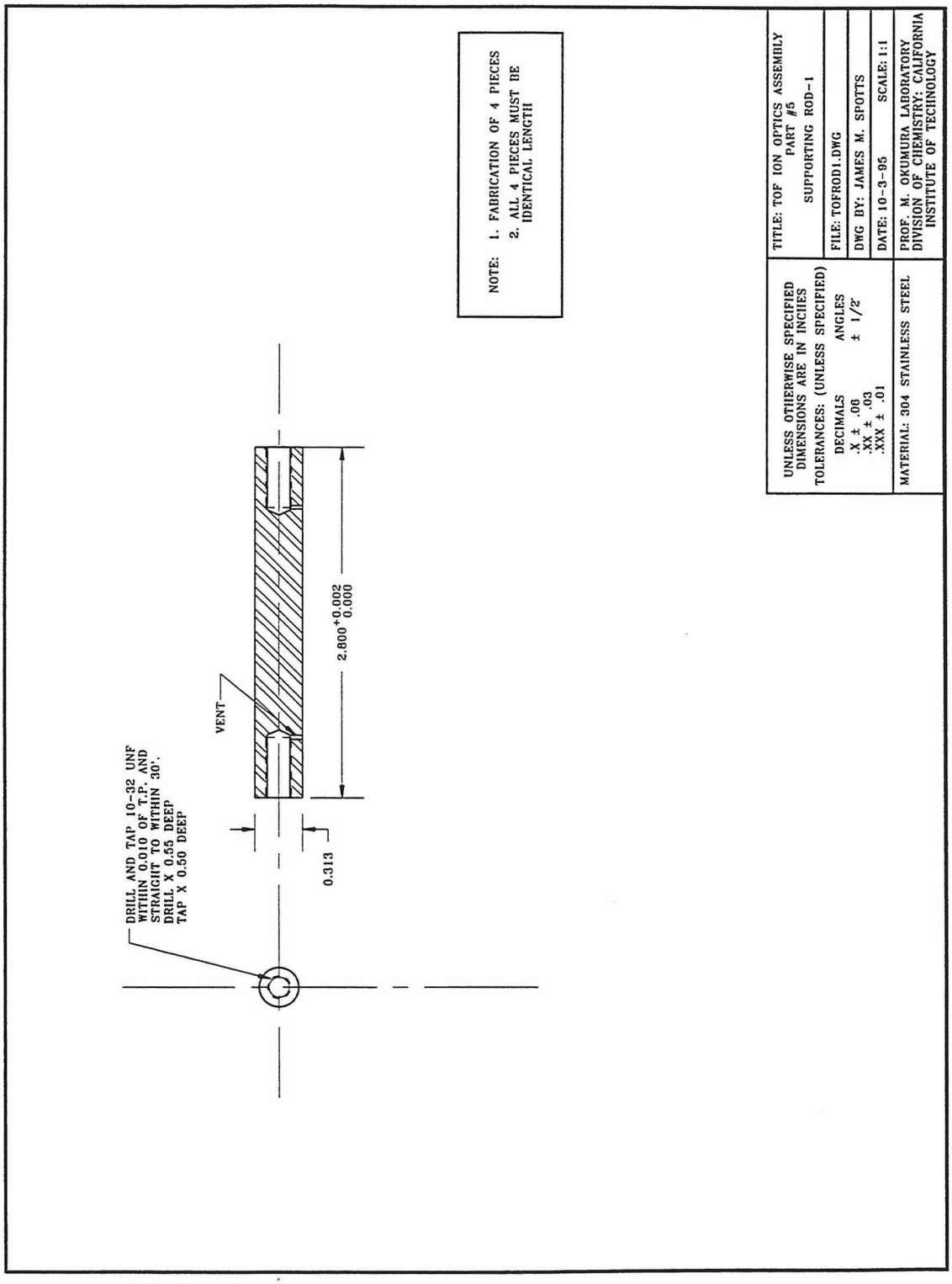

NOTE: 1. FABRICATION OF 4 PIECES
2. ALL 4 PIECES MUST BE IDENTICAL LENGTH
DRILL AND TAP 10-32 UNF WITHIN 0.010 OF T.P. AND STRAIGHT TO WITHIN 30'. DRILL X 0.55 DEEP TAP X 0.50 DEEP
VENT
2.800 +0.002 0.000
0.313
UNLESS OTHERWISE SPECIFIED DIMENSIONS ARE IN INCHES
TOLERANCES: (UNLESS SPECIFIED)
DECIMALS ANGLES
.X ± .06 ± 1/2'
.XX ± .03
.XXX ± .01
MATERIAL: 304 STAINLESS STEEL
TITLE: TOF ION OPTICS ASSEMBLY PART #5 SUPPORTING ROD-1
FILE: TOFROD1.DWG
DWG BY: JAMES M. SPOTTS
DATE: 10-3-95
SCALE: 1:1
PROF. M. OKUMURA LABORATORY DIVISION OF CHEMISTRY: CALIFORNIA INSTITUTE OF TECHINOLOGY

Figure 2-85

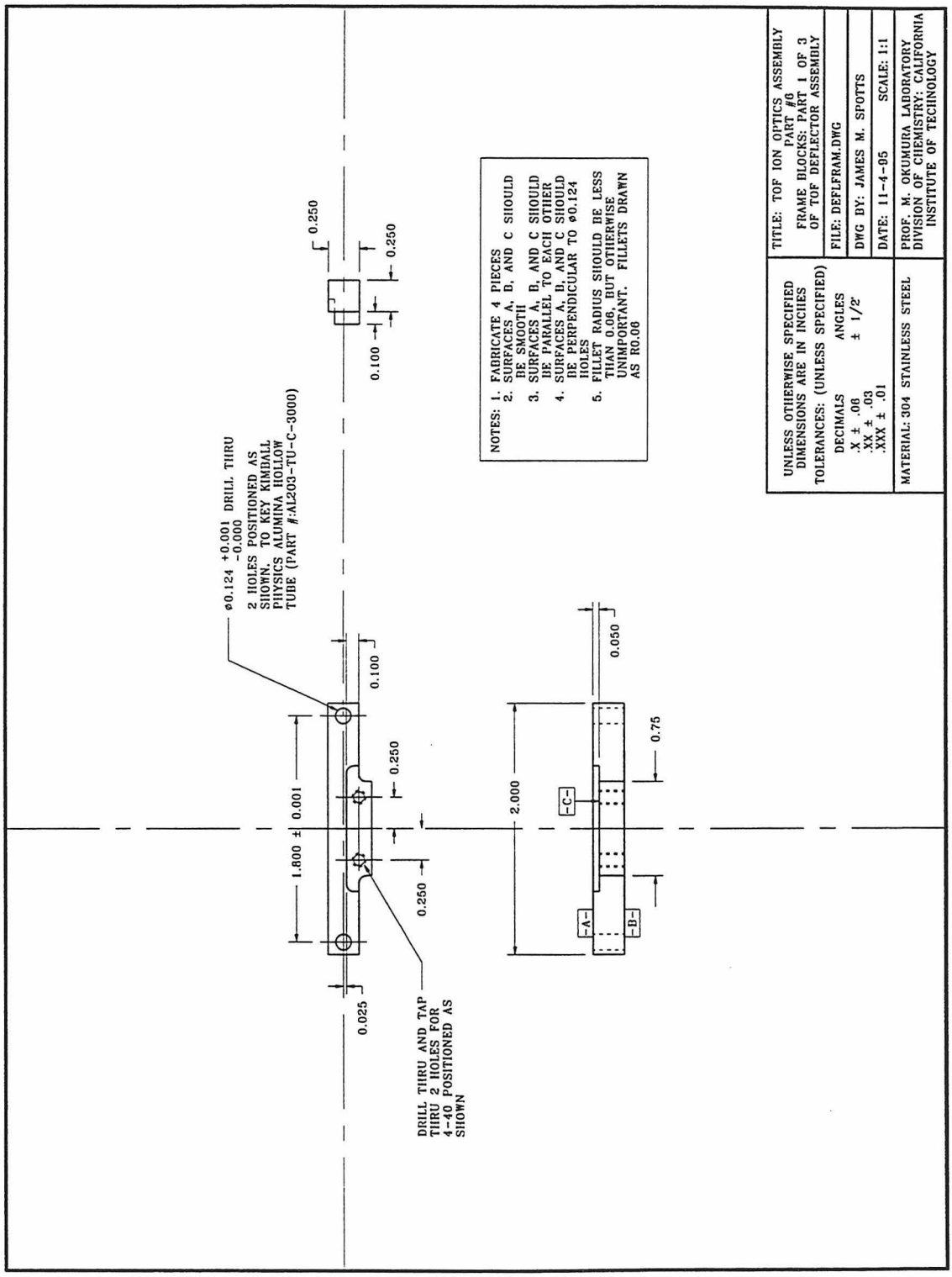

NOTES: 1. FABRICATE 4 PIECES
2. SURFACES A, B, AND C SHOULD BE SMOOTH
3. SURFACES A, B, AND C SHOULD BE PARALLEL TO EACH OTHER
4. SURFACES A, B, AND C SHOULD BE PERPENDICULAR TO ø0.124 HOLES
5. FILLET RADIUS SHOULD BE LESS THAN 0.06, BUT OTHERWISE UNIMPORTANT. FILLETS DRAWN AS R0.06
ø0.124 +0.001 -0.000 DRILL THRU
2 HOLES POSITIONED AS SHOWN. TO KEY KIMBALL PHYSICS ALUMINA HOLLOW TUBE (PART #:AL203-TU-C-3000)
DRILL THRU AND TAP THRU 2 HOLES FOR 4-40 POSITIONED AS SHOWN
1.800 ± 0.001
2.000
0.250
0.100
0.050
0.75
0.025
-A-
-B-
-C-
UNLESS OTHERWISE SPECIFIED DIMENSIONS ARE IN INCHES
TOLERANCES: (UNLESS SPECIFIED)
DECIMALS
.X ± .06
.XX ± .03
.XXX ± .01
ANGLES ± 1/2°
MATERIAL: 304 STAINLESS STEEL
TITLE: TOF ION OPTICS ASSEMBLY PART #6
FRAME BLOCKS: PART 1 OF 3
OF TOF DEFLECTOR ASSEMBLY
FILE: DEFLFRAM.DWG
DWG BY: JAMES M. SPOTTS
DATE: 11-4-95
SCALE: 1:1
PROF. M. OKUMURA LABORATORY
DIVISION OF CHEMISTRY: CALIFORNIA INSTITUTE OF TECHNOLOGY

Figure 2-86

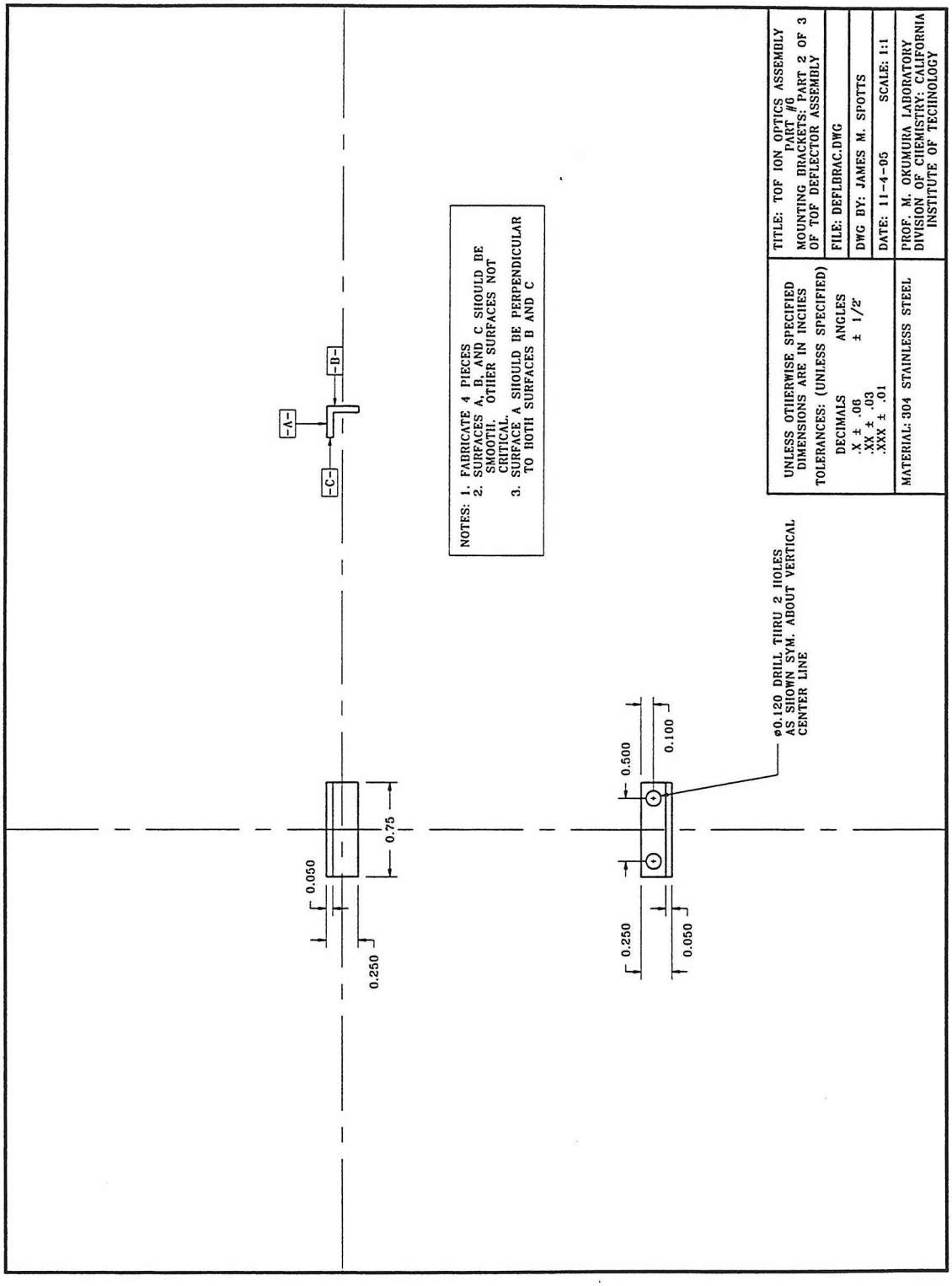

-A-
-B-
-C-
NOTES: 1. FABRICATE 4 PIECES
2. SURFACES A, B, AND C SHOULD BE SMOOTH. OTHER SURFACES NOT CRITICAL.
3. SURFACE A SHOULD BE PERPENDICULAR TO BOTH SURFACES B AND C
UNLESS OTHERWISE SPECIFIED DIMENSIONS ARE IN INCHES
TOLERANCES: (UNLESS SPECIFIED)
DECIMALS ANGLES
.X ± .06 ± 1/2°
.XX ± .03
.XXX ± .01
MATERIAL: 304 STAINLESS STEEL
TITLE: TOF ION OPTICS ASSEMBLY PART #6 MOUNTING BRACKETS: PART 2 OF 3 OF TOF DEFLECTOR ASSEMBLY
FILE: DEFLBRAC.DWG
DWG BY: JAMES M. SPOTTS
DATE: 11-4-05 SCALE: 1:1
PROF. M. OKUMURA LABORATORY DIVISION OF CHEMISTRY: CALIFORNIA INSTITUTE OF TECHNOLOGY
ø0.120 DRILL THRU 2 HOLES AS SHOWN SYM. ABOUT VERTICAL CENTER LINE
0.050
0.75
0.250
0.500
0.100
0.250
0.050

Figure 2-87

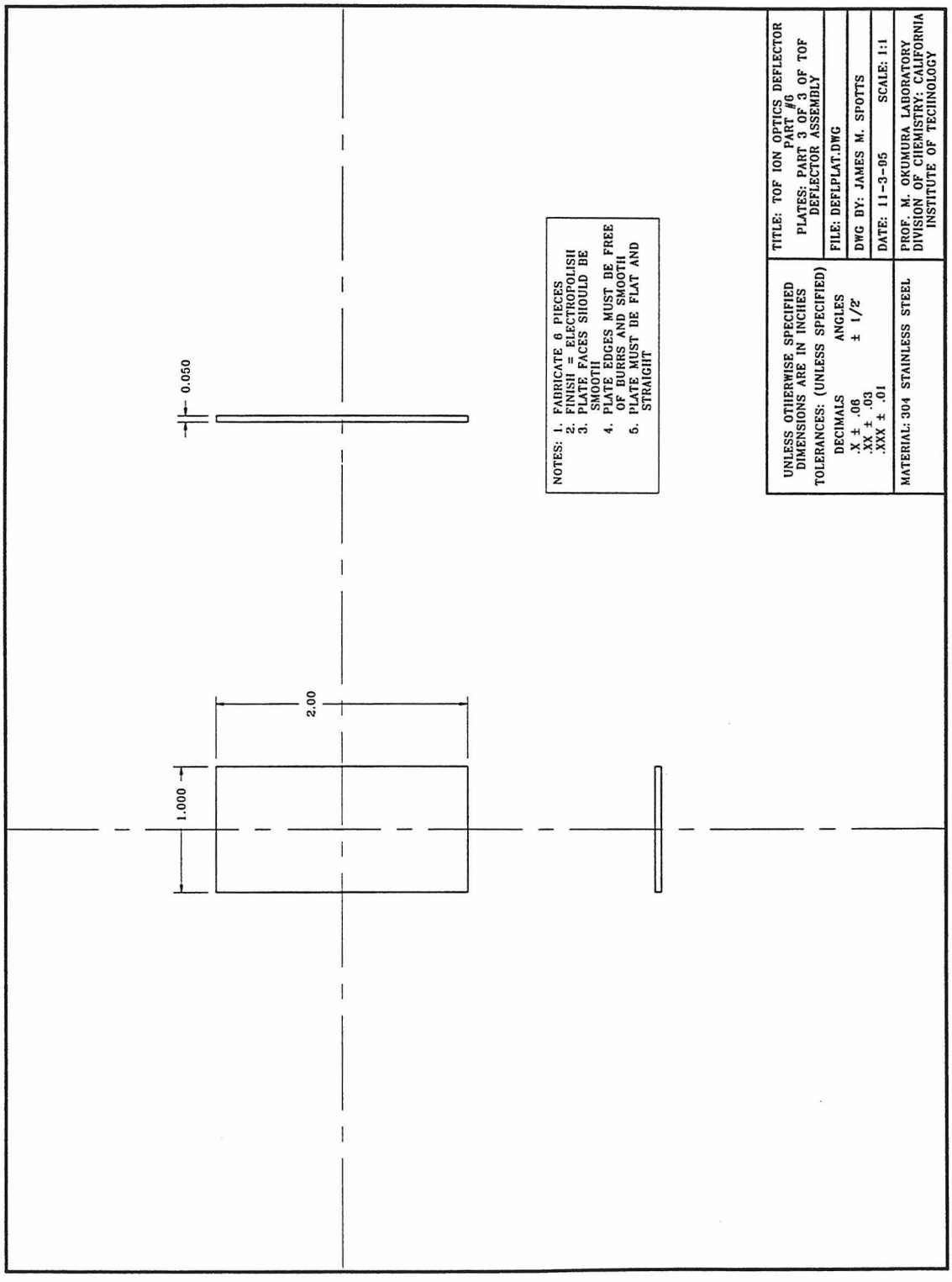

0.050
2.00
1.000
NOTES: 1. FABRICATE 6 PIECES
2. FINISH = ELECTROPOLISH
3. PLATE FACES SHOULD BE SMOOTH
4. PLATE EDGES MUST BE FREE OF BURRS AND SMOOTH
5. PLATE MUST BE FLAT AND STRAIGHT
UNLESS OTHERWISE SPECIFIED DIMENSIONS ARE IN INCHES
TOLERANCES: (UNLESS SPECIFIED)
DECIMALS ANGLES
.X ± .06 ± 1/2°
.XX ± .03
.XXX ± .01
MATERIAL: 304 STAINLESS STEEL
TITLE: TOF ION OPTICS DEFLECTOR PART #6
PLATES: PART 3 OF 3 OF TOF DEFLECTOR ASSEMBLY
FILE: DEFLPLAT.DWG
DWG BY: JAMES M. SPOTTS
DATE: 11-3-05 SCALE: 1:1
PROF. M. OKUMURA LABORATORY
DIVISION OF CHEMISTRY: CALIFORNIA INSTITUTE OF TECHNOLOGY

Figure 2-88

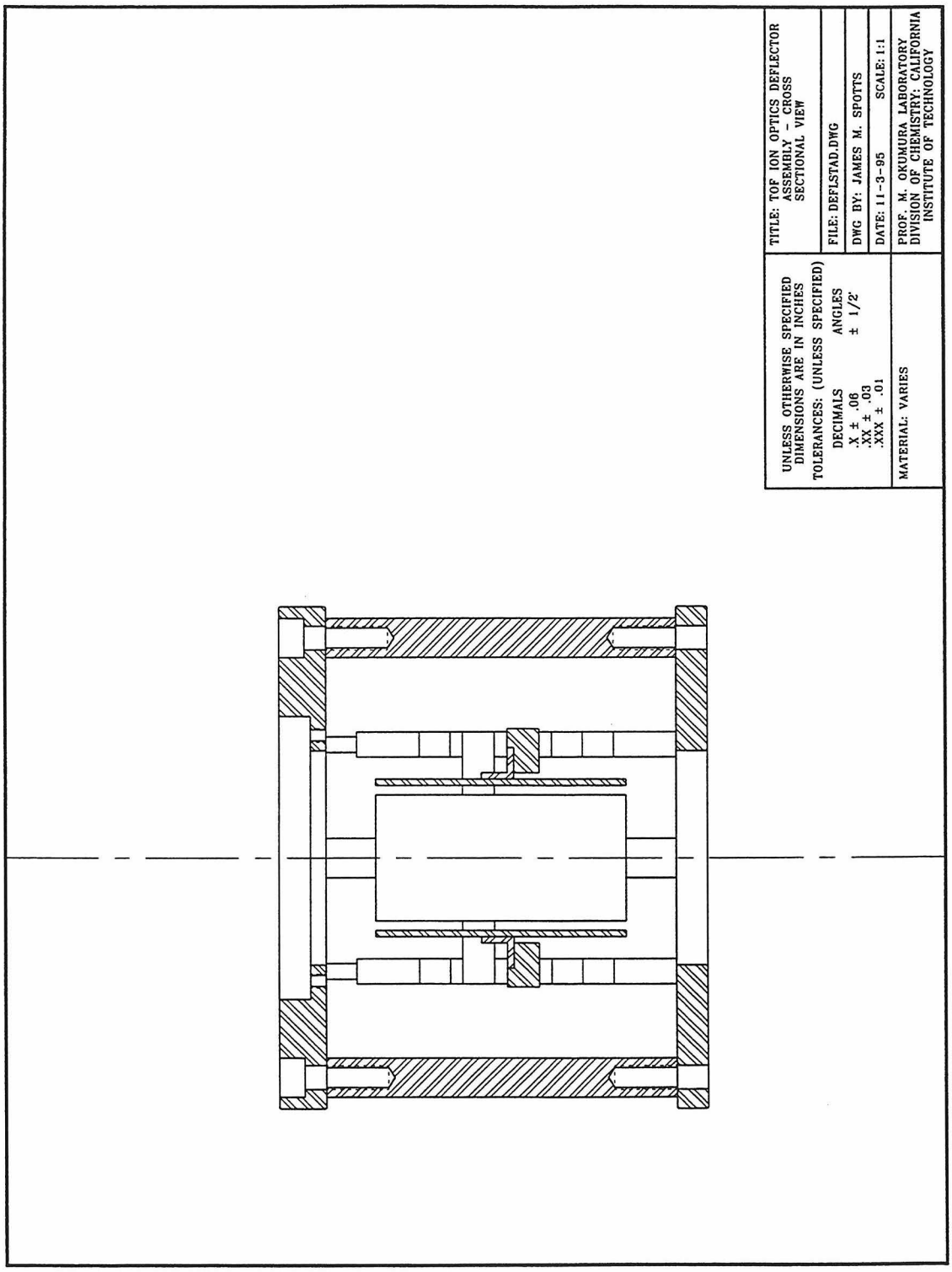

TITLE: TOF ION OPTICS DEFLECTOR ASSEMBLY - CROSS SECTIONAL VIEW
FILE: DEFLSTAD.DWG
DWG BY: JAMES M. SPOTTS
DATE: 11-3-95
SCALE: 1:1
PROF. M. OKUMURA LABORATORY
DIVISION OF CHEMISTRY: CALIFORNIA INSTITUTE OF TECHNOLOGY
UNLESS OTHERWISE SPECIFIED DIMENSIONS ARE IN INCHES
TOLERANCES: (UNLESS SPECIFIED)
DECIMALS
.X ± .06
.XX ± .03
.XXX ± .01
ANGLES
± 1/2'
MATERIAL: VARIES

Figure 2-89

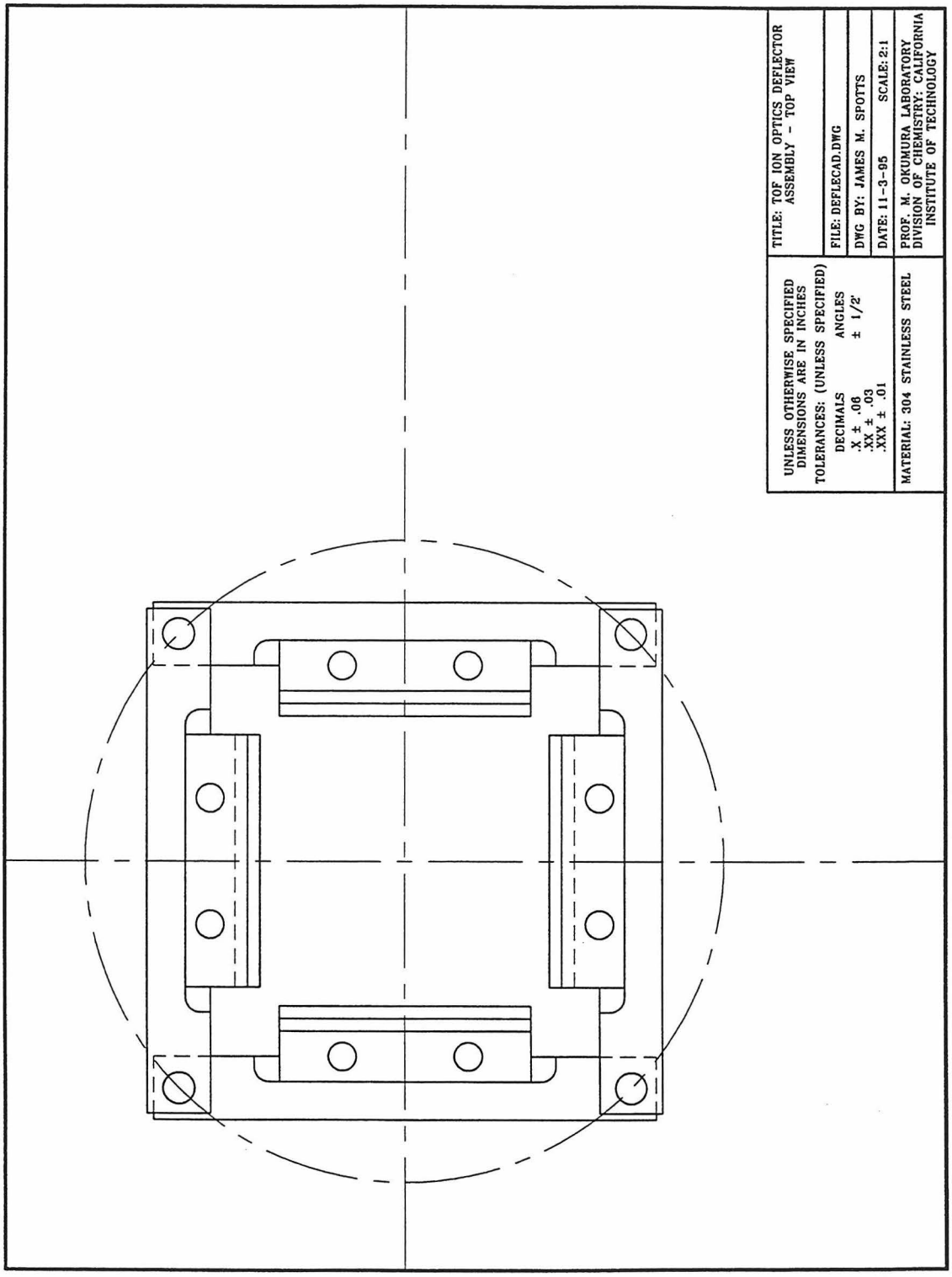

TITLE: TOF ION OPTICS DEFLECTOR ASSEMBLY - TOP VIEW
FILE: DEFLECAD.DWG
DWG BY: JAMES M. SPOTTS
DATE: 11-3-95 SCALE: 2:1
PROF. M. OKUMURA LABORATORY
DIVISION OF CHEMISTRY: CALIFORNIA INSTITUTE OF TECHNOLOGY
UNLESS OTHERWISE SPECIFIED DIMENSIONS ARE IN INCHES
TOLERANCES: (UNLESS SPECIFIED)
DECIMALS ANGLES
.X ± .06 ± 1/2°
.XX ± .03
.XXX ± .01
MATERIAL: 304 STAINLESS STEEL

Figure 2-90

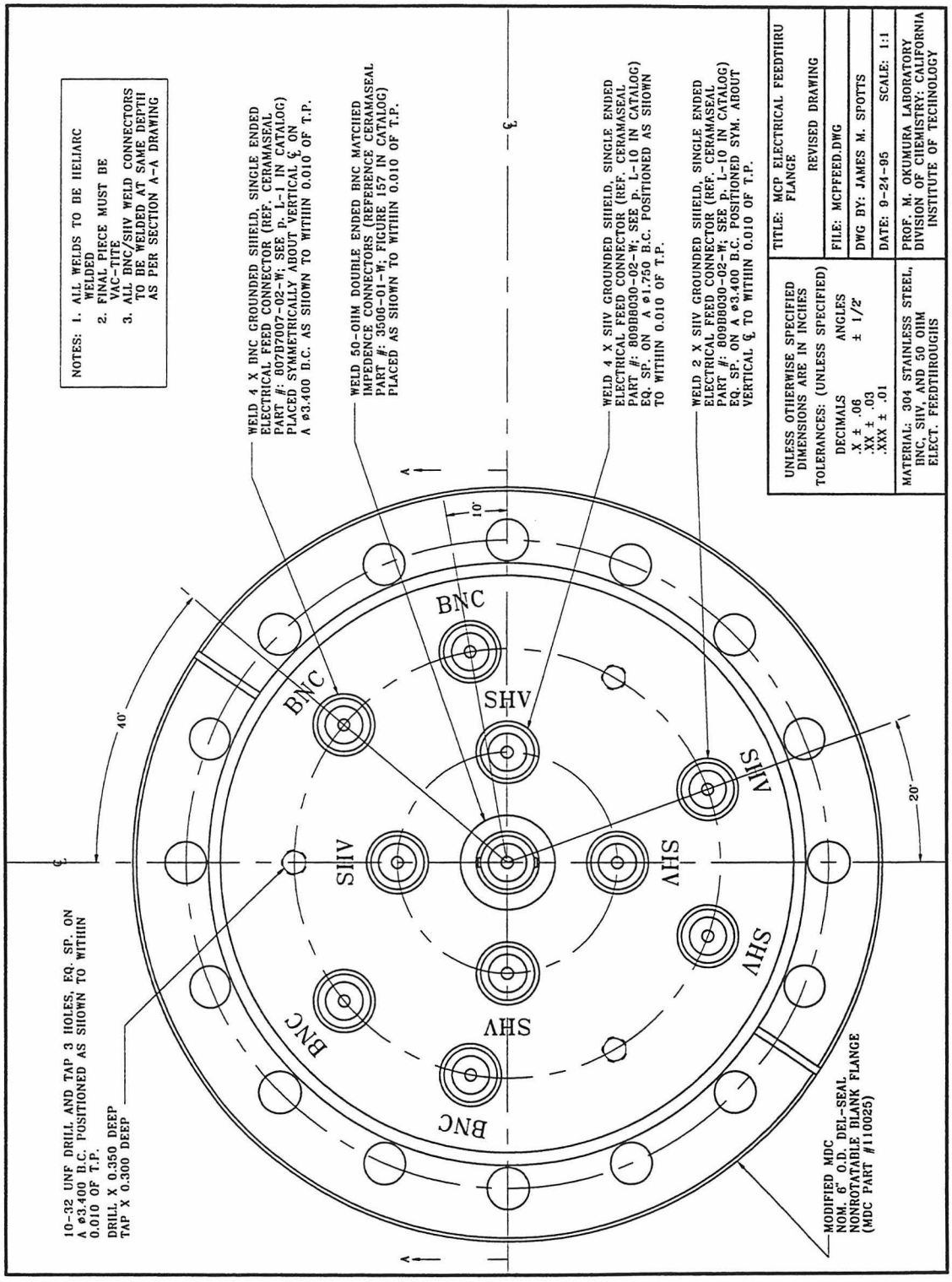

NOTES: 1. ALL WELDS TO BE HELIARC WELDED
2. FINAL PIECE MUST BE VAC-TITE
3. ALL BNC/SHV WELD CONNECTORS TO BE WELDED AT SAME DEPTH AS PER SECTION A-A DRAWING
WELD 4 X BNC GROUNDED SHIELD, SINGLE ENDED ELECTRICAL FEED CONNECTOR (REF. CERAMASEAL PART #: 807D7007-02-W; SEE P. L-1 IN CATALOG) PLACED SYMMETRICALLY ABOUT VERTICAL ℄ ON A ø3.400 B.C. AS SHOWN TO WITHIN 0.010 OF T.P.
WELD 50-OHM DOUBLE ENDED BNC MATCHED IMPEDENCE CONNECTORS (REFERENCE CERAMASEAL PART #: 3500-01-W; FIGURE 157 IN CATALOG) PLACED AS SHOWN TO WITHIN 0.010 OF T.P.
WELD 4 X SHV GROUNDED SHIELD, SINGLE ENDED ELECTRICAL FEED CONNECTOR (REF. CERAMASEAL PART #: 809B8030-02-W; SEE P. L-10 IN CATALOG) EQ. SP. ON A ø1.750 B.C. POSITIONED AS SHOWN TO WITHIN 0.010 OF T.P.
WELD 2 X SHV GROUNDED SHIELD, SINGLE ENDED ELECTRICAL FEED CONNECTOR (REF. CERAMASEAL PART #: 809B8030-02-W; SEE p. L-10 IN CATALOG) EQ. SP. ON A ø3.400 B.C. POSITIONED SYM. ABOUT VERTICAL ℄ TO WITHIN 0.010 OF T.P.
10-32 UNF DRILL AND TAP 3 HOLES, EQ. SP. ON A ø3.400 B.C. POSITIONED AS SHOWN TO WITHIN 0.010 OF T.P.
DRILL X 0.350 DEEP
TAP X 0.300 DEEP
MODIFIED MDC NOM. 6" O.D. DEL-SEAL NONROTATABLE BLANK FLANGE (MDC PART #110025)
BNC
SHV
40°
20°
10°
UNLESS OTHERWISE SPECIFIED DIMENSIONS ARE IN INCHES
TOLERANCES: (UNLESS SPECIFIED)
DECIMALS ANGLES
.X ± .06 ± 1/2°
.XX ± .03
.XXX ± .01
TITLE: MCP ELECTRICAL FEEDTHRU FLANGE
REVISED DRAWING
FILE: MCPFEED.DWG
DWG BY: JAMES M. SPOTTS
DATE: 9-24-95 SCALE: 1:1
MATERIAL: 304 STAINLESS STEEL, BNC, SHV, AND 50 OHM ELECT. FEEDTHROUGHS
PROF. M. OKUMURA LABORATORY
DIVISION OF CHEMISTRY: CALIFORNIA INSTITUTE OF TECHNOLOGY

Figure 2-91

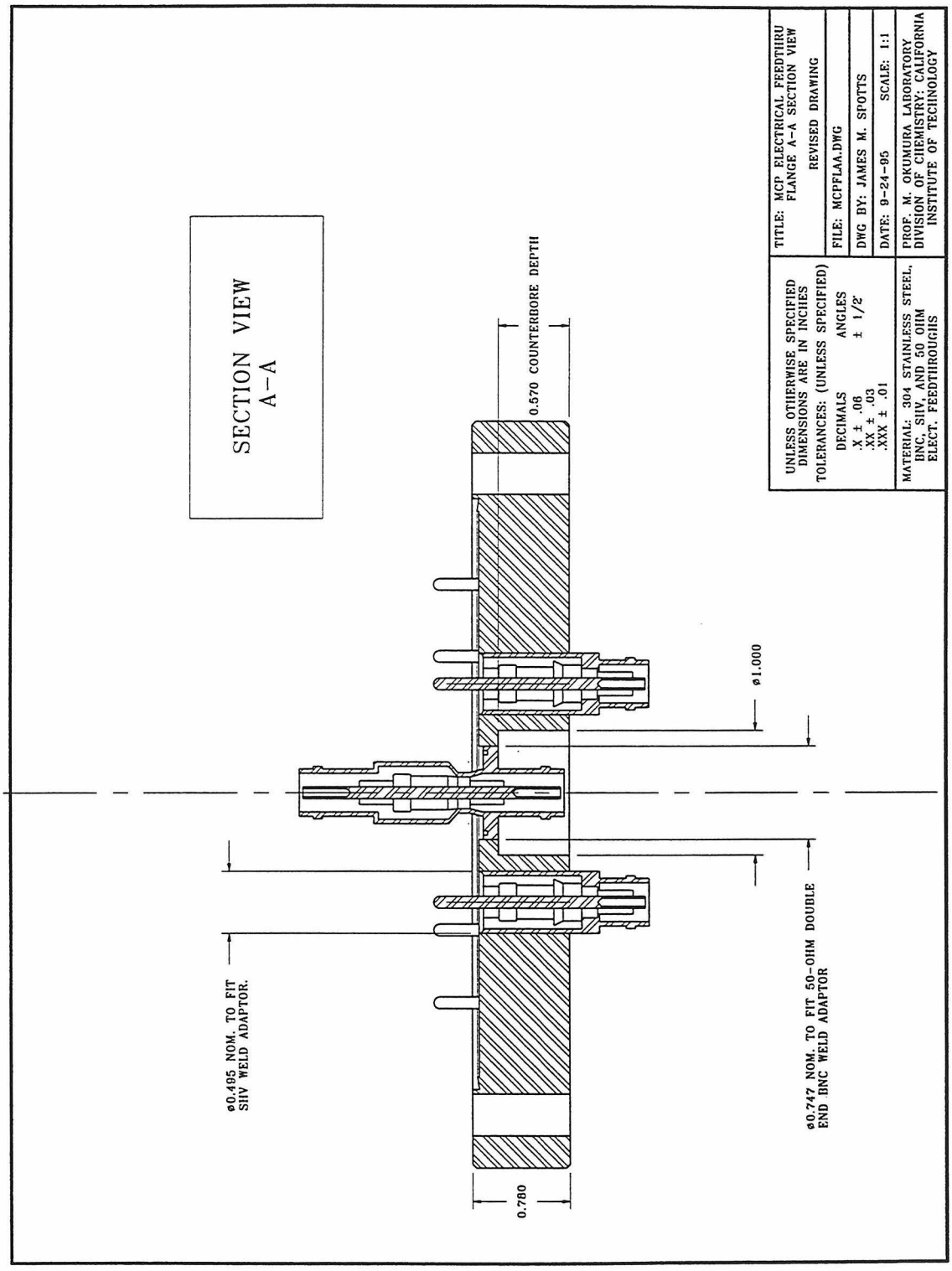

SECTION VIEW
A-A
0.570 COUNTERBORE DEPTH
ø1.000
ø0.495 NOM. TO FIT
SHV WELD ADAPTOR.
ø0.747 NOM. TO FIT 50-OHM DOUBLE
END BNC WELD ADAPTOR
0.780
TITLE: MCP ELECTRICAL FEEDTHRU
FLANGE A-A SECTION VIEW
REVISED DRAWING
FILE: MCPFLAA.DWG
DWG BY: JAMES M. SPOTTS
DATE: 9-24-95
SCALE: 1:1
UNLESS OTHERWISE SPECIFIED
DIMENSIONS ARE IN INCHES
TOLERANCES: (UNLESS SPECIFIED)
DECIMALS
.X ± .06
.XX ± .03
.XXX ± .01
ANGLES
± 1/2°
MATERIAL: 304 STAINLESS STEEL,
BNC, SHV, AND 50 OHM
ELECT. FEEDTHROUGHS
PROF. M. OKUMURA LABORATORY
DIVISION OF CHEMISTRY; CALIFORNIA
INSTITUTE OF TECHNOLOGY

Figure 2-92

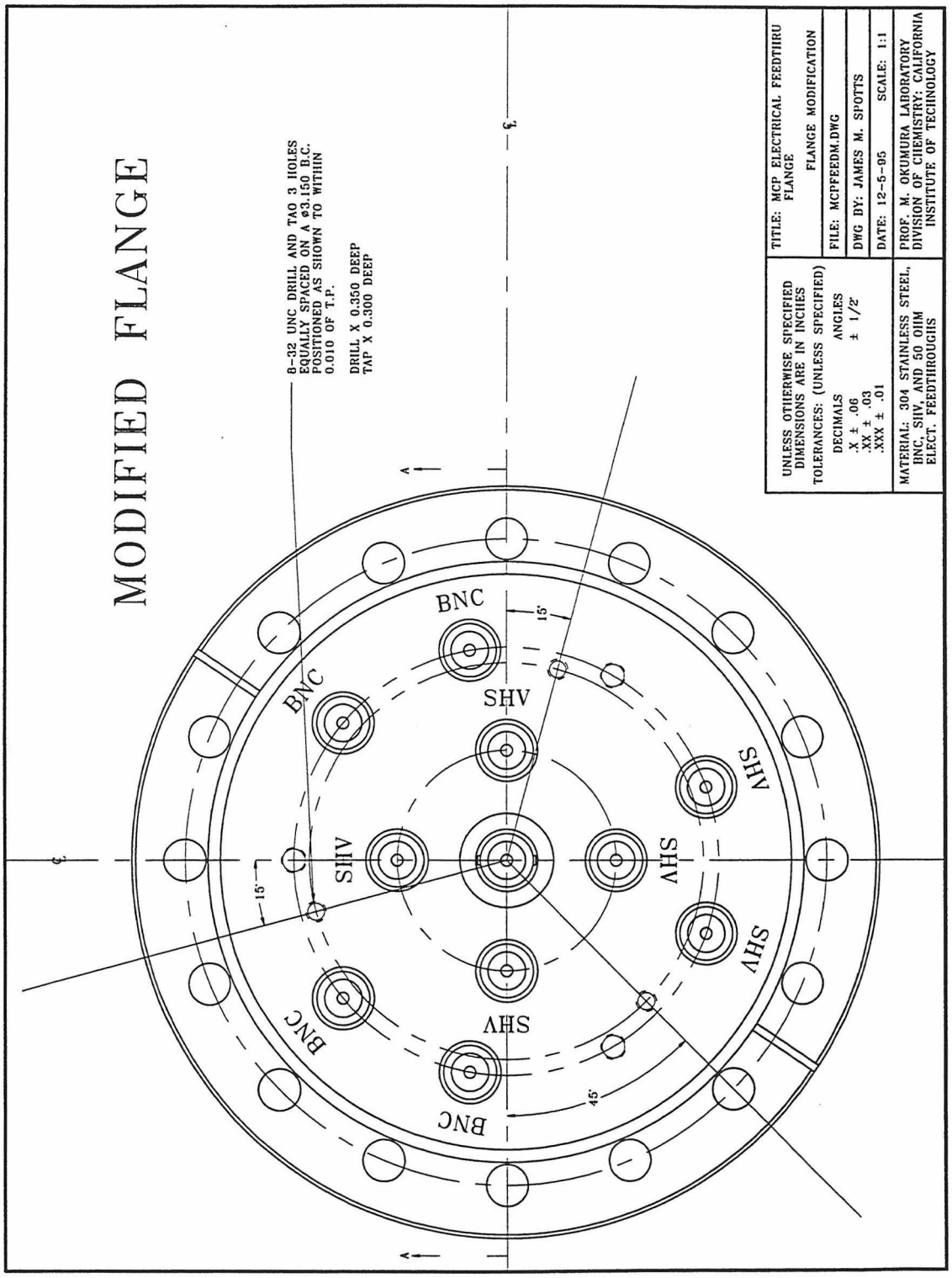

MODIFIED FLANGE
8-32 UNC DRILL AND TAO 3 HOLES
EQUALLY SPACED ON A ø3.150 B.C.
POSITIONED AS SHOWN TO WITHIN
0.010 OF T.P.
DRILL X 0.350 DEEP
TAP X 0.300 DEEP
BNC
SHV
15°
45°
UNLESS OTHERWISE SPECIFIED
DIMENSIONS ARE IN INCHES
TOLERANCES: (UNLESS SPECIFIED)
DECIMALS ANGLES
.X ± .06 ± 1/2°
.XX ± .03
.XXX ± .01
TITLE: MCP ELECTRICAL FEEDTHRU FLANGE
FLANGE MODIFICATION
FILE: MCPFEEDM.DWG
DWG BY: JAMES M. SPOTTS
DATE: 12-5-95
SCALE: 1:1
MATERIAL: 304 STAINLESS STEEL, BNC, SHV, AND 50 OHM ELECT. FEEDTHROUGHS
PROF. M. OKUMURA LABORATORY
DIVISION OF CHEMISTRY: CALIFORNIA INSTITUTE OF TECHNOLOGY

Figure 2-93

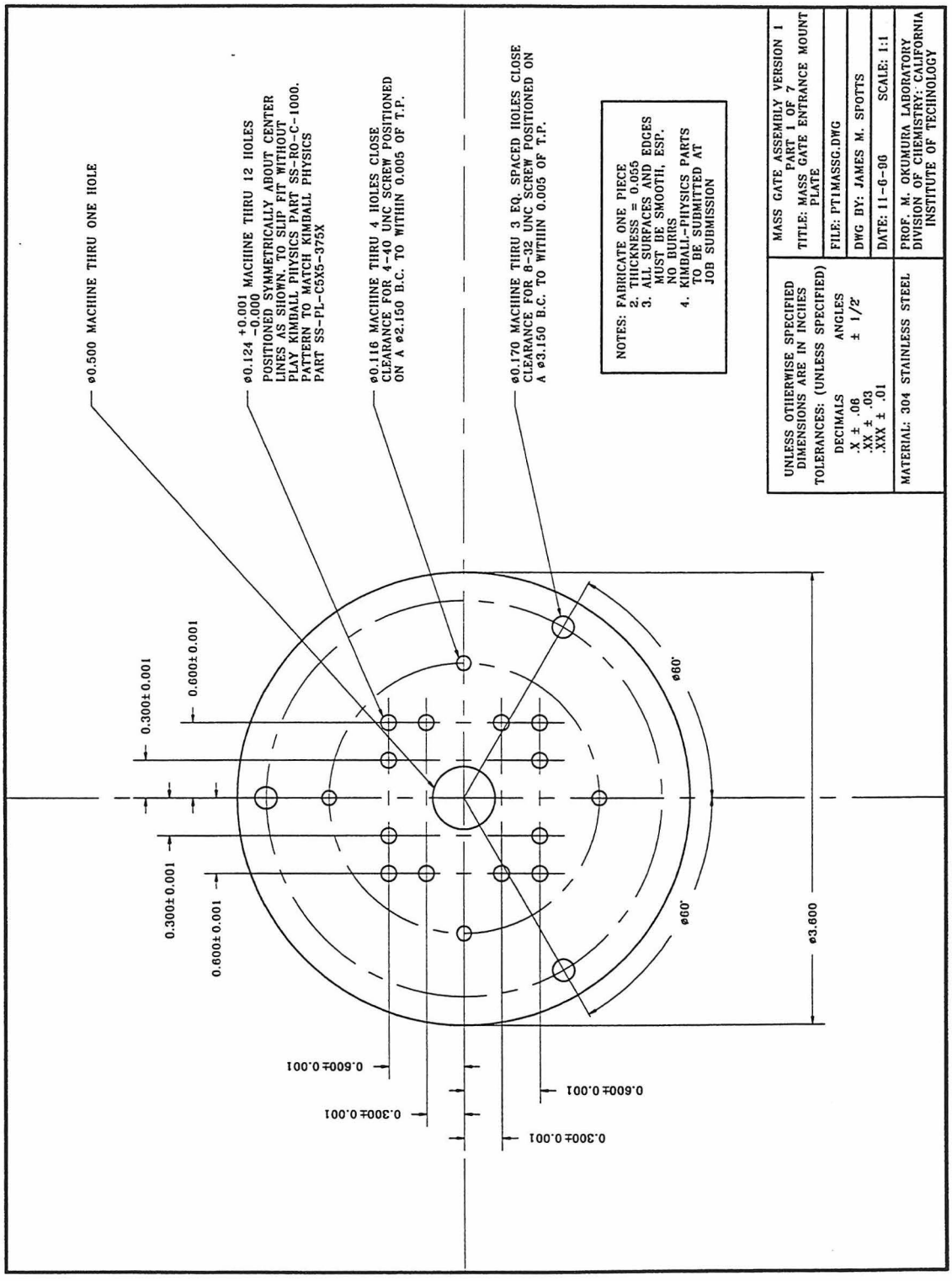

ø0.500 MACHINE THRU ONE HOLE
ø0.124 +0.001 -0.000 MACHINE THRU 12 HOLES POSITIONED SYMMETRICALLY ABOUT CENTER LINES AS SHOWN. TO SLIP FIT WITHOUT PLAY KIMBALL PHYSICS PART SS-RO-C-1000. PATTERN TO MATCH KIMBALL PHYSICS PART SS-PL-C5X5-375X
ø0.116 MACHINE THRU 4 HOLES CLOSE CLEARANCE FOR 4-40 UNC SCREW POSITIONED ON A ø2.150 B.C. TO WITHIN 0.005 OF T.P.
ø0.170 MACHINE THRU 3 EQ. SPACED HOLES CLOSE CLEARANCE FOR 8-32 UNC SCREW POSITIONED ON A ø3.150 B.C. TO WITHIN 0.005 OF T.P.
NOTES: FABRICATE ONE PIECE
2. THICKNESS = 0.055
3. ALL SURFACES AND EDGES MUST BE SMOOTH, ESP. NO BURRS
4. KIMBALL-PHYSICS PARTS TO BE SUBMITTED AT JOB SUBMISSION
0.300±0.001
0.600±0.001
0.300±0.001
0.600±0.001
ø60°
ø60°
ø3.600
0.600±0.001
0.300±0.001
0.300±0.001
0.600±0.001
UNLESS OTHERWISE SPECIFIED DIMENSIONS ARE IN INCHES
TOLERANCES: (UNLESS SPECIFIED)
DECIMALS ANGLES
.X ± .06 ± 1/2°
.XX ± .03
.XXX ± .01
MATERIAL: 304 STAINLESS STEEL
MASS GATE ASSEMBLY VERSION 1 PART 1 OF 7
TITLE: MASS GATE ENTRANCE MOUNT PLATE
FILE: PT1MASSG.DWG
DWG BY: JAMES M. SPOTTS
DATE: 11-6-00 SCALE: 1:1
PROF. M. OKUMURA LABORATORY
DIVISION OF CHEMISTRY: CALIFORNIA INSTITUTE OF TECHNOLOGY

Figure 2-94

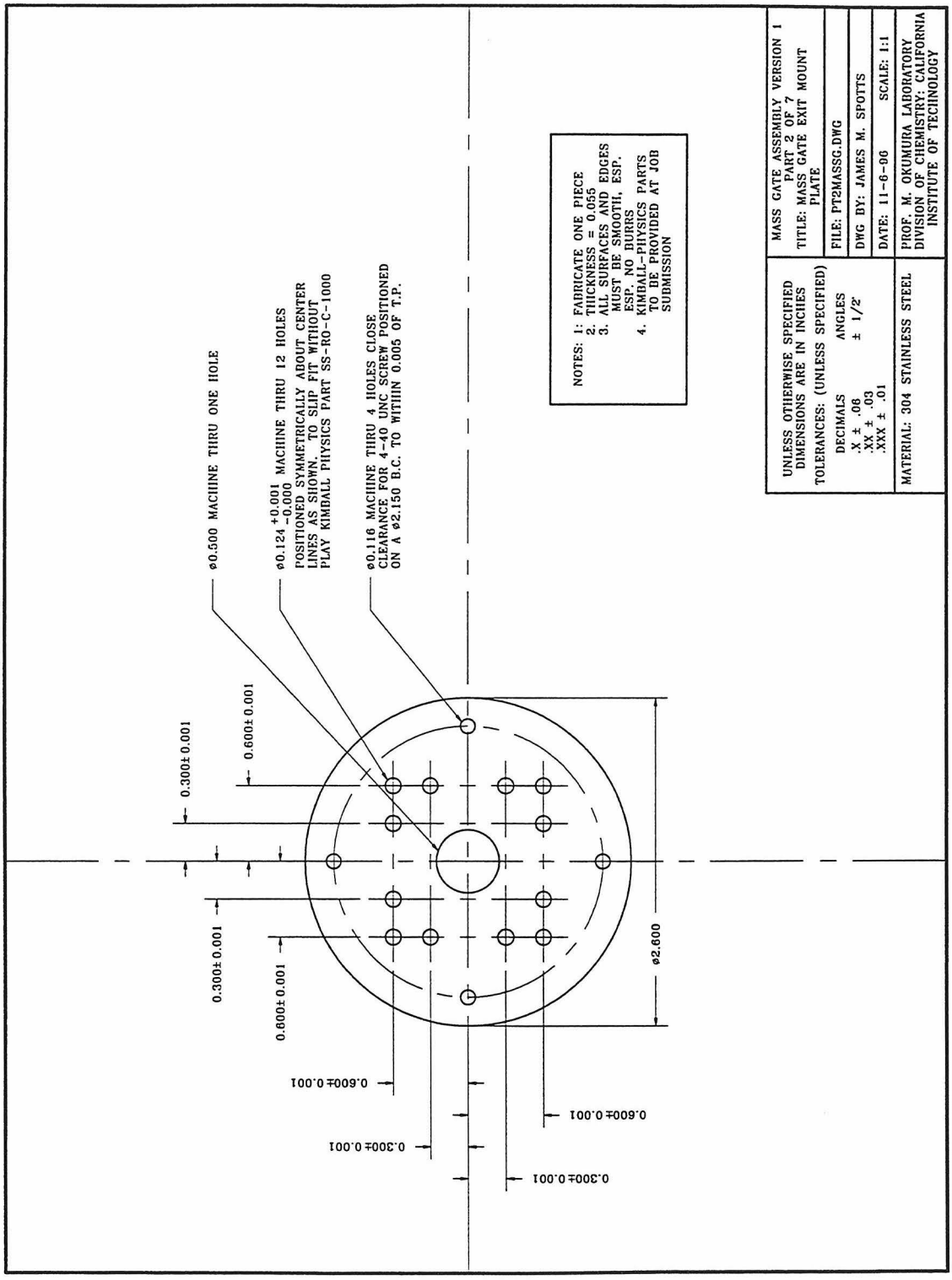

ø0.500 MACHINE THRU ONE HOLE
ø0.124 +0.001 -0.000 MACHINE THRU 12 HOLES POSITIONED SYMMETRICALLY ABOUT CENTER LINES AS SHOWN. TO SLIP FIT WITHOUT PLAY KIMBALL PHYSICS PART SS-RO-C-1000
ø0.116 MACHINE THRU 4 HOLES CLOSE CLEARANCE FOR 4-40 UNC SCREW POSITIONED ON A ø2.150 B.C. TO WITHIN 0.005 OF T.P.
NOTES: 1. FABRICATE ONE PIECE
2. THICKNESS = 0.055
3. ALL SURFACES AND EDGES MUST BE SMOOTH, ESP. ESP. NO BURRS
4. KIMBALL-PHYSICS PARTS TO BE PROVIDED AT JOB SUBMISSION
0.300± 0.001
0.600± 0.001
0.300± 0.001
0.600± 0.001
ø2.600
0.600± 0.001
0.300± 0.001
0.600± 0.001
0.300± 0.001
UNLESS OTHERWISE SPECIFIED DIMENSIONS ARE IN INCHES
TOLERANCES: (UNLESS SPECIFIED)
DECIMALS ANGLES
.X ± .06 ± 1/2°
.XX ± .03
.XXX ± .01
MATERIAL: 304 STAINLESS STEEL
MASS GATE ASSEMBLY VERSION 1
PART 2 OF 7
TITLE: MASS GATE EXIT MOUNT PLATE
FILE: PT2MASSG.DWG
DWG BY: JAMES M. SPOTTS
DATE: 11-6-96
SCALE: 1:1
PROF. M. OKUMURA LABORATORY
DIVISION OF CHEMISTRY; CALIFORNIA INSTITUTE OF TECHNOLOGY

Figure 2-95

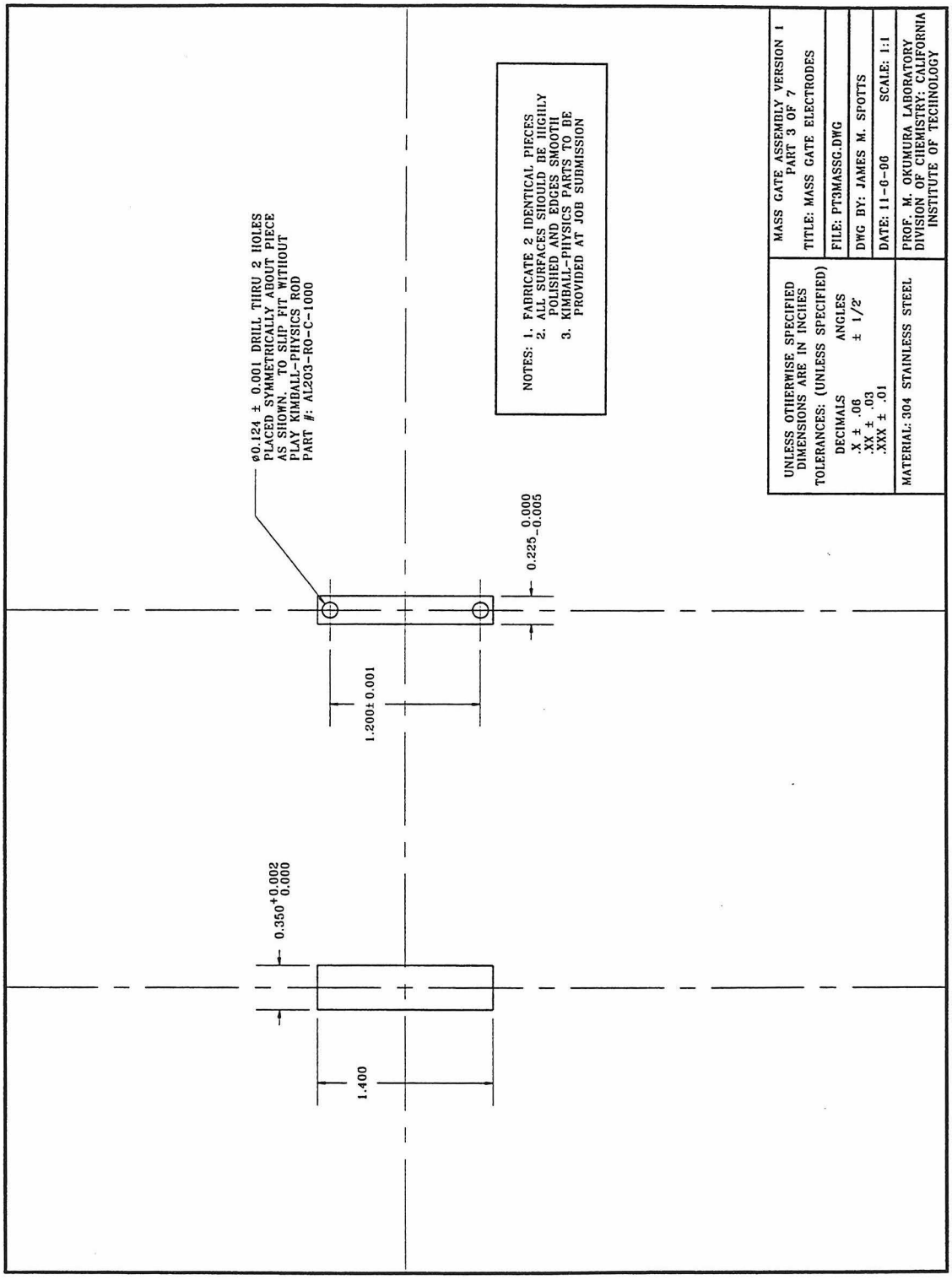

ø0.124 ± 0.001 DRILL THRU 2 HOLES
PLACED SYMMETRICALLY ABOUT PIECE
AS SHOWN. TO SLIP FIT WITHOUT
PLAY KIMBALL-PHYSICS ROD
PART #: AI203-RO-C-1000
NOTES: 1. FABRICATE 2 IDENTICAL PIECES
2. ALL SURFACES SHOULD BE HIGHLY POLISHED AND EDGES SMOOTH
3. KIMBALL-PHYSICS PARTS TO BE PROVIDED AT JOB SUBMISSION
0.225 0.000 −0.005
1.200± 0.001
0.350 +0.002 0.000
1.400
UNLESS OTHERWISE SPECIFIED
DIMENSIONS ARE IN INCHES
TOLERANCES: (UNLESS SPECIFIED)
DECIMALS ANGLES
.X ± .08 ± 1/2°
.XX ± .03
.XXX ± .01
MATERIAL: 304 STAINLESS STEEL
MASS GATE ASSEMBLY VERSION 1
PART 3 OF 7
TITLE: MASS GATE ELECTRODES
FILE: PT3MASSG.DWG
DWG BY: JAMES M. SPOTTS
DATE: 11-6-00 SCALE: 1:1
PROF. M. OKUMURA LABORATORY
DIVISION OF CHEMISTRY: CALIFORNIA
INSTITUTE OF TECHNOLOGY

Figure 2-96

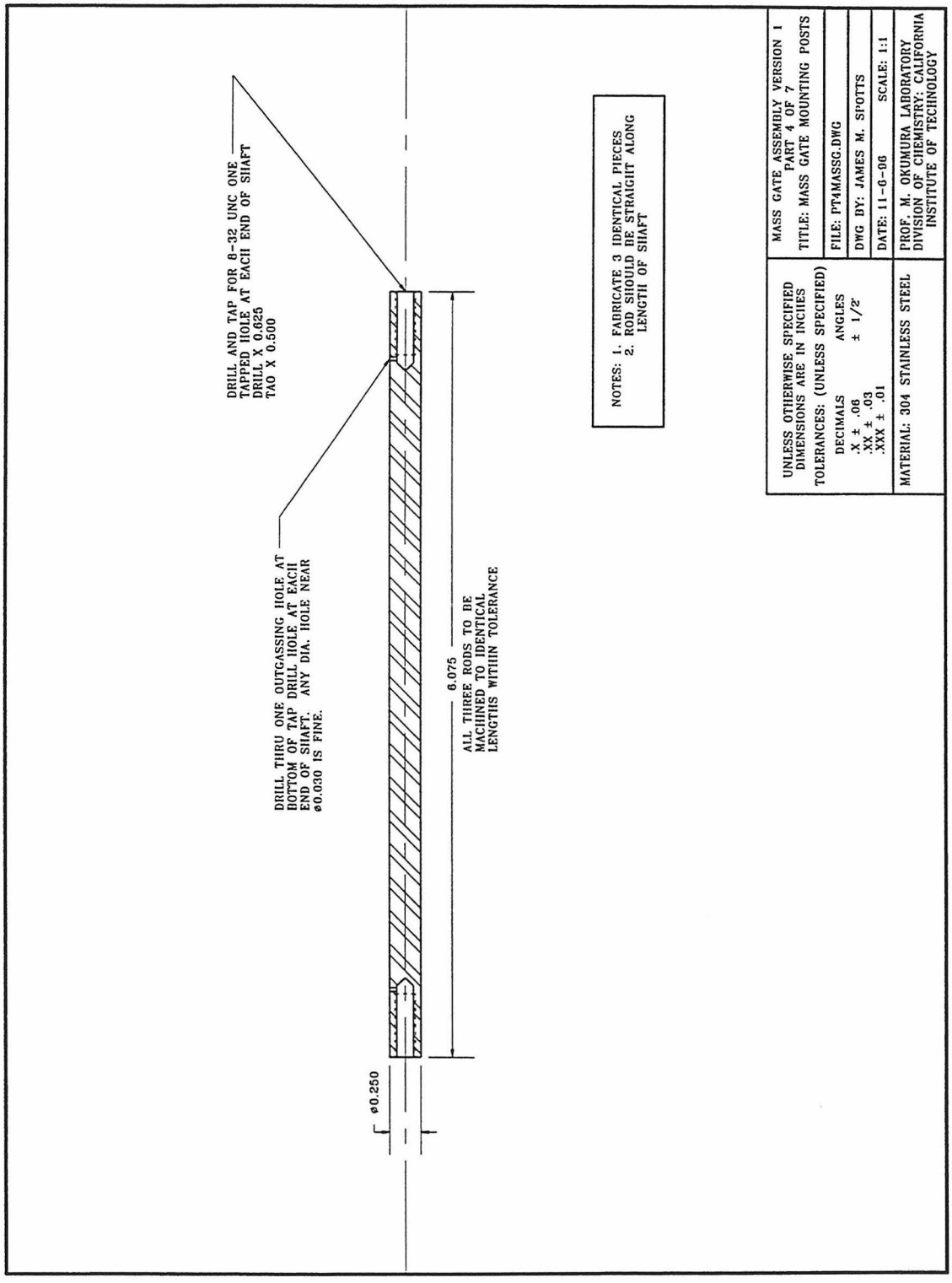

DRILL AND TAP FOR 8-32 UNC ONE
TAPPED HOLE AT EACH END OF SHAFT
DRILL X 0.625
TAO X 0.500
DRILL THRU ONE OUTGASSING HOLE AT
BOTTOM OF TAP DRILL HOLE AT EACH
END OF SHAFT. ANY DIA. HOLE NEAR
ø0.030 IS FINE.
6.075
ALL THREE RODS TO BE
MACHINED TO IDENTICAL
LENGTHS WITHIN TOLERANCE
ø0.250
NOTES: 1. FABRICATE 3 IDENTICAL PIECES
2. ROD SHOULD BE STRAIGHT ALONG
LENGTH OF SHAFT
UNLESS OTHERWISE SPECIFIED
DIMENSIONS ARE IN INCHES
TOLERANCES: (UNLESS SPECIFIED)
DECIMALS ANGLES
.X ± .06 ± 1/2°
.XX ± .03
.XXX ± .01
MATERIAL: 304 STAINLESS STEEL
MASS GATE ASSEMBLY VERSION 1
PART 4 OF 7
TITLE: MASS GATE MOUNTING POSTS
FILE: PT4MASSG.DWG
DWG BY: JAMES M. SPOTTS
DATE: 11-6-96
SCALE: 1:1
PROF. M. OKUMURA LABORATORY
DIVISION OF CHEMISTRY: CALIFORNIA
INSTITUTE OF TECHNOLOGY

Figure 2-97

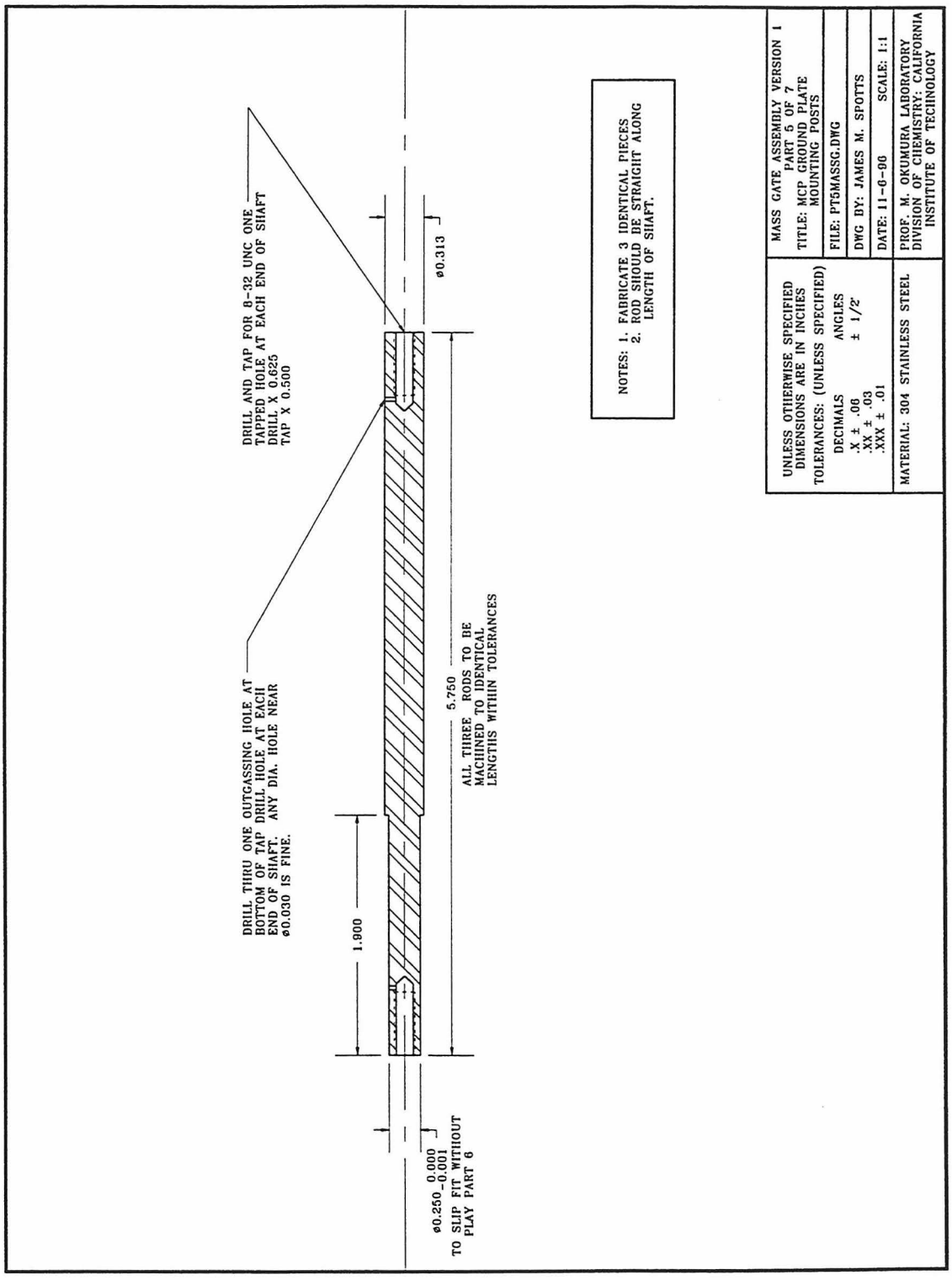

DRILL AND TAP FOR 8-32 UNC ONE TAPPED HOLE AT EACH END OF SHAFT
DRILL X 0.625
TAP X 0.500
DRILL THRU ONE OUTGASSING HOLE AT BOTTOM OF TAP DRILL HOLE AT EACH END OF SHAFT. ANY DIA. HOLE NEAR ø0.030 IS FINE.
1.900
ø0.313
5.750
ALL THREE RODS TO BE MACHINED TO IDENTICAL LENGTHS WITHIN TOLERANCES
ø0.250 0.000 -0.001
TO SLIP FIT WITHOUT PLAY PART 6
NOTES: 1. FABRICATE 3 IDENTICAL PIECES
2. ROD SHOULD BE STRAIGHT ALONG LENGTH OF SHAFT.
UNLESS OTHERWISE SPECIFIED DIMENSIONS ARE IN INCHES
TOLERANCES: (UNLESS SPECIFIED)
DECIMALS ANGLES
.X ± .06 ± 1/2°
.XX ± .03
.XXX ± .01
MATERIAL: 304 STAINLESS STEEL
MASS GATE ASSEMBLY VERSION 1
PART 5 OF 7
TITLE: MCP GROUND PLATE MOUNTING POSTS
FILE: PT5MASSG.DWG
DWG BY: JAMES M. SPOTTS
DATE: 11-6-90 SCALE: 1:1
PROF. M. OKUMURA LABORATORY
DIVISION OF CHEMISTRY: CALIFORNIA INSTITUTE OF TECHNOLOGY

Figure 2-98

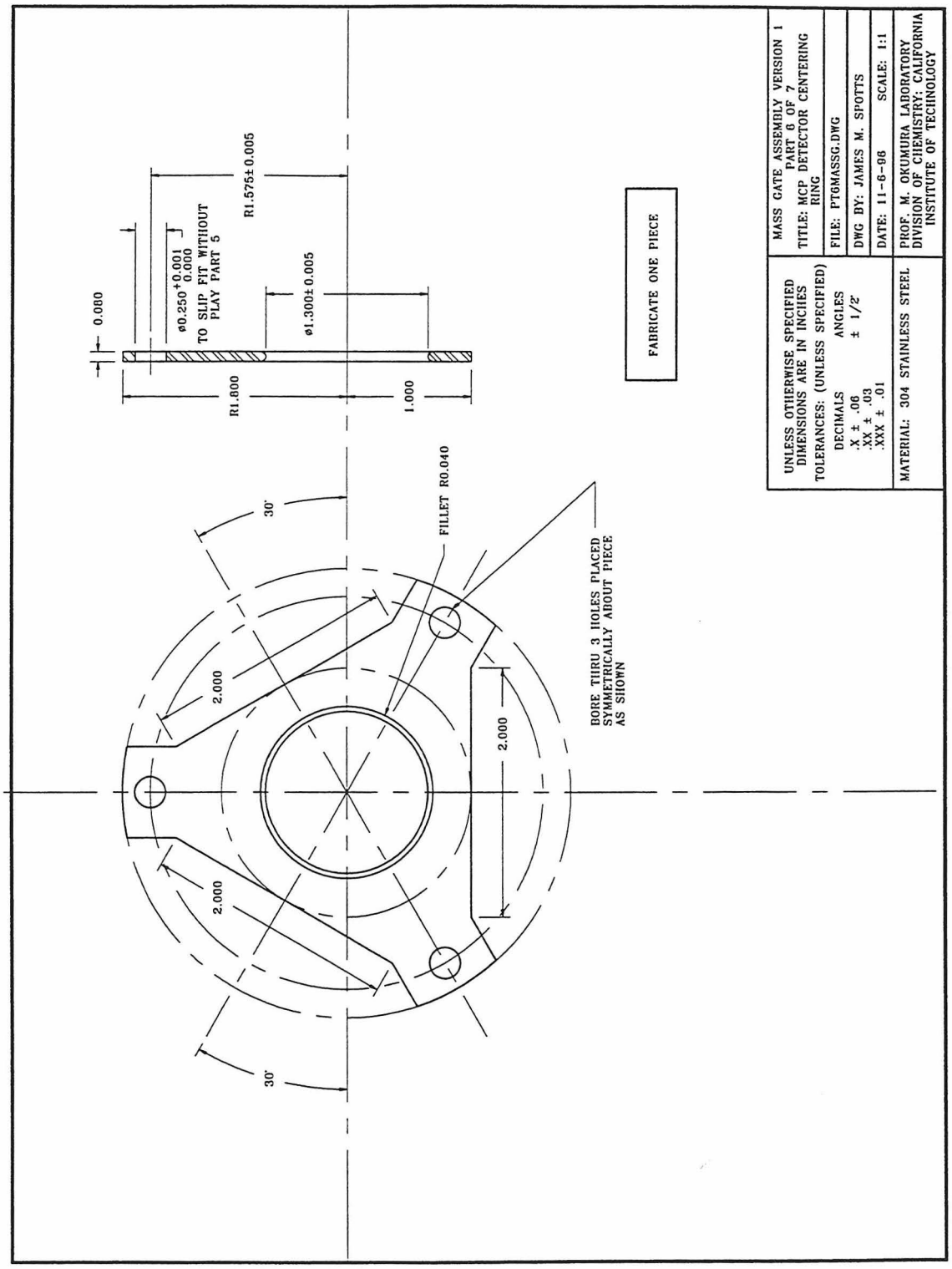

MASS GATE ASSEMBLY VERSION 1
PART 6 OF 7
TITLE: MCP DETECTOR CENTERING RING
FILE: PTGMASSG.DWG
DWG BY: JAMES M. SPOTTS
DATE: 11-6-96
SCALE: 1:1
PROF. M. OKUMURA LABORATORY
DIVISION OF CHEMISTRY: CALIFORNIA INSTITUTE OF TECHNOLOGY
UNLESS OTHERWISE SPECIFIED DIMENSIONS ARE IN INCHES
TOLERANCES: (UNLESS SPECIFIED)
DECIMALS ANGLES
.X ± .06 ± 1/2°
.XX ± .03
.XXX ± .01
MATERIAL: 304 STAINLESS STEEL
FABRICATE ONE PIECE
0.000
ø0.250 +0.001 0.000
TO SLIP FIT WITHOUT PLAY PART 5
R1.575± 0.005
ø1.300± 0.005
R1.000
1.000
FILLET R0.040
30°
2.000
2.000
2.000
30°
BORE THRU 3 HOLES PLACED SYMMETRICALLY ABOUT PIECE AS SHOWN

Figure 2-99

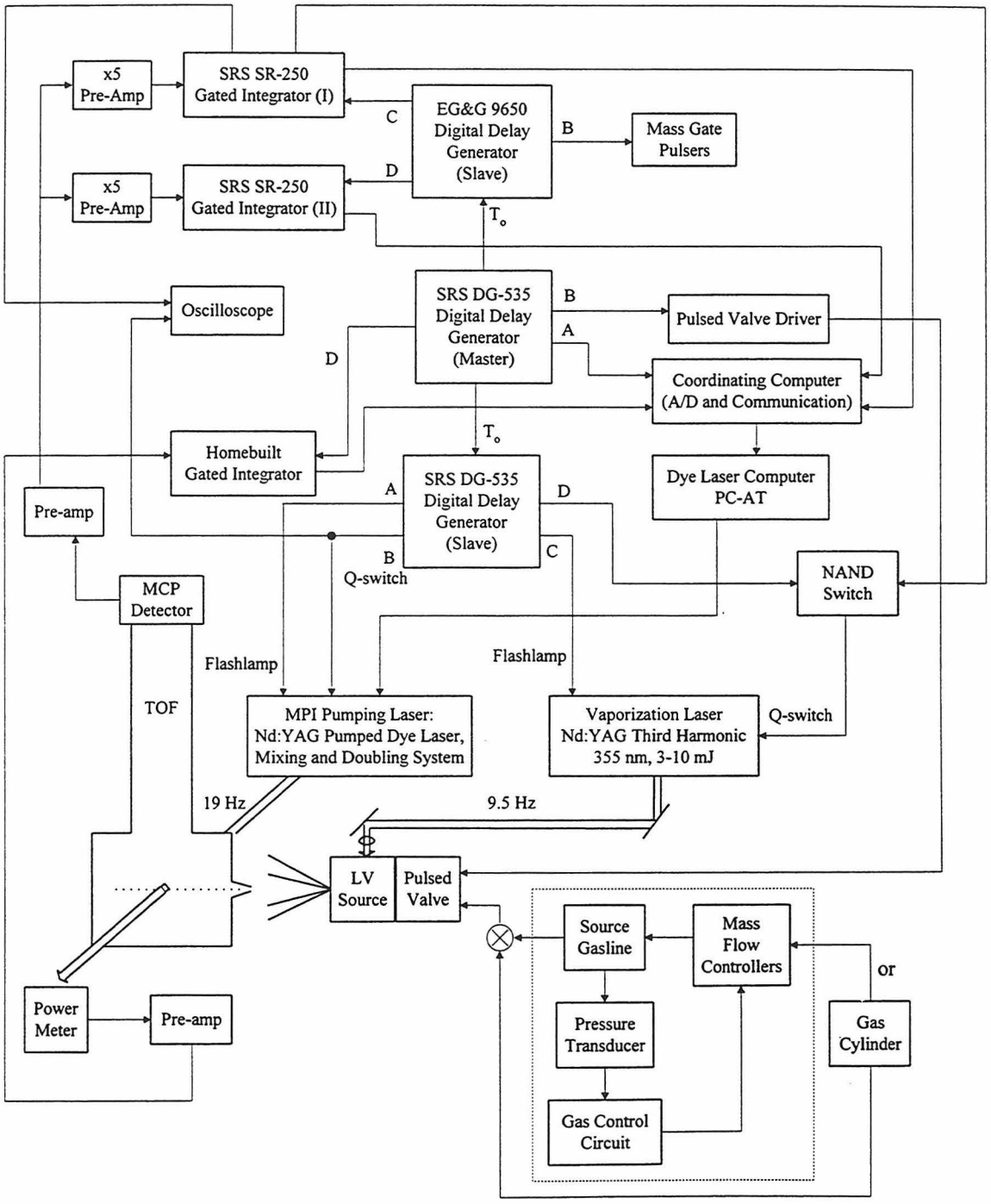

x5
Pre-Amp
SRS SR-250
Gated Integrator (I)
C
EG&G 9650
Digital Delay
Generator
(Slave)
B
Mass Gate
Pulsers
x5
Pre-Amp
SRS SR-250
Gated Integrator (II)
D
T_o
Oscilloscope
SRS DG-535
Digital Delay
Generator
(Master)
B
A
Pulsed Valve Driver
D
Coordinating Computer
(A/D and Communication)
T_o
Homebuilt
Gated Integrator
SRS DG-535
Digital Delay
Generator
(Slave)
Dye Laser Computer
PC-AT
A
D
Pre-amp
B
Q-switch
C
NAND
Switch
MCP
Detector
Flashlamp
Flashlamp
TOF
MPI Pumping Laser:
Nd:YAG Pumped Dye Laser,
Mixing and Doubling System
Vaporization Laser
Nd:YAG Third Harmonic
355 nm, 3-10 mJ
Q-switch
19 Hz
9.5 Hz
LV
Source
Pulsed
Valve
Source
Gasline
Mass
Flow
Controllers
or
Power
Meter
Pre-amp
Pressure
Transducer
Gas
Cylinder
Gas Control
Circuit

Figure 2-100

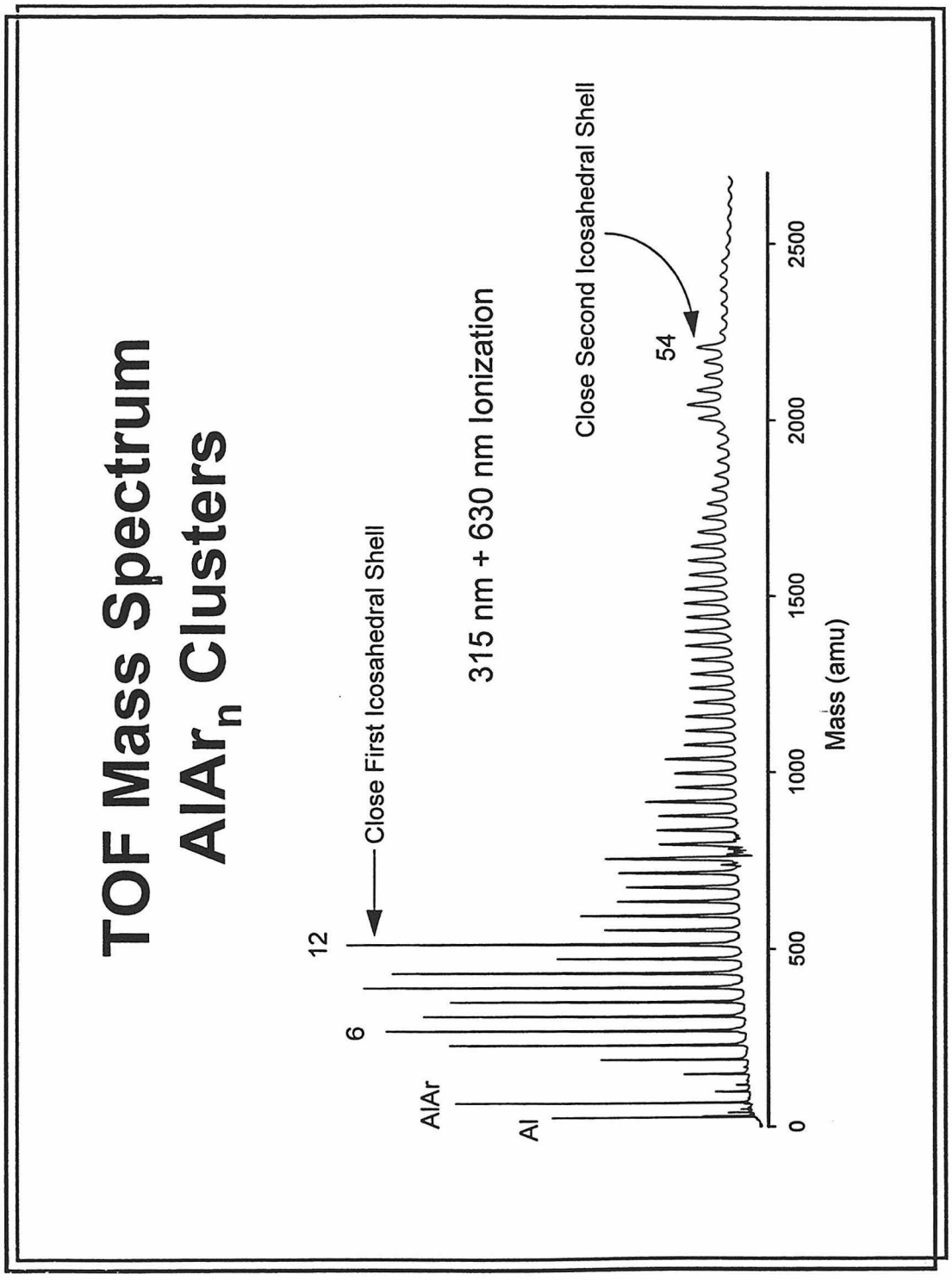

TOF Mass Spectrum
AlAr$_n$ Clusters
315 nm + 630 nm Ionization
Close First Icosahedral Shell
Close Second Icosahedral Shell
12
6
AlAr
Al
54
0
500
1000
1500
2000
2500
Mass (amu)

Figure 2-101

CHAPTER 3

Multiphoton Ionization Studies of the Al(3*d*)•Ar and Al(4*p*)•Ar Electronic Manifolds using both Single-Photon and Two-Photon Excitation Probes

3.1. Introduction

A dynamic model of the condensed phase requires a molecular level description of the N-body potential that govern the interaction of a single atom or molecule with the bulk. However, due to the enormous complexity of condensed phase systems, simplified models of the weak bonding interactions between solute and solvent have been sought. Diatomic systems involving a solute and solvent molecule, whether they be neutral, cationic, or anionic, provide a simplified conceptual framework from which detailed information of the pairwise interactions that govern bulk phase properties can be obtained. Furthermore, diatomic systems are in general amenable to *ab initio* calculations, often enabling a detailed description of the electronic nature of the weak bonding interaction between solute and solvent for both ground and excited electronic states to be understood to a high degree of precision.

3.1.1. Bonding Interactions in Metal-Rare Gas Systems

Neutral metal atom-rare gas molecules (M•RG) have been intensively investigated over the years due to their promise for uncovering the intricacies of how different electronic configurations of a metal solute affect binding to a spherically symmetrical and polarizable rare gas solvent molecule. As has been reviewed recently by Breckenridge,[1] complexes between rare gas atoms and Group 1 (the alkali metals),[2] Group 2 (the alkaline earth metals),[3-16] Group 12 (Zn, Cd, Hg),[3,17-19] or Group 13 (B, Al, In)[20-28] metal atoms have been the focus of considerable spectroscopic effort. A great deal of information has been gleaned as to the nature of the electronic interactions for both the ground (M•RG)

and excited states (M^{*}•RG).[1] In the end, what has arisen from these studies is an intuitively simple picture that has proven quite successful in presenting a unified description regarding the wealth of bond strengths and potential energy curve characteristics presently known for van der Waals complexes.

Due to the weak nature of van der Waals bonding ($1/R^6$ dependence), the degree of electron density placed along the internuclear axis proves to be the critical determinant of whether the nature of a particular M•RG diatomic electronic state will be attractive or repulsive.[1,29-30] A diatomic complex where the electronic state of the atom is spherically symmetric, such as those seen in the ground electronic states of atoms from Groups 1, 2, and 12, range a wide spectrum of bond strengths. The degree of binding in such systems depends critically upon the interplay between two opposing interactions. On one hand, the polarizabilities of the two *s*-type orbitals provides an attractive interaction via induced dipole-induced dipole forces between the two atomic moieties. Countering this bonding force, however, is a repulsive force that arises due to the coulomb repulsion along the internuclear axis between primarily the valance electrons within each of the two *s*-type orbitals on each atomic moiety. Therefore, a delicate balance between atomic orbital polarizability and spatial extent of the individual atomic orbitals along the internuclear axis determines the nature of the bond within such *s*-type σ-complexes.[1]

Electronic states where the metal valance electrons occupy non-spherically symmetric orbitals such as the *p*- or *d*-orbitals, however, are a bit more subtle due to the presence of orbital orientation effects. Electronic states arising from σ-type interactions, namely either M(n*p*σ)•RG or M(n*d*σ)•RG, tend to be predominantly repulsive in character

due to the high degree of electron density directed axially along the internuclear axis. In contrast, π-type states (M(n*p*π)•RG or M(n*d*π)•RG) or δ-type states (M(n*d*δ)•RG) are generally attractive to some degree since the nodal character of the metal atom orbital precludes the accumulation of electron density at the internuclear axis.[1] Furthermore, the directed nature of these orbitals serves to orient the lobes of the metal orbital in such a way as to accommodate the approach of a spherically symmetric rare gas atom along the internuclear axis. As with the case with two interacting *s*-type orbitals, issues of polarizability and orbital spatial extent are important to describe the bonding character of π-type or δ-type M•RG states, except orientation effects must now also be accounted for in conjunction with details of spatial extent. Nevertheless, since *d*-orbitals possess a higher concentration of electron density localised further away from the nucleus (and are hence more polarizable), metal atoms where the electrons reside in *d*-type orbitals are generally more strongly bound than those with electrons in *p*-type orbitals of the same principal quantum number.[1]

An additional facet that must be considered when discussing the energetics of van der Waals molecule binding presents itself in the context of the characterization of the excited electronic states of metal atom-rare gas (M^*•RG) complexes. In particular, a commonly accepted paradigm is that the binding energy of an excited electronic state of a given M^*•RG complex will lie somewhere between that of the neutral ground state (M•RG), and the ionic ground state (M^+•RG).[1] Such a view derives from a reasonable assumption that the electronic structure of an electronically excited M^*•RG complex should become more Rydberg-like as the energy of the electronic state increases. In

essence, with higher electronic excitation, the M^*•RG complex should evolve to a point where the excited electron no longer effectively shields the rare gas molecule from the metal ion core. The evolution of binding character from a weak, van der Waals interaction ($1/R^6$) to one that is more characteristic of an ion-atom/molecule interaction possessing a $1/R^4$ distance dependence has been well established experimentally.[1] While exceptions to this simple bonding picture do exist, particularly in the case of Li•He and Na•He,[2] most van der Waals bonding behavior can be rather accurately described within the context of these relatively uncomplicated atomic orbital-derived interactions.[1]

Recent work by Breckenridge and co-workers has provided a novel example of a doubly excited electronic state of Mg•Ar, namely Mg($3p\pi$,$3p\pi$ ^3P_J)•Ar($^3\Sigma^-$), whose bond strength was found to be 2850 cm^{-1}.[4-5,8] Such a large bond strength is rather unusual for third row complexes, exceeding the 1240 cm^{-1} bond strength of the ground state ion, Mg^+•Ar, by more that a factor of two. While at first appearing anomalous based upon the above discussion, the unusual bond strength for this electronic state can, in fact, be rationalized using the same intuitive picture. Similar to the case involving singly-excited diatomic species, M^*•RG, the doubly-excited magnesium atom is believed to possess a partial doubly-charged core, with the two excited electrons each occupying one of the $3p$ orbitals lying orthogonal to the internuclear axis. The presence of an ionic core with high dicationic character, combined with the absence of electron density along the internuclear axis that accommodates a close approach of the argon atom, is postulated to underlie this rather large bond energy.

3.1.2. State Mixing in Metal-Rare Gas Systems

In the predictive bonding model thus described, the details of the electronic character of the van der Waals bond can be reduced to electrostatic interactions between isolated atomic-like orbitals. However, there is no intrinsic reason to preclude the possibility that complexities in van der Waals bonding behavior due to the presence of energetically-similar electronic states do not exist as they do for covalently-bound species. In particular, one issue that has been rarely observed, and hence remains poorly explored, is how the electronic nature of the bond is perturbed when two diabatic potentials arising from different electronic configurations cross in regions relevant to determining bond character. The opportunity to observe the resultant spectral complexity arising as a consequence of electronic state mixing, especially in cases where the metal moiety possesses a number of closely spaced atomic energy levels, offers a unique challenge to spectroscopists seeking a fundamental understanding of the scope of electronic bonding character present in weakly bound M•RG diatomic systems.

As has been well documented in the recent review by Breckenridge,[1] a common form of state mixing interaction that has been observed in metal-rare gas complexes is due to spin-orbit coupling interactions, either within a particular electronic manifold or between states arising from different electronic manifolds. The degree of the spin-orbit state mixing interaction is generally discussed within the context of the now ubiquitous Hund's cases (a) through (e) - an idealized parametric modeling scheme that provide benchmarks around which the continuum of spin-orbit interactions can be classified.[29-30] The majority of van der Waals systems as well as covalently bound systems are

characterized by either Hund's case (a) or Hund's case (b) behavior. Hund's case (a) and Hund's case (b) pertain to situations where the spin-orbit interaction within an electronic manifold is substantially smaller that the energy difference between adjacent electronic states. The primary difference between these two limiting cases is that Hund's case (a) electronic states possess well-defined total angular momentum values, Ω, while in Hund's case (b), Ω is no longer a good quantum number since the total spin, Σ, becomes decoupled from the internuclear axis. Consequently, electronic states of Hund's case (b) character that derive from the same electronic manifold must be treated as admixtures of states with different total angular momentum, Ω, values.

The other important limiting case of spin-orbit interaction relevant for the classification of van der Waals bond character is that provided by Hund's case (c). In Hund's case (c), the spin-orbit interaction between the electronic states within an electronic manifold becomes comparable to the energy separation between nearly electronic manifolds. The direct consequence of this is that states derived from different electronic manifolds can become significantly coupled to one another, resulting in complex bond character. A recent example of a system exhibiting partial Hund's case (c) character was provided experimentally by Dagdigian and co-workers as a result of the LIF studies on the Al•Ne van der Waals system, as well as subsequent theoretical work by Alexander and co-workers on the same system.[28] In particular, the closely spaced $^2\Pi_{1/2}(3p)$, $^2\Pi_{3/2}(3p)$, and $^2\Sigma^+_{1/2}(3p)$ states (using Hund's case (a) notation for clarity) derived from the ground electronic configurations were found to exhibit complex electrostatic and spin-orbit character. One unusual consequence was the observation that the potential energy

curve derived from the upper $^2\Pi$ state was more strongly bound than that for the lower $^2\Pi$ spin-orbit component.

State mixing effects due to spin-orbit interactions also underlie the existence of spin-orbit-induced predissociation in M•RG systems. For example, the Cd($5s5p\ ^1P_1$)•Xe state[31] was not able to be detected using laser induced fluorescence (LIF) techniques even though the analogous electronic state in the Cd•Ne, Cd•Ar, and Cd•Kr systems was observed.[32] The origin for this mysterious behavior was determined to be the result of a curve crossing with the nearby Cd($5s5p\ ^3P_2$)•Xe state within the bound region of the Cd($5s5p\ ^1P_1$)•Xe state potential. Confirmation of this curve crossing was provided by an action spectrum taken with a second 10 nm-delayed laser tuned to the Cd($5s6s\ ^1P_1 \leftarrow 5s5p\ ^3P_2$) atomic transition.[31] By scanning the first initial pump laser in the vicinity of spectral region where the Cd($5s5p\ ^1P_1$)•Xe state was expected to appear, the action spectrum revealed very efficient spin-orbit-induced predissociation which produced the Cd($5s5p\ ^3P_2$) atomic state exclusively. Likewise, similar observations were observed in the isoelectronic Zn•Xe system in the vicinity of the analogous Zn($4s4p\ ^1P_1 \leftarrow 4s4s\ ^1S_0$) atomic transition.[33-35]

An example of a non-crossing state mixing effect has recently been reported by Massick and Breckenridge during their investigation of the Mg($3s4d\pi\ ^3D_J$)•Ar($^3\Pi$) and Mg($3s5p\pi\ ^3P_J$)•Ar($^3\Pi$) electronic states.[9] Both states were probed by resonant two photon ionization from the metastable Mg($3s3p\pi\ ^3P_J$)•Ar($^3\Pi_{0+,0-}$) state. Transition to the Mg($3s5p\pi\ ^3P_J$)•Ar($^3\Pi$) electronic state is strictly forbidden for single photon excitation, yet this state was observed with comparable intensity to the single photon allowed

transition to the Mg($3s4d\pi\ ^3D_J$)•Ar($^3\Pi$) electronic state. Both states were found to be strongly bound with comparable r_e values. Since the magnesium atomic states that both upper states correlate to differ in energy by only 60 cm^{-1}, significant state mixing between the upper excited diabatic states to create two "nested" adiabatic states was invoked to explain how the nominally forbidden Mg($3s5p\pi\ ^3P_J$)•Ar($^3\Pi$) state was observed. Due to the similarities in binding character between these two states, however, no perturbations due to curve crossings between the Mg($3s4d\pi\ ^3D_J$)•Ar($^3\Pi$) and Mg($3s5p\pi\ ^3P_J$)•Ar($^3\Pi$) electronic states were discovered, suggesting that each mixed adiabatic curve remains separated in energy, each with a regular vibrational progression characteristic to an individual adiabat.

As a result of the spectroscopic work described in Chapter 5 detailing the evolution of electronic character of the Al($3d$) electronic states with increasing Ar solvation, there was strong circumstantial evidence for state mixing effects between the Al($3d$) and Al($4p$) electronic states of the Al•$(Ar)_n$ ($n \leq 60$) clusters. This chapter and the following one describe the first characterization of the Al($4p$)•Ar electronic excited states, as well as a re-evaluation of previously published work by Morse and co-workers describing the electronic spectroscopy of the Al($3d$)•Ar electronic excited state.[36] Analysis of the electronic spectra of the Al($3d$)•Ar and Al($4p$)•Ar states clearly demonstrates complicated electronic state mixing in the diatomic species Al•Ar species - a fact that will bear considerable significance to the spectroscopic behavior observed in the Al•$(Ar)_n$ ($n \leq 60$) cluster systems detailed in Chapter 5.

3.2. Background on the Al•Ar Molecule

Aluminum-rare gas (Al•RG) systems (RG = Ne, Ar, Kr, and Xe) have been the subject of extensive spectroscopic work, with the vibronic states of both Al•Ar and Al•Kr having been characterized up to the ionization limit.[1,36] The ground state of the aluminum atom is open shell with a $3s^2 3p^1$ configuration. Spin-orbit interactions serve to break the degeneracy of the $3p$ orbitals, resulting in the observed Al($^2P_{1/2}$) and Al($^2P_{3/2}$) atomic states that are split by 112.04 cm^{-1} in energy.[37] Interaction with Ar($^1S_0$) gives rise to a total of three electronic states for each of the two atomic aluminum spin-orbit components. The absolute ground state of Al•Ar, the doubly degenerate $X_1\ ^2\Pi_{1/2}$ state, arises from the Al($^2P_{1/2}$) + Ar($^1S_0$) manifold, as does a repulsive $A_1\ ^2\Sigma_{1/2}$ state. Similarly, interaction arising from the Al($^2P_{3/2}$) + Ar($^1S_0$) upper spin-orbit component manifold gives rise to three additional electronic states, $X_2\ ^2\Pi_{3/2}$ and $A_2\ ^2\Sigma_{1/2}$, the former being doubly degenerate.[29-30]

The first excited electronic state of the Al•Ar molecule, the $B\ ^2\Sigma_{1/2}$ state, arises from the interaction of the Al($4s\ ^2S_{1/2}$) atomic state with Ar($^1S_0$). Although the $B\ ^2\Sigma_{1/2} \leftarrow X_1\ ^2\Pi_{1/2}$ transition has been the subject of substantial experimental effort, a definitive characterization of the potential curves underlying this transition has proven difficult, especially with respect to the accurate determination of the ground state bond dissociation energy. Initial work by Lester and co-workers using resonance-enhanced multiphoton ionization (REMPI) placed bounds on the $B\ ^2\Sigma_{1/2}$ state bond dissociation energy (D_o) as 373 cm^{-1} < D_o < 514 cm^{-1}.[38] Callender, Hackett, and Mitchell later extended this work using laser induced fluorescence (LIF) excitation and dispersed

emission.[39] Employing a linear Birge-Sponer analysis, Callender *et al.* reported a D_o value of 136 ± 65 cm^{-1} for the $X_1\ ^2\Pi_{1/2}$ state, and 369 ± 65 cm^{-1} for the $B\ ^2\Sigma_{1/2}$ state. Furthermore, these workers established the spin-orbit splitting between the $X_1\ ^2\Pi_{1/2}$ and $X_2\ ^2\Pi_{3/2}$ states to be 79.8 cm^{-1}. The experiment of Callender *et al.* was later extended by Heaven and co-workers who were able rotationally resolve the $B\ ^2\Sigma_{1/2} \leftarrow X_1\ ^2\Pi_{1/2}$ fluorescence spectrum.[40] This work uncovered an additional vibrational level, $v' = 7$, in the $B\ ^2\Sigma_{1/2}$ state, resulting in a modified D_o value for the $B\ ^2\Sigma_{1/2}$ state of $399\ ^{+35}/_{-8}$ cm^{-1}. This correction enabled Heaven and co-workers to report a modified D_o value for the $X_1\ ^2\Pi_{1/2}$ ground state of $165\ ^{+40}/_{-10}$ cm^{-1}.

Further complicating the determination of the accurate $X_1\ ^2\Pi_{1/2}$ ground state dissociation energy was the report by Morse and co-workers of a $X_1\ ^2\Pi_{1/2}$ D_o value of 122.4 ± 4 cm^{-1}.[36] In contrast to the previous experiments, Morse and co-workers calculated their ground state D_o value from their determination of the D_o value of the electronic states arising from the Al(3*d*) + Ar($^1S_0$) rather than the Al(4*s*) + Ar($^1S_0$) asymptote. Furthermore, this work reported a spin-orbit splitting between the $X_1\ ^2\Pi_{1/2}$ and $X_2\ ^2\Pi_{3/2}$ states of 80.9 ± 2 cm^{-1} as determined by observation of the ionization threshold onset. This value is in close agreement to the 79.8 cm^{-1} value reported by Callender *et al.* using dispersed fluorescence.

This significantly lower value for the dissociation energy of the $X_1\ ^2\Pi_{1/2}$ state was later supported by theoretical work performed by Partridge, Bauschlicher, and Visscher.[41] Using a RHF/CCSD(T)/AANO level of theory, Partridge *et al.* obtained a D_o value of 114.0 cm^{-1} for the $X_1\ ^2\Pi_{1/2}$ state. Clearly, there exists a marked discrepancy between the

$X_1\ ^2\Pi_{1/2}$ D_o values obtained from the experimentally derived Al($4s$) + Ar($^1S_0$) and Al($3d$) + Ar($^1S_0$) asymptotic energies. Using theory as an arbiter, it would appear that D_o values derived from the B state measurements are most likely in error. The origin of this error is presumably due to the presence of a barrier at large internuclear distances for the $B\ ^2\Sigma_{1/2}$ state. Given the measurements from Heaven and co-workers as well as Morse and co-workers, the barrier height for the $B\ ^2\Sigma_{1/2}$ state can be estimated to be roughly 40 cm^{-1}.[36,40]

3.3. Background on the Al($3d$)•Ar and Al($4p$)•Ar States

Electronic states arising from the Al($3d$) + Ar($^1S_0$) and Al($4p$) + Ar($^1S_0$) asymptotes represent the next two excited electronic states following the $B\ ^2\Sigma_{1/2}$ state. Two spin-orbit components are derived from the excited $3s^23d^1$ of atomic aluminum electronic configuration, namely $^2D_{3/2}$ and $^2D_{5/2}$. The spin-orbit splitting between the $^2D_{3/2}$ and $^2D_{5/2}$ states is significantly smaller than that observed in the ground state, only 1.34 cm^{-1} compared to 112.04 cm^{-1} for the latter spin-orbit manifold.[37] Lying roughly 522 cm^{-1} above the Al($3d$) atomic states are those arising from the Al($4p$) state.[37] In direct analogy to the ground state, two atomic spin-orbit components of the Al($4p$) $3s^24p^1$ electronic configuration, $^2P_{1/2}$ and $^2P_{3/2}$, are observed with a splitting of 15.83 cm^{-1}.[37]

The close proximity of the Al($3d$) and Al($4p$) states offers the possibility that state mixing effects might be observed in the Al•Ar molecule, provided that the electronic states derived from the Al($4p$)•Ar manifold possess bond strengths comparable in energy to the separation between the Al($3d$) + Ar($^1S_0$) and Al($4p$) + Ar($^1S_0$) asymptotes. The degree and type of state mixing that might be expected, however, depends critically upon the

electronic symmetries of the states arising from both the Al($3d$)•Ar and Al($4p$)•Ar manifolds.

An attractive yet potentially daunting feature for any spectroscopist interested in the Al($3d$)•Ar and Al($4p$)•Ar region is the large number of electronic states present within a rather small 1000 cm^{-1} energy region. Each $^2D_{3/2}$ and $^2D_{5/2}$ spin-orbit component of the Al($3d$) $3s^2 3d^1$ electronic configuration can interact with an Ar($^1S_0$) atom to form a manifold of Δ, Π, and Σ electronic states.[29-30] Using a Hund's case (a) notation, a total of ten electronic states - $^2\Delta_{5/2}$, $^2\Delta_{3/2}$, $^2\Pi_{3/2}$, $^2\Pi_{1/2}$, and two $^2\Sigma^+_{1/2}$ - derive from the Al($3d$)•Ar manifold, the Δ and Π states being doubly degenerate. Due to the small spin-orbit splitting in the $^2D_{3/2}$ and $^2D_{5/2}$ atomic states, diatomic states of equal orbital angular momentum, Λ, but different total angular momentum, Ω, are expected to lie close in energy.

Analogous to the ground state Al($3p$) + Ar($^1S_0$) manifold, six electronic states arise from the Al($4p$) + Ar($^1S_0$) manifold - three from each spin orbit component (the Π states being doubly degenerate). Interaction of Ar($^1S_0$) with the lower aluminum spin-orbit component, $^2P_{1/2}$, gives rise to $^2\Pi_{1/2}$ and $^2\Sigma^+_{1/2}$ states, while the upper spin-orbit component, $^2P_{3/2}$, gives rise to $^2\Pi_{3/2}$ and $^2\Sigma^+_{1/2}$ states. For the sake of simplicity, the double degeneracy of the Δ and Π diatomic electronic states will be ignored for the remainder of this chapter.

The initial characterization of the Al•Ar vibronic states arising from the Al($3d$) + Ar($^1S_0$) manifold was published by Morse's group as part of their comprehensive survey of all electronic states for Al•Ar and Al•Kr from Al($3d$)•Ar/Kr up to the ionization limit.[36] A

total of four electronic states were assigned to the spectral region around the aluminum atomic $3d \leftarrow 3p$ transition. Three vibronic progressions were assigned as arising from three electronic states converging to the Al($3d$) + Ar($^1S_0$) asymptote, namely $^2\Delta(3d)$, $^2\Pi(3d)$, and $^2\Sigma^+(3d)$. Spin-orbit splittings within the vibronic bands arising from states of equal orbital angular momentum, Λ, were stated to be unresolved, presumably due to the small splitting observed in the atom. In addition, an abrupt cutoff in signal, preceded by an apparent predissociative broadening within the highest vibronic spectral feature, enabled a bond dissociation threshold of 32557.8 cm^{-1} to be determined.[36]

The $^2\Delta(3d)$, $^2\Pi(3d)$, and $^2\Sigma^+(3d)$ bands were assigned according to the magnitude of the bond strength using the rationale discussed in Section 3.1.1. The $^2\Delta(3d)$ state was assigned as the most strongly bound due to the energetically favorable Al($3d\delta$)•Ar δ-type interaction. Vibrational analysis of the $^2\Delta(3d)$ band as well as comparison with isotopic shifts from the analogous Al($3d$)•Kr $^2\Delta(3d)$ band led the authors to conclude that the 0-0 vibronic level had been observed, yielding a D_o for this state of 525 cm^{-1}.[36] The next most strongly bound state was assigned as the $^2\Pi(3d)$ because the π-type interaction was reasonably assumed to lie intermediate in strength to a δ-type and a σ-type bonding interaction. This state was reported to have a D_o value of 136.6 cm^{-1}, only slightly higher than the $X_1\ ^2\Pi_{1/2}$ ground state.[36] Lastly, a narrowly spaced vibronic progression that converged to the proposed dissociation threshold was tentatively assigned as arising from the $^2\Sigma^+(3d)$ state. Nevertheless, the reported D_o for the $^2\Sigma^+(3d)$ state, namely 40.3 cm^{-1},[36] was unexpectedly large, and was apparently inconsistent with the weak bonding character expected from σ-type interactions between third row atomic moieties.

The tentative assignment of the progression within the same spectral region as those assigned to arise from Al(4*p*)•Ar states was intriguing, yet somewhat perplexing. Regardless of the fact that transitions to the Al(4*p*)•Ar manifold were strictly single-photon forbidden from the ground state, what was particularly striking about this assignment was that the Al(4*p*)•Ar 0-0 vibronic band appeared almost 100 cm^{-1} to the red of the $^2\Pi(3d)$ 0-0 vibronic band, yielding a surprisingly large reported D_o value of 744.1 cm^{-1} for the Al(4*p*)•Ar state.[36] State mixing due to the close proximity of the $^2\Pi(3d)$ and $^2\Pi(4p)$ states would have explained the mechanism by which transitions to the Al(4*p*)•Ar state possessed some single-photon character. Nevertheless, the large D_o of the Al(4*p*)•Ar state relative to the Al(3*d*)•Ar state almost certainly implied a significantly smaller equilibrium bond distance, r_e, for the former state. Such a situation required that the two diabatic potential energy curves for these states cross at some point either above or below the dissociation limit for the Al(3*d*)•Ar state, resulting in two mixed adiabatic potentials. Such a crossing should have resulted in perturbations in the $^2\Pi$ vibronic spectra of both states, although none were observed in the vibronic progressions for both the Al(3*d*)•Ar and Al(4*p*)•Ar states assigned by Morse and co-workers.

Another worrisome feature of the assignment proposed by Morse and co-workers was that a number of spectral features remained unassigned. While these extra lines potentially could have been due to spurious signals from fragmentation events in higher clusters, their presence is nevertheless disturbing for one attempting to definitively understand the true nature of the electronic states in this spectral region. Of particular interest was whether any of these allegedly spurious lines were, in fact, the result of

vibronic perturbations due to a curve crossing between the Al(3*d*)•Ar and Al(4*p*)•Ar diabatic states.

These ambiguities, especially with respect to the true nature of the Al(4*p*)•Ar potential, motivated us to re-examine the spectral region containing both Al(3*d*)•Ar and Al(4*p*)•Ar states. In particular, we extended the work from Morse's group by performing single color $2_{vis} + 1_{vis}$ two-photon REMPI within the 31800 cm^{-1} to 33500 cm^{-1} spectral region relevant to both Al(3*d*)•Ar and Al(4*p*)•Ar electronic manifolds. By employing two-photon excitation in addition to the single photon excitation employed previously by Morse and co-workers, our experiments were sensitive to vibronic levels of both Al(3*d*)•Ar or Al(4*p*)•Ar character, as well as any states of mixed electronic character.

3.4. Experimental

Specific details related to the experimental apparatus employed for these experiments have been extensively outlined in Chapter 2. Only a brief synopsis is included here. The reader is also referred to the previous chapter for specific features related to the experimental methodology.

The Al•Ar van der Waals molecule was generated by standard laser ablation techniques. Following the opening of a piezoelectric pulsed valve, the pure argon carrier gas (~8-10 atm. stagnation pressure) was injected into either the second or third generation laser vaporization source described in Chapter 2. The tripled output of a Nd-YAG laser (Continuum Surelite 1) was focused on the surface of a rotatable 2024 alloy aluminum target rod that was positioned directly adjacent to the throat of the supersonic

expansion. Following the supersonic expansion, the jet was skimmed by a 3 mm orifice diameter skimmer (Beam Dynamics), and introduced into the second differential pumping region.

Two principal modes of resonant multi-photon excitation (MPI) were employed for these experiments as shown in Figure 3-1. The first, presented on the left hand side of Figure 3-1, was a $1'_{UV} + 1_{vis}$ mode, where a single UV photon was used excite single-photon allowed transitions to the Al(3*d*)•Ar and Al(4*p*)•Ar manifolds, followed by direct ionization by a single visible photon. For the experiments described, the UV light was generated by frequency doubling the output of a Quantel/Continuum TDL-51 dye laser pumped by a frequency doubled (532 nm) Continuum NY61-20 Nd:YAG laser (1064nm). The laser dyes and dye mixtures used for these experiments - DCM, Rh640, Rh640/Rh610 (50:50 mixture), and Rh610 (all purchased from Exciton) - were all used as straight methanol solutions.

Doubling of the dye fundamental from the TDL-51 was accomplished using a Continuum UVX-3 UV extension unit equipped with mixing, doubling and mixing after doubling capabilities. Straight doubling, using a Continuum DCC-2 crystal (378 nm - 283 nm) was employed to generate all UV photons for these experiments. Manual tracking of the doubling crystal orientation was employed for all $1'_{UV} + 1_{vis}$ by optimizing for maximal UV power.

The visible ionization pulse for the $1'_{UV} + 1_{vis}$ MPI scheme was taken from the residual undoubled dye exiting the DCC-2 crystal. Therefore, the energy of the visible ionization pulse was always half that of the UV pump pulse. The atomic aluminum

ionization potential is 5.986 eV, or 48278 cm^{-1}, while that of Al•Ar was determined to be 47342.6 cm^{-1}.[36,42] For a typical single-photon excitation from the Al(3*d*)•Ar ← Al(3*p*)•Ar region near 32450 cm^{-1}, the visible ionization pulse would be 16225 cm^{-1} or 616 nm. The total energy in this case would be 48675 cm^{-1}. In all cases, therefore, the total photon energy used for the MPI process was always well above the Al•Ar ionization energy of 47342.6 cm^{-1} for all scanned wavelength regions.

The second mode of resonant multi-photon excitation (MPI) that was employed for these experiments is shown on the right-hand side of Figure 3-1, and utilized only the visible color of the $1'_{UV} + 1_{vis}$ experiment outlined above. In essence, this was a single-color $2_{vis} + 1_{vis}$ MPI scheme where excitation to the Al(3*d*)•Ar and Al(4*p*)•Ar manifolds was achieved by a two-photon pump of equal energy to that of the single UV photon utilized for the $1'_{UV} + 1_{vis}$ experiments. In this manner, we could efficiently probe states of Al(4*p*)•Ar character - states where transitions are single-photon forbidden but two-photon allowed. When scanning in this mode, the straight dye output from the TDL-51 dye laser was employed.

For wavelength calibration within the DCM and Rh640 wavelength regions, the atomic Al(3*d*) ← Al(3*p*) transitions were employed.[37] Calibration within the 50:50 Rh640/Rh610 mixture and Rh 610 wavelength range was performed using the atomic Al(4*p*) ← Al(3*p*) transitions via two-photon excitation.[37] In cases where the visible power was low, a 150 mm focal length lens was employed to drive the two-photon transitions. The resolution of the spectra obtained using both $1_{UV} + 1'_{vis}$ and $2_{vis} + 1_{vis}$ modes of excitation was 0.08 cm^{-1}, the specified resolution of the TDL-51 grating. Calibration

scans were performed using the smallest grating step size permissible by the DYEDATA program, namely 0.11 cm^{-1} at 308 nm. The reported absolute peak positions should therefore be accurate to within 0.11 cm^{-1}. Note that simultaneous calibration against a universal calibration spectrum such as that provided by the commonly employed I_2 molecule was not performed for the reported spectral features.

Spectroscopic features were obtained by monitoring the $Al•Ar^+$ (mass 67) and Al^+ (mass 27) signals as a function of pump laser frequency. By monitoring Al^+ fragment signal in addition to the $Al•Ar^+$ signal, we were sensitive to any dissociative transitions that would occur in the spectral region of interest - a feature that proved extremely important during the course of this work.

Following ionization, the clusters were extracted perpendicularly and mass-analyzed by a standard 1 m Wiley-McLaren time-of-flight (TOF) spectrometer,[43] and detected by a chevron dual-microchannel plate detector. A typical TOF mass spectrum can be seen in Figure 2-101 in Chapter 2. Individual scans were recorded by gating the mass peak of interest with a gated integrator (SR-250, Stanford Research Systems). S/N was greatly improved by switching the laser vaporization Q-switch at half the repetition rate and using the gated integrator to subtract the pump background due to DP oil contaminant fragments (LV off) from every signal shot (LV on). Analog-to-digital conversion of the integrated signal was accomplished by a triggered data acquisition on a Keithley-Metrabyte DAS-1602 board. All spectra were power normalized for pump laser fluence as determined by separate power dependence scans.

3.5. Results

In order to simplify the presentation and discussion of the observed vibronic features, the scanned spectral region will be presented as consisting of two distinct regions - the spectral region above the Al(3*d*)•Ar dissociation limit and that below. Note that this is somewhat arbitrary, since some vibronic features are observed to lie within both regions, but will prove a convenient framework nonetheless.

3.5.1. 2_{vis} + 1_{vis} and 1_{UV} + $1'_{vis}$ REMPI Spectra of Al•Ar and Al Fragments Above the Al(3d)•Ar Dissociation Limit

3.5.1.1. 2_{vis} + 1_{vis} REMPI Spectra Above the Al(3d)•Ar Dissociation Limit

The main motivation for this work was to try to characterize the electronic states arising from the Al(4*p*)•Ar manifold. To this end, 2_{vis} + 1_{vis} single color REMPI was employed in the region between the Al(3*d*)•Ar dissociation limit at 32557.8 cm^{-1} to 33050 cm^{-1} above the highest energy atomic Al(4*p*) ← Al(3*p*) transitions. The spectra that we obtained monitoring both the $Al•Ar^+$ signal as well as any Al^+ signal arising from fragmentation of the diatomic molecule is shown in Figure 3-2. The observed band positions of the vibronic features for these spectra are compiled in Table 3-1. Above 32670 cm^{-1}, two clean vibronic progressions were clearly recognizable, distinguished by the letters A and B in Figure 3-2 and Table 3-1. Signal was obtained in both the $Al•Ar^+$ as well as Al^+ channels, indicating significant coupling of these bound vibronic bands with another electronic state possessing dissociative continuum within the same spectral region.

The separation between adjacent bands, e.g., A2-B2, A3-B3, etc., are tabulated in Table 3-2. As shown in Table 3-1, both Al•Ar$^+$ and Al$^+$ fragment signal spectra revealed similar vibronic band positions. The separation of 11-14 cm^{-1} between adjacent vibronic levels above 32670 cm^{-1} compares very well with the atomic Al $^2P_{1/2}(4p)$ - $^2P_{3/2}(4p)$ spin-orbit splitting of 15.83 cm^{-1}. Therefore, the two progressions labeled A and B have been assigned as arising from the $^2\Pi_{1/2}(4p)$ and $^2\Pi_{3/2}(4p)$ electronic states respectively. An incremental decrease in the observed spin-orbit coupling between the $^2\Pi_{1/2}(4p)$ and $^2\Pi_{3/2}(4p)$ electronic states with decreasing vibrational quantum number was indicative of a gradual evolution from strong Hund's case (a) character to include partial Hund's case (b) character. The possible origin of this shift in Hund's case character will be discussed below.

In the region between the Al(3*d*)•Ar dissociation limit and the regular progression above 32670 cm^{-1}, the two-photon spectrum for the $^2\Pi_{1/2}(4p)$ and $^2\Pi_{3/2}(4p)$ electronic states was noticeably perturbed. In particular, the $^2\Pi_{1/2}(4p)$ progression was strongly affected by this perturbation. The first evidence for the effect of this perturbation on the $^2\Pi_{1/2}(4p)$ electronic states was already evident in peak A4. Inspection of peaks A1/B1 through A3/B3 reveal an intensity pattern in the Al•Ar$^+$ spectrum where the $^2\Pi_{1/2}(4p)$ vibronic band was more intense than the $^2\Pi_{3/2}(4p)$ vibronic band. Peak A4 in the Al•Ar$^+$ spectrum demonstrated a reversal in this intensity pattern, with the $^2\Pi_{1/2}(4p)$ vibronic peak demonstrating a marked decrease in intensity relative to the $^2\Pi_{3/2}(4p)$ vibronic band. At the same time, peak A4 exhibited increased fragmentation in the Al$^+$ spectrum, which was strongly indicative of a selective increase in coupling to the dissociative continuum of a

nearby electronic state. With peak A5, evidence of this coupling was even more pronounced. Specifically, the A5 peak was significantly weaker in intensity relative to B5 in the $Al{\bullet}Ar^+$ spectrum, as well as being broadened presumably due to a rapid fragmentation process.

Peak A6 was completely absent in the $Al{\bullet}Ar^+$ spectrum, while the Al^+ fragment signal spectrum exhibited an intense broad (~ 40 cm^{-1} FWHM) feature. This strongly dissociative feature was indicative of the precise curve crossing position between the potentials arising from the $^2\Pi_{1/2}(4p)$ state and the dissociative continuum of the strongly coupled electronic state. The state to which both $^2\Pi_{1/2}(4p)$ and $^2\Pi_{3/2}(4p)$ states were believed to be coupled was a repulsive $^2\Sigma^+_{1/2}(3d)$ state arising from the $Al(3d){\bullet}Ar$ electronic manifold. Note that the peak labeled S in the $Al{\bullet}Ar^+$ spectrum was not believed to be the perturbed $^2\Pi_{1/2}(4p)$ A6 vibronic feature, but rather a quasi-bound level in the $^2\Sigma^+_{1/2}(3d)$ dissociative potential or an accidental resonance. Evidence for this derived from the Al^+ spectrum, where the S peak corresponded to a dip in the broadly dissociative Al^+ signal. This suggested the existence of a state whose lifetime exceeds that of the dissociative $^2\Pi_{1/2}(4p)$ state in this region.

In an attempt to understand what was happening to the $^2\Pi_{1/2}(4p)$ and $^2\Pi_{1/2}(4p)$ electronic states within this perturbed region as well as to the red of this region, the predicted vibronic peak positions for the $^2\Pi_{1/2}(4p)$ and $^2\Pi_{1/2}(4p)$ were derived by linear extrapolation from the largely unperturbed A2, A3, A4, and A5 as well as the B2, B3, B4, and B5 vibronic levels. The predicted A6, A7, A8, and A9 vibronic band positions for the $^2\Pi_{1/2}(4p)$ state are compiled in Table 3-3. Similarly, the predicted B6, B7, B8, and B9

vibronic band positions for the $^2\Pi_{3/2}(4p)$ state are compiled in Table 3-4. As expected, the $^2\Pi_{3/2}(4p)$ state was only moderately perturbed by the curve crossing with the $^2\Sigma^+_{1/2}(3d)$ state. The strongest evidence for a strong perturbation in this electronic state above the Al($3d$)•Ar dissociation limit occurred at vibronic level B6, the higher spin-orbit component of the highly perturbed A6 peak of the $^2\Pi_{1/2}(4p)$ state. While the B6 vibronic band did not appear significantly broadened by the nearby curve crossing, its peak position was nevertheless blue-shifted by 8 cm^{-1} from the predicted position of 32644 cm^{-1} to the observed position at 32652 cm^{-1}. However, the next vibronic level, B7, appeared almost unperturbed, exhibiting a small red-shift of 3 cm^{-1} from the predicted position at 32575 cm^{-1} to the observed position at 32572 cm^{-1}. Hence, this state seemed to manifest only a highly localized strong coupling interaction with the $^2\Sigma^+_{1/2}(3d)$ state.

The same cannot be concluded for the $^2\Pi_{1/2}(4p)$ state. Beyond the A5 vibronic level of the $^2\Pi_{1/2}(4p)$ state, all subsequent lower vibronic levels manifested strongly perturbed character indicative of substantial mixing with the $^2\Sigma^+_{1/2}(3d)$ dissociative state. As shown in Table 3-3, the predicted peak position for the strongly dissociative A6 vibronic level was 32634 cm^{-1}. The maximum of the broad Al^+ fragment signal arising from the A6 peak lay very close to the predicted position, namely 32626 cm^{-1}. The next vibronic level in the progression, the peak labeled by A7, was predicted to be located at 32566 cm^{-1}, only 10 cm^{-1} above the Al($3p$)•Ar dissociation limit. As is evident from the Al•Ar^+ and Al^+ fragment signal spectra in Figure 3-2, no feature was apparent in this region. A peak with high two-photon character lying just below the Al($3p$)•Ar dissociation limit at 32548 cm^{-1} has been assigned as the A7 vibronic level. This implied

an 18 cm^{-1} red-shift in the A7 vibronic level relative to the predicted peak position at 32566 cm^{-1}. Such a strong shift indicated that the electronic wavefunction of the $^2\Pi_{1/2}(4p)$ state was considerably more strongly coupled to the $^2\Sigma^+_{1/2}(3d)$ state in comparison to the $^2\Pi_{3/2}(4p)$ state, consistent with the substantially greater magnitude of the observed vibronic perturbations.

Two features in this spectral range, namely X1 and X2, remain unassigned. In the absence of evidence for other electronic states such as those from the quartet manifold, these features were most likely fragment peaks from higher clusters. Attempts to monitor the Al•Ar_2 spectrum in this spectral region were significantly hampered by our source which produced only negligible amounts Al•Ar_2 ion signal. The resulting spectra were consistently noisy and ambiguous, providing little definitive evidence whether or not peaks X1 and X2 were truly due to fragmentation processes within the Al•Ar_2 trimer.

3.5.1.2. $1'_{UV} + 1_{vis}$ REMPI Spectra Above the Al(3d)•Ar Dissociation Limit

In addition to the two-photon excitation spectra presented above, single-photon UV excitation spectra were also obtained for both the diatomic Al•Ar^+ species and the Al^+ fragments over the same spectral range. The $1'_{UV} + 1_{vis}$ spectra obtained by monitoring both Al•Ar^+ (mass 67) and Al^+ (mass 27) can be seen in Figures 3-3 and 3-4 respectively. From the Al•Ar^+ spectrum three main features were observed, two of which, S and X1, appeared in the two-photon spectra discussed above. The new feature appeared directly to the red of the peak labeled S, and was believed to be the location of A6, the $^2\Pi_{1/2}(4p)$ vibronic band that was absent in the two-photon spectrum due to strong dissociative

coupling to the $^2\Sigma^+_{1/2}(3d)$ state. The A6 peak position was 32612.8 cm^{-1}. Upon examination of the predicted peak positions listed in Table 3-3, the expected location of peak A6 was 32634 cm^{-1}. Therefore, the strong coupling interaction between the $^2\Sigma^+_{1/2}(3d)$ and $^2\Pi_{1/2}(4p)$ states in this region served to red-shift the A6 vibronic band approximately 31 cm^{-1}.

It should be noted that the apparent signals observed above 32900 cm^{-1} were artifacts, caused either by the Al($4p$) ← Al($3p$) atomic transitions being DC coupled into the Al•Ar^+ gate, or surges in signal due to slight instabilities in the source. Since the A6 and S signals were so weak, these instabilities, which were otherwise negligible and buried in baseline noise, became detectable.

The Al^+ fragment signal spectrum obtained above the Al($3d$)•Ar dissociation limit shown in Figure 3-4 exhibited several features that had been previously observed, as well as four additional ones. The new features, labeled X3, X4, X5, and X6 in Figure 3-4, were of unknown origin - possibly due to either fragments of higher clusters or dissociative transitions from some unknown metal-aluminum heteromeric diatomic formed from trace impurities in the target rod. Another unknown feature correlated with the high intensity of the X2 peak at 32587.6 cm^{-1} which appeared weakly in the $2_{vis} + 1_{vis}$ REMPI spectrum seen in Figure 3-2. While it was possible that peak X2 is, in fact, the A6 vibronic band of the $^2\Pi_{1/2}(4p)$ state that is strongly perturbed by strong coupling to the $^2\Sigma^+_{1/2}(3d)$ state, such an assignment would have implied an approximately 46 cm^{-1} red-shift relative to the predicted peak position. While this was possible, it was nonetheless improbable. In light of the peak assigned as A6 that was observed at 32612.8 cm^{-1} in the

$AlAr^+$ $1'_{UV} + 1_{vis}$ REMPI spectrum shown in Figure 3-3, this feature was most likely an artifact.

In addition to these spurious features, two peaks, namely A4 and A5, assigned as arising from the $^2\Pi_{1/2}(4p)$ electronic state appeared with strong intensity to the blue of the region exhibiting strong perturbations. Peak B5, the higher spin-orbit component of peak A5, also appeared, but with significantly reduced intensity. Such observations were consistent with the hypothesis of a curve crossing between the $^2\Pi_{1/2}(4p)$ and $^2\Pi_{3/2}(4p)$ electronic states and the $^2\Sigma^+_{1/2}(3d)$ state. In this case, the $^2\Pi_{1/2}(4p)$ state was expected to couple significantly more strongly to the $^2\Sigma^+_{1/2}(3d)$ state relative to the $^2\Pi_{3/2}(4p)$ state in the limit of Hund's case (a) coupling in the Al($4p$)•Ar manifold.

The broad dissociative feature between 32600 cm^{-1} and 32650 cm^{-1} was due to the single-photon allowed $^2\Sigma^+_{1/2}(3d) \leftarrow X_1\ ^2\Pi_{1/2}(3p)$ dissociative transition. Due to the apparent curve crossing in the Franck-Condon allowed region, however, no attempt was made to model the upper state repulsive surface.

The vibronic peaks labeled A7 and B7 that were assigned as arising from the $^2\Pi_{1/2}(4p)$ and $^2\Pi_{3/2}(4p)$ electronic states respectively, were also observed in the single-photon fragmentation spectrum. The presence of fragmentation from the A7 peak was somewhat puzzling in that it lies below the Al($3d$)•Ar dissociation limit. Possible explanations for this are that these peaks may derive from fragmentation processes occurring in the ion, or possibly predissociative behavior in the $^2\Pi_{1/2}(3d)$ state near the dissociation limit. The latter, however, would be difficult to reconcile with the absence of any obvious broadening in the $^2\Pi_{1/2}(3d)$ vibronic peaks converging on the dissociation

limit discussed below.

3.5.2. $2_{vis} + 1_{vis}$ and $1'_{UV} + 1_{vis}$ REMPI Spectra of Al•Ar and Al Fragments Below the Al(3d)•Ar Dissociation Limit

3.5.2.1. $^2\Pi_{1/2}(3d)$, $^2\Pi_{3/2}(3d)$, $^2\Pi_{1/2}(4p)$, and $^2\Pi_{3/2}(4p)$ States

Having found evidence for the $^2\Pi_{1/2}(4p)$, and $^2\Pi_{3/2}(4p)$ states above the Al(3*d*)•Ar dissociation limit, we proceeded to re-examine the spectral region from 31800 cm^{-1} to 32560 cm^{-1} previously reported by Morse and co-workers.[36] However, we extended Morse's $1'_{UV} + 1_{vis}$ REMPI work by employing $2_{vis} + 1_{vis}$ REMPI as an additional probe of this region in an attempt to discern whether any peaks of Al(4*p*)•Ar character were indeed present below the dissociation limit as had been postulated. During the course of this work, it became evident that the assigned $^2\Pi(3d)$, $^2\Pi(4p)$, and $^2\Sigma(3d)$ progressions from Morse's work were incorrect. Here we report a revised assignment for the spectral region between 32400 cm^{-1} to the Al(3*d*)•Ar dissociation limit.

Both the $1'_{UV} + 1_{vis}$ and $2_{vis} + 1_{vis}$ REMPI spectra obtained during the course of this work by monitoring the $Al•Ar^+$ ion signal are presented in Figure 3-5, as well as being reproduced individually for the sake of labeling clarity in Figures 3-6 and 3-7 respectively. The $1'_{UV} + 1_{vis}$ and $2_{vis} + 1_{vis}$ REMPI spectra obtained by monitoring the Al^+ fragment signal were featureless within the spectral region between 32400 cm^{-1} and the Al(3*d*)•Ar dissociation limit (data not shown). The single-photon UV excitation spectrum appeared identical to that reported by Morse and co-workers, but was perhaps slightly better

resolved. Contrary to Morse's assignment, the previously reported $^2\Pi(3d)$ progression was not believed to terminate in the region of 32490 cm^{-1}, but rather converged all the way to the Al($3d$)•Ar dissociation limit. As shown in Figure 3-6, we have assigned two progressions as arising from $^2\Pi_{1/2}(3d)$ and $^2\Pi_{3/2}(3d)$ electronic states. These are labeled for the ease of discussion by the letters Y and Z respectively. In addition, the observed peak positions for the $^2\Pi_{1/2}(3d) \leftarrow X_1\ ^2\Pi_{1/2}(3p)$ and $^2\Pi_{3/2}(3d) \leftarrow X_1\ ^2\Pi_{1/2}(3p)$ transitions are compiled in Tables 3-5 and 3-6 respectively. In agreement with Morse's work, the peak labeled Y0 was assigned as the presumptive $^2\Pi_{1/2}(3d) \leftarrow X_1\ ^2\Pi_{1/2}(3p)$ 0-0 vibronic transition. Furthermore, we find that the $^2\Pi_{1/2}(3d)$ vibronic progression labeled by Y converged to a dissociation threshold of 32557.7 cm^{-1} taken as the peak maximum of the last observed feature - a value in excellent agreement to that reported by Morse's group.

Nevertheless, there existed some odd behavior in the intensities and vibrational spacing of the assigned $^2\Pi_{1/2}(3d)$ progression, presumably due to some electronic perturbation. This was especially pronounced in the spectral region between vibronic peaks Y3 and Y5. In an attempt to understand this behavior, a Birge-Sponer analysis of the $^2\Pi_{1/2}(3d)$ progression was performed which is shown in Figure 3-8. What was particularly striking about Figure 3-8 is that the $^2\Pi_{1/2}(3d)$ state potential appears to possess two distinct regions of curvature that are delineated between peaks Y4 and Y5.

In order to extract details related to each distinct region of the potential, two additional Birge-Sponer plots were prepared.[29-30] The first includes vibronic levels Y0 through Y3, and is shown in Figure 3-9. The Birge-Sponer plot is clearly linear, from which the following Morse potential parameters were obtained.[30]

$\omega_e = 24.8\ cm^{-1}$ $\omega_e\chi_e = 1.45\ cm^{-1}$

$D_e = 105.9\ cm^{-1}$ $D_o = 93.5\ cm^{-1}$

These parameters would place the Al(3*d*)•Ar dissociation energy at roughly 32514 cm^{-1} which was difficult to reconcile with the observed progression. While Birge-Sponer plots are notorious for their inaccuracy in predicting D_o values, especially for potentials exhibiting considerable anharmonicity such as those common to van der Waals molecules, an error equal to one-third the total well depth would be nevertheless particularly poor.

If, however, we examined the Birge-Sponer plots for the other region of curvature, namely that derived from peaks Y7 through Y15, some interesting behavior emerged. This Birge-Sponer plot can be seen in Figure 3-10. This plot was quite linear, with the exception of a small deviation from linearity arising from a small perturbation in peak Y11. This perturbation was believed to arise from a weak coupling with the adjacent peak A7 derived from the $^2\Pi_{1/2}(4p)$ electronic state as discussed above. By performing a linear fit, the following Morse potential parameters were obtained for this region of $^2\Pi_{1/2}(3d)$ potential.

$\omega_e = 17.8\ cm^{-1}$ $\omega_e\chi_e = 0.53\ cm^{-1}$

$D_e = 149.0\ cm^{-1}$ $D_o = 140.0\ cm^{-1}$

Taking the difference between the Al(3*d*)•Ar dissociation limit and the 0-0 vibronic band

labeled as Y0 in Figure 3-6, we obtained an observed experimental D_o value of 137.7 cm^{-1} for the $^2\Pi_{1/2}(3d)$ state. This was in remarkably good agreement with the value derived from the Birge-Sponer analysis. While it was somewhat questionable whether any quantitative conclusions should be derived from this close correspondence, the similarity between these two D_o values was strongly suggestive that the shape of the upper region of the $^2\Pi_{1/2}(3d)$ potential may be largely undisturbed by whatever perturbation(s) occur(s) in the spectral region between vibronic levels Y3 through Y5.

Furthermore, we can gain additional insight into the potential energy profiles of these two distinct regions of curvature by examining the magnitude of the curvature predicted from the Birge-Sponer analysis. Using such an analysis, the curvature was easily derived as $2\omega_e\chi_e$, suggesting that the lower part of the $^2\Pi_{1/2}(3d)$ potential possessed a higher degree of curvature than the upper region.[30] This implied that whatever perturbation(s) underlay the disruption of the $^2\Pi_{1/2}(3d)$ progression between Y3 through Y5, they served to increase the curvature of the lower aspect of the potential profile while leaving the upper region largely undisturbed.

A second progression observed in the $1'_{UV} + 1_{vis}$ spectrum labeled as Z is seen in Figure 3-6. This progression has been assigned as arising from the higher spin-orbit component of the $^2\Pi(3d)$ state, namely the $^2\Pi_{3/2}(3d)$ state. The spin-orbit splittings observed between the $^2\Pi_{1/2}(3d)$ and $^2\Pi_{3/2}(3d)$ vibronic levels are compiled in Table 3-7. Particularly noteworthy was the observation that with the exception of the Z3-Y3 splitting, the spin-orbit splittings between the $^2\Pi_{1/2}(3d)$ and $^2\Pi_{3/2}(3d)$ states increased with decreasing vibrational quantum number. Recalling the fact that the atomic aluminum $^2D_{1/2}$

and $^2D_{3/2}$ spin-orbit components from which these two states arise are separated by 1.34 cm^{-1}, both $^2\Pi_{1/2}(3d)$ and $^2\Pi_{3/2}(3d)$ states were expected to exhibit at least partial Hund's case (b) character. Therefore, spin-orbit splittings between 4 - 5.5 cm^{-1} that were indicative of substantial Hund's case (a) character were unexpected. Such a trend, however, has been previously observed in several M•Ar systems, in particular Mg($3s3d\pi$ ^3D_J)•Ar($^3\Pi$),[6] Na($3p\pi$ ^2P_J)•Ar($^2\Pi$),[44] and Mg^+($3s4p$ ^2P_J)•Ar($^2\Pi$).[45]

In an attempt to locate any features attributable to additional vibronic transitions to the $^2\Pi_{1/2}(4p)$ and $^2\Pi_{3/2}(4p)$ states to the red of peaks A7 and B7, 2_{vis} + 1_{vis} REMPI spectra were also collected in the region between 32400 cm^{-1} to the Al($3d$)•Ar dissociation limit, monitoring both the Al•Ar^+ and Al^+ fragment signal. The spectrum that was obtained is shown in Figure 3-7, and is directly compared to that obtained by $1'_{UV}$ + 1_{vis} REMPI in Figure 3-5. What was particularly striking about the two-photon spectrum in Figure 3-7 was that within the region between 32400 cm^{-1} and 32490 cm^{-1}, to the red of where a perturbation was believed to disrupt the $^2\Pi_{1/2}(3d)$ progression, both $^2\Pi_{1/2}(3d)$ and $^2\Pi_{3/2}(3d)$ exhibited considerable two-photon character. Above the curve crossing region from 32490 cm^{-1} to the Al($3d$)•Ar dissociation limit, however, the $^2\Pi_{1/2}(3d)$ vibronic levels demonstrated little or no detectable two-photon character. This was consistent with the Birge-Sponer analysis for the $^2\Pi_{1/2}(3d)$ progression that suggested the existence of perturbations increasing the curvature of the lower part of the $^2\Pi_{1/2}(3d)$ state, while leaving the upper regions of the potential relatively undisturbed.

The high two-photon character of a great number of the spectral features observed by $1'_{UV}$ + 1_{vis} REMPI obscured the ability to definitively assign vibronic features

exclusively attributable as arising from lower vibronic levels of the $^2\Pi_{1/2}(4p)$ and $^2\Pi_{3/2}(4p)$ electronic states. Nevertheless, two peaks, A8 (visible in both single- and two-photon spectra in Figures 3-6 and 3-7 respectively) and B8 (visible in the two-photon spectrum in Figure 3-7), were believed to be the next and final vibronic features from the $^2\Pi_{1/2}(4p)$ and $^2\Pi_{3/2}(4p)$ electronic states. Peak A8 was assigned as arising from the lowest observable vibrational level of the $^2\Pi_{1/2}(4p)$ state. This assignment was first based upon the close similarities in peak shape between peaks A7 and A8 as seen in Figure 3-11. The second criteria was the significant single-photon intensity observed in peak A8. This was consistent with strong state mixing with states within the Al($3d$)•Ar manifold, namely the $^2\Pi(3d)$ and $^2\Sigma(3d)$ electronic states. The fact that similar single-photon character was likewise evident in peak A7 strongly suggested a common origin. As seen in Table 3-3, linear extrapolation from the upper $^2\Pi_{1/2}(4p)$ unperturbed vibronic levels predicted that the A8 peak position lay at 32491 cm^{-1}. The observed value at 32502 cm^{-1} exhibited a blue-shift of 11 cm^{-1}, consistent with the fact that it was a curve crossing between the $^2\Pi_{1/2}(4p)$ and $^2\Pi_{1/2}(3d)$ levels that gave rise to the perturbation observed in the $^2\Pi_{1/2}(3d)$ progression between peaks Y3 and Y5. A curve crossing between the $^2\Pi_{1/2}(4p)$ and $^2\Pi_{1/2}(3d)$ around the region of 32480 cm^{-1} could easily account for the 11 cm^{-1} shift in the A8 vibronic level.

The assignment of peak B8 at 32490.7 cm^{-1} as the lowest energy vibronic level arising from the $^2\Pi_{3/2}(4p)$ electronic state was tentative. The peak profile of peak B8 possessed a similar contour to those observed for the other $^2\Pi_{1/2}(4p)$ vibronic levels apparent below the Al($3d$)•Ar dissociation limit - indicative of a common electronic origin.

Further support derived from a linear extrapolation analysis from the upper vibronic $^2\Pi_{3/2}(4p)$ states to predict the lower $^2\Pi_{3/2}(4p)$ vibronic band positions as shown in Table 3-4. This analysis predicted that peak B8 should appear at 32499 cm^{-1}. Assuming that the coupling between the $^2\Pi_{3/2}(4p)$ and $^2\Pi_{3/2}(3d)$ was approximately comparable to that between the $^2\Pi_{1/2}(4p)$ and $^2\Pi_{1/2}(3d)$ states, a shift on the order of 10 cm^{-1} might be expected for peak B8, placing its expected peak position in the region of 32490 cm^{-1} to 32510 cm^{-1}. Given that a) the perturbation in the $^2\Pi_{1/2}(3d)$ progression presumably placed the $^2\Pi_{1/2}(3d)$ - $^2\Pi_{1/2}(4p)$ crossing in the region of 32480 cm^{-1} to 32490 cm^{-1}, and b) the $^2\Pi_{1/2}(4p)$ - $^2\Pi_{3/2}(4p)$ spin-orbit splitting was most likely between 10 cm^{-1} and 15 cm^{-1} within this spectral region, then the $^2\Pi_{3/2}(3d)$ - $^2\Pi_{3/2}(4p)$ curve crossing would be expected to occur in the region between 32490 cm^{-1} and 32510 cm^{-1}. This was consistent with the hypothesis that the diabatic vibrational level for the peak labeled B8 lay very near or in the $^2\Pi_{3/2}(3d)$ - $^2\Pi_{3/2}(4p)$ crossing region, resulting in a significant red-shift to the observed peak position at 32490 cm^{-1}. The observed weak intensity of peak B8 may also be attributable to the fact that the vibrational level that gave rise to vibronic level B8 on the $^2\Pi_{3/2}(4p)$ diabatic potential was presumed to be located very close to the crossing region. Strong perturbations may have caused the nature of the electronic wavefunction as well as the transition dipole matrix element to vary dramatically as a function of internuclear distance within the crossing region, significantly affecting the observed transition intensity relative to that of the $^2\Pi_{1/2}(4p)$ spin-orbit component.

Other interesting characteristics of the two-photon spectrum were the relative intensities of the different progressions relative to the single-photon spectrum, as well as

several frequency shifts evident in certain vibronic levels. Tables 3-5 and 3-6 contain a compilation of the observed peak positions from both the single- and double-photon excitation spectra of the $^2\Pi_{1/2}(3d)$ and $^2\Pi_{3/2}(3d)$ states respectively. Due to the breadth of some of the two-photon peaks and the lower signal to noise, the reported peak values may contain uncertainties on the order of 0.5 - 1.0 cm^{-1}. Whenever possible, the peak positions were taken as peak maxima. However, in cases with no obvious maxima, the approximate center of the peak was used to record the peak position.

On the whole, peaks assigned as arising from the $^2\Pi_{3/2}(3d)$ state appeared with almost equal intensity compared to the $^2\Pi_{1/2}(3d)$ state in the two-photon spectrum, and in the case of Z3, greater intensity. Peaks arising from the $^2\Pi_{1/2}(3d)$ state in the region of the presumed $^2\Pi_{1/2}(3d)$ - $^2\Pi_{1/2}(4p)$ curve crossing, namely Y4 and Y5, were observed to possess much higher intensity in the two-photon spectrum than the other vibronic peaks in the progression. This attribute, coupled to the fact that these two peaks demonstrated significantly decreased single-photon character, lent further credence to the notion of a curve crossing between the $^2\Pi_{1/2}(3d)$ and $^2\Pi_{1/2}(4p)$ states within this spectral region.

As can be seen from comparing the reported peak positions between the single- and double-photon excitation spectra compiled in Tables 3-5 and 3-6, many of the $^2\Pi_{1/2}(3d)$ and $^2\Pi_{1/2}(3d)$ vibronic levels exhibited small blue-shifts on the order of 0-2 cm^{-1} in the two-photon spectrum relative to the single-photon spectrum. The exceptions were peaks Y1 and Z1, both of which demonstrated a strong red-shift of 4.7 cm^{-1} and 4.9 cm^{-1} respectively. The physical basis for this large anomalous shift is not understood. In the next section we will provide evidence for a curve crossing between the $^2\Pi(3d)$ and $^2\Delta(3d)$

states near the 0-0 vibrational levels for both the $^2\Pi_{1/2}(3d)$ and $^2\Pi_{3/2}(3d)$ states. Nevertheless, the absence of a shift of similar magnitude in peaks Y0 and Z0 renders it difficult to argue with confidence that mixing with the $^2\Delta(3d)$ state in this region was the origin of this shift.

Several features in the two-photon spectrum, notably those labeled by the letter O, remain of mysterious origin. One peak in particular, O6, appeared at first as a good candidate for the 0-0 vibronic level of the $^2\Pi_{1/2}(3d)$ state. Nevertheless, close examination of the peak shapes showed that peak O6 was shaded to the blue while those assigned as arising from the $^2\Pi_{1/2}(3d)$ state were shaded to the red. Furthermore, the absence of any evidence for the $^2\Pi_{3/2}(3d)$ state near peak O6 caused us to dismiss this peak as a candidate for the 0-0 vibronic level. Likewise, the spacing between several of these peaks, namely O1, O2, O3, and O6, gave the appearance of possibly arising from the $^2\Pi_{1/2}(4p)$ and $^2\Pi_{3/2}(4p)$ states. Arguing against this was the fact that none of these peaks fit well to the expected peak positions for the $^2\Pi_{1/2}(4p)$ and $^2\Pi_{3/2}(4p)$ states. Furthermore, if O1 were, in fact, the 0-0 vibrational level for the $^2\Pi_{1/2}(4p)$ state, this would have resulted in a D_o value for the $^2\Pi_{1/2}(4p)$ state of approximately 785 cm^{-1}. While this was possible, it was also highly improbable given that the observed zero-point bond strength for the Al•Ar $^2\Pi(6p)$ state is only 787.8 cm^{-1}.[36] Due to the expectation of increased Rydberg-like behavior with increasing electronic excitation, an equal bond strength would imply a virtually identical ionic core for the $^2\Pi$ states derived from the Al(4*p*)•Ar and Al(6*p*)•Ar manifolds.

Ultimately, these peaks remain unassigned. Attempts to positively assign them as fragment peaks due to fragments of $Al•Ar_2$ have been inconclusive so far due to our

inability to generate significant amount of Al•Ar_2 in our source.

3.5.2.2. $^2\Delta(3d)$ States

During the course of this work, the progression assigned as the $^2\Delta(3d)$ in Morse's work was also re-examined. As was the case with the reported work by Morse and co-workers, only a single progression was observed. The absence of a resolvable splitting between the $^2\Delta(3d)$ spin-orbit manifold was suggestive of predominant Hund's case (b) character.

While those bands previously assigned by Morse and co-workers as belonging to the $^2\Delta(3d)$ were found to be correct, the vibrational assignment was incorrect. We have uncovered two additional vibronic features to the red of those previously reported. These new vibronic peaks are shown in Figure 3-12. Figure 3-13 shows the Birge-Sponer plot for the $^2\Delta(3d)$ electronic state including the two newly discovered peaks with those previously reported from the work of Morse and co-workers.[36] By performing a linear fit, the following Morse potential parameters were obtained for the $^2\Delta(3d)$ potential.

$\omega_e = 76.9\ cm^{-1}$ $\omega_e\chi_e = 2.04\ cm^{-1}$

$D_e = 724.3\ cm^{-1}$ $D_o = 685.9\ cm^{-1}$

The experimental D_o taken as the difference between the new $^2\Delta(3d)$ 0-0 band with the Al(3*d*)•Ar dissociation limit yielded a value of 663.5 cm^{-1}. This was reasonable agreement with the predicted Birge-Sponer value given the approximate nature of the analysis.

Furthermore, the revised value of $\omega_e\chi_e$ was in close accordance with the 1.99 cm^{-1} value previously reported by Morse and co-workers.

If an additional vibronic level was present in the $^2\Delta(3d)$ state to the red of the presumed new 0-0 vibronic level, its peak position would have been expected to appear at approximately 31817 cm^{-1}. Extensive signal averaging in the region of 31800 cm^{-1} and 31830 cm^{-1}, however, failed to provide any evidence of an additional vibronic level below the new feature observed at 31894.3 cm^{-1}. We were confident, therefore, that vibronic band at 31894.3 cm^{-1} was the 0-0 vibronic level for the $^2\Delta(3d)$ state.

In addition, two puzzling features observed in both the single- and two-photon spectra between 32400 cm^{-1} and the Al(3*d*)•Ar dissociation limit (see Figures 3-6 and 3-7) can be tentatively assigned as originating from the next higher $^2\Delta(3d)$ state vibronic levels above the last vibronic band assigned by Morse and co-workers. These two features are labeled D10 and D11 in Figures 3-6 and 3-7. The rationale behind this assignment was as follows. If the predicted peak positions for the next vibronic levels from the Birge-Sponer plot shown in Figure 3-13 were extrapolated forward, the $^2\Delta(3d)$ 0-10 (D10) and 0-11 (D11) vibronic peak positions were predicted to be observed at 32416 cm^{-1} and 32444 cm^{-1} respectively. The experimental peak position for D10 was 32427.6 cm^{-1}, and that of D11 was 32449.9 cm^{-1}. Due to the strongly bound nature of the $^2\Delta(3d)$ potential, the outer turning point of the upper portion of the $^2\Delta(3d)$ potential undoubtedly lay close to the outer turning point of the $^2\Pi_{1/2}(3d)$ and $^2\Pi_{3/2}(3d)$ states. Peaks D10 and D11, then, were believed to result due to a state mixing interaction caused by the close proximity of the $^2\Delta(3d)$ and $^2\Pi_{3/2}(3d)$ potentials in a region very close to the bottom of the $^2\Pi_{3/2}(3d)$

potential well. The larger blue-shift in peak D10 relative to D11 in comparison to the extrapolated peak positions was likewise suggestive of a state mixing interaction near the bottom of the potential well.

Since rotational band contours are characterisitic of individual electronic states, examination of the D10 and D11 provided some insight into their possible electronic state origin. The peak contours exhibited by peaks D10 and D11 were both broad and shaded to the blue. Such characteristics were identical to those observed in the other $^2\Delta(3d)$ vibronic bands already assigned. In contrast, all $^2\Pi(3d)$ and $^2\Pi(4p)$ vibronic bands were shaded to the red, making it unlikely that vibronic bands from these states gave rise to these features.

In addition, both peaks D10 and D11 possessed very strong two-photon character. State mixing with the $^2\Pi_{3/2}(3d)$ state, which was already strongly coupled to the $^2\Pi_{3/2}(4p)$ state, provides a mechanism by which the $^2\Delta(3d)$ state acquired two-photon oscillator strength. While such observations were far from definitive, this qualitative evidence was consistent with the proposed assignment. Nevertheless, one cannot rule out the possibility that peaks D10 and D11 were merely artifacts.

3.5.3. *Preliminary ab initio Results on the Al(3d)•Ar and Al(4p)•Ar Electronic Manifolds*

Over the course of performing this work, it became evident that *ab initio* calculations of the Al(3*d*)•Ar and Al(4*p*)•Ar electronic manifolds could provide insight into some of the unusual spectroscopic behavior presented in the preceding sections.

Consequently, theoretical analysis of these states was begun through a collaboration with Jeff Sheehy and Jerry Boatz, both of whom have had considerable success determining the underlying mechanisms behind some unusual spectroscopic behavior observed in systems where alkali metal atoms were embedded in rare gas matrics. The results of the preliminary theoretical calculations described below have been reported,[46] and were all derived from work by Jeff Sheehy and Jerry Boatz performed the at Phillips Laboratory, Edwards Air Force Base. Since these results were preliminary, they will not be presented to argue quantitative details related to the Al(3*d*)•Ar and Al(4*p*)•Ar electronic manifolds, but rather to provide a framework around which some of the observed spectroscopic behavior may be rationalized.

To perform the calculations on the diatomic potential energy curves that correlate with the Al(3*p*)•Ar, Al(4*s*)•Ar, Al(3*d*)•Ar, and Al(4*p*)•Ar electronic manifolds, Sheehy used the (17*s*12*p*5*d*4*f*)/[7*s*6*p*4*d*3*f*] atomic natural basis set (supplemented with diffuse (1*s*1*p*1*d*1*f*) functions), in conjunction with internally contracted multireference configuration interaction (MRCI) calculations from [6331] (3 electrons in 13 orbitals) state-averaged complete active space reference wavefunctions. In addition, the "HFDB2" potential of Aziz and Slaman[46-47] was used in calculating the Al•Ar interaction energies. Spin-orbit interactions within the atomic aluminum moiety were neglected.

The ground and first excited $B\ ^2\Sigma^+_{1/2}(4s)$ states were calculated in order to test whether this level of theory was adequate to describe the weakly bound Al•Ar system. These results are presented in Figures 3-14 and 3-15 for the former and the latter respectively. The ground state calculation compared favorable to that already reported by

Partridge *et al.*[41] Sheehy obtained a ground state equilibrium bond distance of 4 Å, and zero-point bond energy of 115 cm^{-1}. The calculated bond distance was slightly longer than that determined by experiment, namely 3.79 Å, as well as the 3.86 Å value calculated by Partridge *et al.*[41] Sheehy's D_o value, however, was in close accordance with both the 122.4 cm^{-1} experimental value obtained by Morse and co-workers,[36] as well as the calculated value of 112 cm^{-1} derived by Partridge *et al.*

The calculated potential for the $B\ ^2\Sigma_{1/2}(4s)$ state shown in Figure 3-15 demonstrated qualitatively the behavior expected from this state given the experimental results described above. A significant barrier above the Al(4*s*)•Ar dissociation limit was predicted at 4.5 Å, suporting the notion that the D_o values for the $X_1\ ^2\Pi_{1/2}(3p)$ ground state found by Callender *et al.*[39] and Heaven and co-workers[40] were, in fact, due to a barrier in the $B\ ^2\Sigma_{1/2}(4s)$ state at large internuclear distances. Nevertheless, theory appeared to dramatically overestimate the magnitude of this barrier by almost 60 cm^{-1} given the experimental estimate of the presence of a 40 cm^{-1} barrier. Furthermore, the calculated D_e value for the $^2\Sigma_{1/2}(4s)$ state of approximately 240 cm^{-1} was significantly less than the $440\ ^{+35}/_{-8}$ cm^{-1} experimental value obtained by Heaven and co-workers.[40]

The calculated electronic states arising from the Al(3*d*)•Ar, and Al(4*p*)•Ar electronic manifolds shown in Figure 3-16 were quite complicated, even with additional spin-orbit effects neglected. Examination of the calculated potentials presented in Figure 3-16 provided additional evidence for the presence of a strongly-bound $^2\Pi(4p)$ manifold interacting with the $^2\Pi(3d)$ electronic manifold within an internuclear distance range relevant to determining bond character. Nevetheless, the calculations dramatically

underestimated the magnitude of the $^2\Pi(3d)$ well depth, providing an estimate of roughly 35 cm^{-1} rather than the 140 cm^{-1} D_o value observed experimentally.

An extremely strong coupling between the $^2\Pi(3d)$ and $^2\Pi(4p)$ states was evident in the diabatic crossing region at roughly 3.6 Å. This crossing was calculated to lie above the Al(3*d*)•Ar dissociation limit, with a coupling strength of approximately 151 cm^{-1}. Given the accuracy of the excited state calculations, however, the true crossing point could have easily varied by hundreds of wavenumbers either above or below the calculated curve crossing region. The magnitude of the calculated coupling was quite large - on the order of the D_o $^2\Pi(3d)$ potential itself. Such a strong coupling was reminiscent of a strongly-coupled double-well adiabatic potential, where the inner well correlated to the $^2\Pi(4p)$ electronic state, while the outer well correlated to the $^2\Pi(3d)$ electronic state. Such a state, analogous to the intensively investigated $E,F\ ^1\Sigma_g^+$ state of H_2 formed by a strongly avoided crossing between the $(1s2s)\ ^1\Sigma_g^+$ and $(2p\sigma_u)^2\ ^1\Sigma_g^+$ states,[48-58] would be quite novel for a weakly-bound van der Waals system.

The other noteworthy feature from the calculations was the prediction that the $^2\Sigma^+(3d)$ state should be mostly repulsive in character. Near the Al(3*d*)•Ar dissociation limit, however, the potential appeared much flatter, indicative a significant mixing with other nearby electronic states. A very weakly-bound region of this potential was evident at very large internuclear distance - 11 Å - but its shallow nature would have undoubtedly precluded the existence of any bound vibrational levels.

In addition, the $^2\Sigma^+(3d)$ and the $^2\Pi(3d)$ / $^2\Pi(4p)$ electronic state potential energy curves were predicted to be in close proximty around 3.8 Å, near to the internuclear

distance where direct Franck-Condon allowed transitions from the ground state would be expected to occur. The theoretically predicted crossing point was expected to lie approximately 130 cm^{-1} above the Al(3*d*)•Ar dissociation limit. Experimentally, this value appeared to be closer to 60 cm^{-1} above the Al(3*d*)•Ar dissociation limit - a reasonable agreement given the magnitude of the errors evident in the calculated energetics for the *B* $^2\Sigma_{1/2}(4s)$ state. Furthermore, the $^2\Sigma^+(3d)$ potential was predicted to possess a bound region within the internuclear distance range of 3 - 4 Å. Whether this shallow well could have possibly supported a bound vibronic level has not been determined, but the possibility for pseudo-bound character in the $^2\Sigma^+(3d)$ state near the predicted $^2\Pi(3d)$ / $^2\Pi(4p)$ crossing point was consistent with the observation of possible dynamical effects in the spectroscopic behavior within this region.

The calculated $^2\Delta(3d)$ state possessed a calculated D_e value of approximately 480 cm^{-1}, significantly smaller that the revised experimental value on the order of 700 cm^{-1}. Close examination near the Al(3*d*)•Ar dissociation limit revealed that at high vibronic levels, the $^2\Delta(3d)$ state lay within the outer turning point of the $^2\Pi(3d)$ potential before crossing the latter state. Such qualitative behavior was expected due to the strong bonding character presented by the $^2\Delta(3d)$ state. However, since the calculations significantly underestimated the magnitude of the $^2\Delta(3d)$ and $^2\Pi(3d)$ zero-point bond dissociation energies, it was difficult to say definitively where the exact region of interaction between these two states did in fact occur.

3.6. Discussion

3.6.1. Electronic States Originating Above the Al(3d)•Ar Dissociation Limit

3.6.1.1. $^2\Pi_{1/2}(4p)$, $^2\Pi_{3/2}(4p)$, and $^2\Sigma^+_{1/2}(3d)$ Electronic States

As seen in Figure 3-2, the two-photon $2_{vis} + 1_{vis}$ REMPI spectrum showed a clear progression of doublets that have been assigned as arising from the $^2\Pi_{1/2}(4p)$ and $^2\Pi_{3/2}(4p)$ states. While only the $^2\Pi_{1/2}(4p) \leftarrow X_1\,^2\Pi_{1/2}(3p)$ transition was allowed in the single-photon spectrum due to the strict $\Delta\Sigma = 0$ selection rule in Hund's case (a), both $^2\Pi_{1/2}(4p) \leftarrow X_1\,^2\Pi_{1/2}(3p)$ and $^2\Pi_{3/2}(4p) \leftarrow X_1\,^2\Pi_{1/2}(3p)$ transitions were allowed using two-photon excitation.

In the spectral region nearest to the Al(4*p*)•Ar dissociation limit, the $^2\Pi(4p)$ states derived from the Al($^2P_{1/2}$) + Ar($^1S_0$) and Al($^2P_{3/2}$) + Ar($^1S_0$) asymptotes exhibited classic Hund's case (a) character. As is evident from Table 3-2, the highest vibronic levels of the $^2\Pi_{1/2}(4p)$ and $^2\Pi_{3/2}(4p)$ states possessed spin-orbit splittings almost identical to the atomic states from which they derived. For diatomic molecules of Hund's case (a) character, the off-diagonal matrix elements of single-electron spin-orbit operator are essentially zero. The spin-orbit interaction, then, is determined by the diagonal matrix elements of the spin-orbit operator.[1,59]

$$< {}^2\Pi_{3/2}(4p) \mid \hat{a}\, \mathbf{l}_z \bullet \mathbf{s}_z \mid {}^2\Pi_{3/2}(4p) > = 1/2\, a_\pi$$

$$< {}^2\Pi_{1/2}(4p) \mid \hat{a}\, \mathbf{l}_z \bullet \mathbf{s}_z \mid {}^2\Pi_{1/2}(4p) > = -1/2\, a_\pi$$

The value of a_π, the molecular spin-orbit parameter, is directly analogous to the well-known atomic spin-orbit parameter, ζ_k (nl).[59] A spin-orbit value of 15 cm^{-1} such as that observed for the last resolved spin-orbit doublet closely resembled the atomic spin-orbit value of 15.83 cm^{-1}. This is quite consistent with Hund's case (a) character near the Al(4*p*)•Ar dissociation limit.

The lower regions of the $^2\Pi_{1/2}(4p)$ and $^2\Pi_{3/2}(4p)$ potentials near the Al(3*d*)•Ar dissociation limit were complicated by the presence of perturbations. The observation of the Al^+ fragment signal spectrum that closely resembled that obtained by monitoring the $Al•Ar^+$ signal over the same spectral range was compatible with the hypothesis that both the $^2\Pi_{1/2}(4p)$ and $^2\Pi_{3/2}(4p)$ states were coupled to a third electronic state that was principally dissociative in character. Based on the *ab initio* results that predicted the presence of a primarily repulsive $^2\Sigma^+_{1/2}(3d)$ electronic state within the same energetic region manifesting perturbed behavior, a curve crossing that coupled the $^2\Pi_{1/2}(4p)$ and $^2\Pi_{3/2}(4p)$ states with the $^2\Sigma^+_{1/2}(3d)$ state in the region just above the Al(3*d*)•Ar dissociation limit was believed to be the origin of this dissociative character.

The experimental spectra provided several lines of evidence to support this conclusion. Foremost, the $^2\Pi_{1/2}(4p)$ electronic state was perturbed to a much greater degree than the $^2\Pi_{3/2}(4p)$ state. As outlined by Field and Lefebvre-Brion,[59] the magnitude of the coupling between the $^2\Sigma(3d)$ and $^2\Pi(4p)$ states is determined by the off-diagonal matrix elements of the total electronic Hamiltonian. Perturbations arising from off-diagonal couplings between the $^2\Sigma^+_{1/2}(3d)$ and $^2\Pi_{1/2}(4p)$ states can originate from a number of causes, most notably electrostatic as well as spin-electronic sources. The selection rules

for homogeneous electrostatic perturbations are

$$\Delta\Lambda = 0,\ \Delta\Sigma = 0,\ \Delta S = 0 \text{ and } \Delta\Omega = 0$$

while those for homogeneous spin-electronic perturbations are

$$\Delta\Lambda = {}^{+}\!/_{-}1,\ \Delta\Sigma = {}^{-}\!/_{+}1,\ \Delta S = 0 \text{ and } \Delta\Omega = 0.^{59}$$

Both the $^2\Sigma^+_{1/2}(3d)$ and $^2\Pi_{1/2}(4p)$ states could potentially interact to some degree via a spin-electronic interaction governed by the off diagonal matrix element

$$\left\langle \Lambda, S, \Sigma, \Omega, v \right| \frac{1}{2\mu R^2} \mathbf{L}^{\pm}\mathbf{S}^{\mp} \left| \Lambda \mp 1, S, \Sigma \pm 1, \Omega, v' \right\rangle .^{59}$$

In cases where only a single electron configuration is important such as that presented in the ground and excited states of atomic aluminum, the total spin-electronic operator can be safely approximated by the sum of single electron spin-orbit operators as follows:

$$\left\langle\ v\ \left| \frac{\hbar}{2\mu R^2} \right|\ v'\ \right\rangle \left\langle \Lambda, S, \Sigma, \Omega \right| \sum_i \mathbf{l}_i^{\pm} \sum_j \mathbf{s}_j^{\mp} \left| \Lambda \mp 1, S, \Sigma \pm 1, \Omega \right\rangle .^{59}$$

The $^2\Pi_{1/2}(4p)$ electronic state is described by the $|\ \Lambda = 1,\ \Sigma = -1/2,\ \Omega = 1/2\ >$ electronic configuration, while the $^2\Sigma^+_{1/2}(3d)$ is described by $|\ \Lambda = 0,\ \Sigma = 1/2,\ \Omega = 1/2\ >$. Following

Field's notation, these two states can be rewritten as $|\pi\beta>$ and $|\sigma\alpha>$ respectively.[59] These two electronic configurations interact via the one-electron spin-orbit operator as

$$\left\langle {}^2\Pi_{1/2}(4p),\, v \,\middle|\, \frac{1}{2}\,\hat{a}\,\mathbf{l}^+\cdot\mathbf{s}^- \,\middle|\, {}^2\Sigma^+{}_{1/2}(3d),\, v' \right\rangle = \frac{1}{2}\left\langle \pi \,\middle|\, \hat{a}\,\mathbf{l}^+ \,\middle|\, \sigma \right\rangle \left\langle v \,\middle|\, v' \right\rangle .^{1,59}$$

In the limit where the two potential energy curves are of identical character, the vibrational term can be reduced to a delta function, $\delta_{vv'}$, yielding the limiting case of the pure precession hypothesis. In the case of the $^2\Sigma^+{}_{1/2}(3d)$ and $^2\Pi_{1/2}(4p)$ states, however, the potentials are of dramatically different character. Therefore, the vibrational part of the matrix element cannot be factored out, making an evaluation of these matrix elements challenging. The predicted matrix element will be very sensitive to the internuclear distance, as will the magnitude of the spin-orbit coupling in the vicinity of the crossing region.

The effects of this coupling on the $^2\Pi_{1/2}(4p)$ state are apparent for vibronic levels to the blue of the crossing region. From Figure 3-2, a selective augmentation in the dissociative processes within the $^2\Pi_{1/2}(4p)$ state over the $^2\Pi_{3/2}(4p)$ state was apparent for vibronic levels A4/B4 and A5/B5. Furthermore, both A4 and A5 from the $^2\Pi_{1/2}(4p)$ state possessed significant single-photon character as shown in Figure 3-4, while B4 and B5 were barely observed in the single-photon spectrum if at all. All of this was consistent with an avoided curve crossing between the $^2\Sigma^+{}_{1/2}(3d)$ and $^2\Pi_{1/2}(4p)$ states that served to mix Al($3d$) electronic character into the states arising from the Al($4p$) electronic

configuration, and vice versa.

Another interesting feature of the $^2\Pi_{1/2}(4p)$ and $^2\Pi_{3/2}(4p)$ vibronic levels above the perturbed region was the incremental decrease in spin-orbit splitting with decreasing vibrational quantum number. There are two possible explanations that can plausibly account for this observation, either individually or in concert. The first involves direct spin-orbit coupling between the $^2\Sigma^+_{1/2}(3d)$ and $^2\Pi_{1/2}(4p)$ states. As was discussed above, the crossing of these two potentials introduces non-zero off diagonal elements into the spin-electronic Hamiltonian. The effect of this will be that each individual electronic state will possess some spin-orbit character of the other in the weak coupling limit. Due to the significant difference in spin-orbit splitting between the Al($3d$) and the Al($4p$) electronic manifolds, namely 1.34 cm^{-1} versus 15.83 cm^{-1}, a small coupling between these two states might serve to mix atomic spin-orbit character, decreasing the observed spin-orbit splitting in the $^2\Pi_{1/2}(4p)$ and $^2\Pi_{3/2}(4p)$ states more towards those observed from the Al($3d$)•Ar electronic manifold. Upon approaching the crossing region, the coupling should increase in magnitude. Hence, the $^2\Pi_{1/2}(4p)$ and $^2\Pi_{3/2}(4p)$ states would be expected to acquire more and more Al($3d$) character near the crossing point, serving to systematically decrease the observed spin-orbit coupling - the precise effect that has been observed experimentally.

The other underlying cause of the decreased spin-orbit coupling near the crossing point could be selective perturbation of the $^2\Pi_{1/2}(4p)$ state *exclusively* due to the curve crossing with the $^2\Sigma^+_{1/2}(3d)$ state. In essence, state mixing could cause the $^2\Pi_{1/2}(4p)$ vibronic levels to the blue of the crossing region to experience a blue-shift that scaled in some manner proportionally with the energy difference between the crossing point and the

specific vibronic level. Since this blue-shift would be expected to increase closer to the crossing region, the net effect would be to decrease the energy difference between the $^2\Pi_{1/2}(4p)$ and $^2\Pi_{1/2}(4p)$ states as the $^2\Pi_{1/2}(4p)$ state was shifted further and further to the blue. In this case, the spin-orbit character of the $^2\Pi(4p)$ electronic manifold would retain much of its Hund's case (a) character, and demonstrate little or no spin-orbit character of the Al($3d$) manifold. In the absence of a rotationally resolved spectrum of each vibronic band, however, it is impossible to definitively conclude which effect might be dominant.

Near or at the crossing region between the $^2\Pi_{1/2}(4p)$ / $^2\Pi_{3/2}(4p)$ states and $^2\Sigma^+_{1/2}(3d)$ state, the observed single- and two-photon excitation spectra were rather complex. From the single-photon spectrum of the Al^+ dissociative channel shown in Figure 3-4, the broad fragmentation feature was characteristic of a bound→continuum transition between the ground and $^2\Sigma^+_{1/2}(3d)$ states. This implied that the crossing region between the $^2\Sigma^+_{1/2}(3d)$ and $^2\Pi(4p)$ states occurred within an internuclear distance region accessible by direct Franck-Condon-allowed transition from the ground state. Therefore, these excited state potentials most likely crossed within a region very close to the ground state equilibrium bond distance of 3.79 Å.

Both vibronic features A6 and B6 that arose from the $^2\Pi_{1/2}(4p)$ and $^2\Pi_{3/2}(4p)$ states near the crossing region likewise demonstrated strongly perturbed behavior. While maintaining an apparently unperturbed band contour in the two-photon spectrum, peak B6 from the $^2\Pi_{3/2}(4p)$ state nevertheless exhibited a strong blue-shift relative to its predicted peak position derived from linear extrapolation from the higher unperturbed vibronic levels (see Table 3-4). In contrast, peak A6 is completely absent from the two-photon

$Al{\bullet}Ar^+$ spectrum, appearing only in the Al^+ fragment signal spectrum as a broad dissociative feature. A weak feature appearing in the single-photon spectrum has been assigned as being the only evidence for a bound A6 vibronic level (see Figure 3-3). The weak intensity of this peak relative to the Al^+ dissociative channel, along with the absence of two-photon character, strongly suggested that the potentials within this energy region are strongly mixed.

Below the curve crossing region of the $^2\Sigma^+_{1/2}(3d)$ and $^2\Pi(4p)$ states as well as below the $Al(3d){\bullet}Ar$ dissociation limit, vibronic levels believed to arise from the $^2\Pi_{1/2}(4p)$ and $^2\Pi_{3/2}(4p)$ states have been tentatively assigned. The assignment of vibronic level B7 - the last $Al(4p){\bullet}Ar$ feature observed above the $Al(3d){\bullet}Ar$ dissociation limit - can be made with a reasonable degree of confidence. First, this peak lies very close to the expected peak position derived from a linear extrapolation from the upper $^2\Pi_{3/2}(4p)$ vibronic levels. Second, this peak demonstrated strong two-photon character, and no obvious single-photon character. This was consistent with the hypothesis that mixing of the $^2\Pi_{3/2}(4p)$ and $^2\Sigma^+_{1/2}(3d)$ states should exhibit significantly smaller coupling than that between the $^2\Pi_{1/2}(4p)$ and $^2\Sigma^+_{1/2}(3d)$ states.

The assignment of another vibronic level from the $^2\Pi_{3/2}(4p)$ state - a putative 0-0 vibronic band - was complicated due to the presence of the $^2\Pi(3d)$ and $^2\Pi(4p)$ curve crossing near 32490 cm^{-1}. The peak position of the next predicted vibronic level, B8, lies directly within the presumptive $^2\Pi_{3/2}(3d)$ - $^2\Pi_{3/2}(4p)$ curve crossing region. The tentative assignment of B8 has been made on the basis of a number of criteria, none of them definitive. First, the assigned feature was unique to the two-photon spectrum, as expected

for the $^2\Pi_{3/2}(4p)$ state due to its weaker coupling with the $^2\Sigma^+_{1/2}(3d)$ state. Second, the band contour of this peak strongly resembles those assigned to the $^2\Pi_{1/2}(4p)$ vibronic levels below the Al($3d$)•Ar dissociation limit. Third, the assigned peak lay close to the predicted peak position derived from linear extrapolation from the upper unperturbed $^2\Pi_{1/2}(4p)$ levels, appearing just 10 cm^{-1} to the red of the expected position. Such a shift could be readily justified by a nearby $^2\Pi_{3/2}(3d)$ - $^2\Pi_{3/2}(4p)$ curve crossing close to where the diabatic vibronic level would be expected to exist. Lastly, this feature was one of the few orphan features left unassigned in this spectral region from which this state could potentially originate.

The $^2\Pi_{1/2}(4p)$ vibronic levels observed below the Al($3d$)•Ar dissociation limit the can be assigned with a reasonable degree of confidence. A key criterion for assigning these peaks is the expectation that each should possess some single-photon character due to the strong state mixing with the $^2\Sigma^+_{1/2}(3d)$ state just above the Al($3d$)•Ar dissociation limit. The assignment of A7, the next vibronic level directly below the curve crossing, is consistent with the expected degree of state mixing. The A7 peak possessed both significant single- and two-photon character, the single-photon feature being particularly intense. Furthermore, the shape of this band contour resembles those arising from the $^2\Pi_{1/2}(4p)$ above the Al($3d$)•Ar dissociation limit. Peak A7 was observed close to its predicted peak position, appearing approximately 10 cm^{-1} to the red of where the unperturbed peak would be expected to lie. Such a shift was consistent with the nearby $^2\Sigma^+_{1/2}(3d)$ - $^2\Pi_{1/2}(4p)$ curve crossing. Finally, the two-photon spectrum demonstrated that this peak displayed strong two-photon character, suggestive of a $^2\Pi_{1/2}(4p)$ vibronic level.

Peak A8, the final vibronic level assigned as arising from the $^2\Pi_{1/2}(4p)$ state and the putative 0-0 band, manifests much of the same qualitative behavior and characteristics as peak A7. The strong single-photon character, coupled with an almost identical peak contour as peak A7 as seen in Figure 3-11, argued persuasively for the assignment of peak A8 being a $^2\Pi_{1/2}(4p)$ vibronic band. Furthermore, the peak position was in reasonable agreement with that expected from linear extrapolation, albeit blue-shifted by 11 cm^{-1}. Nonetheless, given the close proximity of the $^2\Pi_{1/2}(3d)$ / $^2\Pi_{1/2}(4p)$ curve crossing just to the red of this feature, such a shift would have been reasonable.

Provided that peaks A8 and B8 did, in fact, represent the 0-0 vibronic levels of the $^2\Pi_{1/2}(4p)$ and $^2\Pi_{3/2}(4p)$ state respectively, we can obtain an estimate of approximately 580 cm^{-1} for the $^2\Pi(4p)$ state D_o value. This estimate was significantly lower than the 744.1 cm^{-1} value tentatively reported by Morse and co-workers,[36] and appeared much more reasonable given the other bond strengths characterized for the Al•Ar molecule.[36,38-40] In particular, the D_o value for the $^2\Pi(6p)$ state has been reported to be 787.8 cm^{-1}. A lower value for the Al($4p$)•Ar dissociation energy seemed more plausible. Furthermore, because the $^2\Pi(3d)$ electronic states possessed a zero-point dissociation energy of roughly 140 cm^{-1}, the $^2\Pi(4p)$ electronic state would not have been expected to acquire a significant augmentation in bond energy through state mixing. Hence, the apparent zero-point energy for the diabatic $^2\Pi(4p)$ state probably did not differ much from the experimentally derived D_o value.

In light of the observed single- and two-photon spectra, it was evident that the assignment for the $^2\Sigma^+_{1/2}(3d)$ state by Morse and co-workers was incorrect.[36] Given the

observed spectroscopic behavior as well as the preliminary *ab initio* results, the $^2\Sigma^+_{1/2}(3d)$ state was in all likelihood primarily repulsive. The shape of this potential was nevertheless interesting. Theory predicted that the $^2\Sigma^+_{1/2}(3d)$ state may have possessed slight bonding character within an internuclear distance region potentially accessible from the ground state.[46] The basis for this bonding character was well-characterized, and arises from the prediction that $\Sigma(nl)$ states derived from excited electronic configurations possess a partial positive charge within the ionic core.[1] At large internuclear distances, a rare gas molecule sees only the excited electron along the internuclear axis, causing the observed repulsive character at large internuclear distances. If, however, the rare gas molecule can penetrate into the electronically excited metal orbital, it can begin to "feel" some of the partial positive charage within the ionic core, introducing a partial ion-induced dipole interaction. The strength of this interaction can induce a region of stability to form within the principally repulsive potential. Increased penetration, however, will at some point result in repulsive behavior once again as the rare gas molecule begins to penetrate into the valance orbitals of the metal. Whether the $^2\Sigma^+_{1/2}(3d)$ potential indeed has such a bound region, and if so whether it can support a bound vibrational level, has not been characterized. The presence of the peak labeled by S that was evident in both single- and two-photon spectra suggested that the $^2\Sigma^+_{1/2}(3d)$ may have possessed at least quasi-bound levels near the region of the curve crossing with the $^2\Pi_{1/2}(4p)$ state.

3.6.2. Spectroscopic Region Below the Al(3d)•Ar Dissociation Limit

3.6.2.1. $^2\Pi_{1/2}(3d)$, $^2\Pi_{3/2}(3d)$, and $^2\Delta(3d)$ Electronic States

The spectral assignments proposed by Morse and co-workers for the $^2\Pi(3d)$, $^2\Pi(4p)$, and $^2\Delta(3d)$ states below the Al(3*d*)•Ar disociation limit have been re-evaluated.[36] In contrast to the previously reported spectrum that assigned the $^2\Pi(3d)$ and $^2\Sigma(3d)$ states as the primary spectral progressions from 32420 cm^{-1} to the Al(3*d*)•Ar dissociation limit, the $^2\Pi_{1/2}(3d)$ and $^2\Pi_{3/2}(3d)$ states are now believed to give rise to much of the observed spectral behavior in this region. Other peaks were indeed present, but their appearance was believed to derive either directly or indirectly from electronic interactions with these two states.

The most prominent spectral characteristic within this region was the $^2\Pi_{1/2}(3d)$ progression labeled by the letter Y shown in Figure 3-6. At first inspection, this progression appeared to be fairly regular, except for some irregularities in the transition intensities near where peaks Y3 through Y5 appeared. Closer inspection of this spectral region, however, revealed a striking discontinuity in the vibronic spacing of this progression. A Birge-Sponer analysis of this progression both before and after this discontinuity produced evidence for two distinct regions of curvature within the $^2\Pi_{1/2}(3d)$ potential. This irregularity has been attributed as being at least partially due to an avoided curve crossing between the $^2\Pi_{1/2}(3d)$ and $^2\Pi_{1/2}(3d)$ electronic states in the region between peaks Y3 through Y5. The only other perceptible deviation in the $^2\Pi_{1/2}(3d)$ state apparent from the Birge-Sponer plot occurred at peak Y11. This peak exhibited a small blue-shift,

a fact that has been rationalized as being the result of a vibronic perturbation from the immediately adjacent peak labeled A7 - a substantially mixed $^2\Pi_{1/2}(4p)$ / $^2\Sigma^+_{1/2}(3d)$ vibronic feature.

The exact nature of the $^2\Pi_{1/2}(3d)$ state was somewhat an enigma due to several characteristics that were difficult to explain within the context of a single coherent model. At least initially, the results of the *ab initio* calculations were highly suggestive of the fact that the true nature of this potential was that of a double-well. In particular, the calculated 151 cm^{-1} electronic coupling between the $^2\Pi(3d)$ and $^2\Pi(4p)$ states was greater than the experimentally observed zero-point dissociation energy of roughly 140 cm^{-1} for the $^2\Pi_{1/2}(3d)$ state itself, indicative of a strongly-mixed adiabatic potential. If this were in fact the case, then the region between Y3 and Y5 would have been expected to lie near the top of the "hump" of a double well. In turn, the 151 cm^{-1} calculated adiabatic coupling would have served to push the upper adiabatic potential curve well above the Al($3d$)•Ar dissociation limit. As a result, the upper vibronic levels of the $^2\Pi_{1/2}(3d)$ progression, namely those above peak Y5, would have arisen from a broad potential whose inner turning point derived from the $^2\Pi(4p)$ state while the outer turning point derived from the $^2\Pi(3d)$ state.

In an attempt to gauge the plausibility of a double-well potential, the behavior of a well-characterized double-well potential, the E,F electronic state of H_2, was closely examined. The double-well nature of the E,F state arises from a strongly avoided crossing between the $(1s2s)\ ^1\Sigma_g^+$ and $(2p\sigma_u)^2\ ^1\Sigma_g^+$ states, resulting in a strongly-coupled adiabat.[48-58] This spectrum manifested much of the qualitative behavior expected for a double-well

potential. Below the region of the hump, the observed vibronic levels displayed vibronic spacings characteristic of the potential from which each individual potential arose. Above the hump region, however, one would have expected to observe a more narrow vibronic spacing, approximately half that exhibited by either of the two individual diabatic states. This was, in fact, what was generally observed in the case of the H_2 E,F state - the much flatter region above the hump giving rise to a significantly reduced vibronic spacing compared to the region below the hump.

In the case of the Al•Ar $^2\Pi_{1/2}(3d)$ state, such pronounced behavior was not observed. Above the putative curve crossing between the $^2\Pi_{1/2}(3d)$ and $^2\Pi_{1/2}(4p)$ states, the vibronic spacing, while derived from a potential of lesser curvature, was nonetheless very close to what would have been expected in the absence of any perturbation. In other words, no evidence for a dramatic change in vibronic spacing was observed, merely a disruption of the progression near the crossing region. Such an observation argued persuasively against adiabatic double-well character in the $^2\Pi_{1/2}(3d)$ state, suggesting instead that whatever the electronic nature of the perturbation occurring in the crossing region, it was highly localized.

One observation that was somewhat puzzling in light of the above discussion was the observed significant two-photon character of the $^2\Pi_{1/2}(3d)$ vibronic levels. More specifically, there appeared to be a marked disparity in the two-photon character of the $^2\Pi_{1/2}(3d)$ potential energy profile that originated from the two distinct regions of curvature. The lower vibronic levels of the $^2\Pi_{1/2}(3d)$ potential, that region characterized by the higher degree of curvature, all possessed considerable two-photon character. This

became especially pronounced close to the $^2\Pi_{1/2}(3d)$ / $^2\Pi_{1/2}(4p)$ crossing region. Above the crossing region, however, the opposite behavior was observed. Peaks Y6 through Y15, those $^2\Pi_{1/2}(3d)$ vibronic levels constituting the upper region of the potential that exhibited the lesser degree of curvature, all appeared to possess little or no two-photon character. The precise origin of this behavior was puzzling. Intrinsically, there was no reason to expect that those vibronic levels above a curve crossing region should be mixed to a lesser degree than those below the curve crossing region. The most likely explanation was that above the $^2\Pi_{1/2}(3d)$ / $^2\Pi_{1/2}(4p)$ curve crossing, the $^2\Pi_{1/2}(4p)$ state was still a strong admixture of $^2\Pi_{1/2}(4p)$ and $^2\Sigma^+_{1/2}(3d)$ electronic character. The high degree of $^2\Sigma^+_{1/2}(3d)$ electronic character in the $^2\Pi_{1/2}(4p)$ state would have served to limit the two-photon character of the latter while augmenting single-photon character of any vibronic levels arising from the $^2\Pi_{1/2}(4p)$ state. This was apparently what was observed, since peaks A7 and A8 appear quite strongly in the single-photon spectrum. In contrast, vibronic levels from the $^2\Pi_{1/2}(3d)$ state in the upper region of curvature were barely evident above the $^2\Pi_{1/2}(3d)$ / $^2\Pi_{1/2}(4p)$ curve crossing region in the two-photon spectrum.

A second progression observed within this spectral region, labeled by the letter Z in Figure 3-6, has been assigned as the vibronic levels arising from the $^2\Pi_{3/2}(3d)$ state. The observed intensities of these features were significantly weaker than those assigned to the $^2\Pi_{1/2}(3d)$ state. The low intensity of the $^2\Pi_{1/2}(3d)$ state relative to the $^2\Pi_{1/2}(3d)$ state in the single-photon $1'_{UV} + 1_{vis}$ REMPI spectrum can be most readily attributable to dominant Hund's case (a) character in the $^2\Pi(3d)$ electronic manifold. In strict Hund's case (a), only the $^2\Pi_{1/2}(3d) \leftarrow X_1\,^2\Pi_{1/2}(3p)$ transitions would have been observed due to

the strict $\Delta\Sigma = 0$ selection rule. The fact that a weak $^2\Pi_{3/2}(3d)$ progression was observed suggested that the $^2\Pi(3d)$ electronic manifold was predominantly described by Hund's case (a), in which partial Hund's case (b) character was mixed. Such behavior was consistent with the rotational constants of the Al•Ar molecule. The ground state of Al•Ar possessed a rotational constant, B_o, of 0.07 cm^{-1}, and the expected $^2\Pi_{1/2}(3d)$ state rotational constant will be slightly smaller. At high rotational values, the energy difference between BJ becomes comparable to the spin-orbit energy difference expected from the $^2\Pi(3d)$ states given the atomic spin-orbit splitting of 1.34 cm^{-1}. Hence, some Hund's case (b) character in the $^2\Pi_{3/2}(3d)$ state was expected, accounting for the observed disparity in intensity between the $^2\Pi_{1/2}(3d)$ and $^2\Pi_{3/2}(3d)$ states.

One unusual feature of the assigned $^2\Pi_{1/2}(3d)$ and $^2\Pi_{3/2}(3d)$ states was the large spin-orbit splitting. In particular, the observed spin-orbit splittings between 4 - 5.5 cm^{-1} were significantly larger than expected given the splitting of 1.34 cm^{-1} between the $^2\Pi_{1/2}(3d)$ and $^2\Pi_{3/2}(3d)$ asymptotes. While such splittings were consistent with the predominant Hund's case (a) character apparent from the relative intensities of the $^2\Pi_{1/2}(3d)$ and $^2\Pi_{3/2}(3d)$ states, the fact that the magnitude of the splitting exceeds that of the atomic asymptotes was indicative of some secondary effect presently unaccounted for. Furthermore, examination of Table 3-7 revealed that except for the Z3-Y3 splitting, the spin-orbit splittings between the $^2\Pi_{1/2}(3d)$ and $^2\Pi_{3/2}(3d)$ states appeared to increase with decreasing vibrational quantum number.

In spite of such apparently anomalous behavior, such a trend has, in fact, been previously observed in several M•Ar systems, in particular Mg($3s3d\pi\ ^3D_J$)•Ar($^3\Pi$),[6]

Na($3p\pi$ ^2P_J)•Ar($^2\Pi$),[44] and Mg^+($3s4p$ ^2P_J)•Ar($^2\Pi$).[45] Three lines of argument have been invoked to account for this behavior. The first of these involves an augmentation in spin-orbit character gleaned through state mixing between a state exhibiting a small spin-orbit energy difference with another state of inherently greater spin-orbit character. In the case of the Mg($3s3d\pi$ ^3D_J)•Ar($^3\Pi$) state,[6] the observed 5 - 6 cm^{-1} spin-orbit splittings were unexpected due to sub-wavenumber atomic asymptotic splittings suggestive of Hund's case (b) character. Strong electronic mixing in the region of r_e with a lower energy, close-lying diabatic Mg($3s4p\pi$ ^3P_J)•Ar($^3\Pi$) state was postulated to partially account for the augmented spin-orbit coupling. By direct analogy, state mixing between the $^2\Pi_{1/2}(3d)$ and $^2\Pi_{3/2}(3d)$ states with the $^2\Pi_{1/2}(4p)$ and $^2\Pi_{3/2}(4p)$ states could provide a mechanism by which greater spin-orbit coupling is introduced. Due to the 15.83 cm^{-1} splitting between the $^2\Pi_{1/2}(4p)$ and $^2\Pi_{3/2}(4p)$ atomic asymptotes, partial state mixing between the $^2\Pi(3d)$ and $^2\Pi(4p)$ states could serve to increase the observed $^2\Pi_{1/2}(3d)$ - $^2\Pi_{3/2}(3d)$ splitting.

Nevertheless, it is doubtful whether this was the best explanation in the case of Al•Ar. If state mixing were to completely account for this increased splitting, the energy differences between $^2\Pi_{1/2}(3d)$ and $^2\Pi_{3/2}(3d)$ vibronic components would be expected to become larger closer to the crossing region with the $^2\Pi_{1/2}(4p)$ and $^2\Pi_{3/2}(4p)$ electronic states. In general, this was not observed except in the last two spin-orbit doublets that exhibited a slight increase in the energy difference close to the curve crossing region.

An alternative explanation that has been invoked to explain anomalously large spin-orbit splittings in the Na($3p\pi$ ^2P_J)•Ar($^2\Pi$)[44] and Mg^+($3s4p$ ^2P_J)•Ar($^2\Pi$)[45] systems involved the possibility for partial electron delocalization to the argon atomic moiety.

With increasing electronic excitation, the excited electron becomes more and more Rydberg-like, effectively decoupling from the ion core. Such a decoupling allows for the possibility for electron delocalization along the internuclear axis joining the two atomic moieties. In essence, electronic excitation within the metal atom offers the possibility of delocalizing very small fractions of electron density onto the argon binding partner. Due to the very large spin-orbit difference in the argon atom ground state of approximately 1000 cm^{-1},[60] the electronically-excited electron on the aluminum moiety need only very weakly couple to the argon nucleus to experience a large increase in apparent spin-orbit character.[1] For the magnitude of the observed spin-orbit splittings, only a 0.5% fractional coupling of the aluminum electron density to the argon nucleus would be sufficient to account for the increased spin-orbit character of the $^2\Pi_{1/2}(3d)$ and $^2\Pi_{3/2}(3d)$ states.

A third and final possible explanation also involved state mixing. However, in contrast to the first rationalization where state mixing served to increase the spin-orbit character of both $^2\Pi_{1/2}(3d)$ and $^2\Pi_{3/2}(3d)$ states, selective state mixing between one of the two $^2\Pi(3d)$ states with some other state is also possible. The end result of such a coupling would result in an *apparent* augmented spin-orbit coupling when in fact the aluminum atomic moiety could remain predominately Al($3d$) in character. In other words, a curve crossing to the blue of a given $^2\Pi_{1/2}(3d)$ / $^2\Pi_{3/2}(3d)$ vibronic level that selectively coupled to the $^2\Pi_{1/2}(3d)$ state could cause a red-shift in this band, giving the appearance of an augmented spin-orbit coupling. The inverse scenario with the $^2\Pi_{3/2}(3d)$ state would have an identical effect.

One possible candidate for such an effect would be state mixing between the

$^2\Delta_{3/2}(3d)$ state with the $^2\Pi_{3/2}(3d)$ state. Due to the substantial zero-point dissociation energy of 663.5 cm^{-1} found as a result of this work, the $^2\Delta(3d)$ state was expected to possess an equilibrium bond distance that was significantly shortened relative to the $^2\Pi(3d)$ states that were bound by only 140 cm^{-1}. In this situation, it would be reasonable to conclude that the outer turning point of the upper vibronic levels of the $^2\Delta(3d)$ states lay near the outer turning points of the $^2\Pi(3d)$ potentials. Since the $^2\Delta(3d)$ states were more strongly bound, this implied that the $^2\Delta(3d)$ potentials might interact with the $^2\Pi(3d)$ potentials either along the outer wall of the $^2\Pi(3d)$ potentials or near the minima of the potential energy well. Such qualitative behavior was supported by the preliminary *ab initio* results that demonstrated a crossing between these two potentials close to the dissociation limit.[46] Nevertheless, given the dramatically underestimated bond strengths for both the $^2\Delta(3d)$ and $^2\Pi(3d)$ states, this crossing could have, in reality, lay much lower along the $^2\Pi(3d)$ potential outer wall.

Using the same arguments presented above to describe the nature of the coupling between the $^2\Pi_{1/2}(4p)$ and $^2\Sigma^+_{1/2}(3d)$ states, non-zero off-diagonal matrix elements of the spin-electronic interaction between the $^2\Delta_{3/2}(3d)$ and $^2\Pi_{3/2}(3d)$ electronic states were possible. The $^2\Delta_{3/2}(3d)$ electronic state is described by the $|\ \Lambda = 2, \Sigma = -1/2, \Omega = 3/2\ >$ electronic configuration, while the $^2\Pi_{3/2}(3d)$ is described by $|\ \Lambda = 1, \Sigma = 1/2, \Omega = 3/2\ >$. The off-diagonal selection rules - $\Delta\Lambda = {}^{+}/_{-}1$, $\Delta\Sigma = {}^{-}/_{+}1$, $\Delta S = 0$ and $\Delta\Omega = 0$ - designate that coupling between these states was allowed, although the magnitude of the coupling was difficult to estimate in the absence of a high level electronic structure calculation that explicitly accounts for the effects of spin-orbit coupling.

Both the single- and two-photon spectra provided provisional evidence for a state mixing interaction between the $^2\Delta_{3/2}(3d)$ and $^2\Pi_{3/2}(3d)$ electronic states. Directly adjacent to the blue of the $^2\Pi_{3/2}(3d)$ 0-0 and 0-1 vibronic features were two features whose presence was difficult to assign to any previously discussed electronic state. These features, labeled D10 and D11 in Figures 3-6 and 3-7, have been assigned as tentative vibronic features of the $^2\Delta_{3/2}(3d)$ potential to the red of the $^2\Delta(3d)$ vibronic features assigned previously by Morse and co-workers.[36]

The appearance of these peaks was rationalized as deriving from a state mixing interaction between the $^2\Delta_{3/2}(3d)$ and $^2\Pi_{3/2}(3d)$ electronic states near the minimum of the $^2\Pi_{3/2}(3d)$ potential energy profile. Both peaks D10 and D11 were believed to possess negligible Franck-Condon intensity on the *diabatic* $^2\Delta(3d)$ potentials due to poor overlap with the 0-0 vibronic band of the ground state. State mixing with the $^2\Pi_{3/2}(3d)$ electronic state near its minimum point would have undoubtedly caused large variations to the electronic wavefunctions as well as transition dipole matrix elements of both electronic states in the near vicinity of the interaction region. The appearance of peaks D10 and D11, then, was presumably due to mixing with the $^2\Pi_{3/2}(3d)$ electronic wavefunction that clearly lay within the Franck-Condon region given the strong intensity of the $^2\Pi_{1/2}(3d)$ vibronic bands that lay in the near vicinity.

This assignment of peaks D10 and D11 as arising from the $^2\Delta_{3/2}(3d)$ electronic state was consistent with a number of additional qualitative criteria. Foremost, both peaks lay close to the next expected vibronic features of the $^2\Delta_{3/2}(3d)$ progression derived from extrapolation from the Birge-Sponer plot. Likewise, both peaks demonstrated small

blue-shifts, consistent with the notion of a state mixing interaction near the bottom of the $^2\Pi_{3/2}(3d)$ potential energy well. The observed blue-shifts of peaks D10 and D11 relative to the predicted peak positions are approximately 10.6 cm^{-1} and 6.0 cm^{-1} respectively. The relative magnitude of the blue-shifts was in accordance with the notion that the interaction region occurred closer to the D10 vibronic band. Furthermore, the band contours of peaks D10 and D11 resembled those of the other $^2\Delta(3d)$ vibronic features by being shaded to the blue. Vibronic features arising from the $^2\Pi(3d)$ or $^2\Pi(4p)$ electronic states differed in that they appeared shaded to the red.

The possible existence of a state mixing interaction between the $^2\Delta_{3/2}(3d)$ and $^2\Pi_{3/2}(3d)$ electronic states near the bottom of the $^2\Pi_{3/2}(3d)$ potential well could also explain several characteristics of the $^2\Pi_{3/2}(3d)$ vibronic bands. First, the apparent increase in spin-orbit coupling may not be due to mixing of Al($4p$) orbital character into the Al($3d$) orbitals, but a selective blue-shift of the $^2\Pi_{3/2}(3d)$ vibronic levels relative to those of the $^2\Pi_{1/2}(3d)$ state. The increasing energy difference between $^2\Pi_{1/2}(3d)$ and $^2\Pi_{3/2}(3d)$ vibronic levels with decreasing vibrational quantum number was also consistent with this picture. With an interaction region near the minima of the $^2\Pi_{3/2}(3d)$ state, the lowest vibronic levels would have been expected to exhibit larger red-shifts.

A state mixing interaction can also be invoked to speculate about the observed intensity pattern of the $^2\Pi_{3/2}(3d)$ vibronic levels. If the $^2\Pi(3d)$ state were principally Hund's case (a) in character, one would expect negligible transition intensity to be observed from the $^2\Pi_{3/2}(3d)$ electronic state. State mixing with the $^2\Delta_{3/2}(3d)$ potential may have a local effect on the transition intensities of the $^2\Pi_{3/2}(3d)$ state by relaxing the strict

$^2\Pi_{1/2}(3d) \leftarrow X_1\ ^2\Pi_{1/2}(3p)$ selection rule in Hund's case (a). Since $\Delta\Lambda = 1$, $\Delta\Omega = 0$ transitions are allowed in Hund's case (a), this mixing may serve to permit an otherwise negligible transition to become detectable. The fact that the transition intensities decreased rapidly away from the putative interaction region lent further credence to such a picture. The magnitude of the coupling should decrease rapidly away from the crossing region, quenching the transition intensity in the $^2\Pi_{3/2}(3d)$ state with increasing vibrational quantum number.

Whether or not a state mixing interaction between the $^2\Delta_{3/2}(3d)$ and $^2\Pi_{3/2}(3d)$ states does indeed exist, such a picture presented a means to further understand the origin of the presumptive enhanced curvature of the $^2\Pi(3d)$ state in the lower region of the potential well. In the absence of the $^2\Delta_{3/2}(3d)$ / $^2\Pi_{3/2}(3d)$ interaction, it is difficult to reconcile the increased curvature of the lower $^2\Pi_{1/2}(3d)$ vibronic region as being due solely to a curve crossing with the $^2\Pi_{1/2}(4p)$ state. If, however, we include interactions that might arise due to an additional interaction between the $^2\Delta(3d)$ and $^2\Pi(3d)$ states, this enigmatic aspect became less puzzling. Both the $^2\Delta(3d)$ / $^2\Pi(3d)$ and $^2\Pi(3d)$ / $^2\Pi(4p)$ interaction regions occurred at different points along the $^2\Pi_{1/2}(3d)$ potential. The former would be expected to occur on the outer turning point region of the $^2\Pi_{1/2}(3d)$ potential, while the latter influences the inner region. The presence of a $^2\Delta(3d)$ / $^2\Pi(3d)$ interaction near the minimum of the $^2\Pi(3d)$ potential well would have provided an additional source of localized adiabatic character to explain the apparently greater curvature observed in the lower regions of this potential.

While the previous assignment by Morse and co-workers of the $^2\Delta(3d)$ progression

was correct,[36] the reported 0-0 vibronic level has been found to be incorrect. Two additional vibronic levels were found over the course of this work below the reported 0-0 level. Both of the newly discovered features match well on a Birge-Sponer plot with those features reported by Morse and co-workers.[36] The apparently significant deviation of the 0-1 $^2\Delta(3d)$ band was presumably due to the high harmonic character of the $^2\Delta(3d)$ potential near the minimum of the potential well. With the newly discovered 0-0 vibronic band, a revised experimental $^2\Delta(3d)$ D_o value of 663.5 cm^{-1} was obtained.

3.7. Conclusion

This work provided the first complete characterization of the Al•Ar electronic manifolds arising from the Al(3*d*)•Ar and Al(4*p*)•Ar electronic configurations, with the exception of the $^2\Sigma^+_{1/2}(4p)$ state that is the subject of Chapter 4. Both $1'_{UV} + 1_{vis}$ REMPI as well as $2_{vis} + 1_{vis}$ REMPI have been employed to probe the Al(3*d*)•Ar and Al(4*p*)•Ar manifolds, both extending and re-evaluating the single-photon work reported previously by Morse's group on the Al(3*d*)•Ar states. A definitive assignment of the observed spectral features was difficult due to the substantial complexity arising from the presence of several potential energy curve crossings. While the work reported herein represents the the most plausible assignment based on the presently available spectral resolution of the individual vibronic features, it is not definitive. A systematic dissection of each observed vibronic level with rotational resolution is required if the true electronic character of each of the features is to be understood with certainty.

3.8. References

1. W. H. Breckenridge, C. Jouvet, and B. Soep, in *Advances in Metal and Semiconductor Clusters*, M. A. Duncan, Ed. (JAI Press, Greenwich, 1995), and references therein.
2. S. Bililign, M. Gutowski, J. Simons, and W. H. Breckenridge, *J. Chem. Phys.*, **100**, 8212 (1994), and references therein.
3. J. G. Kaup and W. H. Breckenrigdge, *J. Phys. Chem.*, **99**, 13701 (1995).
4. S. Massick and W. H. Breckenridge, *J. Chem. Phys.*, **104**, 7784 (1996).
5. S. Massick and W. H. Breckenridge, *J. Chem. Phys.*, **105**, 6154 (1996).
6. S. Massick and W. H. Breckenridge, *J. Chem. Phys.*, **105**, 9719 (1996).
7. S. Massick and W. H. Breckenridge, *Chem. Phys. Lett.*, **257**, 465 (1996).
8. A. W. K. Leung, M. Roberson, J. Simons, and W. H. Breckenridge, *Chem. Phys. Lett.*, **259**, 199 (1996).
9. S. Massick and W. H. Breckenridge, *J. Chem. Phys.*, **106**, 2171 (1997).
10. J. G. Kaup and W. H. Breckenridge, *J. Chem. Phys.*, **107**, 2180 (1997).
11. J. G. Kaup and W. H. Breckenridge, *J. Chem. Phys.*, **107**, 4451 (1997).
12. J. G. Kaup and W. H. Breckenridge, *J. Chem. Phys.*, **107**, 5283 (1997).
13. J. G. Kaup and W. H. Breckenridge, *J. Chem. Phys.*, **107**, 5676 (1997).
14. J. G. Kaup and W. H. Breckenridge, *J. Chem. Phys.*, **107**, 6005 (1997).
15. J. G. Kaup and W. H. Breckenridge, *J. Chem. Phys.*, **107**, 6014 (1997).
16. J. G. Kaup, A. W. K. Leung, and W. H. Breckenridge, *J. Chem. Phys.*, **107**, 10492 (1997).
17. K. Onda, K. Yamanouchi, M. Okunishi, and S. Tsuchiya, *J. Chem. Phys.*, **101**, 7290 (1994).
18. K. Onda and K. Yamanouchi, *J. Chem. Phys.*, **102**, 1129 (1995).
19. K. Onda and K. Yamanouchi, *J. Chem. Phys.*, **104**, 9376 (1996).
20. E. Hwang, Y. L. Huang, P. J. Dagdigian, and M. H. Alexander, *J. Chem. Phys.*, **98**, 8484 (1993).

21. E. Hwang, P. J. Dagdigian, and M. H. Alexander, *Can. J. Chem.*, **72**, 821 (1994).
22. E. Hwang and P. J. Dagdigian, *Chem. Phys. Lett.*, **233**, 483 (1995).
23. X. Yang, E. Hwang, P. J. Dagdigian, M. Yang, and M. H. Alexander, *J. Chem. Phys.*, **103**, 2779 (1995).
24. X. Yang, E. Hwang, and P. J. Dagdigian, *J. Chem. Phys.*, **104**, 599 (1996).
25. M. H. Alexander, A. R. Walton, M. Yang, X. Yang, E. Hwang, and P. J. Dagdigian, *J. Chem. Phys.*, **106**, 6320 (1997).
26. X. Yang and P. J. Dagdigian, *J. Chem. Phys.*, **106**, 6596 (1997).
27. X. Yang and P. J. Dagdigian, *J. Phys. Chem. A*, **101**, 3509 (1997).
28. X. Yang, P. J. Dagdigian, and M. H. Alexander, *J. Chem. Phys.*, **108**, 3522 (1998).
29. G. Herzberg, *Molecular Spectra and Molecular Structure I. Spectra of Diatomic Molecules* (Krieger Pub. Co., Malabar, Florida, 1989).
30. P. F. Bernath, *Spectra of Atoms and Molecules* (Oxford University Press, New York, 1995).
31. D. J. Funk and W. H. Breckenridge, *J. Chem. Phys.*, **90**, 2927 (1989).
32. D. J. Funk, A. Kvaran, and W. H. Breckenridge, *J. Chem. Phys.*, **90**, 2915 (1989).
33. I. Wallace, J. G. Kaup, and W. H. Breckenridge, *J. Phys. Chem.*, **95**, 8060 (1991).
34. I. Wallace, R. R. Bennett, and W. H. Breckenridge, *Chem. Phys. Lett.*, **153**, 127 (1988).
35. I. Wallace, J. Ryter, and W. H. Breckenridge, *J. Chem. Phys.*, **96**, 136 (1992).
36. S. A. Heidecke, Z. Fu, J. R. Colt, and M. D. Morse, *J. Chem. Phys.*, **97**, 1692 (1992).
37. S. Bashkin and J. O. Stoner, Jr., *Atomic Energy Levels and Grotrian Diagrams, Vol. I. Hydrogen I - Phosphorus XV* (North-Holland Pub. Co., Amsterdam, 1975).
38. J. M. Gardner and M. I. Lester, *Chem. Phys. Lett.*, **137**, 301 (1987).
39. C. L. Callender, S. A. Mitchell, and P. A. Hackett, *J. Chem. Phys.*, **90**, 5252 (1989).
40. M. J. McQuaid, J. L. Gole, and M. C. Heaven, *J. Chem. Phys.*, **92**, 2733 (1990).
41. H. Partridge, C. W. Bauschlicher, Jr., and L. Visscher, *Chem. Phys. Lett.*, **246**, 33 (1995).

42. K. F. Willey, C. S. Yeh, and M. A. Duncan, *Chem. Phys. Lett.*, **211**, 156 (1993).
43. W. C. Wiley and I. H. McLaren, *Rev. Sci. Instrum.*, **26**, 1150 (1955).
44. R. E. Smalley, D. A. Auerbach, P. S. H. Fitch, D. H. Levy, and L. Wharton, *J. Chem. Phys.*, **66**, 3778 (1977).
45. J. S. Pilgrim, C. S. Yeh, K. R. Berry, and M. A. Duncan, *J. Chem. Phys.*, **100**, 7945 (1994).
46. J. A. Boatz, J. A. Sheehy, and P. W. Langhoff, in *Monte Carlo Simulations of the Structures and the Optical Absorption Spectra of Al/Ar$_N$ Clusters: Applications of the Spectral Theory of Chemical Binding, Proceedings of the High Energy Density (HEDM) Conference*, June 1997 (USAF Office of Scientific Research, Bolling AFB, DC, 1997).
47. R. A. Aziz and M. J. Slaman, *Mol. Phys.*, **58**, 679 (1986).
48. G. H. Dieke, *J. Mol. Spec.*, **2**, 494 (1958).
49. E. R. Davidson, *J. Chem. Phys.*, **35**, 1189 (1961).
50. R. J. Boye, *J. Mol. Spec.*, **26**, 36 (1968).
51. T. E. Sharp, *Atomic Data*, **2**, 119 (1971).
52. J. D. Alemar-Rivera and A. L. Ford, *J. Mol. Spec.*, **67**, 336 (1977).
53. L. Wolniewicz and K. Dressler, *J. Mol. Spec.*, **67**, 416 (1977).
54. D. J. Kliger and C. K. Rhodes, *Phys. Rev. Lett.*, **40**, 309 (1978).
55. D. J. Kliger, J. Bokor, and C. K. Rhodes, *Phys. Rev. A*, **21**, 607 (1980).
56. E. E. Marinero, C. T. Rettner, and R. N. Zare, *Phys. Rev. Lett.*, **48**, 1323 (1982).
57. W. M. Huo and R. L. Jaffe, *Chem. Phys. Lett.*, **101**, 463 (1983).
58. S. L. Anderson, G. D. Kubiak and R. N. Zare, *Chem. Phys. Lett.*, **105**, 22 (1984).
59. H. Lefebvre-Brion and Robert W. Field, *Perturbations in the Spectra of Diatomic Molecules* (Academic Press, Orlando, 1986).
60. S. Bashkin and J. O. Stoner, Jr., *Atomic Energy Levels and Grotrian Diagrams, Vol. II. Sulfur I - Titanium XXII* (North-Holland Pub. Co., Amsterdam, 1978).

TABLE 3-1: Summary of $^2\Pi_{1/2}(4p) \leftarrow X_1\ ^2\Pi_{1/2}(3p)$ and $^2\Pi_{3/2}(4p) \leftarrow X_1\ ^2\Pi_{1/2}(3p)$ Vibronic Features Observed Above the Al(3*d*)•Ar Dissociation Limit Using $2_{vis} + 1_{vis}$ Two-Photon Excitation.

$^2\Pi_{1/2}(4p)$ Label	$^2\Pi_{3/2}(4p)$ Label	Other Label	Al•Ar$^+$ Channel (cm^{-1})	Al$^+$ Fragment Channel (cm^{-1})
A1			32890	---------
	B2		32862	---------
A2			32848	32848
	B3		32816.5	32817.2
A3			32803.7	32803.3
		X1	32775.5	32777.0
	B4		32765.7	32765.0
A4			32753.5	32752.7
	B5		32708.0	32706.4
A5			32697.0	32695.3
	B6		32652.2	32651.0
A6(Broad)			---------	32626 max.
		X2	32587.0	32586.5
	B7		32572.9	32572.0
		S	32618.4	---------

Legend: A# = $^2\Pi_{1/2}(4p) \leftarrow X_1\ ^2\Pi_{1/2}(3p)$ Transition

B# = $^2\Pi_{3/2}(4p) \leftarrow X_1\ ^2\Pi_{1/2}(3p)$ Transition

S# = $^2\Sigma^+_{1/2}(3d) \leftarrow X_1\ ^2\Pi_{1/2}(3p)$ Related Feature (Tentative)

X# = Unassigned Feature

TABLE 3-2: Summary of $^2\Pi_{3/2}(4p)$ - $^2\Pi_{1/2}(4p)$ Spin-Orbit Splittings to the Blue of the Perturbed Region above the Al($3d$)•Ar Dissociation Limit.

Vibronic Levels	ΔE_{so} (cm^{-1}) - Taken from Al•Ar^+ Channel
B2-A2	14
B3-A3	12.8
B4-A4	12.2
B5-A5	11.0

Atomic aluminum $^2P_{3/2}(4p)$ - $^2P_{3/2}(4p)$ ΔE_{so} = 15.83 cm^{-1}

TABLE 3-3: Predicted $^2\Pi_{1/2}(4p)$ Vibronic Bands Above and Below the Al($3d$)•Ar Dissociation Limit Derived by Linear Extrapolation from Peaks A2, A3, A4, and A5 and a Comparison to the Observed Experimental Values.

Vibronic Band Difference	ΔE (cm^{-1})	Predicted Vibronic Band Position (cm^{-1})	Experimental Vibronic Band Position (cm^{-1})
A2-A3	44.3[a]	-------	-------
A3-A4	50.2[a]	-------	-------
A4-A5	56.5[a]	-------	-------
A5-A6	62.5	32634 (A6)	-------
A6-A7	68.6	32566 (A7)	32548 (A7)[b]
Al($3d$)•Ar Dissociation Limit			
A7-A8	74.7	32491 (A8)	32502 (A8)
A8-A9	80.8	32410 (A9)	-------

[a] Observed Experimental Value

[b] Assigned as Below Al($3d$)•Ar Dissociation Limit

TABLE 3-4: Predicted $^2\Pi_{3/2}(4p)$ Vibronic Bands Above and Below the Al($3d$)•Ar Dissociation Limit Derived by Linear Extrapolation from Peaks B2, B3, B4, and B5 and a Comparison to the Observed Experimental Values.

Vibronic Band Difference	ΔE (cm^{-1})	Predicted Vibronic Band Position (cm^{-1})	Experimental Vibronic Band Position (cm^{-1})
B2-B3	45.5[a]	-------	-------
B3-B4	50.8[a]	-------	-------
B4-B5	57.7[a]	-------	-------
B5-B6	63.5	32644 (B6)	32652 (B6)
B6-B7	69.6	32575 (B7)	32572 (B7)
Al($3d$)•Ar Dissociation Limit			
B7-B8	75.7	32499 (B8)	-------
B8-B9	81.8	32417 (B9)	-------

[a] Observed Experimental Value

TABLE 3-5: Summary of the $^2\Pi_{1/2}(3d) \leftarrow X_1\,^2\Pi_{1/2}(3p)$ Vibronic Features Observed Up to the Al(3*d*)•Ar Dissociation Limit.

Label	Single-Photon Excitation (cm^{-1})	Two-Photon Excitation (cm^{-1})[a]
Y0	32420.0	32420.7
Y1	32440.9	32436.2
Y2	32458.0	32458.7
Y3	32472.3	32472.9
Y4	32484.4	32485.6
Y5	32495.4	32496.4
Y6	32507.5	32508.6
Y7	32517.2	32518.2
Y8	32526.0	---------
Y9	32533.9	32534.4
Y10	32540.5	32541.8
Y11	32545.5	---------
Y12	32551.0	---------
Y13	32554.1	---------
Y14	32556.4	---------
Y15	32557.7	---------

[a] Due to the spectral breadth of many of the two-photon vibronic features, the reported peak positions should be considered accurate to within ± 0.5-1.0 cm^{-1}.

Note: All reported vibronic bands from the single-photon excitation spectrum were calibrated against the atomic Al(3*d*) ← Al(3*p*) transitions

$^2D_{3/2} \leftarrow {}^2P_{1/2}$ at 32435.45 cm^{-1}

$^2D_{5/2} \leftarrow {}^2P_{3/2}$ at 32324.75 cm^{-1}

$^2D_{3/2} \leftarrow {}^2P_{3/2}$ at 32323.41 cm^{-1}

and are accurate to within ± 0.11 cm^{-1}.

TABLE 3-6: Summary of the $^2\Pi_{3/2}(3d) \leftarrow X_1\ ^2\Pi_{1/2}(3p)$ Vibronic Features Observed Up to the Al(3*d*)•Ar Dissociation Limit.

Label	Single Photon Excitation (cm^{-1})	Two-Photon Excitation (cm^{-1})[a]
Z0	32425.5	32425.8
Z1	32445.8	32440.9
Z2	32461.9	32463.0
Z3	32476.4	32477.2

[a] Due to the spectral breadth of many of the two-photon vibronic features, the reported peak positions should be considered accurate to within ± 0.5-1.0 cm^{-1}.

Note: All reported vibronic bands from the single-photon excitation spectrum were calibrated against the atomic Al(3*d*) ← Al(3*p*) transitions

$^2D_{3/2} \leftarrow {}^2P_{1/2}$ at 32435.45 cm^{-1}

$^2D_{5/2} \leftarrow {}^2P_{3/2}$ at 32324.75 cm^{-1}

$^2D_{3/2} \leftarrow {}^2P_{3/2}$ at 32323.41 cm^{-1}

and are accurate to within ± 0.11 cm^{-1}.

TABLE 3-7: Summary of the $^2\Pi_{1/2}(3d)$ - $^2\Pi_{3/2}(3d)$ Spin-Orbit Splitting.

Vibronic Levels	ΔE_{so} (cm^{-1})
Z0-Y0	5.5
Z1-Y1	4.9
Z2-Y2	3.9
Z3-Y3	4.1

3.9. Figure Captions

Figure 3-1 Resonant multiphoton excitation schemes employed during the course of the experiment. The left-hand side shows the $1'_{UV} + 1_{vis}$ two-color multiphoton ionization (MPI) methodology used to probe electronic states of predominantly Al($3d$)•Ar character. The right-hand side shows the $2_{vis} + 1_{vis}$ single-color MPI methodology used to probe electronic states of predominantly Al($4p$)•Ar character.

Figure 3-2 $2_{vis} + 1_{vis}$ single-color multiphoton ionization (MPI) spectra obtained above the Al($3d$)•Ar dissociation limit at 32557.8 cm^{-1}. At the top is the spectrum obtained by monitoring the $Al•Ar^+$ ion signal, while the bottom spectrum shows the Al^+ ion fragment signal recorded over the same spectral region. Peaks labeled by A# or B# correspond to transitions from the $^2\Pi_{1/2}(3p)$ ground state to the $^2\Pi_{1/2}(4p)$ and $^2\Pi_{3/2}(4p)$ electronic states respectively.

Figure 3-3 $1'_{UV} + 1_{vis}$ two-color multiphoton ionization (MPI) spectra obtained above the Al($3d$)•Ar dissociation limit at 32557.8 cm^{-1} by monitoring the $Al•Ar^+$ ion signal. The presumed location of the $^2\Pi_{1/2}(4p)$ vibronic band obscured in the $2_{vis} + 1_{vis}$ single-color MPI spectra is labeled as A6.

Figure 3-4 $1'_{UV} + 1_{vis}$ two-color multiphoton ionization (MPI) spectrum obtained above the Al($3d$)•Ar dissociation limit at 32557.8 cm^{-1} by monitoring the Al^+ ion fragment signal. Peaks labeled by A# or B# correspond to the nominally single-photon forbidden electronic transitions from the $^2\Pi_{1/2}(3p)$ ground state to the $^2\Pi_{1/2}(4p)$ and $^2\Pi_{3/2}(4p)$ electronic states respectively.

Figure 3-5 Comparison of the $2_{vis} + 1_{vis}$ single-color multiphoton ionization (MPI) spectrum (top) and $1'_{UV} + 1_{vis}$ two-color MPI spectrum (bottom) obtained below the Al($3d$)•Ar dissociation limit at 32557.8 cm^{-1} by monitoring the $Al•Ar^+$ ion signal. Peaks labeled by O# in the $2_{vis} + 1_{vis}$ MPI spectrum correspond to unidentified spectral features.

Figure 3-6 $1'_{UV} + 1_{vis}$ two-color multiphoton ionization (MPI) spectra obtained below the Al($3d$)•Ar dissociation limit at 32557.8 cm^{-1} by monitoring the Al•Ar^+ ion signal. Peaks labeled by Y#, Z#, and D# have been assigned to transitions arising from the $^2\Pi_{1/2}(3p)$ ground state to the $^2\Pi_{1/2}(3d)$, $^2\Pi_{3/2}(3d)$, and $^2\Delta(3d)$ electronic states respectively. Also shown are the putative 0-0 and 0-1 vibronic levels of the $^2\Pi_{1/2}(4p)$ electronic state labeled by A8 and A7 respectively.

Figure 3-7 $2_{vis} + 1_{vis}$ single-color multiphoton ionization (MPI) spectra obtained below the Al($3d$)•Ar dissociation limit at 32557.8 cm^{-1} by monitoring the Al•Ar^+ ion signal. Peaks labeled by Y#, Z#, and D# have been assigned to transitions arising from the $^2\Pi_{1/2}(3p)$ ground state to the $^2\Pi_{1/2}(3d)$, $^2\Pi_{3/2}(3d)$, and $^2\Delta(3d)$ electronic states respectively. Also shown are both the putative 0-0 and 0-1 vibronic levels of the $^2\Pi_{1/2}(4p)$ electronic state labeled by A8 and A7 respectively, as well as the putative 0-0 and 0-1 vibronic levels of the $^2\Pi_{3/2}(4p)$ electronic state labeled by B8 and B7 respectively.

Figure 3-8 Birge-Sponer plot of the vibronic progression arising from the $^2\Pi_{1/2}(3d) \leftarrow X_1\ ^2\Pi_{1/2}(3p)$ transitions (Y0 through Y15).

Figure 3-9 Birge-Sponer plot of the lowest four vibronic transitions (Y0 through Y3) between the $^2\Pi_{1/2}(3p)$ ground state and the $^2\Pi_{1/2}(3d)$ electronic state below the presumptive $^2\Pi_{1/2}(3d)$ / $^2\Pi_{1/2}(4p)$ curve crossing region.

Figure 3-10 Birge-Sponer plot of the upper vibronic transitions (Y7 through Y15) between the $^2\Pi_{1/2}(3p)$ ground state and the $^2\Pi_{1/2}(3d)$ electronic state above the presumptive $^2\Pi_{1/2}(3d)$ / $^2\Pi_{1/2}(4p)$ curve crossing region.

Figure 3-11 Comparison of the peak contours for both $^2\Pi_{1/2}(4p)$ vibronic levels (A8 and A7) assigned below the Al($3d$)•Ar dissociation limit.

Figure 3-12 New vibronic levels attributed to the $^2\Delta(3d)$ electronic state to the red of the previously assigned 0-0 $^2\Delta(3d)$ vibronic level by Morse and co-workers.[36] (a) the new $^2\Delta(3d)$ 0-0 vibronic band. (b) the new $^2\Delta(3d)$ 0-1 vibronic band.

Figure 3-13 Birge-Sponer plot for the $^2\Delta(3d)$ electronic state including the newly discovered 0-0 and 0-1 vibronic bands together with those previously reported by Morse and co-workers.[36]

Figure 3-14 The Al•Ar ground state $^2\Pi(3p)$ and $^2\Sigma^+(3p)$ potential energy curves derived from the calculations by Jeff Sheehy.[46]

Figure 3-15 The Al•Ar first excited state $B\ ^2\Sigma^+(4s)$ potential energy curve derived from the calculations by Jeff Sheehy.[46]

Figure 3-16 Potential energy curves arising from the Al($3d$)•Ar and Al($4p$)•Ar electronic manifolds from the calculations by Jeff Sheehy.[46] Note that spin-orbit effects have been neglected, so three electronic states - $^2\Delta(3d)$, $^2\Pi(3d)$, and $^2\Sigma^+(3d)$ - converge to the Al($3d$) + Ar asymptote, and two electronic states - $^2\Pi(4p)$ and $^2\Sigma^+(4p)$ - converge to the Al($4p$) + Ar asymptote.

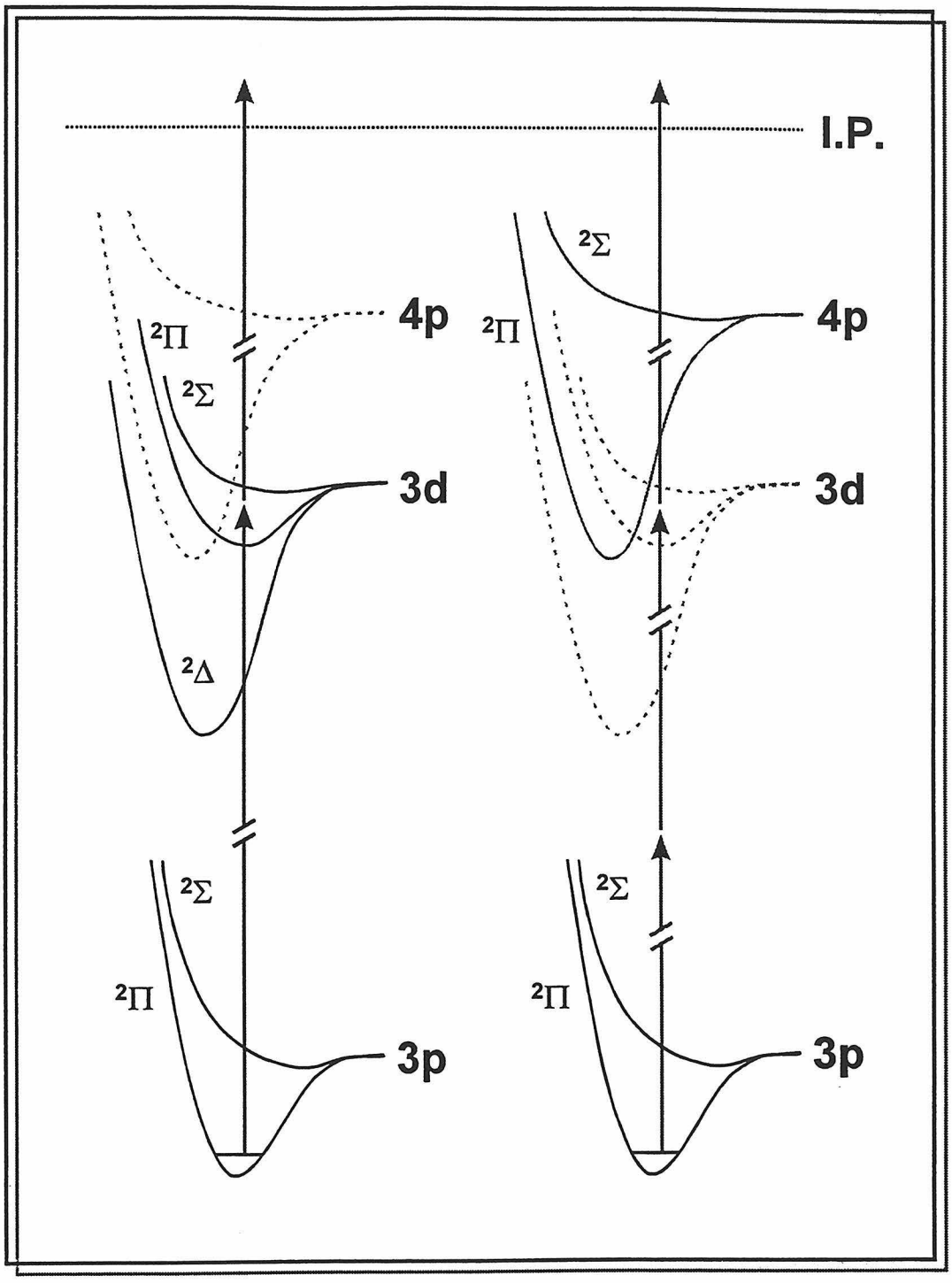


Figure 3-1

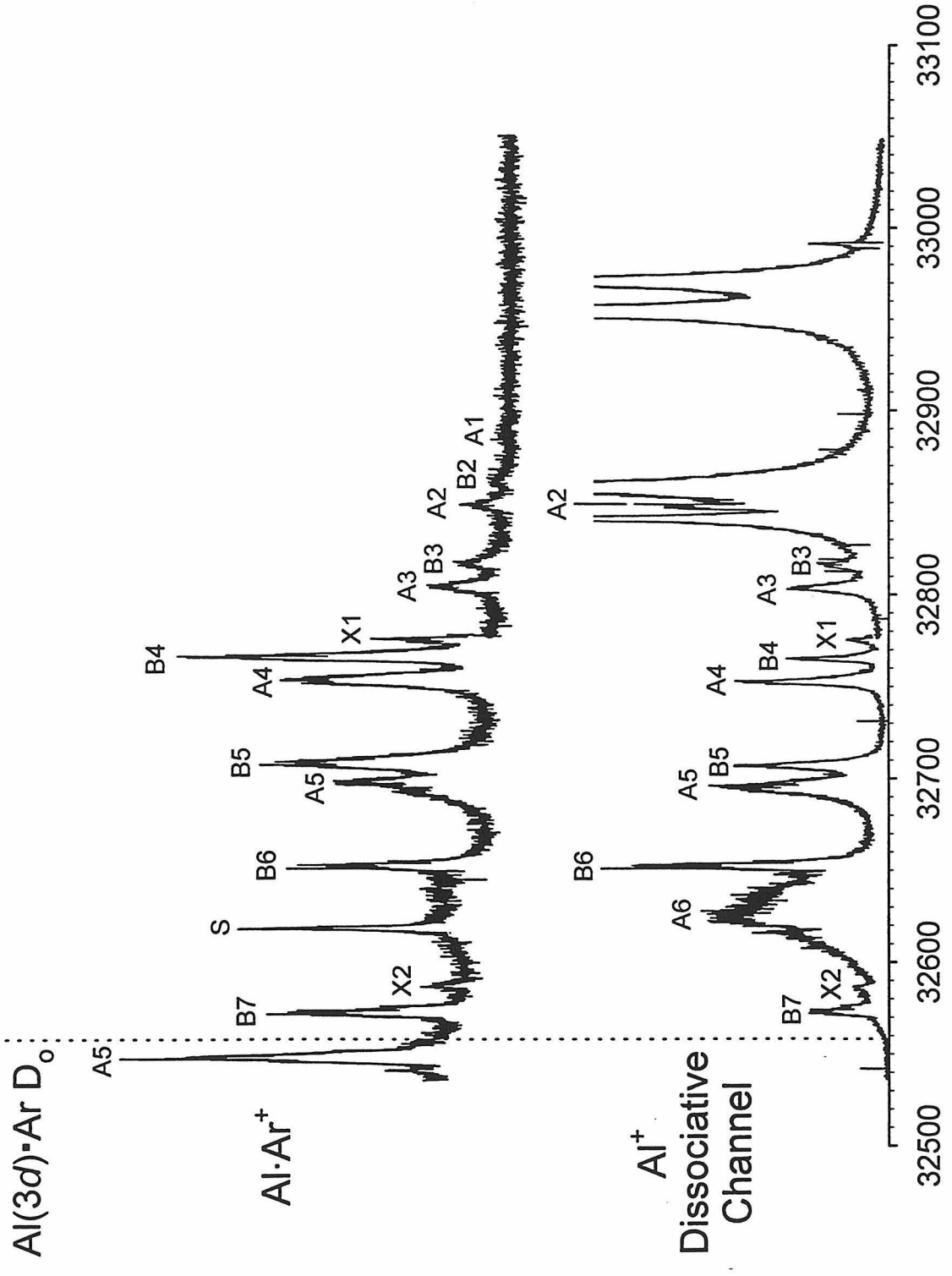

Al(3d)•Ar D0
Al·Ar+
Al+
Dissociative
Channel
A5
B7
X2
S
B6
A5
B5
A4
B4
X1
A3
B3
A2
B2
A1
A6
B7
X2
B6
A5
B5
A4
B4
X1
A3
B3
A2
32500
32600
32700
32800
32900
33000
33100

Figure 3-2

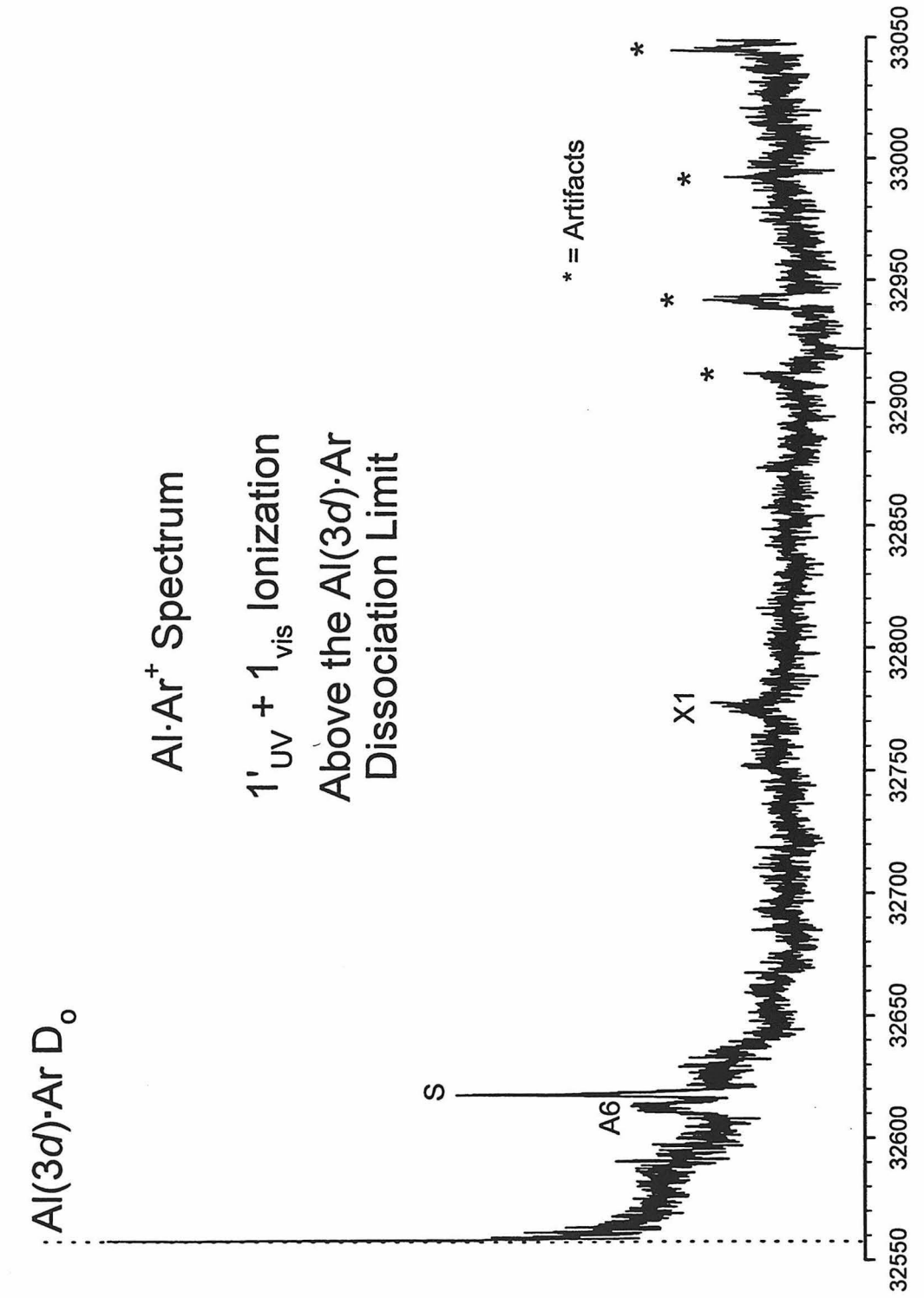

Al(3d)-Ar D$_o$
Al·Ar$^+$ Spectrum
1'$_{UV}$ + 1$_{vis}$ Ionization
Above the Al(3d)·Ar
Dissociation Limit
S
A6
X1
* = Artifacts
*
*
*
*
32550
32600
32650
32700
32750
32800
32850
32900
32950
33000
33050
cm^{-1}

Figure 3-3

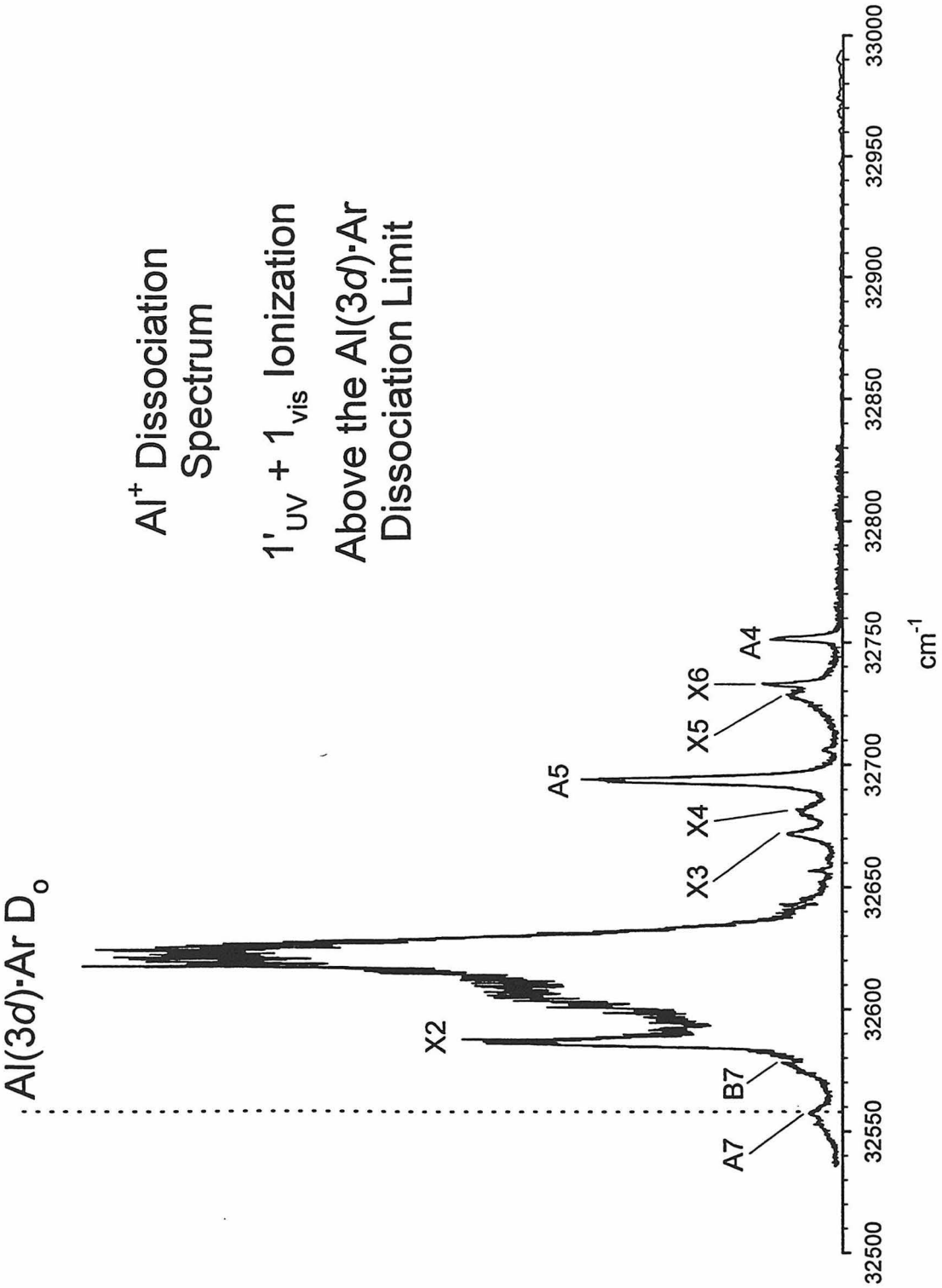

Al(3d)·Ar D$_o$
Al$^+$ Dissociation Spectrum
1'$_{UV}$ + 1$_{vis}$ Ionization Above the Al(3d)·Ar Dissociation Limit
A7
B7
X2
A5
X3
X4
X5
X6
A4
32500
32550
32600
32650
32700
32750
32800
32850
32900
32950
33000
cm^{-1}

Figure 3-4

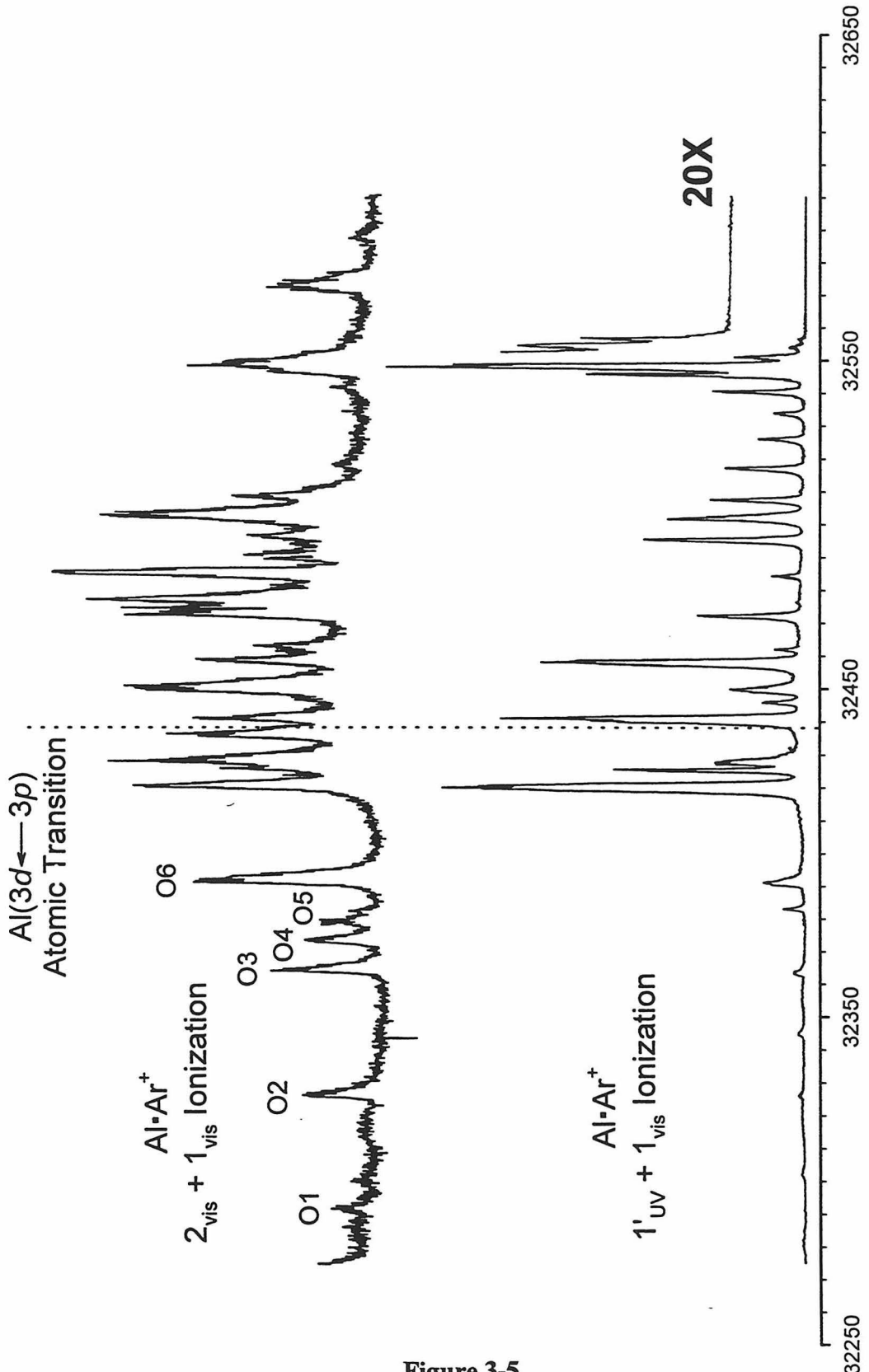

Al(3d←3p)
Atomic Transition
Al·Ar+
2vis + 1vis Ionization
O1
O2
O3
O4
O5
O6
Al·Ar+
1'UV + 1vis Ionization
20X
32250
32350
32450
32550
32650

Figure 3-5

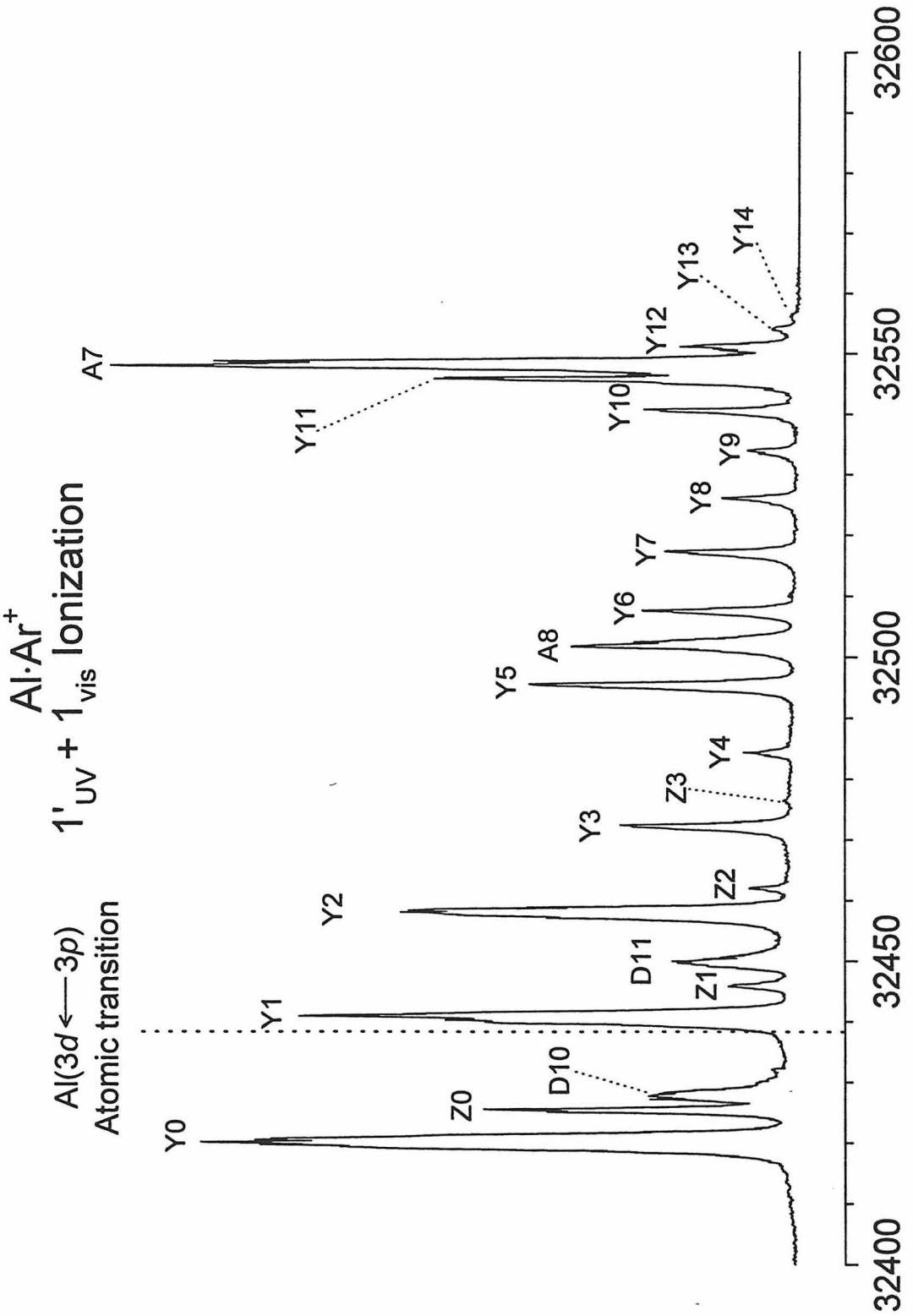

Al·Ar+
1'UV + 1vis Ionization
Al(3d ← 3p)
Atomic transition
Y0
Z0
D10
Y1
Y2
D11
Z1
Z2
Y3
Z3
Y4
Y5
A8
Y6
Y7
Y8
Y9
Y10
Y11
A7
Y12
Y13
Y14
32400
32450
32500
32550
32600

Figure 3-6

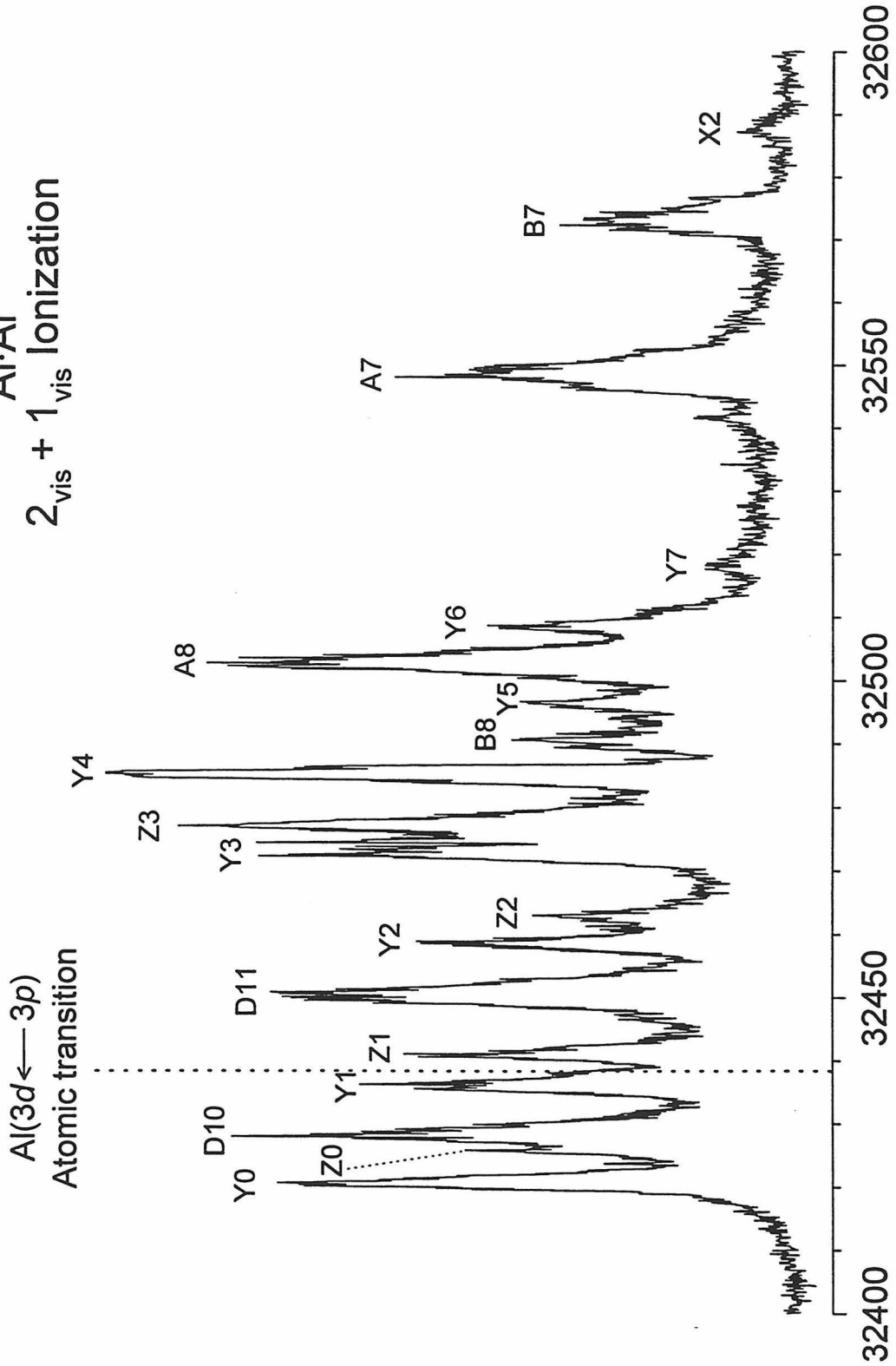

Al·Ar+
2vis + 1vis Ionization
Al(3d ← 3p)
Atomic transition
Y0
D10
Z0
Y1
Z1
D11
Y2
Z2
Y3
Z3
Y4
A8
B8
Y5
Y6
A7
Y7
B7
X2
32400
32450
32500
32550
32600

Figure 3-7

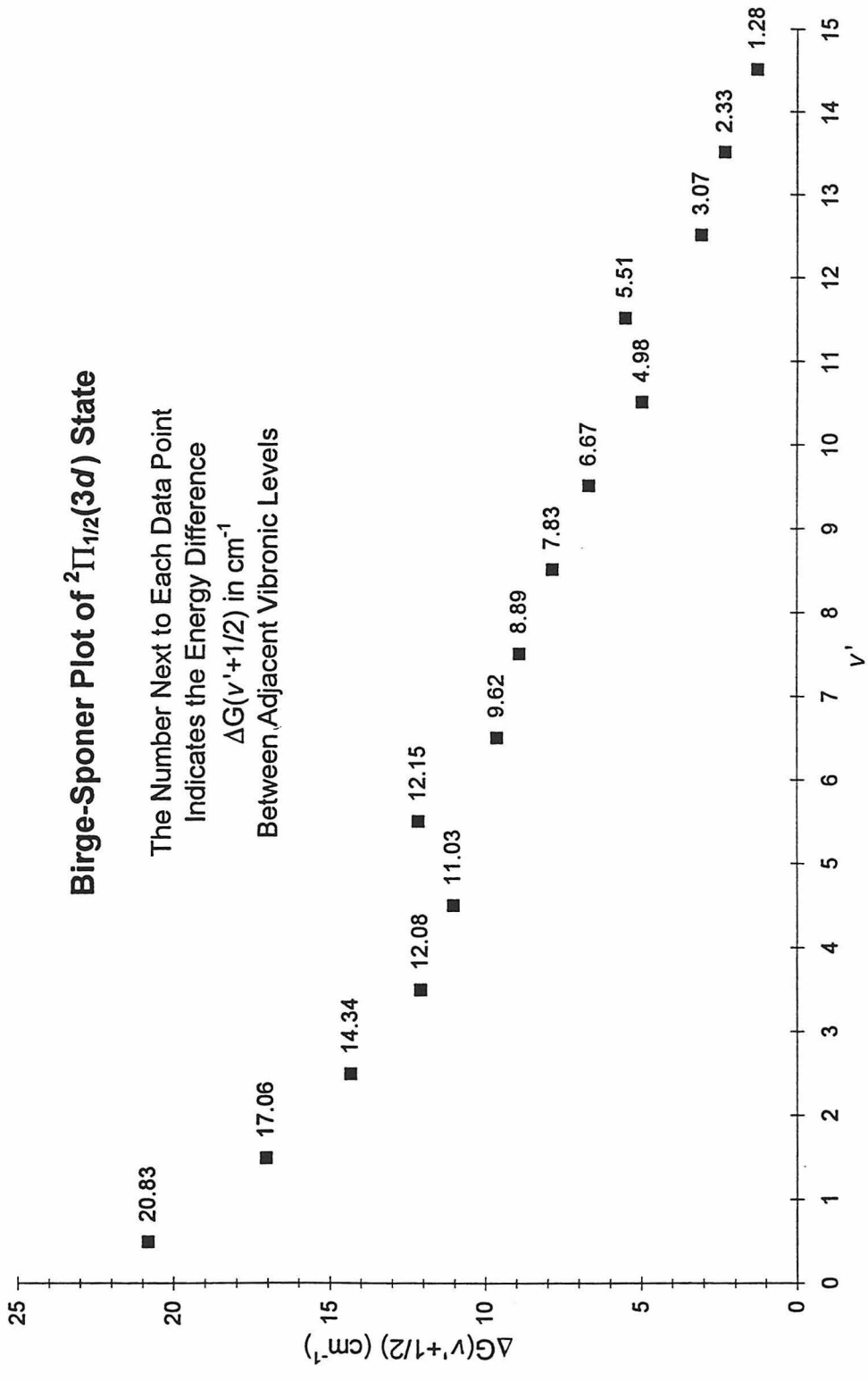

Birge-Sponer Plot of $^2\Pi_{1/2}(3d)$ State
The Number Next to Each Data Point
Indicates the Energy Difference
$\Delta G(v'+1/2)$ in cm^{-1}
Between Adjacent Vibronic Levels
$\Delta G(v'+1/2)$ (cm^{-1})
v'
20.83
17.06
14.34
12.08
11.03
12.15
9.62
8.89
7.83
6.67
4.98
5.51
3.07
2.33
1.28
0
5
10
15
20
25
0
1
2
3
4
5
6
7
8
9
10
11
12
13
14
15

Figure 3-8

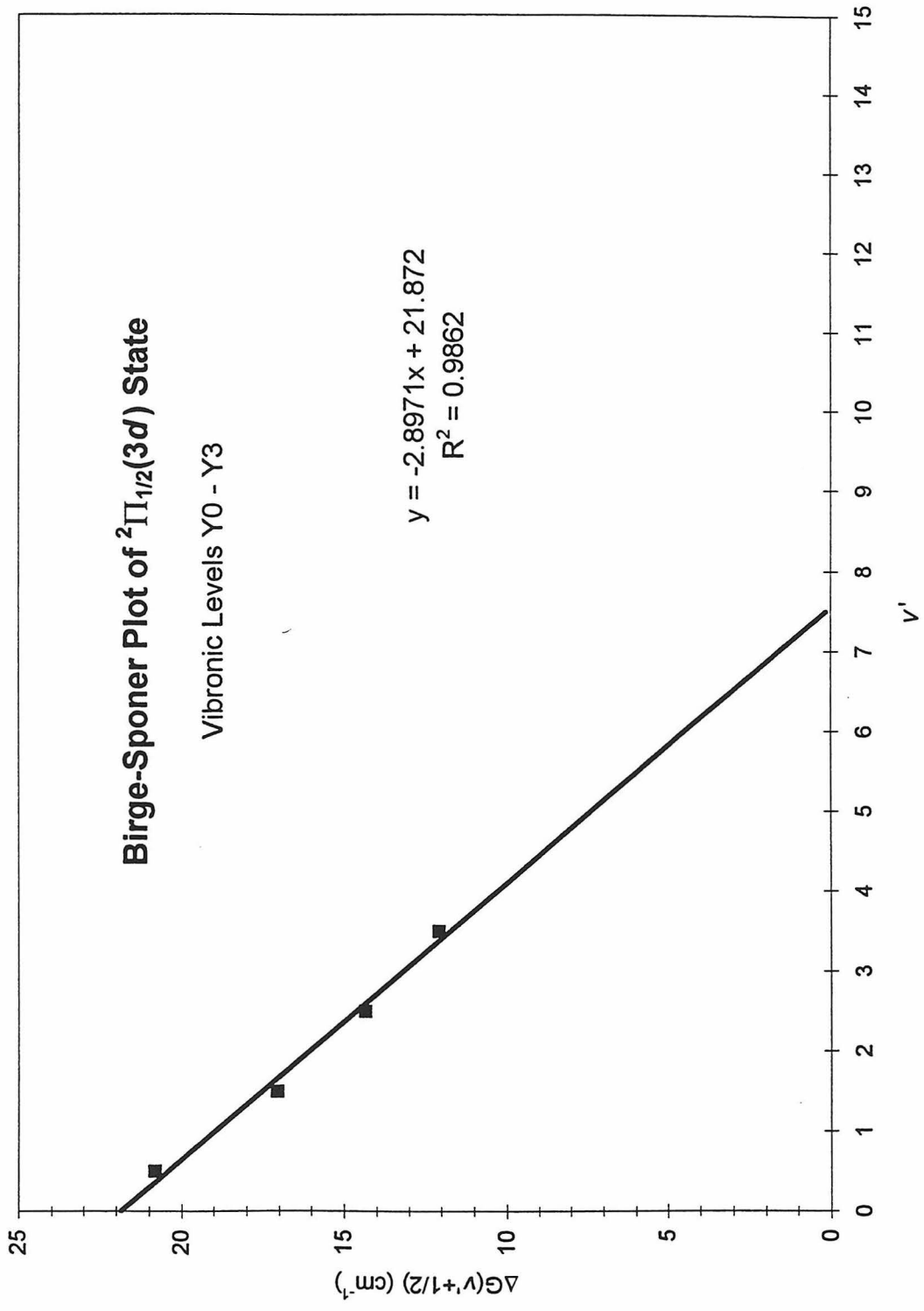

Birge-Sponer Plot of $^2\Pi_{1/2}(3d)$ State
Vibronic Levels Y0 - Y3
y = -2.8971x + 21.872
R^2 = 0.9862
$\Delta G(v'+1/2)$ (cm^{-1})
v'
0
5
10
15
20
25
0 1 2 3 4 5 6 7 8 9 10 11 12 13 14 15

Figure 3-9

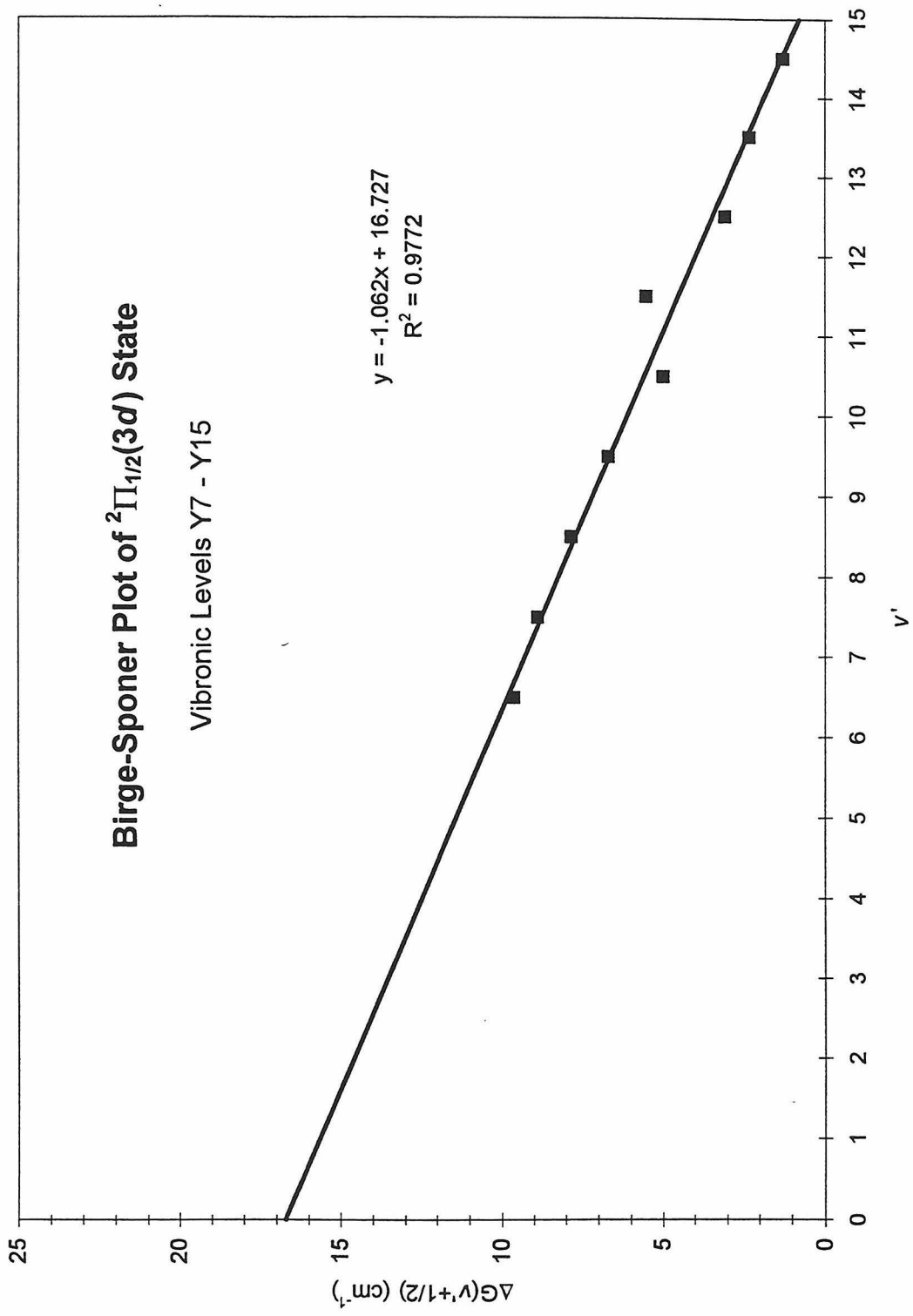

Birge-Sponer Plot of $^2\Pi_{1/2}(3d)$ State
Vibronic Levels Y7 - Y15
y = -1.062x + 16.727
R^2 = 0.9772
ΔG(v'+1/2) (cm^{-1})
v'
0
5
10
15
20
25
0 1 2 3 4 5 6 7 8 9 10 11 12 13 14 15

Figure 3-10

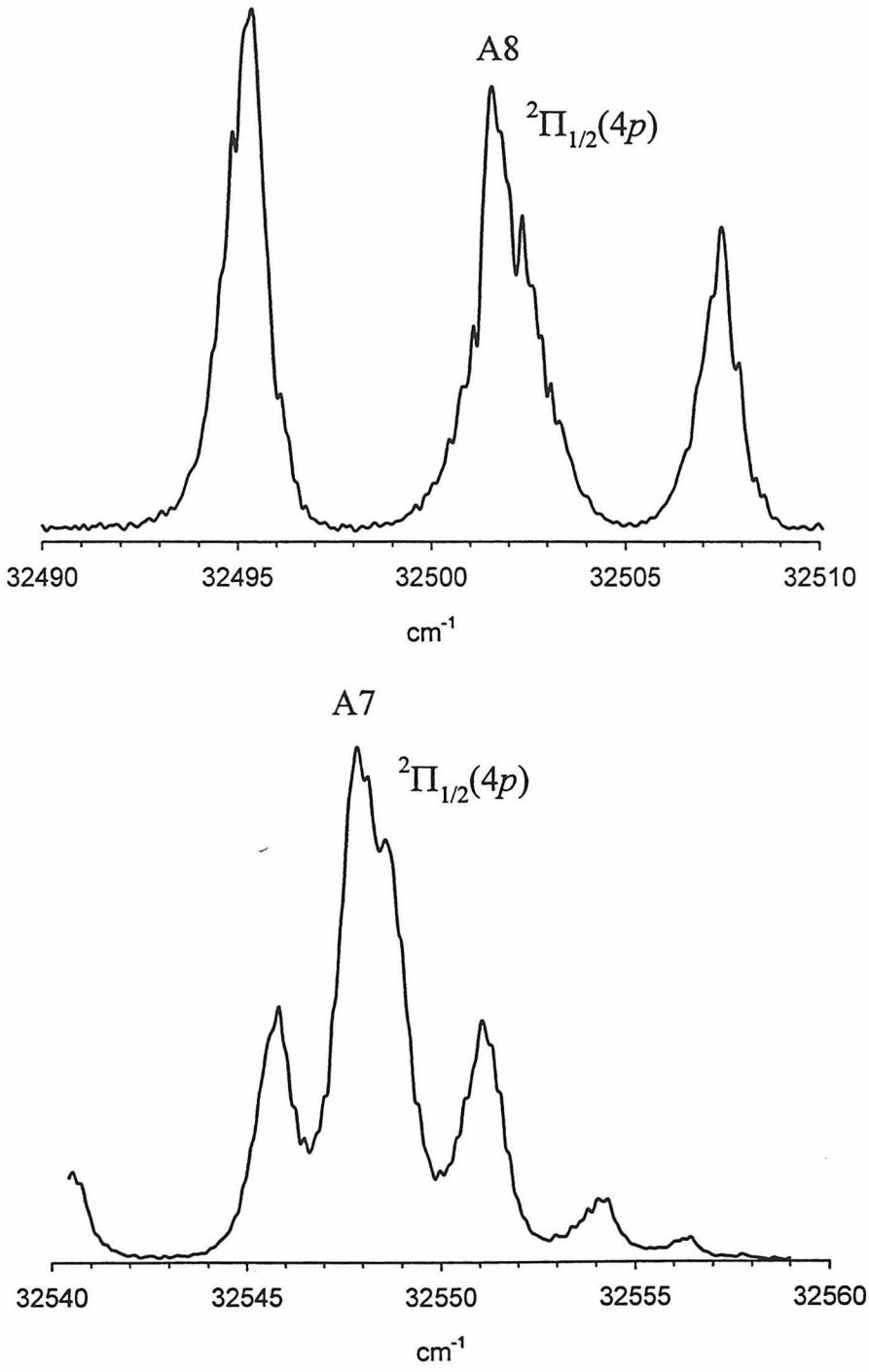
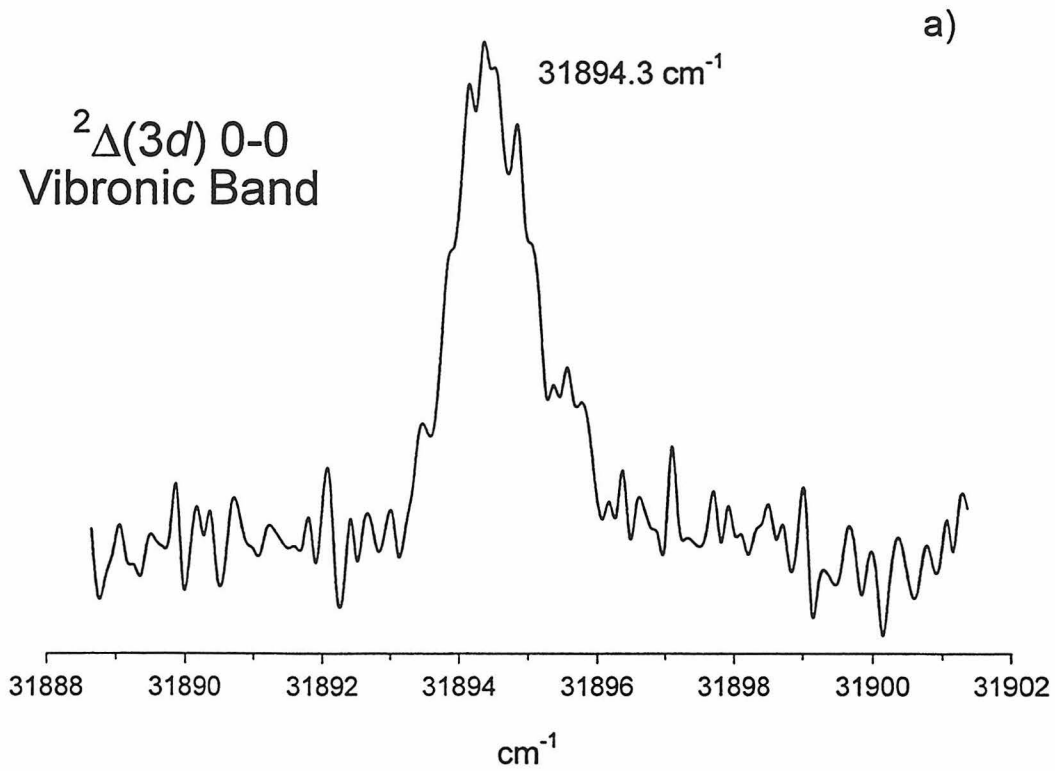
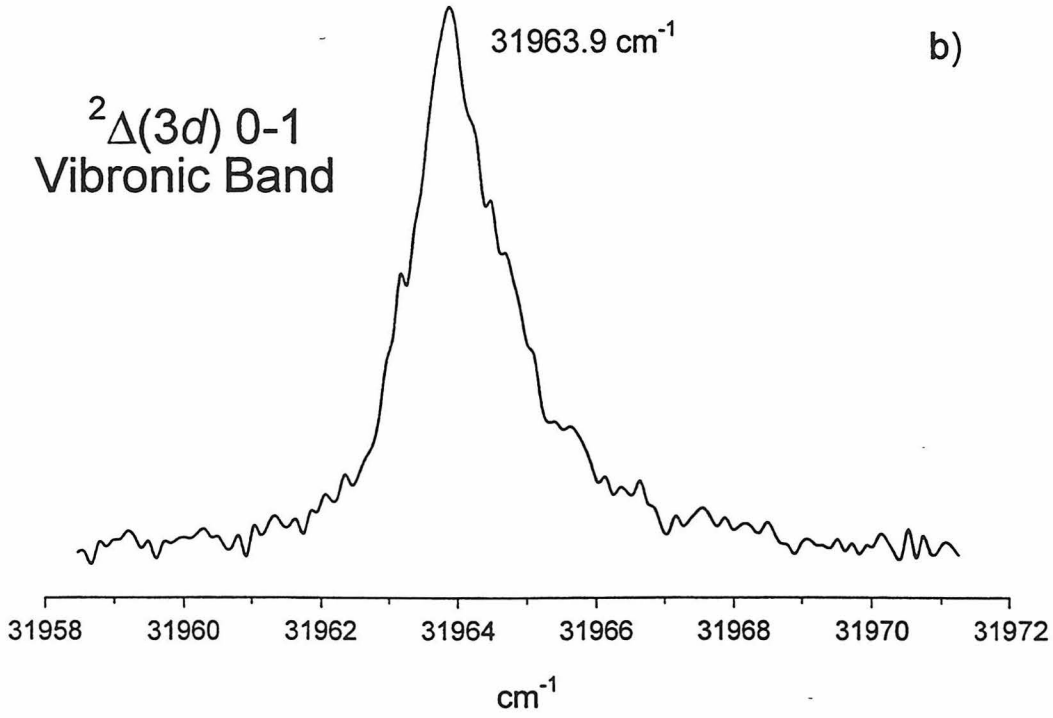

A8
$^2\Pi_{1/2}(4p)$
32490
32495
32500
32505
32510
cm^{-1}
A7
$^2\Pi_{1/2}(4p)$
32540
32545
32550
32555
32560
cm^{-1}

Figure 3-11





Figures 3-12a and 3-12b

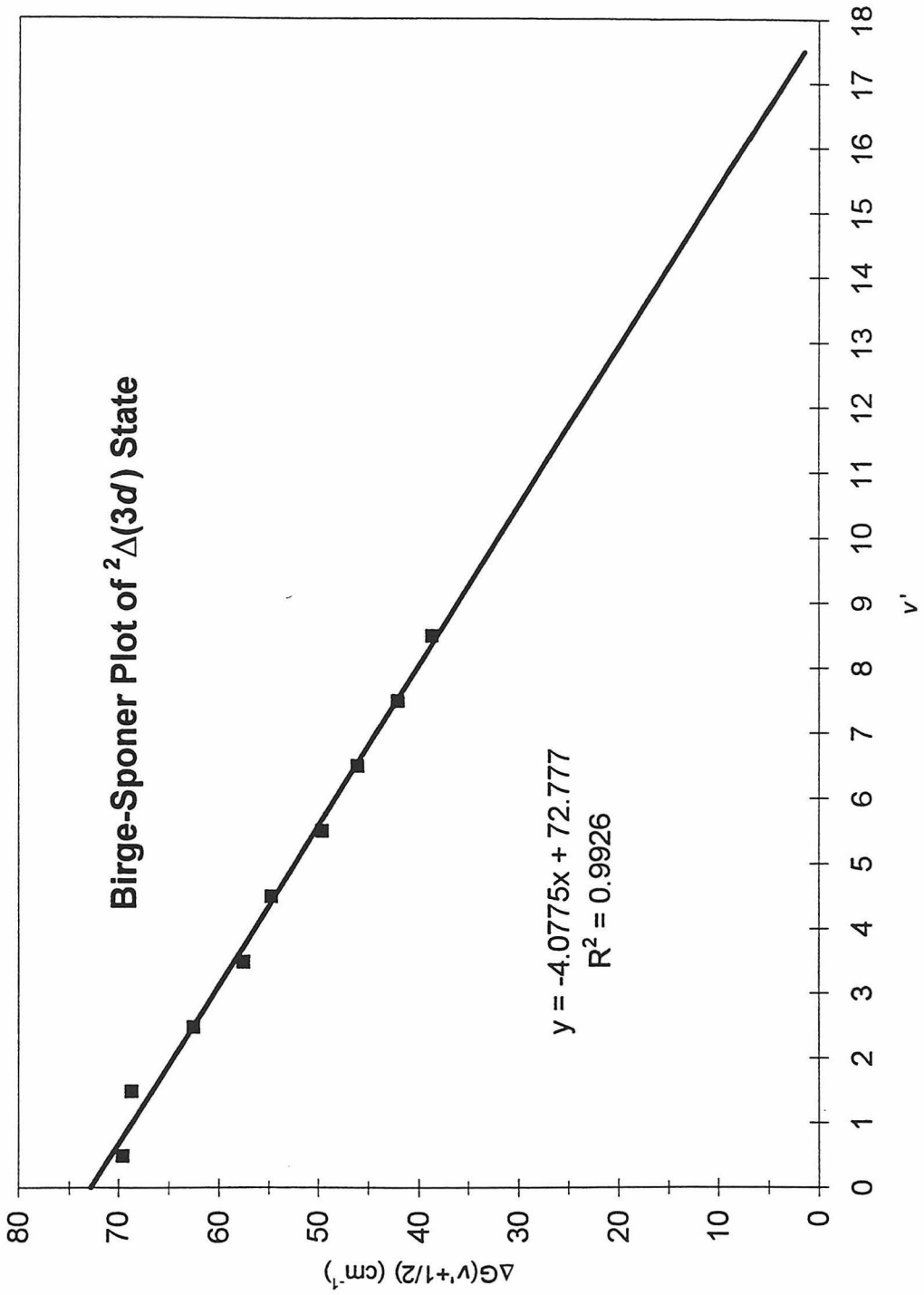

Birge-Sponer Plot of $^2\Delta(3d)$ State
y = -4.0775x + 72.777
R^2 = 0.9926
$\Delta G(v'+1/2)$ (cm^{-1})
v'
0
10
20
30
40
50
60
70
80
0 1 2 3 4 5 6 7 8 9 10 11 12 13 14 15 16 17 18

Figure 3-13

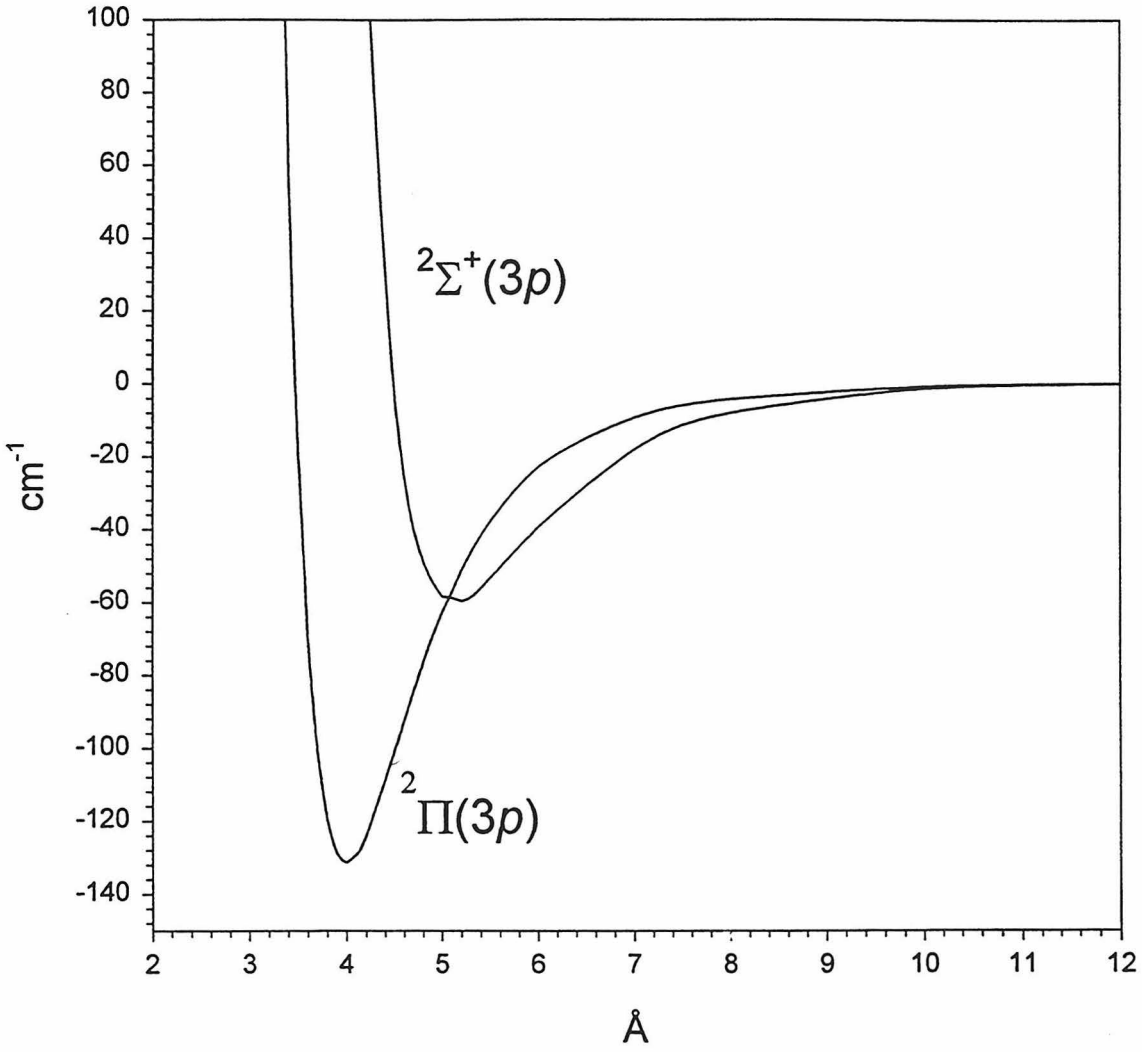

100
80
60
40
20
0
-20
-40
-60
-80
-100
-120
-140
cm-1
2
3
4
5
6
7
8
9
10
11
12
Å
2Σ+(3p)
2Π(3p)

Figure 3-14

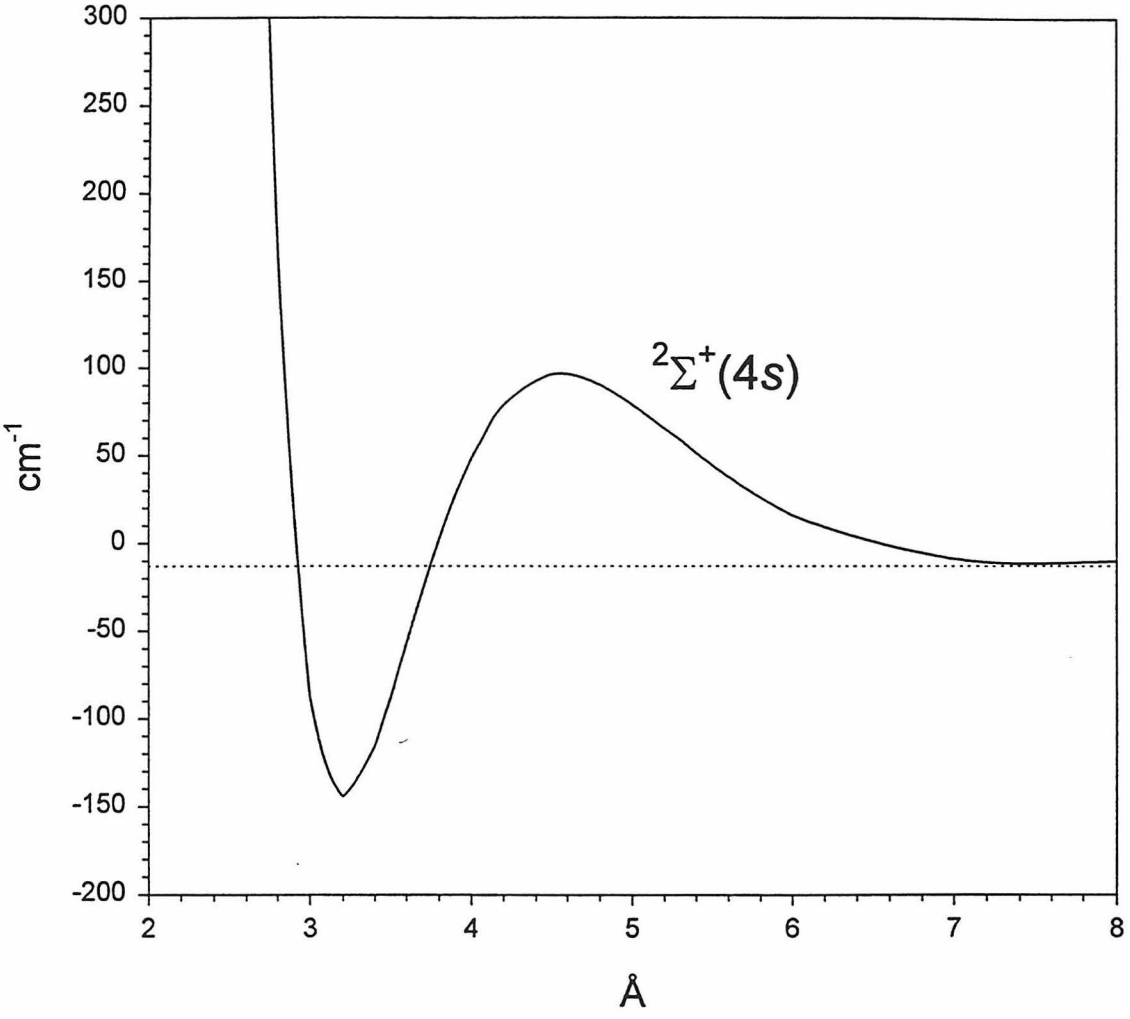


Figure 3-15

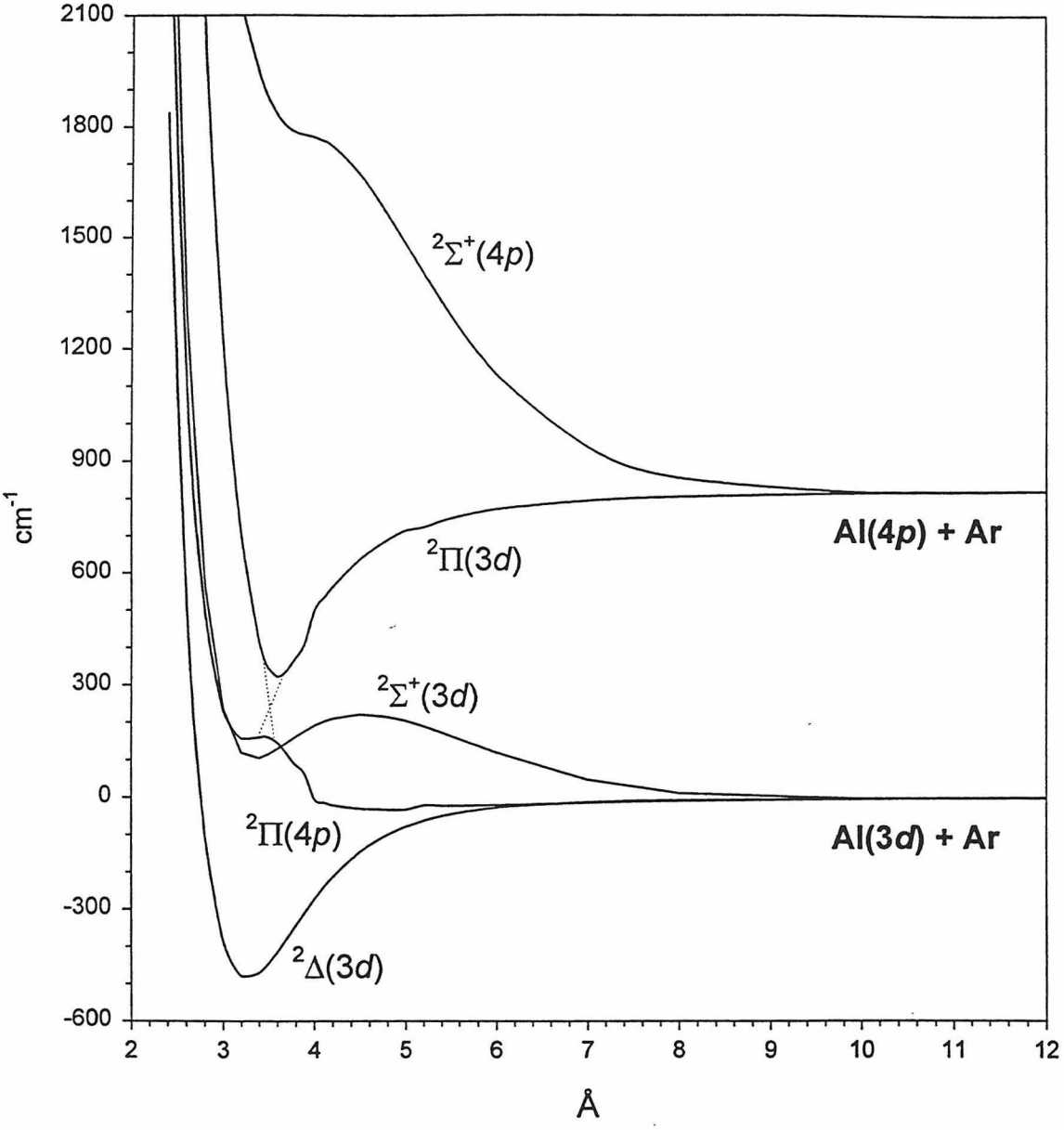

2100
1800
1500
1200
900
600
300
0
-300
-600
cm-1
2
3
4
5
6
7
8
9
10
11
12
Å
2Σ+(4p)
2Π(3d)
2Σ+(3d)
2Π(4p)
2Δ(3d)
Al(4p) + Ar
Al(3d) + Ar

Figure 3-16

CHAPTER 4

Characterization of a Direct Two-Photon Bound→Continuum Transition Between the $X_1\ ^2\Pi_{1/2}(3p)$ Ground State and the $^2\Sigma^+_{1/2}(4p)$ Excited State of Al•Ar

4.1 Introduction

The electronic spectroscopy of the Al•Ar van der Waals molecule has been the subject of numerous investigations over the years.[1-4] In particular, bound→bound single-photon allowed transitions originating from the ground $^2\Pi_{1/2}(3p)$ electronic state have been extensively characterized up to the ionization limit.[1-4] Nevertheless, two key facets of Al•Ar spectroscopy have remained unexplored during the course of the past work, namely the characterization of 1) bound→continuum transitions arising from ground state to excited Al•Ar electronic configurations and 2) two-photon allowed transitions from the ground $^2\Pi_{1/2}(3p)$ electronic state to the excited Al(n*p*)•Ar (n > 3) manifolds.

The first experimental example of a bound→continuum transition in the Al•Ar van der Waals system was reported in Chapter 3 of this thesis as a result of the systematic examination of the electronic states derived from the Al(3*d*) + Ar and Al(4*p*) + Ar asymptotes. A substantially broadened, single-photon allowed $^2\Sigma^+_{1/2}(3d) \leftarrow {}^2\Pi_{1/2}(3p)$ transition lying approximately 70 cm^{-1} above the Al(3*d*)•Ar dissociation limit was prominently observed in the aluminum atom fragmentation channel. Such spectral behavior was highly indicative of a direct Franck-Condon transition to a repulsive region of the upper potential, followed by rapid dissociation of the excited state complex. Preliminary *ab initio* calculations performed in collaboration with Jeff Sheehy (see Section 3.5.3. in Chapter 3) supported the notion that the potential was mostly repulsive, although slight bonding character of 125 cm^{-1} was predicted near 3.4 Å - a region that nevertheless lay above the Al(3*d*)•Ar dissociation limit.[5] However, evidence of a curve crossing between the $^2\Pi_{1/2}(4p)$ and $^2\Sigma^+_{1/2}(3d)$ potential energy curves precisely in the Franck-

Condon allowed region of the $^2\Sigma^+_{1/2}(3d)$ potential hindered a quantitative simulation of the dissociative peak profile, rendering a comprehensive comparison between the predicted theoretical and experimental peak profiles unattainable.

Prior to the work presented in Chapter 3 of this thesis, no direct observation of an allowed two-photon transition in the Al•Ar molecule had been reported. During the course of characterizing all single-photon allowed transitions in Al•Ar from 31000 cm^{-1} up to the ionization limit, Morse and co-workers tentatively assigned two progressions as arising from the $^2\Pi(4p)$ and $^2\Pi(6p)$ electronic states.[4] Detection of these two nominally electric dipole forbidden transitions was rationalized by invoking electronic state mixing interactions - the former state arising due to interactions with the $^2\Pi(3d)$ state and the latter arising due to interactions possibly with the $^2\Pi(5f)$ or $^2\Delta(5f)$ states. However, the results of the single- and two-photon spectroscopy performed on the Al($3d$)•Ar and Al($4p$)•Ar electronic states detailed in Chapter 3 demonstrated that the previous assignment of the $^2\Pi(4p)$ electronic state was incorrect, and a new assignment was proposed. Likewise, there remains some doubt as to the true nature of the progression presently assigned to the $^2\Pi(6p)$ electronic state due to considerable spectral congestion within the region in which the progression was observed. In the end, the conclusion that very little is presently known about the electronic spectroscopy of the excited Al(np)•Ar ($n > 3$) states would properly summarize the current state of affairs.

While some information exists regarding two $^2\Pi(np)$ electronic states, there has been no characterization to date of any transition from the ground $^2\Pi_{1/2}(3p)$ state to any excited $^2\Sigma^+_{1/2}(np)$ state in Al•Ar. As a consequence of the single- and two-photon

spectroscopy performed on the Al(3*d*)•Ar and Al(4*p*)•Ar electronic states presented in Chapter 3, spectroscopic evidence for the $^2\Sigma^+_{1/2}(4p)$ state was sought. This chapter introduces the first spectroscopic evidence of a direct two-photon allowed bound→continuum transition from the ground $^2\Pi_{1/2}(3p)$ state to the $^2\Sigma^+_{1/2}(4p)$ state. This discovery represents the first report of a direct two-photon allowed bound→continuum transition that originates from the ground state electronic manifold for *any* metal-rare gas van der Waals diatomic system.

Electronic states of metal-rare gas van der Waals molecules possessing Σ-type symmetry are of fundamental interest due to the intrinsically complicated basis of the observed bonding, or, as is often the case, non-bonding behavior. In particular, states of Σ symmetry often exhibit subtleties that render a detailed understanding of the electronic interaction difficult to infer at the most fundamental levels. By definition, Σ states in metal-rare gas systems arise from orbital configurations on the metal atom that serve to restrict the electron density of the valance or excited Rydberg electron along the internuclear axis.[6-7] Therefore, in contrast to electronic states manifesting higher degrees of orbital angular momentum, Λ, that serve to draw electron density away from the internuclear axis in orthogonal directions, bonding/non-bonding interactions in electronic states of Σ symmetry arise from a delicate balance between attractive and repulsive contributions to the diatomic potential.

As a direct consequence of the high degree of electron repulsion between the metal valance or excited Rydberg electron and the closed-shell rare gas molecule, electronic states of Σ symmetry can often demonstrate primarily repulsive potentials.[8] Such a

generalization is especially true of Σ states that arise from metal atom electronic configurations whose atomic orbital angular momentum, *l*, is greater than or equal to one.[8] Under these circumstances, electron density from the metal atom moiety is specifically oriented directly along the internuclear axis, resulting in higher degrees of repulsion than Σ(n*s*) states where the metal atom possesses a spherical electron distribution ($l = 0$). Although exceptions exist,[9-10] Σ(n*s*) states often demonstrate significant bonding character with the more polarizable rare gas species (Ar, Kr, Xe), since the weakly attractive ($1/R^6$) van der Waals force can overcome the weak repulsion derived from the partial electron density produced by the diffuse, spherically symmetric *s*-orbital on the metal moiety.[8] In the case of Σ(n*l*) ($l \geq 1$) states, however, the magnitude of the repulsive force often dramatically overwhelms the weak van der Waals attractive force, causing the potentials to exhibit often nearly exponential repulsive potentials.[6-8] Although such potentials may exhibit very weakly bound potentials at very large internuclear distances, these regions are generally far from the Franck-Condon overlap region with the ground state equilibrium bond distance, thus rendering them effectively inaccessible by direct excitation from the ground state potential.

Needless to say, as soon as one moves beyond these more extreme limiting cases of Σ(n*l*) state bonding or non-bonding behavior, a number of secondary interactions acquire considerable influence on the true shape of a given Σ(n*l*) potential. Most notably, theoretical calculations on Σ(n*l*) states manifolds quite often predict subtle inflections within the repulsive regions of the potential, sometimes to the extent that the potential becomes almost flat over a small internuclear distance region.[11-13] These inflections can

occasionally become so pronounced as to generate a bound region nested within a principally repulsive potential. Such bound regions have been calculated to exist even above the nominal bond dissociation limit for the electronic manifold from which the particular $\Sigma(n\ell)$ state derives, resulting in a quasi-bound metastable region.

Although the precise fundamental origin of these non-exponential curvature regions often lie concealed within the treatment of the electron correlation effects in a specific calculation, there are, nonetheless, two physical explanations that can be invoked to rationalize why such behavior *should* be evident. The first involves coupling between nearby electronic states with identical total angular momentum, Ω. Numerous calculations have demonstrated that the inclusion of a sufficient basis set is critical if proper potential shapes are to be obtained.[11-13] This is especially true of repulsive $\Sigma(n\ell)$ ($\ell \geq 0$) states where higher lying $\Sigma(n\ell)$ states as well as nearby $\Pi(n\ell)$, $\Delta(n\ell)$, etc., can significantly influence the final curvature of the potential.

The second primary determinant of the curvature that specifically influences mostly $\Sigma(n\ell)$ states arising from excited electronic configurations involves the degree to which a rare gas atom can penetrate within the outer Rydberg orbital.[8] In particular, with increasing electronic excitation within the metal atom moiety, the excited electron becomes more and more Rydberg-like - a fairly weakly bound electron orbiting around a partially-charged cationic core at large distances away from the nucleus. Since the region of highest electron probability density shifts further from the nucleus with increasing excitation, the rare gas atom can often lie partially within the regions of highest electron density - thus experiencing the partial positive charge at the nucleus. Under these

circumstances, the interaction between the metal atom moiety and the rare gas atom acquires significantly stronger bonding character due to the presence of partial ion-induced dipole forces that are considerably stronger than simple van der Waals forces.[8] Furthermore, in the event that a metal and a rare gas atomic moiety encounter each other in such a way that the rare gas atom comes to lie near or at a nodal region of electron probability density on the metal atom, the bonding force for a $\Sigma(n\ell)$ state can be substantial.[8] Such situations can result in the manifestation of a strongly bound, metastable region on an otherwise purely repulsive $\Sigma(n\ell)$ state whose minima can lie either near or well above the nominal bond dissociation energy for the electronic manifold from which the particular state arises.

A final influence on the shape of $\Sigma(n\ell)$ state potential was recently discovered by Yamanouchi and co-workers during their optical-optical double resonance (OODR) studies of the singlet $^1\Sigma^+$ Hg($ns\ ^1S_0$)•Ne (n = 7-9) Rydberg series as well as the analogous triplet Rydberg series.[9-10] Rather unexpectedly, the results of these studies showed that the singlet states possessed a more strongly bound attractive interatomic potential that the triplet states - an observation clearly at odds with the fundamental tenets of Hund's rules.[10] In order to rationalize these results, Yamanouchi and co-workers presented a novel hypothesis whereby a superexchange interaction was invoked that served to preferentially stabilize the singlet Rydberg states. The presumptive origin of the superexchange interactions derived from the notion that partial electron density from the filled $2p_z$ orbital on neon can transfer to the $6s$ partially-ionic core of the mercury moiety due to the high Rydberg character of the excited electron. As a result of this partial

charge exchange, the electron spin alignment of the remaining $2p_z$ electron density localized on the neon moiety becomes preferentially aligned parallel to the lone 6*s* electron within the mercury ionic core. For singlet states, the partial alignment of the electron density on the neon $2p_z$ orbital becomes antiparallel to the electron spin on the excited Rydberg n*s*-electron (n = 7-9). Consequently, a superexchange interaction arises between the excited Rydberg electron and the non-orthogonal neon $2p_z$ orbital. For the triplet states, however, the excited Rydberg electron is necessarily aligned parallel to the neon $2p_z$ orbital, effecting no superexchange interaction. The calculated stabilization was comparable to that observed in the singlet Rydberg series, a fact that is strongly supportive of the notion that superexchange interactions may be found to play an increasingly significant role in determining the absolute shapes of $\Sigma(n\ell)$ potentials.[10]

The only published example of a direct bound→continuum transition from the ground state to an excited electronic configuration in a metal-rare gas system was reported by Dagdigian and co-workers.[14] Using a single-photon pump and laser induced fluorescence (LIF) and dispersed emission detection, Dagdigian and co-workers characterized the $B\,^2\Sigma^+(3s) \leftarrow X\,^2\Pi_{1/2}(2p)$ transition whose upper state potential was determined to be completely repulsive. Subsequent *ab initio* calculations performed by Alexander and co-workers confirmed the repulsive nature of the $^2\Sigma^+(3s)$ potential, as well as providing the means to simulate the experimentally-derived dissociative peak contour (determined monitoring the free boron atomic fluorescence).[14] By employing primarily two highly correlated *ab initio* methods - multireference, internally-contracted, configuration interaction (MRCI) and coupled cluster (UCCSD) with additional provisions

for the inclusion of higher-order excitations - reasonable agreement was achieved in the simulations with the experimental contour, especially at the MRCI + Q level of theory.

4.2 Experimental

The Al•Ar van der Waals molecule was generated by a standard laser ablation techniques. Following the opening of a piezoelectric pulsed valve, the pure Ar carrier gas (~8 - 10 atm. stagnation pressure) was injected into the third generation laser vaporization source described in Chapter 2. The tripled output of a Nd-YAG laser (Continuum Surelite 1) was focused on the surface of a rotatable 2024 alloy aluminum rod that was positioned directly adjacent to the throat of the supersonic expansion. Following the supersonic expansion, the jet was skimmed by a 3 mm orifice diameter skimmer (Beam Dynamics), and introduced into the second differential pumping region. The $^2\Sigma^+_{1/2}(4p)$ electronic state was then ionized by three different methodologies. The first employed a $2_{vis} + 1_{vis}$ single-color multiphoton ionization scheme consisting of solely the fundamental output wavelength from a dye laser (Quantel TDL-51) pumped by the doubled output of a Nd:YAG laser (Continuum NY61-20). The laser dye Rhodamine 610 (Exciton) was used as a straight methanol solution for all the experiments presented in this chapter. The dye fundamental was tightly focused using a 150 mm focal length lens to drive the initial two-photon excitation step. Dye fundamental power attenuation was achieved by passing the visible laser pulses through one to three sheets of stainless steel wire mesh.

The second method used to probe the $^2\Sigma^+_{1/2}(4p)$ electronic state was a $1'_{UV} + 1_{vis}$ resonant two-color multiphoton ionization scheme. The UV wavelength was generated by

frequency-doubling the Rhodamine 610 dye output from the TDL-51 dye laser using a UV extension system (UVX-3, Continuum) that was equipped with both DCC-3 and DCC-2 doubling crystals (both purchased from Continuum). The former crystal provided a 367 nm - 295 nm UV tuning range from while the latter permitted a UV tuning range from 295 nm to 265 nm. The $^2\Sigma^+_{1/2}(4p)$ spectral feature lay within the blue extreme of the DCC-3 crystal and the red extreme of the DCC-2 crystal, necessitating the exchange of the crystals over the UV spectral tuning range explored for this experiment. The visible ionization pulse was taken from the residual undoubled dye fundamental that exits the doubling crystal coaxially with the UV laser pulse. Power attenuation of the UV laser pulse was accomplished by passing the beam through an UV absorbing stack of glass plates.

The final manner employed to probe the $^2\Sigma^+_{1/2}(4p)$ state was $1'_{UV} + 1'_{UV}$ single-color multiphoton ionization. To separate the UV light from the residual dye fundamental that emerged coaxially from the doubling crystal, a Pellin-Broca prism was installed following the doubling stage.

The atomic sodium D lines positioned (in air) at 589.5924 nm and 588.9950 nm were employed to calibrate the TDL-51 dye laser within the Rhodamine 610 dye fundamental tuning range.[15] To accomplish this calibration, the output from a sodium lamp was focused onto the entrance slits of a Jarrell-Ash 0.5 m monochrometer. The monochrometer grating was then adjusted to one of the two maximum intensity positions of the sodium D line transitions. After significant power attenuation, the straight output of the dye laser was introduced through the monochrometer slits coaxial to the lamp input.

The dye laser grating was then adjusted until the output wavelength of the dye laser was coincident with one of the two sodium transitions.

Following ionization, the clusters were extracted perpendicularly and mass-analyzed by a standard 1 m Wiley-McLaren time-of-flight (TOF) spectrometer,[16] and detected by a chevron dual-microchannel plate detector. A typical TOF mass spectrum can be seen in Figure 2-101 in Chapter 2. Individual scans were recorded by gating the mass peak of interest with a gated integrator (SR-250, Stanford Research Systems). S/N was greatly improved by switching the laser vaporization Q-switch at half the repetition rate and using the gated integrator to subtract the pump background due to DP oil contaminant fragments (LV off) from every signal shot (LV on). All spectra were power normalized for pump laser fluence as determined by separate power dependence scans (approximately a 2.5 power dependence for the $2_{vis} + 1_{vis}$ mode, a 1.6 power dependence for the $1'_{UV} + 1'_{UV}$ mode, and a linear power dependence for the $1'_{UV} + 1_{vis}$ mode).

4.3. Results and Discussion

4.3.1. Experimental Spectra

4.3.1.1. $2_{vis} + 1_{vis}$ Spectra

The $^2\Sigma^+_{1/2}(4p) \leftarrow {}^2\Pi_{1/2}(3p)$ transition is nominally electric dipole forbidden. Consequently, evidence of this transition was initially sought by monitoring both the $Al{\bullet}Ar^+$ and the Al^+ dissociative channel using two-photon excitation above the $Al(4p){\bullet}Ar$ dissociation limit near 33080 cm^{-1}. For clarity, it is important to note that the dissociation

limit has been calculated by neglecting the spin-orbit splitting in the atomic Al($4p$) manifold for the sake of simplicity. The true Al($4p$) + Ar asymptotes lie approximately $\pm$ 8 cm^{-1} (i.e., $\pm A/2$) above and below this average value.

A single broad, unstructured feature was uncovered approximately 820 cm^{-1} above the Al($4p$) + Ar dissociation limit using 2_{vis} + 1_{vis} single-color multiphoton ionization with a visible pump power of roughly 20 mJ/pulse. Centered near 33920 cm^{-1} with a full-width at half-maximum (FWHM) of approximately 80 cm^{-1}, this feature was strongly visible in the Al^+ fragmentation channel shown in Figure 4-1, but was only weakly apparent in the $Al{\bullet}Ar^+$ channel shown in Figure 4-2. The lack of any distinct structure in the observed feature in either the Al^+ fragment signal channel or the $Al{\bullet}Ar^+$ channel strongly suggested that this feature arose from a rapid photodissociation process induced by a direct two-photon Franck-Condon transition to a repulsive region of the $^2\Sigma^+_{1/2}(4p)$ potential.

As is evident in Figure 4-1, the observed dissociative profile was noticeably asymmetric. Compared to the blue edge, the red edge of the peak profile sloped much less dramatically toward the baseline. Furthermore, upon approaching the baseline, the red edge exhibited an extended tail that caused the base of the peak profile to appear considerably shaded to the red. The blue edge of the dissociative peak profile likewise was observed to manifest an extended tail very close to the baseline. However, unlike the tail apparent on the red edge, the blue edge tail appeared to adjoin the main spectral feature in a discontinuous manner.

Figure 4-3 shows a second Al^+ fragmentation peak profile that was collected using a higher visible pump power of approximately 30 mJ/pulse. While the overall peak shape

was quite similar to that obtained using lower power, the higher power spectrum was considerably broadened, exhibiting a FWHM of approximately 120 cm^{-1}. Furthermore, the tail on the red edge of the peak profile showed evidence of a substantial fragmentation background relative to the spectrum collected at low power.

4.3.1.2. $1'_{UV} + 1_{vis}$ Spectra

To verify the intrinsic two-photon character of the $^2\Sigma^+_{1/2}(4p) \leftarrow {}^2\Pi_{1/2}(3p)$ transition, single-photon excitation spectra were collected with both high and low UV pump powers to drive the initial excitation step. No UV transition to the $^2\Sigma^+_{1/2}(4p)$ state would be expected due to the forbidden nature of the electric dipole selection rule, rendering these experiments, in principle, negative controls. Nevertheless, as is evident from Figures 4-4 and 4-5, single-photon $1'_{UV} + 1_{vis}$ dissociative fragmentation spectra were detectable, indicative of the fact that the $^2\Sigma^+_{1/2}(4p)$ state was strongly coupled to nearby electronic manifolds that were accessible by single-photon excitation. The most likely candidate(s) for mixing with the $^2\Sigma^+_{1/2}(4p)$ state would be the $\Omega = 1/2$ electronic states derived from the Al(3*d*) + Ar asymptote that lay approximately 522 cm^{-1} below the Al(4*p*) + Ar asymptote. In particular, the $^2\Sigma^+_{1/2}(3d)$ electronic state was undoubtedly strongly coupled to the $^2\Sigma^+_{1/2}(4p)$ state, given the previous theoretical calculations showing the importance of including close lying electronic states of equal total angular momentum, Ω, if a proper $\Sigma(nl)$ potential shape was to be attained.[11-13]

Two other electronic states of $\Sigma(ns)$ symmetry that lie directly above and below the Al(3*d*)•Ar and Al(4*p*)•Ar electronic manifolds could also be potentially mixed to a

minor degree with the $^2\Sigma^+_{1/2}(4p)$ state. The first was the $B\ ^2\Sigma^+_{1/2}(4s)$ state, whose asymptote lay approximately 7610 cm^{-1} below the Al($4p$) + Ar asymptote.[17] Second, lying asymptotically 4730 cm^{-1} above the Al($4p$) + Ar asymptote, the $^2\Sigma^+_{1/2}(5s)$ state was likewise a good candidate for state mixing with the $^2\Sigma^+_{1/2}(4p)$ state.[17] Nevertheless, given the strongly bound character of the $^2\Sigma^+_{1/2}(4s)$ and $^2\Sigma^+_{1/2}(5s)$ potentials as well as the significant energy separation relative to the $^2\Sigma^+_{1/2}(4p)$ state, these two states probably contribute much less to the true $^2\Sigma^+_{1/2}(4p)$ potential shape than the $^2\Sigma^+_{1/2}(3d)$ state.[1-4]

Figure 4-4 shows the dissociative peak profile obtained by monitoring the Al^+ fragment signal using a UV pump power of 300-500 μJ/pulse. Overall, the peak profile was rather similar to that acquired using $2_{vis} + 1_{vis}$ single-color excitation (see Figure 4-1), exhibiting an almost identical FWHM of 80 cm^{-1}. One subtle difference in the $1'_{UV} + 1_{vis}$ two-color excitation spectrum was that the blue edge of the peak was no longer almost linear, but instead appeared to possess at least one shoulder near the bottom half of the peak profile. Whether this shoulder was real or perhaps an artifact due to preferential fragmentation during the ionization step has been difficult to definitively ascertain.

In addition to the low power spectrum, a high-power $1'_{UV} + 1_{vis}$ two-color excitation spectrum was obtained using a UV pump power in the range of 3-5 mJ/pulse. This dissociative spectrum obtained by monitoring the Al^+ fragment signal is presented in Figure 4-5. This spectrum was considerably power broadened relative to the low-power spectrum. Furthermore, both the red and blue edges of the peak showed a marked fragmentation enhancement reminiscent of the high power spectrum collected using $2_{vis} + 1_{vis}$ single-color excitation (see Figure 4-3). Nevertheless, the magnitude of the

fragmentation background on both the red and blue edges of the peak profile was noticeably altered. Particularly noteworthy was the strong dissociative feature shaded for approximately 200 cm^{-1} to the blue of the main peak. This contrasts distinctly with the 2_{vis} + 1_{vis} single-color excitation where essentially no additional fragmentation background was noted on the blue edge of the peak profile upon increasing the power employed for the excitation step. The broad blue-shaded dissociation profile appeared to originate in the same vicinity as the shoulder noted on the blue-edge of the main peak profile obtained using low-power excitation, suggestive of the fact that these two spectral features had a common physical origin.

Compared to the high power 2_{vis} + 1_{vis} single-color excitation, the red edge of the primary peak obtained by $1'_{UV}$ + 1_{vis} two-color excitation exhibited considerably less fragmentation - gradually approaching the baseline after almost 200 cm^{-1}. The overall shape of the red-shaded tail, however, was quite similar in profile to both low-power spectra collected using 2_{vis} + 1_{vis} single-color and $1'_{UV}$ + 1_{vis} two-color excitation after allowing for its broadened spectral extent.

4.3.1.3. $1'_{UV}$ + $1'_{UV}$ Spectra

In an attempt to definitively identify any spectral features in the single-photon excitation spectra arising from the visible laser pulse - either in the initial excitation step (in this case a two-photon excitation) or the ionization step - $1'_{UV}$ + $1'_{UV}$ single-color ionization was employed using both low and high initial excitation pump powers. The low-power $1'_{UV}$ + $1'_{UV}$ single-color dissociation spectrum collected by monitoring the Al^+

fragment signal using a UV pump power of 300-500 μJ/pulse is presented in Figure 4-6. In general, the overall peak profile was quite similar to that obtained using the $1'_{UV} + 1_{vis}$ two-color excitation method (see Figure 4-4). The primary difference was the shape of the peak maximum which was observed to be considerably broadened and flattened, rendering it difficult to judge whether the true contour of the peak maxima had been obtained. It remained possible that the observed contour of the peak maximum may not have been intrinsic to the feature itself, but rather represented the low amount of ion signal that hindered an accurate peak maximum to be acquired even after substantial signal averaging.

As was the case with the low power $1'_{UV} + 1_{vis}$ two-color excitation spectrum, the $1'_{UV} + 1'_{UV}$ single-color dissociation spectrum likewise exhibited a slight shoulder on the blue edge of the peak profile near the peak half maximum. Because the peak maximum was indeterminate for the low power $1'_{UV} + 1'_{UV}$ single-color excitation mode, it was difficult to determine whether or not this shoulder was perhaps slightly diminished in this spectrum relative to the low power $1'_{UV} + 1_{vis}$ two-color excitation spectrum.

A high-power $1'_{UV} + 1'_{UV}$ single-color dissociation spectrum was also obtained by monitoring the Al^+ fragment signal using UV pump powers of 3-5 mJ/pulse. This high-power spectrum is presented in Figure 4-7. Unlike the other spectra obtained during the course of the experiment, the high-power dissociative peak profile clearly exhibited two well-defined spectral features. Specifically, a prominent spectral feature was apparent on the blue edge of the peak profile that was shifted approximately 120 cm^{-1} to the blue of the main dissociative feature. While a slight trace of a shoulder was noted on the blue edge of

the peak profile in both low- and high-power $1'_{UV} + 1_{vis}$ two-color spectra as well as the low-power $1'_{UV} + 1'_{UV}$ single-color spectrum, this small shoulder was apparently close to 33970 cm^{-1} as opposed to 34040 cm^{-1} for the spectral feature in the high-power $1'_{UV} + 1'_{UV}$ single-color spectrum. Whether or not these two features possess a common origin has not been able to be determined.

Even ignoring the increased spectral breadth of the high-power $1'_{UV} + 1'_{UV}$ single-color dissociative feature caused by the additional blue-shifted peak, the spectrum presented in Figure 4-7 was considerably more power broadened than the other high-power spectra obtained using the alternate excitation modes. Specifically, the primary spectral feature in the high-power $1'_{UV} + 1'_{UV}$ single-color dissociative spectrum appeared with a FWHM of approximately 180 cm^{-1} - substantially greater than that observed in any of the other spectra. The fundamental physical basis for why the high-power $1'_{UV} + 1'_{UV}$ single-color dissociative spectrum and the high-power $1'_{UV} + 1_{vis}$ two-color dissociative spectrum appear substantially different is presently not understood, especially given the fact that the same UV pump power was used to drive the initial excitation step in both cases.

4.3.2 Simulation of the $1'_{UV} + 1_{vis}$ Single-Photon Excitation Spectrum

In direct analogy to the B•Ne work,[14] *ab initio* calculations on the Al•Ar $^2\Sigma^+_{1/2}(4p)$ state were performed in collaboration with Jeff Sheehy at the Phillips Laboratory, Edwards Air Force Base.[5] The theoretical characterization of the Al•Ar $^2\Sigma^+_{1/2}(4p)$ potential were derived from the comprehensive set of calculations for the Al($3p$)•Ar,

Al(4*s*)•Ar, Al(3*d*)•Ar, and Al(4*p*)•Ar electronic manifolds that were presented in Section 3.5.3. of Chapter 3. In contrast to the *ab initio* calculation by Alexander and co-workers on the B•Ne system, only a single level of theory - internally contracted multireference configuration interaction (MRCI) calculations from [6331] (3 electrons in 13 orbitals) state-averaged complete active space reference wavefunctions using a (17*s*12*p*5*d*4*f*)/[7*s*6*p*4*d*3*f*] atomic natural basis set (supplemented with diffuse (1*s*1*p*1*d*1*f*) functions) - has been performed to predict the potential energy profile of the Al•Ar $^2\Sigma^+_{1/2}(4p)$ state.[5] As a result, a comprehensive comparison between different levels of theory and experiment as was achieved in the case of the B•Ne work is not possible at the present time. Nevertheless, these initial *ab initio* results from Jeff Sheehy have permitted a preliminary characterization of the Al•Ar $^2\Sigma^+_{1/2}(4p)$ potential energy profile.

As shown in Figure 4-8a, the calculated $^2\Sigma^+_{1/2}(4p)$ potential energy profile was found to be completely repulsive in nature, consistent with the experimental results. However, the potential energy curve did not exhibit simple exponentially repulsive behavior. Rather, a conspicuous inflection was predicted approximately 1000 cm^{-1} above the Al(4*p*) + Ar asymptote. This inflection point was found to lie directly above the calculated equilibrium internuclear bond distance for the $^2\Pi_{1/2}(3p)$ ground state potential at 4 Å (see Section 3.5.3. in Chapter 3). A direct, Franck-Condon-allowed bound→continuum transition was predicted to access the central region of the inflection almost precisely as is shown in Figure 4-8b.

To clarify any ambiguities, it should be noted that the calculated ground state equilibrium bond distance was somewhat larger than the experimentally derived value of

3.79 Å. For the sake of this discussion and subsequent theoretical simulations presented below, the calculated ground state equilibrium bond distance *was not* shifted to match the experimental value. Hence, all simulations will treat the 4 Å region on the $^2\Sigma^+_{1/2}(4p)$ potential as the direct Franck-Condon accessible region regardless of the experimentally-derived values for the ground state.

With the calculated $^2\Pi_{1/2}(3p)$ ground state and $^2\Sigma^+_{1/2}(4p)$ excited potentials in hand, simulations of the bound→continuum dissociative peak profiles were undertaken using the public domain computer program, BCONT, written and distributed by Le Roy.[18] The one drawback of this program for the purposes of simulating the experimentally-derived spectra was that BCONT cannot properly treat Franck-Condon transitions to virtual intermediate states such as those excited in the $2_{vis} + 1_{vis}$ single-color excitation mode. As a result, the most informative spectra, namely those generated using a two-photon initial excitation step, cannot be properly simulated. Nevertheless, BCONT was capable of predicting dissociation profiles generated by direct single-photon transitions to the $^2\Sigma^+_{1/2}(4p)$ state, rendering those spectra obtained using $1'_{UV} + 1'_{UV}$ single-color and $1'_{UV} + 1_{vis}$ two-color excitation schemes amenable to comparison with their simulated spectral behavior.

A single simulation has been performed on the direct, single-photon Franck-Condon $^2\Sigma^+_{1/2}(4p) \leftarrow {}^2\Pi_{1/2}(3p)$ continuum←bound transition near the 4 Å region. The BCONT parameters used for this simulation are presented in Tables 4-1 and 4-2. For these simulations, the transition dipole matrix elements were considered to be constant over the accessible excitation region. Consequently, the simulated dissociative peak

profiles effectively represented the Franck-Condon overlap profiles between the $^2\Pi_{1/2}(3p)$ ground state and the $^2\Sigma^+_{1/2}(4p)$ excited state. Calculations of the transition dipole matrix elements recently performed by Sheehy demonstrated only a very small variation over the Franck-Condon allowed excitation region (data not shown). This indicated that approximating the transition dipole matrix elements as constant for the purpose of this simulation would not seriously hinder the ability to extract physically meaningful results from the dissociative peak profiles.

The simulated dissociative peak profile generated by BCONT is shown in Figure 4-9. Qualitatively, the overall shape of the predicted dissociative peak profile was reminiscent of those obtained from the low power $1'_{UV} + 1_{vis}$ two-color (see Figure 4-4) and $1'_{UV} + 1'_{UV}$ single-color (see Figure 4-6) excitation schemes. As was the case with the experimental spectra, the simulated dissociative peak profile was asymmetric and shaded slightly to the red. Likewise, the extended tail shaded to the red of the main feature was clearly apparent in the simulated peak profile. In addition, a very weak intensity peak shifted to the blue of the main spectral feature was also predicted (see x38 inset in Figure 4-9). Whether or not the blue shaded shoulders observed in the low power $1'_{UV} + 1_{vis}$ two-color and $1'_{UV} + 1'_{UV}$ single-color excitation spectra could possibly be of common origin to this particularly low intensity feature, however, remained indeterminate.

One primary discrepancy in the simulated profile was the fact that the predicted FWHM of approximately 50 cm^{-1} was considerably less than that noted in the experimental spectrum. By employing small pump powers of approximately 300-500 μJ/pulse, power broadening effects in the $1'_{UV} + 1_{vis}$ two-color and $1'_{UV} + 1'_{UV}$ single-

color excitation schemes should have been minimized if not eliminated. Hence, the most probable explanation for the narrow width of the simulated peak profile was the flat nature of the $^2\Sigma^+_{1/2}(4p)$ potential energy profile within the Franck-Condon allowed region. If the location of the Franck-Condon transition in the $^2\Sigma^+_{1/2}(4p)$ state was shifted slightly to either larger or smaller internuclear bond distances, then regions of increasingly significant degrees of repulsive character would become accessible - undoubtedly broadening the simulated dissociative peak profile. Therefore, in all likelihood, the true nature of the $^2\Sigma^+_{1/2}(4p)$ potential energy profile within the dissociative region was probably not as flat as predicted at the present level of theory - a supposition that can be tested through future theoretical work.

Figures 4-10 and 4-11 show the simulated peak profile superimposed with the low power $1'_{UV} + 1_{vis}$ two-color and $1'_{UV} + 1'_{UV}$ single-color spectra respectively. Since the peak maximum for the $1'_{UV} + 1'_{UV}$ single-color spectrum was ill-defined, the simulated peak profile was aligned in both Figures 4-10 and 4-11 such that the maximum was positioned identically to that observed in the $1'_{UV} + 1_{vis}$ two-color dissociative spectrum. The superposition of the two profiles clearly demonstrated the presence of a broadened shoulder on the blue-edge of both the $1'_{UV} + 1_{vis}$ two-color and $1'_{UV} + 1'_{UV}$ single-color peak profiles. Despite the discrepancies noted at the blue edge, the red edge of both the simulated and experimental peak profiles correlated rather well with one another, especially in the case of the low power $1'_{UV} + 1'_{UV}$ single-color spectrum.

4.4. Conclusion

The first observation of a direct two-photon bound→continuum transition from the ground state in a metal atom-rare gas van der Waals molecule has been characterized. Two-photon transitions between the Al•Ar $^2\Pi_{1/2}(3p)$ ground state and the $^2\Sigma^+_{1/2}(4p)$ excited state were observed to result in the observation of a broad, structureless feature predominantly in the Al^+ fragment signal channel, indicative of a direct transition onto a purely repulsive upper state potential. Characterization of this feature using single-photon excitation revealed significant state mixing between the $^2\Sigma^+_{1/2}(4p)$ state and nearby electronic states with total angular momentum values of $\Omega = 1/2$, thus inducing partial single-photon character in the observed dissociative peak profile. Both the precise details of the states responsible for state mixing interactions with the $^2\Sigma^+_{1/2}(4p)$ state as well as the magnitude of the coupling between the various mixed states remains an open question for future theoretical inquiry.

Simulations of the single-photon excitation dissociative peak profile predicted from *ab initio* calculations of the Al•Ar $^2\Pi_{1/2}(3p)$ ground state and the $^2\Sigma^+_{1/2}(4p)$ excited state potential showed reasonable similarity to those collected experimentally. Future theoretical work will need to focus on both modifying the BCONT bound→continuum simulation program to permit two-photon excitation profiles to be generated as well as trying to understand the fundamental physical origin of the broadened spectral behavior on the blue edge of the primary dissociation peak profile observed with single-photon excitation.

4.5. References

1. J. M. Gardner and M. I. Lester, *Chem. Phys. Lett.*, **137**, 301 (1987).
2. C. L. Callender, S. A. Mitchell, and P. A. Hackett, *J. Chem. Phys.*, **90**, 5252 (1989).
3. M. J. McQuaid, J. L. Gole, and M. C. Heaven, *J. Chem. Phys.*, **92**, 2733 (1990).
4. S. A. Heidecke, Z. Fu, J. R. Colt, and M. D. Morse, *J. Chem. Phys.*, **97**, 1692 (1992).
5. J. A. Boatz, J. A. Sheehy, and P. W. Langhoff, in *Monte Carlo Simulations of the Structures and the Optical Absorption Spectra of Al/Ar$_N$ Clusters: Applications of the Spectral Theory of Chemical Binding, Proceedings of the High Energy Density (HEDM) Conference*, June 1997 (USAF Office of Scientific Research, Bolling AFB, DC, 1997).
6. G. Herzberg, *Molecular Spectra and Molecular Structure I. Spectra of Diatomic Molecules* (Krieger Pub. Co., Malabar, Florida, 1989).
7. P. F. Bernath, *Spectra of Atoms and Molecules* (Oxford University Press, New York, 1995).
8. W. H. Breckenridge, C. Jouvet, and B. Soep, in *Advances in Metal and Semiconductor Clusters*, M. A. Duncan, Ed. (JAI Press, Greenwich, 1995), and references therein.
9. K. Onda, K. Yamanouchi, M. Okunishi, and S. Tsuchiya, *J. Chem. Phys.*, **101**, 7290 (1994).
10. K. Onda and K. Yamanouchi, *J. Chem. Phys.*, **102**, 1129 (1995).
11. J. Pasacale and J. Vandeplanque, *J. Chem. Phys.*, **60**, 2278 (1974).
12. M. Hliwa, J. C. Barthelat, and J. P. Malrieu, *J. Phys. B: At. Mol. Phys.*, **18**, 2433 (1985).
13. E. Czuchaj, H. Stoll, and H. Preuss, *J. Phys. B: At. Mol. Phys.*, **20**, 1487 (1987).
14. X. Yang, E. Hwang, P. J. Dagdigian, M. Yang, and M. H. Alexander, *J. Chem. Phys.*, **103**, 2779 (1995).

15. R. C. Weast, Ed., *CRC Handbook of Chemistry and Physics, 68th Ed.* (CRC Press, Boca Raton, Florida, 1987).
16. W. C. Wiley and I. H. McLaren, *Rev. Sci. Instrum.*, **26**, 1150 (1955).
17. S. Bashkin and J. O. Stoner, Jr., *Atomic Energy Levels and Grotrian Diagrams, Vol. I. Hydrogen I - Phosphorus XV* (North-Holland Pub. Co., Amsterdam, 1975).
18. R. J. Le Roy, *Computer Physics Communications*, **52**, 383 (1989).

Table 4-1: Input parameters for the BCONT 1.4 calculations of absorption coefficients for Al·Ar $^2\Sigma_{1/2}$ ($4p$) ← $X_1\,^2\Pi_{1/2}$ ($3p$); Part 1.

NFIT	IORD	IFREE	NV	NJ	IRDAT	NEWPOT	IWR	IPNCH	OVRCRT
0	2	1	1	0	1	1	-1	1	4d-4

NT	NFR	IRWAVL	IFRPW
0	160	1	1

WAVL

296.30	296.31	296.32	296.33	296.34	296.35	296.36	296.37	296.38	295.39
296.40	296.41	296.42	296.43	296.44	296.45	296.46	296.47	296.48	296.49
296.50	296.51	296.52	296.53	296.54	296.55	296.56	296.57	296.58	296.59
296.60	296.61	296.62	296.63	296.64	296.65	296.66	296.67	296.68	296.69
296.70	296.71	296.72	296.73	296.74	296.75	296.76	296.77	296.78	296.79
296.80	296.81	296.82	296.83	296.84	296.85	296.86	296.87	296.88	296.89
296.90	296.91	296.92	296.93	296.94	296.95	296.96	296.97	296.98	296.99
297.00	297.01	297.02	297.03	297.04	297.05	297.06	297.07	297.08	297.09
297.10	297.11	297.12	297.13	297.14	297.15	297.16	297.17	297.18	297.19
297.20	297.21	297.22	297.23	297.24	297.25	297.26	297.27	297.28	297.29
297.30	297.31	297.32	297.33	297.34	297.35	297.36	297.37	297.38	297.39
297.40	297.41	297.42	297.43	297.44	297.45	297.46	297.47	297.48	297.49
297.50	297.51	297.52	297.53	297.54	297.55	297.56	297.57	297.58	297.59
297.60	297.61	297.62	297.63	297.64	297.65	297.66	297.67	297.68	297.69
297.70	297.71	297.72	297.73	297.74	297.75	297.76	297.77	297.78	297.79
297.80	297.81	297.82	297.83	297.84	297.85	297.86	297.87	297.88	297.89

EV
-123.697

BV
0.0727

IVFIX	JFIX
0	0

ZMU	RMIN	RH	REX
16.10438	2	0.002	4

NTPI	VLIMI
26	138.718

NUSEI	VSHFTI	RFACTI	VFACTI
8	-138.718	1.d0	1.d0

Table 4-2: Input parameters for the BCONT 1.4 calculations of absorption coefficients for Al·Ar $^2\Sigma_{1/2}$ ($4p$) ← $X_1\,^2\Pi_{1/2}$ ($3p$); Part 2.

RTPI	VTPI	RTPI	VTPI	RTPI	VTPI	RTPI	VTPI
2.00	17230.34	2.40	5590.11	2.60	3185.50	2.80	1754.53
3.00	914.72	3.20	439.70	3.40	186.34	3.50	112.44
3.60	62.60	3.70	30.65	3.80	11.87	3.90	2.57
4.00	0.00	4.10	2.10	4.20	7.20	4.50	30.50
4.80	54.86	5.00	68.71	5.20	80.31	5.40	89.80
6.00	108.57	7.00	122.10	8.00	127.16	10.00	130.45
12.00	131.32	100.00	131.72				

PRM(1)	PRM(2)	PRM(3)
1	0	0

NTPF	VLIMF1
26	32894.34

NUSEF	VSHFTF	RFACTF	VFACTF
8	-138.718	1.d0	1.d0

RTPF	VTPF	RTPF	VTPF
2.00	49409.33	2.40	38266.35
2.60	36231.54	2.80	35174.78
3.00	34624.54	3.20	34321.52
3.40	34138.63	3.50	34077.06
3.60	34033.14	3.70	34005.11
3.80	33990.04	3.90	33982.80
4.00	33977.24	4.10	33967.31
4.20	33952.34	4.50	33875.37
4.80	33766.14	5.00	33687.14
5.20	33607.80	5.40	33531.47
6.00	33337.46	7.00	33144.25
8.00	33061.35	10.00	33022.60
12.00	33022.85	100.00	33026.06

PRM(4)	PRM(5)	PRM6)
5.60	0.00	0.00

4.6. Figure Captions

Figure 4-1 Low-power (about 20 mJ/pulse) $2_{vis} + 1_{vis}$ single-color multiphoton ionization (MPI) spectrum of the bound→continuum transition between the $^2\Pi_{1/2}(3p)$ ground state and the excited $^2\Sigma^+{}_{1/2}(4p)$ electronic state obtained by monitoring the Al^+ fragment signal channel.

Figure 4-2 Low-power (about 20 mJ/pulse) $2_{vis} + 1_{vis}$ single-color multiphoton ionization (MPI) spectrum of the bound→continuum transition between the $^2\Pi_{1/2}(3p)$ ground state and the excited $^2\Sigma^+{}_{1/2}(4p)$ electronic state obtained by monitoring the $Al{\bullet}Ar^+$ channel.

Figure 4-3 High-power (about 30 mJ/pulse) $2_{vis} + 1_{vis}$ single-color multiphoton ionization (MPI) spectrum of the bound→continuum transition between the $^2\Pi_{1/2}(3p)$ ground state and the excited $^2\Sigma^+{}_{1/2}(4p)$ electronic state obtained by monitoring the Al^+ fragment signal channel.

Figure 4-4 Low UV power (about 300-500 μJ/pulse) $1'_{UV} + 1_{vis}$ two-color multiphoton ionization (MPI) spectrum of the bound→continuum transition between the $^2\Pi_{1/2}(3p)$ ground state and the excited $^2\Sigma^+{}_{1/2}(4p)$ electronic state obtained by monitoring the Al^+ fragment signal channel.

Figure 4-5 High UV power (about 3-5 mJ/pulse) $1'_{UV} + 1_{vis}$ two-color multiphoton ionization (MPI) spectrum of the bound→continuum transition between the $^2\Pi_{1/2}(3p)$ ground state and the excited $^2\Sigma^+{}_{1/2}(4p)$ electronic state obtained by monitoring the Al^+ fragment signal channel.

Figure 4-6 Low UV power (about 300-500 μJ/pulse) $1'_{UV} + 1'_{UV}$ single-color multiphoton ionization (MPI) spectrum of the bound→continuum transition between the $^2\Pi_{1/2}(3p)$ ground state and the excited $^2\Sigma^+{}_{1/2}(4p)$ electronic state obtained by monitoring the Al^+ fragment signal channel.

Figure 4-7 High UV power (about 3-5 mJ/pulse) $1'_{UV} + 1'_{UV}$ single-color multiphoton ionization (MPI) spectrum of the bound→continuum transition between the $^2\Pi_{1/2}(3p)$ ground state and the excited $^2\Sigma^+_{1/2}(4p)$ electronic state obtained by monitoring the Al^+ fragment signal channel.

Figure 4-8 Potential energy curves arising from the Al(4*p*)•Ar electronic manifold from the calculations by Jeff Sheehy.[5] (a) The calculated potential energy profiles for the $^2\Pi(4p)$ and $^2\Sigma^+(4p)$ electronic states (note that spin-orbit effects have been neglected in these calculations) (b) Enlargement of the region on the $^2\Sigma^+(4p)$ potential that is accessible by a direct Franck-Condon-allowed transition from the $^2\Pi_{1/2}(3p)$ ground state.

Figure 4-9 BCONT 1.4 simulation of the single-photon $^2\Sigma^+(4p) \leftarrow {}^2\Pi(3p)$ continuum←bound transition using the calculated potential energy curves provided by Jeff Sheehy.[5]

Figure 4-10 Comparison of the simulated dissociative $^2\Sigma^+(4p)$ peak profile generated from the BCONT 1.4 program with the experimental low UV power (about 300-500 μJ/pulse) $1'_{UV} + 1_{vis}$ two-color multiphoton ionization (MPI) spectrum obtained by monitoring the Al^+ fragment signal channel.

Figure 4-11 Comparison of the simulated dissociative $^2\Sigma^+(4p)$ peak profile generated from the BCONT 1.4 program with the experimental low UV power (about 300-500 μJ/pulse) $1'_{UV} + 1_{UV}$ single-color multiphoton ionization (MPI) spectrum obtained by monitoring the Al^+ fragment signal channel.

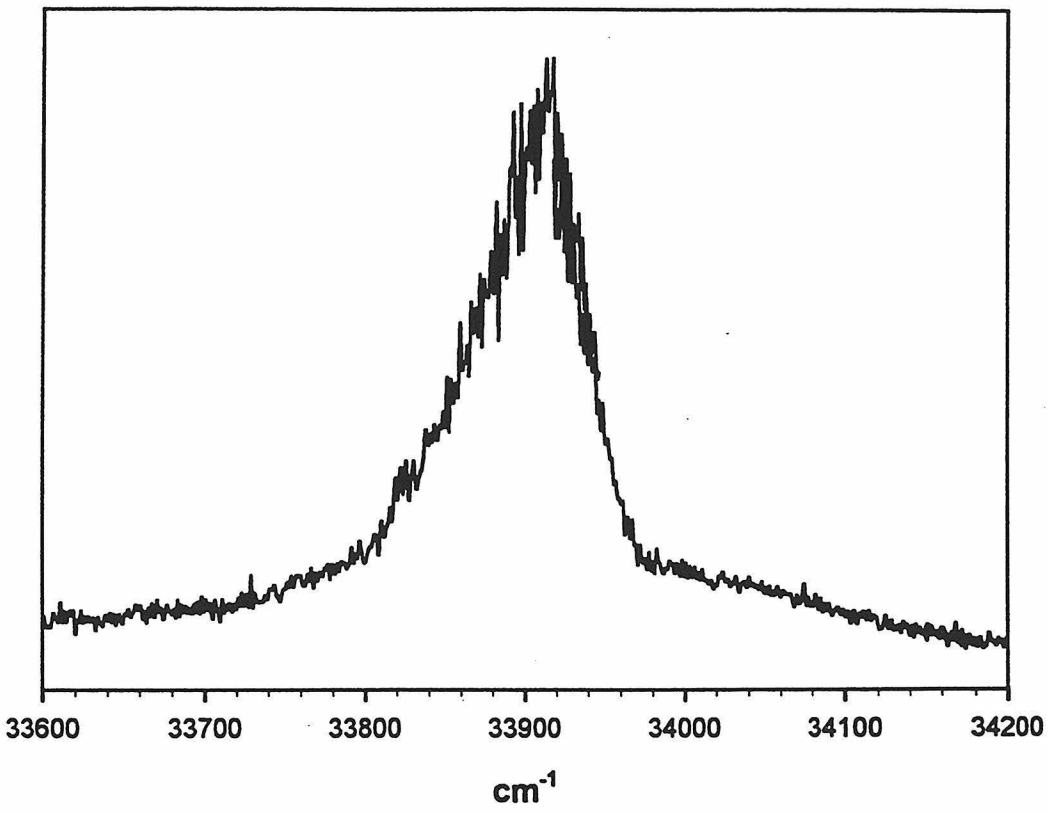


Figure 4-1

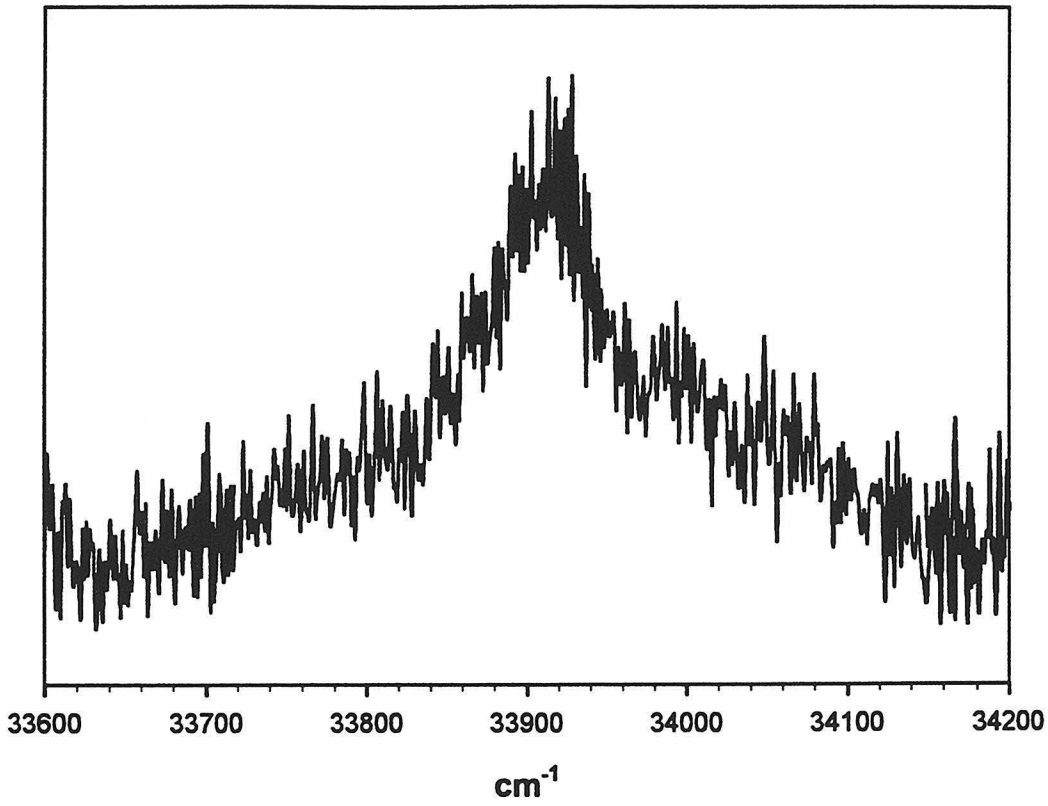


Figure 4-2

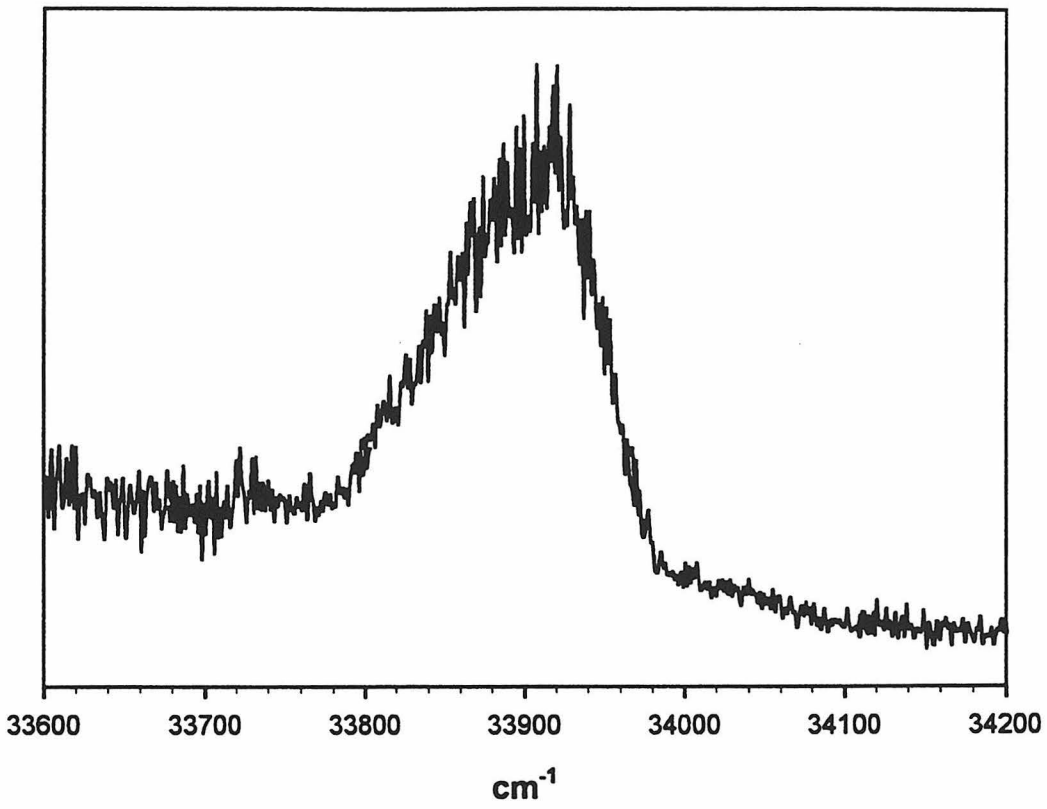


Figure 4-3

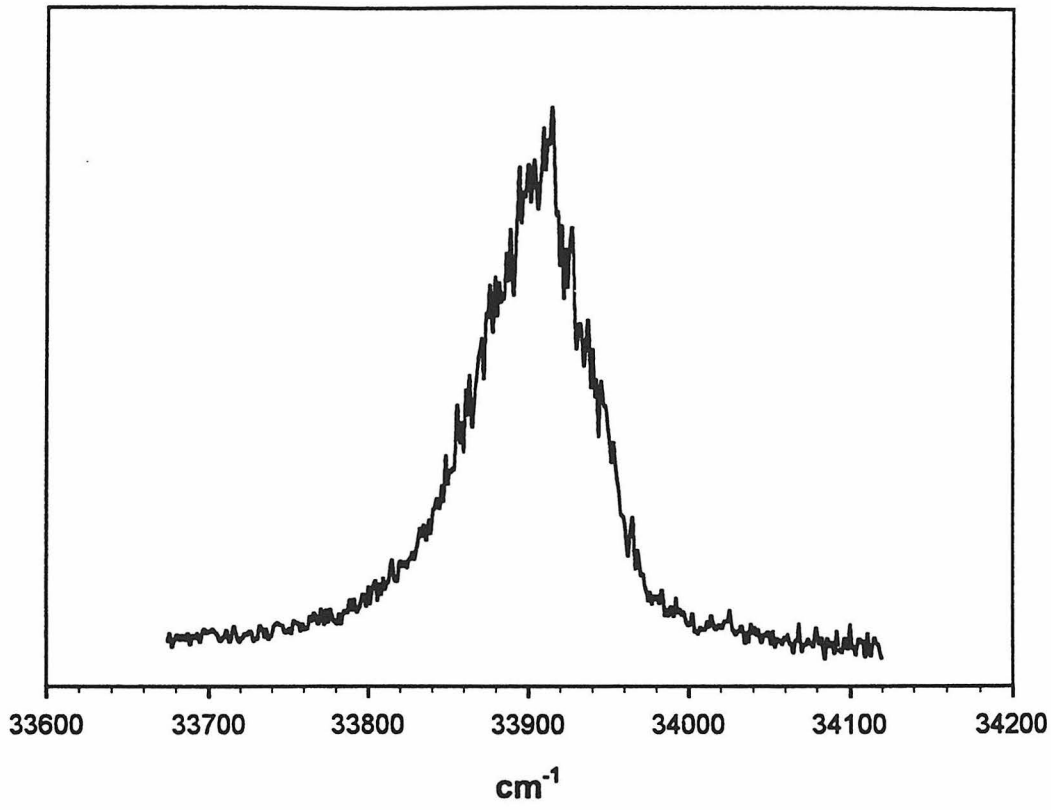


Figure 4-4

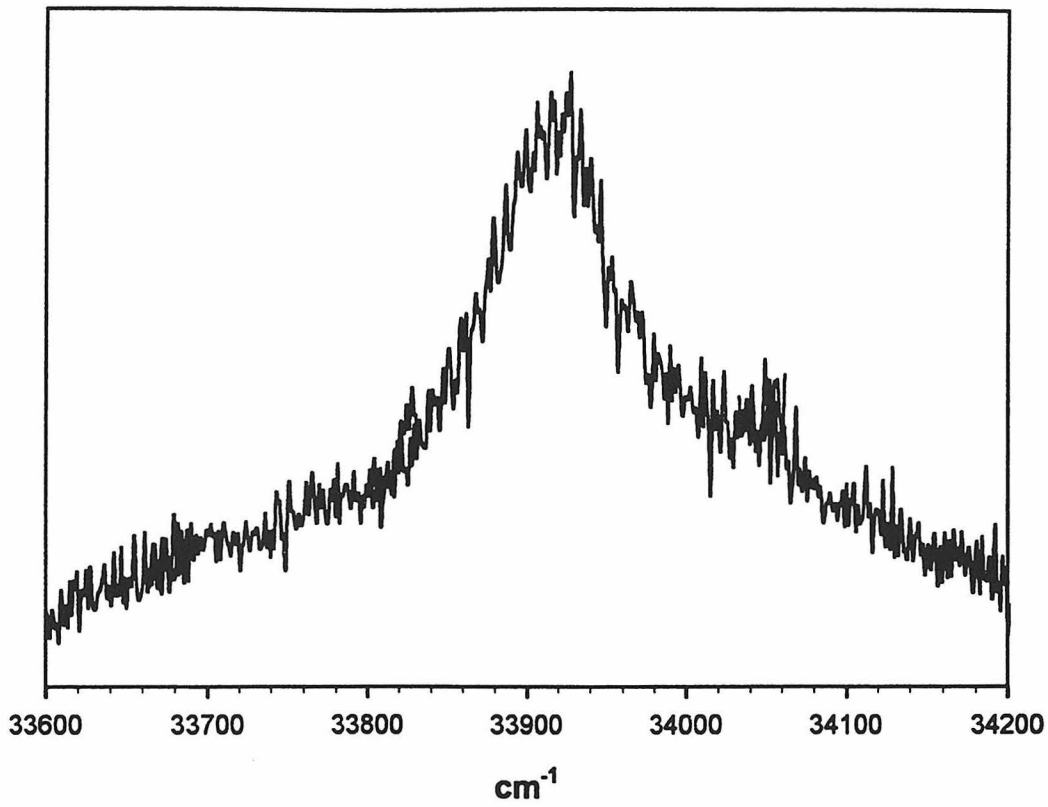


Figure 4-5

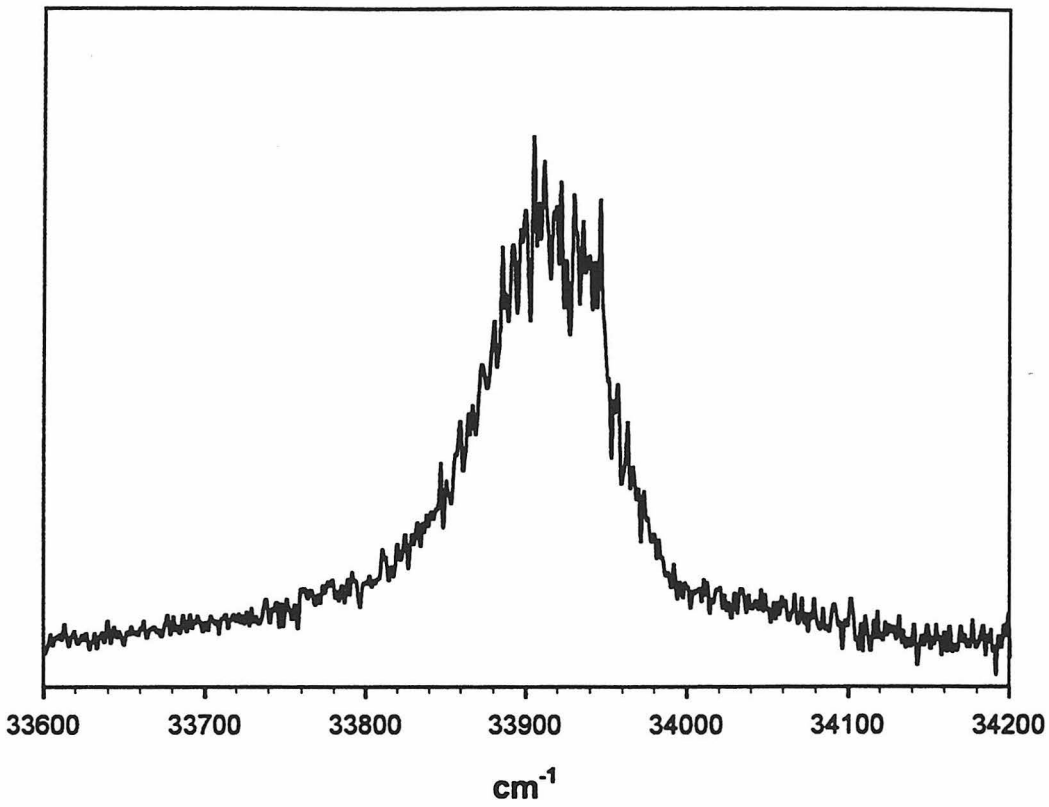


Figure 4-6

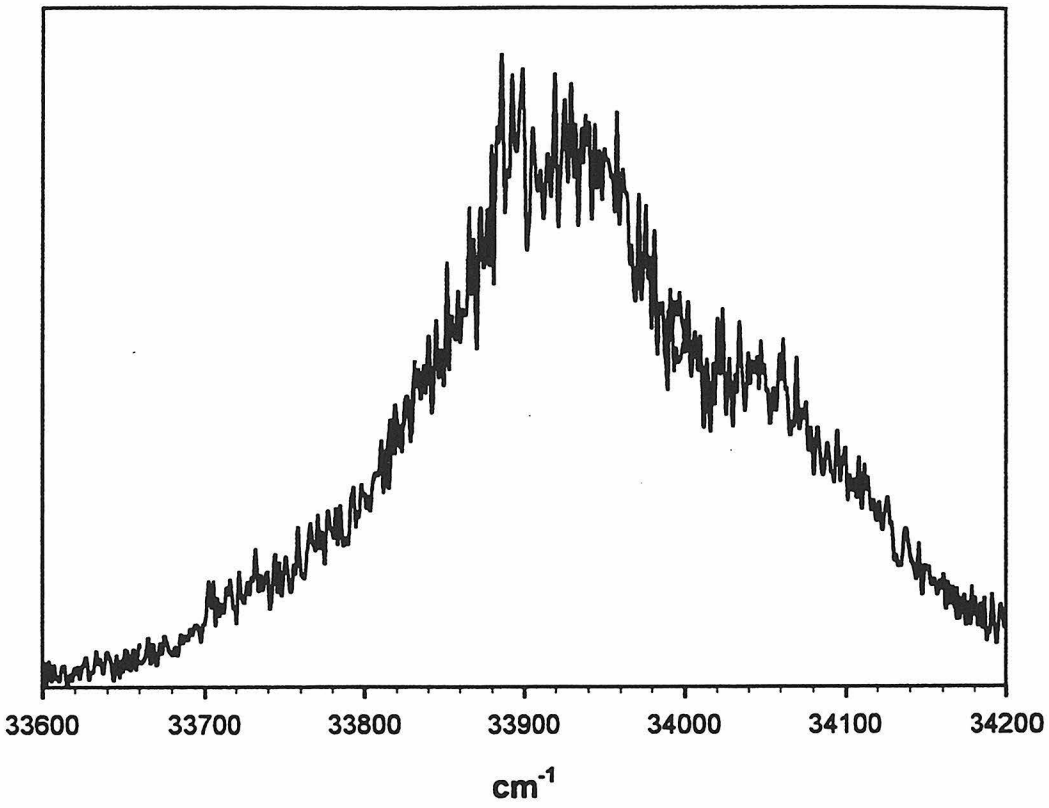
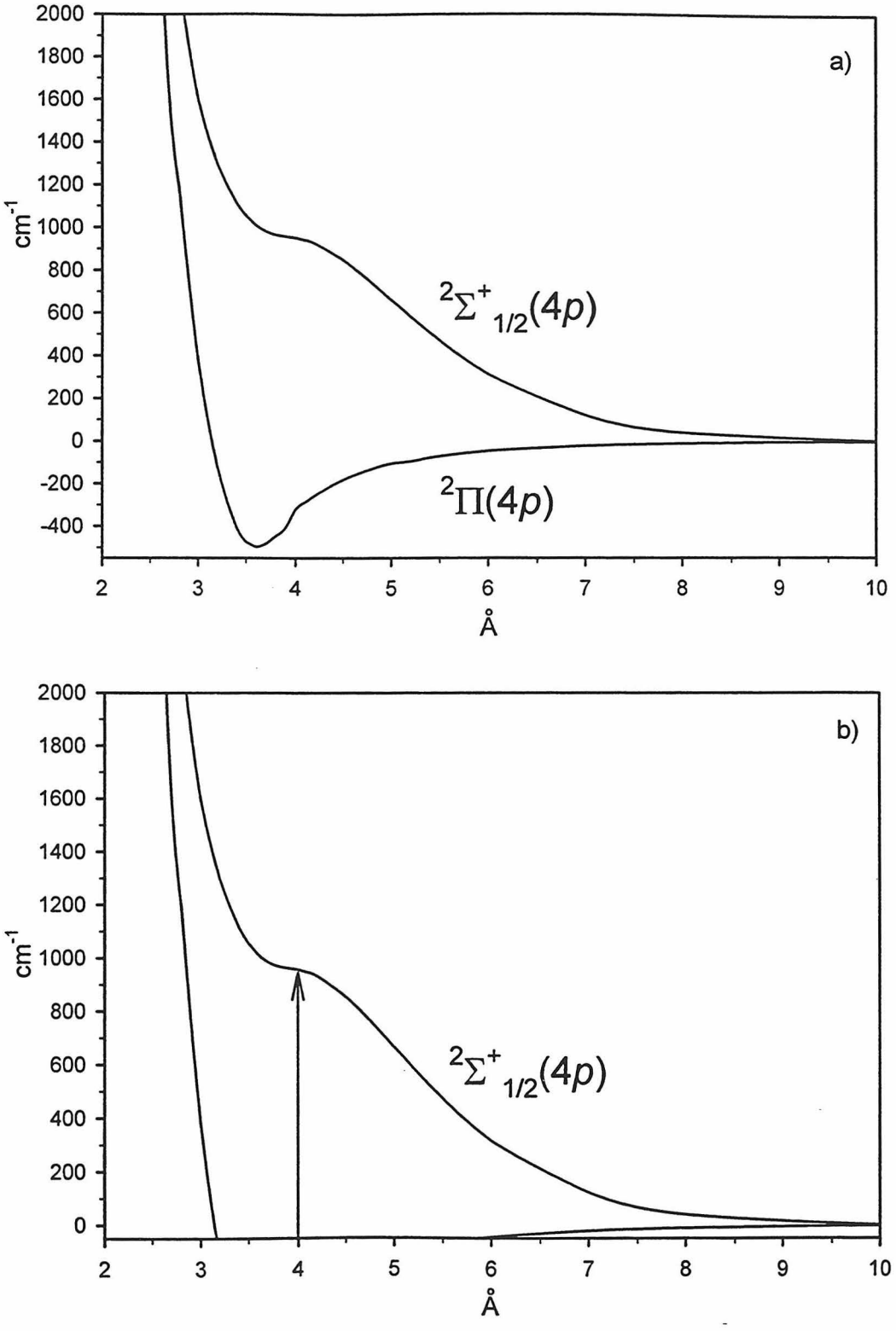


Figure 4-7



Figures 4-8a and 4-8b

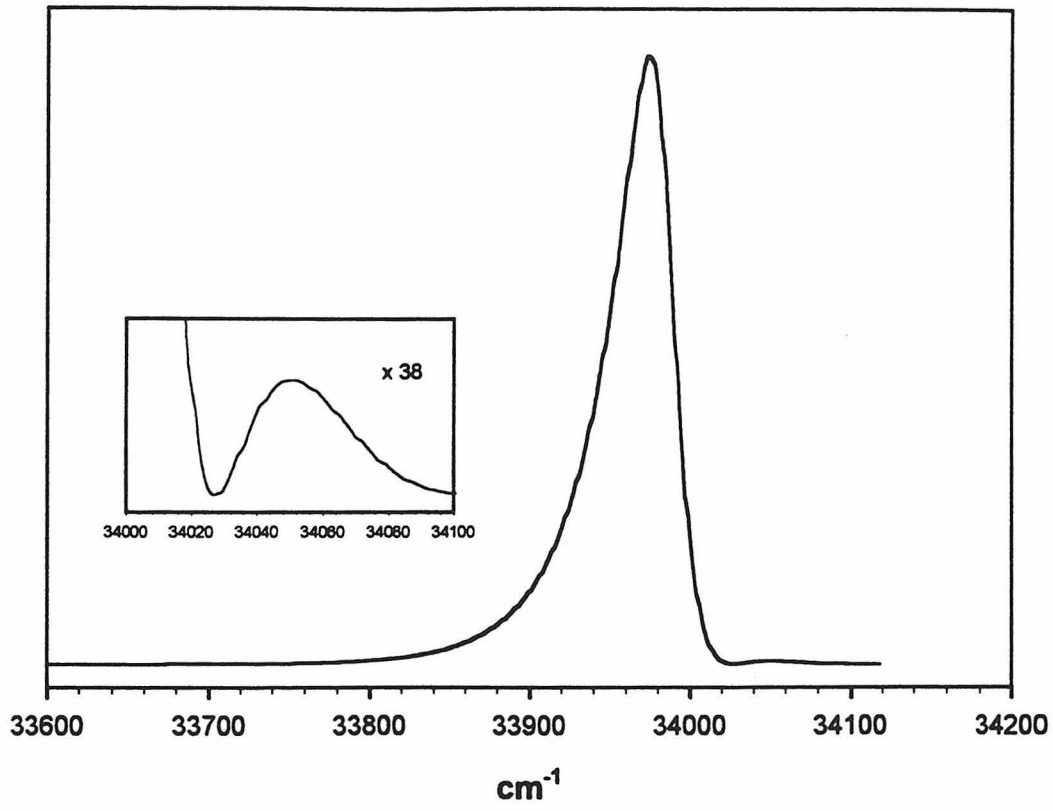

x 38
34000
34020
34040
34060
34080
34100
33600
33700
33800
33900
34000
34100
34200
cm-1

Figure 4-9

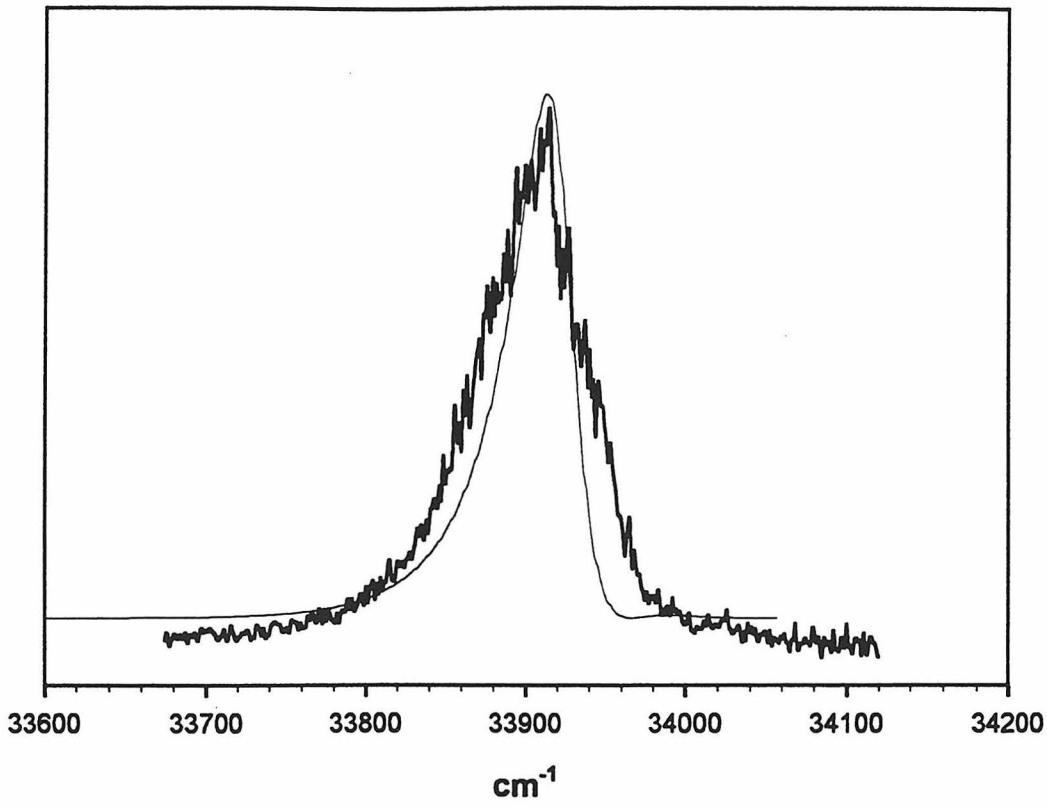


Figure 4-10

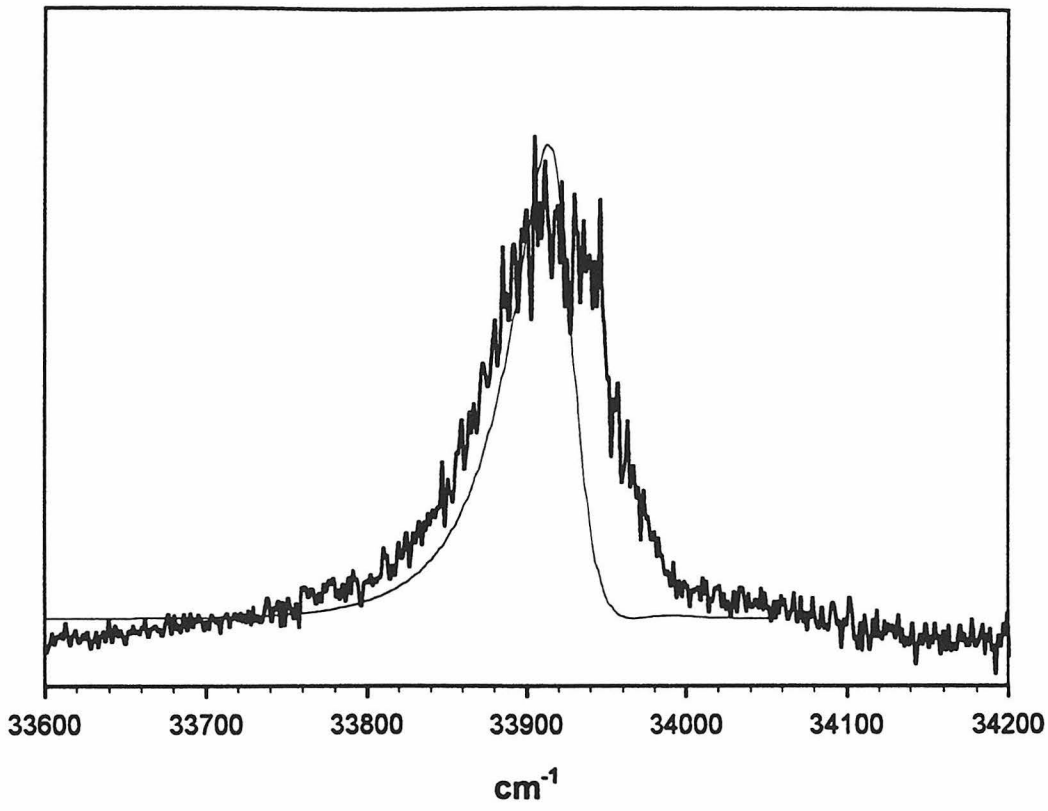


Figure 4-11

CHAPTER 5

The Observation of Novel Spectroscopic Behavior in $Al \cdot Ar_n$ Clusters ($n \leq 60$) in the Vicinity of the $Al(3d) \leftarrow Al(3p)$ Atomic Transition

5.1 Introduction

The nature of the electronic structure of single metal atoms doped into rare gas matrices has been examined extensively over the years by optical absorption spectroscopy.[1-2] The principal contribution of this accumulated work has been a systematic survey of the spectral shifts, and in some cases electronic splittings, that result when a metal atom is solvated within a condensed phase matrix. However, due to the breadth of and often unresolvable nature of the spectral features observed in condensed phase work, interpretation of a spectrum often yields little more than qualitative generalities related to the inferred size of the binding site - i.e., whether or not the dopant atom finds itself in a "tight" binding site within the matrix. Ultimately, such work has often provided little insight in and of itself regarding the intricacies of the electronic interactions that give rise to the observed spectral features, nor the size or symmetry of the binding site surrounding the metal atom itself.

In order to simplify an otherwise intractable problem of solving for the N-dimensional potential that governs the interactions in a condensed phase system, approximate model systems have been sought that serve to reduce the enormity of the problem while still retaining the fundamental physical properties of the bulk. Such an approach has invariably been the domain of cluster chemistry, a field dedicated to the use of small molecular aggregates as models for the condensed phase. The advantage to studying such small systems is that a reasonably precise description of the pair-wise and many-body potentials between a small, finite number of atomic or molecular species that comprise the model system can be obtained. Because solvent atoms or molecules can be

added to a solute in a sequential manner, a microscopic model of the dopant surrounded by the initial few solvation shells representative of a liquid or solid can begin to emerge, providing a core model from which the properties of the bulk may eventually be successfully extrapolated.

Despite the simplicity offered by the use of rare gas molecules as a model solvent, cluster studies seeking to systematically characterize the evolution of the electronic interactions between a metal atom and increasing numbers of rare gas solvating atoms have been rarely pursued. Two examples, however, that have arisen out of collaborative efforts between experimentalists and theorists have been particularly informative. The first relates to the systematic study of small $HgAr_n$ ($n \leq 5$) near the atomic $Hg(6s6p\ ^3P_1 \leftarrow 6s^2\ ^1S_0)$ transition.[3] From matrix absorption work, the electronic states arising from transitions between these two electronic manifolds were revealed to undergo large blue shifts of 1250 cm^{-1}.[4-5] An intriguing aspect about these cluster systems was the observation that excitation to the $\Omega = 0^{(+)}$ component of the excited state, namely $^3\Pi_{0+}$ in Hund's case (a) notation, exhibited an initial red shift of 60 cm^{-1} in the $Hg{\bullet}Ar_2$ clusters which was subsequently not observed with larger clusters sizes.[6-8]

Molecular dynamics simulations, however, predicted substantial red-shifts for the $^3\Pi_{0+}$ electronic state on the order of 100 cm^{-1} for $Hg{\bullet}Ar_2$ (C_{2v}), $Hg{\bullet}Ar_3$ (C_{3v}), $Hg{\bullet}Ar_4$ (C_{3v}).[8] Other isomers of these small clusters were predicted to exhibit smaller spectral red-shifts: $Hg{\bullet}Ar_4$ (C_{2v}) = 25 cm^{-1}, $Hg{\bullet}Ar_5$ (C_{4v}) = 15 cm^{-1}, and $Hg{\bullet}Ar_5$ (C_s) = 49 cm^{-1}.[8] By $Hg{\bullet}Ar_6$, this state was predicted to give rise to a blue-shifted feature of 216 cm^{-1} according to the simulations.[8] What is striking about these molecular dynamical

predictions is that all of the red-shifted features arise from isomeric configurations where the mercury atom lies at the surface of the rare gas cluster.[8] In particular, the atomic $Hg(^3P_1)$ electronic state (J = 1) can be envisioned as the shape of a torus where the electron density arising from the excited *p*-electron is aligned parallel to the rare gas cluster surface.[3] This suggests, therefore, that in cases where a metal atom can reside on the exterior of the rare gas cluster, electronic states that serve to sequester electron density oriented away from the cluster surface can experience a net stabilization. Such a conclusion was reinforced by the results of the $Hg{\bullet}Ar_6$ and larger clusters. The origin of the calculated blue shifts derived from the fact that $Hg{\bullet}Ar_6$ and subsequent larger cluster sizes were predicted to become solvated within the interior of the rare gas cluster, thus residing in a more matrix-like site characteristic of the bulk.[8]

A second noteworthy example of metal-rare gas interactions within the context of cluster systems arose from the work performed by Visticot and co-workers using barium atoms as a probe of argon cluster structure.[9-12] Rather than employing the standard method for generating metal rare gas clusters, namely laser vaporization/pulsed beam expansion methods, these experiments applied a "pick-up" technique whereby barium atoms are were deposited onto argon clusters that had already undergone expansion cooling.[11] Through such an approach, one avoids the necessity of dissipating the additional heat of the laser vaporization plasma that can otherwise limit the clustering efficiency of the source. Consequently, these experiments were able to generate large-sized argon clusters ranging from 300 to 4000 rare gas atoms.

Laser induced fluorescence (LIF) as well as dispersed emission spectra were

performed on the large $Ba•Ar_n$ clusters around the atomic $Ba(6s6p\ ^1P_1 \leftarrow 6s6s\ ^1S_0)$ transition.[11] The resultant spectra showed evidence for two main spectral features, one blue-shifted 400 cm^{-1} relative to the atomic transition and the other red-shifted by about 100 cm^{-1}. Both transitions were observed to red-shift about 100 cm^{-1} with increasing solvation, the red-shifted band lying approximately 200 cm^{-1} to the red of the atomic transition in $Ba•Ar_{3850}$.

Subsequent classical molecular dynamic simulations were performed in order to simulate the spectra.[11-12] The results of the simulations were strongly suggestive that the observed spectrum was due to surface solvation of the barium atom. Attempts to place the barium atom within the interior of the cluster resulted only in the observation of a triplet structure that was slightly more strongly blue-shifted than that experimentally observed blue-shifted feature.[11] No red-shifted feature was observed with interior solvation of the barium atom. In contrast, simulations that placed the barium atom at the surface of the cluster were able to reproduce both the red- and blue-shifted features observed experimentally with remarkable accuracy - even reproducing the small splitting observed in the red-shifted feature.[11-12]

These two examples clearly demonstrate that use of metal-rare gas clusters as models for condensed phase solvation offers a means to explore a completely new facet of binding interactions within condensed phase systems, namely as a probe of the electronic interactions of a metal atom bound to an interface. Such interactions have essentially remained unexplored in the bulk phase work performed to date. Nevertheless, there is considerable promise for the use of cluster model systems to reveal key insights into the

intricacies of binding interactions directly at the surface interface in addition to interior sites within the cluster.

As a result of these previous studies, we have pursued a systematic spectroscopic study of aluminum atoms solvated by Ar_n ($n < 55$) clusters. Aluminum was chosen as a potentially informative probe of argon cluster structure for two reasons. First, the ground state binding energy of Al•Ar[13-17] is slightly greater than the Ar•Ar pair potential by roughly 30 to 40 cm^{-1}.[3,11,18] This contrasts with the barium case where the Ba•Ar pair-potential is slightly less strongly bound than that of Ar•Ar.[11] Consequently, aluminum can serve as a sensitive probe of the role of pair-potential energetics on the site of metal atom binding within the cluster. Furthermore, aluminum, being a third row atom, is significantly smaller than either barium or mercury, both sixth row atoms. Therefore, aluminum serves as a useful probe of how atomic size may or may not affect the preferred binding site of a metal atom with a rare gas cluster. Therefore, by using a cluster approach, we sought to gain insight into the size dependent behavior of both cluster structure and the electronic band frequency shifts resulting from sequential solvation. Such measurements can, in turn, provide a stringent benchmark for testing the accuracy and reliability of the theories used to describe both bulk doped matrices as well as interfacial surfaces.

The UV absorption spectrum of aluminum trapped in argon matrices has been extensively investigated.[19-21] These studies have concentrated on the spectral region corresponding to the lowest energy atomic aluminum transitions between 400 nm and 240 nm where the matrix bands appear relatively uncongested and are, therefore, assignable with reasonable accuracy. One band of particular interest is the matrix band assigned to

the lowest energy atomic aluminum transition, namely the Al(4*s*) ← Al(3*p*).[22] While the Al(4*s*) ← Al(3*p*) transition appears around 395 nm, the matrix band assigned to result from the Al(4*s*) ← Al(3*p*) transition exhibits a blue-shift to roughly 340 nm.[19] Such a large blue shift is rather unusual, and the exact interactions that give rise to this shift are still unquantified.

Whetten and co-workers have studied the Al•$(Ar)_n$ cluster ($n < 150$) Al(4*s*) ← Al(3*p*) frequency shifts as a function of increasing solvation using a cluster approach.[23-25] The Al(4*s*) ← Al(3*p*) band exhibited a strong monotonic blue shift with increasing cluster size up to $Al(Ar)_{12}$, after which the observed spectral shift leveled off. The maximum extent of the cluster Al(4*s*) ← Al(3*p*) blue-shift was +1000 cm^{-1}, only a moderate fraction of the +4200 cm^{-1} matrix shift.[25] However, due to the spherically symmetric nature of the excited Al(4*s*) orbital, these authors were unable to infer structural details from merely the solvent shifts, only concluding that these cluster systems do not yet resemble the bulk.

The next excited electronic band observed in argon matrices doped with aluminum atoms, a doublet or possibly triplet near 290 nm, has been assigned to the Al(3*d*) ← Al(3*p*) transitions that occur near 308 nm in the isolated atom.[19,22] Far more insight could potentially be gained by investigating the matrix band spectral shifts arising from the Al(3*p*) ground state to the excited Al(3*d*) states because asymmetries in the aluminum atom binding site can lift the five-fold degeneracy of the Al(3*d*) states, leading to the possibility of a splitting in the excited electronic states. By studying the size dependent frequency shifts and band splittings arising from transitions to the Al(3*d*) manifold with

sequential solvation, a great deal of insight may be gleaned into both the nature of the electronic interaction of the metal atom trapped within a matrix site as well as the intrinsic symmetry of the matrix site in which the metal atom resides. As a result, we have investigated the UV spectra of Al•$(Ar)_n$ clusters ($n < 60$) about the atomic aluminum Al($3d$) ← Al($3p$) transitions by $1'_{UV} + 1_{vis}$ resonant two-color multiphoton ionization spectroscopy (R2MPI) as well as $2_{vis} + 1_{vis}$ non-resonant single-color multiphoton ionization spectroscopy.

5.2 Experimental

Al•$(Ar)_n$ clusters were generated by a standard laser ablation techniques. Following the opening of a piezoelectric pulsed valve, the pure Ar carrier gas (~8 atm. stagnation pressure) was injected into either the second or third generation laser vaporization sources described in Chapter 2. The tripled output of a Nd-YAG laser (Continuum Surelite 1) was focused on the surface of a rotatable 2024 alloy aluminum rod that was positioned directly adjacent to the throat of the supersonic expansion. Following the supersonic expansion, the clusters passed through a 3 mm orifice diameter skimmer into the second differential region. The clusters were then ionized by $1'_{UV} + 1_{vis}$ resonant two-color multiphoton ionization by crossing the jet with an unfocused pump beam consisting of both the residual fundamental and doubled fundamental of the appropriate laser dye wavelength (DCM, Rhodamine 640, Rhodamine 640/Rhodamine 610 (50:50 mixture), and Rhodamine 610). The UV laser pulse (1 - 4 mJ/pulse) was derived from the doubled output of a dye laser (Quantel TDL-51) pumped by the doubled output of a

Nd:YAG laser (Continuum NY61-20). Figure 5-1 shows the ionization scheme employed. The clusters were scanned through the UV region from 330 nm to 296 nm, first exciting the atomic Al(3*d*) ← Al(3*p*) transitions with the doubled UV photon, and subsequently ionizing with the residual visible fundamental dye output (10-50 mJ/pulse) that exited the doubling crystal coaxially with the UV laser pulse. In the current single dye laser experiments, the UV and visible wavelengths were forced to tune simultaneously. Based on data by Whetten and co-workers,[23] absorption of the second, visible photon ($\nu_{vis} = (\nu_{UV})/2$) was near the ionization threshold. The total photon energy ($\nu_{UV} + \nu_{vis}$) was always within 0.75 eV or less of the ionization threshold of the clusters.

Following ionization, the clusters were extracted perpendicularly and mass-analyzed by a standard 1 m Wiley-McLaren time-of-flight (TOF) spectrometer,[26] and detected by a chevron dual-microchannel plate detector. A typical TOF mass spectrum can be seen in Figure 2-101 in Chapter 2. Individual scans were recorded by gating the mass peak of interest with a gated integrator (SR-250, Stanford Research Systems). S/N was greatly improved by switching the laser vaporization Q-switch at half the repetition rate and using the gated integrator to subtract the pump background due to DP oil contaminant fragments (LV off) from every signal shot (LV on). All spectra were power normalized for UV fluence.

5.3 Results

5.3.1 Experimental Spectra

The experimental UV spectra of Al•$(Ar)_n$ clusters ($n < 60$) about the atomic

aluminum Al($3d$) ← Al($3p$) transitions obtained by $1'_{UV} + 1_{vis}$ resonant two-color multiphoton ionization are presented in Figures 5-2 through 5-12. The Al•Ar_n cluster sizes for which spectra were acquired over the course of the experiment were the following: Al•Ar_3, Al•Ar_5, Al•Ar_6, Al•Ar_7, Al•Ar_{12}, Al•Ar_{18}, Al•Ar_{25}, Al•Ar_{34}, Al•Ar_{40}, Al•Ar_{47}, and Al•Ar_{54}. Each of the spectra presented in Figures 5-2 through 5-12 represented the results derived over four complete dye laser tuning ranges (DCM, Rhodamine 640, Rhodamine 640/Rhodamine 610 (50:50 mixture), and Rhodamine 610) that have been joined together to form the complete total spectrum for a given cluster size. Whenever possible, care was taken to ensure overlapping wavelength ranges between the different dye tuning ranges so that sufficient spectral overlap between the various regions was achieved. This served to remove (to the best of our ability) the subjectiveness inherent to scaling and offsetting the spectral features observed between different dye regions. Therefore, while the spectral features themselves presented in the combined spectra were believed to be truly characteristic of a specific cluster size, there nevertheless existed some ambiguity as to the absolute relative intensities of features arising between individual dye tuning ranges. Consequently, care should be exercised before drawing definitive comparisons between the relative intensities of spectral features collected from different dye tuning ranges. Furthermore, a number of the spectra exhibited a gap in the region between 312 nm and 310 nm. Such spectral gaps are the result of insufficient overlap in the signal between the DCM and Rhodamine 640 dye tuning ranges, rendering a reasonable combined spectrum difficult to infer.

Due to the time intensive nature of accumulating a complete spectrum for a given

cluster size across four different dye tuning ranges, specific cluster sizes were chosen for study rather than scanning every cluster size as had been performed in the case of the $Al{\bullet}Ar_n$ cluster spectra taken about the $Al(4s) \leftarrow Al(3p)$ transition by Whetten and co-workers.[23-25] The cluster sizes for which complete spectra were obtained were chosen for two reasons. First, as is seen from inspection of the characteristic mass spectrum presented in Figure 2-101 in Chapter 2, a number of the cluster sizes pursued for study were "magic numbers." Due to the supposed enhanced thermodynamic stability of these cluster sizes, it was believed that the spectra arising from magic number cluster sizes might be representative of particularly stable geometrical isomers that might in turn give rise to clean, well-defined spectral features characteristic of this atomic configuration. Second, the cluster sizes for which spectra were obtained were interspersed in size along the solvation shell closings characteristic of Mackay icosahedra that describe the solvation behavior of rare gas clusters.[27-28] In particular, complete spherical shells of Mackay icosahedra would be expected at $Al{\bullet}Ar_{12}$ and $Al{\bullet}Ar_{54}$, masses for which distinct changes can be observed in the mass spectrum (see Figure 2-101 in Chapter 2) characteristic of shell closing behavior. The cluster sizes chosen for study were representative of both the complete solvation shell closing themselves as well as varying degrees of solvation within the first and second Mackay icosahedral solvation shells.

As is suggested in Figure 5-1, an additional variable that remained unquantified in the spectra presented in Figures 5-2 through 5-12 was the degree to which features derived from higher clusters fragmenting into the detected cluster size contributed to the observed spectral features. To test this, cluster sizes directly adjacent to those presented

were scanned over one or more of the dye tuning ranges (data not shown). In no case above the Al•Ar_6 cluster size was there observed dramatic differences in the absorption spectrum between adjacent cluster sizes. Therefore, while cluster fragmentation undoubtedly influenced the observed spectrum to some degree, the cluster sizes for which complete spectra were obtained are believed to be mostly representative of a fairly narrow size distribution.

A final comment is warranted regarding the presence of structural isomers in the observed spectrum for a particular mass. During the course of the experiments, it was discovered that the relative intensities of certain spectral features were highly sensitive to changes in the source conditions employed to generate the clusters - an observation highly indicative of the presence of structural isomers present in the UV cluster absorption spectra characteristic for each mass. Therefore, there exists some ambiguity by mere examination of the experimental spectra whether closely spaced features derive from different electronic interactions within a single cluster isomer, or from interactions of a single electronic state among many different isomers of a specific cluster size.

5.3.1.1. Solvation Trends up to Al•Ar_6

A comparison of the optical absorption spectra for Al•Ar_3, Al•Ar_5, and Al•Ar_6 is presented in Figure 5-13. All of the spectra exhibit two primary features, one peak being red-shifted relative to the atomic Al($3d$) ← Al($3p$) transitions centered around 308 nm, the other blue-shifted. For the Al•Ar_3 cluster, the red-shifted absorption feature was fairly broad, and was centered at approximately 312.5 nm. This represented a sizable shift of

roughly 450 cm^{-1} relative to the atomic aluminum transitions. For Al•Ar_5, a similar absorption feature centered at approximately 313.5 nm was observed that strongly resembled that seen in the Al•Ar_3 cluster. In addition, a second absorption feature was present that manifested itself as a red-shifted shoulder relative to the main peak centered at roughly 316 nm. A weak intensity red-shifted feature relative to the main peak of Al•Ar_3 centered at 318 nm was also present, but whether these two features are of the same origin remained unclear.

The apparent red-shifted doublet feature observed with the Al•Ar_5 cluster became especially pronounced by Al•Ar_6, appearing as two equally intense and distinct peaks. Intriguingly, the red-shifted doublet seen in the Al•Ar_5 cluster underwent a slight blue-shift from Al•Ar_5 to Al•Ar_6 such that the center of the doublet feature lay at approximately the same energy as the peak maximum for the Al•Ar_3 cluster. The peak maxima for the red-shifted features in the Al•Ar_6 cluster appear at approximately 311 nm and 314 nm.

As shown in Figure 5-13, all three cluster sizes exhibited a broad blue-shifted feature that varied considerably in spectral breadth between the three different cluster sizes. For Al•Ar_3, the blue-shifted peak maximum appeared to be centered at about 302 nm, which shifted slightly to the blue upon higher degrees of solvation seen in the Al•Ar_5 and Al•Ar_6 spectra.

5.3.1.2. Solvation Trends up from Al•Ar_6 to Al•Ar_{12}

As the clusters evolve towards the icosahedral shell closing of the first solvation shell, the spectral trends remain fairly static, resembling strongly the spectral

characteristics exhibited by the $Al•Ar_5$ and $Al•Ar_6$ cluster sizes. Figure 5-14 shows the UV absorption spectral changes that occur between the $Al•Ar_6$, $Al•Ar_7$, and $Al•Ar_{12}$ clusters. The $Al•Ar_7$ cluster exhibited a red-shifted feature that was significantly broadened relative to $Al•Ar_6$, even though the peak maximum remained centered between the doublet feature of the latter cluster. In addition, there may have been an additional weak feature centered near the atomic aluminum transitions centered near 308 nm. However, due to the difficulty mentioned above concerning the best manner to join the DCM and Rhodamine 640 spectra in the region between 312 nm and 310 nm, this feature may merely be the blue edge of a significantly broadened feature.

By $Al•Ar_{12}$, a well-defined red-shifted doublet was once again apparent that was significantly less broadened than the absorption feature present in the $Al•Ar_7$ cluster. Both peaks of the doublet were slightly red-shifted relative to those seen in $Al•Ar_6$, appearing at 316.5 nm and 313.5 nm. Somewhat surprisingly, the spectra obtained for red-shifted feature of the $Al•Ar_5$ and the $Al•Ar_{12}$ cluster were almost perfectly identical both with respect to relative frequency shifts and relative peak intensities. In fact, if the two are overlapped, almost no distinction can be made between the two spectra. This was strongly suggestive of a similar metal atom binding site in both the $Al•Ar_5$ and $Al•Ar_{12}$ clusters.

As was the case with the $Al•Ar_3$ to $Al•Ar_6$ cluster size range, a broad blue-shifted feature was observed in both the $Al•Ar_7$ and $Al•Ar_{12}$ spectra. A rather distinct peak maximum was evident in the case of $Al•Ar_7$ at approximately 301.5 nm. The peak maximum for the blue-shifted feature for the $Al•Ar_{12}$ cluster was only slightly more blue-

shifted relative to Al•Ar_7, centered at perhaps 300.5 nm.

Overall, for the first solvation shell, one observed a prominent red-shifted absorption relative to the atomic aluminum transitions near 308 nm. Upon increasing solvation by argon beyond the Al•Ar_3 cluster size, this feature manifested pronounced doublet character, the two individual features exhibiting red-shifts on the order of 870 cm^{-1} and 570 cm^{-1} respectively. In addition, a broad, blue-shifted feature was consistently observed centered in the region of 302 nm to 300 nm, an overall blue-shift of approximately 850 cm^{-1}.

5.3.1.3. Solvation Behavior Within the Second Solvation Shell: Al•Ar_{12} to Al•Ar_{47}

Figure 5-15 presents the progressive solvation behavior observed upon increasing solvation within the second icosahedral solvation shell. As was the case with the spectra collected for the different cluster sizes of the first solvation shell, the spectra of the clusters composing the second solvation shell consisted of a prominent red-shifted feature relative to the atomic aluminum transitions near 308 nm, as well as a broad blue-shifted feature. With the Al•Ar_{18} cluster, one observed essentially no additional spectral shift in the red-shifted feature, although the appearance of an extended tail on the blue edge of the feature was noted. The blue-shifted feature for the Al•Ar_{18} cluster is difficult to discern above the background, presumably due to a high degree of fragmentation of the larger clusters. By Al•Ar_{25}, the red-shifted feature began to show a slight additional spectral shift to the red on the red edge of the absorption feature. Both red-shifted absorption features for the Al•Ar_{25} and Al•Ar_{34} clusters are similar in their spectral breadth and

relative position. The extensive broadening of the red-shifted absorption features for the $Al{\bullet}Ar_{25}$ and $Al{\bullet}Ar_{34}$ clusters was presumably due to a number of isomeric forms of each cluster being detected. Similar to the case of the $Al{\bullet}Ar_{18}$ cluster, the blue-shifted feature for $Al{\bullet}Ar_{25}$ and $Al{\bullet}Ar_{34}$ was largely obscured by a significant fragmentation background.

Unexpectedly, the absorption spectrum for the $Al{\bullet}Ar_{47}$ cluster was remarkably uncongested, with clearly defined spectral features evident. Two red-shifted features were discernible. The most red-shifted feature was an almost symmetrical peak centered at almost 319 nm. The exact peak maximum and contour for the other red-shifted feature was indeterminate due to a gap in the spectrum between 312 nm and 310 nm caused by an inability to unambiguously join the spectra collected from the DCM and Rhodamine 640 dye tuning ranges. Nevertheless, a reasonable estimate for the peak maximum appearing at approximately 311 nm can be inferred.

A broad-blue-shifted feature can be clearly distinguished centered between 302 nm to 301 nm. The shape and spectral shift of the blue-shifted feature was similar between $Al{\bullet}Ar_{12}$ and $Al{\bullet}Ar_{47}$, indicative of the fact that the electronic interactions that gave rise to this feature were largely unaffected by increasing solvation within the second solvation shell.

A comparison between the red-shifted feature observed in the $Al{\bullet}Ar_{25}$ and $Al{\bullet}Ar_{34}$ clusters and that of the $Al{\bullet}Ar_{47}$ cluster revealed that the overall spectral breadth of the observed absorption feature were very similar. Nevertheless, the $Al{\bullet}Ar_{47}$ cluster was relatively uncongested near the center of the absorption feature unlike the other two cluster sizes. The lack of spectral congestion within the $Al{\bullet}Ar_{47}$ cluster may be indicative

of a lack of different isomeric forms of this cluster in favor of a single particularly stable atomic configuration.

An additional interesting observation was that the two red-shifted features of the Al•Ar_{47} cluster may derive from the doublet features observed in both the Al•Ar_6 and Al•Ar_{12} cluster sizes. If, in fact, these features do arise from analogous electronic interactions, then we see that the more red-shifted peak of the doublet undergoes an additional red-shift of approximately 200 cm^{-1} upon increasing solvation from Al•Ar_{12} to Al•Ar_{47}. Likewise the more blue-shifted peak undergoes a slight blue-shift upon increasing solvation from Al•Ar_{12} to Al•Ar_{47}, exhibiting a spectral shift of approximately 250 cm^{-1}.

5.3.1.4. The Second Icosahedral Solvation Shell Closing at Al•Ar_{54}: Comparisons with the Al•Ar_6 and Al•Ar_{12} Clusters As Well As the Bulk Matrix Spectrum

The absorption spectrum for the Al•Ar_{54} cluster corresponding to the completion of the second icosahedral solvation shell is shown in Figure 5-16. In addition, Figure 5-16 directly compares the Al•Ar_{54} absorption spectrum to those collected for the Al•Ar_6 and Al•Ar_{12} clusters as well as that obtained from the bulk matrix work. The Al•Ar_{54} absorption spectrum was dominated by a prominent, broad red-shifted absorption feature centered at approximately 319.5 nm. The absorption maximum for this peak was slightly more red-shifted that that observed for the Al•Ar_{47} cluster. In addition, the spectral breadth of the Al•Ar_{54} cluster was significantly broadened on both the red and blue wings of the absorption feature relative to the most red-shifted feature of the Al•Ar_{47} cluster.

Overall the main Al•Ar_{54} red-shifted absorption feature demonstrated a significant spectral shift of approximately 1150 cm^{-1} to the red of the atomic transition at 308 nm.

While being largely obscured by a sizable fragmentation background, there existed nevertheless some evidence that a second absorption feature may be present near the atomic aluminum transitions near 308 nm. Such a feature would correspond to the more red-shifted absorption feature of the red-shifted doublet observed in the Al•Ar_{47} cluster, albeit shifted slightly more to the blue relative to the latter cluster. Any evidence for a blue-shifted feature observed in a number of the cluster sizes within the first and second solvation shells was obscured by a large fragmentation background in the Al•Ar_{54} cluster.

A rather unusual solvation trend, therefore, was exhibited by the clusters. As is clearly shown in Figure 5-16, the most prominent cluster absorption feature shifted strongly to the red with increasing solvation. In fact, the magnitude of the spectral shift trend observed in the clusters was dramatically *opposite* to that observed in the bulk matrix spectrum. By Al•Ar_{54}, the magnitude of the red-shift for the primary absorption feature, namely 1150 cm^{-1}, represented a sizable fraction of the magnitude of the spectral shifts (1900 cm^{-1} and 2500 cm^{-1} respectively) for matrix absorption doublet feature presently assigned as arising from the Al($3d$) ← Al($3p$) transitions.

5.3.1.5. 2_{vis} + 1_{vis} Single-Color Multiphoton Ionization of Al•Ar_6 and Al•Ar_{12}

In addition to the $1'_{UV}$ + 1_{vis} two-color multiphoton ionization spectra collected for the different sized clusters within the first and second icosahedral solvation shells, 2_{vis} + 1_{vis} single-color ionization studies were also attempted on these same cluster sizes.

By employing such an approach, we became sensitive to nominally two-photon allowed transitions that would arise from transitions to the Al($4p$) + Ar electronic manifold whose asymptotic energy lies approximately 520 cm^{-1} above the asymptote for the Al($3d$) + Ar electronic manifold.[22] Experimental characterization of the electronic spectroscopy of the Al($3d$) ← Al($3p$) and Al($4p$) ← Al($3p$) transitions in the diatomic Al•Ar molecule have been comprehensively detailed in Chapter 3 of this thesis. The results from the diatomic work provided convincing evidence for electronic state mixing within the diatomic Al•Ar van der Waals molecule between the electronic states arising from the excited Al($4p$) + Ar and Al($3d$) + Ar electronic manifolds. As a result, the larger cluster spectra were likewise probed to explore the possibility whether electronic state mixing effects between the Al($3d$) and Al($4p$) electronic manifolds were indeed observable within the same spectral region.

Due to the weak nature of the Al($4p$) ← Al($3p$) transition intensities, single-color, two-photon spectra of the clusters were difficult to obtain. Significant intensity was not observed in clusters larger than Al•Ar_{12}. Furthermore, only within the DCM dye tuning range was the ion intensity significant enough to achieve a reasonable signal to noise spectrum. Therefore, the 2_{vis} + 1_{vis} single-color spectra on the cluster systems was not able to be acquired to the breadth that was achieved with the $1'_{UV}$ + 1_{vis} two-color multiphoton ionization work presented above.

Nevertheless, two spectra that were successfully acquired were particularly noteworthy. Figures 5-17 and 5-18 show the 2_{vis} + 1_{vis} single-color ionization spectra collected for Al•Ar_6 and Al•Ar_{12} over the DCM dye tuning range, a region lying to the red

of the atomic aluminum transitions near 308 nm. Comparison with the $1'_{UV} + 1_{vis}$ two-color multiphoton ionization spectra for $Al{\bullet}Ar_6$ and $Al{\bullet}Ar_{12}$ presented in Figure 5-18 clearly demonstrates noticeable coincidence in the spectral behavior. Namely, both of the spectral features obtained from the $2_{vis} + 1_{vis}$ spectrum coincided remarkably well with the more red-shifted peak of the red-shifted doublet feature observed in the $1'_{UV} + 1_{vis}$ spectra for $Al{\bullet}Ar_6$ and $Al{\bullet}Ar_{12}$ - even mimicking the slight red-shift observed in going from $Al{\bullet}A_6$ to $Al{\bullet}Ar_{12}$. Such behavior raised the intriguing possibility that the red-shifted doublet features observed in the $1'_{UV} + 1_{vis}$ spectra for $Al{\bullet}Ar_6$ and $Al{\bullet}Ar_{12}$ were derived from two dramatically different electronic interactions within the Al(3*d*) electronic manifold, one being largely uncoupled from the Al(4*p*) electronic manifold while the other having acquired substantial Al(4*p*) character. Likewise, the fact that the mixed electronic state band exhibited the more extreme red-shift was suggestive of the fact that a net stabilization between the aluminum atom and the bulk of the cluster was attained as a direct consequence of the state mixing interaction.

5.3.2. Balling and Wright Model Simulations of $Al{\bullet}Ar_n$ Cluster Structure and Electronic Spectrum

In an attempt to rationalize the unusual spectral behavior observed in the $Al{\bullet}Ar_n$ clusters by $1'_{UV} + 1_{vis}$ two-color and $2_{vis} + 1_{vis}$ single-color multiphoton ionization spectroscopy, classical Monte Carlo simulation techniques were performed as a result of a collaborative effort with Jeff Sheehy and Jerry Boatz. All of the theoretical work described in this chapter derived from work performed by Jeff Sheehy and Jerry Boatz at

Phillips Laboratory, Edwards Air Force Base, and for which preliminary results have been reported.[29]

Presently, the absorption spectrum of three cluster sizes - Al•A_6, Al•Ar_{12}, and Al•Ar_{54} - have been simulated using a methodology originally proposed by Balling and Wright.[30-31] The Balling and Wright model is a simple pair-wise potential additivity approach that neglects all higher order interactions beyond the two-body terms. In addition, this model also neglects subtle electronic effects since the transition dipole moment is assumed to be constant across the region where vertical allowed transitions between the ground and excited potentials occur.

The Al•Ar diatomic potential curves generated by Jeff Sheehy for the Al($3p$)•Ar, Al($4s$)•Ar, Al($3d$)•Ar, and Al($4p$)•Ar electronic manifolds were presented in Section 3.5.3. of Chapter 3. These potentials were then used by Jerry Boatz to generate minimum energy structures for the Al•A_6, Al•Ar_{12}, and Al•Ar_{54} clusters. In all cases, the most energetically favorable site for the aluminum atom was on the surface of the cluster as was observed in the case of the Ba•Ar_n clusters.[11] The simulated minimum energy cluster structures are presented in Figures 5-19 and 5-20. In general, the aluminum atom was observed to cause minimal distortions to the icosahedral packing structure of the Ar_n clusters directly adjacent to the aluminum atom binding site, nearly maintaining the original cluster symmetry. Attempts to uncover a stable interior site were hampered by the proclivity demonstrated by the aluminum atom for migration to the cluster surface, yielding only metastable interior sites.[32]

Using these calculated minimum energy structures, absorption spectra for the three

cluster sizes were generated at three different temperatures about the Al($3d$) ← Al($3p$) atomic transitions. These simulated absorption spectra are presented in Figure 5-21. As is evident from inspection of Figure 5-21, three main spectral features were predicted, although two remained incompletely resolved in the Al•Ar_{12} and Al•Ar_{54} clusters. For Al•Ar_6, one absorption feature was predicted to lie slightly to the red of the atomic aluminum transitions near 308 nm, centered almost exactly at 310 nm. In addition, two blue-shifted features were observed with the Al•Ar_6 cluster, one appearing at approximately 306.2 nm while the other was apparent near 303.4 nm.

For the Al•Ar_{12} and Al•Ar_{54} cluster sizes, two primary features were predicted. The first was an intense, fairly narrow absorption feature centered at 308.8 nm and 308.6 nm for the Al•Ar_{12} and Al•Ar_{54} clusters respectively. This feature was essentially coincident with the atomic transition. The other feature, a broad blue-shifted feature, was predicted that was centered around 303.8 nm and 303.6 nm for the Al•Ar_{12} and Al•Ar_{54} clusters respectively.

In an attempt to determine whether an interior site could possibly give rise to the observed red-shifted feature, constraints were placed on the relaxation method by which the minimum energy structure was derived. The constraints placed on the model were somewhat unreasonable since they prevented the minimum energy relaxation pathway for the aluminum atom to migrate to the surface of the cluster. Nevertheless, a simulated absorption spectrum could be attained for these metastable interior states. All the observed spectral features were predicted to undergo a significant blue-shift in the case of interior solvation.[32] In fact, the simulated spectra that were generated were more

characteristic of the bulk matrix spectrum rather those derived from the surface solvated minimum energy structure.

5.4. Discussion

At present, there remains an incongruity between the observed cluster spectra derived from $1'_{UV} + 1_{vis}$ two-color and $2_{vis} + 1_{vis}$ single-color multiphoton ionization spectroscopy and the results of the classical simulations. While Balling and Wright level models have successfully predicted the small spectral red-shifts observed in the electronic spectroscopy of single barium atoms surface solvated on Ar_n clusters, the red-shifts were nevertheless small in magnitude - only about 200 cm^{-1} for a cluster as large as $Ba•Ar_{3850}$. The observed spectral red-shifts for the $Al•Ar_n$ were therefore anomalous in two respects. First, the sheer magnitude of the red-shifted absorption features for the $Al•Ar_n$ clusters was uncommonly large. In particular, the 1150 cm^{-1} red-shift for the main absorption feature of the $Al•Ar_{54}$ cluster was unprecedented compared to other previously studied metal-rare gas cluster systems. Such large shifts were in marked contrast to the results of the simulations that predict a small red-shift of 200 cm^{-1} in one of the three primary spectral features only for the smallest $Al•Ar_6$ cluster. After the $Al•Ar_6$ cluster, increasing degrees of solvation such as those present in the larger $Al•Ar_{12}$ and $Al•Ar_{54}$ clusters were predicted exhibit no red-shifted absorption features - a prediction which is clearly contradicted by the experimental results.

The second exceptional characteristic of the spectroscopic $Al•Ar_n$ cluster results was that such a prominent spectral red-shift was present with such relatively small cluster

sizes. The initial red-shift noted in the $Ba•Ar_n$ experiments was 100 cm^{-1} which occurred at $Ba•Ar_{300}$,[11] a cluster size approximately an order of magnitude larger than any studied during the $Al•Ar_n$ work. Furthermore, the less red-shifted of the doublet absorption features noted in the $Al•Ar_6$ cluster demonstrated a 300 cm^{-1} red-shift, already exceeding the 200 cm^{-1} red-shift predicted by the classical simulations of the $Al•Ar_6$ cluster.

From a theoretical perspective, the fundamental origin of the unusual spectroscopic behavior manifested in the $Al•Ar_n$ clusters was enigmatic. In all probability, the prediction from the Balling and Wright simulations that the aluminum atom lay at the surface of the cluster was correct. Such a conjecture has been recently supported by Alexander and co-workers who have employed a modified deterministic/stochastic genetic algorithm (DS-GA) approach to predict the minimum energy structures of $B•Ar_n$ clusters, another Group 13 atom solvated by multiple argon atoms.[33] The results of these calculations predicted that in the case of boron, the preferred binding site was on the surface of the cluster capping one or more of the polyhedral faces of the Ar_n cluster. The cluster face to which the boron atom was most favored to bind was determined to be that polyhedral face to which a maximal number of attractive π-type interactions with the bulk cluster would be achieved. In light of the fact that the ground state B•Ar binding energy was only approximately 40 cm^{-1} less than that for ground state Al•Ar,[13-17,34-37] coupled with the results of the Balling and Wright simulation, strong evidence suggested that surface binding of the aluminum atom to the Ar_n clusters to be the most plausible solvation structure.

In light of the presumptive surface solvation, the question remained as to the

fundamental physical origin of the unusually large red-shifted absorption in the Al•Ar_n clusters. Intuitively, one might expect that the spectroscopic behavior of an atomic species bound to the surface of a cluster might strongly resemble that of the bare aluminum atom or the diatomic Al•Ar molecule - a statement that essentially reiterates the results of the classical simulations. To uncover why this was apparently not the case, a complete characterization of the $1'_{UV} + 1_{vis}$ two-color and $2_{vis} + 1_{vis}$ single-color multiphoton ionization spectroscopy of the Al($3d$)•Ar ← Al($3p$)•Ar and Al($4p$)•Ar ← Al($3p$)•Ar electronic transitions were undertaken. The results of this study have been extensively documented in Chapter 3 of this thesis.

Two results that derived from the Al•Ar spectroscopy were potentially relevant the possible origin of the extensively red-shifted spectral feature present in the Al•Ar_n clusters. The first was the characterization of a strongly attractive $^2\Delta$ electronic state arising from the Al($3d$)•Ar electronic manifold. The experimentally observed zero-point bond dissociation energy for this state was found to be 663.5 cm^{-1}, yielding a $^2\Delta$ 0-0 vibronic level that lay approximately 541 cm^{-1} to the red of the atomic aluminum transitions near 308 nm. The second exceptional result that arose from the diatomic work was evidence for significant state mixing between the $^2\Pi(3d)$ and $^2\Pi(4p)$ electronic states - a result that was likewise observed from the $2_{vis} + 1_{vis}$ single-color multiphoton ionization spectroscopy performed on the Al•Ar_6 and Al•Ar_{12} clusters.

The current hypothesis, therefore, to rationalize the spectroscopy of the Al•Ar_n clusters is as follows. The red-shifted doublet feature most likely arises from two separate electronic interactions. The less red-shifted of the doublet absorption features presumably

derives from a δ-type interaction from the Al(3*d*) electronic state with the bulk cluster. Such an explanation is consistent with the other primary example of metal atom surface solvation on a Ar_n cluster, namely $Ba•Ar_n$, where the red-shifted feature derives from a π-type interaction from a lone *p*-electron in the excited state.[9-12]

The more red-shifted feature of the doublet absorption features is believed to originate from electronic state mixing between the $^2\Pi(3d)$ and $^2\Pi(4p)$ electronic states. A primary consequence of such an interaction is the possibility for the formation of hybrid orbitals such as those presented in Figure 5-22. For example, the upper schematic of Figure 5-22 shows a hypothetical state mixing interaction between a d_{z^2} and a p_z orbital within the aluminum moiety, and its subsequent effect on cluster binding. As a result of such a state mixing interaction, the aluminum atom can draw electron density away from the cluster surface while at the same time creating a localized partial positive charge directly adjacent to the cluster surface. Both of these effects can serve to dramatically stabilize the binding interaction of aluminum to the cluster surface, altering what was initially a van der Waals-type interaction to a significantly stronger partial ion-induced dipole interaction. In fact, one can imagine a scenario where further solvation of the aluminum atom by argon serves to systematically increase the coupling between the two mixed states - creating an almost synergistic correlation between cluster size (and hence net polarizability) and the degree of partial charge character of the hybrid orbital. While this hypothesis has no theoretical basis at present, the observation that the $2_{vis} + 1_{vis}$ single-color multiphoton ionization spectroscopy absorption feature observed in both the $Al•Ar_6$ and $Al•Ar_{12}$ clusters closely correlated to the more red-shifted of the doublet features

tends to support such a hypothetical picture.

In an attempt to provide definitive proof of the importance of state mixing interactions, new theoretical calculations based on the spectral theory developed by Peter Langhoff are presently being pursued by Jeff Sheehy and Jerry Boatz in collaboration with Peter Langhoff.[38] Unlike the Balling and Wright model, spectral theory can explicitly account for electronic state mixing effects by the inclusion of the transition dipole moments to the upper state mixed adiabatic potentials. The results of these new calculations will be quite useful in trying to definitively support the postulate that state mixing effects can have a dramatic effect on the spectroscopy of metal atoms bound at interfacial regions.

5.5. Conclusion

The results of the $1'_{UV} + 1_{vis}$ two-color and $2_{vis} + 1_{vis}$ single-color multiphoton ionization spectra on $Al{\bullet}Ar_n$ clusters ($n \leq 60$) present an interesting dilemma presently unaccounted for in simple solvation models. The possibility that state mixing effects may underlie the dramatic deviation from the expected spectral behavior observed in the $Al{\bullet}Ar_n$ clusters ($n \leq 60$) is quite novel, potentially revealing a hitherto unforeseen facet of the intricacies present within solute-solvent interactions.

5.6. References

1. N. Schwentner, E. E. Koch, and J. Jortner, *Electronic Excitations in Condensed Rare Gases* (Springer-Verlag, Berlin, 1985), and references therein.
2. *A Bibliography of Matrix Isolation Spectroscopy 1954-1985*, D. W. Ball, Z. H. Kafafi, L. Fredin, R. H. Hauge, and J. L. Margrave, Eds. (Rice University, Houston, 1988).
3. W. H. Breckenridge, C. Jouvet, and B. Soep, in *Advances in Metal and Semiconductor Clusters*, M. A. Duncan, Ed. (JAI Press, Greenwich, 1995), and references therein.
4. M. Chergui, C. Crépin, T. Hebert, and A. Tramer, *Chem. Phys. Lett.*, **197**, 476 (1992).
5. C. Crépin and A. Tramer, *J. Chem. Phys.*, **97**, 4772 (1992).
6. M. Okunishi, K. Yamanouchi, and S. Tsuchiya, *J. Chem. Phys.*, **97**, 2305 (1992).
7. R. D. van Zee, S. C. Blankespoor, T. S. Zwier, *Chem. Phys. Lett.*, **158**, 306 (1989).
8. S. Martrenchard-Barra, C. Dedonder-Lardeaux, C. Jouvet, and D. Solgadi, *J. Chem. Phys.*, **98**, 528 (1993).
9. J. P. Visticot, J. Berlande, J. Cuvellier, A. Lallement, J. M. Mestagh, P. Maynadier, P. de Pujo, and O. Sublemontier, *Chem. Phys. Lett.*, **191**, 107 (1992).
10. P. de Pujo, J. M. Mestagh, J. P. Visticot, J. Cuvellier, P. Maynadier, O. Sublemontier, A. Lallement, and J. Berlande, *Z. Phys. D.*, **25**, 357 (1993).
11. J. P. Visticott, P. de Pujo, J. M. Mestdagh, A. Lallement, J. Berlande, O. Sublemontier, P. Meynadier and J. Cuvellier, *J. Chem. Phys.*, **100**, 158 (1994).
12. A. I. Krylov, R. B. Gerber, M. A. Gaveau, J. M. Mestdagh, B. Schilling, and J. P. Visticot, *J. Chem. Phys.*, **104**, 3651 (1996).
13. S. A. Heidecke, Z. Fu, J. R. Colt, and M. D. Morse, *J. Chem. Phys.*, **97**, 1692 (1992).
14. J. M. Gardner and M. I. Lester, *Chem. Phys. Lett.*, **137**, 301 (1987).

15. C. L. Callender, S. A. Mitchell, and P. A. Hackett, *J. Chem. Phys.*, **90**, 5252 (1989).
16. M. J. McQuaid, J. L. Gole, and M. C. Heaven, *J. Chem. Phys.*, **92**, 2733 (1990).
17. H. Partridge, C. W. Bauschlicher, Jr., and L. Visscher, *Chem. Phys. Lett.*, **246**, 33 (1995).
18. J. Barker, in Rare Gas Solids, M. Klein and J. Venables, Eds. (Academic Press, New York, 1976).
19. H. Abe and D. M. Kolb, *Ber. Bunsenges. Phys. Chem.* **87**, 523 (1983).
20. J. H. Ammeter and D. C. Schlosnagle, *J. Chem. Phys.*, **59**, 4784 (1973).
21. R. Grinter and R. J. Singer, *Chem. Phys.* **113**, 87 (1987).
22. S. Bashkin and J. O. Stoner, Jr., *Atomic Energy Levels and Grotrian Diagrams, Vol. I. Hydrogen I - Phosphorus XV* (North-Holland Pub. Co., Amsterdam, 1975).
23. K. E. Schriver, M. Y. Hahn, J. L. Persson, M. E. LaVilla, and R. L. Whetten, *J. Phys. Chem.*, **93**, 2869 (1989).
24. R. L. Whetten. K. E. Schriver, J. L. Persson, and M. Y. Hahn, *J. Chem. Soc. Farad. Trans.*, **86**, 2375 (1990).
25. X. Li., M. Y. Hahn, M. S. El-Shall, and R. L. Whetten, *J. Phys. Chem.* **95**, 8524 (1991).
26. W. C. Wiley and I. H. McLaren, *Rev. Sci. Instrum.*, **26**, 1150 (1955).
27. A. C. Mackay, *Acta Crystallogr.*, **15**, 916 (1962).
28. J. C. Phillips, *Chem. Rev.*, **86**, 619 (1986).
29. J. A. Boatz, J. A. Sheehy, and P. W. Langhoff, in *Monte Carlo Simulations of the Structures and the Optical Absorption Spectra of Al/Ar$_N$ Clusters: Applications of the Spectral Theory of Chemical Binding, Proceedings of the High Energy Density (HEDM) Conference*, June 1997 (USAF Office of Scientific Research, Bolling AFB, DC, 1997).
30. L. C. Balling and J. J. Wright, *J. Chem. Phys.*, **79**, 2941 (1983).
31. L. C. Balling and J. J. Wright, *J. Chem. Phys.*, **81**, 675 (1984).
32. J. A. Boatz, personal communication.
33. S. K. Gregurick, M. H. Alexander, and Bernd Hartke, *J. Chem. Phys.*, **104**, 2684 (1996).

34. E. Hwang, Y. L. Huang, P. J. Dagdigian, and M. H. Alexander, *J. Chem. Phys.*, **98**, 8484 (1993).

35. E. Hwang, P. J. Dagdigian, and M. H. Alexander, *Can. J. Chem.*, **72**, 821 (1994).

36. E. Hwang and P. J. Dagdigian, *Chem. Phys. Lett.*, **233**, 483 (1995).

37. M. H. Alexander, A. R. Walton, M. Yang, X. Yang, E. Hwang, and P. J. Dagdigian, *J. Chem. Phys.*, **106**, 6320 (1997).

38. P. W. Langhoff, *J. Phys. Chem.*, **100**, 2974 (1996).

5.7. Figure Captions

Figure 5-1 Schematic showing the $1'_{UV} + 1_{vis}$ multiphoton ionization (MPI) methodology used for most of the experimental work presented in Chapter 5. Also depicted are the possible points at which cluster fragmentation could occur during the laser excitation/ionization process. For the $2_{vis} + 1_{vis}$ MPI scheme discussed in Section 5.3.1.5., the initial UV excitation was replaced with a two-photon pump of equal total energy to the original UV single-photon pump.

Figure 5-2 $1'_{UV} + 1_{vis}$ multiphoton ionization (MPI) spectrum of Al•Ar_3 taken about the Al($3d$) ← Al($3p$) atomic transitions.

Figure 5-3 $1'_{UV} + 1_{vis}$ multiphoton ionization (MPI) spectrum of Al•Ar_5 taken about the Al($3d$) ← Al($3p$) atomic transitions.

Figure 5-4 $1'_{UV} + 1_{vis}$ multiphoton ionization (MPI) spectrum of Al•Ar_6 taken about the Al($3d$) ← Al($3p$) atomic transitions.

Figure 5-5 $1'_{UV} + 1_{vis}$ multiphoton ionization (MPI) spectrum of Al•Ar_7 taken about the Al($3d$) ← Al($3p$) atomic transitions.

Figure 5-6 $1'_{UV} + 1_{vis}$ multiphoton ionization (MPI) spectrum of Al•Ar_{12} taken about the Al($3d$) ← Al($3p$) atomic transitions.

Figure 5-7 $1'_{UV} + 1_{vis}$ multiphoton ionization (MPI) spectrum of Al•Ar_{18} taken about the Al($3d$) ← Al($3p$) atomic transitions.

Figure 5-8 $1'_{UV} + 1_{vis}$ multiphoton ionization (MPI) spectrum of Al•Ar_{25} taken about the Al($3d$) ← Al($3p$) atomic transitions.

Figure 5-9 $1'_{UV} + 1_{vis}$ multiphoton ionization (MPI) spectrum of Al•Ar_{34} taken about the Al($3d$) ← Al($3p$) atomic transitions.

Figure 5-10 $1'_{UV} + 1_{vis}$ multiphoton ionization (MPI) spectrum of Al•Ar_{40} taken about the Al($3d$) ← Al($3p$) atomic transitions.

Figure 5-11 $1'_{UV} + 1_{vis}$ multiphoton ionization (MPI) spectrum of $Al{\bullet}Ar_{47}$ taken about the Al($3d$) ← Al($3p$) atomic transitions.

Figure 5-12 $1'_{UV} + 1_{vis}$ multiphoton ionization (MPI) spectrum of $Al{\bullet}Ar_{54}$ taken about the Al($3d$) ← Al($3p$) atomic transitions.

Figure 5-13 Comparison of the UV absorption spectra obtained for the $Al{\bullet}Ar_3$, $Al{\bullet}Ar_5$, and $Al{\bullet}Ar_6$ clusters taken about the Al($3d$) ← Al($3p$) atomic transitions.

Figure 5-14 Comparison of the UV absorption spectra obtained for the $Al{\bullet}Ar_6$, $Al{\bullet}Ar_7$, and $Al{\bullet}Ar_{12}$ clusters taken about the Al($3d$) ← Al($3p$) atomic transitions. The $Al{\bullet}Ar_{12}$ cluster size represents the closing of the first icosahedral solvation shell.

Figure 5-15 Comparison of the UV absorption spectra obtained for the $Al{\bullet}Ar_{12}$, $Al{\bullet}Ar_{18}$, $Al{\bullet}Ar_{25}$, $Al{\bullet}Ar_{34}$, and $Al{\bullet}Ar_{47}$ clusters taken about the Al($3d$) ← Al($3p$) atomic transitions. The cluster sizes are representative of increasing degrees of solvation within the second icosahedral solvation shell.

Figure 5-16 The UV absorption spectrum obtained for the $Al{\bullet}Ar_{54}$ cluster representing the completion of the second icosahedral solvation shell. The UV absorption spectrum of the $Al{\bullet}Ar_{54}$ cluster is directly compared to that obtained for the $Al{\bullet}Ar_6$ and $Al{\bullet}Ar_{12}$ cluster sizes (top) as well as the bulk matrix spectrum (bottom).

Figure 5-17 $2_{vis} + 1_{vis}$ single-color multiphoton ionization (MPI) spectrum of $Al{\bullet}Ar_6$ and $Al{\bullet}Ar_6$ taken to the red of the Al($3d$) ← Al($3p$) atomic transitions.

Figure 5-18 Comparison of the $2_{vis} + 1_{vis}$ single-color spectra collected to the red of the Al($3d$) ← Al($3p$) atomic transitions with the UV absorption spectra obtained using $1'_{UV} + 1_{vis}$ two-color excitation. (a) $Al{\bullet}Ar_6$. (b) $Al{\bullet}Ar_{12}$.

Figure 5-19 Balling and Wright calculated minimum energy structures for the $Al{\bullet}Ar_6$ and $Al{\bullet}Ar_{12}$ clusters generated by classical Monte Carlo simulations performed by Jeff Sheehy and Jerry Boatz.[29]

Figure 5-20 Balling and Wright calculated minimum energy structures for the $Al{\bullet}Ar_{54}$ cluster generated by classical Monte Carlo simulations performed by Jeff Sheehy and Jerry Boatz.[29]

Figure 5-21 Predicted UV absorption spectra for the $Al{\bullet}Ar_6$, $Al{\bullet}Ar_{12}$, and $Al{\bullet}Ar_{54}$ cluster sizes using the Balling and Wright model.[29]

Figure 5-22 Schematic showing how electronic state mixing between the Al(3*d*) and Al(4*p*) atomic states can influence the nature of the electronic interaction between a surface-solvated aluminum atom and a rare gas cluster. The top figure shows the hybrid orbital that results from a state mixing interaction between a d_z^2 and a p_z atomic orbital. The result of this state mixing interaction is to draw electron density on the aluminum atom away from the cluster surface while creating a localized partial positive charge adjacent to the cluster. The bottom figure shows a schematic of analogous hybrid orbitals derived from state mixing interactions between d_{xz}, d_{yz} with p_x, p_y atomic orbital configurations.

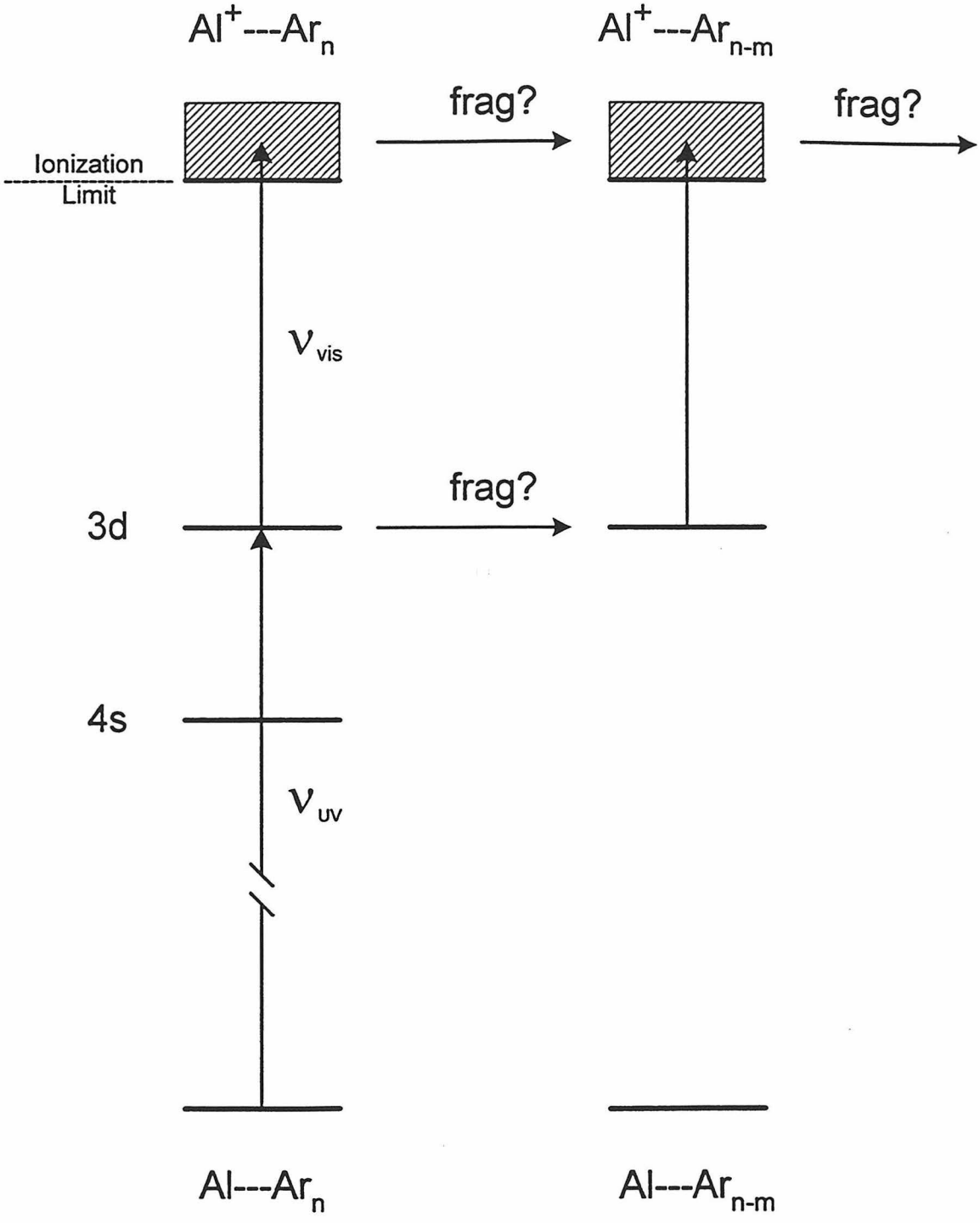

Al+---Arn
Al+---Arn-m
frag?
frag?
Ionization
Limit
νvis
frag?
3d
4s
νuv
Al---Arn
Al---Arn-m

Figure 5-1

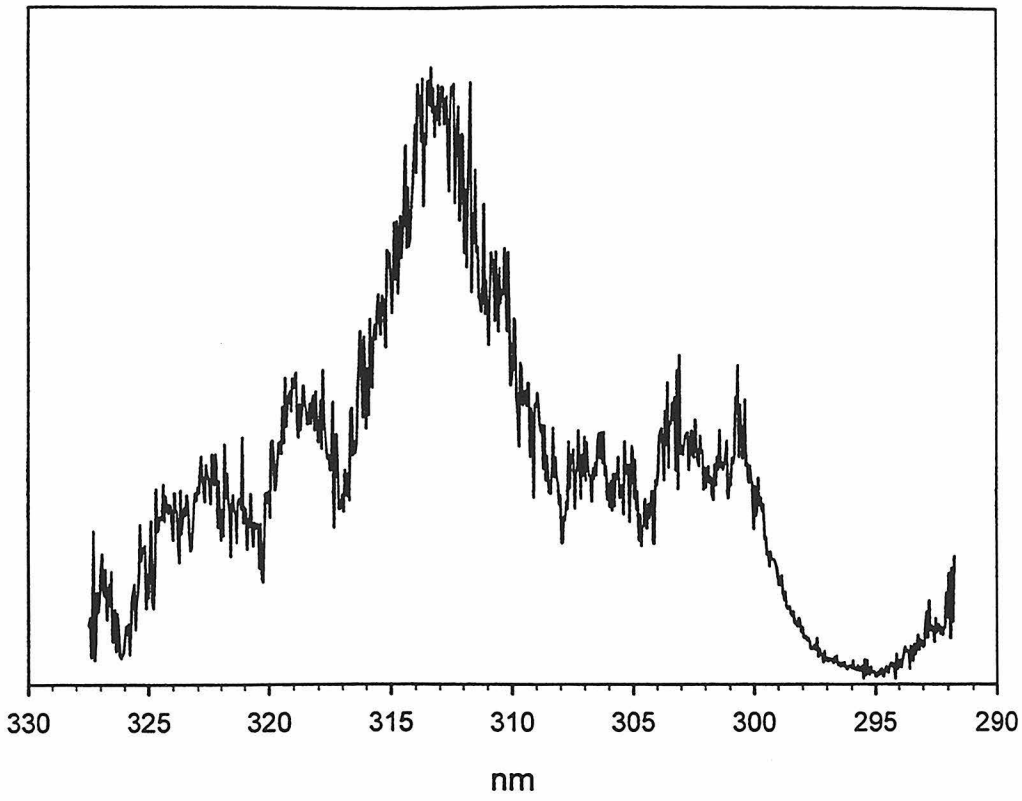


Figure 5-2

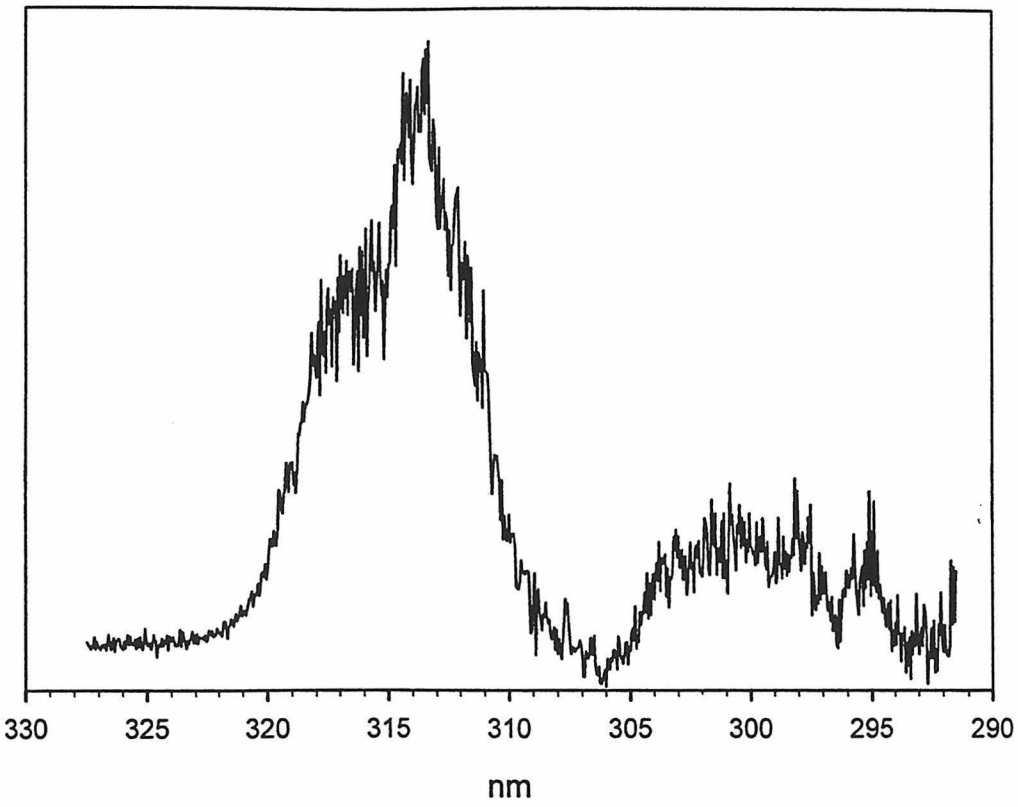


Figure 5-3

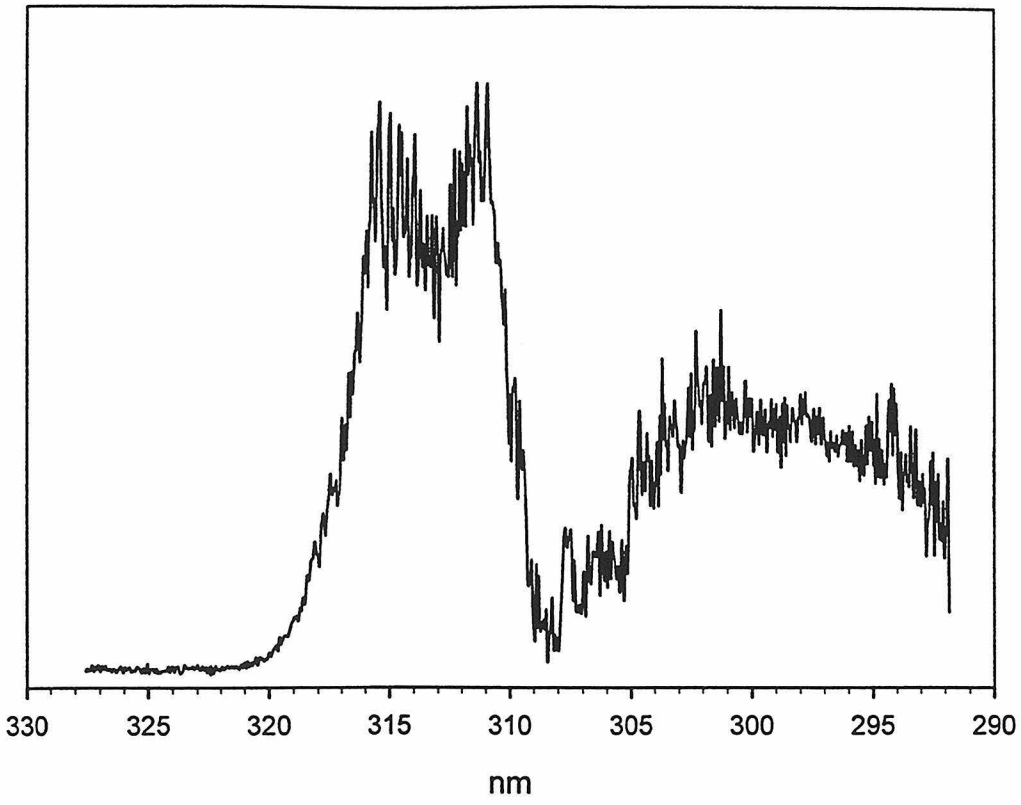


Figure 5-4

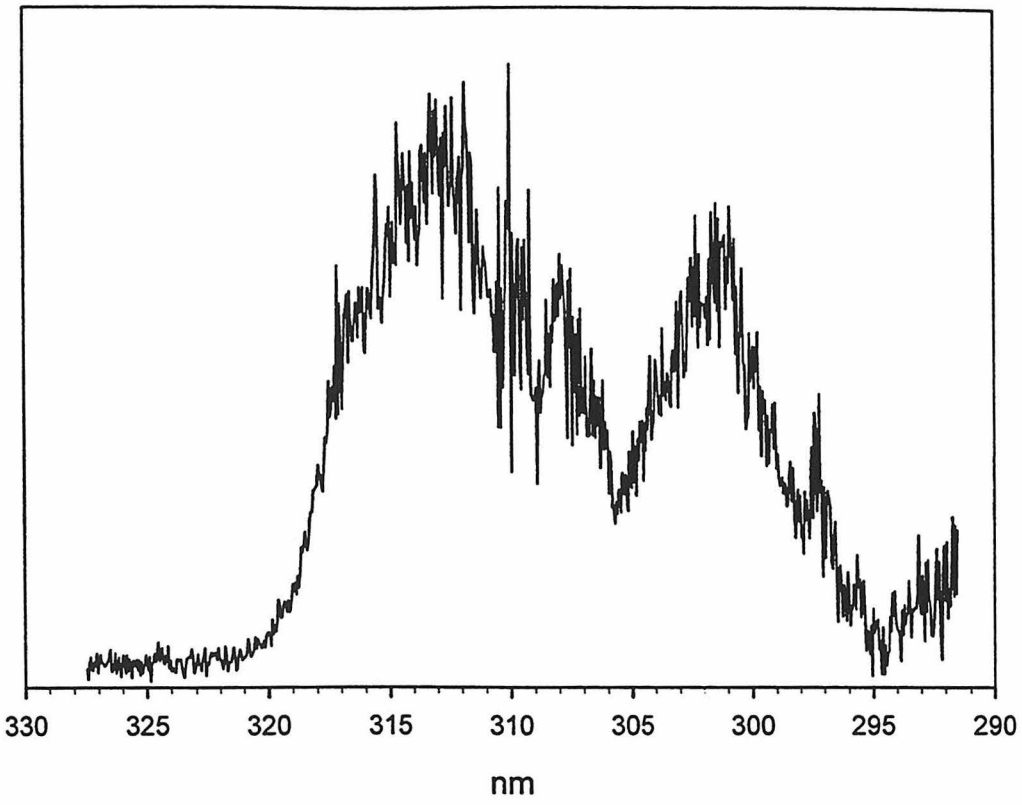


Figure 5-5

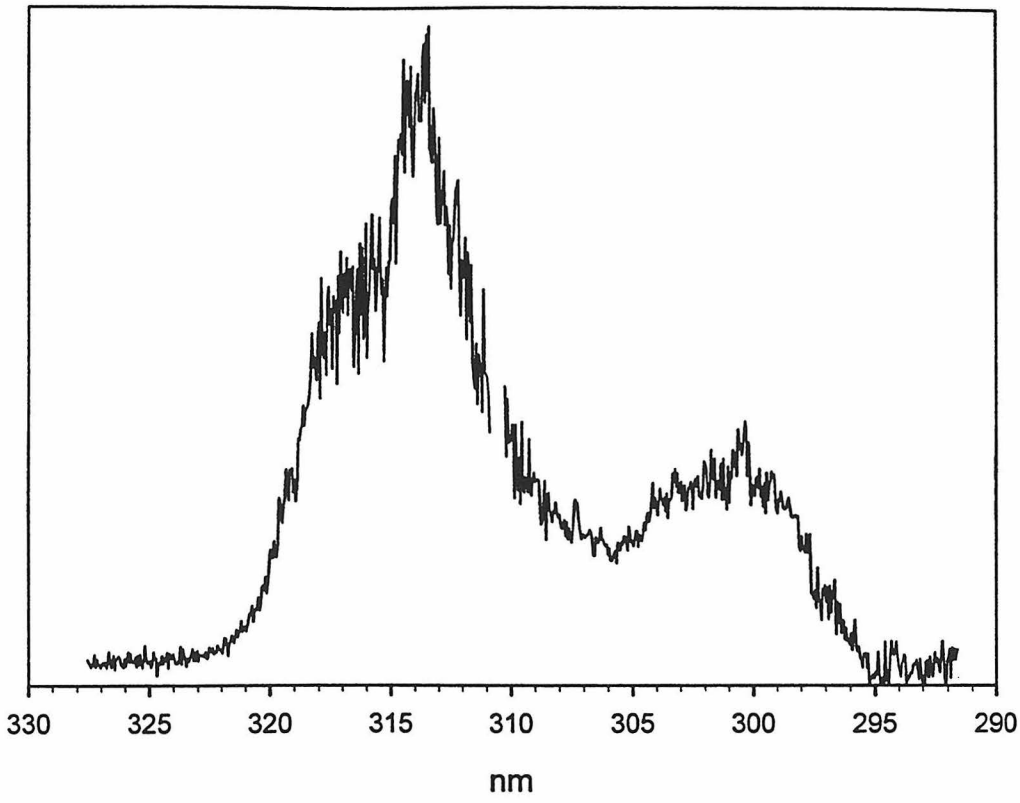


Figure 5-6

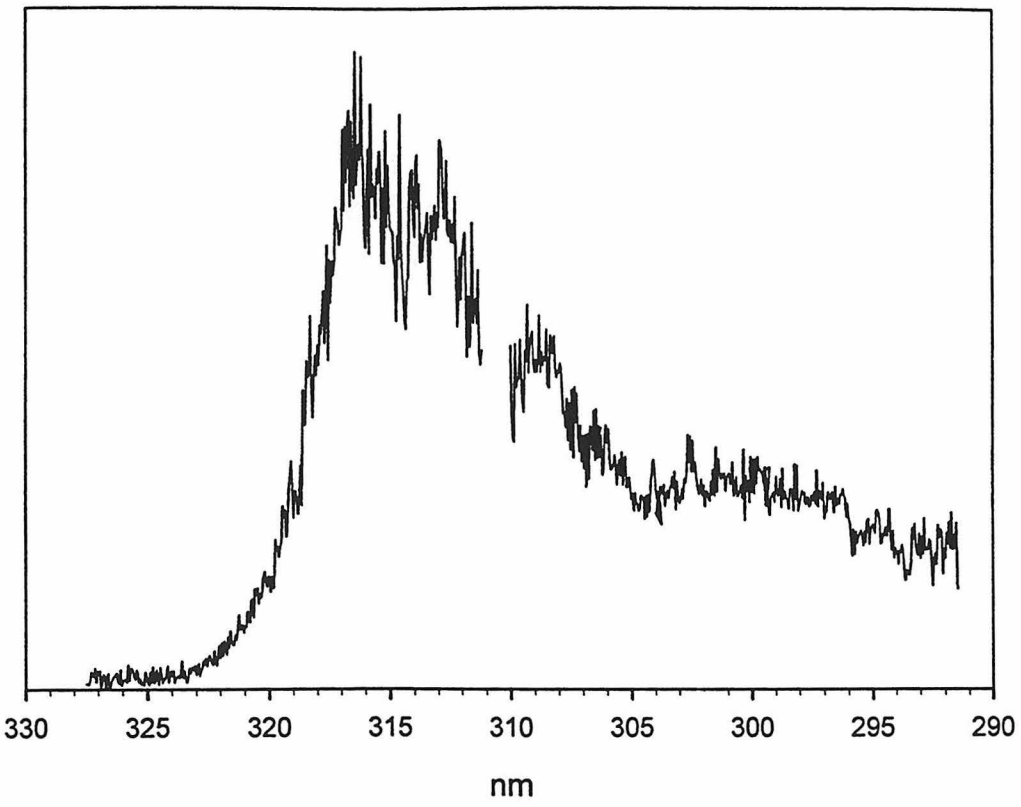


Figure 5-7

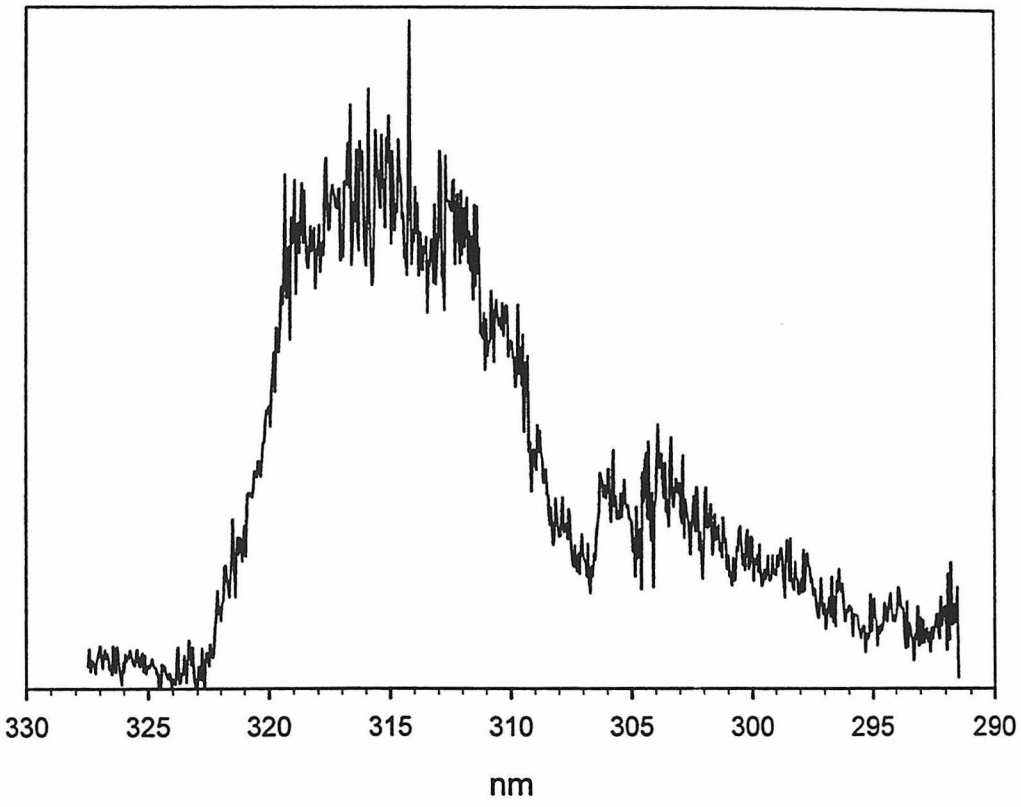


Figure 5-8

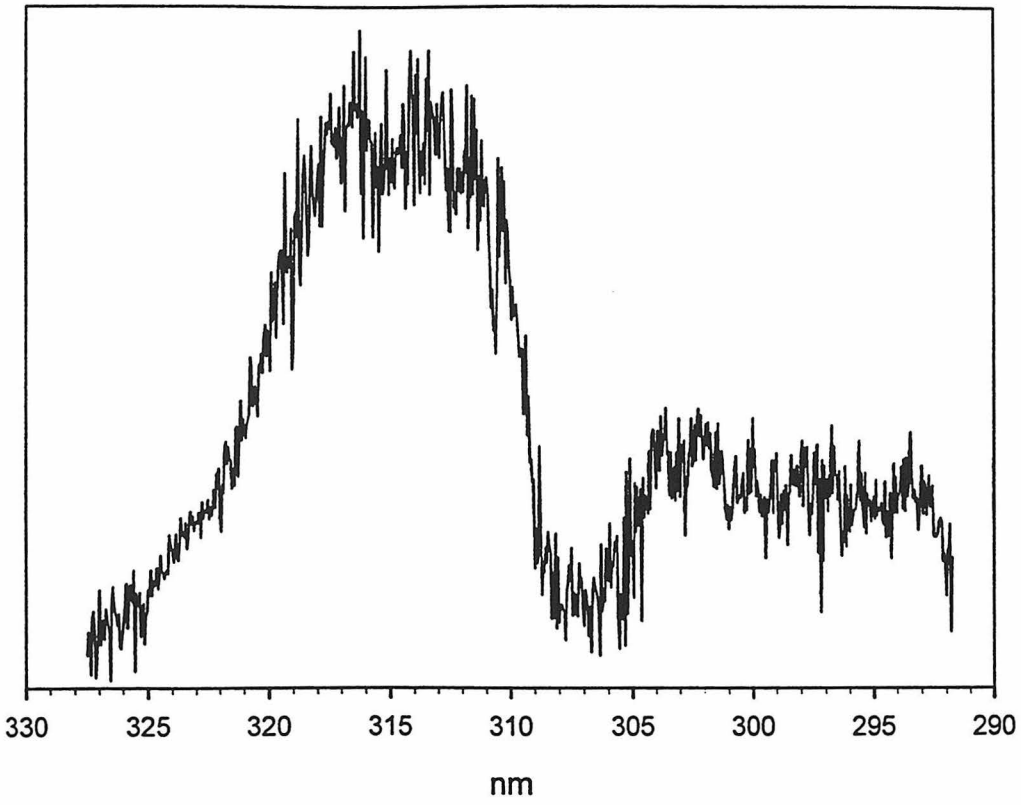


Figure 5-9

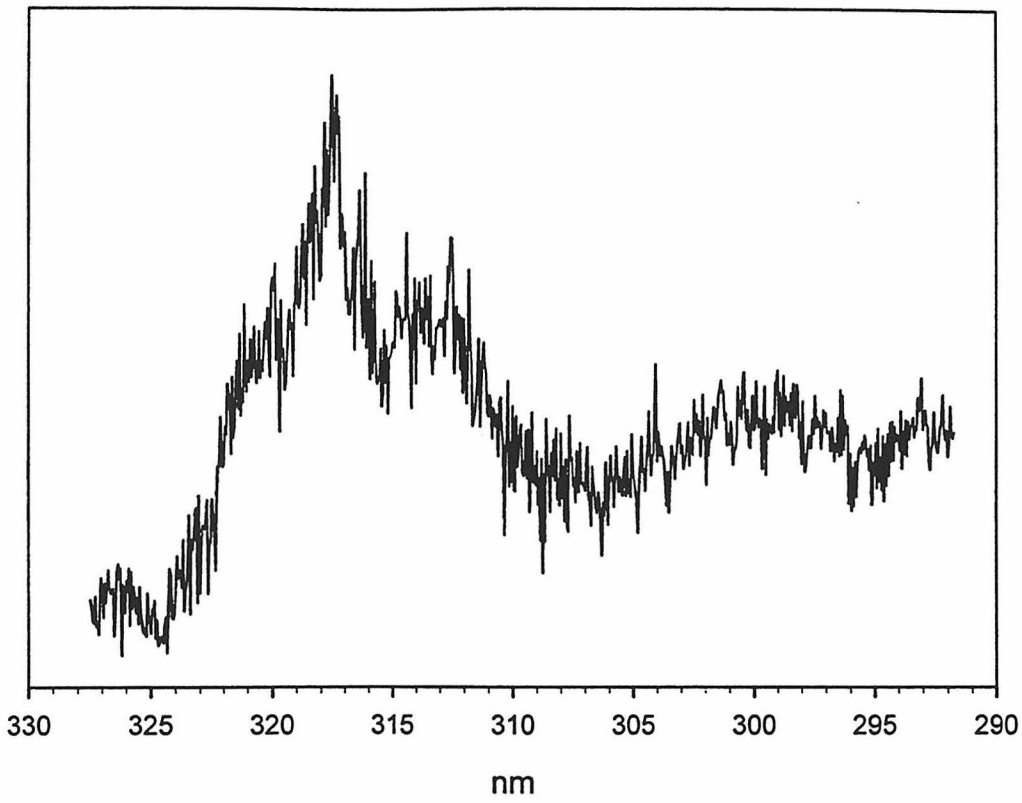


Figure 5-10

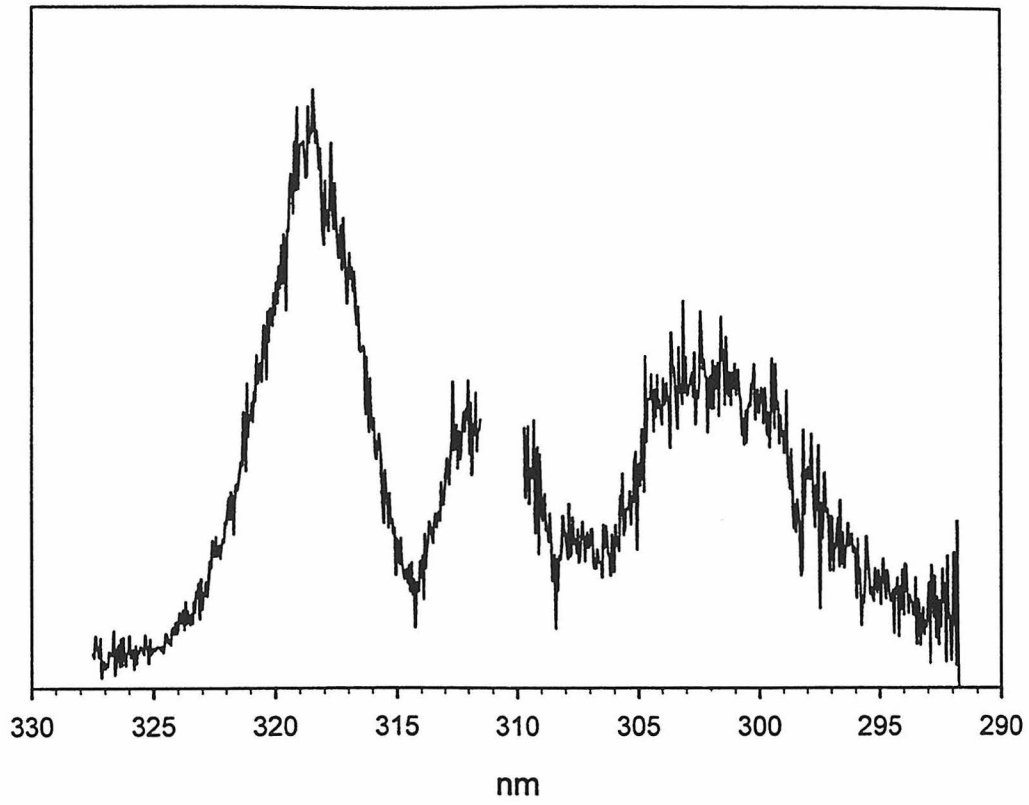


Figure 5-11

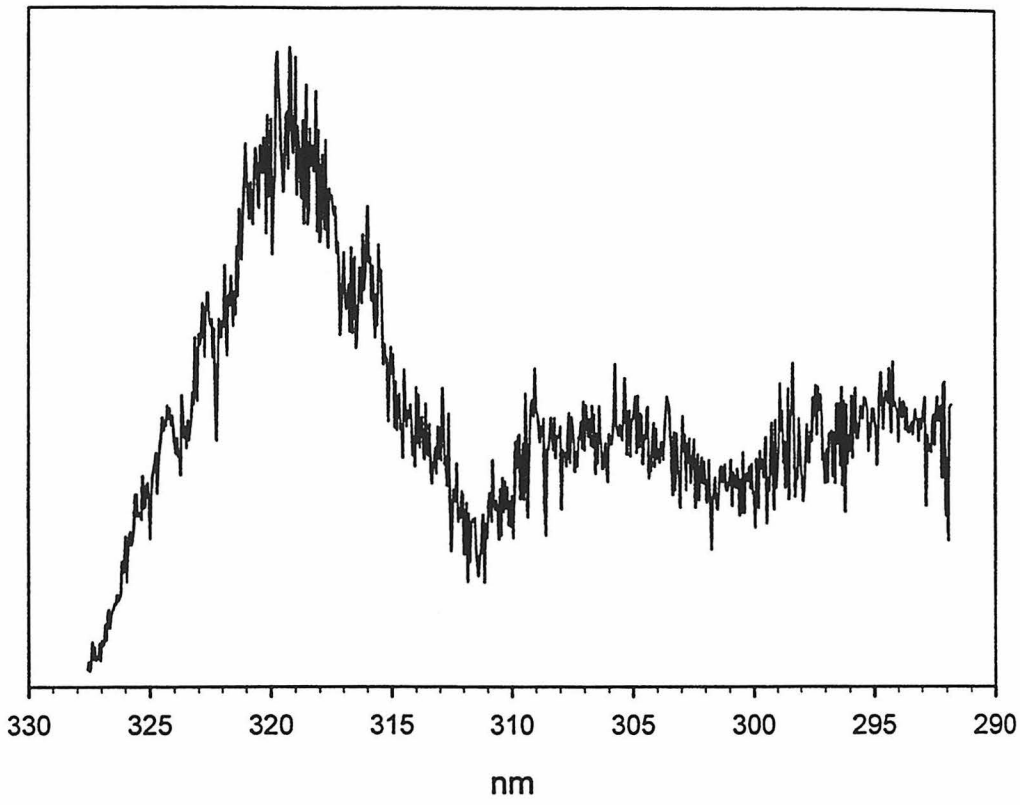


Figure 5-12

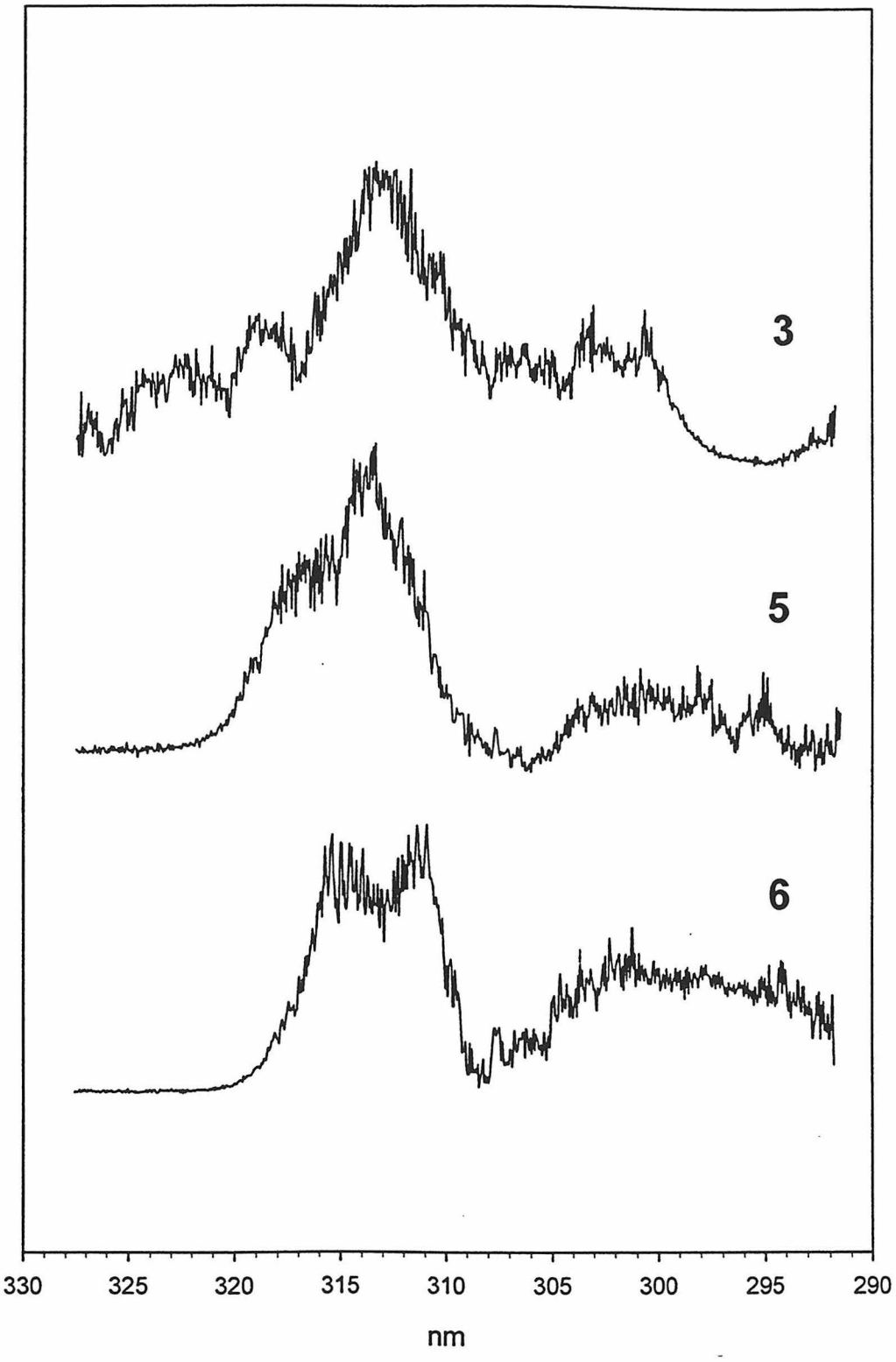


Figure 5-13

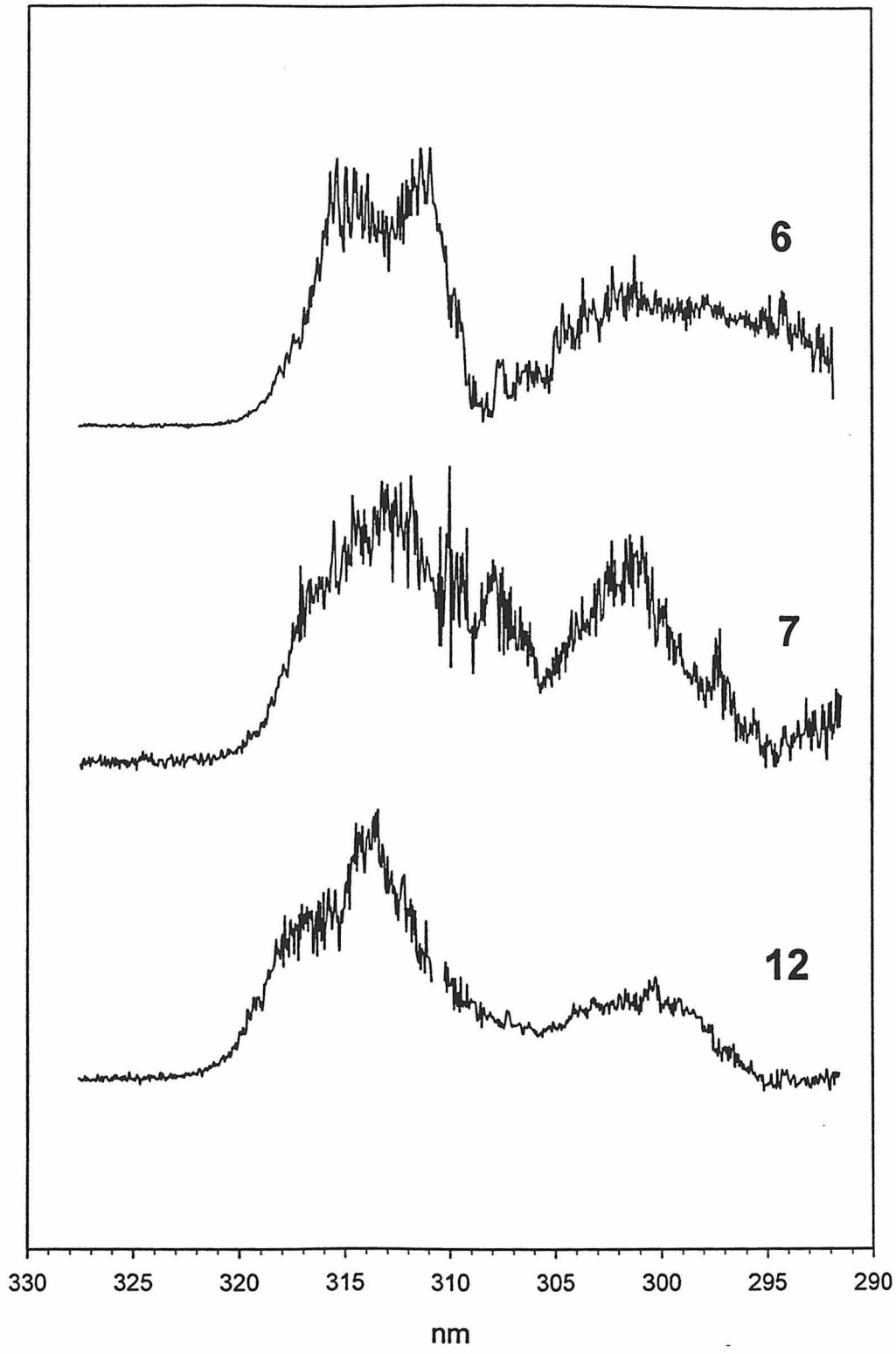


Figure 5-14

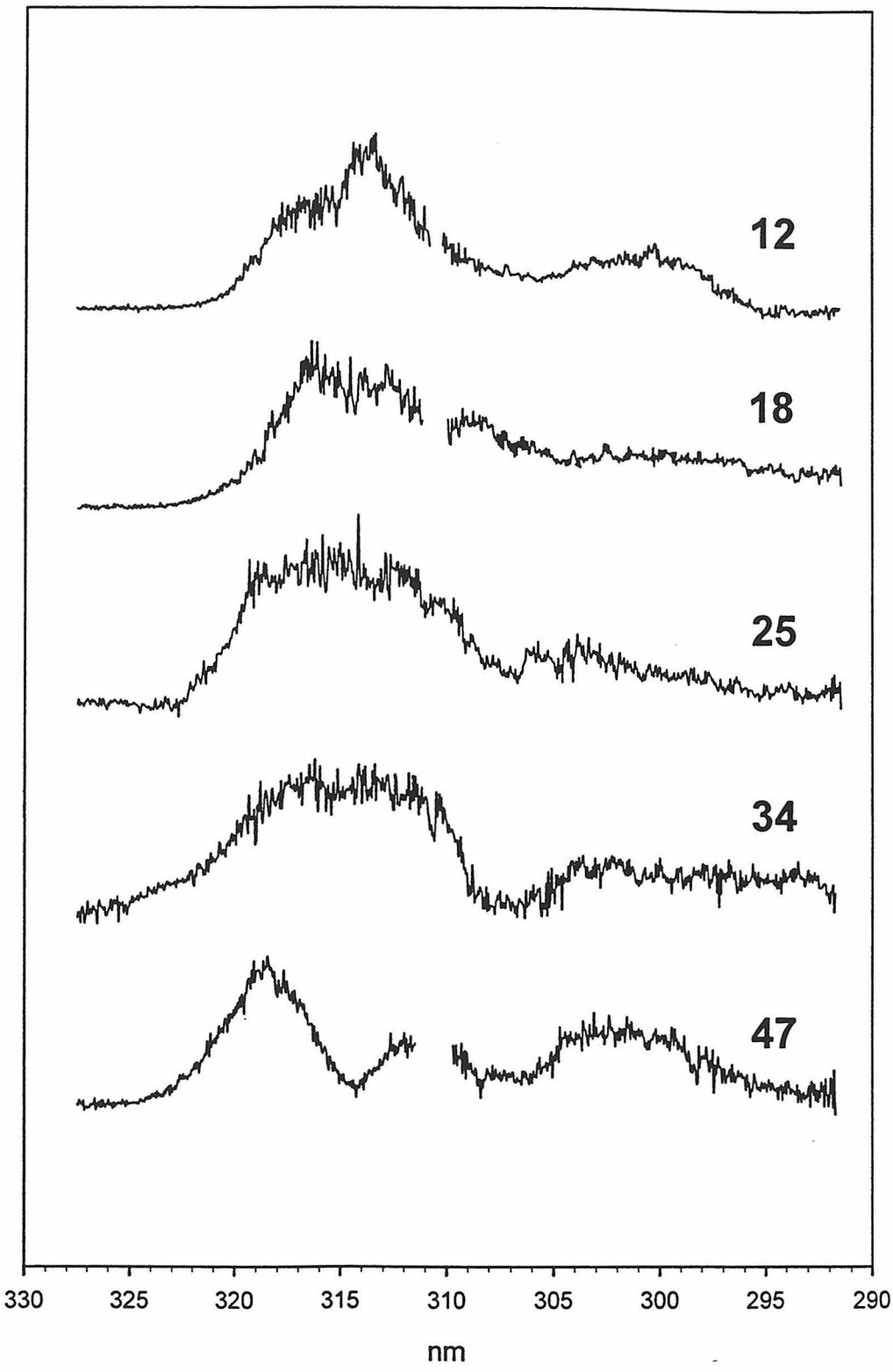
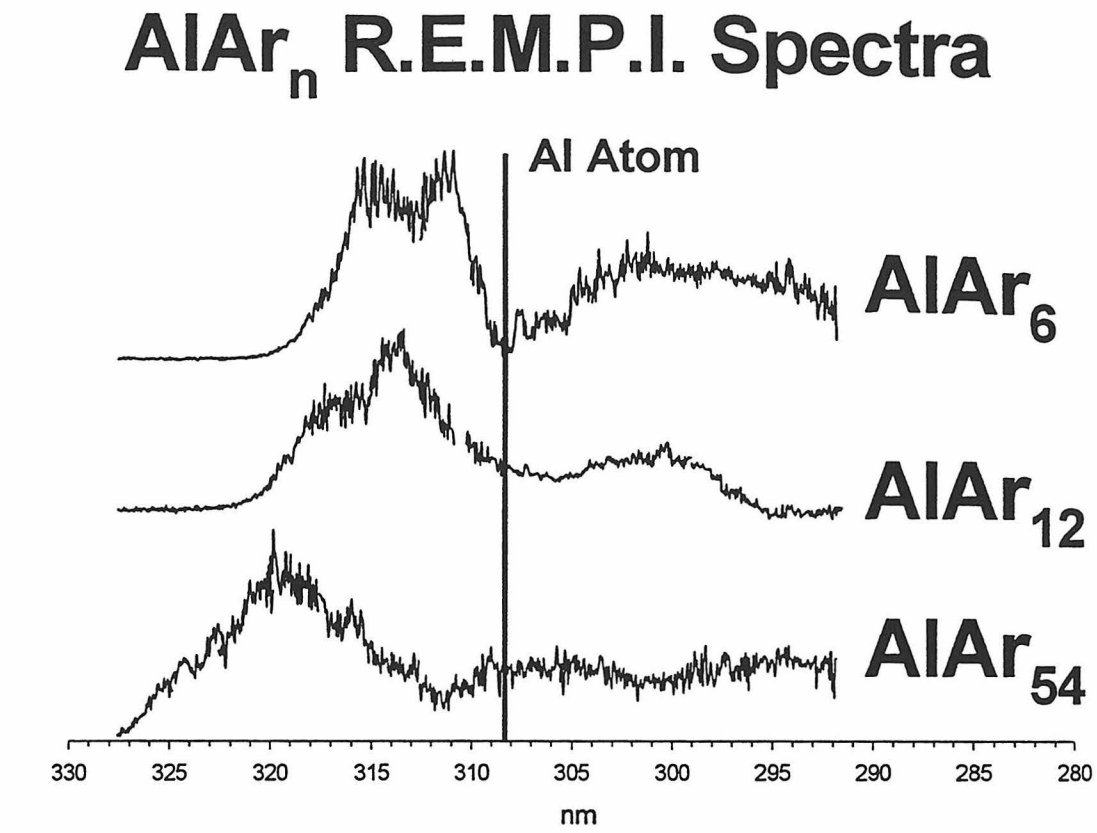
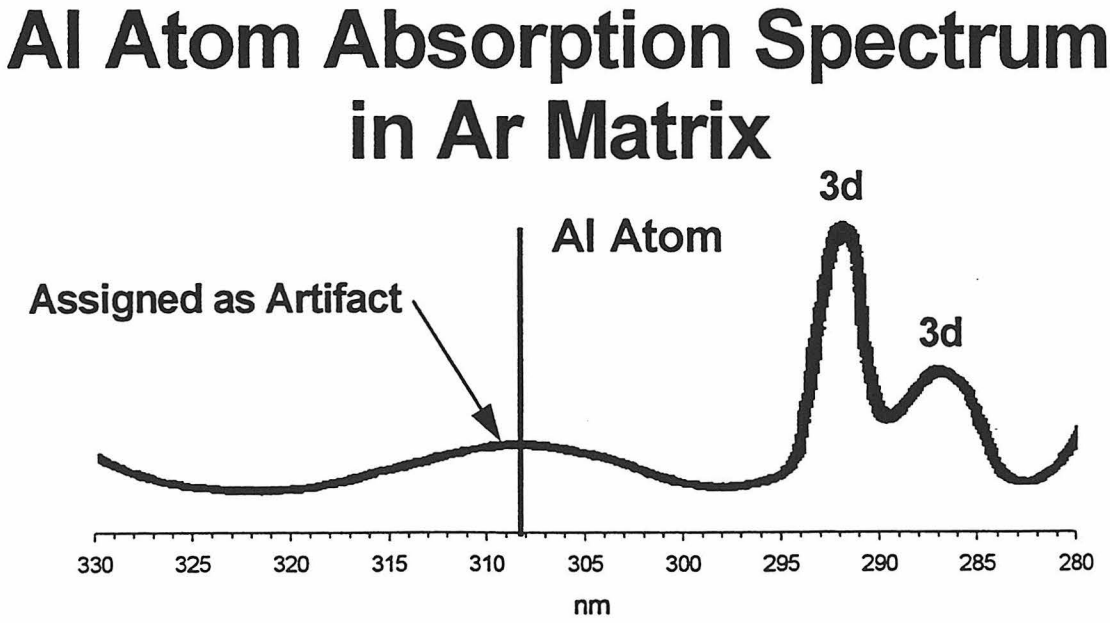


Figure 5-15





Abe and Kolb, *Ber. Bunsenges Phys. Chem.* **87**, 523-527 (1983).

Figure 5-16

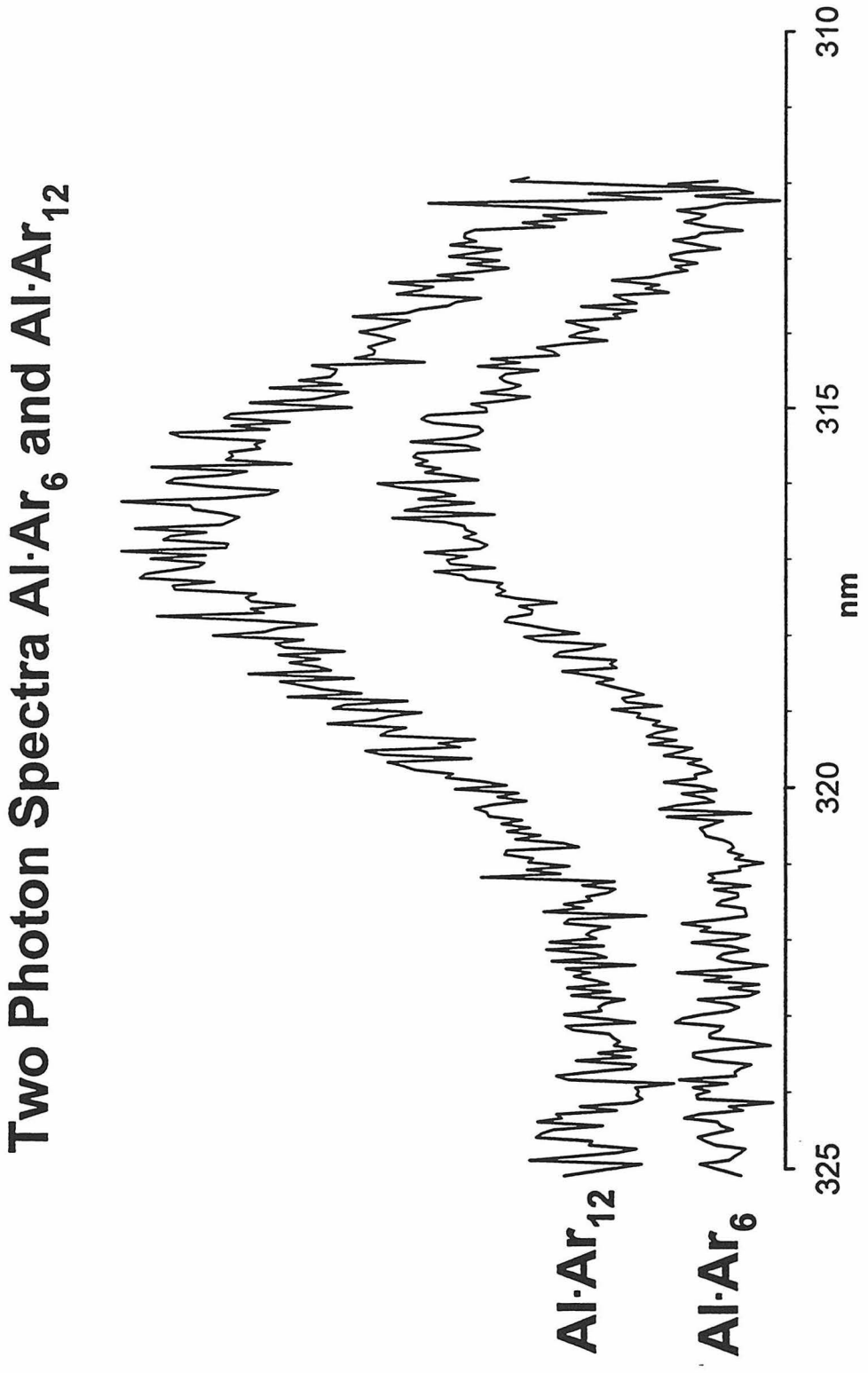
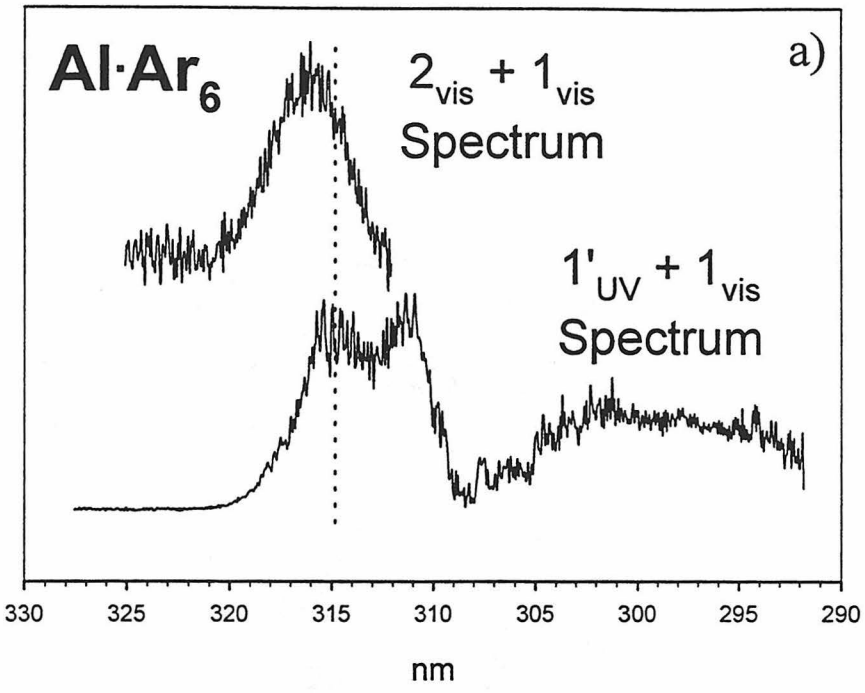
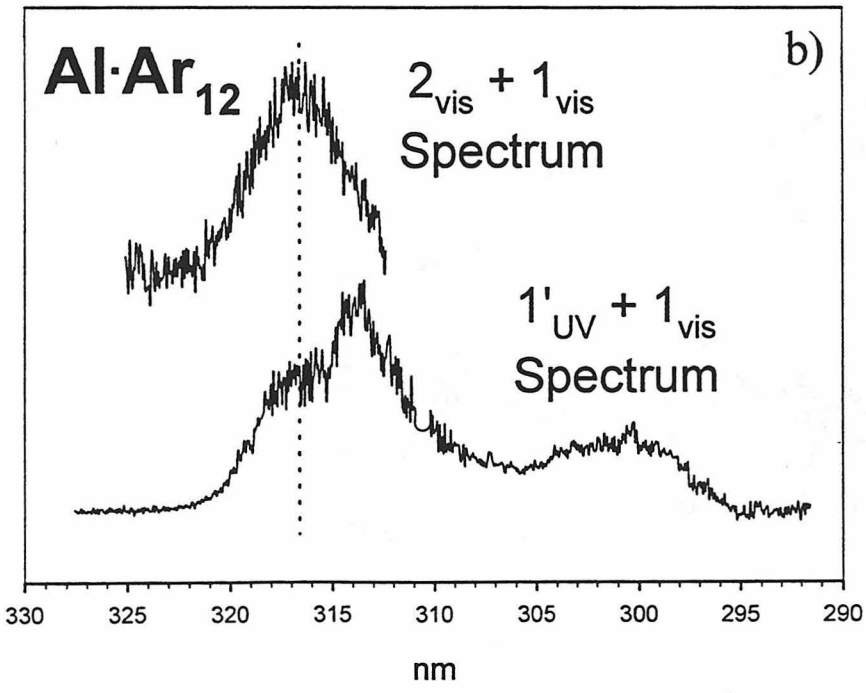

Two Photon Spectra Al·Ar6 and Al·Ar12
Al·Ar12
Al·Ar6
325
320
315
310
nm

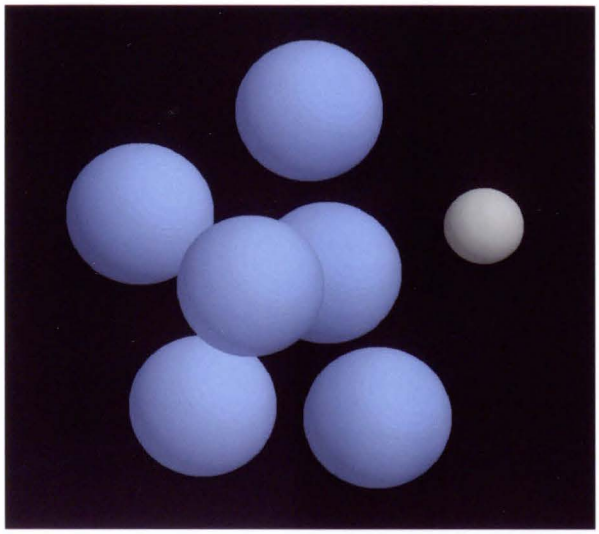
Figure 5-17





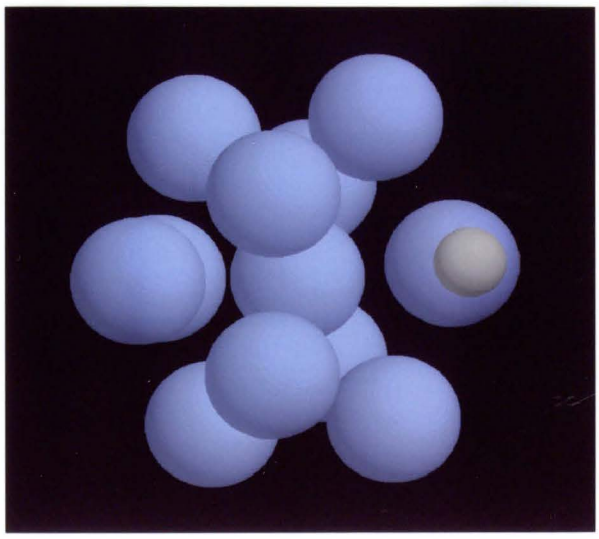
Figures 5-18a and 5-18b

Balling and Wright Calculated Minimum Energy Structures



$Al{\cdot}Ar_6$

$Al{\cdot}Ar_{12}$

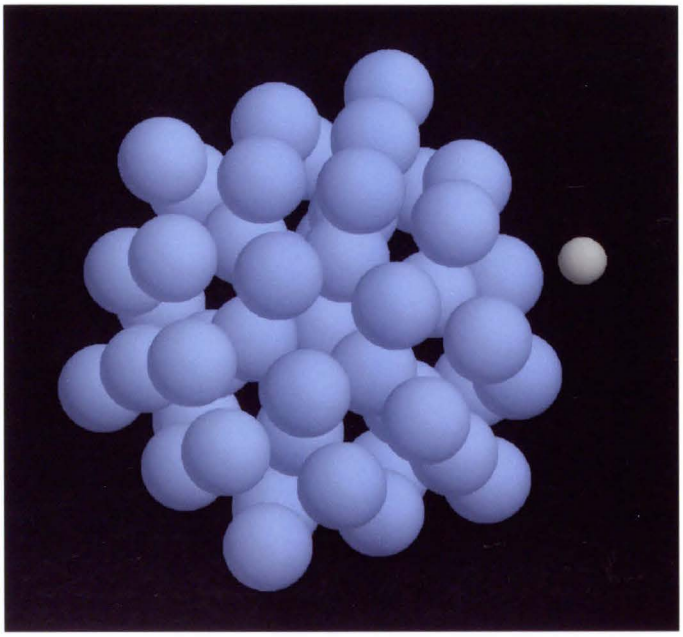


Potential: Jeff Sheehy

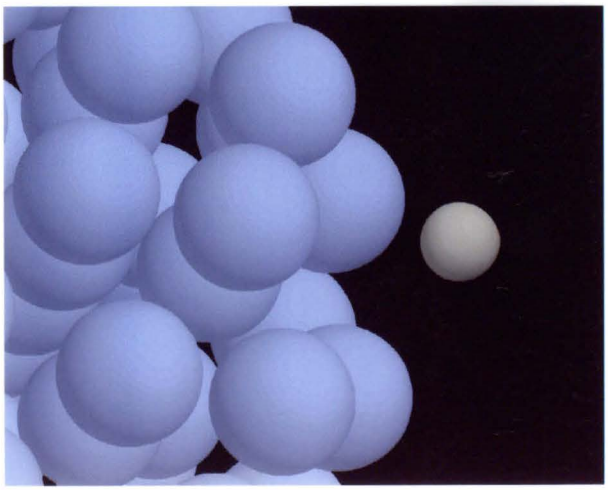
Simulations: Jerry Boatz

Figure 5-19

Balling and Wright Calculated Minimum Energy Structure



$Al{\cdot}Ar_{54}$



Potential: Jeff Sheehy

Simulations: Jerry Boatz

Figure 5-20

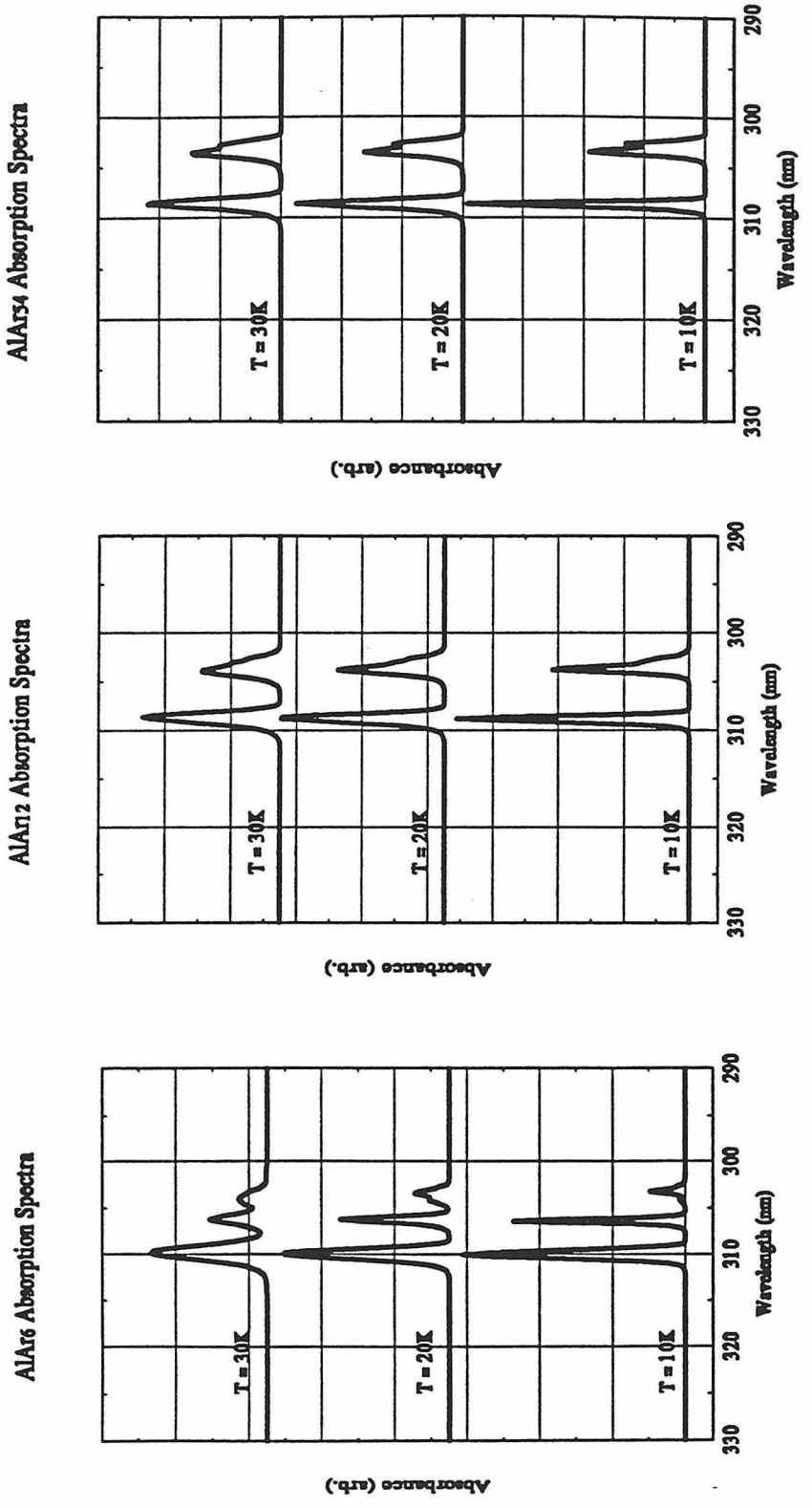
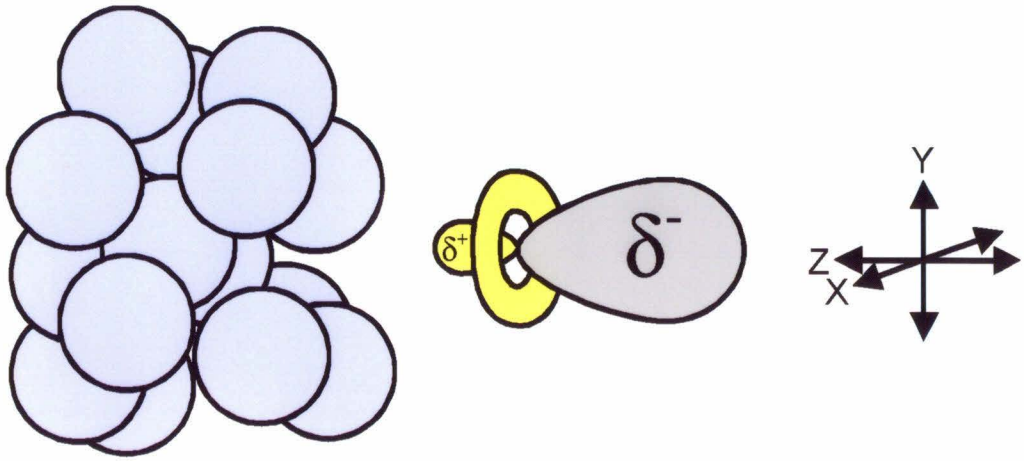

AlAr34 Absorption Spectra
T = 30K
T = 20K
T = 10K
Absorbance (arb.)
Wavelength (nm)
290
300
310
320
330
AlAr12 Absorption Spectra
T = 30K
T = 20K
T = 10K
Absorbance (arb.)
Wavelength (nm)
290
300
310
320
330
AlAr6 Absorption Spectra
T = 30K
T = 20K
T = 10K
Absorbance (arb.)
Wavelength (nm)
290
300
310
320
330

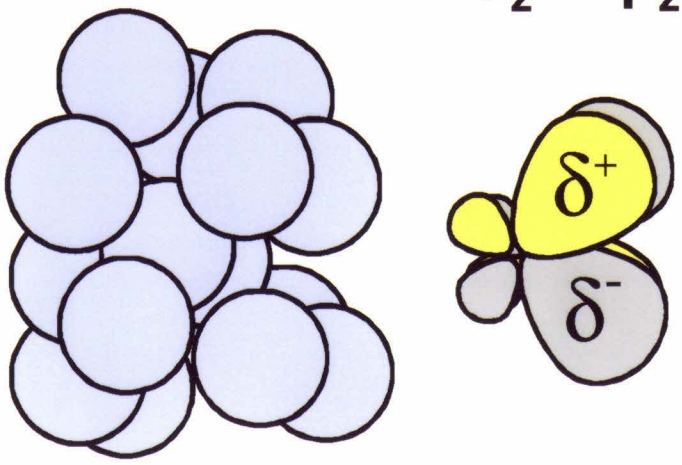
Figure 5-21

3d/4p State Mixing



σ-Type Hybrid Orbital

$d_{z^2} + p_z$



Note: Two Hybrid Orbitals Shown

π-Type Hybrid Orbital

$(d_{xz} ; d_{yz}) + (p_x ; p_y)$

Figure 5-22

CHAPTER 6

Design of a Disk Target Laser Vaporization Source for the Production of van der Waals Complexes between Alkali Metal Atoms and Polyatomic Solvents

6.1. Introduction

Alkali metal ions are central to the maintenance of the homeostatic state throughout the wide spectrum of living organisms from the simplest single-celled entity to human beings. At the most fundamental level, life itself depends upon a proper electrolytic balance to control both osmotic pressure within cells as well as electrostatic gradients across cell membranes - a role for which sodium and potassium ions are unequivocally required.[1-2] Furthermore, the evolutionary process has conferred upon many different phyla the ability to rapidly transmit electrical signals over great distances.[1] Such adaptations, which ultimately underlie the fundamental cognitive functioning of human beings, derive primarily from the acquisition of the ability to control the flux of small metal ions, and in particular the sodium ion, across the outer cell membrane.

The ubiquity of alkali metal ions within living systems suggests that their interactions with the constitutive proteins that compose a cell may possibly exert some influence upon function. In particular, acidic side-chains from amino acid residues can potentially form strong ionic bonds with the solvated metal ions that surround a given protein. Rather than serving merely as a cationic counterions for these acidic residues, however, the possibility exists that these metal ions could serve a structural role by stabilizing interactions between acidic side chains via the formation of salt bridges.[2] Nevertheless, whether or not the presence of metal ions has any influence on protein structure or function at any level remains mostly uncharacterized at the present time.

One key metal ion-protein interaction that has been elucidated by Dougherty and co-workers is the cation-π interaction.[3-6] Previous to this work, a commonly-held

assumption was that the interior pore of a channel protein or binding site that served to either transport or directly bind some positively charged species must be lined with acidic amino acid residues to provide a negatively-charged attractive surface. Using model cage compounds consisting of a primarily hydrocarbon-based aromatic framework, Dougherty and co-workers somewhat unexpectedly discovered that an unusually strong interaction could be observed between the aromatic moieties lining the cage and the cationic end of a heterophillic protonated alkylamine compound within the cage.[6] The subsequent discovery of aromatic side chains near the binding site for acetylcholine from x-ray analysis of acetylcholine esterase and the nicotinic acetylcholine receptor provided strong evidence that the presence of aromatic residues could in fact stabilize the binding of positively-charged ligand within functional biological systems.[6] Similar observations have been obtained from the x-ray structure analysis of the interior pore of potassium ion and sodium ion channels - those that directly underlie the physiology of neurotransmission among other key activities.[6] Ultimately, a simple model where coulomb electrostatics primarily determines the binding behavior between a charged species and the target protein has been superseded by a more subtle model. In particular, the dipole and higher multipole moments each amino acid side-chain residing within the active site of the protein are now recognized as exerting considerable influence on functional behavior, and hence must be characterized in order to obtain a proper description of a particular physiological interaction.

Working at the level of the solvated protein, it is exceedingly difficult to obtain quantitative details of the electrostatic interactions between a specific amino acid side-

chain residue and a charged species. To remove these complexities, gas phase molecular beam spectroscopy of the weakly-bound dimeric species consisting of only the portion of the amino acid side-chain most critical to determining the binding interaction with the charged moiety can be fruitful. Such an approach permits a detailed dissection of the electrostatic contributions ranging from purely coulombic forces all the way down to the van der Waals induced dipole-induced dipole interaction.

Following the experiments related to the Al•Ar_n (n = 1-60) work presented in Chapter 3 through Chapter 5, complexes between alkali metals and both carbon dioxide (CO_2) and benzene were chosen as experimental targets. Both of these alkali atom-solvent systems bear considerable relevance to the systematic investigation of alkali metal ion interactions with amino acid side-chain residues. With respect to the alkali metal-(CO_2) system, theoretical calculations predict that the ground states for both the Li•(CO_2) and Na•(CO_2) species possess considerable charge-transfer character.[7] In other words, the ground electronic state is better characterized as being highly ionic, resembling Li^+•$(CO_2)^-$ and Na^+•$(CO_2)^-$ rather than a weakly bound van der Waals complex. In addition, the ground state CO_2 bond angle in both complexes is calculated to be significantly bent to an angle of 130° due to the charge transfer from the alkali atom valance orbital into the CO_2 π^*-antibonding molecular orbital.[7] The presence of a bent, highly negatively-charged CO_2 species is reminiscent of both the geometry and charge distribution of the carboxyl end group present in aspartate as well as glutamate amino acid side-chain residues.[2] Therefore, characterization of these alkali metal-(CO_2) complexes by either REMPI or ion dip methods offers the possibility that detailed information concerning the contributions of

the principal electrostatic interactions between an alkali metal ion and the acidic side-chains of aspartate and glutamate may be quantitatively achieved.

The other system targeted for study, namely alkali metal-benzene complexes, is likewise highly relevant because it provides a means by which to definitively probe the fundamental nature of the cation-π interaction. In particular, aromatic amino acid residues such as those possessed by tyrosine, tryptophan, and phenylalanine can be approximated to a reasonable degree as being composed of a single benzene molecule.[2] While some of the subtle secondary electrostatic effects due to the additional substituents of the native amino acid aromatic ring are lost in such an approximation, the basic physical character of the π-cation interaction should nonetheless remain largely intact.

Alkali metal-benzene complexes are quite amenable for the systematic investigation of the π-cation interaction because of the development of several high-resolution photoelectron methodologies developed over the past decade. Specifically, techniques based on the zero electron kinetic energy (ZEKE)[8] and mass-analyzed threshold ionization (MATI)[9-12] methodologies have both been successfully demonstrated to yield vibrationally-resolved spectra of the ionic ground state of weakly-bound complexes. In the case of the former, even subwavenumber resolution can be commonly achieved. As a result, the implementation of the ZEKE or MATI techniques towards the study of alkali metal-benzene complexes offers the possibility for the direct observation of high-resolution spectra of the *ionic* ground state of alkali metal-benzene complexes.

The salient strength of both of the ZEKE and MATI approaches originates in part from the fact that they are both intrinsically ionization-based techniques that are, in

principal, no more difficult to perform than other MPI-based techniques. Both methodologies are based upon the initial excitation of a valance electron from the ground state of the neutral complex into the high-density manifold of electronic Rydberg states that converge to the ionic ground state.[8-12] This initial excitation can occur either through a resonantly-enhanced scheme via some intermediate excited state of the neutral complex, or by direct single-photon excitation to an energy region just beneath the ionization threshold. With the ZEKE method, a small DC stark shift is employed to field-ionize and subsequently detect the excited Rydberg electrons just under threshold after a fixed time delay (typically about 1-10 μs).[8] The MATI technique (as well as other close variants) are similar in spirit to ZEKE, except that the formation of the ionic species itself rather than the photoelectron is detected as a result of a temporally-controlled threshold ionization process.[9-12]

In order to begin the investigation of alkali metal-containing van der Waals complexes, a new laser vaporization source needed to be developed in order to accommodate the complications involved when employing an ablation target other than those from refractory elements such as aluminum. Due to the soft nature of the alkali metals, a target rod source such as that used in the third generation laser vaporization source (see Section 2.2.4.3. in Chapter 2) was deemed somewhat impractical due to the difficulty in obtaining (or creating) a mechanically stable alkali rod. Consequently, a new source design was envisioned that utilized a flat, circular target disk as the ablation target. The remainder of this chapter serves to detail the development of this new disk target laser vaporization source that will be implemented over the course of the following months to

produce alkali metal-solvent van der Waals complexes.

6.2. Design of the Disk Target Laser Vaporization Source

A complete set of machine drawings for the component parts of the new laser vaporization source design are presented in Appendix 1. The part numbers referred to throughout the remainder of this chapter correspond to the individual part numbers designated on the machine drawing for each of the various components.

The first consideration that needed to be accounted for in the new design was the best manner in which to properly mount the alkali target material into the source. Rather than rely on the mechanical stability (or lack thereof) of the target material, a OFHC copper target sample holder (see Part #2 in Appendix 1) was designed to mechanically support the alkali target material of interest. In order to install the alkali material into the target sample holder, a custom designed stainless steel target press (see Parts #19a-19d in Appendix 1) was designed. The manner in which functional alkali metal targets can be fabricated is as follows. First, the target sample holder is inserted directly into Part # 19a as shown in the assembly drawing for Part #19. Part #19a was designed with two 2-56 UNC tapped holes positioned on opposite sides of the piece that were tapped directly into the center region of the piece. These 2-56 UNC tapped holes served to mount a 2-56 UNC threaded rod. The purpose of this rod was to support the stainless steel drive pins that were press fit into the target sample holder (see Part #2 in Appendix 1). By threading the 2-56 UNC threaded rods such that they seated directly onto the ends of the stainless steel drive pins of the target sample holder, one could ensure that the drive pins would not

be dislodged as a result of the force of the press. Once positioned, these 2-56 UNC threaded rods were to be secured into position by a 2-56 UNC locknut that seated directly against a flat positioned around each of the 2-56 UNC tapped holes.

To assemble the press, Part #19a (with Part #2 already mounted inside) was then precisely positioned between Part #19b and Part #19c (see Part #19 assembly drawing in Appendix 1) via the use of a 1.250" diameter precision keyed counterbore machined into both pieces. Part #19b was then firmly bolted to Part #19c by a set of four 8-32 UNC socket head cap screws. With the press now assembled, the target sample holder was effectively sandwiched into the center of the press. In addition, the 0.500" inner diameter of the target sample holder was perfectly aligned with the 0.500" diameter central channel of Part #19c.

The target press was specially designed such that the alkali targets could be generated under oil to limit the oxidation of the exposed surfaces upon exposure to air. In order to make a target, the entire press is to be submerged within a bath of mineral oil. The alkali metal of choice is then inserted down the central channel of Part #19c and loosely installed within the target sample holder. The amount of alkali material should be sufficient to completely fill the target sample holder once the target material has been compressed. The stainless steel press plunger (see Part #19d in Appendix 1) is then inserted into the central channel of Part #19c. A vice or press can then be employed to forcibly compress the soft alkali material into a solid contiguous mass that completely fills the target sample holder. Relief channels machined into the bottom surface of Part 19c then extended radially from the target sample holder to the exterior surface of the press

serve to remove the mineral oil displaced as a result of the compression process.

The press has been designed in such a way that the smooth target face will always be formed against the flat surface of Part #19b. The opposite side of the target sample holder will typically possess excess material that extends beyond the edge of the target sample holder. To remove this material, Part #19c can be unbolted from Part #19b and removed, leaving Part # 19a seated within Part #19b for support. At this point, the excess alkali material extending from the end of the target sample holder will be exposed, and can be trimmed away with a razor blade to create a flat surface. Once the alkali target sample holder is subsequently removed from Part #19a of the press assembly, it is ready for installation into the source.

The other primary design consideration that needed to be addressed was the problem posed by the reactivity of the alkali metal surface. Previous experience with alkali metal laser vaporization targets *in vacuo* from work performed in the Whetten group had demonstrated that stable sources of alkali metal atoms were difficult to achieve.[13-14] The underlying cause was found to derive from the fact that all alkali metals act as very effective "getters" even in a UHV environment. Consequently, a clean target surface was difficult to obtain even after several passes of the ablation laser since the freshly exposed surface quickly re-oxidized due to trace oxygen and water in the UHV environment. To combat the oxidation problem, it was found that cooling the alkali metal target to liquid nitrogen temperatures dramatically reduced to reactivity of the exposed surface, and in turn significantly improved the stability of the laser vaporization source. While it was found that lithium could often be used without liquid nitrogen cooling due to

its lower degree of reactivity with respect to oxidation, use of all other alkali metals was found to absolutely require cooling of the ablation target.

In order to permit the alkali target to be cooled to liquid nitrogen temperatures, the new source was designed around an OFHC copper liquid nitrogen reservoir housing (see Part #3 in Appendix 1). The housing possessed a 0.375" diameter through-hole through the face of the piece along the vertical center line that served to mount a stack of four precision radial ball bearings (57155K36. McMaster-Carr) that were press-fit into place. The 0.250" diameter central bore of the precision radial ball bearing stack was designed to slip fit the neck of the OFHC copper rotatable disk target mount (see Part #1 in Appendix 1). In essence, the rotatable disk target mount served two purposes. First, this piece was designed to slip-fit the target sample holder, thus serving as the new target mount for the new source design. Two 0.100" wide grooves were likewise machined into the disk target mount to accommodate the stainless steel drive pins of the target sample holder. This design feature ensured that the alkali target could be effectively rotated without the possibility that the target sample holder would rotate freely within the target mount should the target sample contact the nozzle piece during the course of an experiment. The second function of the rotatable target mount was that it served as a thermal coupling between the liquid nitrogen reservoir and the target sample itself. To ensure maximal thermal coupling between the alkali target sample and the target mount, a chemically inert grease should be applied to the base of the target mount to guarantee maximal thermal conductivity to the target disk. This grease, once frozen, would also effectively act as adhesive to secure the target disk securely within the mount.

The remaining components of the source design consisted of pieces that served to form a cart around the liquid nitrogen-cooled reservoir similar to that designed for the third generation laser vaporization source discussed in Section 2.2.4.3. While somewhat different in design than the cart designed for the target rod laser vaporization source, the two cart designs were nevertheless completely interchangeable. In addition, both cart designs were mounted within the same structural framework designed and implemented as a result of the development of the third generation laser vaporization source as will be discussed in more detail below.

As was the case with the target rod laser vaporization sources presented in Chapter 2, two degrees of motion were desired for the target alkali metal disk mounted to the liquid nitrogen reservoir. The first was rotary motion of the target disk sample that could be achieved merely by rotating the target sample mount within the frictionless rotary ball bearings of the liquid nitrogen-cooled housing. The second degree of freedom envisioned for the new source was vertical motion that would be implemented in concert with the rotary motion. The rationale behind this design was that such concerted motion would permit a continually spiraling ablation pattern to become etched into the surface of the target that would only infrequently overlap with a previously ablated point. By randomizing the ablation surface rather than constantly ablating along a single radial track, the stability of the source should be markedly improved.

Because of the usable face of the alkali metal target sample is only 0.500" in diameter in the new source design, the vertical motion of the new cart would exhibit a much faster temporal period compared to the cart designed for the third generation target

rod laser vaporization source. In the latter cart, stainless steel drill bushings were employed to secure without play the target rod cart to the vertical rails along which the cart executed its vertical motion. For the new disk target cart, however, the decision was made to mount the cart to the rails through the use of linear ball bearings. This ensured that smooth travel would be maintained at the extrema points of the vertical motion which had been observed to offer slight mechanical resistance in the target rod cart design.

To implement a linear ball bearing design, however, a slight modification was required to the vertical rails assembly along which the cart would execute its travel. In particular, the wider diameter of linear ball bearing housings compared to the drill bushings necessitated that the vertical rails that originally installed in the third generation laser vaporization be more widely separated from the original 0.440" center-to-center distance to a new 0.675" center-to-center distance. To retrofit the new rails to the third generation laser vaporization source, adapter pieces (see Part # 15 through Part #18 in Appendix 1) were designed that would enable the new vertical rail system to be installed without any additional changes to the rest of the third generation source design. To convert from the target rod source to the target disk source, the original vertical rails are removed from the internal frame and replaced with four short 1.000" - 1.500" long precision ground shafts of equal diameter - two placed in each the upper and lower carts mounted to the internal frame (see Part #3a and Part #6 in Figure 2-64 in Chapter 2). These shortened shafts were then secured to the internal frame carts by the use of the custom collar (see Part #3b in Appendix 4) previously employed in the target rod design. The target disk vertical rail system then directly mounted to the shaft stubs extending from

both the upper and lower internal frame cart. In particular, Part #15 and Part #17 were custom-designed collars that clamped directly onto the shaft stubs present in the upper and lower internal frame carts respectively. Finally, Part #16 and Part #18 were bolted to Part #15 and Part #17 respectively to complete the retrofit. Both Part #16 and Part #18 possessed a drill bushings that has been press-fit into place to accommodate the new pair of vertical rails at the proper center-to-center distance.

The basic framework of the cart into which the liquid nitrogen-cooled housing is mounted was composed of Part #4, Part #5, Part #6, and Part #10. Both Part #4 and Part #5 have been specifically designed to minimize heat conduction since they both lie immediately adjacent to the liquid nitrogen-cooled housing. Part #4 was a stainless steel adapter piece that served to couple the Vespel SP-1 standoffs (Part #5) to the liquid nitrogen-cooled housing. Part #4 was secured to the liquid nitrogen cooled housing by an intrinsic clamp mechanism that mounted through two pairs of holes machined near the upper and lower edges of the liquid nitrogen-cooled housing. The purpose of the standoffs was to permit the liquid nitrogen-cooled housing to be coupled to the rest of the cart frame while minimizing heat conduction. Vespel SP-1 was a perfect choice of material for this function because of its strength, its low thermal conductivity, and its usable temperature range that extends into liquid nitrogen temperature regime. Likewise, by tapping a 4-40 UNC threaded central hole along the length of the Vespel SP-1 standoff, heat conduction was further limited.

To complete the frame of the cart, the liquid nitrogen-cooled housing with the attached Vespel SP-1 standoffs was fastened to the stainless steel upper and lower cart

plates (see Part #6 in Appendix 1) by bolting both plates directly to the Vespel SP-1 standoffs. The stainless steel back plate of the cart (see Part #6 in Appendix 1) was then joined to the upper and lower cart plated by standard right angle brackets purchased from Kimball-Physics, thus resulting in a rigid frame. The thicknesses of all the stainless steel plated was minimized to limit heat conduction through the frame. Similarly, significant portions of the back plate were machined away to further limit heat conduction through the assembled piece.

In order to permit precise linear motion of the cart along the vertical rails, four custom linear ball bearing housings were designed. After the linear ball bearings (6064K51, McMaster-Carr) were press-fit into place, a pair of linear bearing housings were directly bolted to each the upper and lower plates of the disk target cart. To couple the cart to the screw drive assembly of the third generation laser source that would drive the vertical motion of the cart, a custom rotary ball bearing mount (see Part #8 in Appendix 1) was designed. Since the vertical motion was to be driven by the 1/4-80 drive screw of the screw drive assembly installed within the third generation laser vaporization source, a freely-rotating coupling needed to be designed to join the drive screw to the target disk cart. Part #8 was designed to permit the installation of an rotary ball bearing that would serve as the basis for the requisite rotary motion. Within the central bore of the rotary ball bearing was then installed a stainless steel coupling (see Part #9 in Appendix 1). This coupling possessed a flange on its lower surface rather than an external retaining ring to ensure that the piece would bear the weight of the cart without any risk of slippage. With the coupling installed within the rotary bearing, Part #8 was then fastened

to the upper plate of the target disk cart, and subsequently joined to the drive screw of the screw drive assembly of the third generation laser vaporization source.

As a result of the complete assembly of the previously described components, the desired vertical motion of the new disk cart laser vaporization source was fully operational. The remaining components of the design were related to the implementation of the second desired degree of motion, namely the rotary motion of the mounted disk target itself. To drive the rotary motion of the target sample holder, a small DC-gearmotor was employed. The DC-gearmotor was mounted directly to a stainless steel plate (see Part #11 in Appendix 1). This plate was then to be bolted directly to the back plate of the assembled target disk cart, and positioned directly behind the rotable disk target mount (see Part #1 in Appendix 1). While appearing convoluted, such a design offered the distinct advantage that the DC-gearmotor could be installed or removed from the assembled disk target cart without having to disassemble any component of the cart itself. This ensured that replacing burned-out motors could be performed in a minimal amount of time. It is important to note that no effort was placed in designing a cooling mechanism for the DC-gearmotor mounted in the UHV environment. Nevertheless, a thermal equilibrium will undoubtedly be achieved between the hot motor and the cold liquid nitrogen reservoir. With luck, the heat conduction through the cart may have the dual benefit of maintaining the mechanical components of the cart at a reasonable temperature while simultaneously cooling the DC-gearmotor to a some degree - thus extending the operational lifetime of the motor.

The final three components of the disk target laser vaporization source design

couple the rotary motion produced by the DC-gearmotor to the target sample mount itself (see Part #1 in Appendix 1). To minimize heat conduction between the liquid nitrogen-cooled target sample mount and the DC-gearmotor, a strand of 0.063" diameter stranded stainless steel wire rope fastened to both components at each end was envisioned as a suitable coupling mechanism. In order to join one end of the wire rope to the 2 mm diameter drive shaft of the DC-gearmotor, two components were employed. The first was a custom-designed clamp (see Part #13 in Appendix 1) that served to fit over the gear motor drive shaft at one end while securing the wire rope within a clamp on the other end. Part #13 was then securely fastened to the DC-gearmotor drive shaft by a custom designed shaft collar (see Part #12 in Appendix 1) that served to compress the split-hub of Part #13 tightly onto the shaft. On the opposite end of the wire rope, a second clamp (see Part #14 in Appendix 1) that was similar to Part #13 was designed to couple the wire rope to the target sample mount. At one end of Part #14 was a cable clamp in direct analogy to Part #13. The opposite end of Part #14 was a 0.125" square drive pin that keyed directly into a square mating channel that had been machined into the back of the target sample mount (see Part #1 in Appendix 1). Ultimately, to assemble the rotary motion drive coupling, one first inserts Part #14 into Part #1, and secures Part #13 to the drive shaft of the DC-gearmotor. A strand of wire rope is then cut that will span the distance between the two clamps, and each end is subsequently secured into place.

6.3 Conclusion

The design of a new target disk laser vaporization source has been presented, one

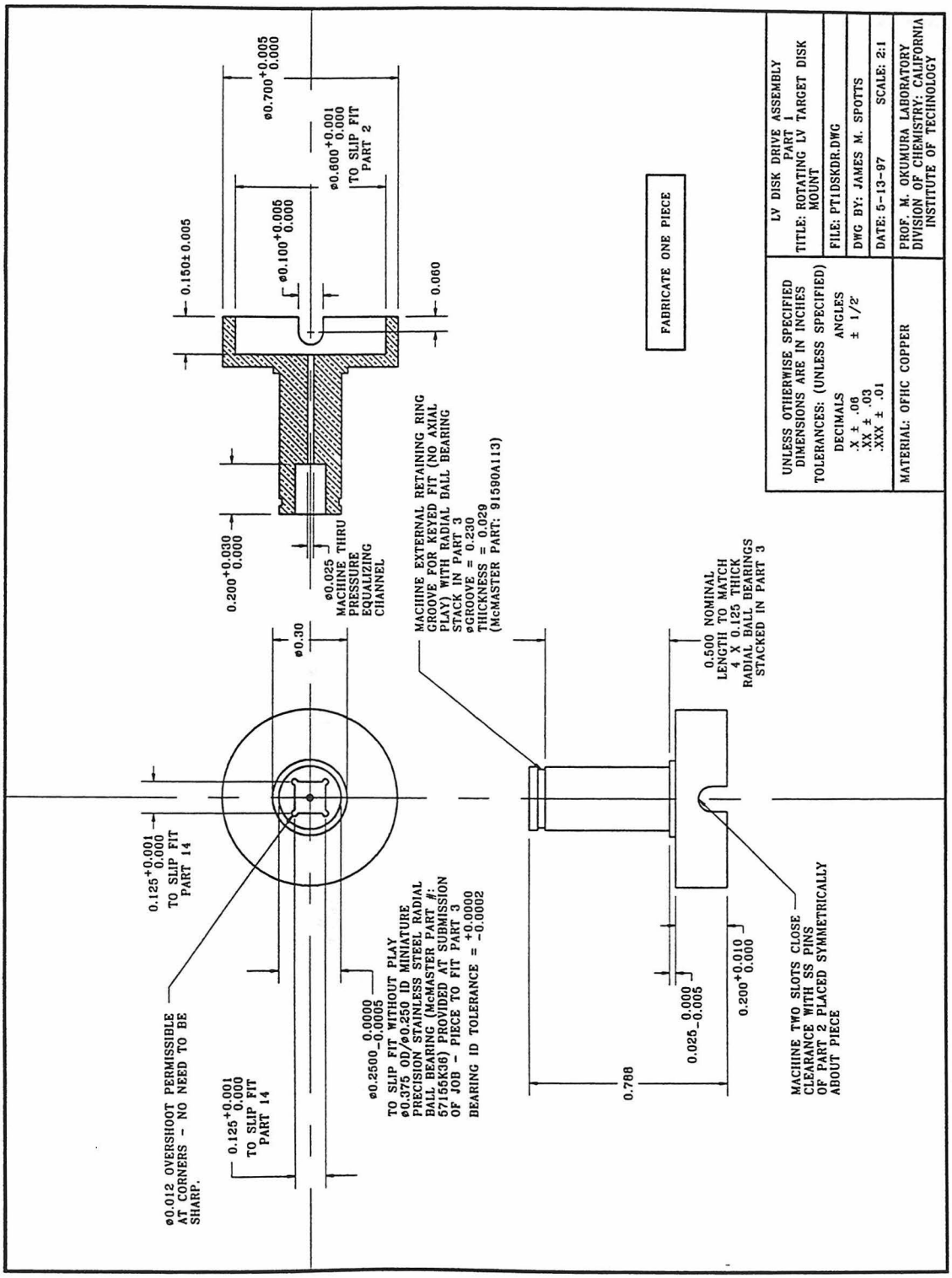
that will permit the systematic investigation of van der Waals complexes containing alkali metal atoms. While special consideration was taken to ensure that the design would accommodate the distinctive physical properties and chemical behavior inherent to alkali metals, there is no loss of generality in its use. In fact, the new source design is very flexible, and can be easily modified or adapted for use with almost any target material that can be acquired in the form of a disk, thus opening up a wide spectrum of experimental systems beyond aluminum-containing van der Waals systems that have been the focus of the majority of this thesis work.

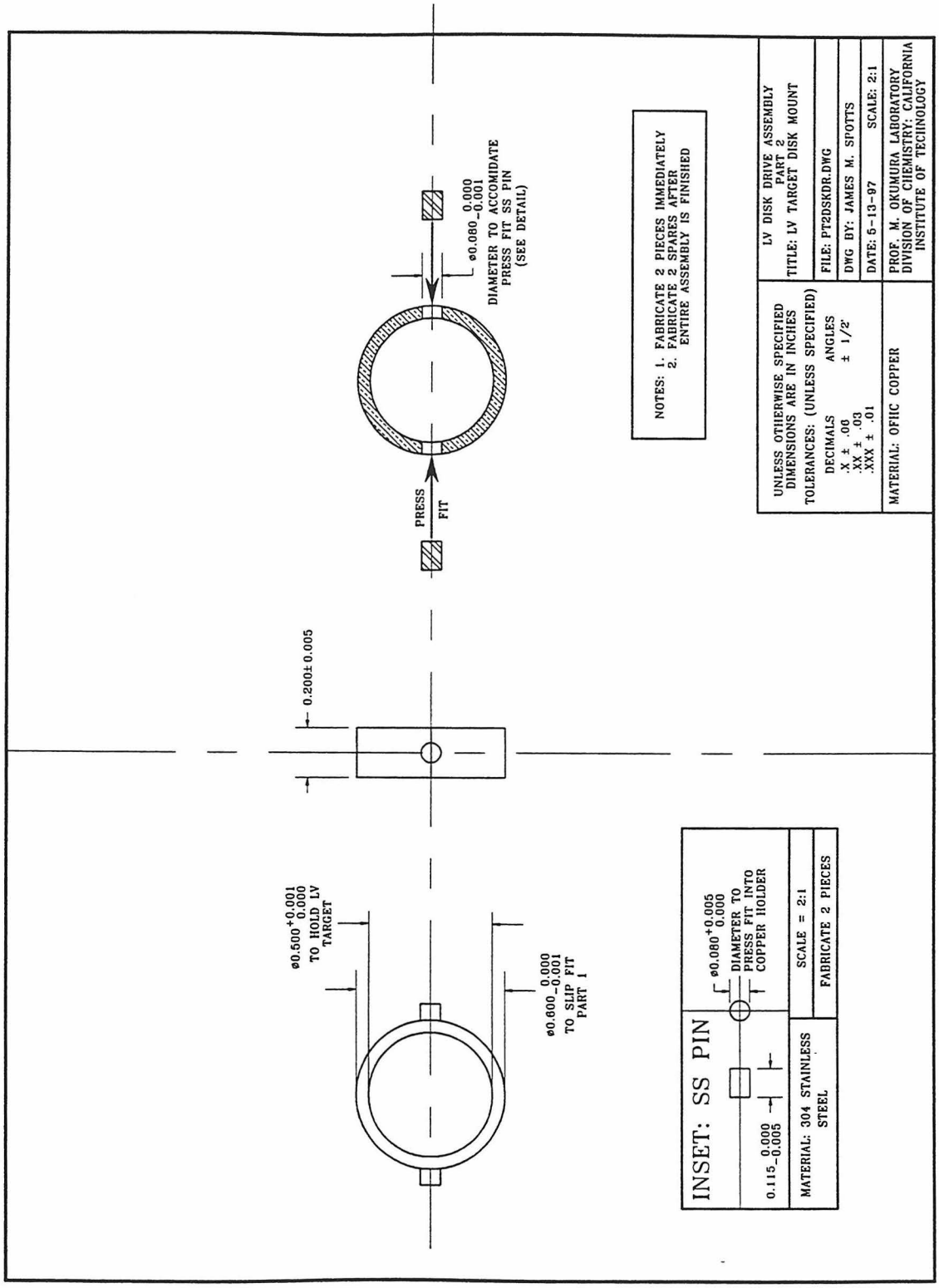
6.4. References

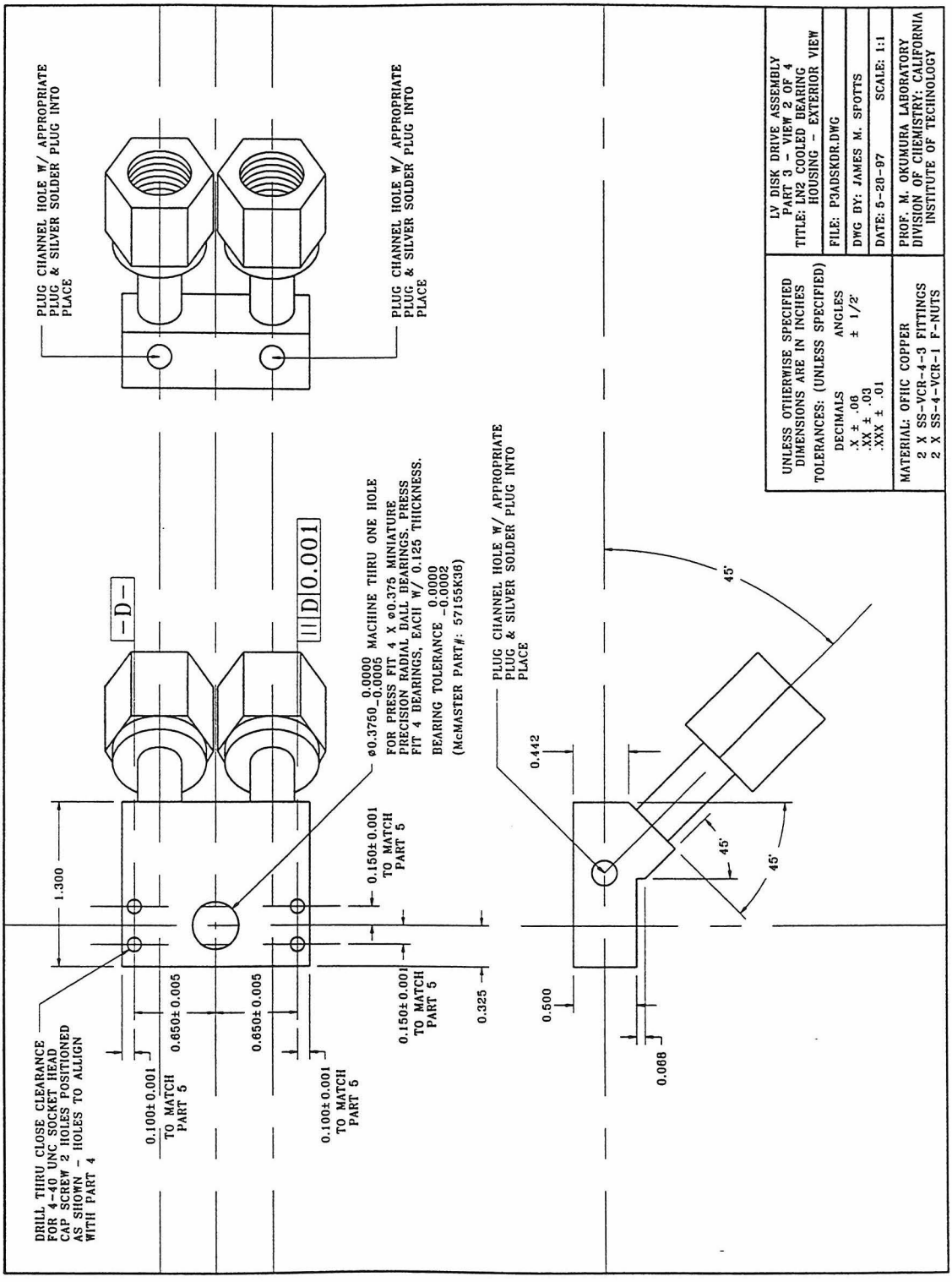
1. B. Alberts, D. Bray, J. Lewis, M. Raff, K. Roberts, and J. D. Watson, *Molecular Biology of the Cell, Third Edition* (Garland Publishing, Inc., New York, 1994), and references therein.
2. L. Stryer, *Biochemistry, Fourth Edition* (W. H. Freeman, New York, 1995).
3. S. Mecozzi, A. P. West, Jr., and D. A. Dougherty, *Proc. Natl. Acad. Sci. USA*, **93**, 10566 (1996).
4. D. A. Dougherty, *Science*, **271**, 163 (1996).
5. S. Mecozzi, A. P. West, Jr., and D. A. Dougherty, *J. Am. Chem. Soc.*, **118**, 2307 (1996).
6. J. C. Ma and D. A. Dougherty, *Chem. Rev.*, **97**, 1303 (1997).
7. H. Tachikawa, Y. Takatori, A. Ohtake, J. Kumagai, and H. Yoshida, *J. Mol. Struct. (Theochem)*, **342**, 1 (1995).
8. K. Muller-Dethlefs and E. W. Schlag, *Ann. Rev. Phys. Chem.*, **42**, 109 (1991).
9. L. Zhu and P. Johnson, *J. Chem. Phys.*, **94**, 5769 (1991).
10. H. Krause and H. J. Neusser, *J. Chem. Phys.*, **97**, 5923 (1992).
11. C. Jouvet, C. Dedonder-Lardeaux, S. Martrenchard-Barra, and D. Solgadi, *Chem. Phys. Lett.*, **198**, 419 (1992).
12. K. F. Willey, C. S. Yeh, and M. A. Duncan, *Chem. Phys. Lett.*, **211**, 156 (1993).
13. E. C. Honea, M. L. Homer, and R. L. Whetten. *Phys. Rev. B*, **47**, 7480 (1993).
14. M. L. Homer, personal communication.

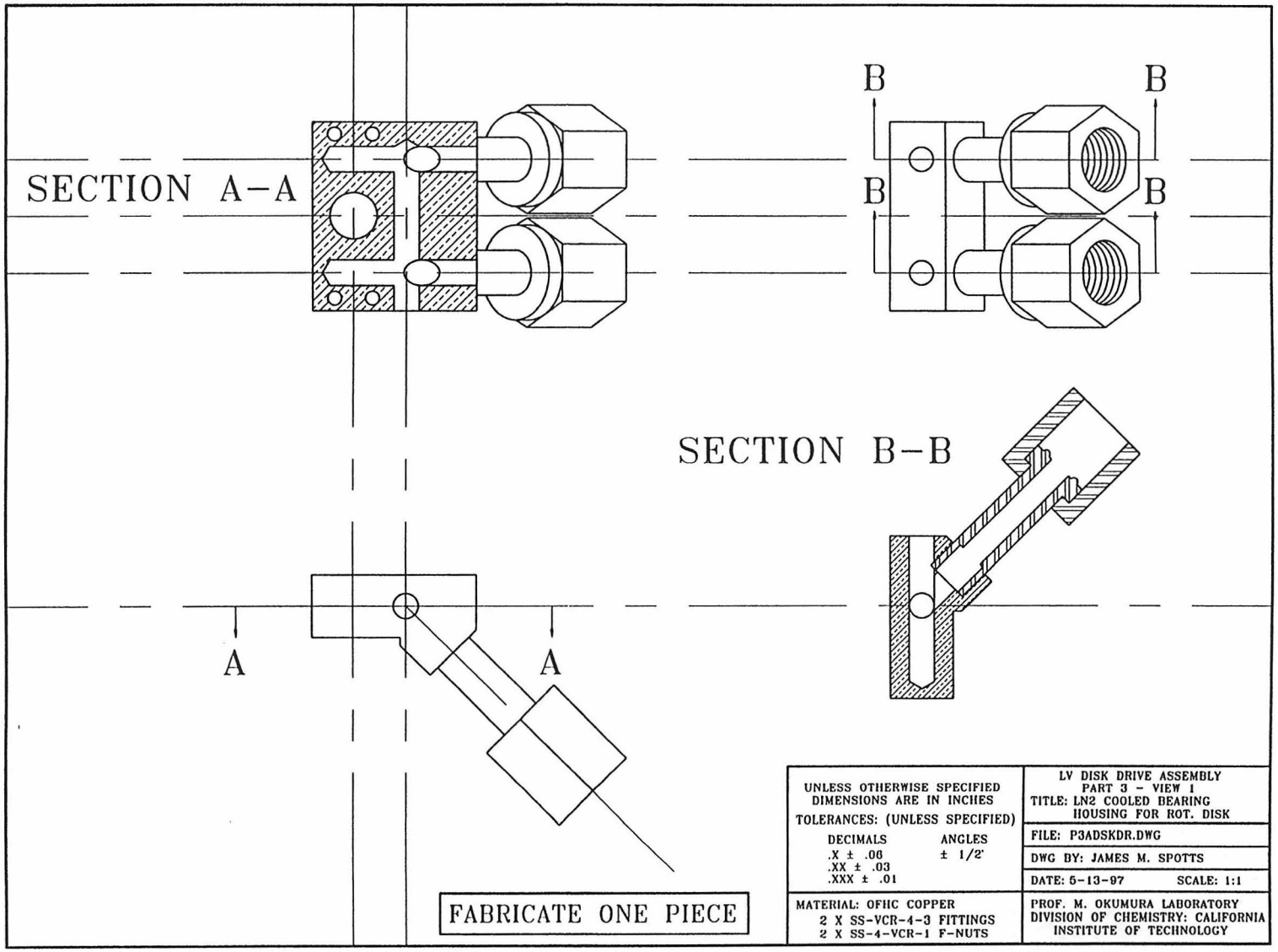
APPENDIX 1

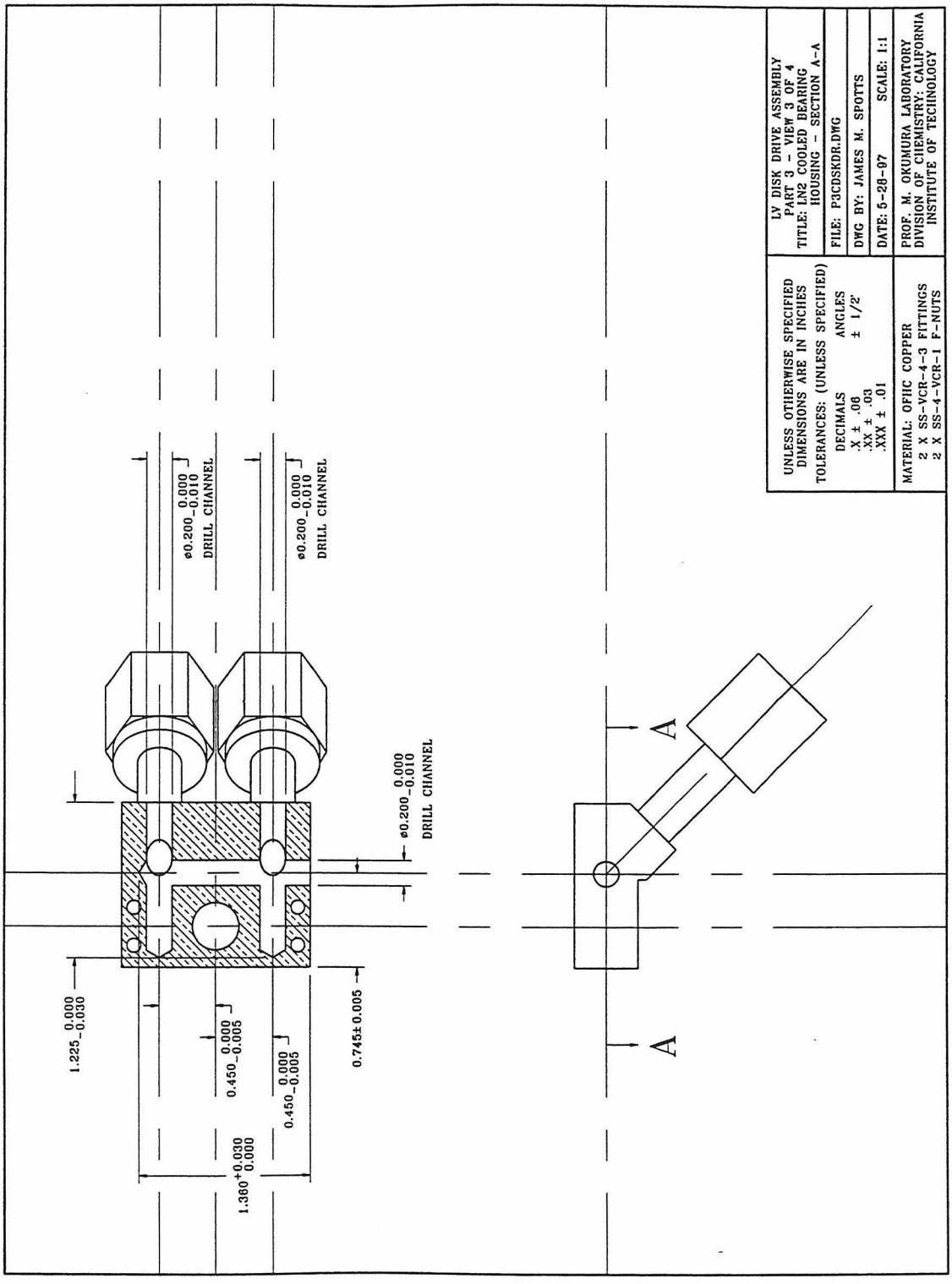
Drawings for the Disk Target Laser Vaporization Source

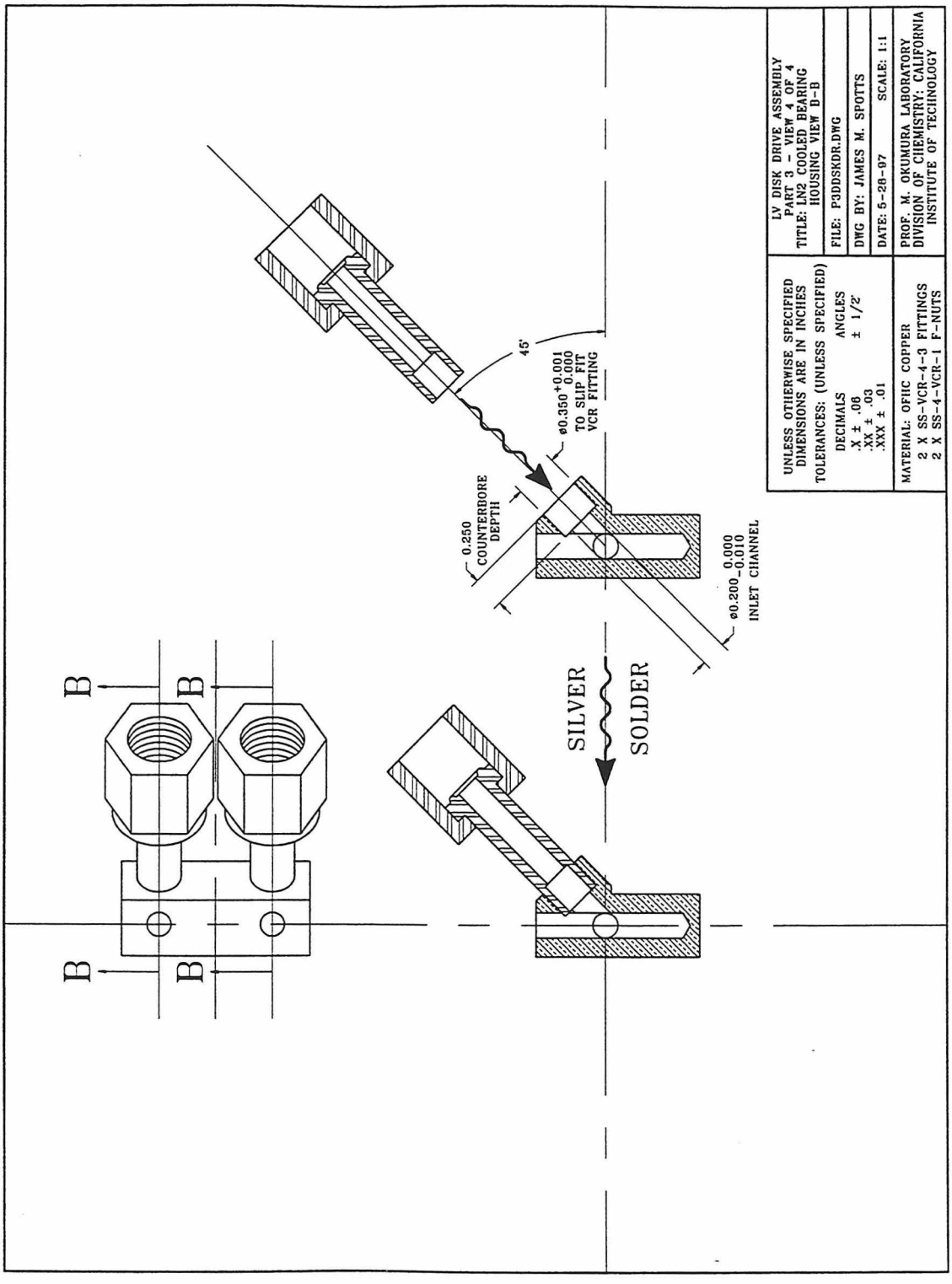

0.150±0.005
ø0.700 +0.005 0.000
ø0.100 +0.005 0.000
ø0.600 +0.001 0.000
TO SLIP FIT PART 2
0.060
0.200 +0.030 0.000
ø0.025 MACHINE THRU PRESSURE EQUALIZING CHANNEL
ø0.30
MACHINE EXTERNAL RETAINING RING GROOVE FOR KEYED FIT (NO AXIAL PLAY) WITH RADIAL BALL BEARING STACK IN PART 3
øGROOVE = 0.230
THICKNESS = 0.029
(McMASTER PART: 91590A113)
FABRICATE ONE PIECE
0.500 NOMINAL LENGTH TO MATCH 4 X 0.125 THICK RADIAL BALL BEARINGS STACKED IN PART 3
0.125 +0.001 0.000 TO SLIP FIT PART 14
ø0.012 OVERSHOOT PERMISSIBLE AT CORNERS - NO NEED TO BE SHARP.
0.125 +0.001 0.000 TO SLIP FIT PART 14
ø0.2500 -0.0000 -0.0005
TO SLIP FIT WITHOUT PLAY
ø0.375 OD/ø0.250 ID MINIATURE PRECISION STAINLESS STEEL RADIAL BALL BEARING (McMASTER PART #: 57155K36) PROVIDED AT SUBMISSION OF JOB - PIECE TO FIT PART 3
BEARING ID TOLERANCE = +0.0000 -0.0002
0.788
0.025 -0.000 -0.005
0.200 +0.010 0.000
MACHINE TWO SLOTS CLOSE CLEARANCE WITH SS PINS OF PART 2 PLACED SYMMETRICALLY ABOUT PIECE
UNLESS OTHERWISE SPECIFIED DIMENSIONS ARE IN INCHES
TOLERANCES: (UNLESS SPECIFIED)
DECIMALS ANGLES
.X ± .06 ± 1/2°
.XX ± .03
.XXX ± .01
MATERIAL: OFHC COPPER
LV DISK DRIVE ASSEMBLY PART 1
TITLE: ROTATING LV TARGET DISK MOUNT
FILE: PT1DSKDR.DWG
DWG BY: JAMES M. SPOTTS
DATE: 5-13-97 SCALE: 2:1
PROF. M. OKUMURA LABORATORY
DIVISION OF CHEMISTRY: CALIFORNIA INSTITUTE OF TECHNOLOGY

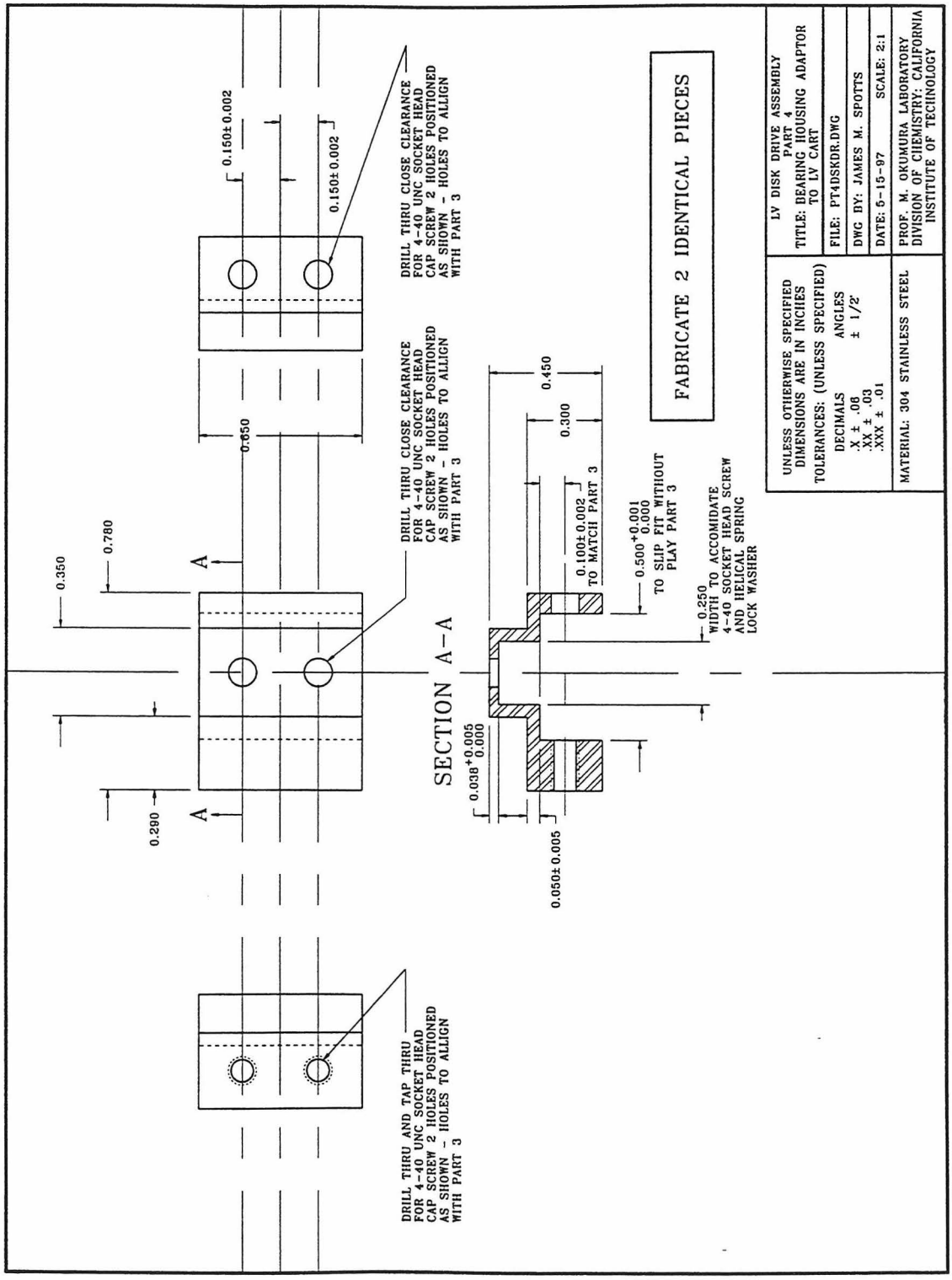

NOTES: 1. FABRICATE 2 PIECES IMMEDIATELY
2. FABRICATE 2 SPARES AFTER ENTIRE ASSEMBLY IS FINISHED
LV DISK DRIVE ASSEMBLY PART 2
TITLE: LV TARGET DISK MOUNT
UNLESS OTHERWISE SPECIFIED DIMENSIONS ARE IN INCHES
TOLERANCES: (UNLESS SPECIFIED)
DECIMALS ANGLES
.X ± .06 ± 1/2°
.XX ± .03
.XXX ± .01
FILE: PT2DSKDR.DWG
DWG BY: JAMES M. SPOTTS
DATE: 6-13-97 SCALE: 2:1
MATERIAL: OFHC COPPER
PROF. M. OKUMURA LABORATORY
DIVISION OF CHEMISTRY: CALIFORNIA INSTITUTE OF TECHNOLOGY
PRESS FIT
ø0.080 0.000 -0.001
DIAMETER TO ACCOMIDATE PRESS FIT SS PIN (SEE DETAIL)
0.200± 0.005
ø0.500 +0.001 0.000
TO HOLD LV TARGET
ø0.600 0.000 -0.001
TO SLIP FIT PART 1
INSET: SS PIN
ø0.080 +0.005 0.000
DIAMETER TO PRESS FIT INTO COPPER HOLDER
0.115 0.000 -0.005
MATERIAL: 304 STAINLESS STEEL
SCALE = 2:1
FABRICATE 2 PIECES

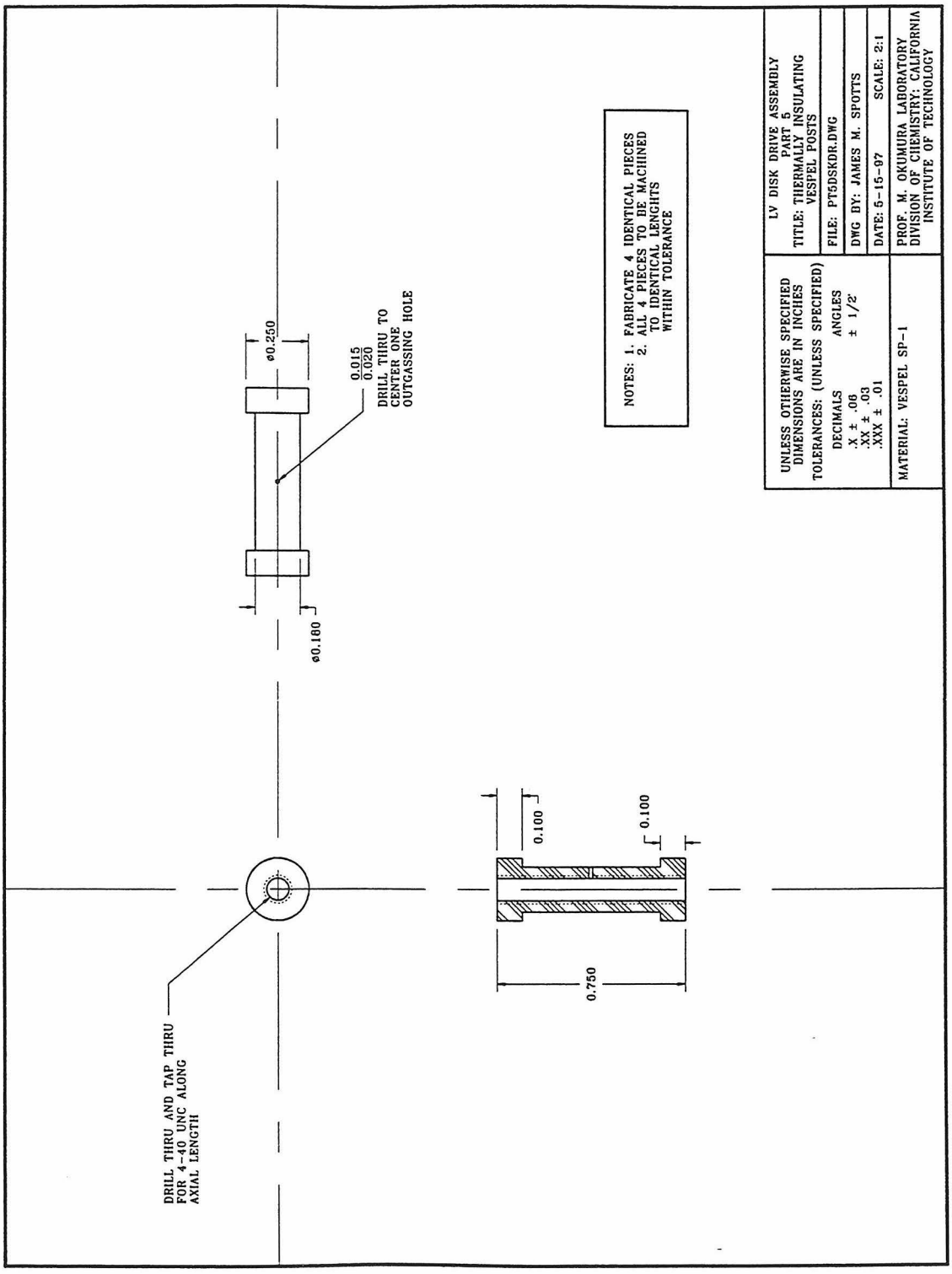

PLUG CHANNEL HOLE W/ APPROPRIATE PLUG & SILVER SOLDER PLUG INTO PLACE
PLUG CHANNEL HOLE W/ APPROPRIATE PLUG & SILVER SOLDER PLUG INTO PLACE
-D-
|D|0.001
DRILL THRU CLOSE CLEARANCE FOR 4-40 UNC SOCKET HEAD CAP SCREW 2 HOLES POSITIONED AS SHOWN - HOLES TO ALIGN WITH PART 4
1.300
0.100± 0.001 TO MATCH PART 5
0.650± 0.005
0.650± 0.005
0.100± 0.001 TO MATCH PART 5
ø0.3750 -0.0000 -0.0005 MACHINE THRU ONE HOLE FOR PRESS FIT 4 X ø0.375 MINIATURE PRECISION RADIAL BALL BEARINGS. PRESS FIT 4 BEARINGS, EACH W/ 0.125 THICKNESS.
BEARING TOLERANCE -0.0000 -0.0002
(McMASTER PART#: 57155K36)
0.150± 0.001 TO MATCH PART 5
0.150± 0.001 TO MATCH PART 5
0.325
PLUG CHANNEL HOLE W/ APPROPRIATE PLUG & SILVER SOLDER PLUG INTO PLACE
0.442
0.500
0.088
45°
45°
45°
UNLESS OTHERWISE SPECIFIED DIMENSIONS ARE IN INCHES
TOLERANCES: (UNLESS SPECIFIED)
DECIMALS ANGLES
.X ± .06 ± 1/2°
.XX ± .03
.XXX ± .01
LV DISK DRIVE ASSEMBLY
PART 3 - VIEW 2 OF 4
TITLE: LN2 COOLED BEARING HOUSING - EXTERIOR VIEW
FILE: P3ADSKDR.DWG
DWG BY: JAMES M. SPOTTS
DATE: 6-20-97
SCALE: 1:1
MATERIAL: OFHC COPPER
2 X SS-VCR-4-3 FITTINGS
2 X SS-4-VCR-1 F-NUTS
PROF. M. OKUMURA LABORATORY
DIVISION OF CHEMISTRY: CALIFORNIA INSTITUTE OF TECHNOLOGY

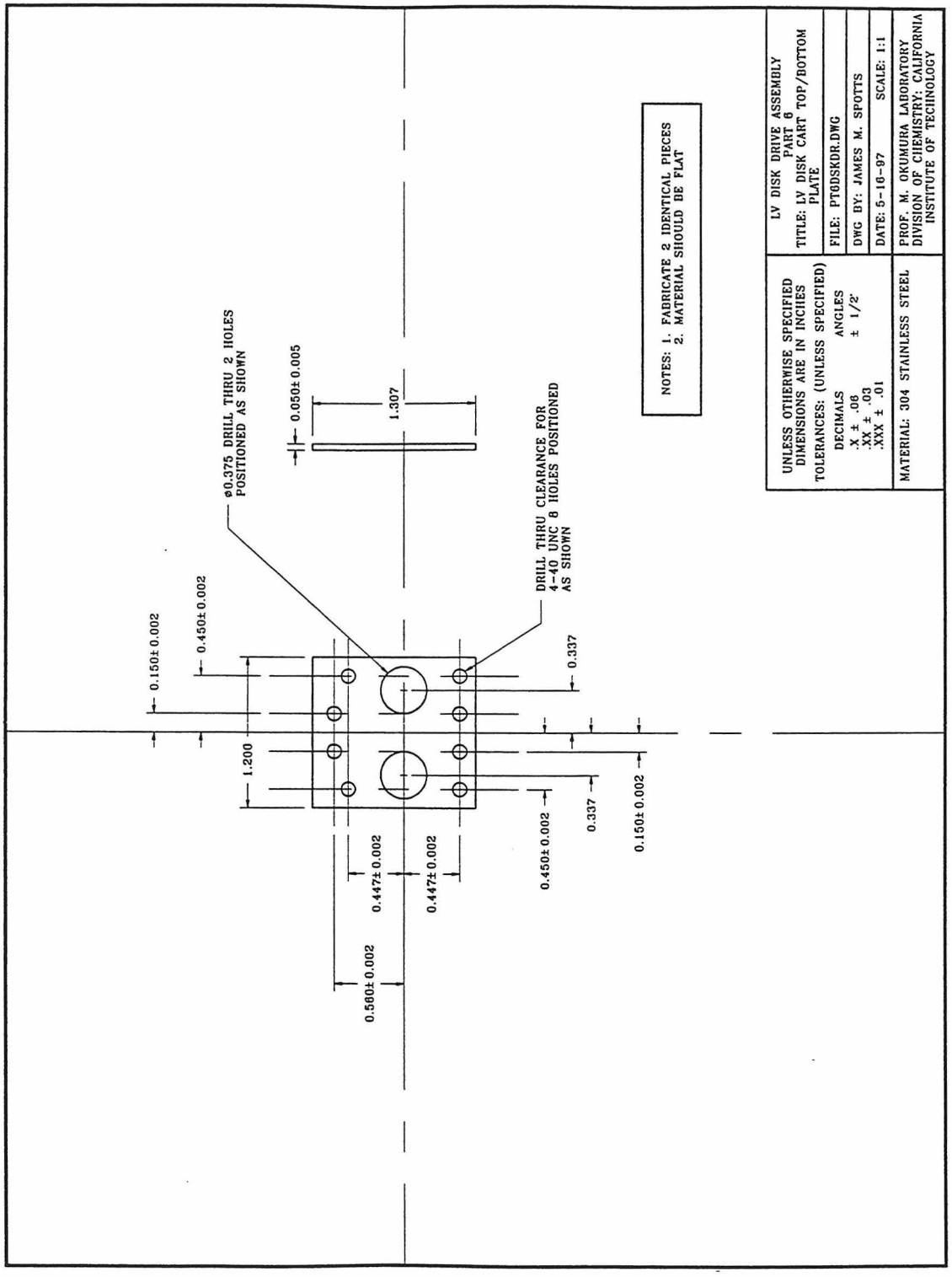

SECTION A–A
B
B
B
B
SECTION B–B
A
A
FABRICATE ONE PIECE
UNLESS OTHERWISE SPECIFIED
DIMENSIONS ARE IN INCHES
TOLERANCES: (UNLESS SPECIFIED)
DECIMALS
.X ± .06
.XX ± .03
.XXX ± .01
ANGLES
± 1/2'
MATERIAL: OFHC COPPER
2 X SS-VCR-4-3 FITTINGS
2 X SS-4-VCR-1 F-NUTS
LV DISK DRIVE ASSEMBLY
PART 3 - VIEW 1
TITLE: LN2 COOLED BEARING
HOUSING FOR ROT. DISK
FILE: P3ADSKDR.DWG
DWG BY: JAMES M. SPOTTS
DATE: 5-13-97
SCALE: 1:1
PROF. M. OKUMURA LABORATORY
DIVISION OF CHEMISTRY: CALIFORNIA
INSTITUTE OF TECHNOLOGY

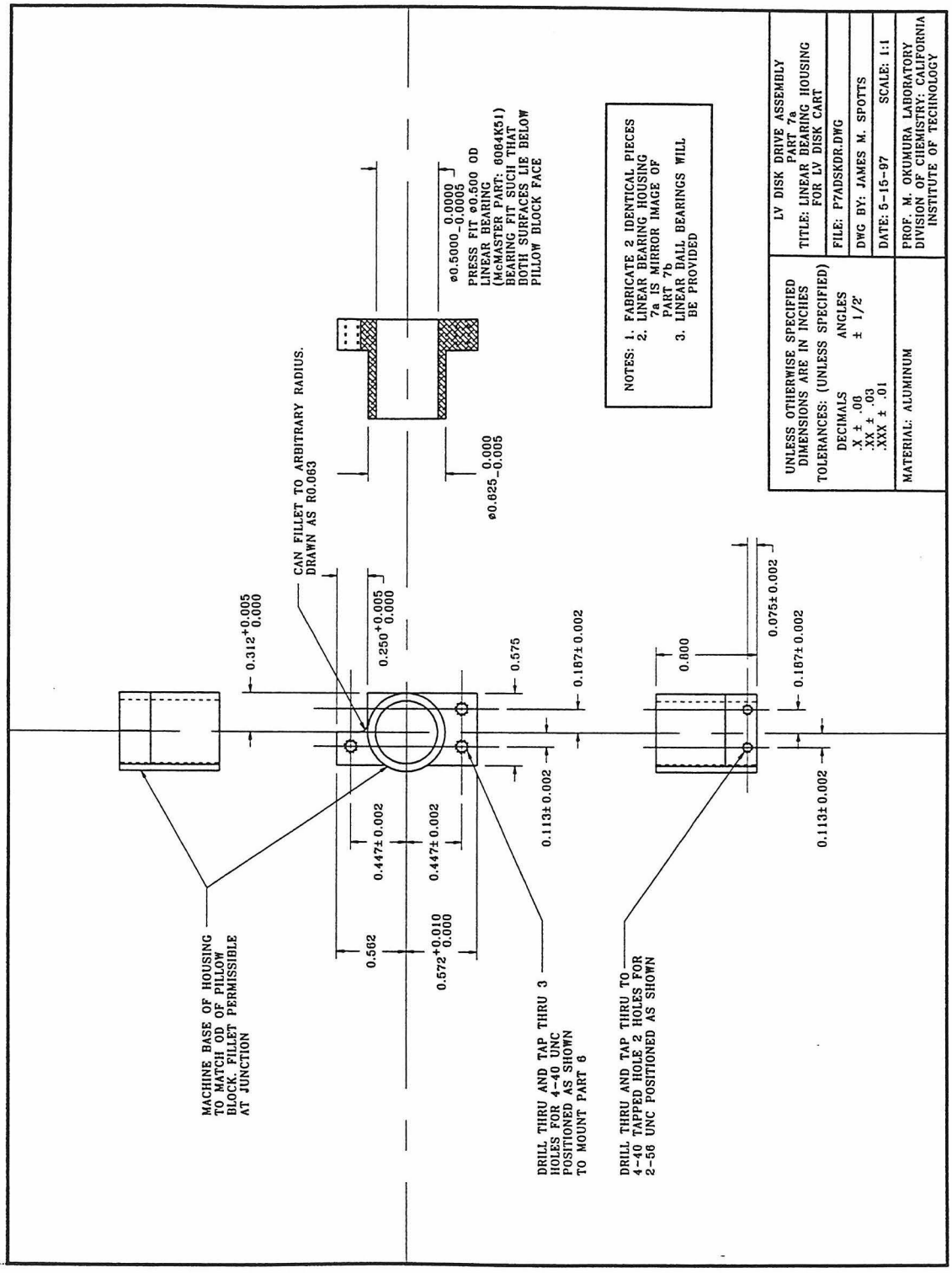

ø0.200 0.000 -0.010
DRILL CHANNEL
ø0.200 0.000 -0.010
DRILL CHANNEL
ø0.200 0.000 -0.010
DRILL CHANNEL
1.225 0.000 -0.030
0.450 0.000 -0.005
0.450 0.000 -0.005
0.745± 0.005
1.360 +0.030 0.000
A
A
UNLESS OTHERWISE SPECIFIED
DIMENSIONS ARE IN INCHES
TOLERANCES: (UNLESS SPECIFIED)
DECIMALS ANGLES
.X ± .06 ± 1/2°
.XX ± .03
.XXX ± .01
MATERIAL: OFHC COPPER
2 X SS-VCR-4-3 FITTINGS
2 X SS-4-VCR-1 F-NUTS
LV DISK DRIVE ASSEMBLY
PART 3 - VIEW 3 OF 4
TITLE: LN2 COOLED BEARING
HOUSING - SECTION A-A
FILE: P3CDSKDR.DWG
DWG BY: JAMES M. SPOTTS
DATE: 5-28-97 SCALE: 1:1
PROF. M. OKUMURA LABORATORY
DIVISION OF CHEMISTRY: CALIFORNIA
INSTITUTE OF TECHINOLOGY

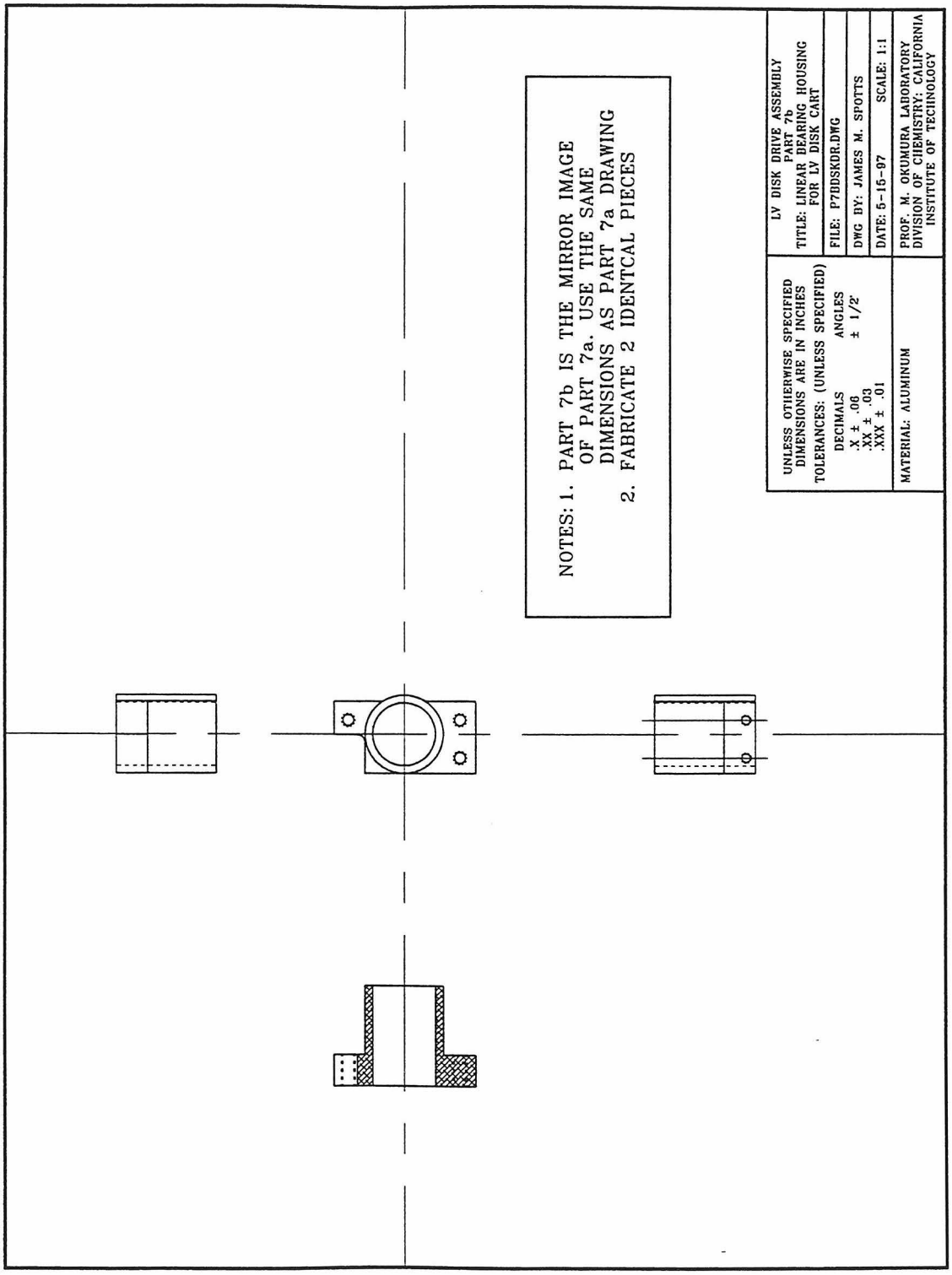

B
B
B
B
45°
ø0.350 +0.001 0.000
TO SLIP FIT
VCR FITTING
0.250
COUNTERBORE
DEPTH
ø0.200 −0.000 0.010
INLET CHANNEL
SILVER
SOLDER
UNLESS OTHERWISE SPECIFIED
DIMENSIONS ARE IN INCHES
TOLERANCES: (UNLESS SPECIFIED)
DECIMALS ANGLES
.X ± .06 ± 1/2°
.XX ± .03
.XXX ± .01
MATERIAL: OFHC COPPER
2 X SS-VCR-4-3 FITTINGS
2 X SS-4-VCR-1 F-NUTS
LV DISK DRIVE ASSEMBLY
PART 3 - VIEW 4 OF 4
TITLE: LN2 COOLED BEARING
HOUSING VIEW B-B
FILE: P3DDSKDR.DWG
DWG BY: JAMES M. SPOTTS
DATE: 5-28-97 SCALE: 1:1
PROF. M. OKUMURA LABORATORY
DIVISION OF CHEMISTRY; CALIFORNIA
INSTITUTE OF TECHNOLOGY

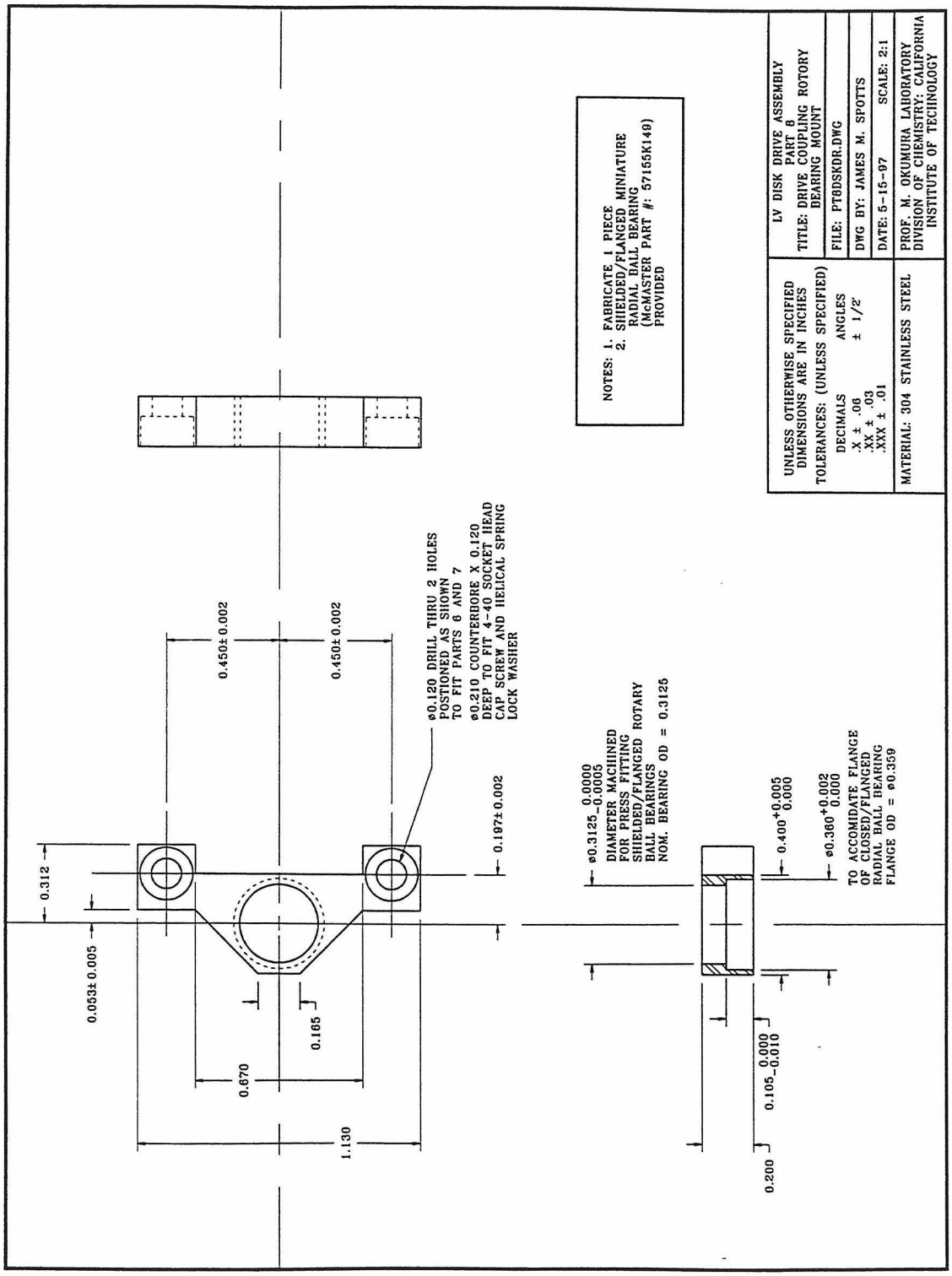

0.350
0.780
0.650
0.150± 0.002
0.150± 0.002
0.290
A
A
DRILL THRU CLOSE CLEARANCE FOR 4-40 UNC SOCKET HEAD CAP SCREW 2 HOLES POSITIONED AS SHOWN - HOLES TO ALLIGN WITH PART 3
DRILL THRU CLOSE CLEARANCE FOR 4-40 UNC SOCKET HEAD CAP SCREW 2 HOLES POSITIONED AS SHOWN - HOLES TO ALLIGN WITH PART 3
DRILL THRU AND TAP THRU FOR 4-40 UNC SOCKET HEAD CAP SCREW 2 HOLES POSITIONED AS SHOWN - HOLES TO ALLIGN WITH PART 3
SECTION A-A
0.038+0.005 0.000
0.050± 0.005
0.450
0.300
0.100± 0.002 TO MATCH PART 3
0.500+0.001 0.000 TO SLIP FIT WITHOUT PLAY PART 3
0.250 WIDTH TO ACCOMIDATE 4-40 SOCKET HEAD SCREW AND HELICAL SPRING LOCK WASHER
FABRICATE 2 IDENTICAL PIECES
UNLESS OTHERWISE SPECIFIED DIMENSIONS ARE IN INCHES
TOLERANCES: (UNLESS SPECIFIED)
DECIMALS ANGLES
X ± .08 ± 1/2°
.XX ± .03
.XXX ± .01
MATERIAL: 304 STAINLESS STEEL
LV DISK DRIVE ASSEMBLY
PART 4
TITLE: BEARING HOUSING ADAPTOR TO LV CART
FILE: PT4DSKDR.DWG
DWG BY: JAMES M. SPOTTS
DATE: 5-15-97 SCALE: 2:1
PROF. M. OKUMURA LABORATORY
DIVISION OF CHEMISTRY: CALIFORNIA INSTITUTE OF TECHNOLOGY

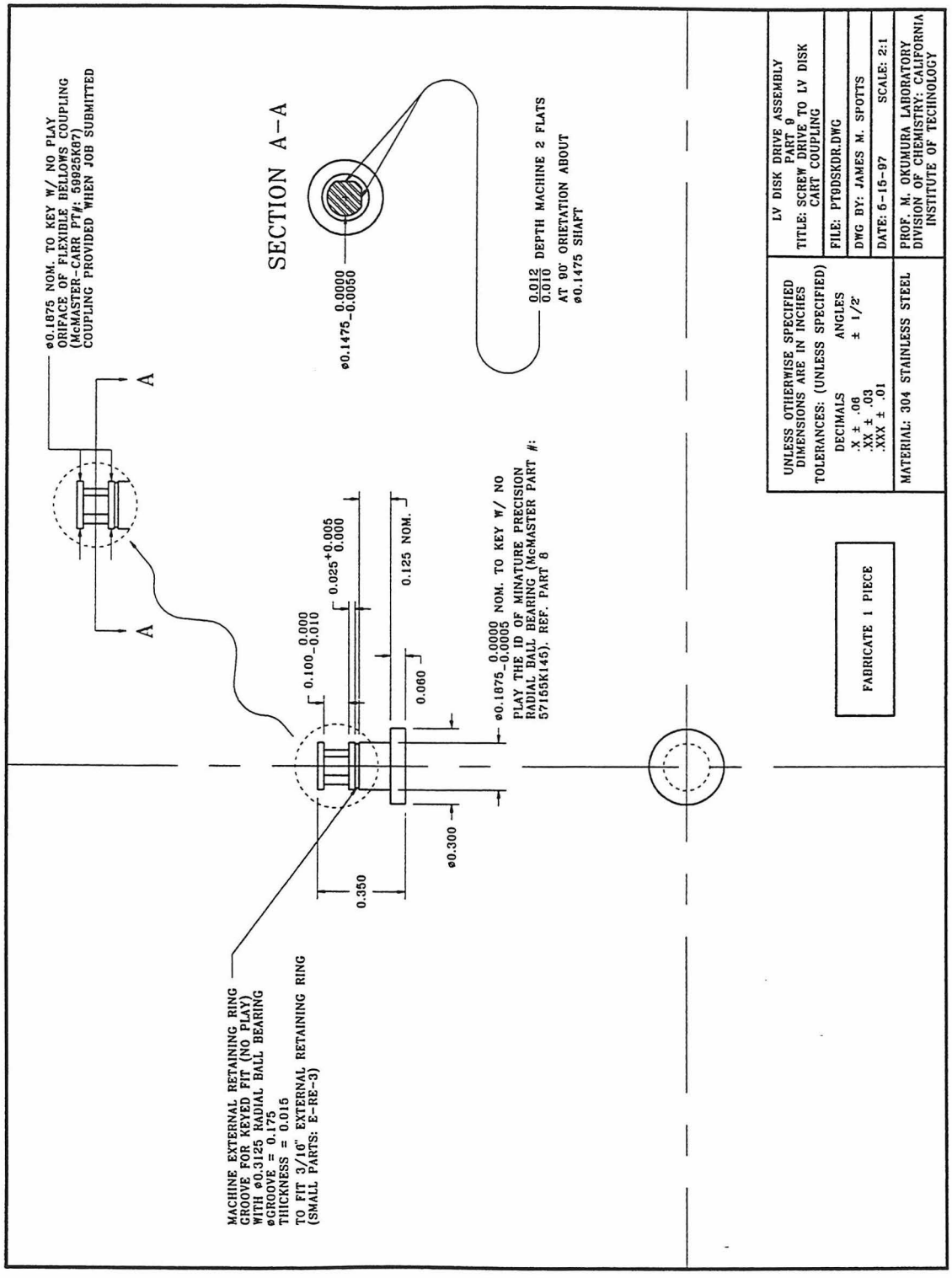

ø0.250
0.015
0.020
DRILL THRU TO
CENTER ONE
OUTGASSING HOLE
ø0.180
NOTES: 1. FABRICATE 4 IDENTICAL PIECES
2. ALL 4 PIECES TO BE MACHINED
TO IDENTICAL LENGHTS
WITHIN TOLERANCE
0.100
0.100
0.750
DRILL THRU AND TAP THRU
FOR 4-40 UNC ALONG
AXIAL LENGTH
UNLESS OTHERWISE SPECIFIED
DIMENSIONS ARE IN INCHES
TOLERANCES: (UNLESS SPECIFIED)
DECIMALS ANGLES
.X ± .06 ± 1/2°
.XX ± .03
.XXX ± .01
MATERIAL: VESPEL SP-1
LV DISK DRIVE ASSEMBLY
PART 5
TITLE: THERMALLY INSULATING
VESPEL POSTS
FILE: PT5DSKDR.DWG
DWG BY: JAMES M. SPOTTS
DATE: 6-15-97 SCALE: 2:1
PROF. M. OKUMURA LABORATORY
DIVISION OF CHEMISTRY: CALIFORNIA
INSTITUTE OF TECHNOLOGY

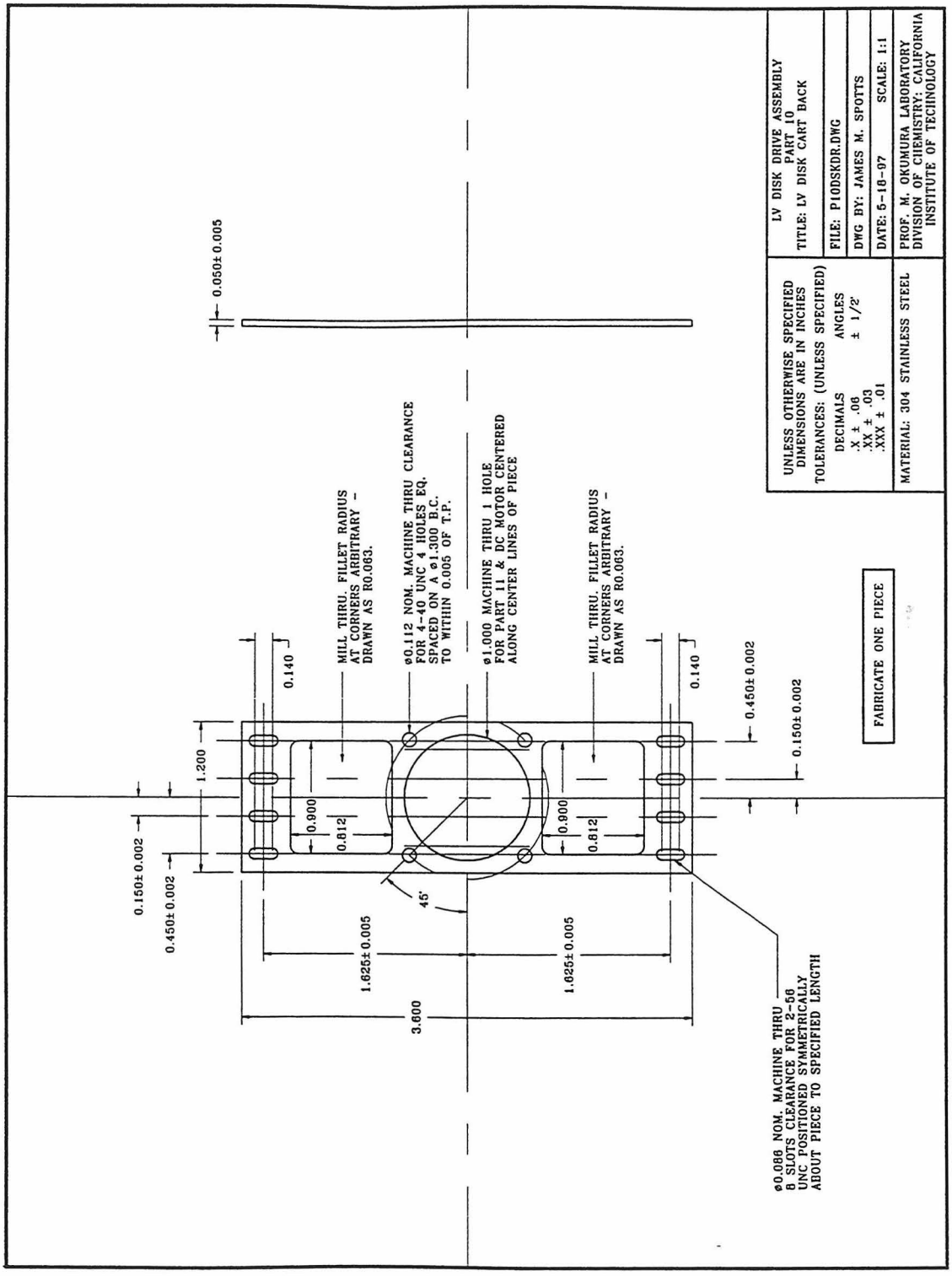

NOTES: 1. FABRICATE 2 IDENTICAL PIECES
2. MATERIAL SHOULD BE FLAT
UNLESS OTHERWISE SPECIFIED
DIMENSIONS ARE IN INCHES
TOLERANCES: (UNLESS SPECIFIED)
DECIMALS ANGLES
.X ± .06 ± 1/2°
.XX ± .03
.XXX ± .01
MATERIAL: 304 STAINLESS STEEL
LV DISK DRIVE ASSEMBLY
PART 6
TITLE: LV DISK CART TOP/BOTTOM PLATE
FILE: PT6DSKDR.DWG
DWG BY: JAMES M. SPOTTS
DATE: 5-10-97 SCALE: 1:1
PROF. M. OKUMURA LABORATORY
DIVISION OF CHEMISTRY: CALIFORNIA INSTITUTE OF TECHNOLOGY
ø0.375 DRILL THRU 2 HOLES POSITIONED AS SHOWN
0.050± 0.005
1.307
DRILL THRU CLEARANCE FOR 4-40 UNC 6 HOLES POSITIONED AS SHOWN
0.150± 0.002
0.450± 0.002
1.200
0.337
0.447± 0.002
0.447± 0.002
0.560± 0.002
0.450± 0.002
0.337
0.150± 0.002

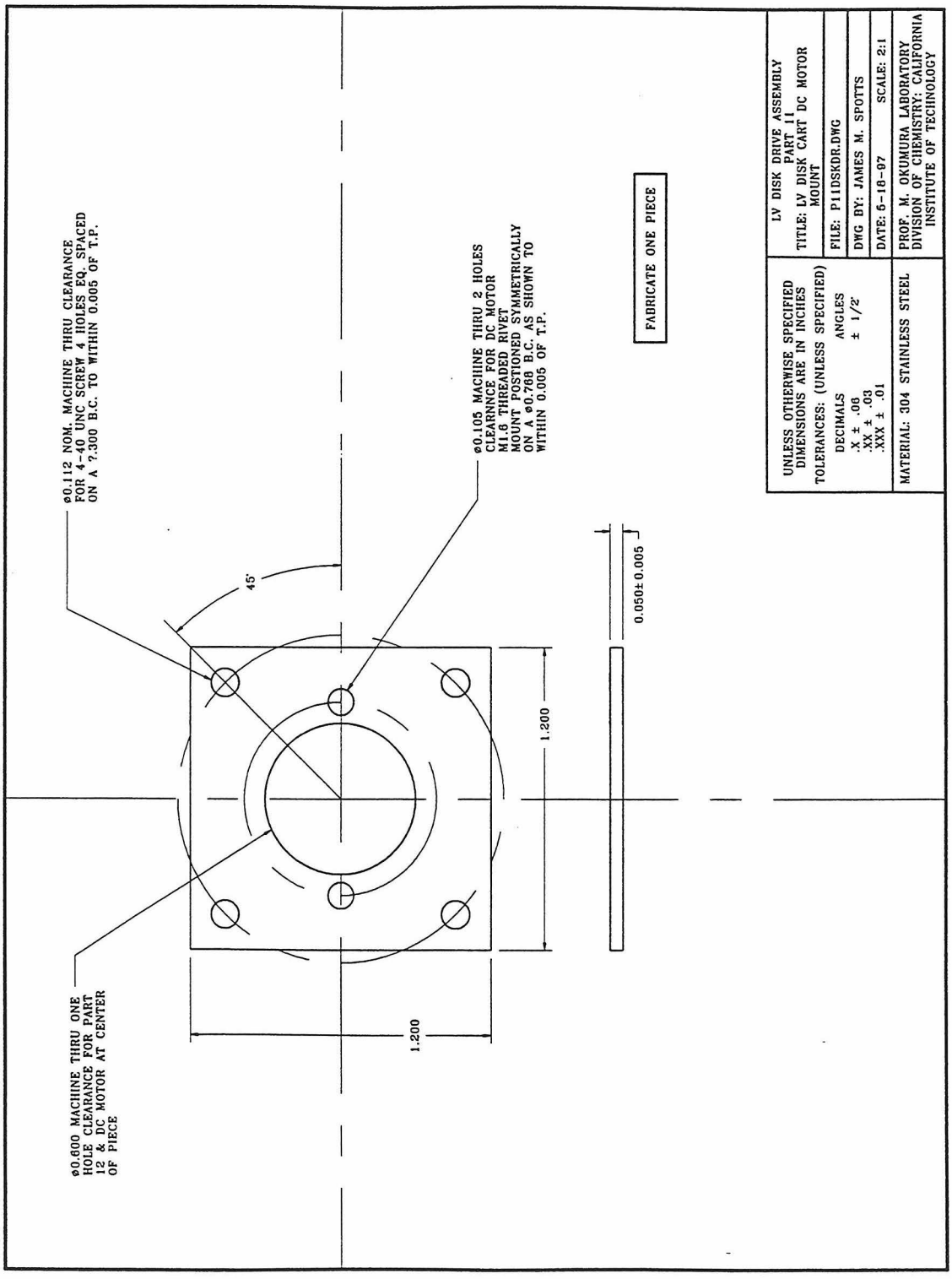

NOTES: 1. FABRICATE 2 IDENTICAL PIECES
2. LINEAR BEARING HOUSING 7a IS MIRROR IMAGE OF PART 7b
3. LINEAR BALL BEARINGS WILL BE PROVIDED
UNLESS OTHERWISE SPECIFIED DIMENSIONS ARE IN INCHES
TOLERANCES: (UNLESS SPECIFIED)
DECIMALS ANGLES
X ± .00 ± 1/2°
.XX ± .03
.XXX ± .01
MATERIAL: ALUMINUM
LV DISK DRIVE ASSEMBLY
PART 7a
TITLE: LINEAR BEARING HOUSING FOR LV DISK CART
FILE: P7ADSKDR.DWG
DWG BY: JAMES M. SPOTTS
DATE: 5-15-97 SCALE: 1:1
PROF. M. OKUMURA LABORATORY
DIVISION OF CHEMISTRY: CALIFORNIA INSTITUTE OF TECHNOLOGY
PRESS FIT ø0.500 OD LINEAR BEARING (McMASTER PART: 6084K51) BEARING FIT SUCH THAT BOTH SURFACES LIE BELOW PILLOW BLOCK FACE
ø0.5000 0.0000 -0.0005
ø0.625 0.000 -0.005
CAN FILLET TO ARBITRARY RADIUS. DRAWN AS R0.063
0.312 +0.005 0.000
0.250 +0.005 0.000
0.575
0.187± 0.002
0.075± 0.002
0.800
0.187± 0.002
0.113± 0.002
0.113± 0.002
0.447± 0.002
0.447± 0.002
0.562
0.572 +0.010 0.000
MACHINE BASE OF HOUSING TO MATCH OD OF PILLOW BLOCK. FILLET PERMISSIBLE AT JUNCTION
DRILL THRU AND TAP THRU 3 HOLES FOR 4-40 UNC POSITIONED AS SHOWN TO MOUNT PART 6
DRILL THRU AND TAP THRU TO 4-40 TAPPED HOLE 2 HOLES FOR 2-56 UNC POSITIONED AS SHOWN

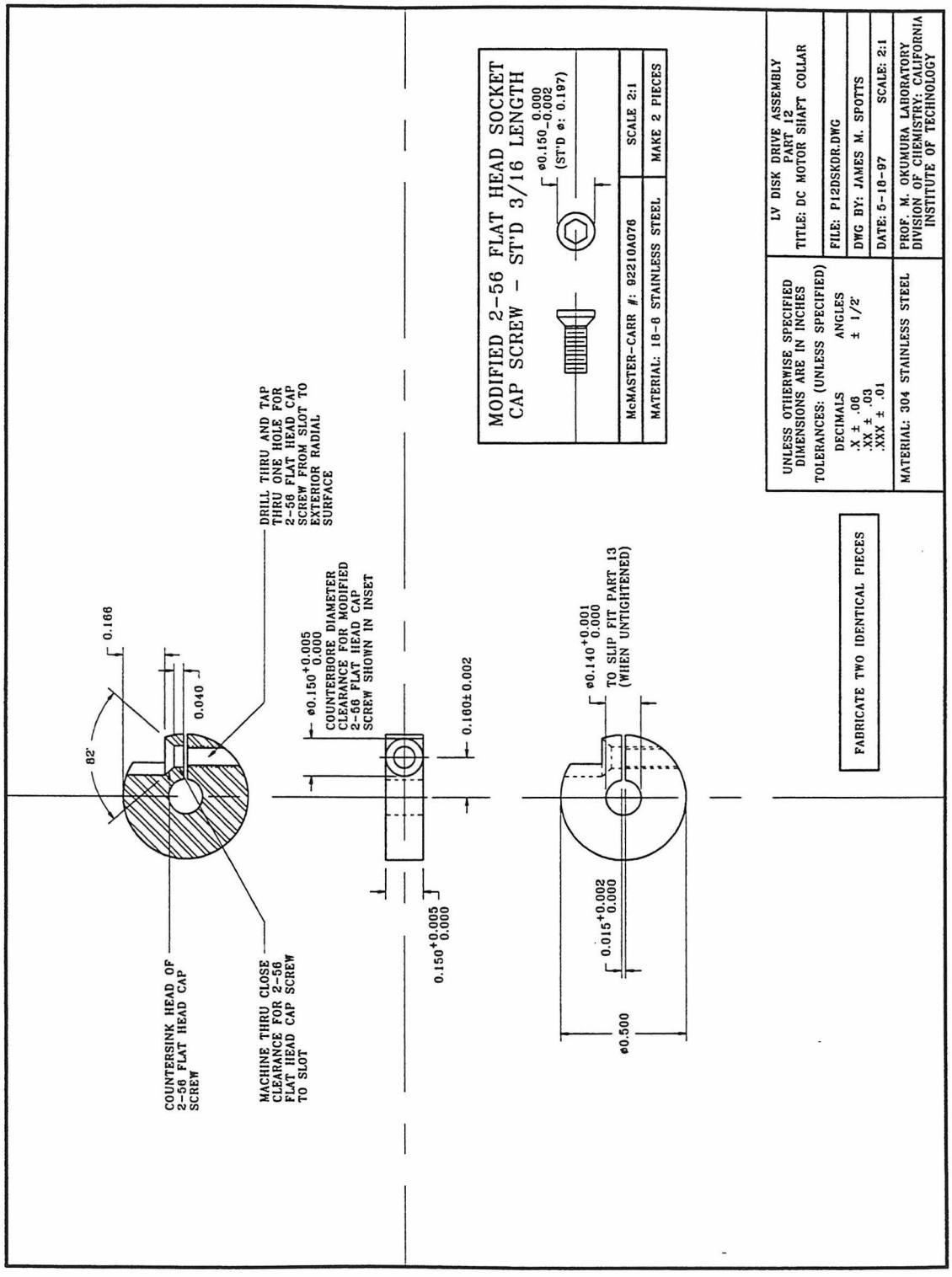

NOTES: 1. PART 7b IS THE MIRROR IMAGE
OF PART 7a. USE THE SAME
DIMENSIONS AS PART 7a DRAWING
2. FABRICATE 2 IDENTCAL PIECES
LV DISK DRIVE ASSEMBLY
PART 7b
TITLE: LINEAR BEARING HOUSING
FOR LV DISK CART
FILE: P7BDSKDR.DWG
DWG BY: JAMES M. SPOTTS
DATE: 5-15-97
SCALE: 1:1
PROF. M. OKUMURA LABORATORY
DIVISION OF CHEMISTRY: CALIFORNIA
INSTITUTE OF TECHNOLOGY
UNLESS OTHERWISE SPECIFIED
DIMENSIONS ARE IN INCHES
TOLERANCES: (UNLESS SPECIFIED)
DECIMALS
.X ± .06
.XX ± .03
.XXX ± .01
ANGLES
± 1/2°
MATERIAL: ALUMINUM

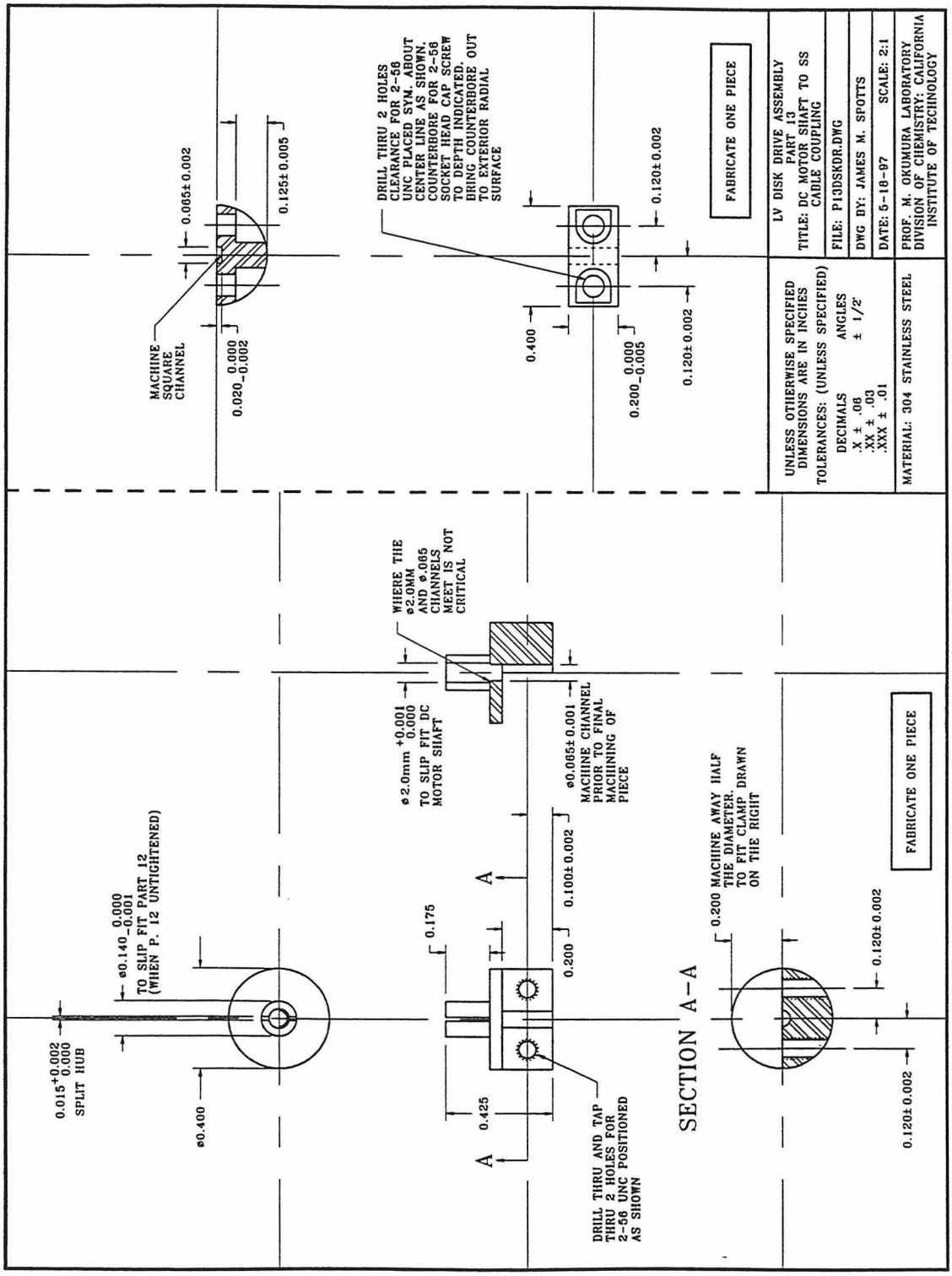

NOTES: 1. FABRICATE 1 PIECE
2. SHIELDED/FLANGED MINIATURE RADIAL BALL BEARING (McMASTER PART #: 57155K149) PROVIDED
UNLESS OTHERWISE SPECIFIED DIMENSIONS ARE IN INCHES
TOLERANCES: (UNLESS SPECIFIED)
DECIMALS ANGLES
.X ± .06 ± 1/2°
.XX ± .03
.XXX ± .01
MATERIAL: 304 STAINLESS STEEL
LV DISK DRIVE ASSEMBLY
PART 8
TITLE: DRIVE COUPLING ROTORY BEARING MOUNT
FILE: PT8DSKDR.DWG
DWG BY: JAMES M. SPOTTS
DATE: 5-15-97 SCALE: 2:1
PROF. M. OKUMURA LABORATORY
DIVISION OF CHEMISTRY: CALIFORNIA INSTITUTE OF TECHNOLOGY
ø0.120 DRILL THRU 2 HOLES POSTIONED AS SHOWN TO FIT PARTS 6 AND 7
ø0.210 COUNTERBORE X 0.120 DEEP TO FIT 4-40 SOCKET HEAD CAP SCREW AND HELICAL SPRING LOCK WASHER
0.450± 0.002
0.450± 0.002
0.197± 0.002
0.312
0.053± 0.005
0.165
0.670
1.130
ø0.3125 -0.0000 -0.0005
DIAMETER MACHINED FOR PRESS FITTING SHIELDED/FLANGED ROTARY BALL BEARINGS NOM. BEARING OD = 0.3125
0.400 +0.005 0.000
ø0.360 +0.002 0.000
TO ACCOMIDATE FLANGE OF CLOSED/FLANGED RADIAL BALL BEARING FLANGE OD = ø0.359
0.105 -0.000 -0.010
0.200

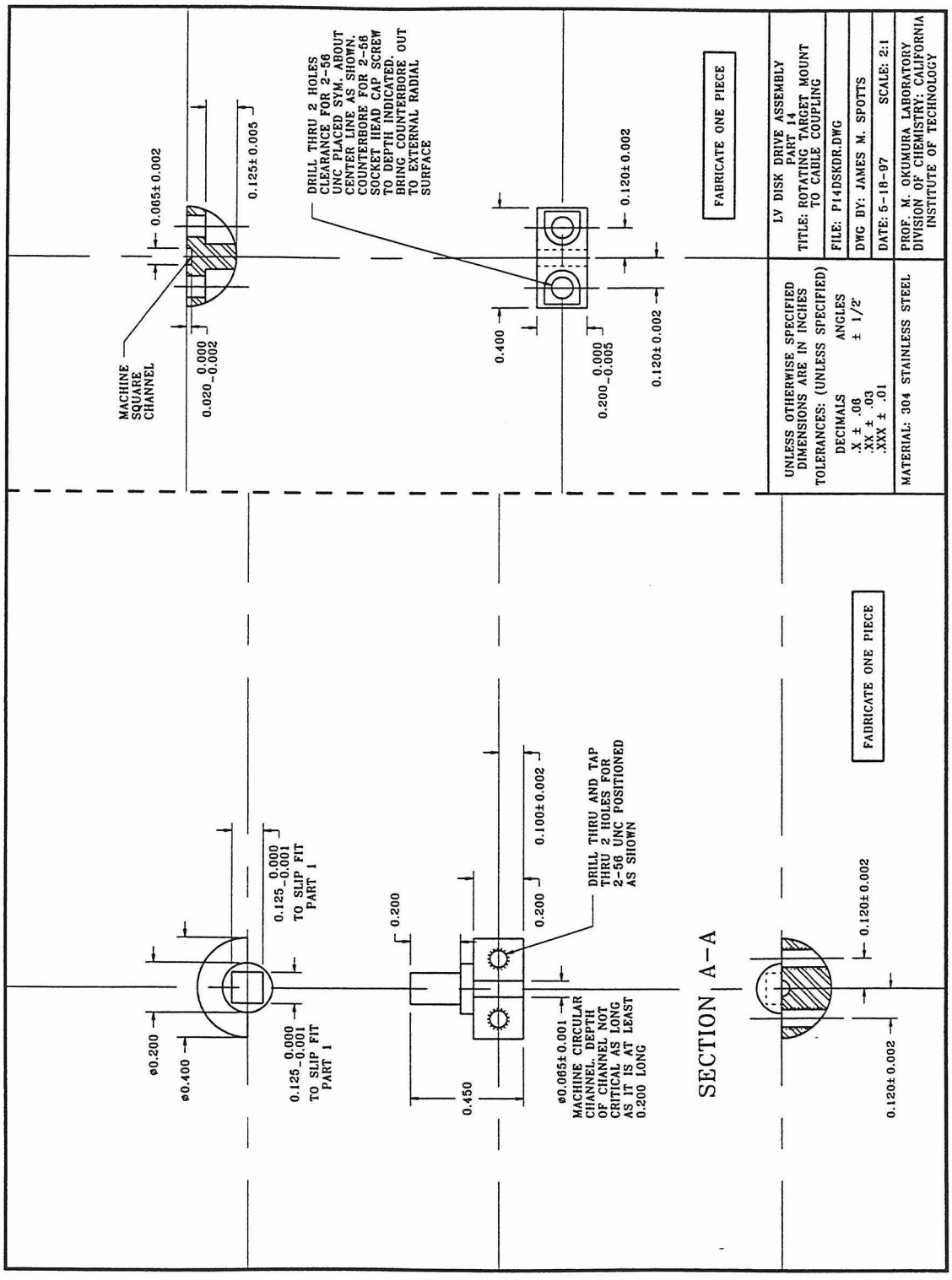

SECTION A-A
ø0.1875 NOM. TO KEY W/ NO PLAY
ORIFACE OF FLEXIBLE BELLOWS COUPLING
(McMASTER-CARR PT#: 59925K87)
COUPLING PROVIDED WHEN JOB SUBMITTED
A
A
ø0.1475 0.0000 -0.0050
0.012 0.010 DEPTH MACHINE 2 FLATS
AT 90° ORIETATION ABOUT
ø0.1475 SHAFT
0.100 0.000 -0.010
0.025 +0.005 0.000
0.125 NOM.
0.080
ø0.1875 0.0000 -0.0005 NOM. TO KEY W/ NO
PLAY THE ID OF MINATURE PRECISION
RADIAL BALL BEARING (McMASTER PART #:
57155K145). REF. PART 8
ø0.300
0.350
MACHINE EXTERNAL RETAINING RING
GROOVE FOR KEYED FIT (NO PLAY)
WITH ø0.3125 RADIAL BALL BEARING
øGROOVE = 0.175
THICKNESS = 0.015
TO FIT 3/16" EXTERNAL RETAINING RING
(SMALL PARTS: E-RE-3)
FABRICATE 1 PIECE
UNLESS OTHERWISE SPECIFIED
DIMENSIONS ARE IN INCHES
TOLERANCES: (UNLESS SPECIFIED)
DECIMALS ANGLES
X ± .06 ± 1/2°
.XX ± .03
.XXX ± .01
MATERIAL: 304 STAINLESS STEEL
LV DISK DRIVE ASSEMBLY
PART 9
TITLE: SCREW DRIVE TO LV DISK
CART COUPLING
FILE: PT9DSKDR.DWG
DWG BY: JAMES M. SPOTTS
DATE: 6-15-97 SCALE: 2:1
PROF. M. OKUMURA LABORATORY
DIVISION OF CHEMISTRY: CALIFORNIA
INSTITUTE OF TECHNOLOGY

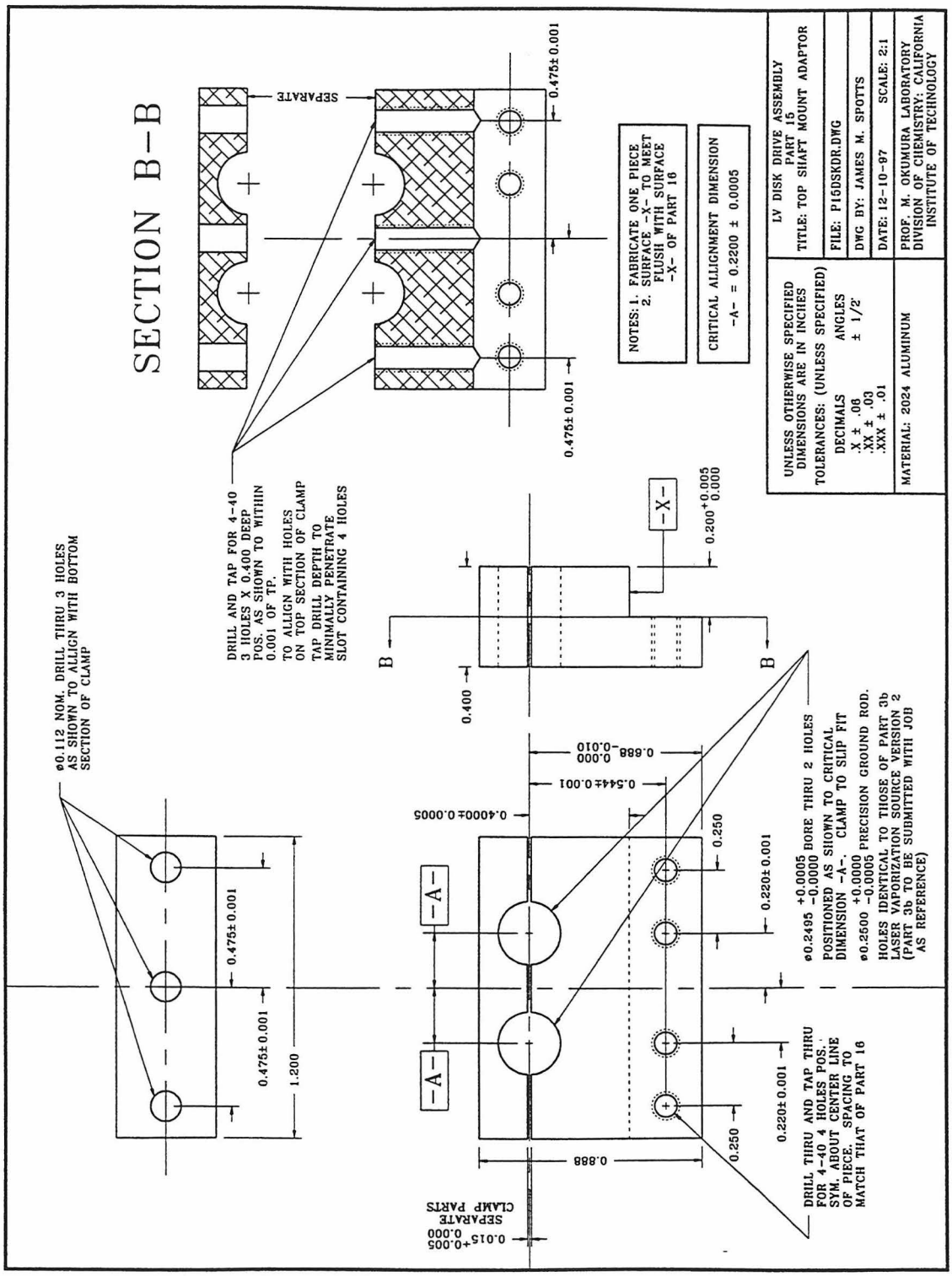

0.050± 0.005
MILL THRU. FILLET RADIUS
AT CORNERS ARBITRARY -
DRAWN AS R0.063.
ø0.112 NOM. MACHINE THRU CLEARANCE
FOR 4-40 UNC 4 HOLES EQ.
SPACED ON A ø1.300 B.C.
TO WITHIN 0.005 OF T.P.
ø1.000 MACHINE THRU 1 HOLE
FOR PART 11 & DC MOTOR CENTERED
ALONG CENTER LINES OF PIECE
MILL THRU. FILLET RADIUS
AT CORNERS ARBITRARY -
DRAWN AS R0.063.
0.140
0.140
0.450± 0.002
0.150± 0.002
1.200
0.900
0.812
0.900
0.812
45°
0.150± 0.002
0.450± 0.002
1.625± 0.005
1.625± 0.005
3.600
ø0.086 NOM. MACHINE THRU
8 SLOTS CLEARANCE FOR 2-56
UNC POSITIONED SYMMETRICALLY
ABOUT PIECE TO SPECIFIED LENGTH
FABRICATE ONE PIECE
UNLESS OTHERWISE SPECIFIED
DIMENSIONS ARE IN INCHES
TOLERANCES: (UNLESS SPECIFIED)
DECIMALS ANGLES
.X ± .06 ± 1/2°
.XX ± .03
.XXX ± .01
MATERIAL: 304 STAINLESS STEEL
LV DISK DRIVE ASSEMBLY
PART 10
TITLE: LV DISK CART BACK
FILE: P10DSKDR.DWG
DWG BY: JAMES M. SPOTTS
DATE: 5-10-97 SCALE: 1:1
PROF. M. OKUMURA LABORATORY
DIVISION OF CHEMISTRY: CALIFORNIA
INSTITUTE OF TECHNOLOGY

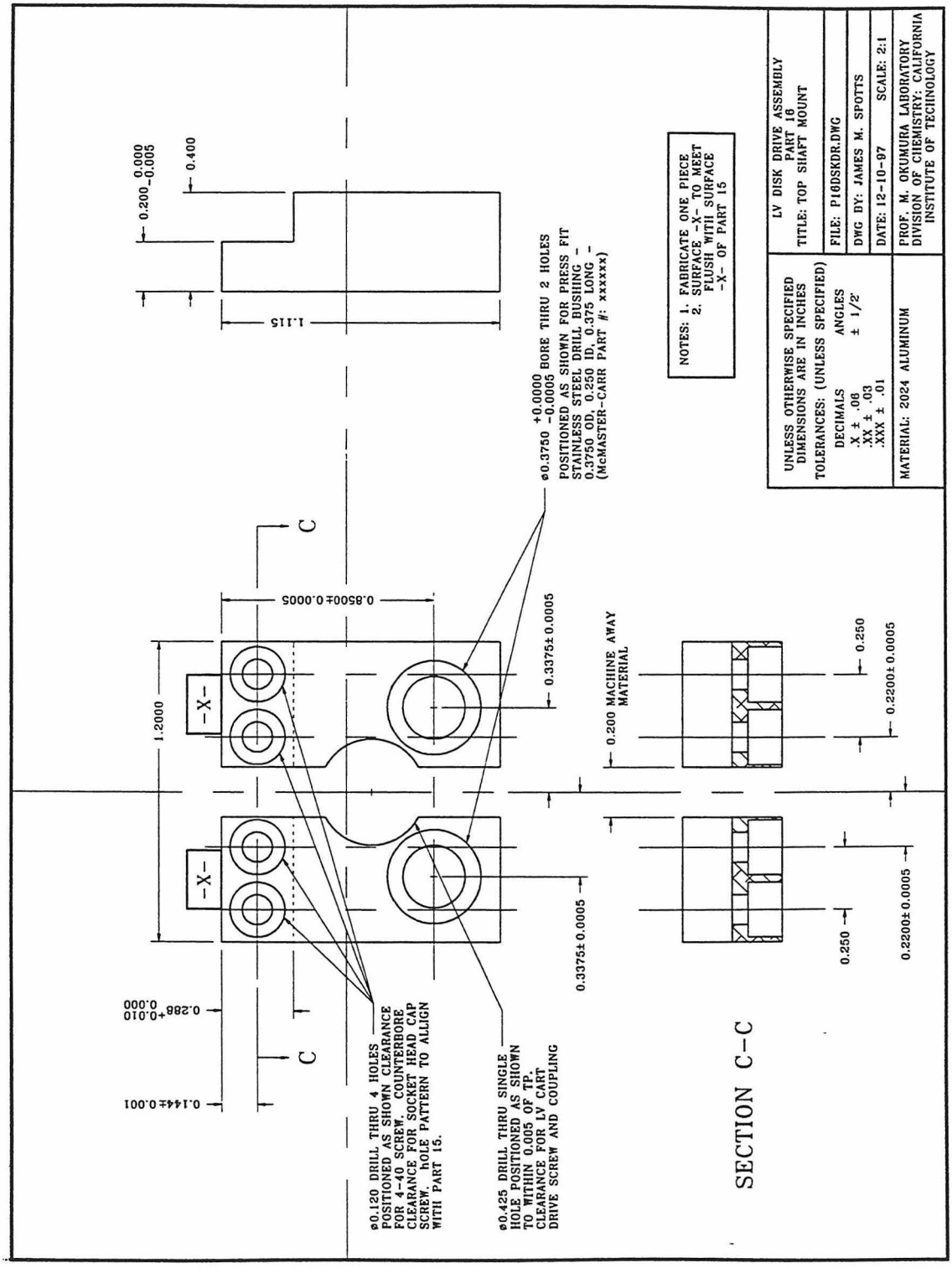

ø0.112 NOM. MACHINE THRU CLEARANCE
FOR 4-40 UNC SCREW 4 HOLES EQ. SPACED
ON A ?.300 B.C. TO WITHIN 0.005 OF T.P.
ø0.105 MACHINE THRU 2 HOLES
CLEARNNCE FOR DC MOTOR
M1.6 THREADED RIVET
MOUNT POSTIONED SYMMETRICALLY
ON A ø0.760 B.C. AS SHOWN TO
WITHIN 0.005 OF T.P.
45°
1.200
1.200
0.050±0.005
FABRICATE ONE PIECE
ø0.600 MACHINE THRU ONE
HOLE CLEARANCE FOR PART
12 & DC MOTOR AT CENTER
OF PIECE
UNLESS OTHERWISE SPECIFIED
DIMENSIONS ARE IN INCHES
TOLERANCES: (UNLESS SPECIFIED)
DECIMALS ANGLES
.X ± .06 ± 1/2°
.XX ± .03
.XXX ± .01
MATERIAL: 304 STAINLESS STEEL
LV DISK DRIVE ASSEMBLY
PART 11
TITLE: LV DISK CART DC MOTOR
MOUNT
FILE: P11DSKDR.DWG
DWG BY: JAMES M. SPOTTS
DATE: 6-18-97
SCALE: 2:1
PROF. M. OKUMURA LABORATORY
DIVISION OF CHEMISTRY: CALIFORNIA
INSTITUTE OF TECHNOLOGY

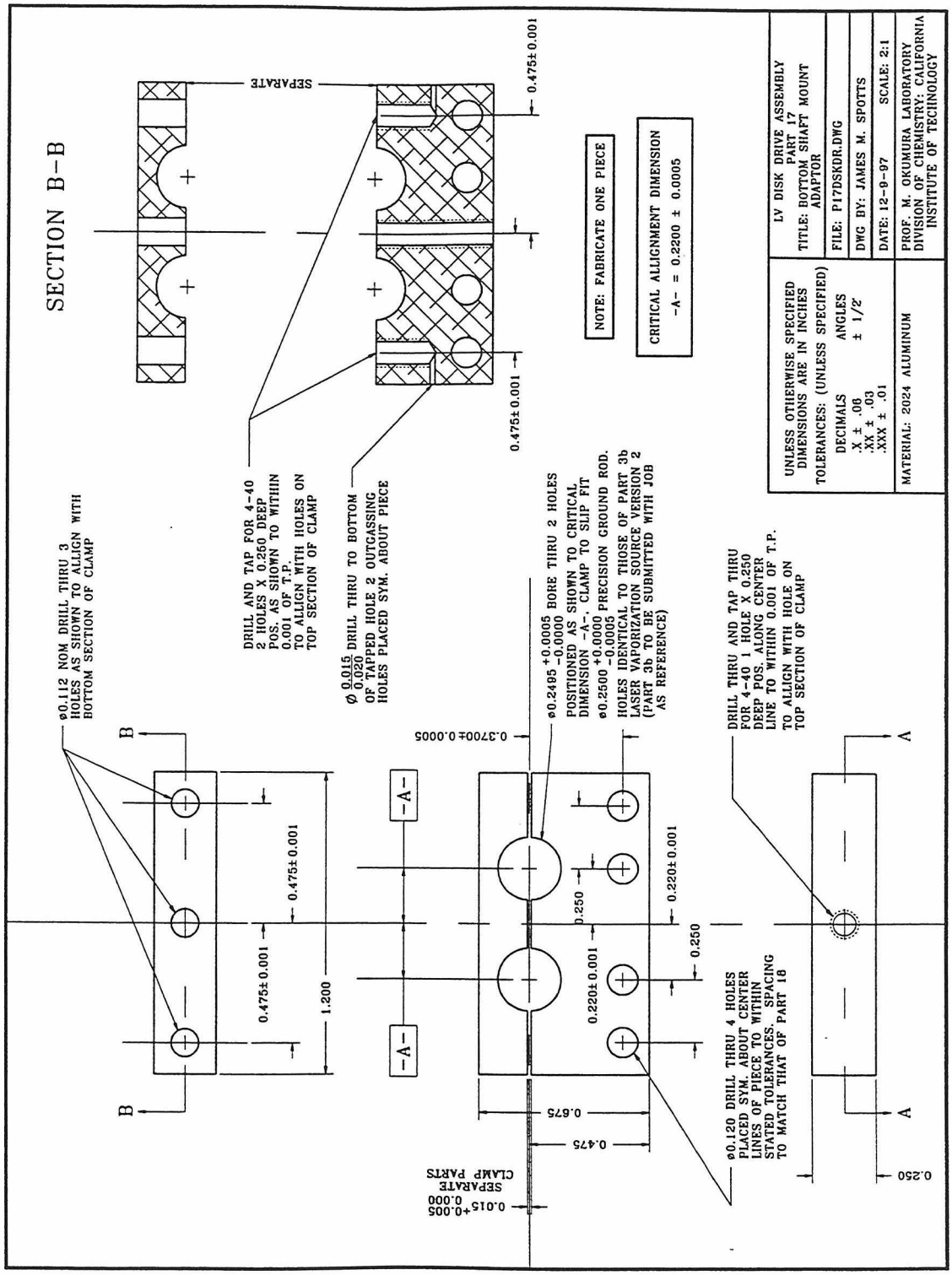

MODIFIED 2-56 FLAT HEAD SOCKET CAP SCREW - ST'D 3/16 LENGTH
ø0.150 0.000 -0.002 (ST'D ø: 0.197)
McMASTER-CARR #: 92210A076
SCALE 2:1
MATERIAL: 18-8 STAINLESS STEEL
MAKE 2 PIECES
0.166
0.040
82°
COUNTERSINK HEAD OF 2-56 FLAT HEAD CAP SCREW
MACHINE THRU CLOSE CLEARANCE FOR 2-56 FLAT HEAD CAP SCREW TO SLOT
DRILL THRU AND TAP THRU ONE HOLE FOR 2-56 FLAT HEAD CAP SCREW FROM SLOT TO EXTERIOR RADIAL SURFACE
ø0.150 +0.005 0.000
COUNTERBORE DIAMETER CLEARANCE FOR MODIFIED 2-56 FLAT HEAD CAP SCREW SHOWN IN INSET
0.160± 0.002
0.150 +0.005 0.000
ø0.140 +0.001 0.000
TO SLIP FIT PART 13 (WHEN UNTIGHTENED)
0.015 +0.002 0.000
ø0.500
FABRICATE TWO IDENTICAL PIECES
UNLESS OTHERWISE SPECIFIED DIMENSIONS ARE IN INCHES
TOLERANCES: (UNLESS SPECIFIED)
DECIMALS ANGLES
.X ± .06 ± 1/2°
.XX ± .03
.XXX ± .01
MATERIAL: 304 STAINLESS STEEL
LV DISK DRIVE ASSEMBLY PART 12
TITLE: DC MOTOR SHAFT COLLAR
FILE: P12DSKDR.DWG
DWG BY: JAMES M. SPOTTS
DATE: 5-16-97
SCALE: 2:1
PROF. M. OKUMURA LABORATORY
DIVISION OF CHEMISTRY: CALIFORNIA INSTITUTE OF TECHNOLOGY

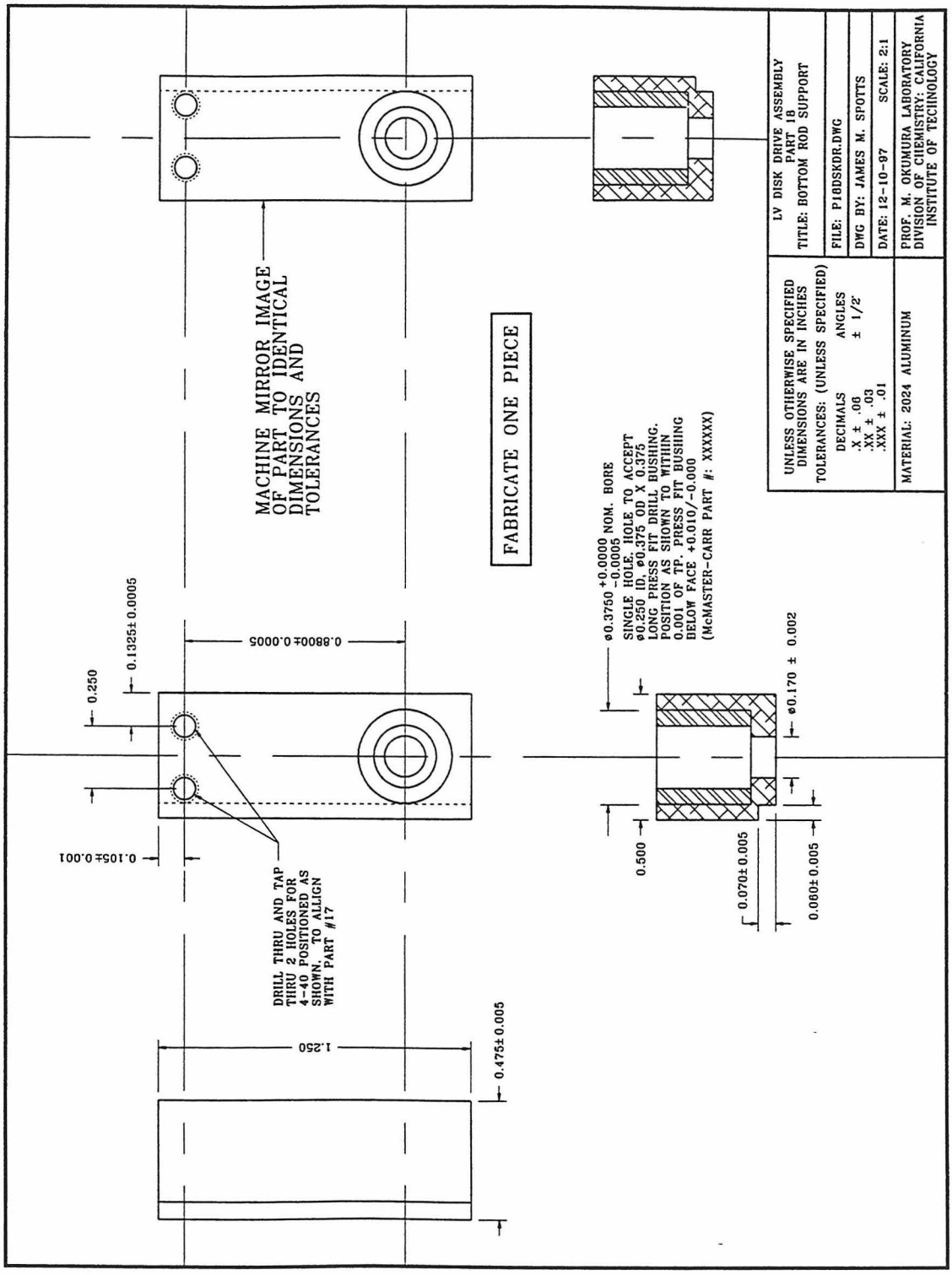

0.015+0.002 0.000
SPLIT HUB
ø0.140 0.000 -0.001
TO SLIP FIT PART 12
(WHEN P. 12 UNTIGHTENED)
ø0.400
0.175
A
A
0.425
ø2.0mm +0.001 0.000
TO SLIP FIT DC
MOTOR SHAFT
WHERE THE
ø2.0MM
AND ø.065
CHANNELS
MEET IS NOT
CRITICAL
ø0.065± 0.001
MACHINE CHANNEL
PRIOR TO FINAL
MACHINING OF
PIECE
0.200
0.100± 0.002
DRILL THRU AND TAP
THRU 2 HOLES FOR
2-56 UNC POSITIONED
AS SHOWN
SECTION A-A
0.200 MACHINE AWAY HALF
THE DIAMETER.
TO FIT CLAMP DRAWN
ON THE RIGHT
0.120± 0.002
0.120± 0.002
FABRICATE ONE PIECE
MACHINE
SQUARE
CHANNEL
0.020 0.000 -0.002
0.065± 0.002
0.125± 0.005
DRILL THRU 2 HOLES
CLEARANCE FOR 2-56
UNC PLACED SYM. ABOUT
CENTER LINE AS SHOWN.
COUNTERBORE FOR 2-56
SOCKET HEAD CAP SCREW
TO DEPTH INDICATED.
BRING COUNTERBORE OUT
TO EXTERIOR RADIAL
SURFACE
0.400
0.200 0.000 -0.005
0.120± 0.002
0.120± 0.002
FABRICATE ONE PIECE
LV DISK DRIVE ASSEMBLY
PART 13
TITLE: DC MOTOR SHAFT TO SS
CABLE COUPLING
FILE: P13DSKDR.DWG
DWG BY: JAMES M. SPOTTS
DATE: 5-18-97 SCALE: 2:1
UNLESS OTHERWISE SPECIFIED
DIMENSIONS ARE IN INCHES
TOLERANCES: (UNLESS SPECIFIED)
DECIMALS ANGLES
.X ± .06 ± 1/2°
.XX ± .03
.XXX ± .01
MATERIAL: 304 STAINLESS STEEL
PROF. M. OKUMURA LABORATORY
DIVISION OF CHEMISTRY: CALIFORNIA
INSTITUTE OF TECHNOLOGY

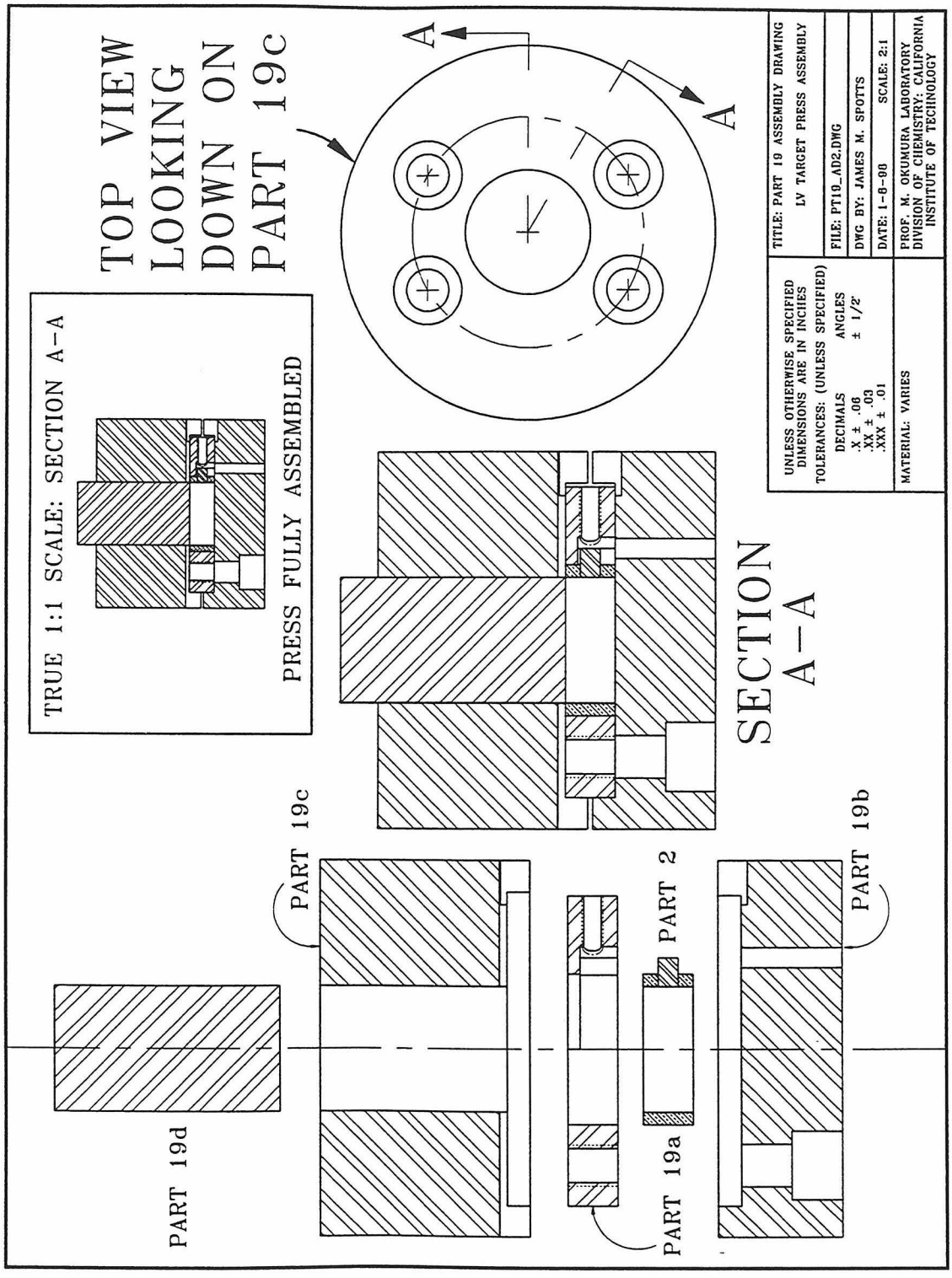

MACHINE SQUARE CHANNEL
0.020 0.000 -0.002
0.005± 0.002
0.125± 0.005
DRILL THRU 2 HOLES CLEARANCE FOR 2-56 UNC PLACED SYM. ABOUT CENTER LINE AS SHOWN. COUNTERBORE FOR 2-56 SOCKET HEAD CAP SCREW TO DEPTH INDICATED. BRING COUNTERBORE OUT TO EXTERNAL RADIAL SURFACE
0.400
0.200 0.000 -0.005
0.120± 0.002
0.120± 0.002
FABRICATE ONE PIECE
LV DISK DRIVE ASSEMBLY
PART 14
TITLE: ROTATING TARGET MOUNT
TO CABLE COUPLING
FILE: P14DSKDR.DWG
DWG BY: JAMES M. SPOTTS
DATE: 5-18-97
SCALE: 2:1
UNLESS OTHERWISE SPECIFIED
DIMENSIONS ARE IN INCHES
TOLERANCES: (UNLESS SPECIFIED)
DECIMALS
.X ± .06
.XX ± .03
.XXX ± .01
ANGLES
± 1/2'
MATERIAL: 304 STAINLESS STEEL
PROF. M. OKUMURA LABORATORY
DIVISION OF CHEMISTRY: CALIFORNIA
INSTITUTE OF TECHNOLOGY
ø0.200
ø0.400
0.125 0.000 -0.001
TO SLIP FIT
PART 1
0.125 0.000 -0.001
TO SLIP FIT
PART 1
0.200
0.450
0.200
0.100± 0.002
DRILL THRU AND TAP
THRU 2 HOLES FOR
2-56 UNC POSITIONED
AS SHOWN
ø0.065± 0.001
MACHINE CIRCULAR
CHANNEL, DEPTH
OF CHANNEL NOT
CRITICAL AS LONG
AS IT IS AT LEAST
0.200 LONG
SECTION A-A
FABRICATE ONE PIECE
0.120± 0.002
0.120± 0.002

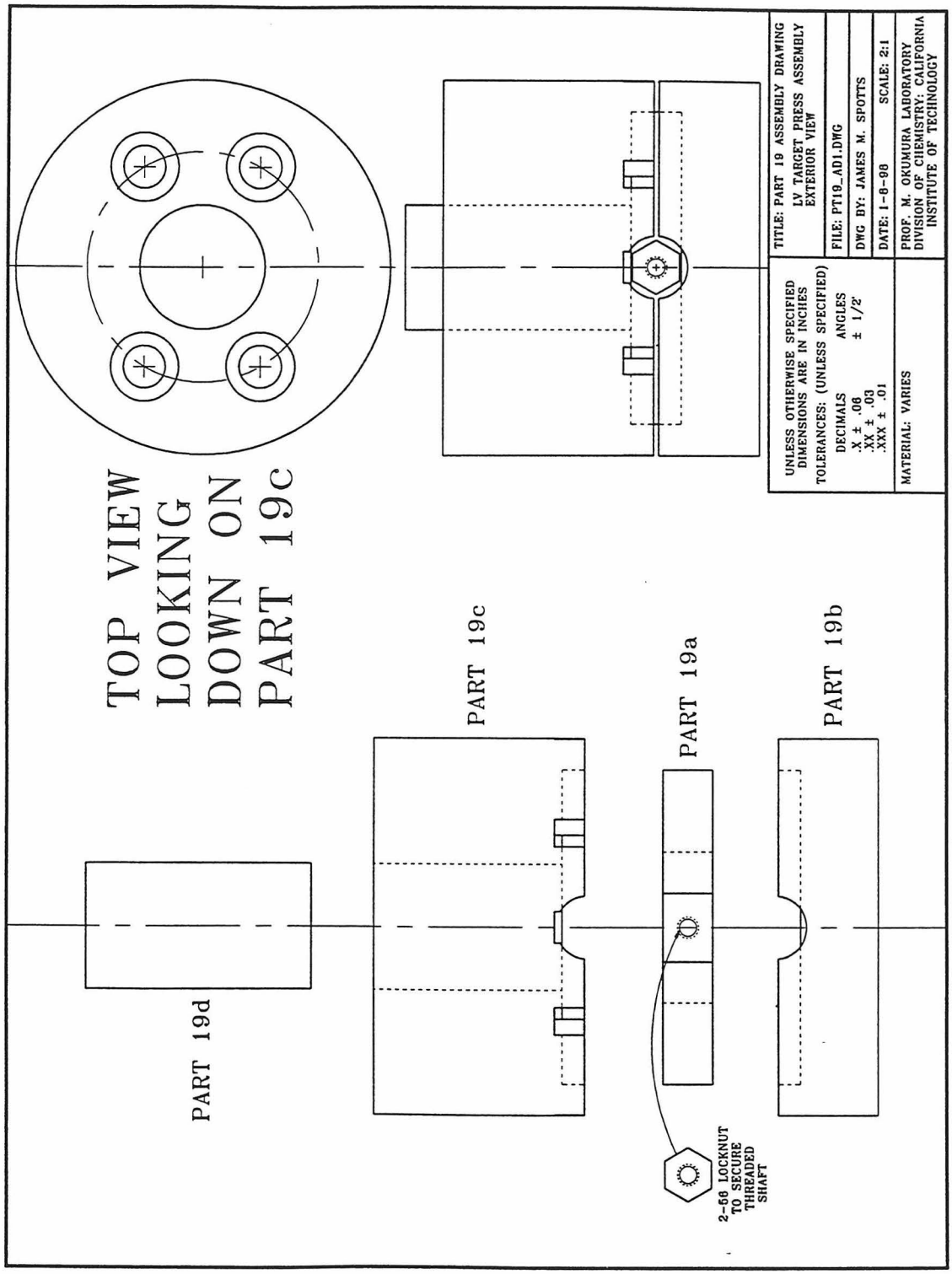

SECTION B-B
SEPARATE
0.475± 0.001
0.475± 0.001
DRILL AND TAP FOR 4-40
3 HOLES X 0.400 DEEP
POS. AS SHOWN TO WITHIN
0.001 OF TP.
TO ALLIGN WITH HOLES
ON TOP SECTION OF CLAMP
TAP DRILL DEPTH TO
MINIMALLY PENETRATE
SLOT CONTAINING 4 HOLES
NOTES: 1. FABRICATE ONE PIECE
2. SURFACE -X- TO MEET
FLUSH WITH SURFACE
-X- OF PART 16
CRITICAL ALLIGNMENT DIMENSION
-A- = 0.2200 ± 0.0005
UNLESS OTHERWISE SPECIFIED
DIMENSIONS ARE IN INCHES
TOLERANCES: (UNLESS SPECIFIED)
DECIMALS ANGLES
.X ± .06 ± 1/2°
.XX ± .03
.XXX ± .01
MATERIAL: 2024 ALUMINUM
LV DISK DRIVE ASSEMBLY
PART 15
TITLE: TOP SHAFT MOUNT ADAPTOR
FILE: P15DSKDR.DWG
DWG BY: JAMES M. SPOTTS
DATE: 12-10-97 SCALE: 2:1
PROF. M. OKUMURA LABORATORY
DIVISION OF CHEMISTRY: CALIFORNIA
INSTITUTE OF TECHNOLOGY
ø0.112 NOM. DRILL THRU 3 HOLES
AS SHOWN TO ALIGN WITH BOTTOM
SECTION OF CLAMP
0.475± 0.001
0.475± 0.001
1.200
B
B
0.400
0.200 +0.005 0.000
-X-
0.868 0.000 -0.010
0.544± 0.001
0.4000± 0.0005
0.250
0.220± 0.001
-A-
-A-
0.220± 0.001
0.250
0.868
0.015 +0.005 0.000
SEPARATE
CLAMP PARTS
ø0.2495 +0.0005 -0.0000 BORE THRU 2 HOLES
POSITIONED AS SHOWN TO CRITICAL
DIMENSION -A-. CLAMP TO SLIP FIT
ø0.2500 +0.0000 -0.0005 PRECISION GROUND ROD.
HOLES IDENTICAL TO THOSE OF PART 3b
LASER VAPORIZATION SOURCE VERSION 2
(PART 3b TO BE SUBMITTED WITH JOB
AS REFERENCE)
DRILL THRU AND TAP THRU
FOR 4-40 4 HOLES POS.
SYM. ABOUT CENTER LINE
OF PIECE. SPACING TO
MATCH THAT OF PART 16

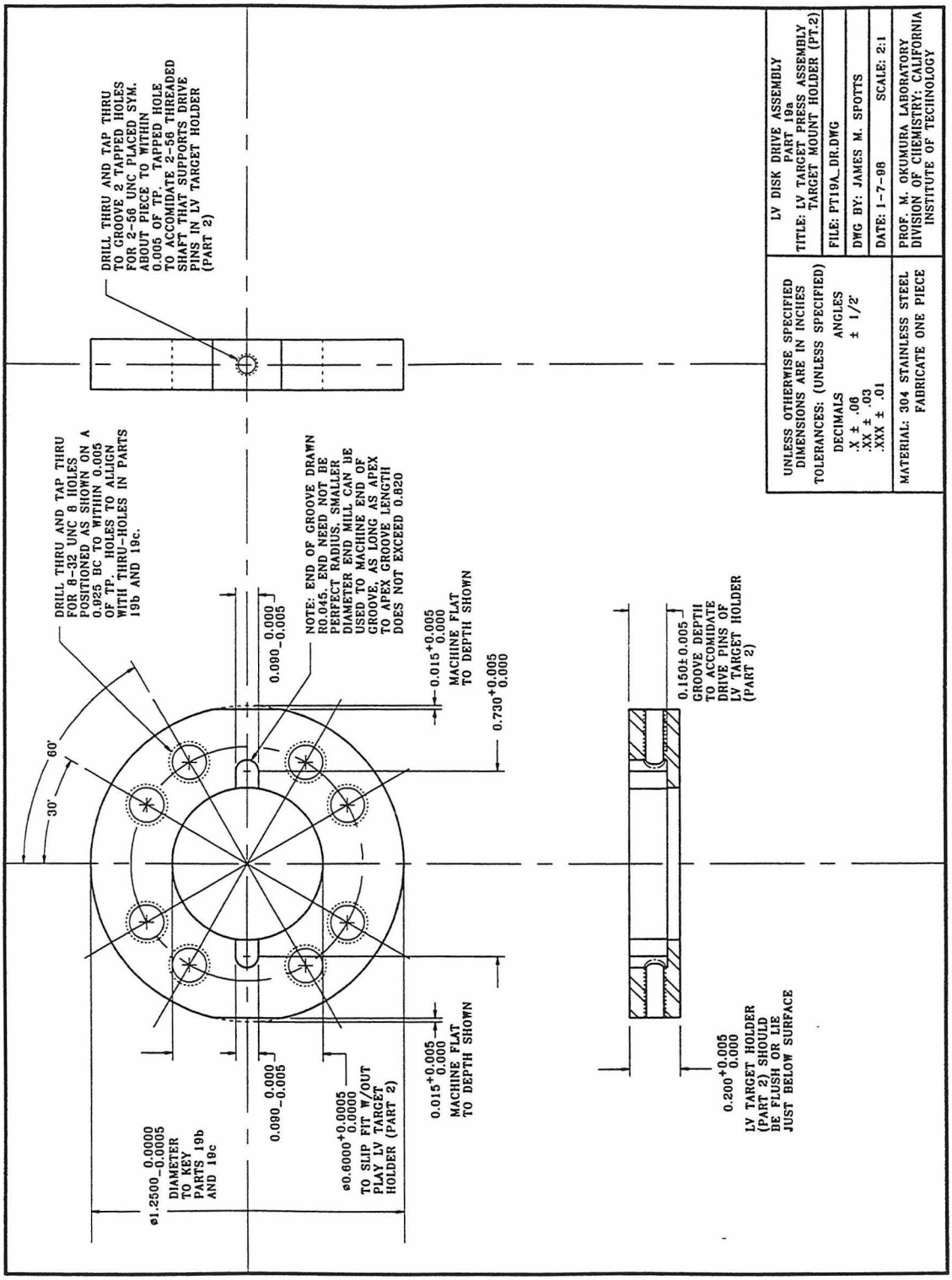

NOTES: 1. FABRICATE ONE PIECE
2. SURFACE -X- TO MEET FLUSH WITH SURFACE -X- OF PART 15
UNLESS OTHERWISE SPECIFIED DIMENSIONS ARE IN INCHES
TOLERANCES: (UNLESS SPECIFIED)
DECIMALS
.X ± .06
.XX ± .03
.XXX ± .01
ANGLES ± 1/2°
MATERIAL: 2024 ALUMINUM
LV DISK DRIVE ASSEMBLY
PART 16
TITLE: TOP SHAFT MOUNT
FILE: P16DSKDR.DWG
DWG BY: JAMES M. SPOTTS
DATE: 12-10-97
SCALE: 2:1
PROF. M. OKUMURA LABORATORY
DIVISION OF CHEMISTRY: CALIFORNIA
INSTITUTE OF TECHNOLOGY
SECTION C-C
ø0.120 DRILL THRU 4 HOLES POSITIONED AS SHOWN CLEARANCE FOR 4-40 SCREW. COUNTERBORE CLEARANCE FOR SOCKET HEAD CAP SCREW. hOLE PATTERN TO ALLIGN WITH PART 15.
ø0.425 DRILL THRU SINGLE HOLE POSITIONED AS SHOWN TO WITHIN 0.005 OF TP. CLEARANCE FOR LV CART DRIVE SCREW AND COUPLING
ø0.3750 +0.0000 -0.0005 BORE THRU 2 HOLES POSITIONED AS SHOWN FOR PRESS FIT STAINLESS STEEL DRILL BUSHING - 0.3750 OD, 0.250 ID, 0.375 LONG - (McMASTER-CARR PART #: xxxxx)
0.200 MACHINE AWAY MATERIAL
0.200 -0.000 -0.005
0.400
1.115
1.2000
0.8500± 0.0005
0.3375± 0.0005
0.250
0.2200± 0.0005
0.288 +0.010 0.000
0.144± 0.001
-X-
C

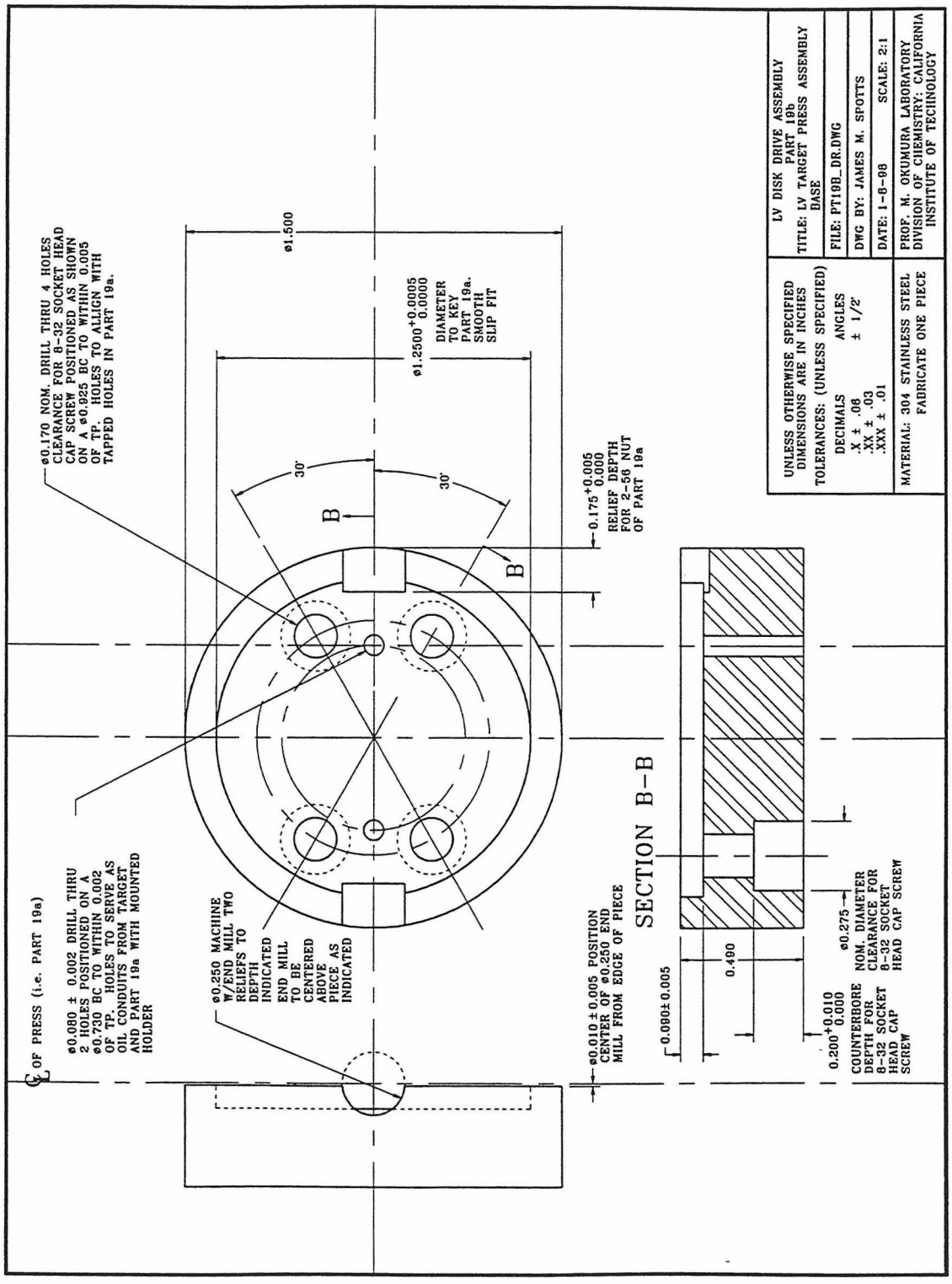

SECTION B-B
SEPARATE
0.475± 0.001
DRILL AND TAP FOR 4-40
2 HOLES X 0.250 DEEP
POS. AS SHOWN TO WITHIN
0.001 OF T.P.
TO ALIGN WITH HOLES ON
TOP SECTION OF CLAMP
Ø 0.015 / 0.020 DRILL THRU TO BOTTOM
OF TAPPED HOLE 2 OUTGASSING
HOLES PLACED SYM. ABOUT PIECE
NOTE: FABRICATE ONE PIECE
CRITICAL ALIGNMENT DIMENSION
-A- = 0.2200 ± 0.0005
Ø0.112 NOM DRILL THRU 3
HOLES AS SHOWN TO ALLIGN WITH
BOTTOM SECTION OF CLAMP
0.3700± 0.0005
Ø0.2495 +0.0005 -0.0000 BORE THRU 2 HOLES
POSITIONED AS SHOWN TO CRITICAL
DIMENSION -A-, CLAMP TO SLIP FIT
Ø0.2500 +0.0000 -0.0005 PRECISION GROUND ROD.
HOLES IDENTICAL TO THOSE OF PART 3b
LASER VAPORIZATION SOURCE VERSION 2
(PART 3b TO BE SUBMITTED WITH JOB
AS REFERENCE)
DRILL THRU AND TAP THRU
FOR 4-40 1 HOLE X 0.250
DEEP POS. ALONG CENTER
LINE TO WITHIN 0.001 OF T.P.
TO ALIGN WITH HOLE ON
TOP SECTION OF CLAMP
0.475± 0.001
1.200
0.220± 0.001
0.250
0.675
0.475
0.250
0.015 +0.005 0.000
SEPARATE
CLAMP PARTS
Ø0.120 DRILL THRU 4 HOLES
PLACED SYM. ABOUT CENTER
LINES OF PIECE TO WITHIN
STATED TOLERANCES. SPACING
TO MATCH THAT OF PART 18
UNLESS OTHERWISE SPECIFIED
DIMENSIONS ARE IN INCHES
TOLERANCES: (UNLESS SPECIFIED)
DECIMALS ANGLES
.X ± .00 ± 1/2°
.XX ± .03
.XXX ± .01
MATERIAL: 2024 ALUMINUM
LV DISK DRIVE ASSEMBLY
PART 17
TITLE: BOTTOM SHAFT MOUNT
ADAPTOR
FILE: P17DSKDR.DWG
DWG BY: JAMES M. SPOTTS
DATE: 12-9-97 SCALE: 2:1
PROF. M. OKUMURA LABORATORY
DIVISION OF CHEMISTRY: CALIFORNIA
INSTITUTE OF TECHINOLOGY

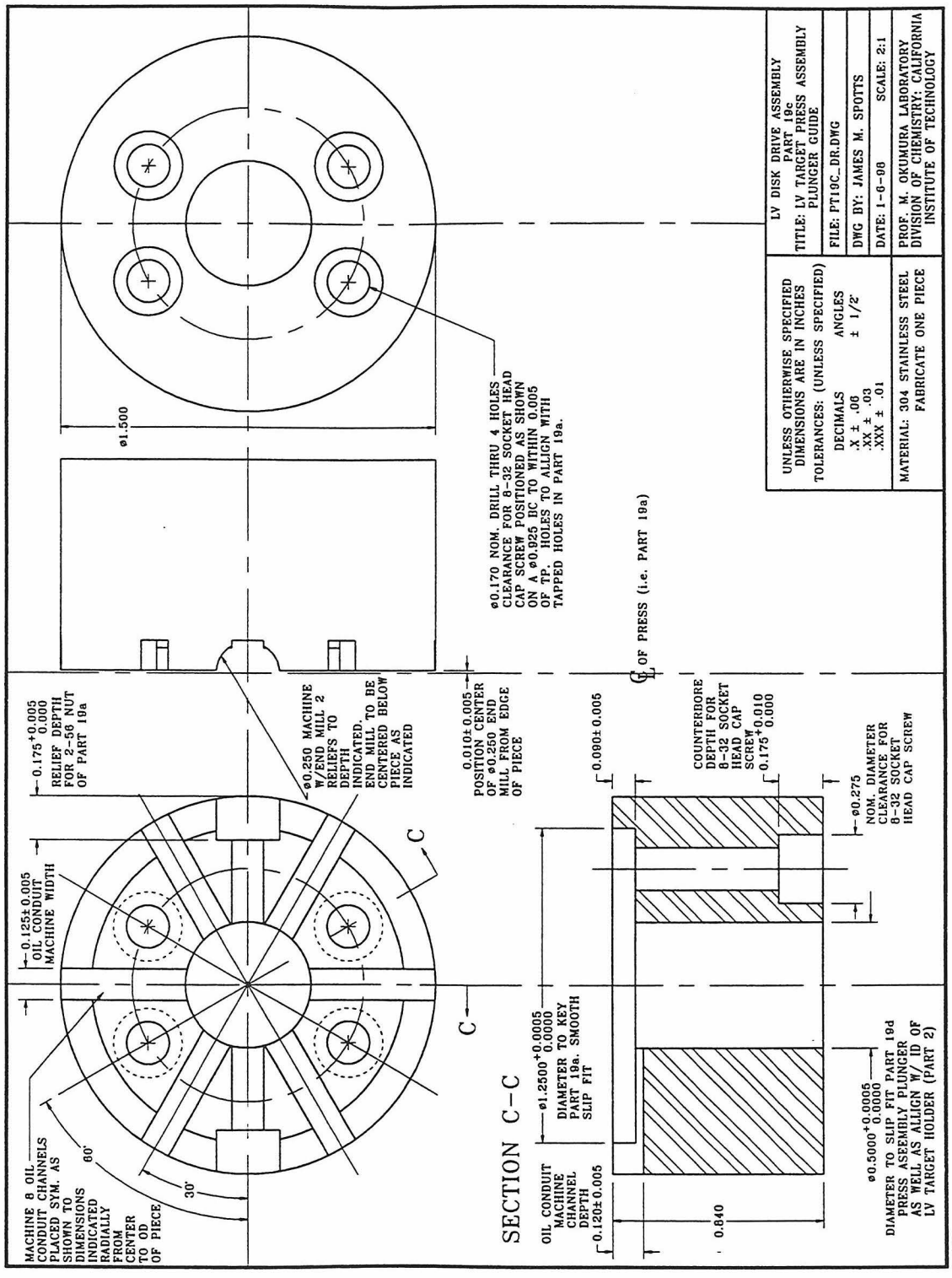

MACHINE MIRROR IMAGE
OF PART TO IDENTICAL
DIMENSIONS AND
TOLERANCES
FABRICATE ONE PIECE
0.8800± 0.0005
0.1325± 0.0005
0.250
0.105± 0.001
DRILL THRU AND TAP
THRU 2 HOLES FOR
4-40 POSITIONED AS
SHOWN. TO ALLIGN
WITH PART #17
1.250
0.475± 0.005
ø0.3750 +0.0000 -0.0005 NOM. BORE
SINGLE HOLE. HOLE TO ACCEPT
ø0.250 ID, ø0.375 OD X 0.375
LONG PRESS FIT DRILL BUSHING.
POSITION AS SHOWN TO WITHIN
0.001 OF TP. PRESS FIT BUSHING
BELOW FACE +0.010/-0.000
(McMASTER-CARR PART #: XXXXXX)
ø0.170 ± 0.002
0.500
0.070± 0.005
0.060± 0.005
UNLESS OTHERWISE SPECIFIED
DIMENSIONS ARE IN INCHES
TOLERANCES: (UNLESS SPECIFIED)
DECIMALS ANGLES
.X ± .06 ± 1/2°
.XX ± .03
.XXX ± .01
MATERIAL: 2024 ALUMINUM
LV DISK DRIVE ASSEMBLY
PART 1B
TITLE: BOTTOM ROD SUPPORT
FILE: P1BDSKDR.DWG
DWG BY: JAMES M. SPOTTS
DATE: 12-10-97
SCALE: 2:1
PROF. M. OKUMURA LABORATORY
DIVISION OF CHEMISTRY: CALIFORNIA
INSTITUTE OF TECHNOLOGY

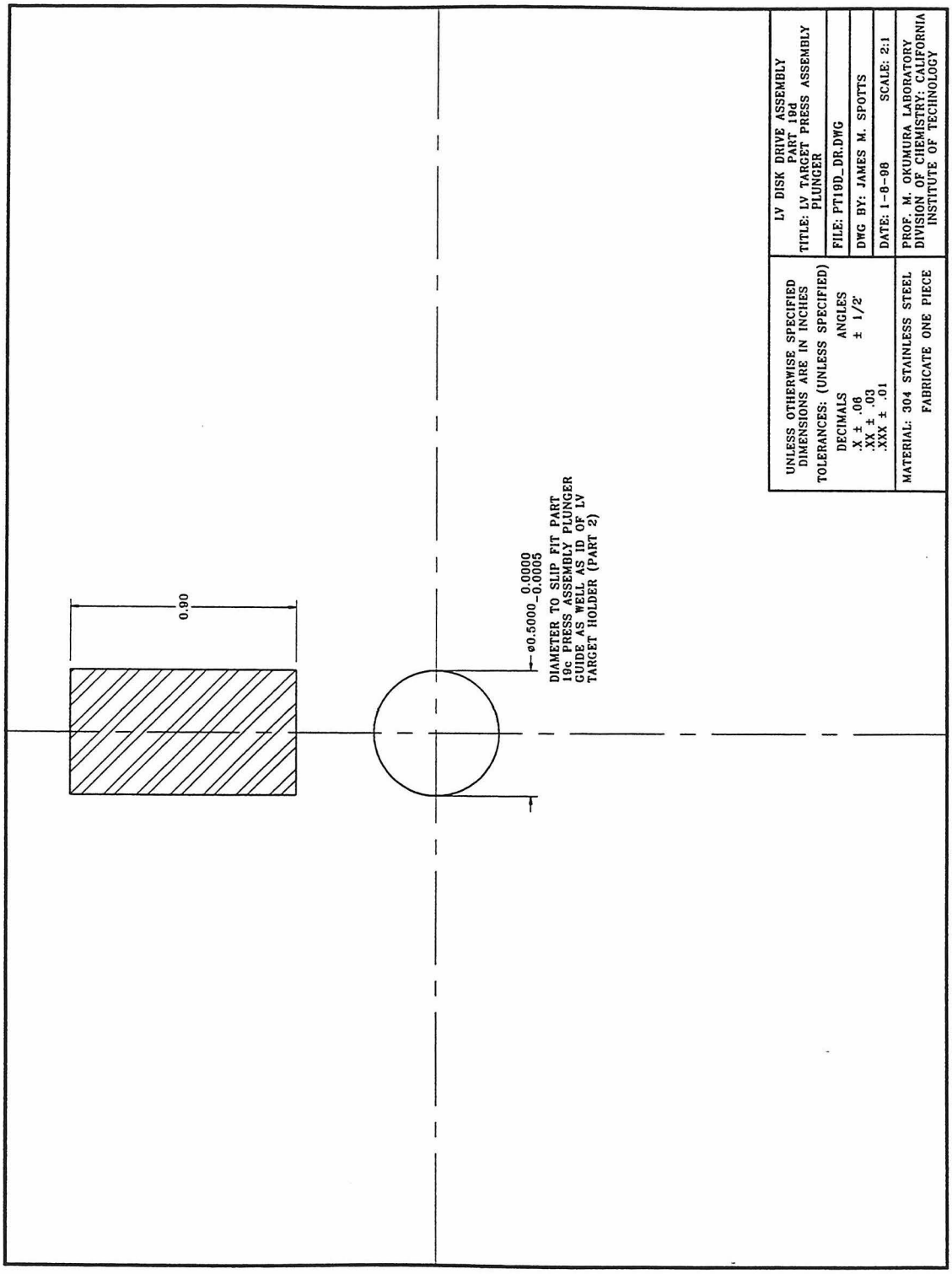

TOP VIEW
LOOKING
DOWN ON
PART 19c
A
A
TRUE 1:1 SCALE: SECTION A-A
PRESS FULLY ASSEMBLED
SECTION
A-A
PART 19c
PART 19d
PART 2
PART 19a
PART 19b
UNLESS OTHERWISE SPECIFIED
DIMENSIONS ARE IN INCHES
TOLERANCES: (UNLESS SPECIFIED)
DECIMALS ANGLES
.X ± .06 ± 1/2°
.XX ± .03
.XXX ± .01
MATERIAL: VARIES
TITLE: PART 19 ASSEMBLY DRAWING
LV TARGET PRESS ASSEMBLY
FILE: PT19_AD2.DWG
DWG BY: JAMES M. SPOTTS
DATE: 1-8-98 SCALE: 2:1
PROF. M. OKUMURA LABORATORY
DIVISION OF CHEMISTRY: CALIFORNIA
INSTITUTE OF TECHNOLOGY


TOP VIEW
LOOKING
DOWN ON
PART 19c
PART 19d
PART 19c
PART 19a
PART 19b
2-56 LOCKNUT
TO SECURE
THREADED
SHAFT
UNLESS OTHERWISE SPECIFIED
DIMENSIONS ARE IN INCHES
TOLERANCES: (UNLESS SPECIFIED)
DECIMALS ANGLES
.X ± .06 ± 1/2°
.XX ± .03
.XXX ± .01
MATERIAL: VARIES
TITLE: PART 19 ASSEMBLY DRAWING
LV TARGET PRESS ASSEMBLY
EXTERIOR VIEW
FILE: PT19_AD1.DWG
DWG BY: JAMES M. SPOTTS
DATE: 1-8-98
SCALE: 2:1
PROF. M. OKUMURA LABORATORY
DIVISION OF CHEMISTRY: CALIFORNIA
INSTITUTE OF TECHNOLOGY


DRILL THRU AND TAP THRU TO GROOVE 2 TAPPED HOLES FOR 2-56 UNC PLACED SYM. ABOUT PIECE TO WITHIN 0.005 OF TP. TAPPED HOLE TO ACCOMIDATE 2-56 THREADED SHAFT THAT SUPPORTS DRIVE PINS IN LV TARGET HOLDER (PART 2)
DRILL THRU AND TAP THRU FOR 8-32 UNC 8 HOLES POSITIONED AS SHOWN ON A 0.925 BC TO WITHIN 0.005 OF TP. HOLES TO ALLIGN WITH THRU-HOLES IN PARTS 19b AND 19c.
60°
30°
NOTE: END OF GROOVE DRAWN R0.045. END NEED NOT BE PERFECT RADIUS. SMALLER DIAMETER END MILL CAN BE USED TO MACHINE END OF GROOVE, AS LONG AS APEX TO APEX GROOVE LENGTH DOES NOT EXCEED 0.820
0.090 -0.000 -0.005
0.015 +0.005 0.000
MACHINE FLAT TO DEPTH SHOWN
0.730 +0.005 0.000
0.150±0.005
GROOVE DEPTH TO ACCOMIDATE DRIVE PINS OF LV TARGET HOLDER (PART 2)
ø1.2500 -0.0000 -0.0005
DIAMETER TO KEY PARTS 19b AND 19c
0.090 -0.000 -0.005
ø0.6000 +0.0005 0.0000
TO SLIP FIT W/OUT PLAY LV TARGET HOLDER (PART 2)
0.015 +0.005 0.000
MACHINE FLAT TO DEPTH SHOWN
0.200 +0.005 0.000
LV TARGET HOLDER (PART 2) SHOULD BE FLUSH OR LIE JUST BELOW SURFACE
UNLESS OTHERWISE SPECIFIED DIMENSIONS ARE IN INCHES
TOLERANCES: (UNLESS SPECIFIED)
DECIMALS ANGLES
.X ± .06 ± 1/2°
.XX ± .03
.XXX ± .01
MATERIAL: 304 STAINLESS STEEL FABRICATE ONE PIECE
LV DISK DRIVE ASSEMBLY PART 19a
TITLE: LV TARGET PRESS ASSEMBLY TARGET MOUNT HOLDER (PT.2)
FILE: PT19A_DR.DWG
DWG BY: JAMES M. SPOTTS
DATE: 1-7-98
SCALE: 2:1
PROF. M. OKUMURA LABORATORY DIVISION OF CHEMISTRY: CALIFORNIA INSTITUTE OF TECHNOLOGY


ø0.170 NOM. DRILL THRU 4 HOLES
CLEARANCE FOR 8-32 SOCKET HEAD
CAP SCREW POSITIONED AS SHOWN
ON A ø0.925 BC TO WITHIN 0.005
OF TP. HOLES TO ALLIGN WITH
TAPPED HOLES IN PART 19a.
ø1.500
ø1.2500 +0.0005 0.0000
DIAMETER
TO KEY
PART 19a.
SMOOTH
SLIP FIT
30°
30°
B
B'
0.175 +0.005 0.000
RELIEF DEPTH
FOR 2-56 NUT
OF PART 19a
℄ OF PRESS (i.e. PART 19a)
ø0.080 ± 0.002 DRILL THRU
2 HOLES POSITIONED ON A
ø0.730 BC TO WITHIN 0.002
OF TP. HOLES TO SERVE AS
OIL CONDUITS FROM TARGET
AND PART 19a WITH MOUNTED
HOLDER
ø0.250 MACHINE
W/END MILL TWO
RELIEFS TO
DEPTH
INDICATED
END MILL
TO BE
CENTERED
ABOVE
PIECE AS
INDICATED
ø0.010 ± 0.005 POSITION
CENTER OF ø0.250 END
MILL FROM EDGE OF PIECE
SECTION B-B
0.090± 0.005
0.490
0.200 +0.010 0.000
COUNTERBORE
DEPTH FOR
8-32 SOCKET
HEAD CAP
SCREW
ø0.275
NOM. DIAMETER
CLEARANCE FOR
8-32 SOCKET
HEAD CAP SCREW
UNLESS OTHERWISE SPECIFIED
DIMENSIONS ARE IN INCHES
TOLERANCES: (UNLESS SPECIFIED)
DECIMALS
.X ± .06
.XX ± .03
.XXX ± .01
ANGLES
± 1/2°
MATERIAL: 304 STAINLESS STEEL
FABRICATE ONE PIECE
LV DISK DRIVE ASSEMBLY
PART 19b
TITLE: LV TARGET PRESS ASSEMBLY
BASE
FILE: PT19B_DR.DWG
DWG BY: JAMES M. SPOTTS
DATE: 1-8-98
SCALE: 2:1
PROF. M. OKUMURA LABORATORY
DIVISION OF CHEMISTRY: CALIFORNIA
INSTITUTE OF TECHNOLOGY


MACHINE 8 OIL CONDUIT CHANNELS PLACED SYM. AS SHOWN TO DIMENSIONS INDICATED RADIALLY FROM CENTER TO OD OF PIECE
60°
30°
0.125± 0.005 OIL CONDUIT MACHINE WIDTH
0.175 +0.005 0.000 RELIEF DEPTH FOR 2-56 NUT OF PART 19a
ø0.250 MACHINE W/END MILL 2 RELIEFS TO DEPTH INDICATED. END MILL TO BE CENTERED BELOW PIECE AS INDICATED
C
C
SECTION C-C
ø1.500
ø0.170 NOM. DRILL THRU 4 HOLES CLEARANCE FOR 8-32 SOCKET HEAD CAP SCREW POSITIONED AS SHOWN ON A ø0.925 BC TO WITHIN 0.005 OF TP. HOLES TO ALLIGN WITH TAPPED HOLES IN PART 19a.
0.010± 0.005 POSITION CENTER OF ø0.250 END MILL FROM EDGE OF PIECE
℄ OF PRESS (i.e. PART 19a)
0.090± 0.006
COUNTERBORE DEPTH FOR 8-32 SOCKET HEAD CAP SCREW 0.175 +0.010 0.000
ø0.275 NOM. DIAMETER CLEARANCE FOR 8-32 SOCKET HEAD CAP SCREW
ø1.2500 +0.0005 0.0000 DIAMETER TO KEY PART 19a. SMOOTH SLIP FIT
OIL CONDUIT MACHINE CHANNEL DEPTH 0.120± 0.005
0.840
ø0.5000 +0.0005 0.0000 DIAMETER TO SLIP FIT PART 19d PRESS ASEEMBLY PLUNGER AS WELL AS ALLIGN W/ ID OF LV TARGET HOLDER (PART 2)
UNLESS OTHERWISE SPECIFIED DIMENSIONS ARE IN INCHES TOLERANCES: (UNLESS SPECIFIED)
DECIMALS ANGLES
.X ± .06 ± 1/2°
.XX ± .03
.XXX ± .01
MATERIAL: 304 STAINLESS STEEL FABRICATE ONE PIECE
LV DISK DRIVE ASSEMBLY PART 19c
TITLE: LV TARGET PRESS ASSEMBLY PLUNGER GUIDE
FILE: PT19C_DR.DWG
DWG BY: JAMES M. SPOTTS
DATE: 1-6-98 SCALE: 2:1
PROF. M. OKUMURA LABORATORY DIVISION OF CHEMISTRY: CALIFORNIA INSTITUTE OF TECHNOLOGY


0.90
ø0.5000 0.0000 -0.0005
DIAMETER TO SLIP FIT PART
19c PRESS ASSEMBLY PLUNGER
GUIDE AS WELL AS ID OF LV
TARGET HOLDER (PART 2)
UNLESS OTHERWISE SPECIFIED
DIMENSIONS ARE IN INCHES
TOLERANCES: (UNLESS SPECIFIED)
DECIMALS ANGLES
.X ± .06 ± 1/2°
.XX ± .03
.XXX ± .01
MATERIAL: 304 STAINLESS STEEL
FABRICATE ONE PIECE
LV DISK DRIVE ASSEMBLY
PART 19d
TITLE: LV TARGET PRESS ASSEMBLY
PLUNGER
FILE: PT19D_DR.DWG
DWG BY: JAMES M. SPOTTS
DATE: 1-8-98
SCALE: 2:1
PROF. M. OKUMURA LABORATORY
DIVISION OF CHEMISTRY: CALIFORNIA
INSTITUTE OF TECHNOLOGY

APPENDIX 2

Drawings for the Original Piezoelectric Pulsed Valve Based of the Design of Trickl and Proch

PARTS LIST FOR AFOSR PULSED VALVE

1. REQUIRED PARTS SHOWN ON DRAWINGS

Part #	Part Name	Material	Quantity
1	Back Housing	304 Stainless Steel	1
2	Front Plate	304 Stainless Steel	1
3	Nozzle Plate	304 Stainless Steel	2
4	Bolt	304 Stainless Steel	4
5	Holder for Plunger	Aluminum	1
6	Nut	Hard Plastic (Electrical Insulator)	1
7	Plunger	Aluminum	1
8	Nut	Aluminum	1
9	Holder for Damping O-Ring	304 Stainless Steel	1
10	Pulsed Valve Mount	304 Stainless Steel	1
11	BNC Feedthrough (Welded to Pt. 1) ⇨ Not Shown	304 Stainless Steel	1
12	Wrench 1	Brass/304 Stainless Steel	1
13	Wrench 2	Brass/304 Stainless Steel	1

2. O-RINGS

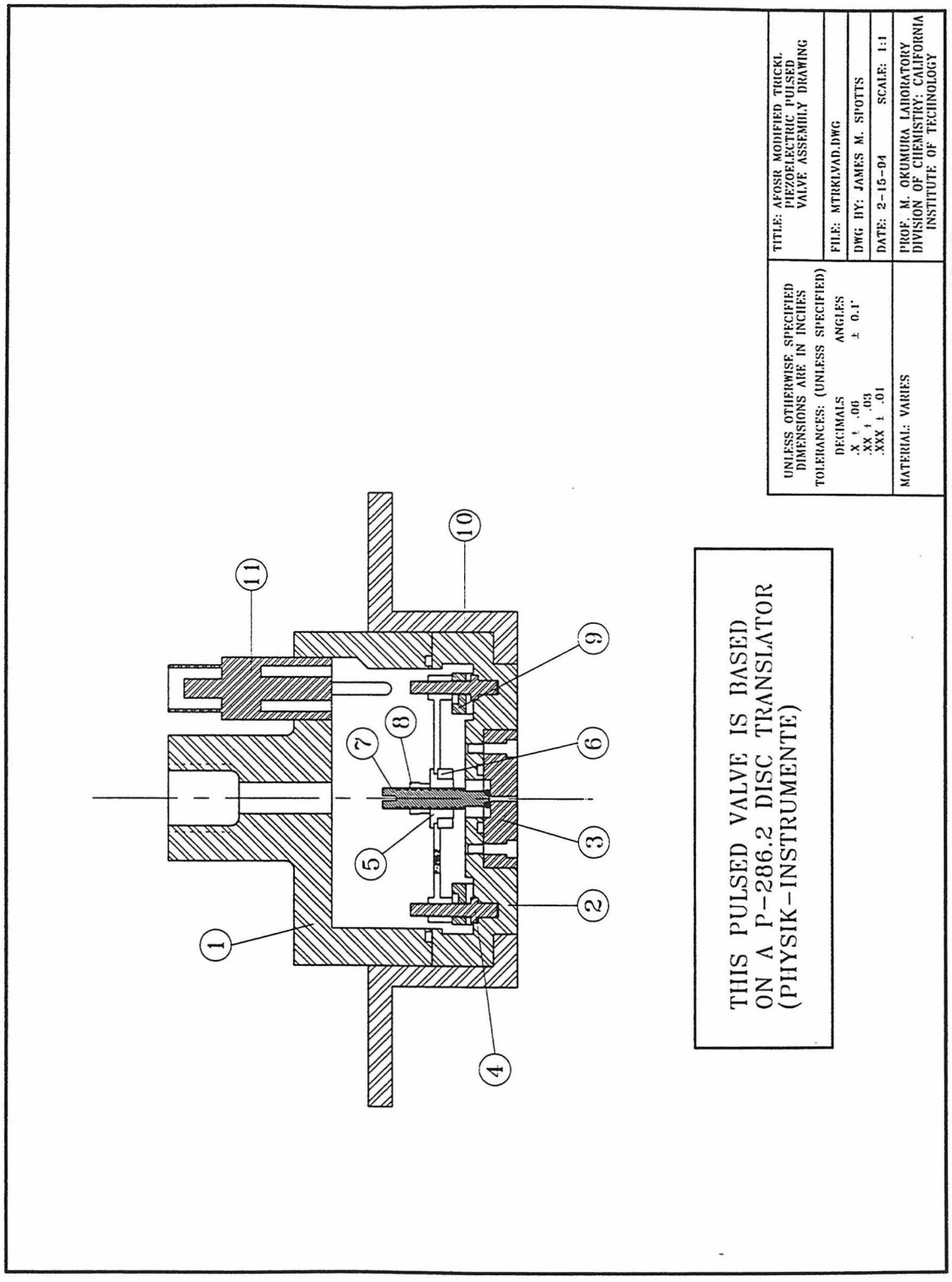
Parker #	Size (ID x Thick.)	Material	Quantity
2-002	0.042 x .050	Viton	1
2-012	0.364 x .070	Viton	1
2-029	1.489 x .070	Viton	1
2-034	2.114 x .070	Viton	1

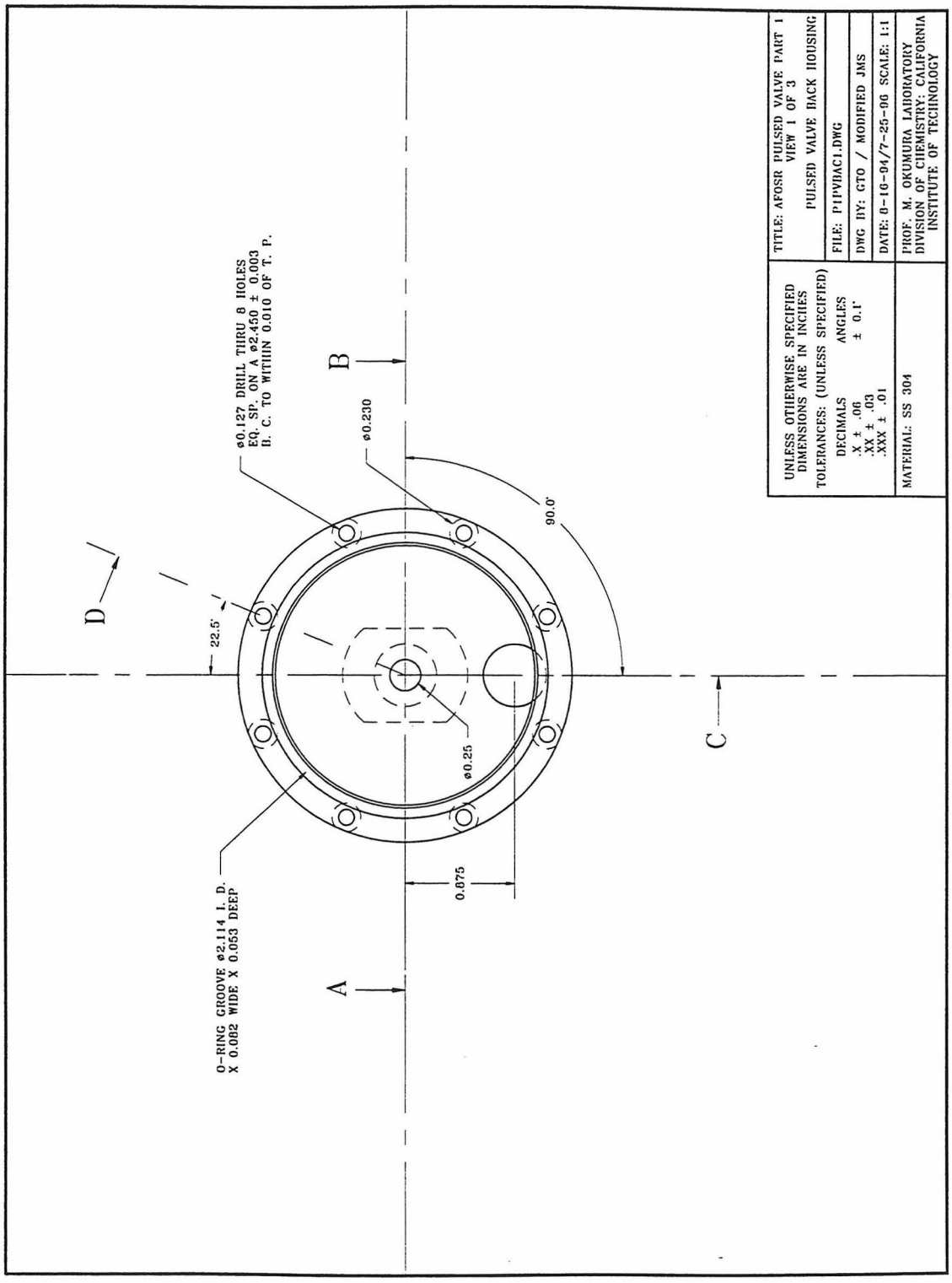
3. SCREWS

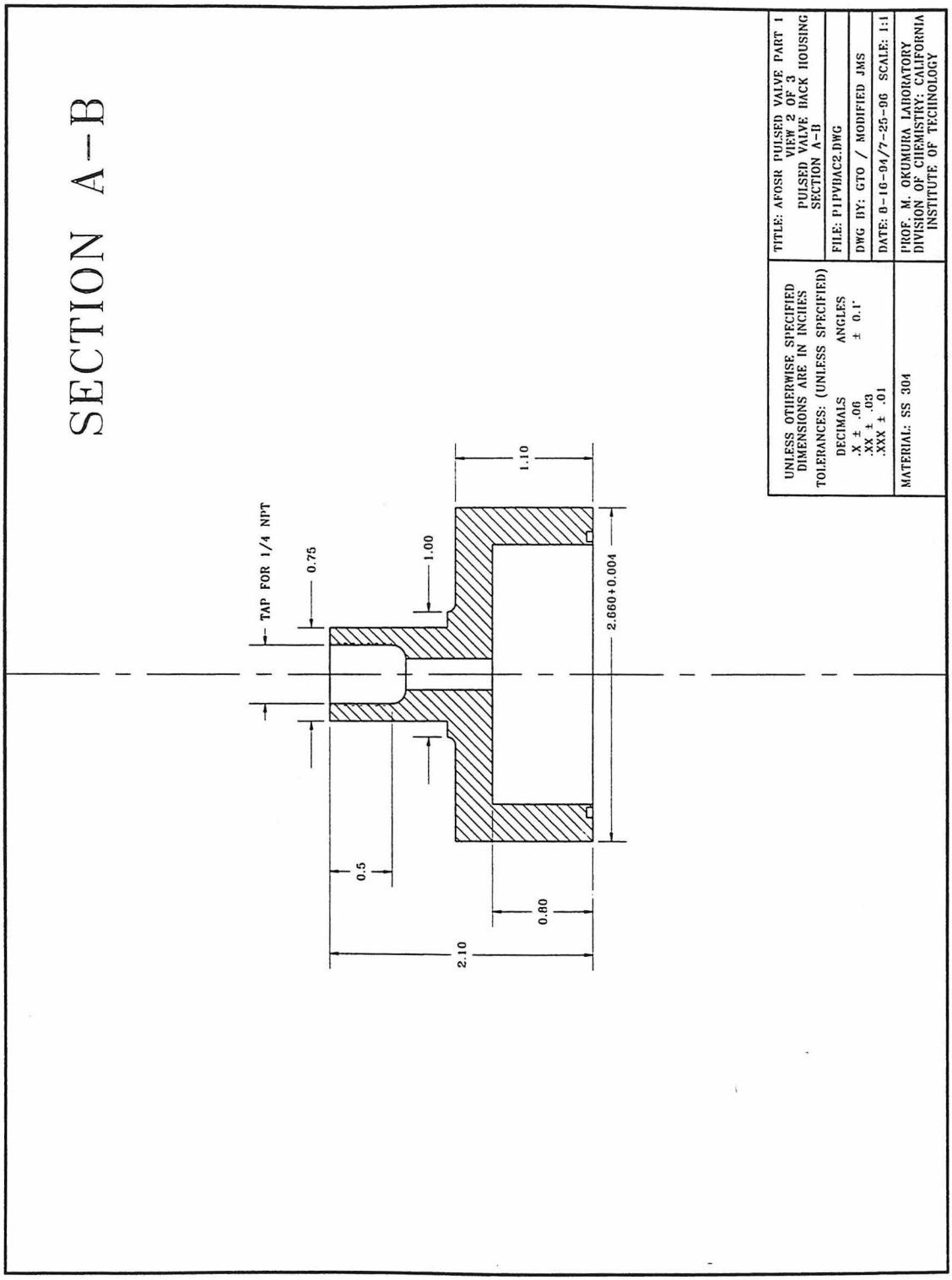
Size	Type	Material	Quantity
5-40 UNC	Socket Head	Stainless Steel	8
2-56 UNC	Socket Head	Stainless Steel	4
6-32 UNC	Socket Head	Stainless Steel	4

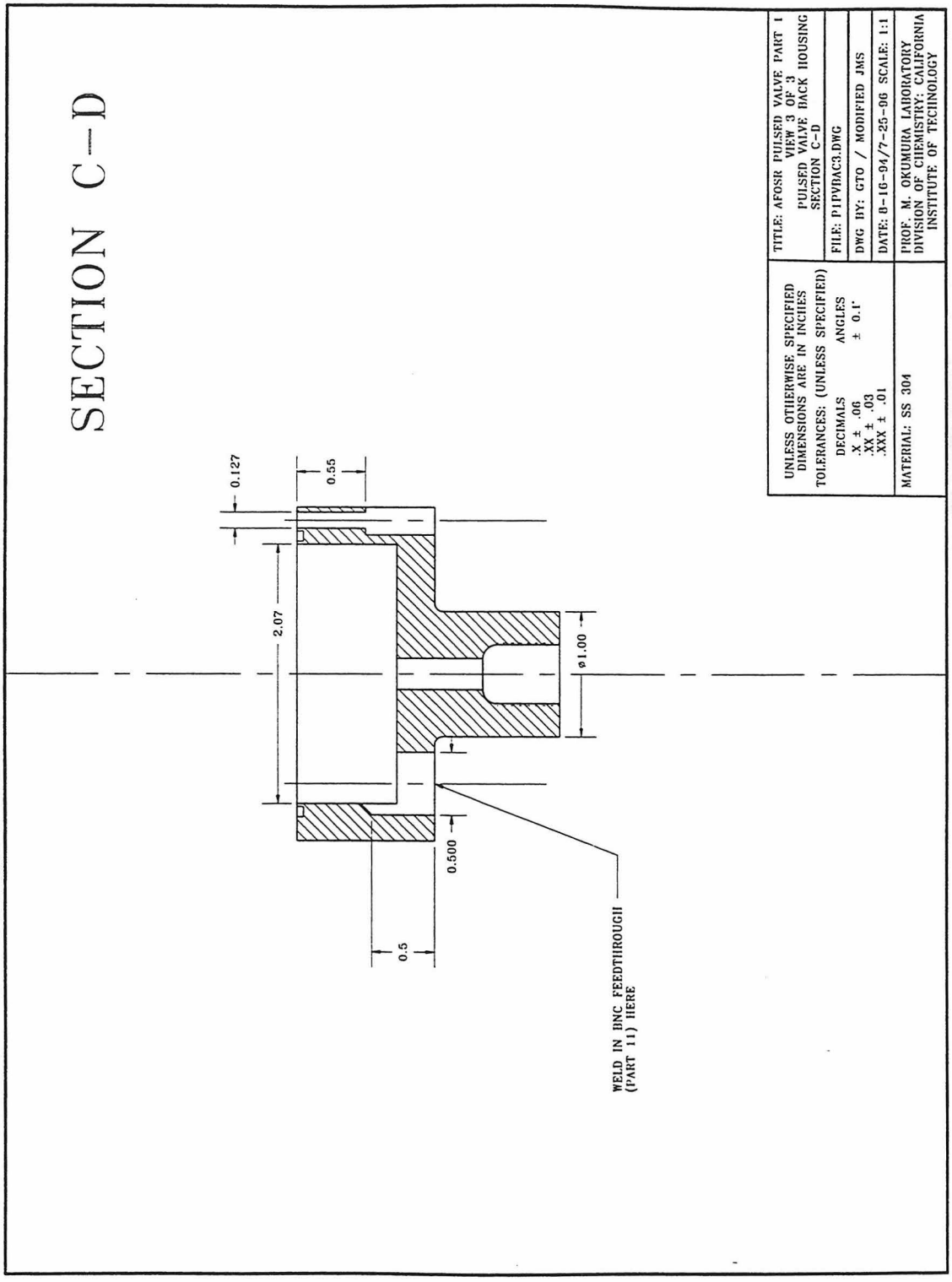
4. NUTS

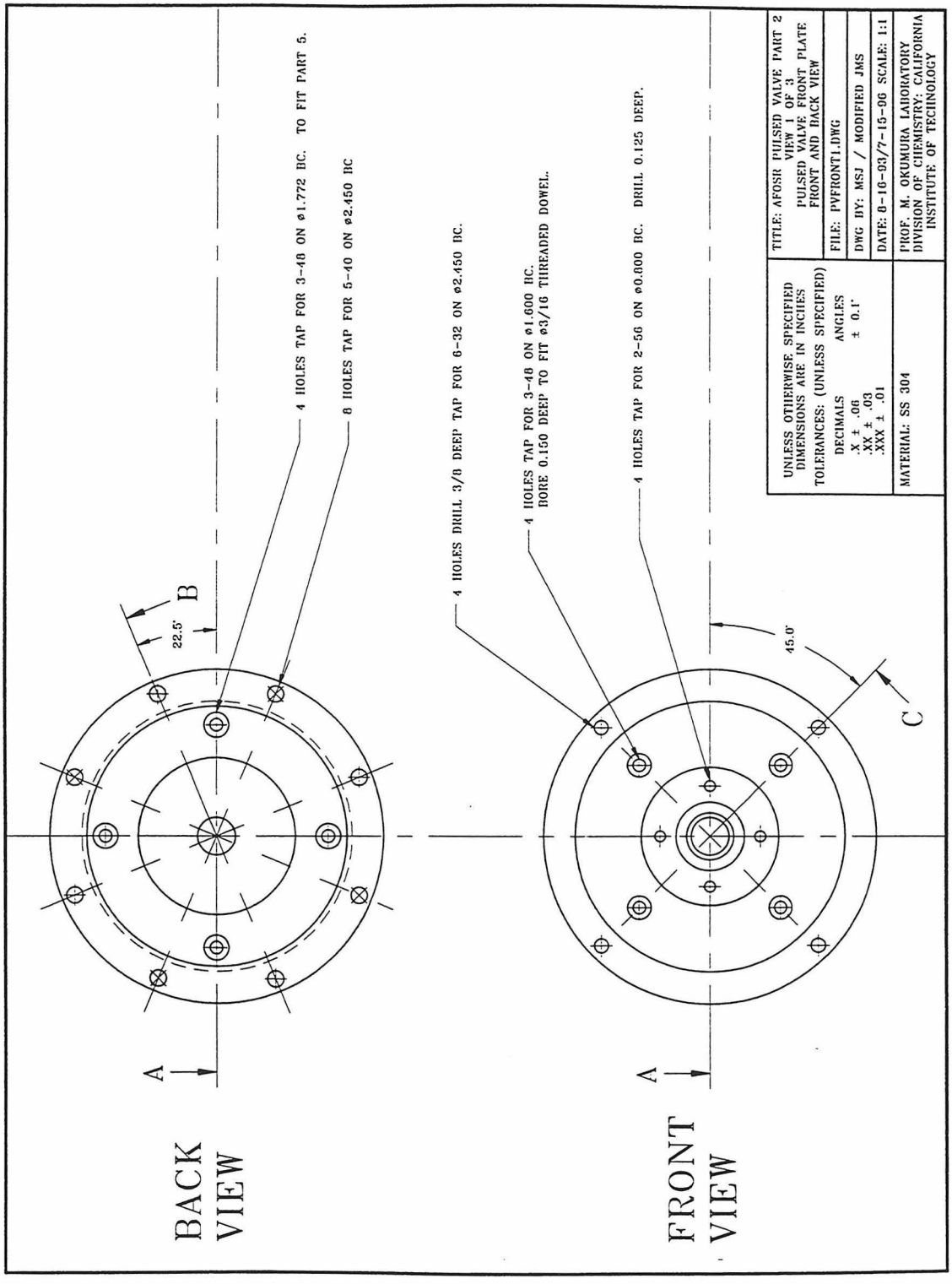
Size	Type	Material	Quantity
3-48 UNC	Hexagon	Stainless Steel	4

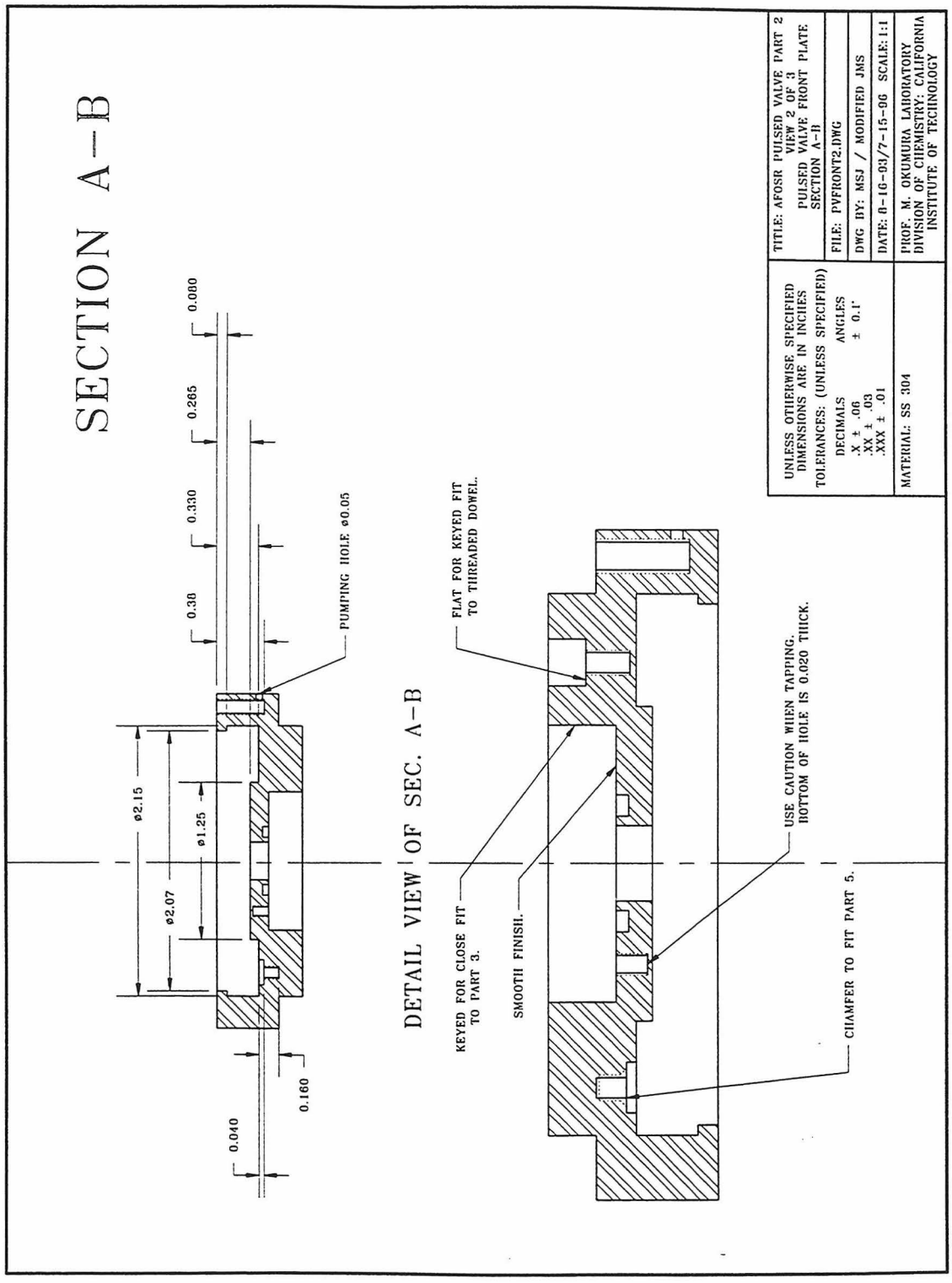

TITLE: AFOSR MODIFIED TRICKL PIEZOELECTRIC PULSED VALVE ASSEMBLY DRAWING
FILE: MTRKLVAD.DWG
DWG BY: JAMES M. SPOTTS
DATE: 2-15-04 SCALE: 1:1
PROF. M. OKUMURA LABORATORY
DIVISION OF CHEMISTRY; CALIFORNIA INSTITUTE OF TECHNOLOGY
UNLESS OTHERWISE SPECIFIED DIMENSIONS ARE IN INCHES
TOLERANCES: (UNLESS SPECIFIED)
DECIMALS ANGLES
.X ± .06 ± 0.1°
.XX ± .03
.XXX ± .01
MATERIAL: VARIES
THIS PULSED VALVE IS BASED ON A P-286.2 DISC TRANSLATOR (PHYSIK-INSTRUMENTE)
1
2
3
4
5
6
7
8
9
10
11

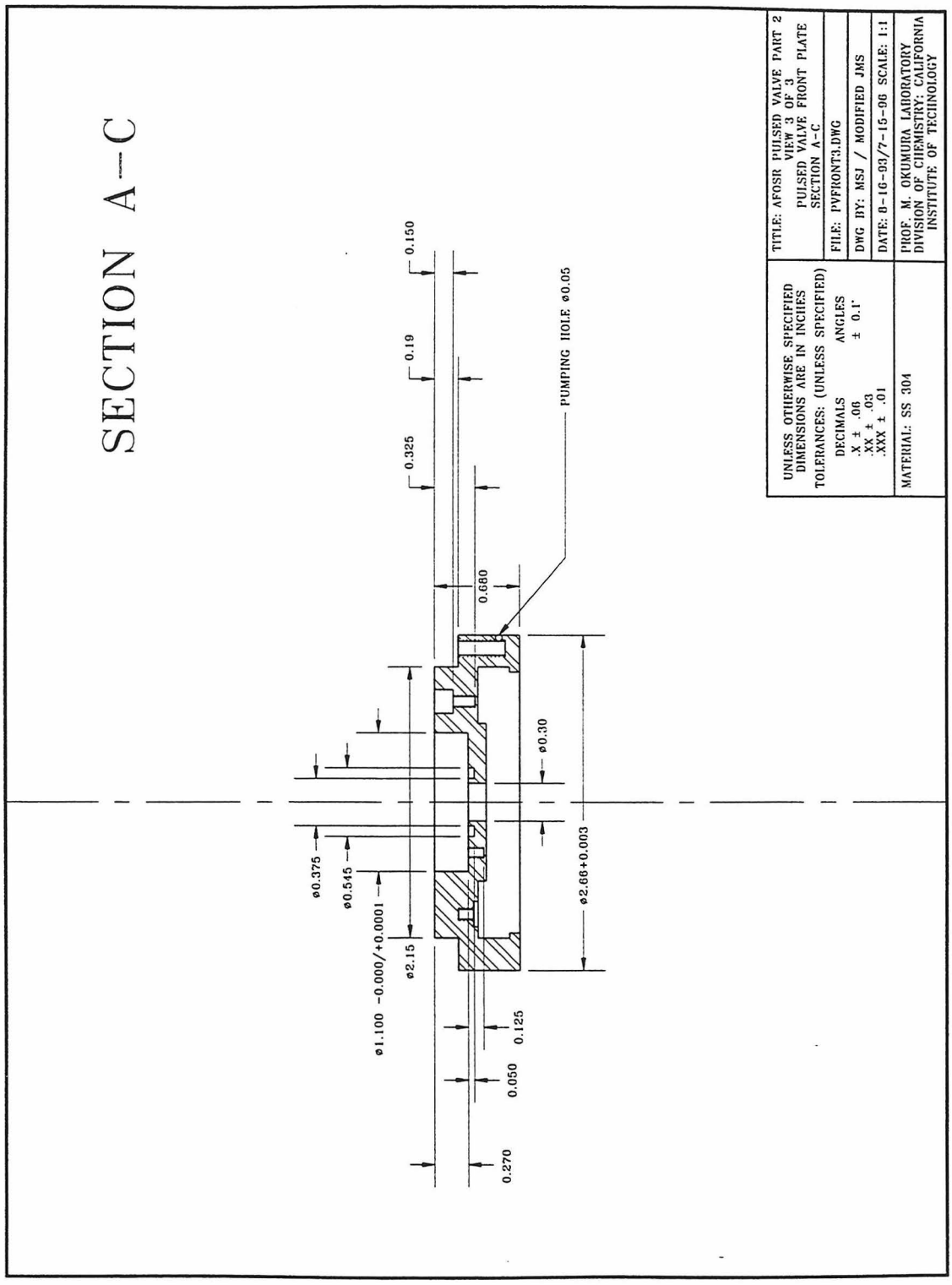

ø0.127 DRILL THRU 8 HOLES
EQ. SP. ON A ø2.450 ± 0.003
B. C. TO WITHIN 0.010 OF T. P.
ø0.230
90.0°
22.5°
ø0.25
0.075
O-RING GROOVE ø2.114 I. D.
X 0.082 WIDE X 0.053 DEEP
A
B
C
D
UNLESS OTHERWISE SPECIFIED
DIMENSIONS ARE IN INCHES
TOLERANCES: (UNLESS SPECIFIED)
DECIMALS ANGLES
.X ± .06 ± 0.1°
.XX ± .03
.XXX ± .01
MATERIAL: SS 304
TITLE: AFOSR PULSED VALVE PART 1
VIEW 1 OF 3
PULSED VALVE BACK HOUSING
FILE: P1PVBAC1.DWG
DWG BY: GTO / MODIFIED JMS
DATE: 8-16-94/7-25-96 SCALE: 1:1
PROF. M. OKUMURA LABORATORY
DIVISION OF CHEMISTRY: CALIFORNIA
INSTITUTE OF TECHNOLOGY

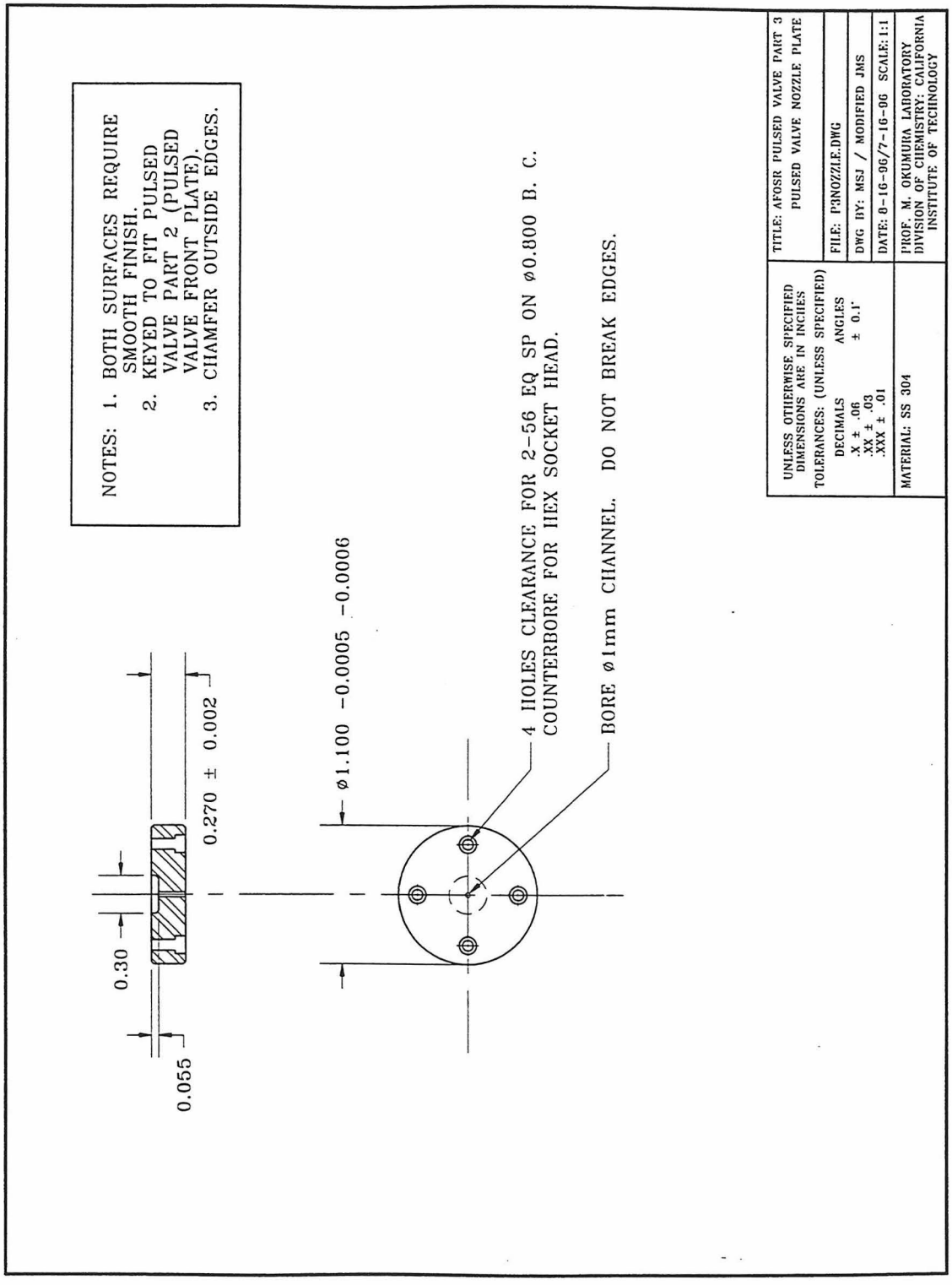

SECTION A-B
TAP FOR 1/4 NPT
0.75
1.00
1.10
2.660+0.004
0.5
0.80
2.10
UNLESS OTHERWISE SPECIFIED
DIMENSIONS ARE IN INCHES
TOLERANCES: (UNLESS SPECIFIED)
DECIMALS ANGLES
.X ± .06 ± 0.1°
.XX ± .03
.XXX ± .01
TITLE: AFOSR PULSED VALVE PART 1
VIEW 2 OF 3
PULSED VALVE BACK HOUSING
SECTION A-B
FILE: P1PVBAC2.DWG
DWG BY: GTO / MODIFIED JMS
DATE: 8-16-94/7-25-96 SCALE: 1:1
MATERIAL: SS 304
PROF. M. OKUMURA LABORATORY
DIVISION OF CHEMISTRY: CALIFORNIA
INSTITUTE OF TECHNOLOGY

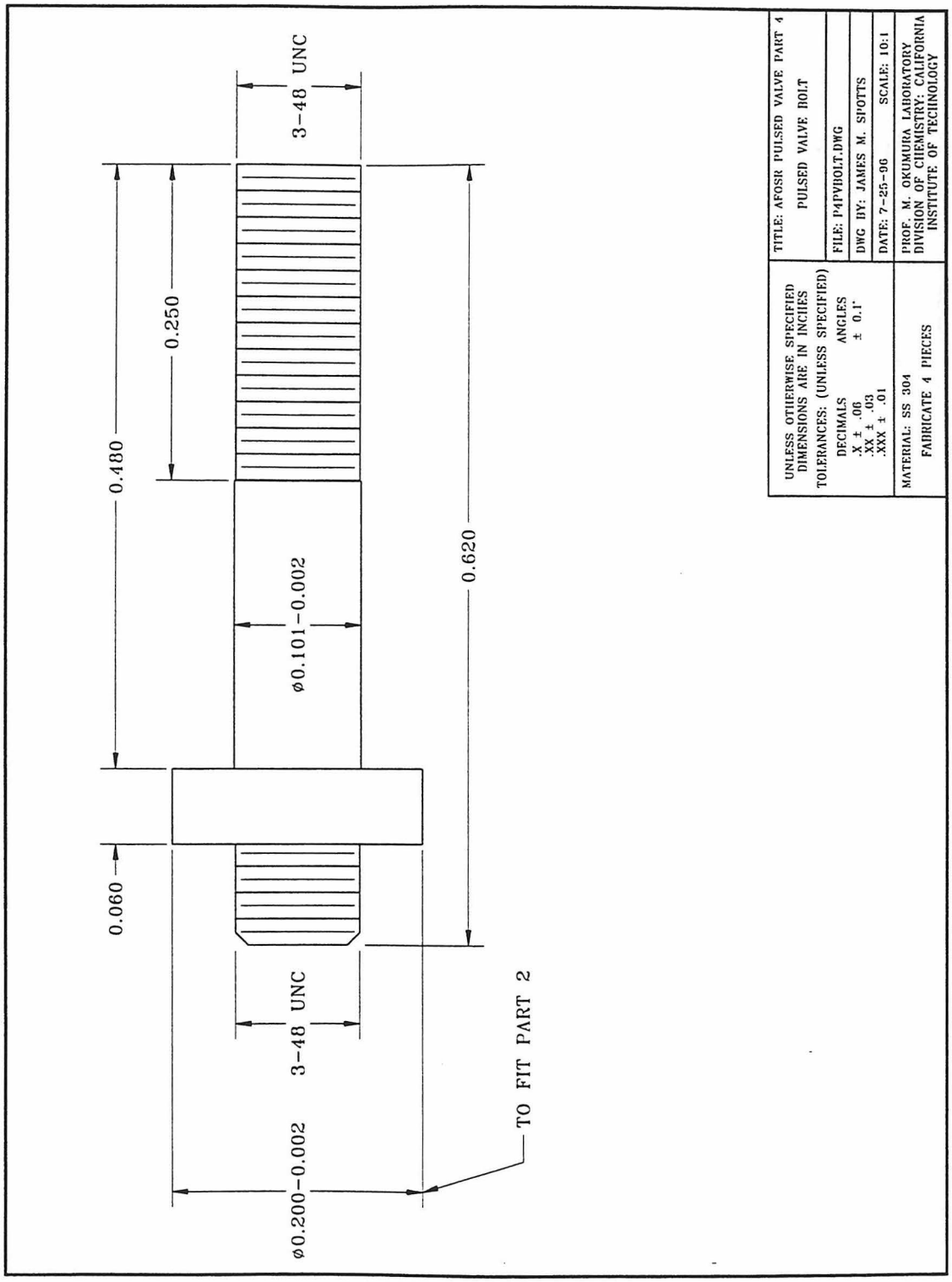

SECTION C–D
0.127
0.55
2.07
ø1.00
0.500
0.5
WELD IN INC FEEDTHROUGH
(PART 11) HERE
UNLESS OTHERWISE SPECIFIED
DIMENSIONS ARE IN INCHES
TOLERANCES: (UNLESS SPECIFIED)
DECIMALS ANGLES
.X ± .06 ± 0.1°
.XX ± .03
.XXX ± .01
MATERIAL: SS 304
TITLE: AFOSR PULSED VALVE PART 1
VIEW 3 OF 3
PULSED VALVE BACK HOUSING
SECTION C–D
FILE: P1PVBAC3.DWG
DWG BY: GTO / MODIFIED JMS
DATE: 8–16–94/7–25–96 SCALE: 1:1
PROF. M. OKUMURA LABORATORY
DIVISION OF CHEMISTRY: CALIFORNIA
INSTITUTE OF TECHNOLOGY

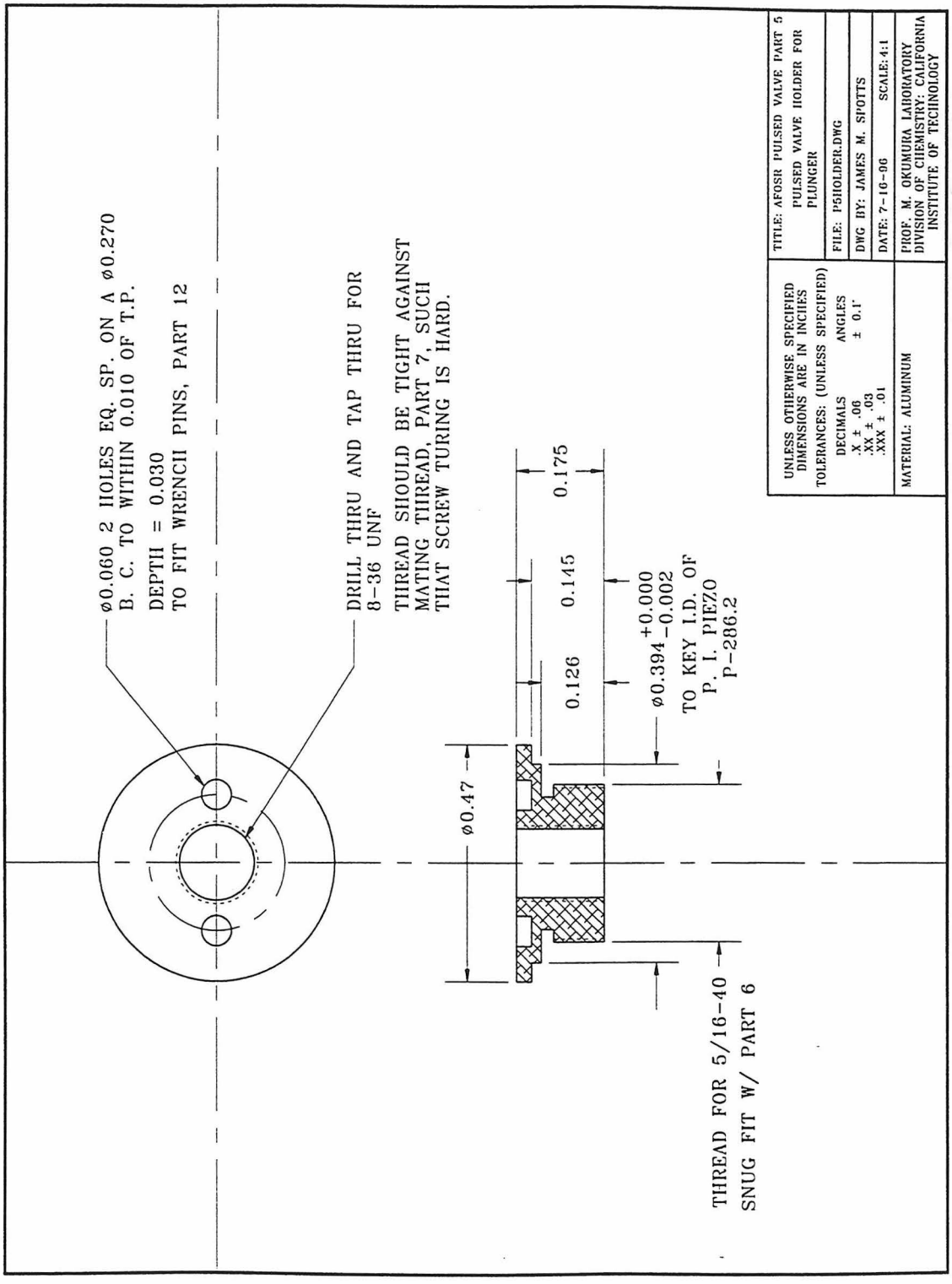

BACK VIEW
FRONT VIEW
A
B
C
22.5°
45.0°
4 HOLES TAP FOR 3-48 ON ø1.772 BC. TO FIT PART 5.
8 HOLES TAP FOR 5-40 ON ø2.450 BC
4 HOLES DRILL 3/8 DEEP TAP FOR 6-32 ON ø2.450 BC.
4 HOLES TAP FOR 3-48 ON ø1.600 BC.
BORE 0.150 DEEP TO FIT ø3/16 THREADED DOWEL.
4 HOLES TAP FOR 2-56 ON ø0.000 BC. DRILL 0.125 DEEP.
UNLESS OTHERWISE SPECIFIED
DIMENSIONS ARE IN INCHES
TOLERANCES: (UNLESS SPECIFIED)
DECIMALS
.X ± .06
.XX ± .03
.XXX ± .01
ANGLES
± 0.1°
MATERIAL: SS 304
TITLE: AFOSR PULSED VALVE PART 2
VIEW 1 OF 3
PULSED VALVE FRONT PLATE
FRONT AND BACK VIEW
FILE: PVFRONT1.DWG
DWG BY: MSJ / MODIFIED JMS
DATE: 8-16-03/7-15-96 SCALE: 1:1
PROF. M. OKUMURA LABORATORY
DIVISION OF CHEMISTRY: CALIFORNIA
INSTITUTE OF TECHNOLOGY

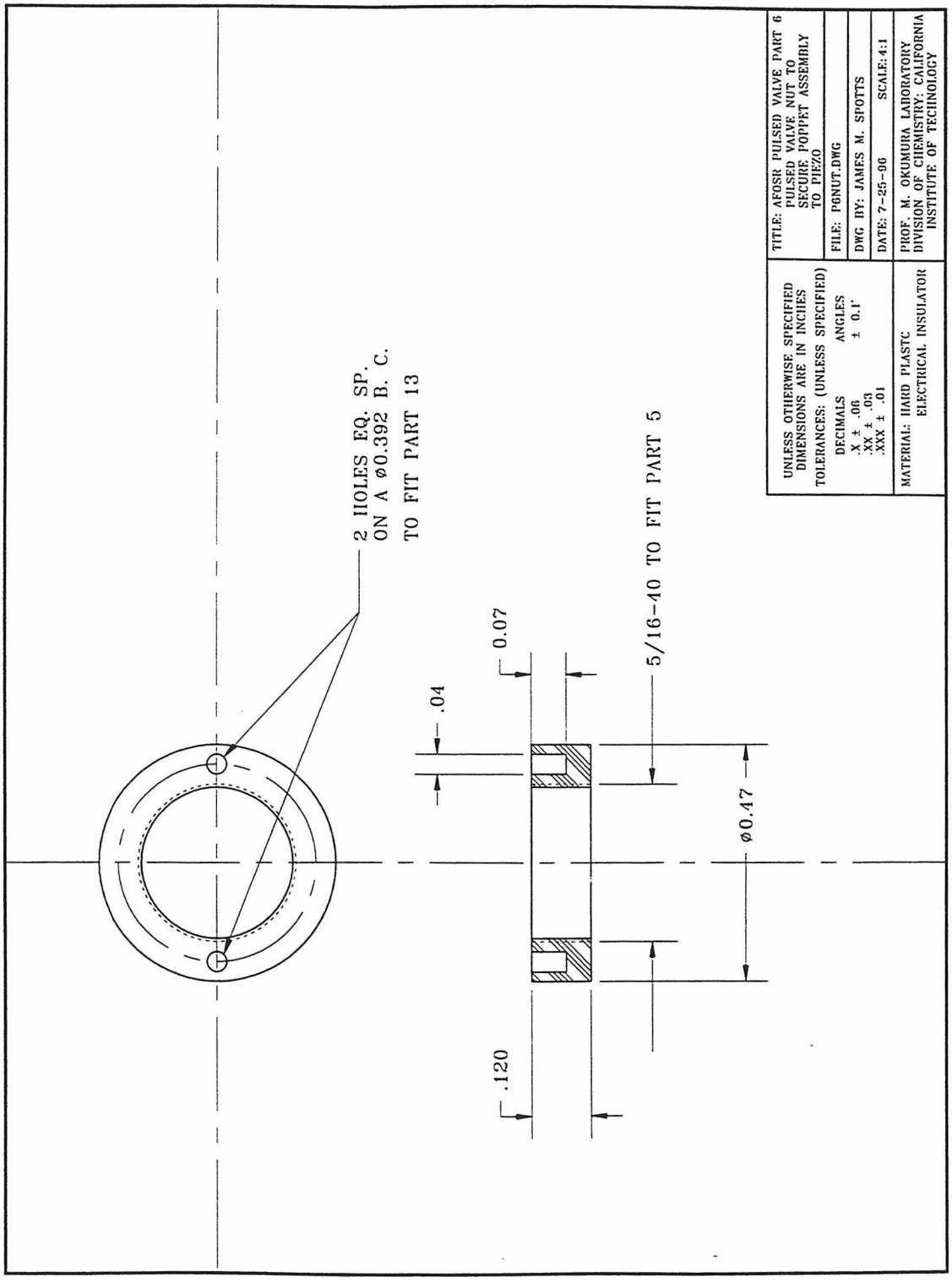

SECTION A–B
0.080
0.265
0.330
0.30
PUMPING HOLE ø0.05
ø2.15
ø2.07
ø1.25
0.040
0.160
DETAIL VIEW OF SEC. A–B
FLAT FOR KEYED FIT TO THREADED DOWEL.
KEYED FOR CLOSE FIT TO PART 3.
SMOOTH FINISH.
USE CAUTION WHEN TAPPING. BOTTOM OF HOLE IS 0.020 THICK.
CHAMFER TO FIT PART 5.
UNLESS OTHERWISE SPECIFIED DIMENSIONS ARE IN INCHES
TOLERANCES: (UNLESS SPECIFIED)
DECIMALS ANGLES
.X ± .06 ± 0.1°
.XX ± .03
.XXX ± .01
MATERIAL: SS 304
TITLE: AFOSR PULSED VALVE PART 2 VIEW 2 OF 3
PULSED VALVE FRONT PLATE SECTION A–B
FILE: PVFRONT2.DWG
DWG BY: MSJ / MODIFIED JMS
DATE: 8–16–03/7–15–06 SCALE: 1:1
PROF. M. OKUMURA LABORATORY
DIVISION OF CHEMISTRY; CALIFORNIA INSTITUTE OF TECHNOLOGY

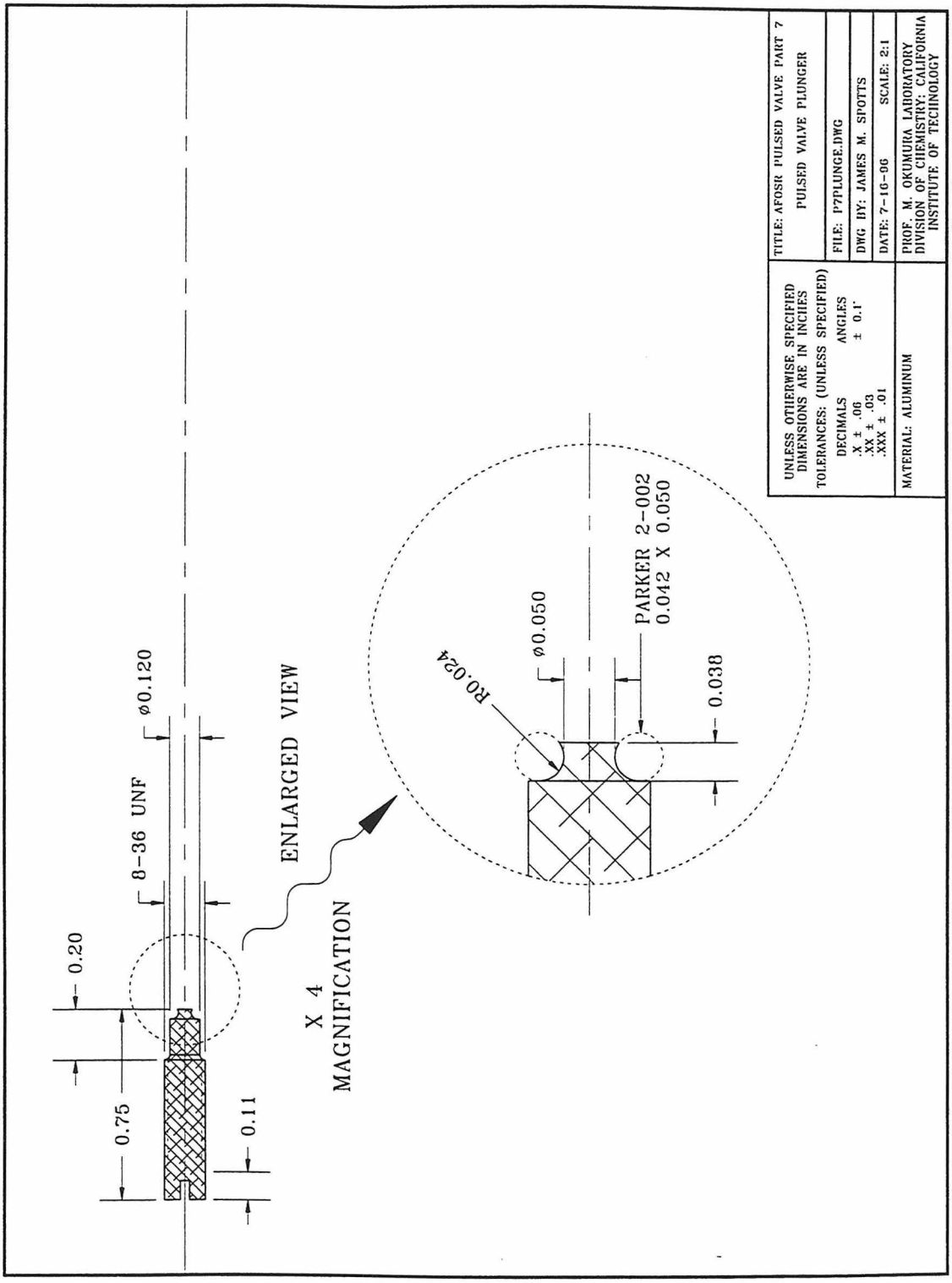

SECTION A–C
0.150
0.19
0.325
PUMPING HOLE ø0.05
0.680
ø0.30
ø0.375
ø0.545
ø1.100 -0.000/+0.0001
ø2.15
ø2.66+0.003
0.125
0.050
0.270
TITLE: AFOSR PULSED VALVE PART 2
VIEW 3 OF 3
PULSED VALVE FRONT PLATE
SECTION A-C
FILE: PVFRONT3.DWG
DWG BY: MSJ / MODIFIED JMS
DATE: 8-16-93/7-15-96 SCALE: 1:1
UNLESS OTHERWISE SPECIFIED
DIMENSIONS ARE IN INCHES
TOLERANCES: (UNLESS SPECIFIED)
DECIMALS ANGLES
.X ± .06 ± 0.1°
.XX ± .03
.XXX ± .01
MATERIAL: SS 304
PROF. M. OKUMURA LABORATORY
DIVISION OF CHEMISTRY; CALIFORNIA
INSTITUTE OF TECHNOLOGY

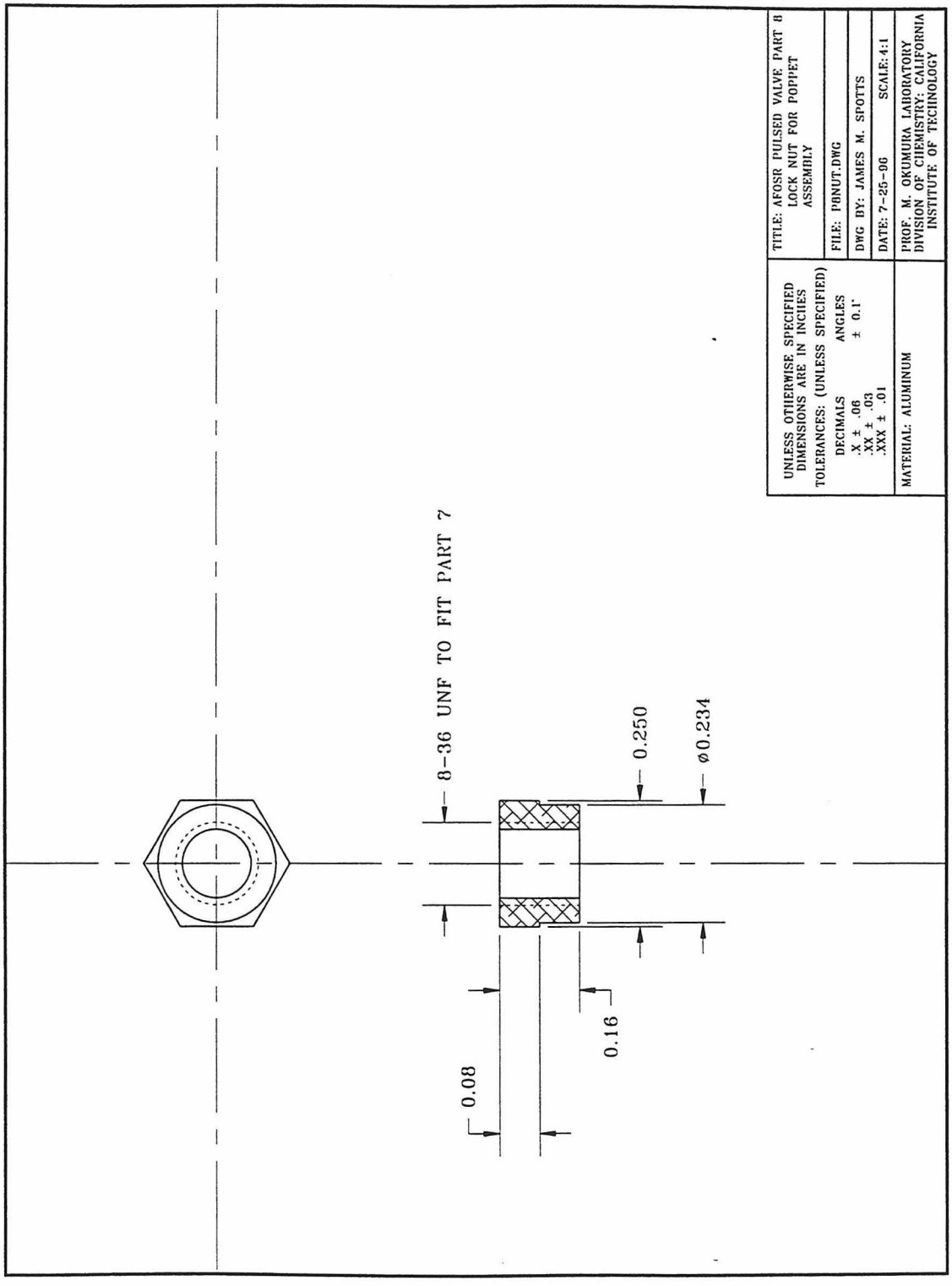

NOTES: 1. BOTH SURFACES REQUIRE SMOOTH FINISH.
2. KEYED TO FIT PULSED VALVE PART 2 (PULSED VALVE FRONT PLATE).
3. CHAMFER OUTSIDE EDGES.
0.30
0.055
0.270 ± 0.002
ø1.100 -0.0005 -0.0006
4 HOLES CLEARANCE FOR 2-56 EQ SP ON ø0.800 B. C.
COUNTERBORE FOR HEX SOCKET HEAD.
BORE ø1mm CHANNEL. DO NOT BREAK EDGES.
UNLESS OTHERWISE SPECIFIED
DIMENSIONS ARE IN INCHES
TOLERANCES: (UNLESS SPECIFIED)
DECIMALS ANGLES
.X ± .06 ± 0.1°
.XX ± .03
.XXX ± .01
MATERIAL: SS 304
TITLE: AFOSR PULSED VALVE PART 3
PULSED VALVE NOZZLE PLATE
FILE: P3NOZZLE.DWG
DWG BY: MSJ / MODIFIED JMS
DATE: 8-16-96/7-16-96 SCALE: 1:1
PROF. M. OKUMURA LABORATORY
DIVISION OF CHEMISTRY: CALIFORNIA
INSTITUTE OF TECHNOLOGY

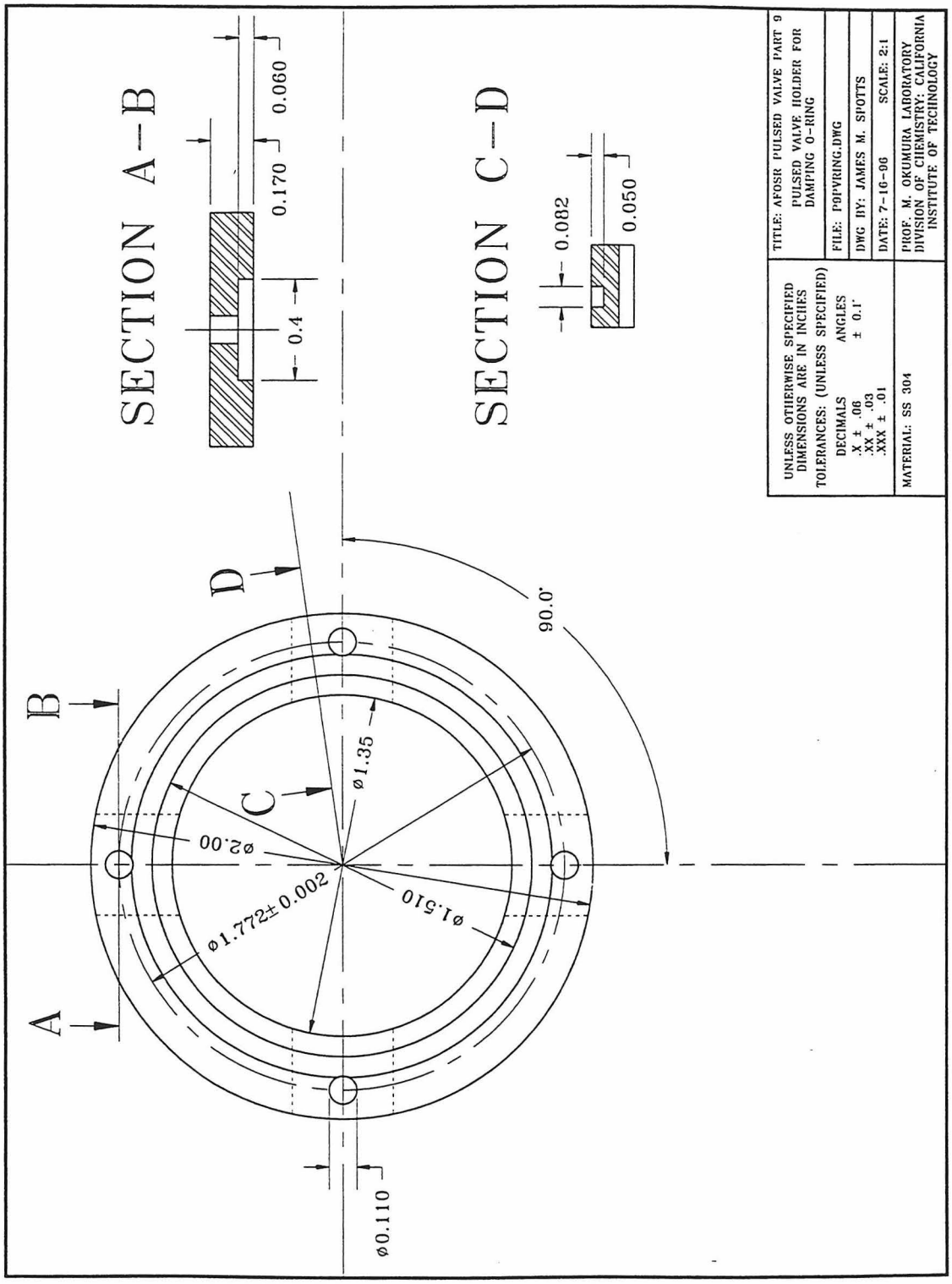

3-48 UNC
0.250
0.480
ø0.101-0.002
0.620
0.060
3-48 UNC
ø0.200-0.002
TO FIT PART 2
UNLESS OTHERWISE SPECIFIED
DIMENSIONS ARE IN INCHES
TOLERANCES: (UNLESS SPECIFIED)
DECIMALS
X ± .06
.XX ± .03
.XXX ± .01
ANGLES
± 0.1°
MATERIAL: SS 304
FABRICATE 4 PIECES
TITLE: AFOSR PULSED VALVE PART 4
PULSED VALVE BOLT
FILE: P4PVBOLT.DWG
DWG BY: JAMES M. SPOTTS
DATE: 7-25-96
SCALE: 10:1
PROF. M. OKUMURA LABORATORY
DIVISION OF CHEMISTRY: CALIFORNIA
INSTITUTE OF TECHNOLOGY

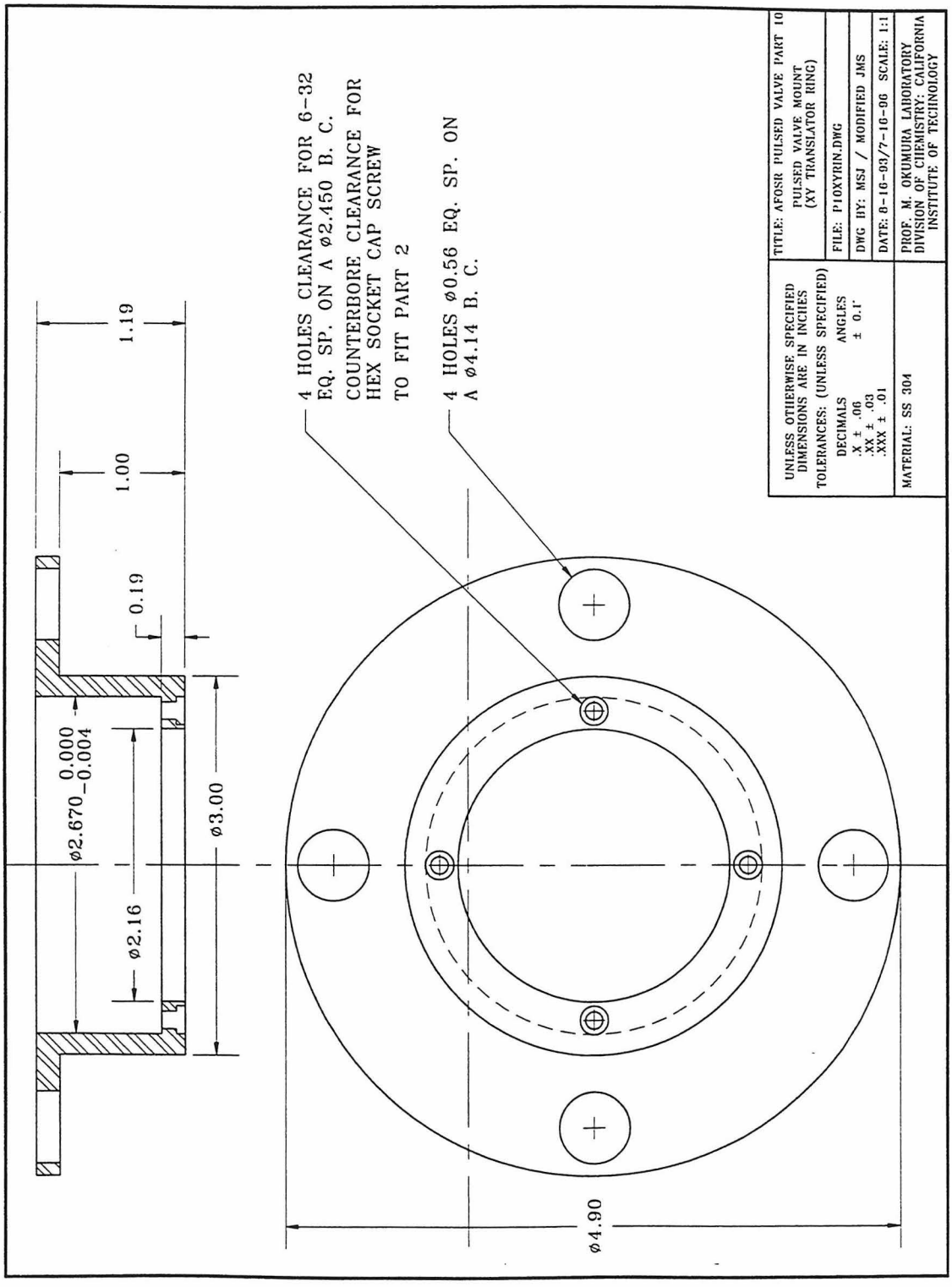

ø0.060 2 HOLES EQ. SP. ON A ø0.270
B. C. TO WITHIN 0.010 OF T.P.
DEPTH = 0.030
TO FIT WRENCH PINS, PART 12
DRILL THRU AND TAP THRU FOR
8-36 UNF
THREAD SHOULD BE TIGHT AGAINST
MATING THREAD, PART 7, SUCH
THAT SCREW TURING IS HARD.
ø0.47
0.126
0.145
0.175
ø0.394 +0.000 -0.002
TO KEY I.D. OF
P. I. PIEZO
P-286.2
THREAD FOR 5/16-40
SNUG FIT W/ PART 6
UNLESS OTHERWISE SPECIFIED
DIMENSIONS ARE IN INCHES
TOLERANCES: (UNLESS SPECIFIED)
DECIMALS
X ± .06
.XX ± .03
.XXX ± .01
ANGLES
± 0.1°
MATERIAL: ALUMINUM
TITLE: AFOSR PULSED VALVE PART 5
PULSED VALVE HOLDER FOR
PLUNGER
FILE: P5HOLDER.DWG
DWG BY: JAMES M. SPOTTS
DATE: 7-16-96
SCALE: 4:1
PROF. M. OKUMURA LABORATORY
DIVISION OF CHEMISTRY: CALIFORNIA
INSTITUTE OF TECHNOLOGY

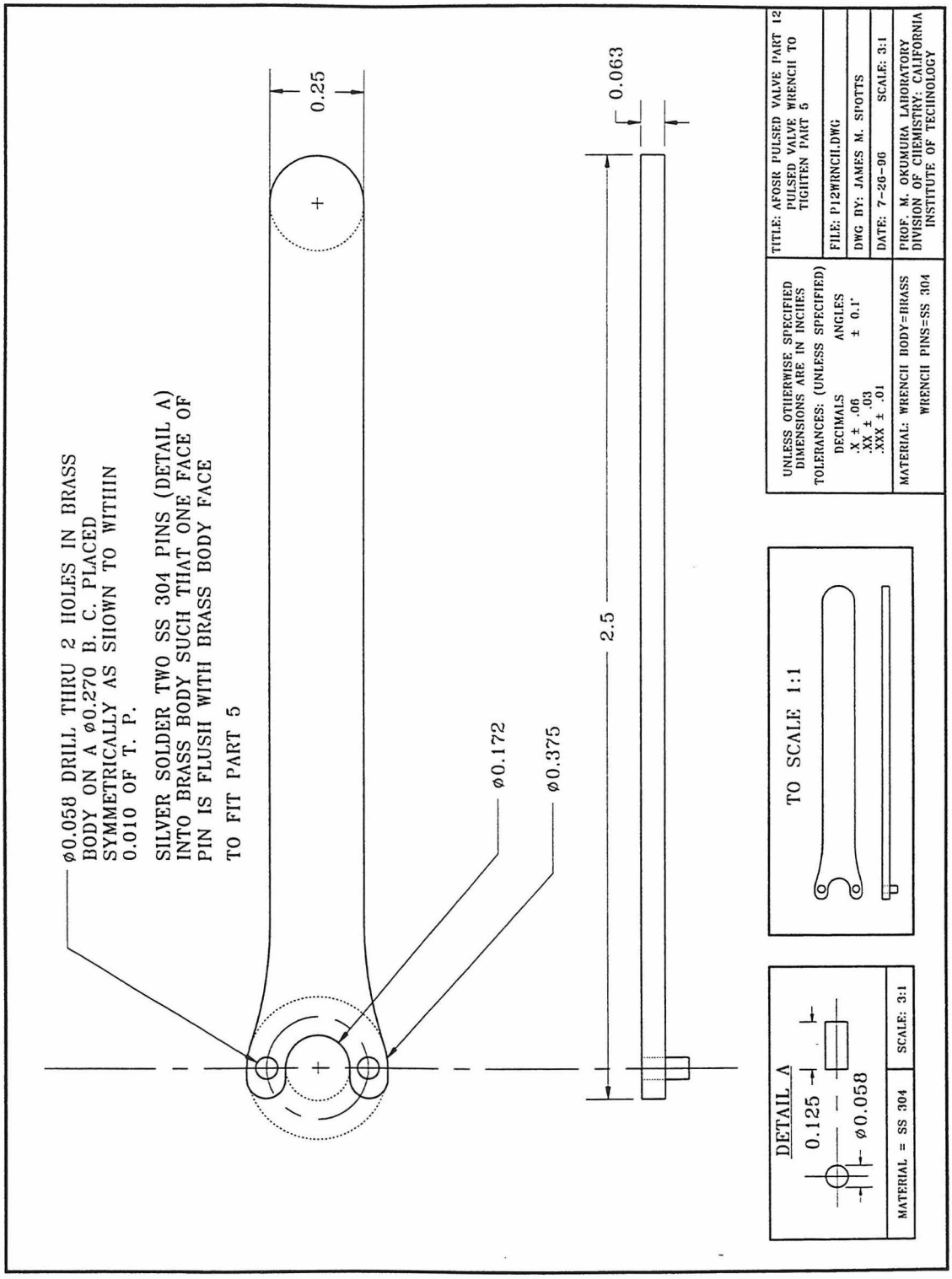

2 HOLES EQ. SP.
ON A ø0.392 B. C.
TO FIT PART 13
.04
0.07
5/16-40 TO FIT PART 5
ø0.47
.120
UNLESS OTHERWISE SPECIFIED
DIMENSIONS ARE IN INCHES
TOLERANCES: (UNLESS SPECIFIED)
DECIMALS
X ± .06
.XX ± .03
.XXX ± .01
ANGLES
± 0.1°
MATERIAL: HARD PLASTC
ELECTRICAL INSULATOR
TITLE: AFOSR PULSED VALVE PART 6
PULSED VALVE NUT TO
SECURE POPPET ASSEMBLY
TO PIEZO
FILE: P6NUT.DWG
DWG BY: JAMES M. SPOTTS
DATE: 7-25-06
SCALE:4:1
PROF. M. OKUMURA LABORATORY
DIVISION OF CHEMISTRY: CALIFORNIA
INSTITUTE OF TECHNOLOGY

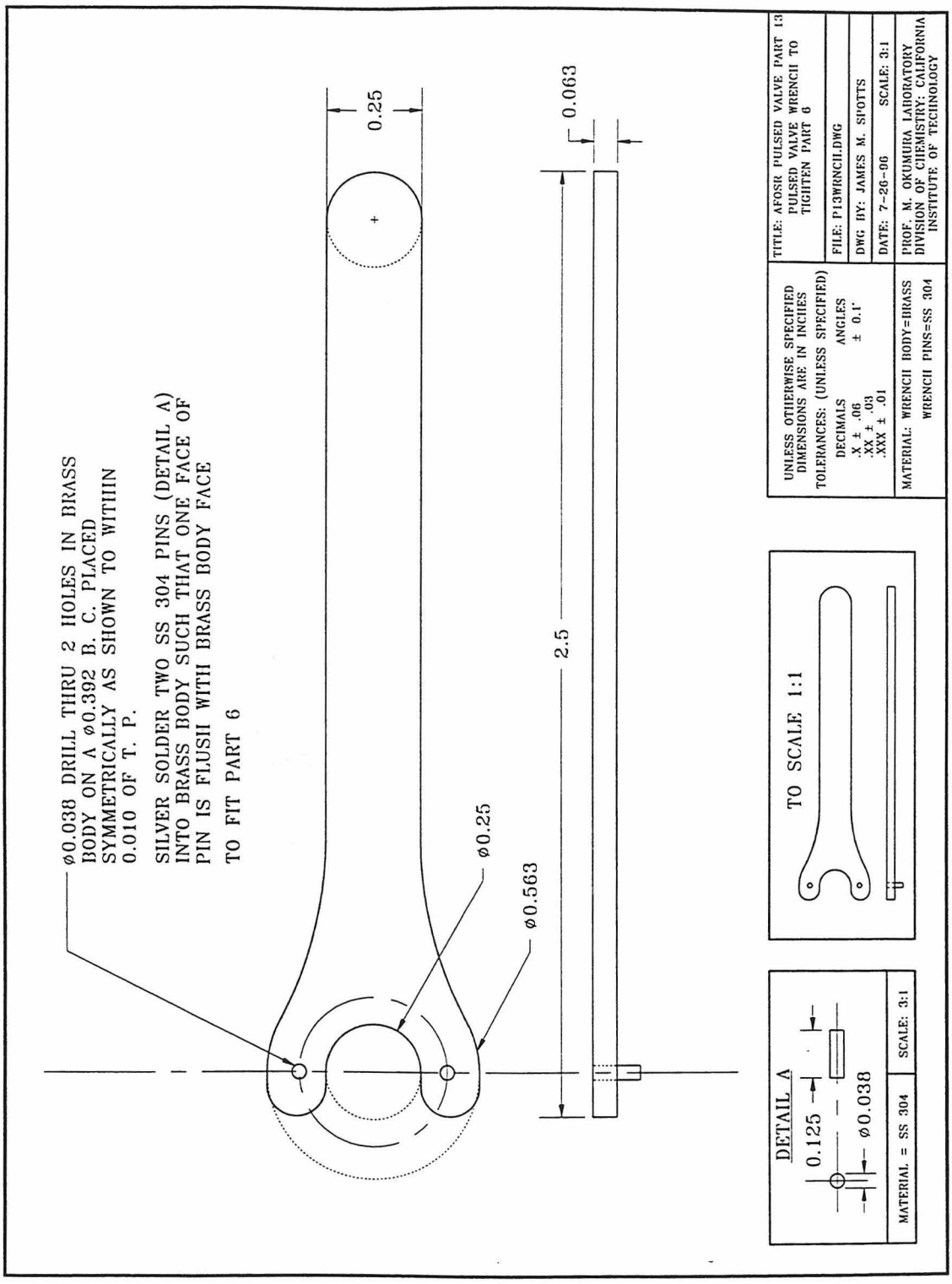

0.20
0.75
0.11
8-36 UNF
ø0.120
ENLARGED VIEW
X 4
MAGNIFICATION
R0.024
ø0.050
PARKER 2-002
0.042 X 0.050
0.038
UNLESS OTHERWISE SPECIFIED DIMENSIONS ARE IN INCHES
TOLERANCES: (UNLESS SPECIFIED)
DECIMALS
.X ± .06
.XX ± .03
.XXX ± .01
ANGLES
± 0.1°
MATERIAL: ALUMINUM
TITLE: AFOSR PULSED VALVE PART 7
PULSED VALVE PLUNGER
FILE: P7PLUNGE.DWG
DWG BY: JAMES M. SPOTTS
DATE: 7-16-96
SCALE: 2:1
PROF. M. OKUMURA LABORATORY
DIVISION OF CHEMISTRY: CALIFORNIA
INSTITUTE OF TECHNOLOGY


8-36 UNF TO FIT PART 7
0.250
ø0.234
0.08
0.16
UNLESS OTHERWISE SPECIFIED
DIMENSIONS ARE IN INCHES
TOLERANCES: (UNLESS SPECIFIED)
DECIMALS ANGLES
.X ± .06 ± 0.1°
.XX ± .03
.XXX ± .01
MATERIAL: ALUMINUM
TITLE: AFOSR PULSED VALVE PART 8
LOCK NUT FOR POPPET
ASSEMBLY
FILE: P8NUT.DWG
DWG BY: JAMES M. SPOTTS
DATE: 7-25-06
SCALE: 4:1
PROF. M. OKUMURA LABORATORY
DIVISION OF CHEMISTRY: CALIFORNIA
INSTITUTE OF TECHNOLOGY


SECTION A–B
0.060
0.170
0.4
SECTION C–D
0.082
0.050
A
B
C
D
90.0°
ø1.35
ø2.00
ø1.772±0.002
ø1.510
ø0.110
UNLESS OTHERWISE SPECIFIED
DIMENSIONS ARE IN INCHES
TOLERANCES: (UNLESS SPECIFIED)
DECIMALS
.X ± .06
.XX ± .03
.XXX ± .01
ANGLES
± 0.1°
MATERIAL: SS 304
TITLE: AFOSR PULSED VALVE PART 9
PULSED VALVE HOLDER FOR
DAMPING O-RING
FILE: P9PVRING.DWG
DWG BY: JAMES M. SPOTTS
DATE: 7-16-96
SCALE: 2:1
PROF. M. OKUMURA LABORATORY
DIVISION OF CHEMISTRY: CALIFORNIA
INSTITUTE OF TECHNOLOGY

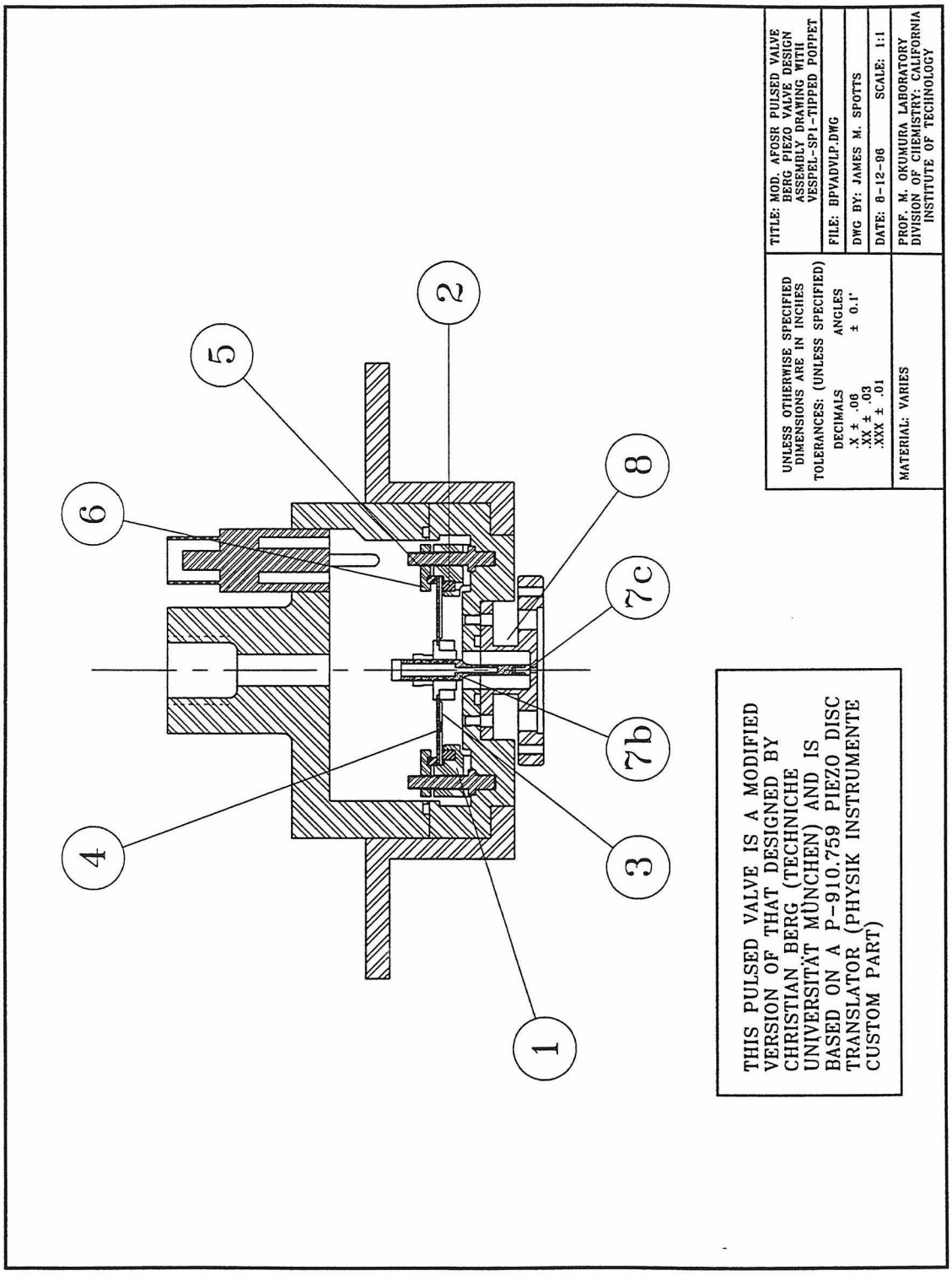

4 HOLES CLEARANCE FOR 6-32
EQ. SP. ON A ø2.450 B. C.
COUNTERBORE CLEARANCE FOR
HEX SOCKET CAP SCREW
TO FIT PART 2
4 HOLES ø0.56 EQ. SP. ON
A ø4.14 B. C.
1.19
1.00
0.19
ø2.670 0.000 -0.004
ø2.16
ø3.00
ø4.90
UNLESS OTHERWISE SPECIFIED
DIMENSIONS ARE IN INCHES
TOLERANCES: (UNLESS SPECIFIED)
DECIMALS
.X ± .06
.XX ± .03
.XXX ± .01
ANGLES
± 0.1°
MATERIAL: SS 304
TITLE: AFOSR PULSED VALVE PART 10
PULSED VALVE MOUNT
(XY TRANSLATOR RING)
FILE: P10XYRIN.DWG
DWG BY: MSJ / MODIFIED JMS
DATE: 8-16-93/7-16-96 SCALE: 1:1
PROF. M. OKUMURA LABORATORY
DIVISION OF CHEMISTRY: CALIFORNIA
INSTITUTE OF TECHNOLOGY

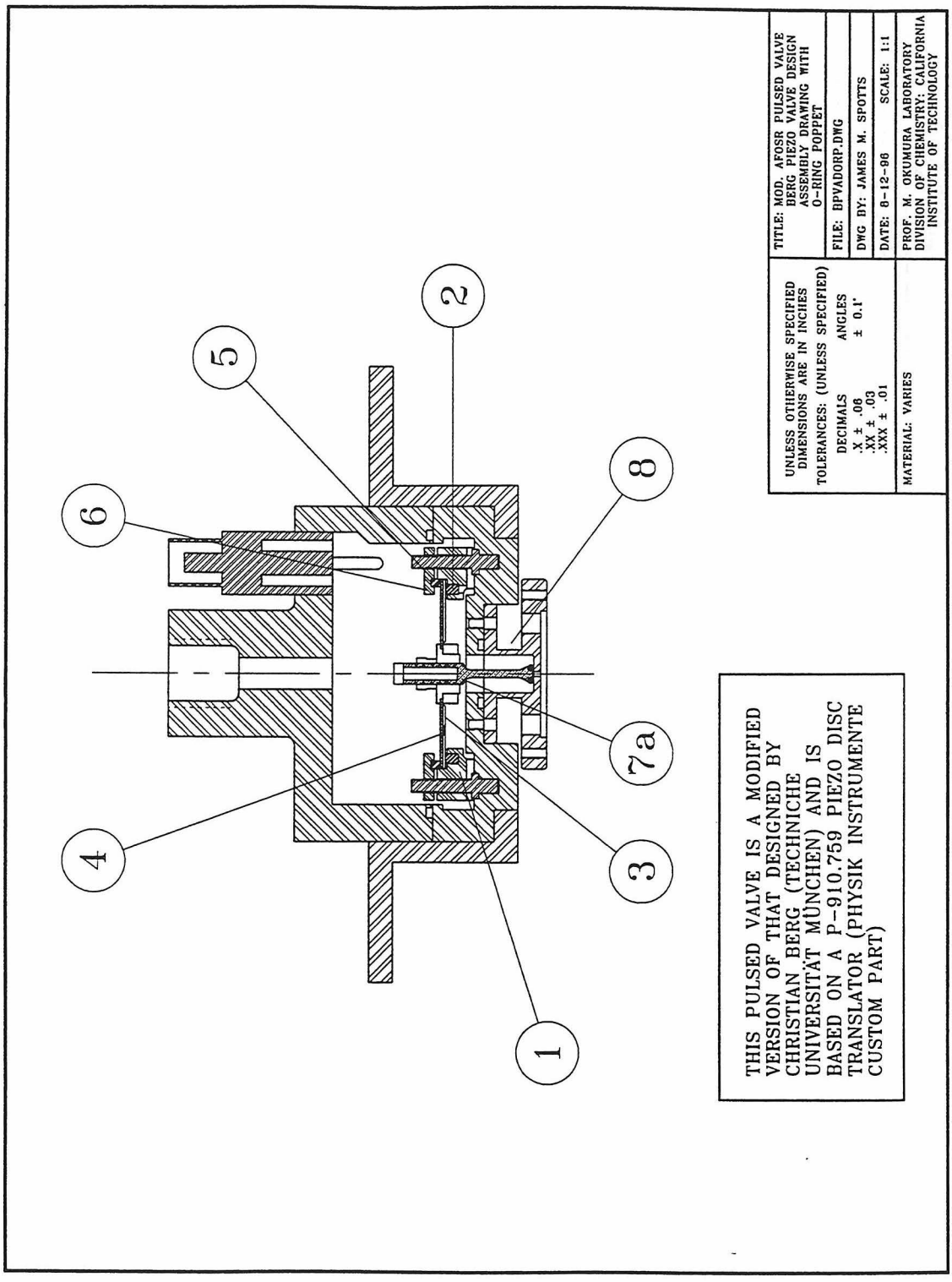

ø0.058 DRILL THRU 2 HOLES IN BRASS BODY ON A ø0.270 B. C. PLACED SYMMETRICALLY AS SHOWN TO WITHIN 0.010 OF T. P.
SILVER SOLDER TWO SS 304 PINS (DETAIL A) INTO BRASS BODY SUCH THAT ONE FACE OF PIN IS FLUSH WITH BRASS BODY FACE TO FIT PART 5
0.25
0.063
2.5
ø0.172
ø0.375
TO SCALE 1:1
DETAIL A
0.125
ø0.058
MATERIAL = SS 304
SCALE: 3:1
UNLESS OTHERWISE SPECIFIED DIMENSIONS ARE IN INCHES
TOLERANCES: (UNLESS SPECIFIED)
DECIMALS
X ± .06
.XX ± .03
.XXX ± .01
ANGLES
± 0.1°
MATERIAL: WRENCH BODY=BRASS
WRENCH PINS=SS 304
TITLE: AFOSR PULSED VALVE PART 12
PULSED VALVE WRENCH TO TIGHTEN PART 5
FILE: P12WRNCH.DWG
DWG BY: JAMES M. SPOTTS
DATE: 7-26-96
SCALE: 3:1
PROF. M. OKUMURA LABORATORY
DIVISION OF CHEMISTRY: CALIFORNIA INSTITUTE OF TECHNOLOGY

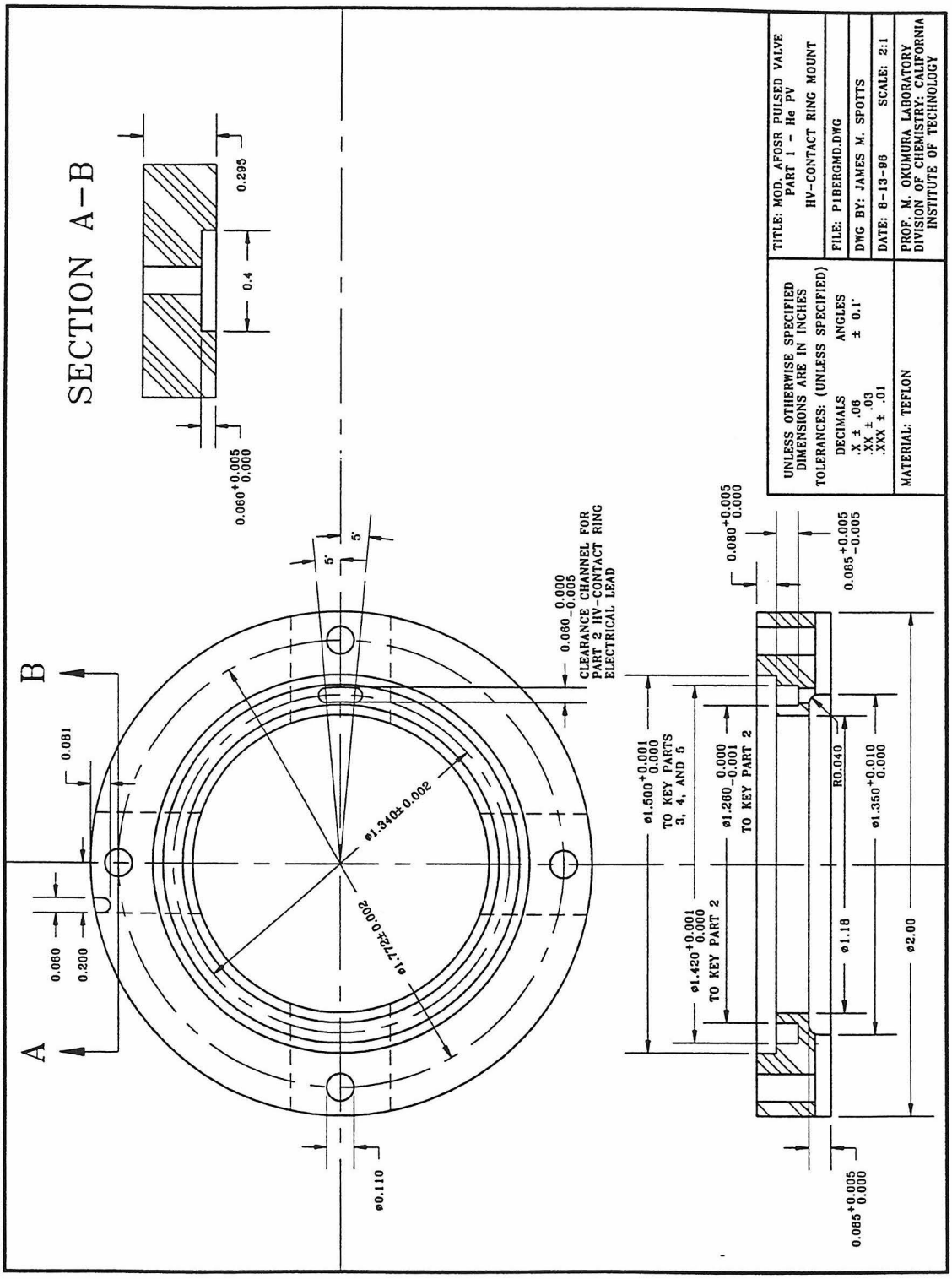

ø0.038 DRILL THRU 2 HOLES IN BRASS BODY ON A ø0.392 B. C. PLACED SYMMETRICALLY AS SHOWN TO WITHIN 0.010 OF T. P.
SILVER SOLDER TWO SS 304 PINS (DETAIL A) INTO BRASS BODY SUCH THAT ONE FACE OF PIN IS FLUSH WITH BRASS BODY FACE TO FIT PART 6
0.25
0.063
2.5
ø0.25
ø0.563
TO SCALE 1:1
DETAIL A
0.125
ø0.038
MATERIAL = SS 304
SCALE: 3:1
UNLESS OTHERWISE SPECIFIED DIMENSIONS ARE IN INCHES
TOLERANCES: (UNLESS SPECIFIED)
DECIMALS
.X ± .06
.XX ± .03
.XXX ± .01
ANGLES
± 0.1°
MATERIAL: WRENCH BODY=BRASS
WRENCH PINS=SS 304
TITLE: AFOSR PULSED VALVE PART 13 PULSED VALVE WRENCH TO TIGHTEN PART 6
FILE: P13WRNCH.DWG
DWG BY: JAMES M. SPOTTS
DATE: 7-26-96
SCALE: 3:1
PROF. M. OKUMURA LABORATORY
DIVISION OF CHEMISTRY: CALIFORNIA INSTITUTE OF TECHNOLOGY

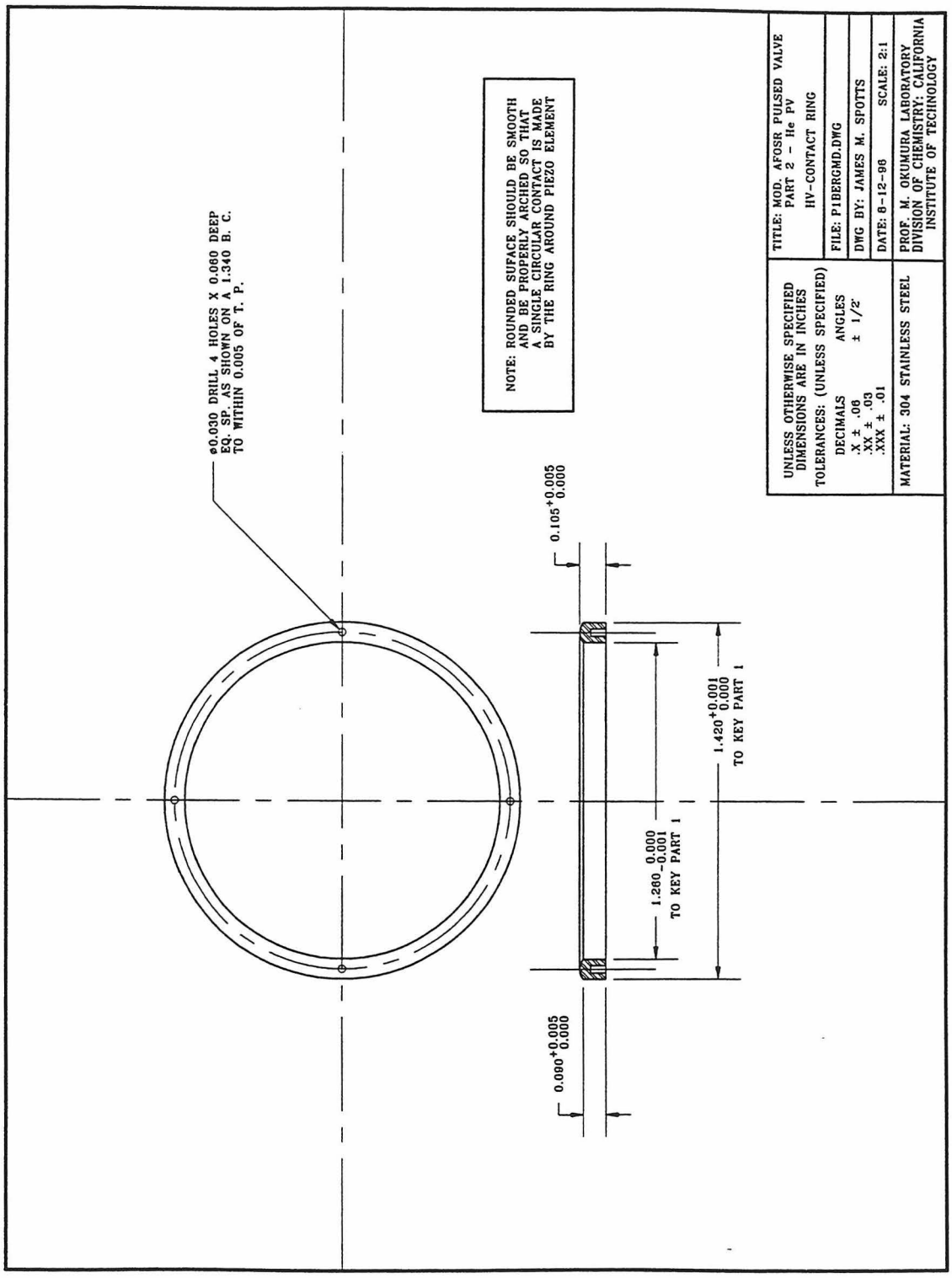
APPENDIX 3

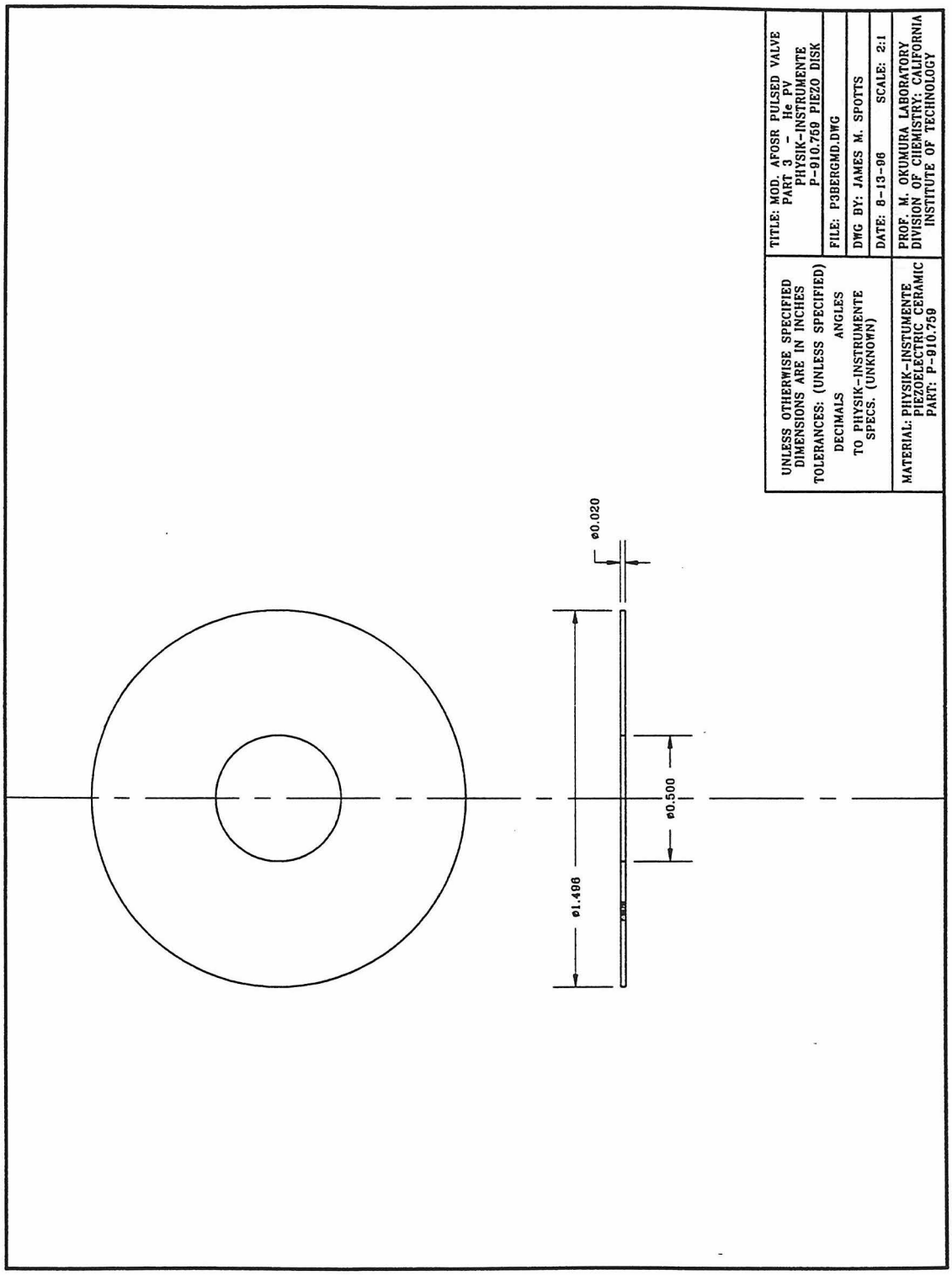
Drawings for the Modified Piezoelectric Pulsed Valve Based of the Design of Christian Berg

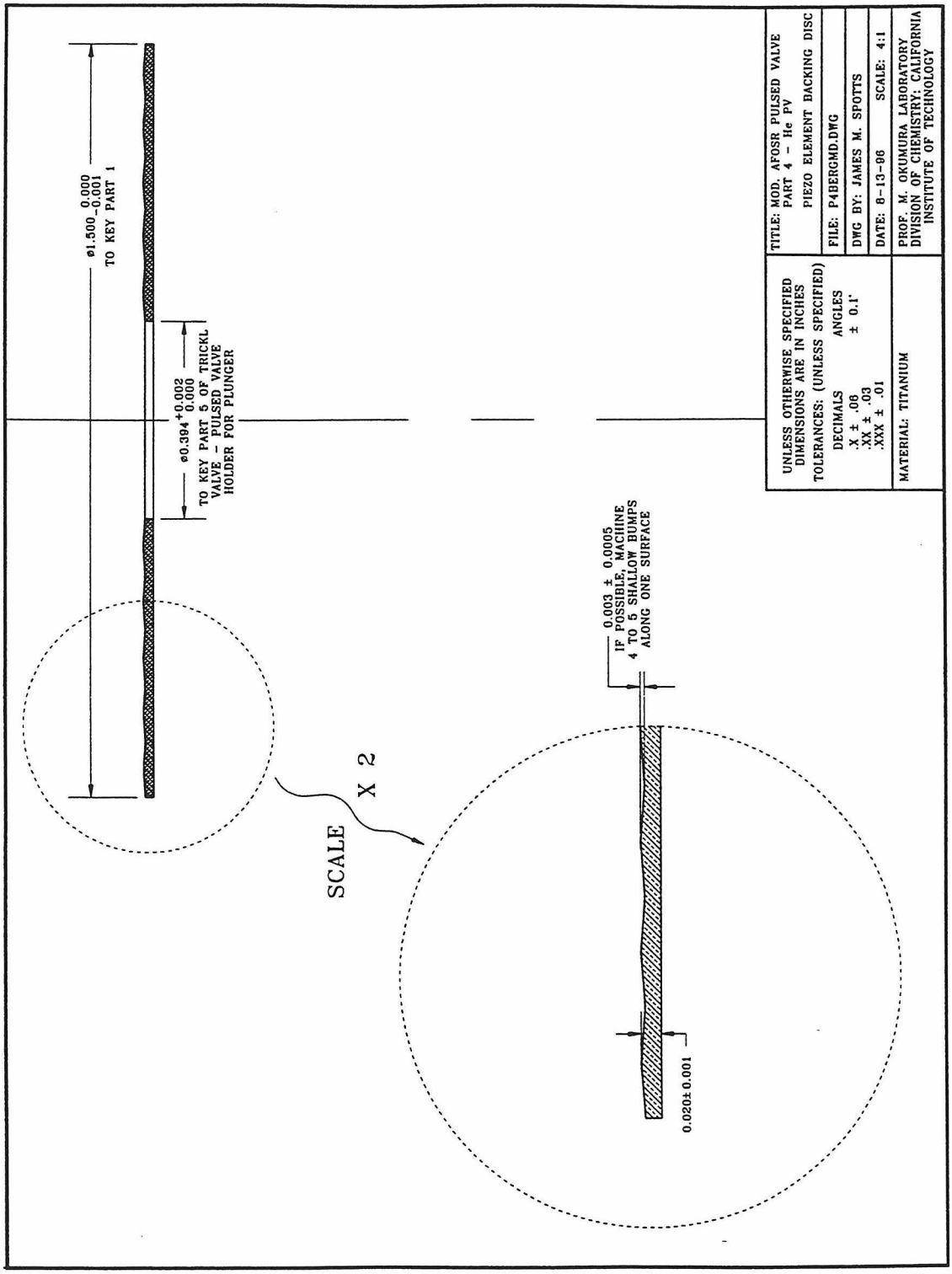

1
2
3
4
5
6
7b
7c
8
THIS PULSED VALVE IS A MODIFIED VERSION OF THAT DESIGNED BY CHRISTIAN BERG (TECHNICHE UNIVERSITÄT MÜNCHEN) AND IS BASED ON A P-910.759 PIEZO DISC TRANSLATOR (PHYSIK INSTRUMENTE CUSTOM PART)
UNLESS OTHERWISE SPECIFIED DIMENSIONS ARE IN INCHES
TOLERANCES: (UNLESS SPECIFIED)
DECIMALS ANGLES
X ± .06 ± 0.1°
.XX ± .03
.XXX ± .01
MATERIAL: VARIES
TITLE: MOD. AFOSR PULSED VALVE BERG PIEZO VALVE DESIGN ASSEMBLY DRAWING WITH VESPEL-SP1-TIPPED POPPET
FILE: BPVADVLP.DWG
DWG BY: JAMES M. SPOTTS
DATE: 8-12-96 SCALE: 1:1
PROF. M. OKUMURA LABORATORY
DIVISION OF CHEMISTRY: CALIFORNIA INSTITUTE OF TECHNOLOGY

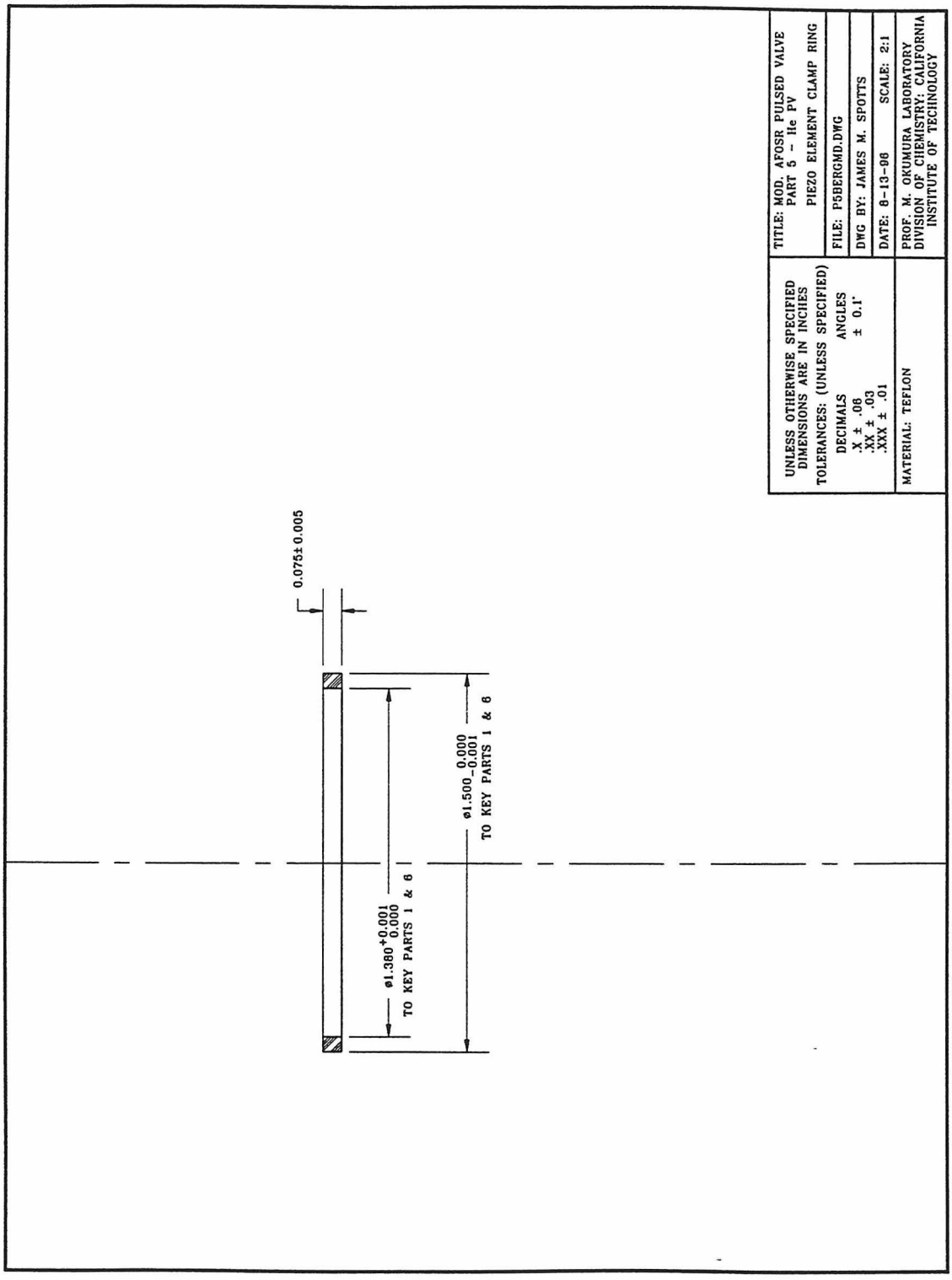

1
2
3
4
5
6
7a
8
THIS PULSED VALVE IS A MODIFIED VERSION OF THAT DESIGNED BY CHRISTIAN BERG (TECHNICHE UNIVERSITÄT MÜNCHEN) AND IS BASED ON A P-910.759 PIEZO DISC TRANSLATOR (PHYSIK INSTRUMENTE CUSTOM PART)
UNLESS OTHERWISE SPECIFIED DIMENSIONS ARE IN INCHES
TOLERANCES: (UNLESS SPECIFIED)
DECIMALS ANGLES
.X ± .06 ± 0.1°
.XX ± .03
.XXX ± .01
MATERIAL: VARIES
TITLE: MOD. AFOSR PULSED VALVE BERG PIEZO VALVE DESIGN ASSEMBLY DRAWING WITH O-RING POPPET
FILE: BPVADORP.DWG
DWG BY: JAMES M. SPOTTS
DATE: 8-12-96 SCALE: 1:1
PROF. M. OKUMURA LABORATORY
DIVISION OF CHEMISTRY: CALIFORNIA INSTITUTE OF TECHNOLOGY

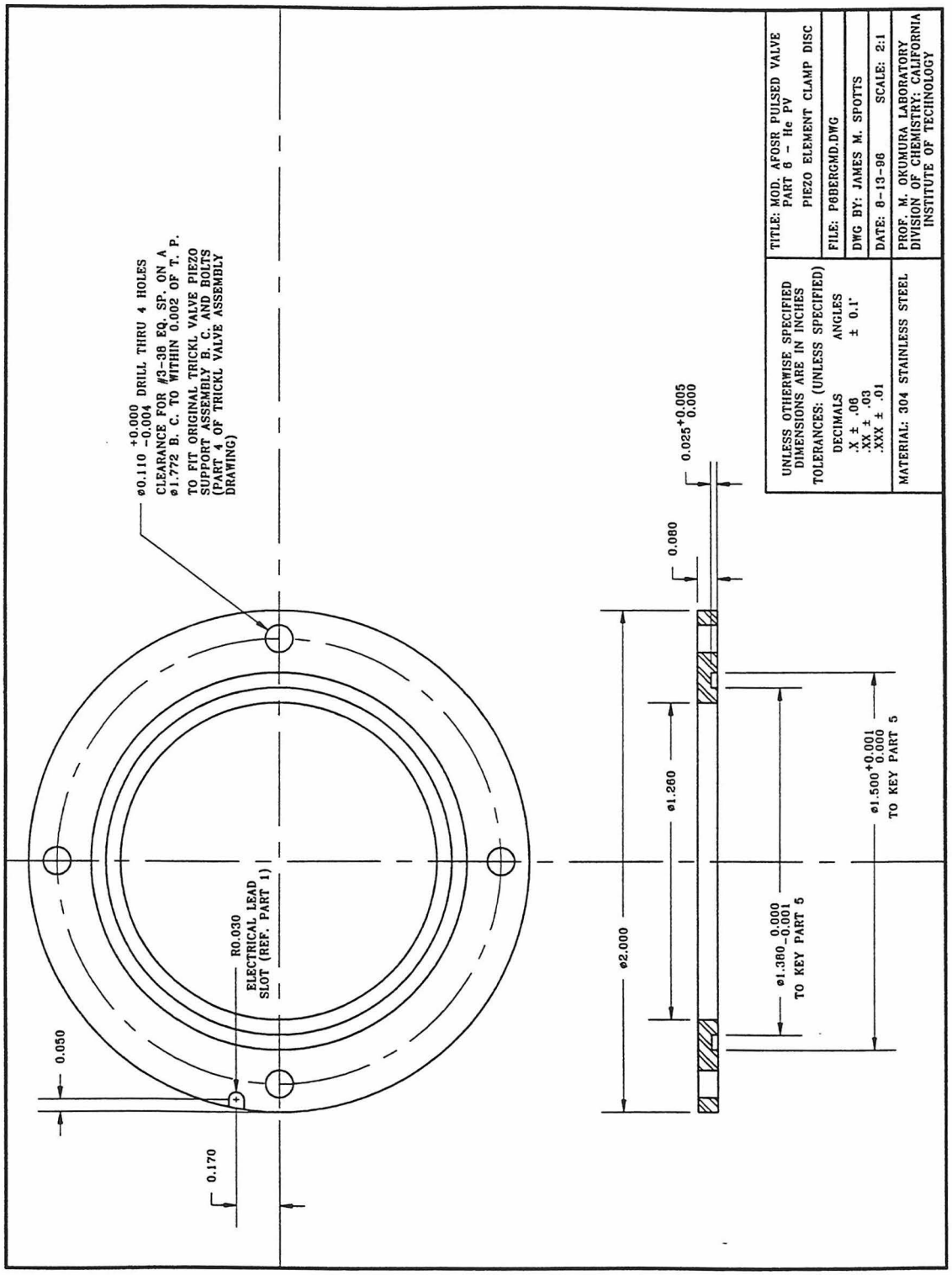

SECTION A–B
A
B
0.080
0.200
0.081
0.060 +0.005 0.000
0.295
0.4
5°
5°
ø1.340±0.002
ø1.772±0.002
0.060 0.000 −0.005
CLEARANCE CHANNEL FOR PART 2 HV-CONTACT RING ELECTRICAL LEAD
ø0.110
0.080 +0.005 0.000
0.085 +0.005 −0.005
ø1.500 +0.001 0.000
TO KEY PARTS 3, 4, AND 5
ø1.260 0.000 −0.001
TO KEY PART 2
ø1.420 +0.001 0.000
TO KEY PART 2
R0.040
ø1.350 +0.010 0.000
ø1.18
ø2.00
0.085 +0.005 0.000
UNLESS OTHERWISE SPECIFIED DIMENSIONS ARE IN INCHES
TOLERANCES: (UNLESS SPECIFIED)
DECIMALS
.X ± .06
.XX ± .03
.XXX ± .01
ANGLES
± 0.1°
MATERIAL: TEFLON
TITLE: MOD. AFOSR PULSED VALVE PART 1 - He PV HV-CONTACT RING MOUNT
FILE: P1BERGMD.DWG
DWG BY: JAMES M. SPOTTS
DATE: 8-13-96
SCALE: 2:1
PROF. M. OKUMURA LABORATORY
DIVISION OF CHEMISTRY: CALIFORNIA INSTITUTE OF TECHNOLOGY

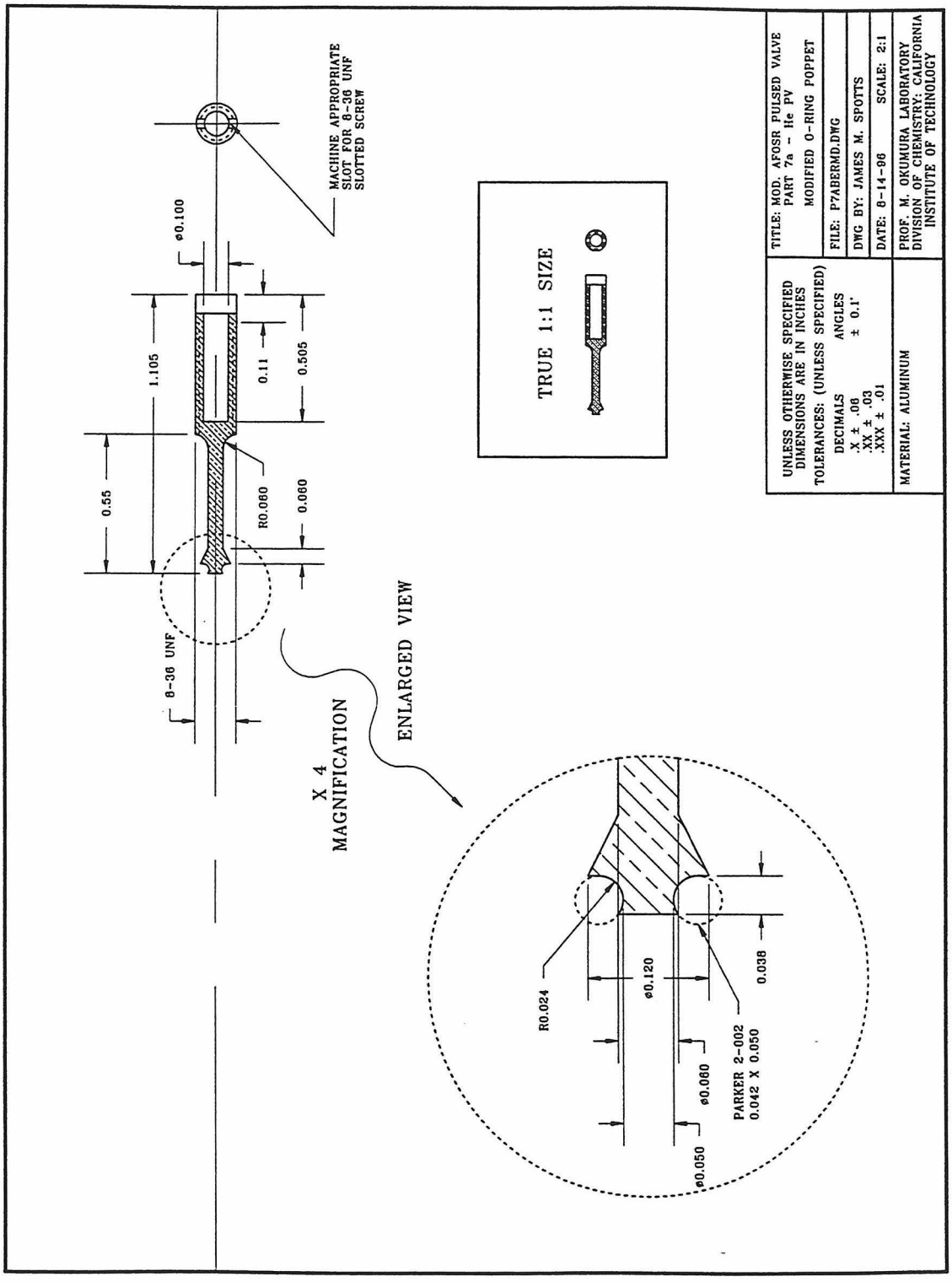

ø0.030 DRILL 4 HOLES X 0.060 DEEP
EQ. SP. AS SHOWN ON A 1.340 B. C.
TO WITHIN 0.005 OF T. P.
NOTE: ROUNDED SUFACE SHOULD BE SMOOTH AND BE PROPERLY ARCHED SO THAT A SINGLE CIRCULAR CONTACT IS MADE BY THE RING AROUND PIEZO ELEMENT
0.105 +0.005 0.000
1.420 +0.001 0.000 TO KEY PART 1
1.280 0.000 -0.001 TO KEY PART 1
0.090 +0.005 0.000
UNLESS OTHERWISE SPECIFIED DIMENSIONS ARE IN INCHES
TOLERANCES: (UNLESS SPECIFIED)
DECIMALS ANGLES
.X ± .06 ± 1/2°
.XX ± .03
.XXX ± .01
MATERIAL: 304 STAINLESS STEEL
TITLE: MOD. AFOSR PULSED VALVE PART 2 - He PV HV-CONTACT RING
FILE: P1BERGMD.DWG
DWG BY: JAMES M. SPOTTS
DATE: 8-12-96 SCALE: 2:1
PROF. M. OKUMURA LABORATORY DIVISION OF CHEMISTRY: CALIFORNIA INSTITUTE OF TECHNOLOGY

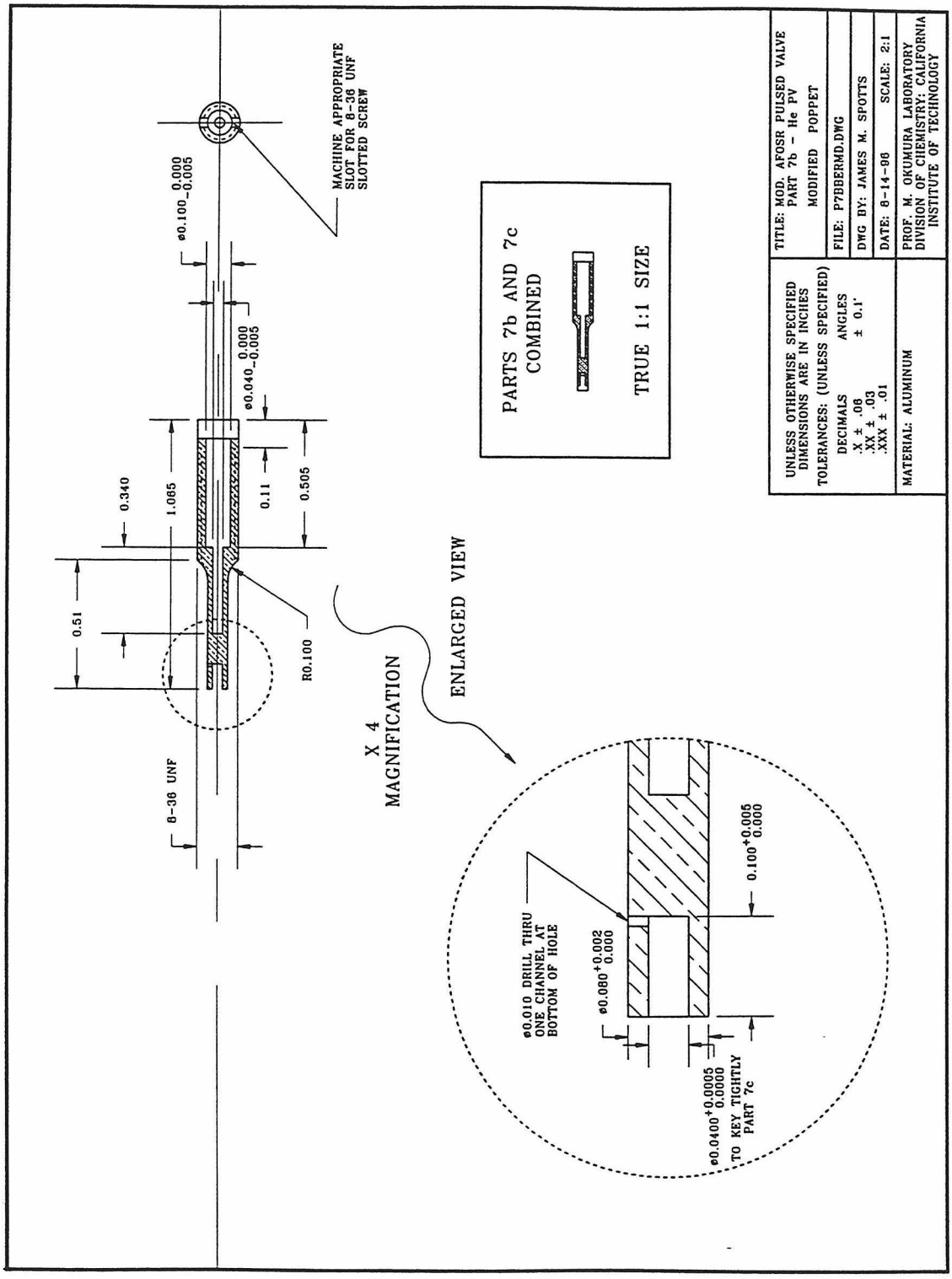

ø0.020
ø0.500
ø1.400
UNLESS OTHERWISE SPECIFIED
DIMENSIONS ARE IN INCHES
TOLERANCES: (UNLESS SPECIFIED)
DECIMALS ANGLES
TO PHYSIK-INSTRUMENTE SPECS. (UNKNOWN)
TITLE: MOD. AFOSR PULSED VALVE PART 3 - He PV
PHYSIK-INSTRUMENTE P-910.759 PIEZO DISK
FILE: P3BERGMD.DWG
DWG BY: JAMES M. SPOTTS
DATE: 8-13-98 SCALE: 2:1
MATERIAL: PHYSIK-INSTUMENTE PIEZOELECTRIC CERAMIC PART: P-910.759
PROF. M. OKUMURA LABORATORY
DIVISION OF CHEMISTRY: CALIFORNIA INSTITUTE OF TECHNOLOGY

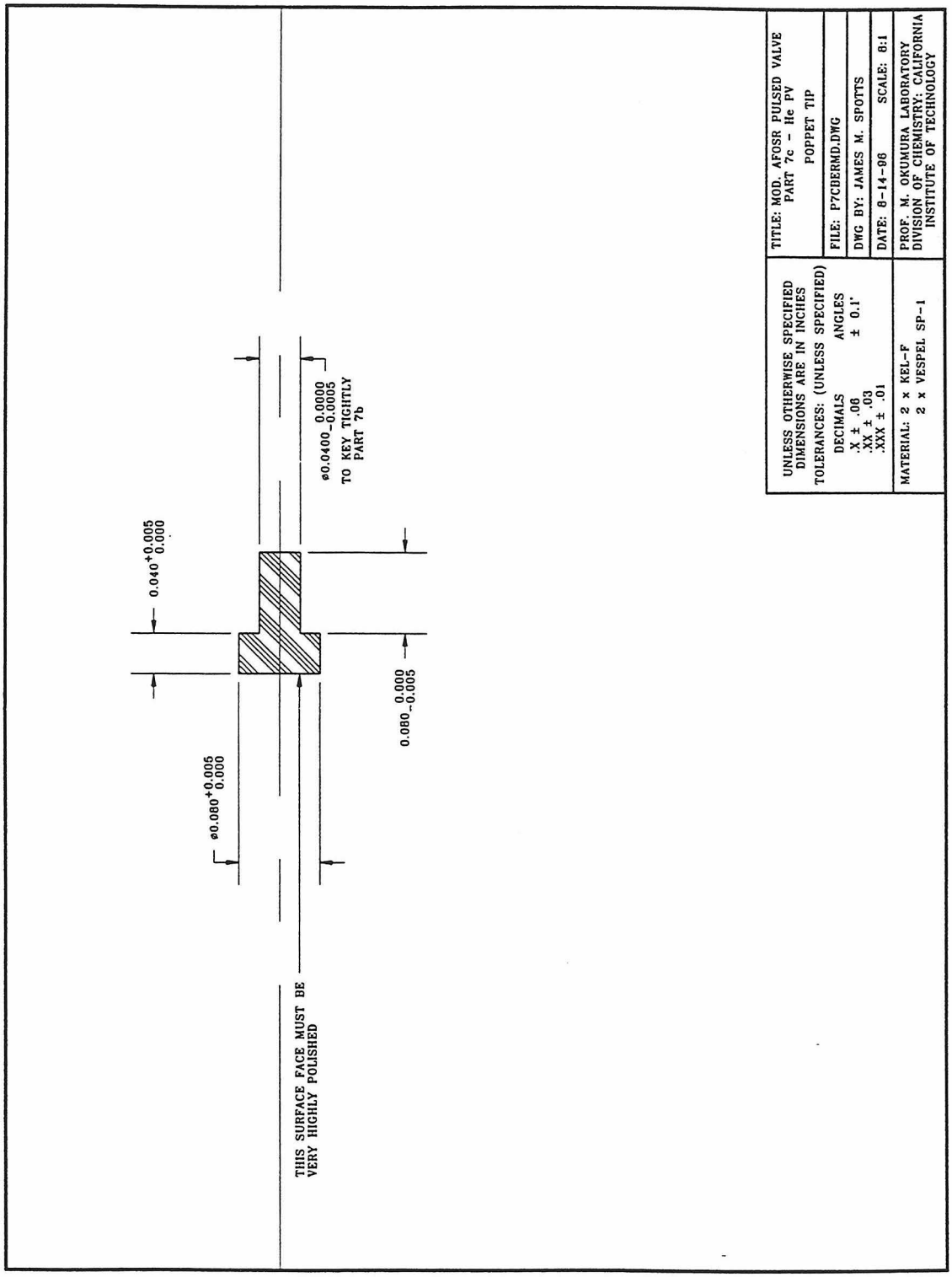

ø1.500 0.000 -0.001
TO KEY PART 1
ø0.394 +0.002 0.000
TO KEY PART 5 OF TRICKL VALVE - PULSED VALVE HOLDER FOR PLUNGER
0.003 ± 0.0005
IF POSSIBLE, MACHINE 4 TO 5 SHALLOW BUMPS ALONG ONE SURFACE
SCALE X 2
0.020± 0.001
UNLESS OTHERWISE SPECIFIED DIMENSIONS ARE IN INCHES
TOLERANCES: (UNLESS SPECIFIED)
DECIMALS ANGLES
.X ± .06 ± 0.1°
.XX ± .03
.XXX ± .01
MATERIAL: TITANIUM
TITLE: MOD. AFOSR PULSED VALVE PART 4 - He PV
PIEZO ELEMENT BACKING DISC
FILE: P4BERGMD.DWG
DWG BY: JAMES M. SPOTTS
DATE: 8-13-96
SCALE: 4:1
PROF. M. OKUMURA LABORATORY
DIVISION OF CHEMISTRY: CALIFORNIA INSTITUTE OF TECHNOLOGY

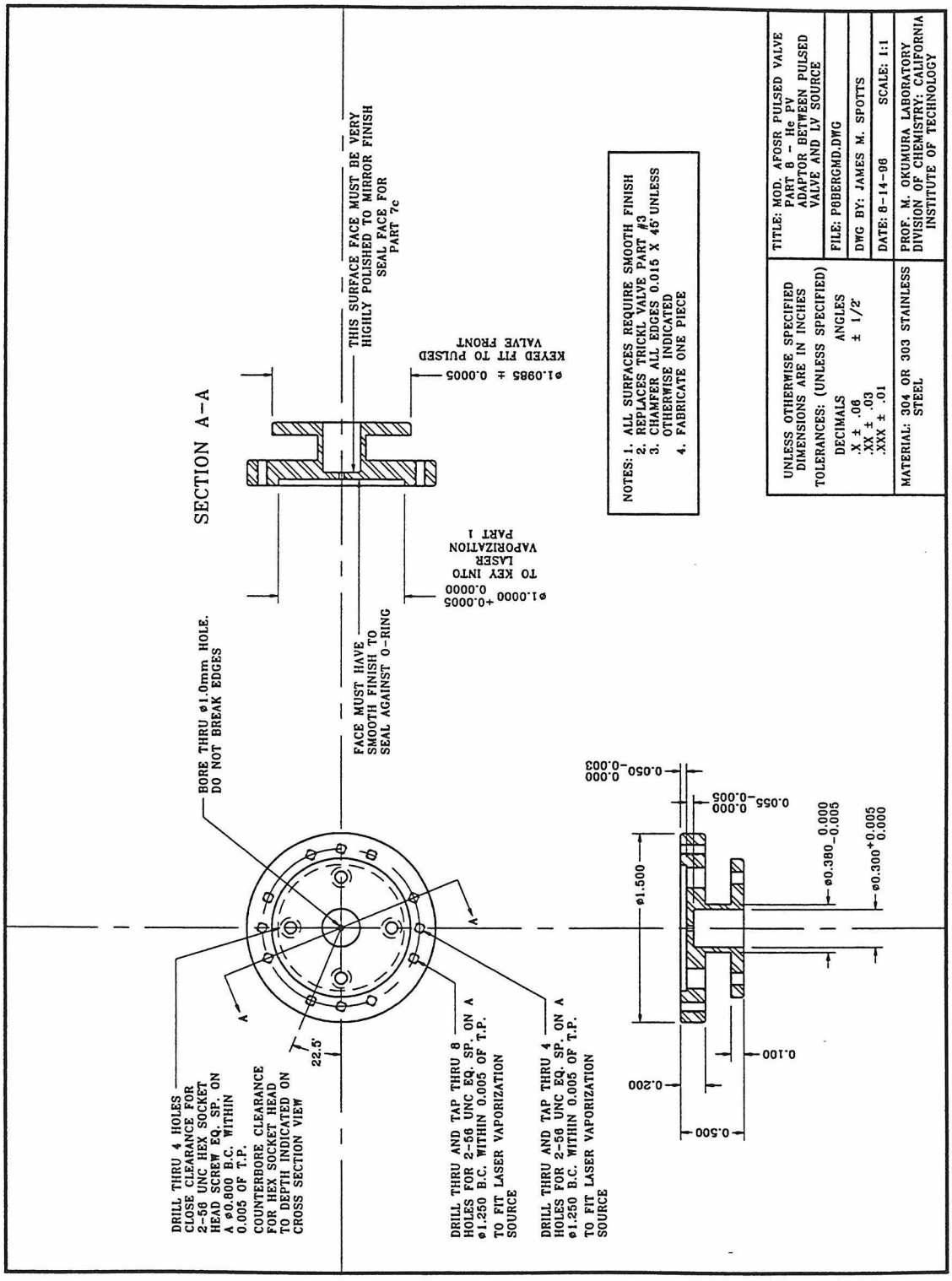

0.075±0.005
ø1.380 +0.001 0.000
TO KEY PARTS 1 & 6
ø1.500 0.000 -0.001
TO KEY PARTS 1 & 6
UNLESS OTHERWISE SPECIFIED
DIMENSIONS ARE IN INCHES
TOLERANCES: (UNLESS SPECIFIED)
DECIMALS
.X ± .06
.XX ± .03
.XXX ± .01
ANGLES
± 0.1°
MATERIAL: TEFLON
TITLE: MOD. AFOSR PULSED VALVE
PART 5 - IIe PV
PIEZO ELEMENT CLAMP RING
FILE: P5BERGMD.DWG
DWG BY: JAMES M. SPOTTS
DATE: 8-13-96
SCALE: 2:1
PROF. M. OKUMURA LABORATORY
DIVISION OF CHEMISTRY: CALIFORNIA
INSTITUTE OF TECHNOLOGY


ø0.110 +0.000 -0.004 DRILL THRU 4 HOLES
CLEARANCE FOR #3-38 EQ. SP. ON A ø1.772 B. C. TO WITHIN 0.002 OF T. P.
TO FIT ORIGINAL TRICKL VALVE PIEZO SUPPORT ASSEMBLY B. C. AND BOLTS (PART 4 OF TRICKL VALVE ASSEMBLY DRAWING)
R0.030
ELECTRICAL LEAD SLOT (REF. PART 1)
0.050
0.170
0.025 +0.005 0.000
0.080
ø2.000
ø1.280
ø1.380 0.000 -0.001
TO KEY PART 5
ø1.500 +0.001 0.000
TO KEY PART 5
UNLESS OTHERWISE SPECIFIED DIMENSIONS ARE IN INCHES
TOLERANCES: (UNLESS SPECIFIED)
DECIMALS
.X ± .06
.XX ± .03
.XXX ± .01
ANGLES
± 0.1°
MATERIAL: 304 STAINLESS STEEL
TITLE: MOD. AFOSR PULSED VALVE PART 6 - He PV
PIEZO ELEMENT CLAMP DISC
FILE: P6BERGMD.DWG
DWG BY: JAMES M. SPOTTS
DATE: 8-13-96
SCALE: 2:1
PROF. M. OKUMURA LABORATORY
DIVISION OF CHEMISTRY; CALIFORNIA INSTITUTE OF TECHNOLOGY


MACHINE APPROPRIATE SLOT FOR 8-36 UNF SLOTTED SCREW
ø0.100
1.105
0.11
0.505
0.55
R0.060
0.060
8-36 UNF
TRUE 1:1 SIZE
X 4 MAGNIFICATION
ENLARGED VIEW
R0.024
ø0.120
0.038
ø0.060
ø0.050
PARKER 2-002
0.042 X 0.050
UNLESS OTHERWISE SPECIFIED DIMENSIONS ARE IN INCHES
TOLERANCES: (UNLESS SPECIFIED)
DECIMALS ANGLES
.X ± .06 ± 0.1°
.XX ± .03
.XXX ± .01
MATERIAL: ALUMINUM
TITLE: MOD. AFOSR PULSED VALVE PART 7a - He PV MODIFIED O-RING POPPET
FILE: P7ABERMD.DWG
DWG BY: JAMES M. SPOTTS
DATE: 8-14-96
SCALE: 2:1
PROF. M. OKUMURA LABORATORY
DIVISION OF CHEMISTRY; CALIFORNIA INSTITUTE OF TECHNOLOGY

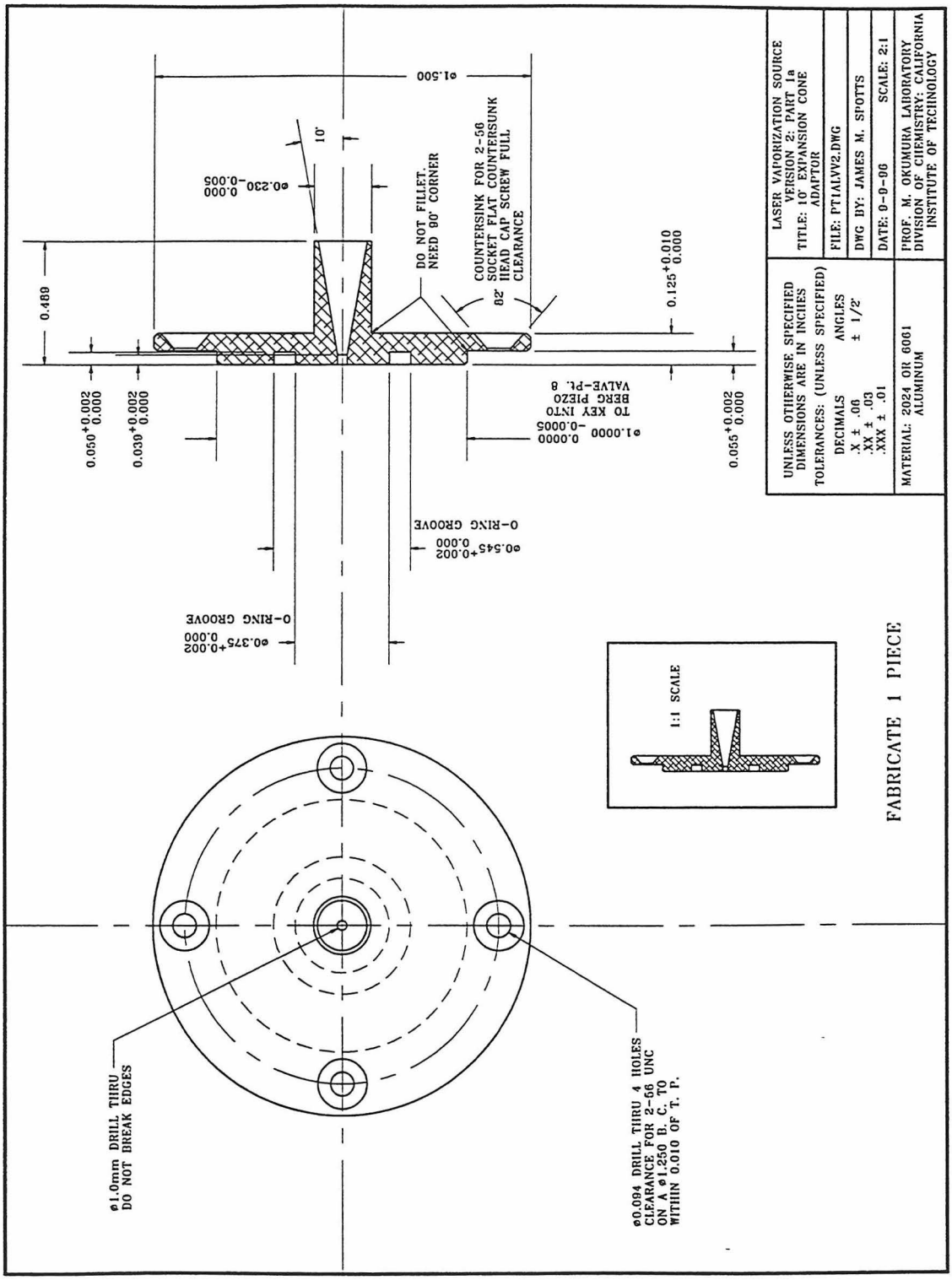

MACHINE APPROPRIATE SLOT FOR 8-36 UNF SLOTTED SCREW
ø0.100 0.000 -0.005
ø0.040 0.000 -0.005
0.340
1.085
0.11
0.505
0.51
R0.100
8-36 UNF
X 4 MAGNIFICATION
ENLARGED VIEW
PARTS 7b AND 7c COMBINED
TRUE 1:1 SIZE
ø0.010 DRILL THRU ONE CHANNEL AT BOTTOM OF HOLE
ø0.080 +0.002 0.000
0.100 +0.005 0.000
ø0.0400 +0.0005 0.0000
TO KEY TIGHTLY PART 7c
UNLESS OTHERWISE SPECIFIED DIMENSIONS ARE IN INCHES
TOLERANCES: (UNLESS SPECIFIED)
DECIMALS ANGLES
.X ± .06 ± 0.1°
.XX ± .03
.XXX ± .01
MATERIAL: ALUMINUM
TITLE: MOD. AFOSR PULSED VALVE PART 7b - He PV MODIFIED POPPET
FILE: P7BBERMD.DWG
DWG BY: JAMES M. SPOTTS
DATE: 8-14-00 SCALE: 2:1
PROF. M. OKUMURA LABORATORY DIVISION OF CHEMISTRY; CALIFORNIA INSTITUTE OF TECHNOLOGY

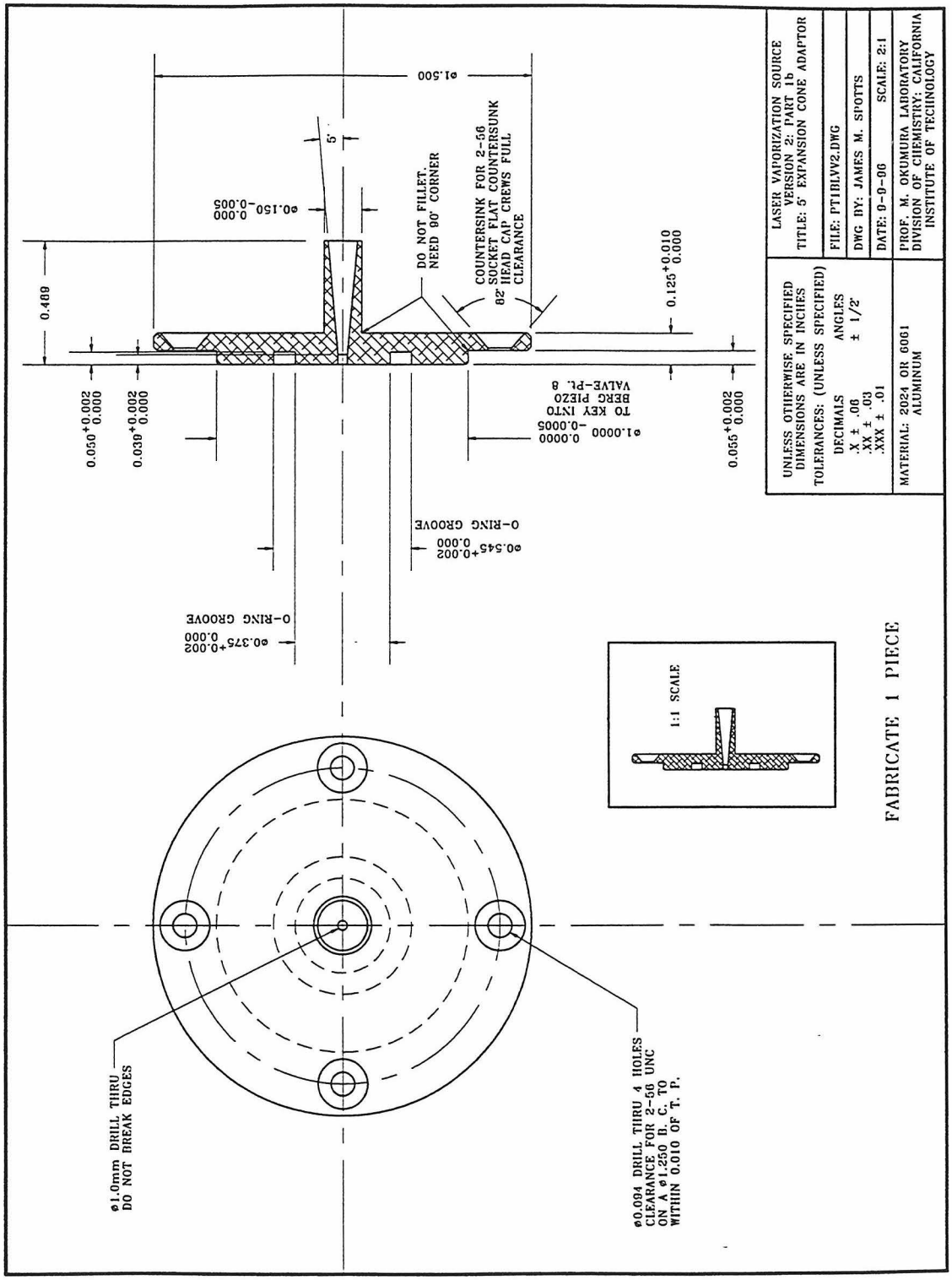

0.040 +0.005 0.000
ø0.0400 0.0000 -0.0005
TO KEY TIGHTLY
PART 7b
0.080 0.000 -0.005
ø0.080 +0.005 0.000
THIS SURFACE FACE MUST BE
VERY HIGHLY POLISHED
UNLESS OTHERWISE SPECIFIED
DIMENSIONS ARE IN INCHES
TOLERANCES: (UNLESS SPECIFIED)
DECIMALS ANGLES
.X ± .06 ± 0.1°
.XX ± .03
.XXX ± .01
TITLE: MOD. AFOSR PULSED VALVE
PART 7c - He PV
POPPET TIP
FILE: P7CDERMD.DWG
DWG BY: JAMES M. SPOTTS
DATE: 8-14-96
SCALE: 8:1
MATERIAL: 2 x KEL-F
2 x VESPEL SP-1
PROF. M. OKUMURA LABORATORY
DIVISION OF CHEMISTRY: CALIFORNIA
INSTITUTE OF TECHNOLOGY

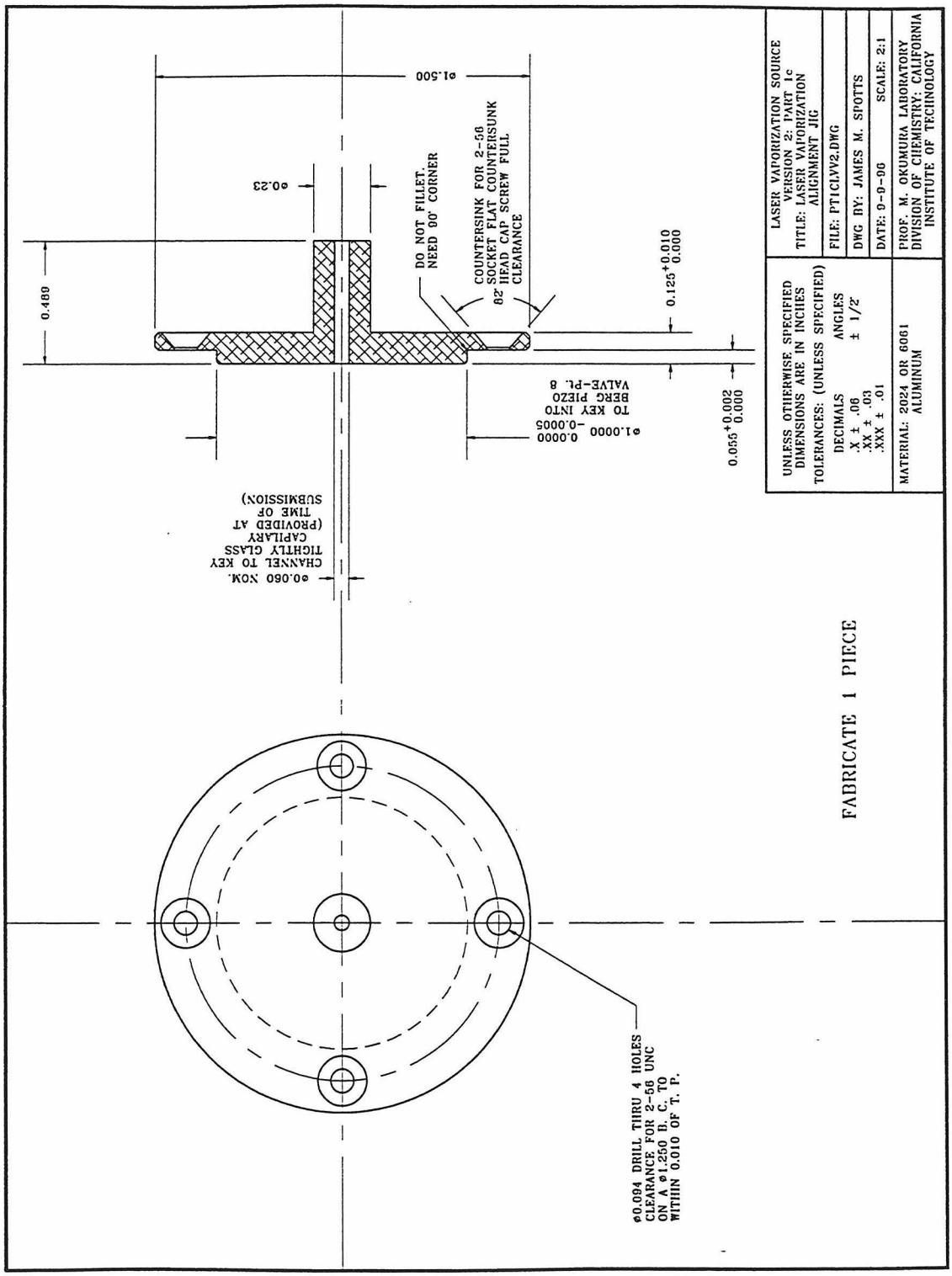

SECTION A-A
THIS SURFACE FACE MUST BE VERY HIGHLY POLISHED TO MIRROR FINISH SEAL FACE FOR PART 7c
KEYED FIT TO PULSED VALVE FRONT
ø1.0985 ± 0.0005
TO KEY INTO LASER VAPORIZATION PART 1
ø1.0000 +0.0005 0.0000
FACE MUST HAVE SMOOTH FINISH TO SEAL AGAINST O-RING
BORE THRU ø1.0mm HOLE. DO NOT BREAK EDGES
DRILL THRU 4 HOLES CLOSE CLEARANCE FOR 2-56 UNC HEX SOCKET HEAD SCREW EQ. SP. ON A ø0.800 B.C. WITHIN 0.005 OF T.P. COUNTERBORE CLEARANCE FOR HEX SOCKET HEAD TO DEPTH INDICATED ON CROSS SECTION VIEW
22.5°
DRILL THRU AND TAP THRU 8 HOLES FOR 2-56 UNC EQ. SP. ON A ø1.250 B.C. WITHIN 0.005 OF T.P. TO FIT LASER VAPORIZATION SOURCE
DRILL THRU AND TAP THRU 4 HOLES FOR 2-56 UNC EQ. SP. ON A ø1.250 B.C. WITHIN 0.005 OF T.P. TO FIT LASER VAPORIZATION SOURCE
0.050 0.000 -0.003
0.055 0.000 -0.005
ø1.500
ø0.380 0.000 -0.005
ø0.300 +0.005 0.000
0.200
0.100
0.500
NOTES: 1. ALL SURFACES REQUIRE SMOOTH FINISH
2. REPLACES TRICKL VALVE PART #3
3. CHAMFER ALL EDGES 0.015 X 45° UNLESS OTHERWISE INDICATED
4. FABRICATE ONE PIECE
UNLESS OTHERWISE SPECIFIED DIMENSIONS ARE IN INCHES
TOLERANCES: (UNLESS SPECIFIED)
DECIMALS ANGLES
X ± .06 ± 1/2°
.XX ± .03
.XXX ± .01
MATERIAL: 304 OR 303 STAINLESS STEEL
TITLE: MOD. AFOSR PULSED VALVE PART 8 - He PV ADAPTOR BETWEEN PULSED VALVE AND LV SOURCE
FILE: P8BERGMD.DWG
DWG BY: JAMES M. SPOTTS
DATE: 8-14-98
SCALE: 1:1
PROF. M. OKUMURA LABORATORY DIVISION OF CHEMISTRY: CALIFORNIA INSTITUTE OF TECHNOLOGY

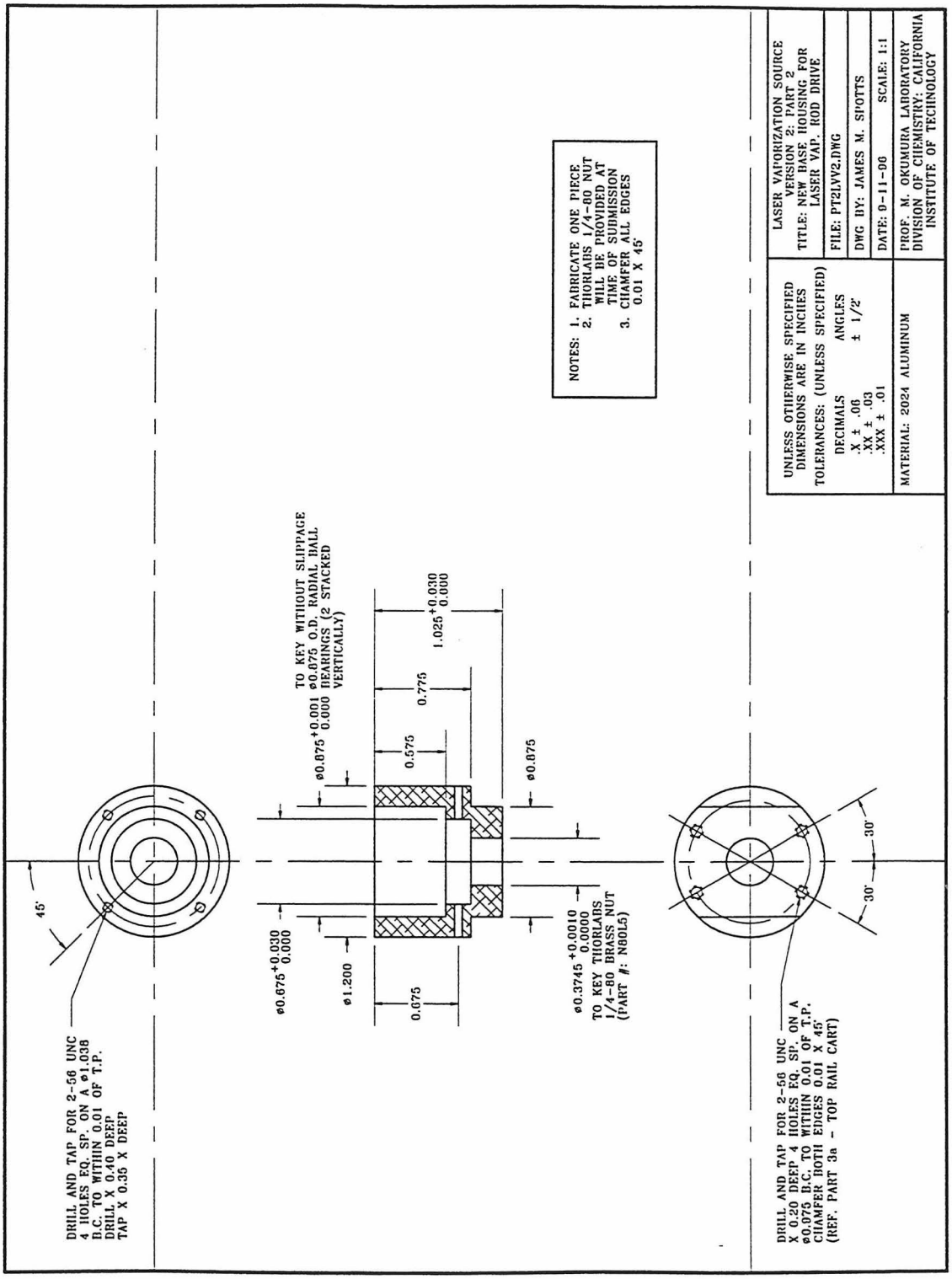
APPENDIX 4

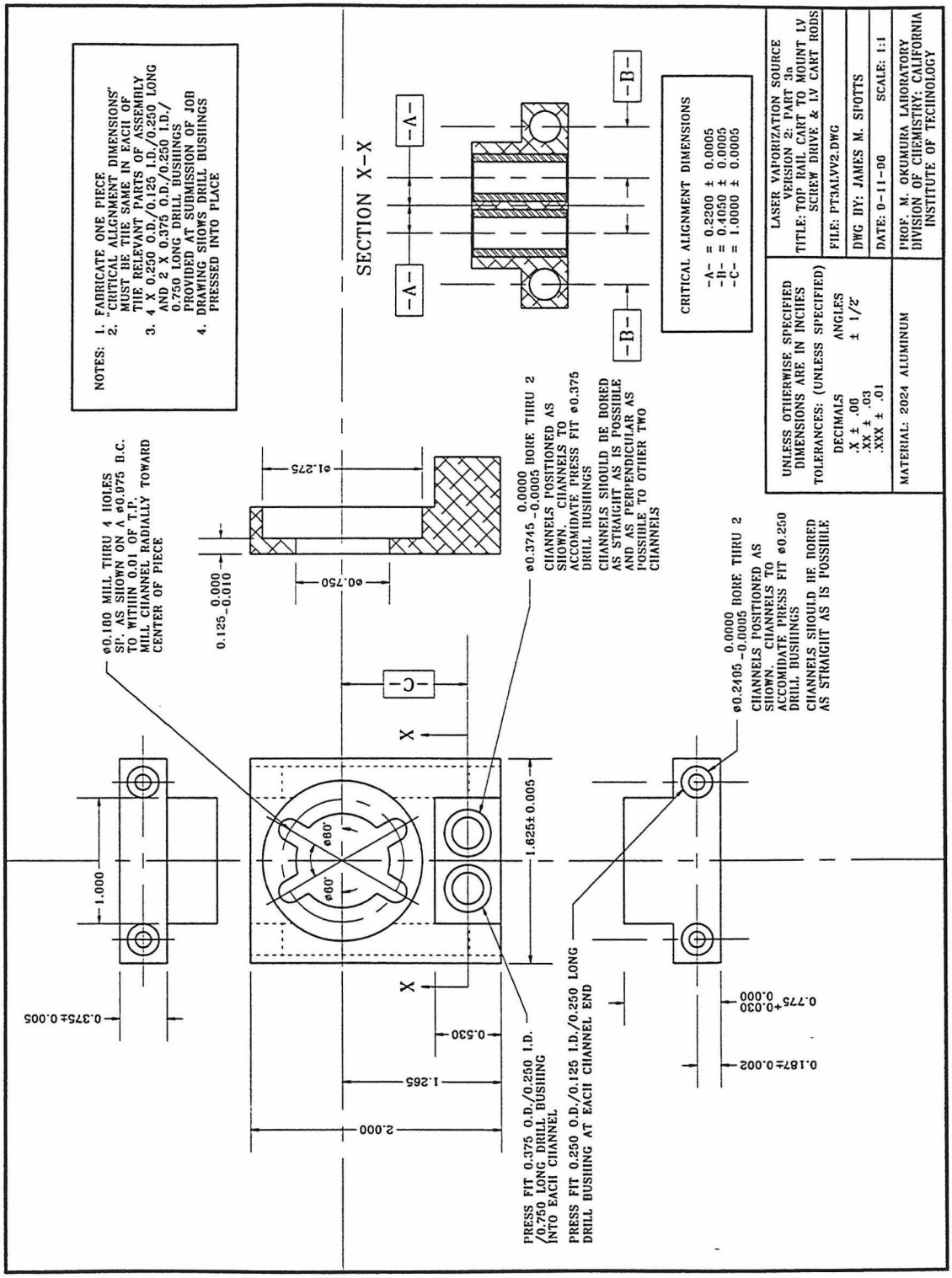
Drawings for the Third Generation Laser Vaporization Source

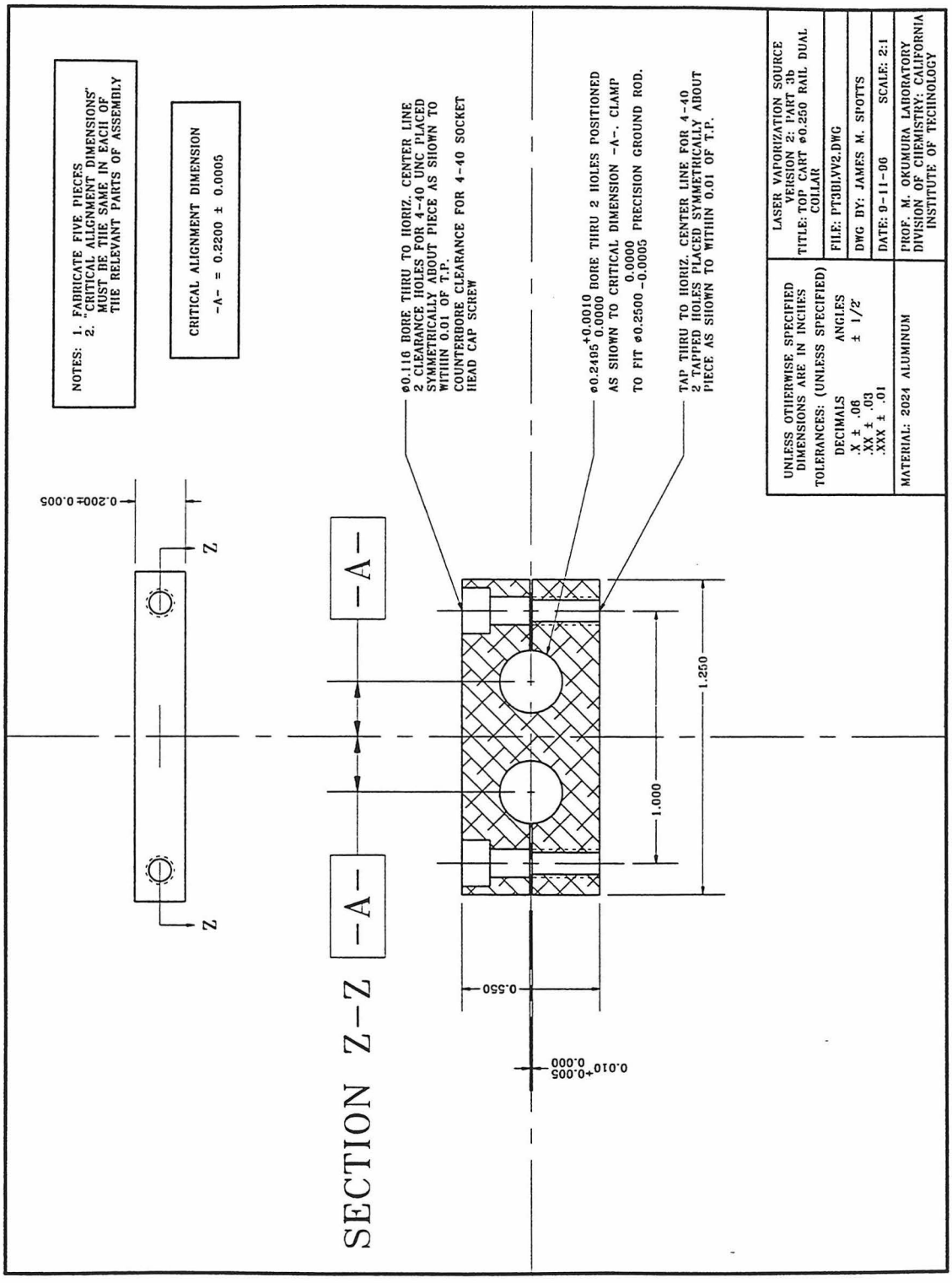

LASER VAPORIZATION SOURCE
VERSION 2: PART 1a
TITLE: 10° EXPANSION CONE
ADAPTOR
FILE: PT1ALVV2.DWG
DWG BY: JAMES M. SPOTTS
DATE: 9-9-96
SCALE: 2:1
PROF. M. OKUMURA LABORATORY
DIVISION OF CHEMISTRY: CALIFORNIA
INSTITUTE OF TECHNOLOGY
UNLESS OTHERWISE SPECIFIED
DIMENSIONS ARE IN INCHES
TOLERANCES: (UNLESS SPECIFIED)
DECIMALS
.X ± .06
.XX ± .03
.XXX ± .01
ANGLES
± 1/2°
MATERIAL: 2024 OR 6061
ALUMINUM
FABRICATE 1 PIECE
1:1 SCALE
ø1.500
10°
ø0.230 -0.000 -0.005
DO NOT FILLET.
NEED 90° CORNER
COUNTERSINK FOR 2-56
SOCKET FLAT COUNTERSUNK
HEAD CAP SCREW FULL
CLEARANCE
82°
0.125 +0.010 0.000
0.489
0.050 +0.002 0.000
0.039 +0.002 0.000
ø1.0000 -0.0000 -0.0005
TO KEY INTO
BERG PIEZO
VALVE-PL. 8
0.055 +0.002 0.000
O-RING GROOVE
ø0.545 +0.002 0.000
O-RING GROOVE
ø0.375 +0.002 0.000
ø1.0mm DRILL THRU
DO NOT BREAK EDGES
ø0.094 DRILL THRU 4 HOLES
CLEARANCE FOR 2-56 UNC
ON A ø1.250 B. C. TO
WITHIN 0.010 OF T. P.

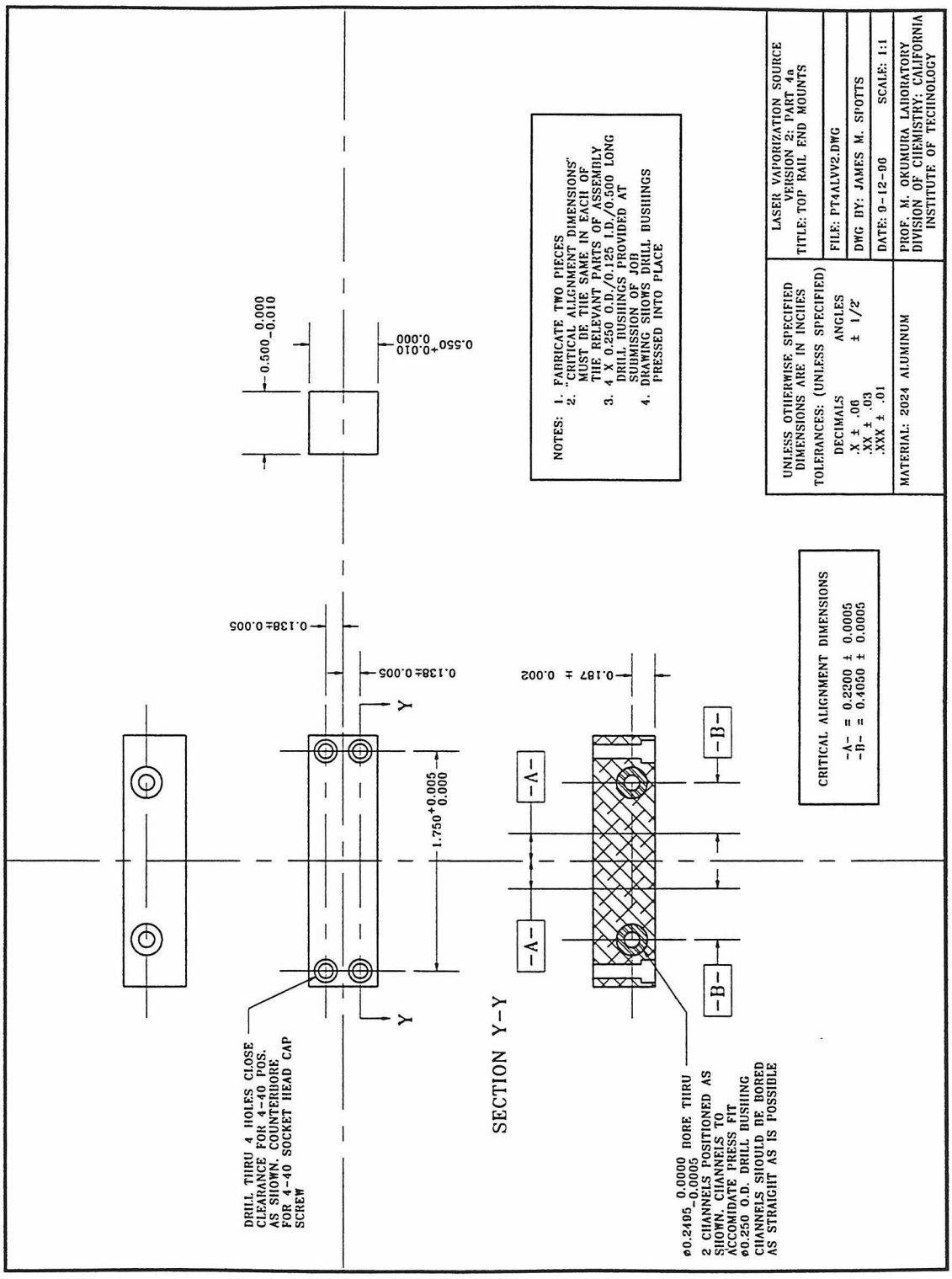

LASER VAPORIZATION SOURCE
VERSION 2: PART 1b
TITLE: 5° EXPANSION CONE ADAPTOR
FILE: PTIBLVV2.DWG
DWG BY: JAMES M. SPOTTS
DATE: 9-9-96
SCALE: 2:1
PROF. M. OKUMURA LABORATORY
DIVISION OF CHEMISTRY: CALIFORNIA
INSTITUTE OF TECHNOLOGY
UNLESS OTHERWISE SPECIFIED
DIMENSIONS ARE IN INCHES
TOLERANCES: (UNLESS SPECIFIED)
DECIMALS
.X ± .06
.XX ± .03
.XXX ± .01
ANGLES
± 1/2°
MATERIAL: 2024 OR 6061
ALUMINUM
FABRICATE 1 PIECE
1:1 SCALE
ø1.500
5°
ø0.150 0.000 -0.005
DO NOT FILLET.
NEED 90° CORNER
COUNTERSINK FOR 2-56
82° HEAD CAP CREWS FULL
CLEARANCE
0.125 +0.010 0.000
0.489
0.050 +0.002 0.000
0.039 +0.002 0.000
ø1.0000 0.0000 -0.0005
TO KEY INTO
BERG PIEZO
VALVE-PL. 8
0.056 +0.002 0.000
O-RING GROOVE
ø0.545 +0.002 0.000
O-RING GROOVE
ø0.375 +0.002 0.000
ø1.0mm DRILL THRU
DO NOT BREAK EDGES
ø0.094 DRILL THRU 4 HOLES
CLEARANCE FOR 2-56 UNC
ON A ø1.250 B. C. TO
WITHIN 0.010 OF T. P.

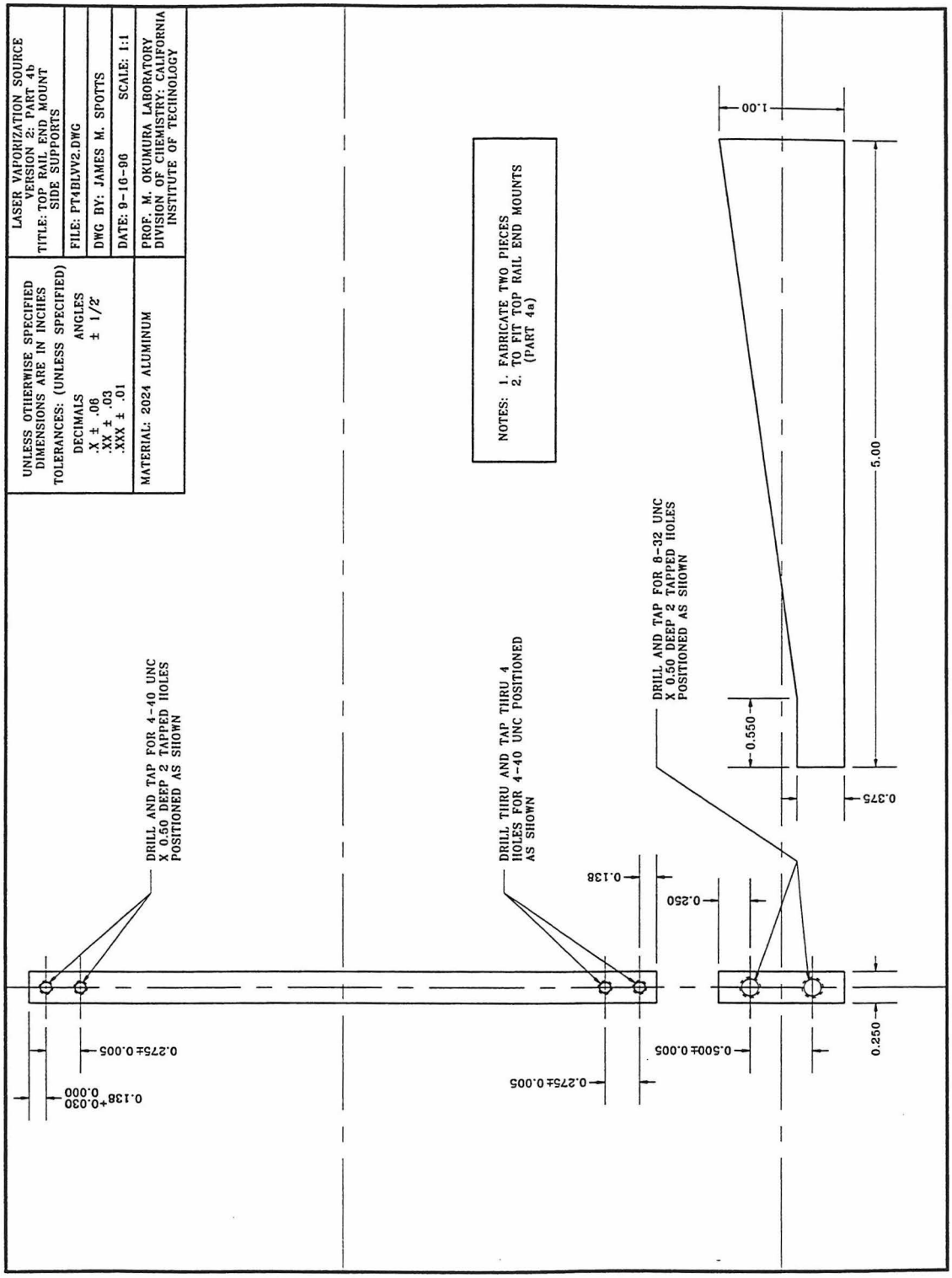

ø1.500
ø0.23
DO NOT FILLET.
NEED 90° CORNER
COUNTERSINK FOR 2-56
SOCKET FLAT COUNTERSUNK
82° HEAD CAP SCREW FULL
CLEARANCE
0.125+0.010 0.000
0.480
ø1.0000 0.0000 -0.0005
TO KEY INTO
BERG PIEZO
VALVE-PL. 8
0.055+0.002 0.000
ø0.060 NOM.
CHANNEL TO KEY
TIGHTLY GLASS
CAPILLARY
(PROVIDED AT
TIME OF
SUBMISSION)
ø0.094 DRILL THRU 4 HOLES
CLEARANCE FOR 2-56 UNC
ON A ø1.250 B. C. TO
WITHIN 0.010 OF T. P.
FABRICATE 1 PIECE
UNLESS OTHERWISE SPECIFIED
DIMENSIONS ARE IN INCHES
TOLERANCES: (UNLESS SPECIFIED)
DECIMALS ANGLES
.X ± .06 ± 1/2°
.XX ± .03
.XXX ± .01
MATERIAL: 2024 OR 6061
ALUMINUM
LASER VAPORIZATION SOURCE
VERSION 2: PART 1c
TITLE: LASER VAPORIZATION
ALIGNMENT JIG
FILE: PT1CLVV2.DWG
DWG BY: JAMES M. SPOTTS
DATE: 9-0-96
SCALE: 2:1
PROF. M. OKUMURA LABORATORY
DIVISION OF CHEMISTRY: CALIFORNIA
INSTITUTE OF TECHNOLOGY

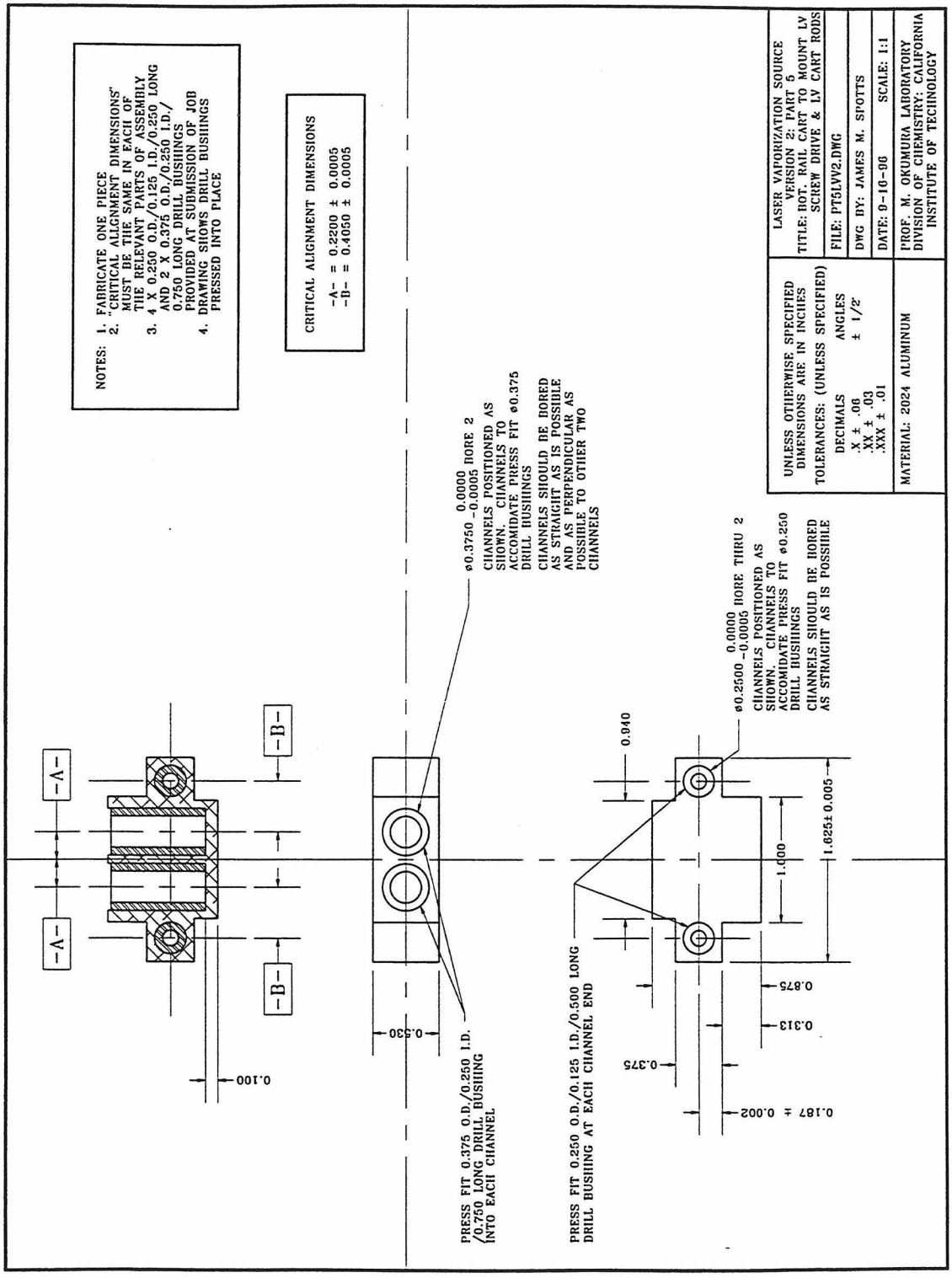

NOTES: 1. FABRICATE ONE PIECE.
2. THORLABS 1/4-80 NUT WILL BE PROVIDED AT TIME OF SUBMISSION
3. CHAMFER ALL EDGES 0.01 X 45°
UNLESS OTHERWISE SPECIFIED DIMENSIONS ARE IN INCHES
TOLERANCES: (UNLESS SPECIFIED)
DECIMALS ANGLES
.X ± .06 ± 1/2°
.XX ± .03
.XXX ± .01
MATERIAL: 2024 ALUMINUM
LASER VAPORIZATION SOURCE VERSION 2: PART 2
TITLE: NEW BASE HOUSING FOR LASER VAP. ROD DRIVE
FILE: PT2LVV2.DWG
DWG BY: JAMES M. SPOTTS
DATE: 9-11-96
SCALE: 1:1
PROF. M. OKUMURA LABORATORY
DIVISION OF CHEMISTRY: CALIFORNIA INSTITUTE OF TECHNOLOGY
DRILL AND TAP FOR 2-56 UNC 4 HOLES EQ. SP. ON A ø1.038 B.C. TO WITHIN 0.01 OF T.P. DRILL X 0.40 DEEP TAP X 0.35 X DEEP
45°
TO KEY WITHOUT SLIPPAGE ø0.875 +0.001 0.000 ø0.075 O.D. RADIAL BALL BEARINGS (2 STACKED VERTICALLY)
ø0.675 +0.030 0.000
ø1.200
0.675
0.575
0.775
1.025 +0.030 0.000
ø0.875
ø0.3745 +0.0010 0.0000
TO KEY THORLABS 1/4-80 BRASS NUT (PART #: N80L5)
DRILL AND TAP FOR 2-56 UNC X 0.20 DEEP 4 HOLES EQ. SP. ON A ø0.075 B.C. TO WITHIN 0.01 OF T.P. CHAMFER BOTH EDGES 0.01 X 45° (REF. PART 3a - TOP RAIL CART)
30°
30°

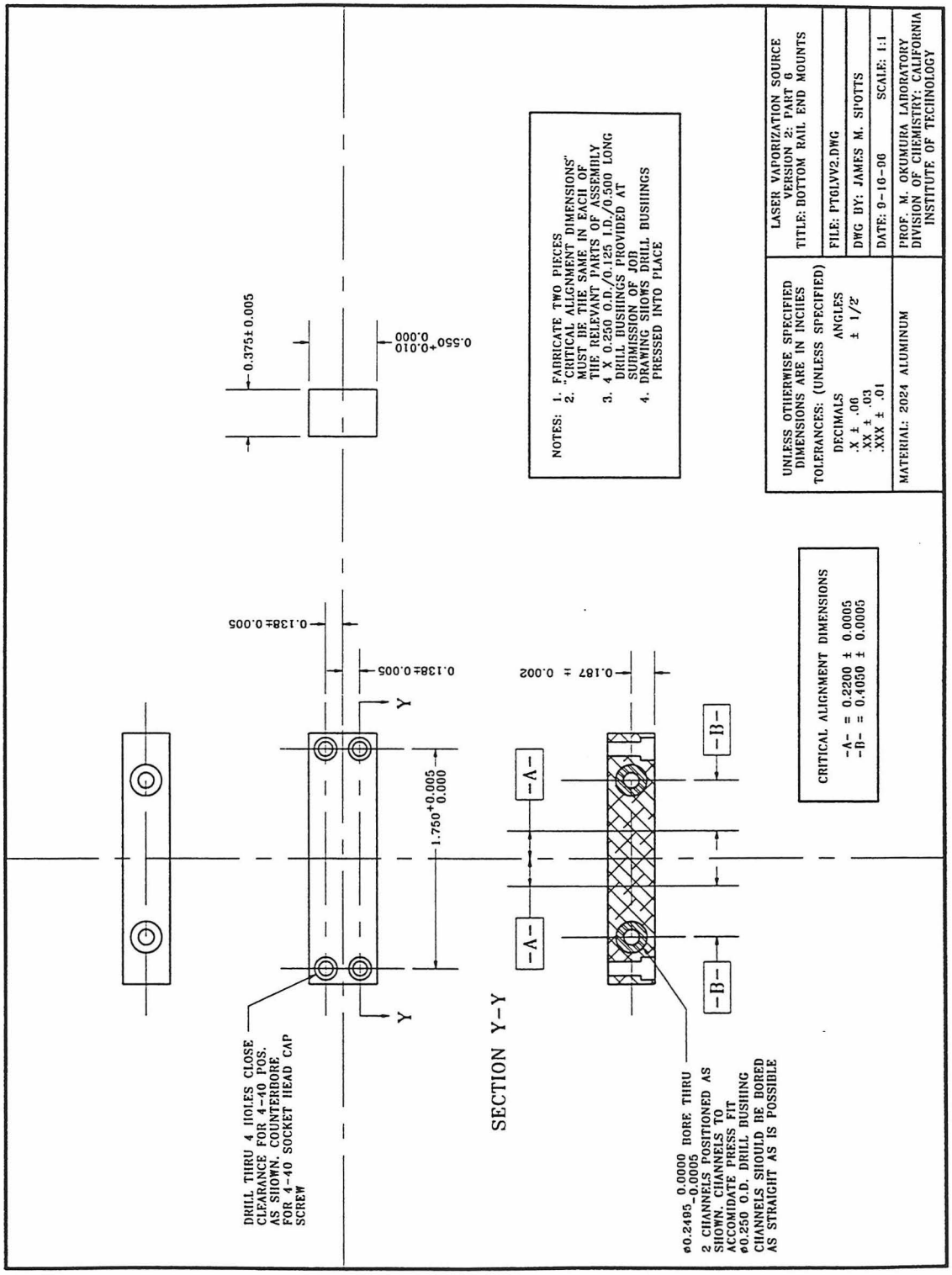

NOTES: 1. FABRICATE ONE PIECE
2. *CRITICAL ALIGNMENT DIMENSIONS* MUST BE THE SAME IN EACH OF THE RELEVANT PARTS OF ASSEMBLY
3. 4 X 0.250 O.D./0.125 I.D./0.250 LONG AND 2 X 0.375 O.D./0.250 I.D./ 0.750 LONG DRILL BUSHINGS PROVIDED AT SUBMISSION OF JOB
4. DRAWING SHOWS DRILL BUSHINGS PRESSED INTO PLACE
SECTION X-X
CRITICAL ALIGNMENT DIMENSIONS
-A- = 0.2200 ± 0.0005
-B- = 0.4050 ± 0.0005
-C- = 1.0000 ± 0.0005
ø0.180 MILL THRU 4 HOLES SP. AS SHOWN ON A ø0.975 B.C. TO WITHIN 0.01 OF T.P. MILL CHANNEL RADIALLY TOWARD CENTER OF PIECE
ø0.3745 0.0000 -0.0005 BORE THRU 2 CHANNELS POSITIONED AS SHOWN. CHANNELS TO ACCOMIDATE PRESS FIT ø0.375 DRILL BUSHINGS
CHANNELS SHOULD BE BORED AS STRAIGHT AS IS POSSIBLE AND AS PERPENDICULAR AS POSSIBLE TO OTHER TWO CHANNELS
ø0.2405 0.0000 -0.0005 BORE THRU 2 CHANNELS POSITIONED AS SHOWN. CHANNELS TO ACCOMIDATE PRESS FIT ø0.250 DRILL BUSHINGS
CHANNELS SHOULD BE BORED AS STRAIGHT AS IS POSSIBLE
PRESS FIT 0.375 O.D./0.250 I.D. /0.750 LONG DRILL BUSHING INTO EACH CHANNEL
PRESS FIT 0.250 O.D./0.125 I.D./0.250 LONG DRILL BUSHING AT EACH CHANNEL END
UNLESS OTHERWISE SPECIFIED DIMENSIONS ARE IN INCHES
TOLERANCES: (UNLESS SPECIFIED)
DECIMALS ANGLES
.X ± .00 ± 1/2°
.XX ± .03
.XXX ± .01
MATERIAL: 2024 ALUMINUM
LASER VAPORIZATION SOURCE VERSION 2: PART 3a
TITLE: TOP RAIL CART TO MOUNT LV SCREW DRIVE & LV CART RODS
FILE: PT3A1VV2.DWG
DWG BY: JAMES M. SPOTTS
DATE: 0-11-00
SCALE: 1:1
PROF. M. OKUMURA LABORATORY
DIVISION OF CHEMISTRY; CALIFORNIA INSTITUTE OF TECHNOLOGY
1.000
0.375± 0.005
0.125 0.000 -0.010
ø1.275
ø0.750
ø60°
ø60°
1.625± 0.005
0.530
1.265
2.000
0.775 +0.030 0.000
0.187± 0.002

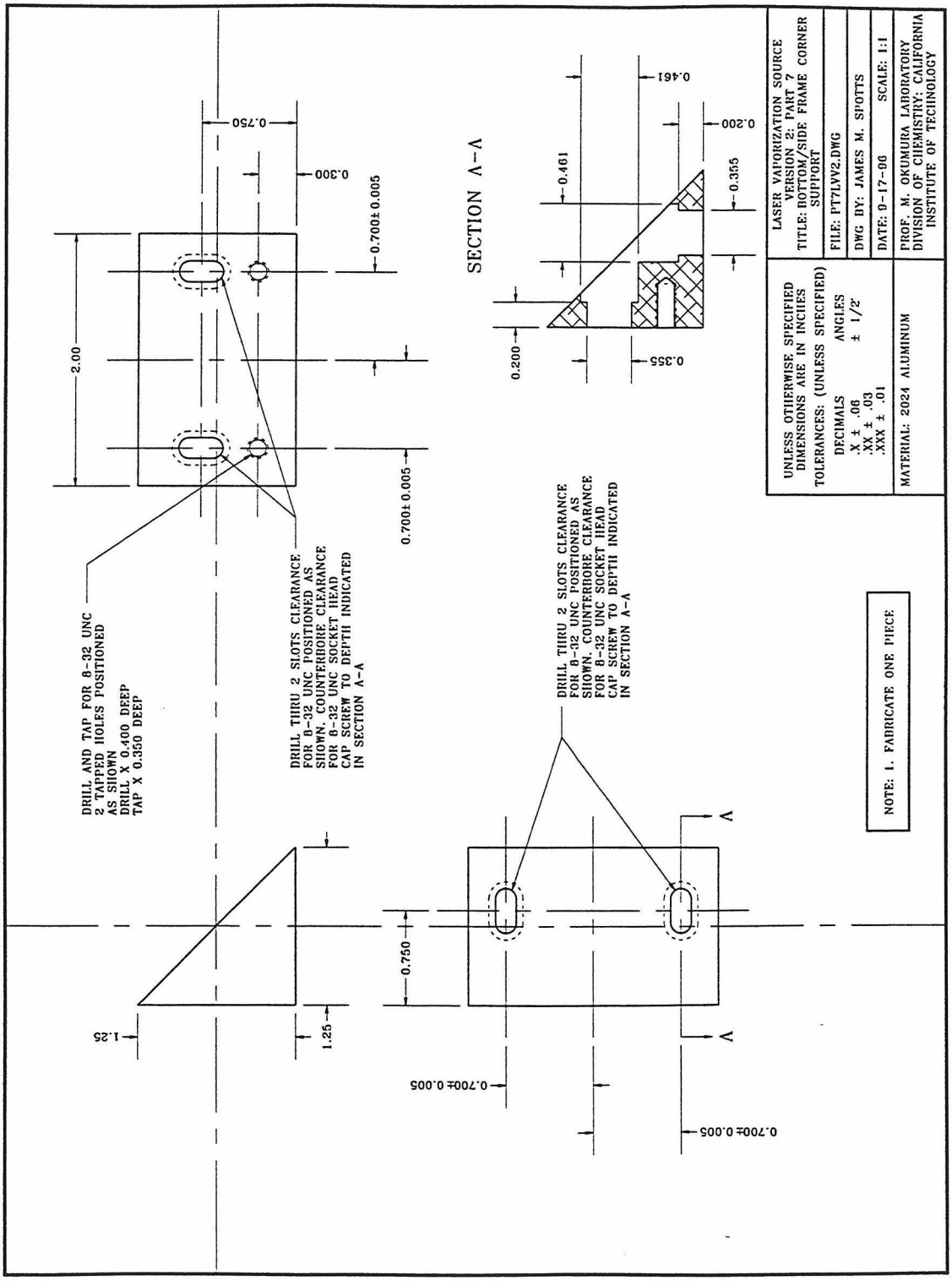

NOTES: 1. FABRICATE FIVE PIECES
2. "CRITICAL ALIGNMENT DIMENSIONS" MUST BE THE SAME IN EACH OF THE RELEVANT PARTS OF ASSEMBLY
CRITICAL ALIGNMENT DIMENSION
-A- = 0.2200 ± 0.0005
0.200±0.005
Z
Z
SECTION Z-Z
-A-
-A-
ø0.116 BORE THRU TO HORIZ. CENTER LINE
2 CLEARANCE HOLES FOR 4-40 UNC PLACED
SYMMETRICALLY ABOUT PIECE AS SHOWN TO
WITHIN 0.01 OF T.P.
COUNTERBORE CLEARANCE FOR 4-40 SOCKET
HEAD CAP SCREW
ø0.2495+0.0010 0.0000 BORE THRU 2 HOLES POSITIONED
AS SHOWN TO CRITICAL DIMENSION -A-. CLAMP
TO FIT ø0.2500 0.0000 -0.0005 PRECISION GROUND ROD.
TAP THRU TO HORIZ. CENTER LINE FOR 4-40
2 TAPPED HOLES PLACED SYMMETRICALLY ABOUT
PIECE AS SHOWN TO WITHIN 0.01 OF T.P.
1.250
1.000
0.550
0.010+0.005 0.000
UNLESS OTHERWISE SPECIFIED
DIMENSIONS ARE IN INCHES
TOLERANCES: (UNLESS SPECIFIED)
DECIMALS ANGLES
.X ± .06 ± 1/2°
.XX ± .03
.XXX ± .01
MATERIAL: 2024 ALUMINUM
LASER VAPORIZATION SOURCE
VERSION 2: PART 3b
TITLE: TOP CART ø0.250 RAIL DUAL COLLAR
FILE: PT3BLVV2.DWG
DWG BY: JAMES M. SPOTTS
DATE: 9-11-90
SCALE: 2:1
PROF. M. OKUMURA LABORATORY
DIVISION OF CHEMISTRY: CALIFORNIA INSTITUTE OF TECHNOLOGY

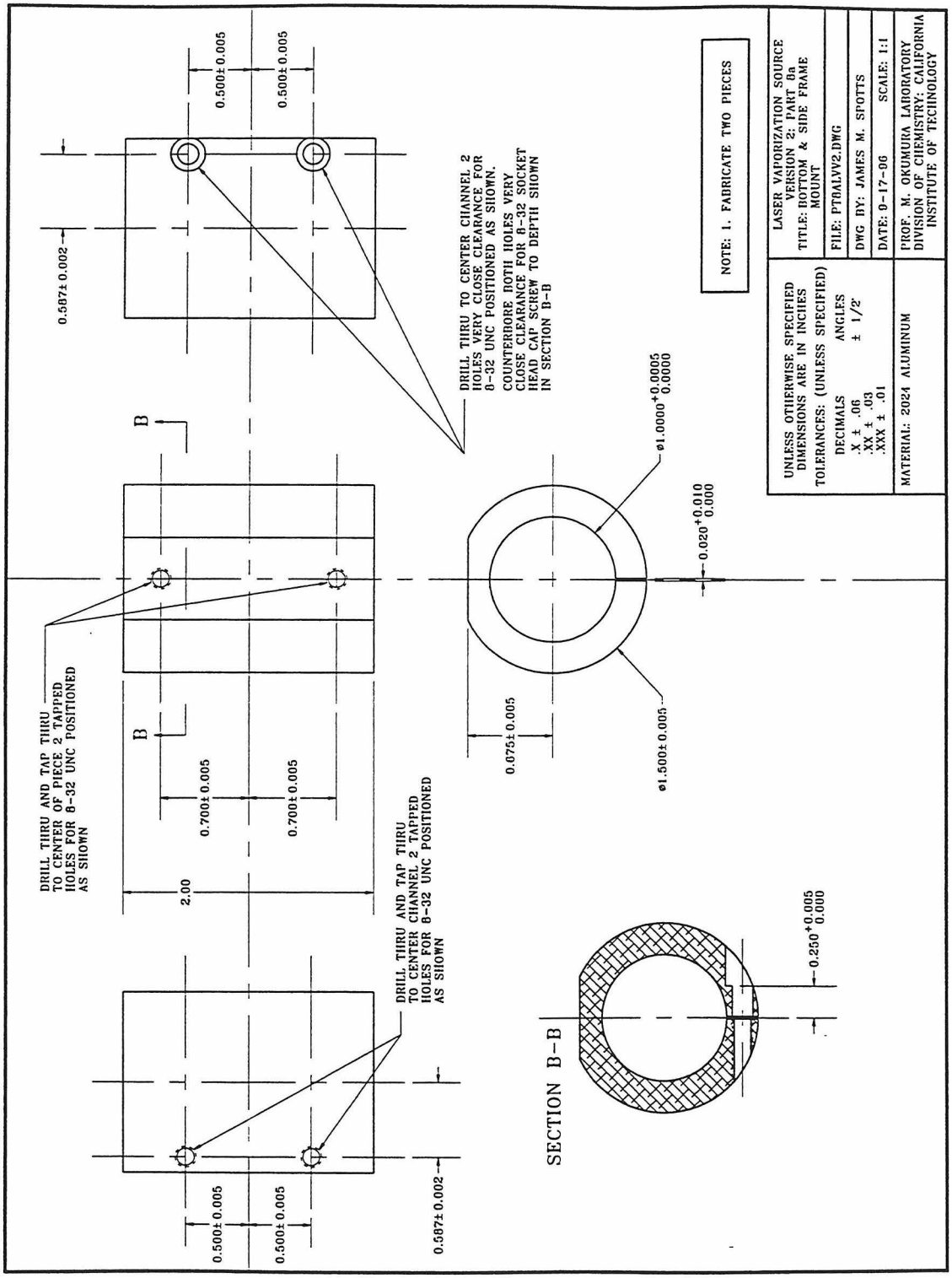

NOTES: 1. FABRICATE TWO PIECES
2. "CRITICAL ALIGNMENT DIMENSIONS" MUST BE THE SAME IN EACH OF THE RELEVANT PARTS OF ASSEMBLY
3. 4 X 0.250 O.D./0.125 I.D./0.500 LONG DRILL BUSHINGS PROVIDED AT SUBMISSION OF JOB
4. DRAWING SHOWS DRILL BUSHINGS PRESSED INTO PLACE
UNLESS OTHERWISE SPECIFIED DIMENSIONS ARE IN INCHES
TOLERANCES: (UNLESS SPECIFIED)
DECIMALS ANGLES
.X ± .06 ± 1/2°
.XX ± .03
.XXX ± .01
MATERIAL: 2024 ALUMINUM
LASER VAPORIZATION SOURCE VERSION 2: PART 4a
TITLE: TOP RAIL END MOUNTS
FILE: PT4ALVV2.DWG
DWG BY: JAMES M. SPOTTS
DATE: 9-12-96 SCALE: 1:1
PROF. M. OKUMURA LABORATORY
DIVISION OF CHEMISTRY: CALIFORNIA INSTITUTE OF TECHNOLOGY
CRITICAL ALIGNMENT DIMENSIONS
-A- = 0.2300 ± 0.0005
-B- = 0.4050 ± 0.0005
SECTION Y-Y
DRILL THRU 4 HOLES CLOSE CLEARANCE FOR 4-40 POS. AS SHOWN. COUNTERBORE FOR 4-40 SOCKET HEAD CAP SCREW
ø0.2495 0.0000 -0.0005 BORE THRU
2 CHANNELS POSITIONED AS SHOWN. CHANNELS TO ACCOMIDATE PRESS FIT ø0.250 O.D. DRILL BUSHING CHANNELS SHOULD BE BORED AS STRAIGHT AS IS POSSIBLE
0.500 0.000 -0.010
0.550 +0.010 0.000
0.138 ± 0.005
0.138 ± 0.005
1.750 +0.005 0.000
0.187 ± 0.002
-A-
-B-
Y
Y

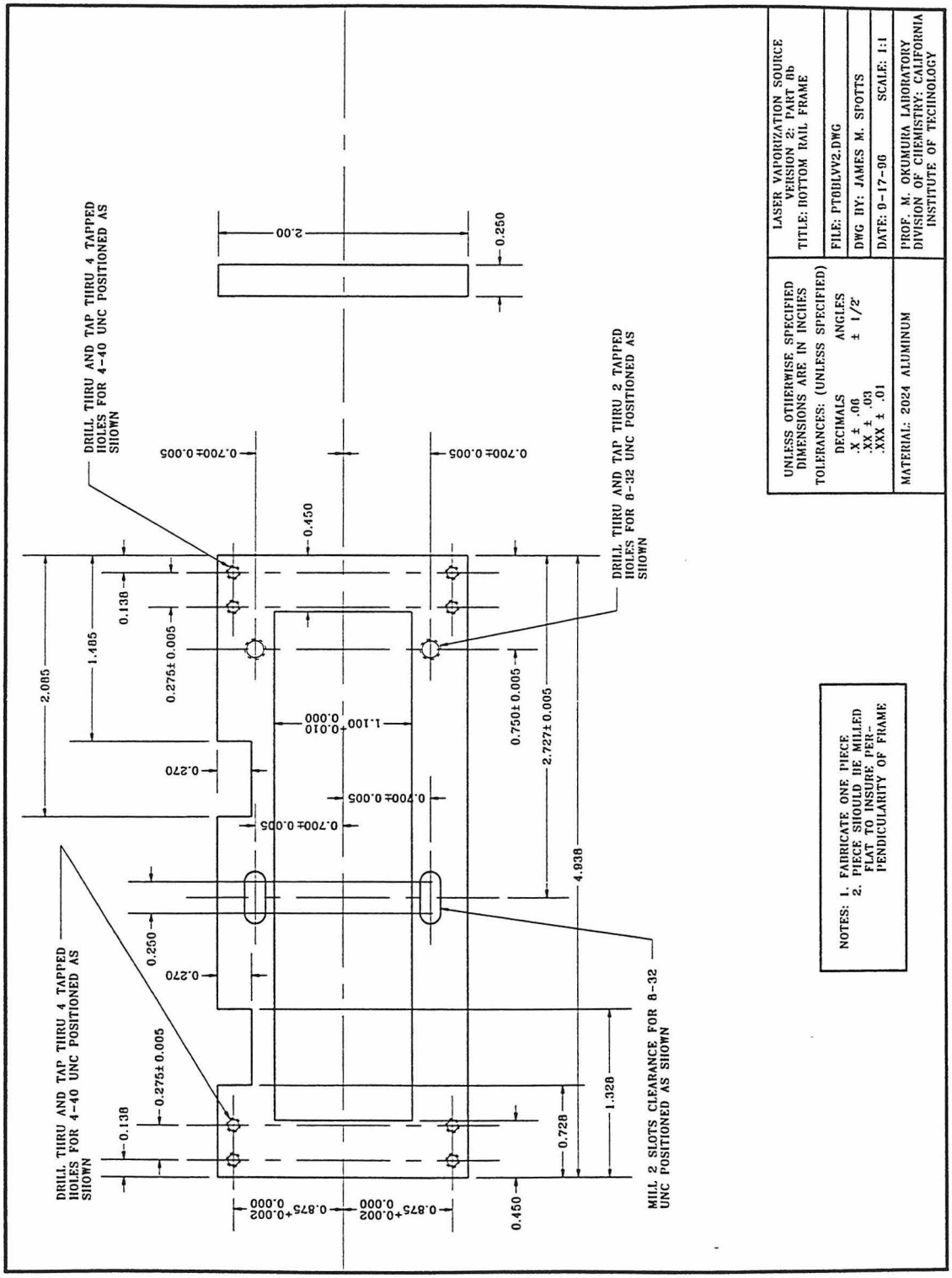

LASER VAPORIZATION SOURCE
VERSION 2: PART 4b
TITLE: TOP RAIL END MOUNT
SIDE SUPPORTS
FILE: PT4BLVV2.DWG
DWG BY: JAMES M. SPOTTS
DATE: 9-16-96
SCALE: 1:1
PROF. M. OKUMURA LABORATORY
DIVISION OF CHEMISTRY: CALIFORNIA
INSTITUTE OF TECHNOLOGY
UNLESS OTHERWISE SPECIFIED
DIMENSIONS ARE IN INCHES
TOLERANCES: (UNLESS SPECIFIED)
DECIMALS
.X ± .06
.XX ± .03
.XXX ± .01
ANGLES
± 1/2'
MATERIAL: 2024 ALUMINUM
NOTES: 1. FABRICATE TWO PIECES
2. TO FIT TOP RAIL END MOUNTS
(PART 4a)
DRILL AND TAP FOR 4-40 UNC
X 0.50 DEEP 2 TAPPED HOLES
POSITIONED AS SHOWN
DRILL THRU AND TAP THRU 4
HOLES FOR 4-40 UNC POSITIONED
AS SHOWN
DRILL AND TAP FOR 8-32 UNC
X 0.50 DEEP 2 TAPPED HOLES
POSITIONED AS SHOWN
1.00
5.00
0.550
0.375
0.138
0.250
0.138 +0.030 0.000
0.2754 0.005
0.2754 0.005
0.5004 0.005
0.250

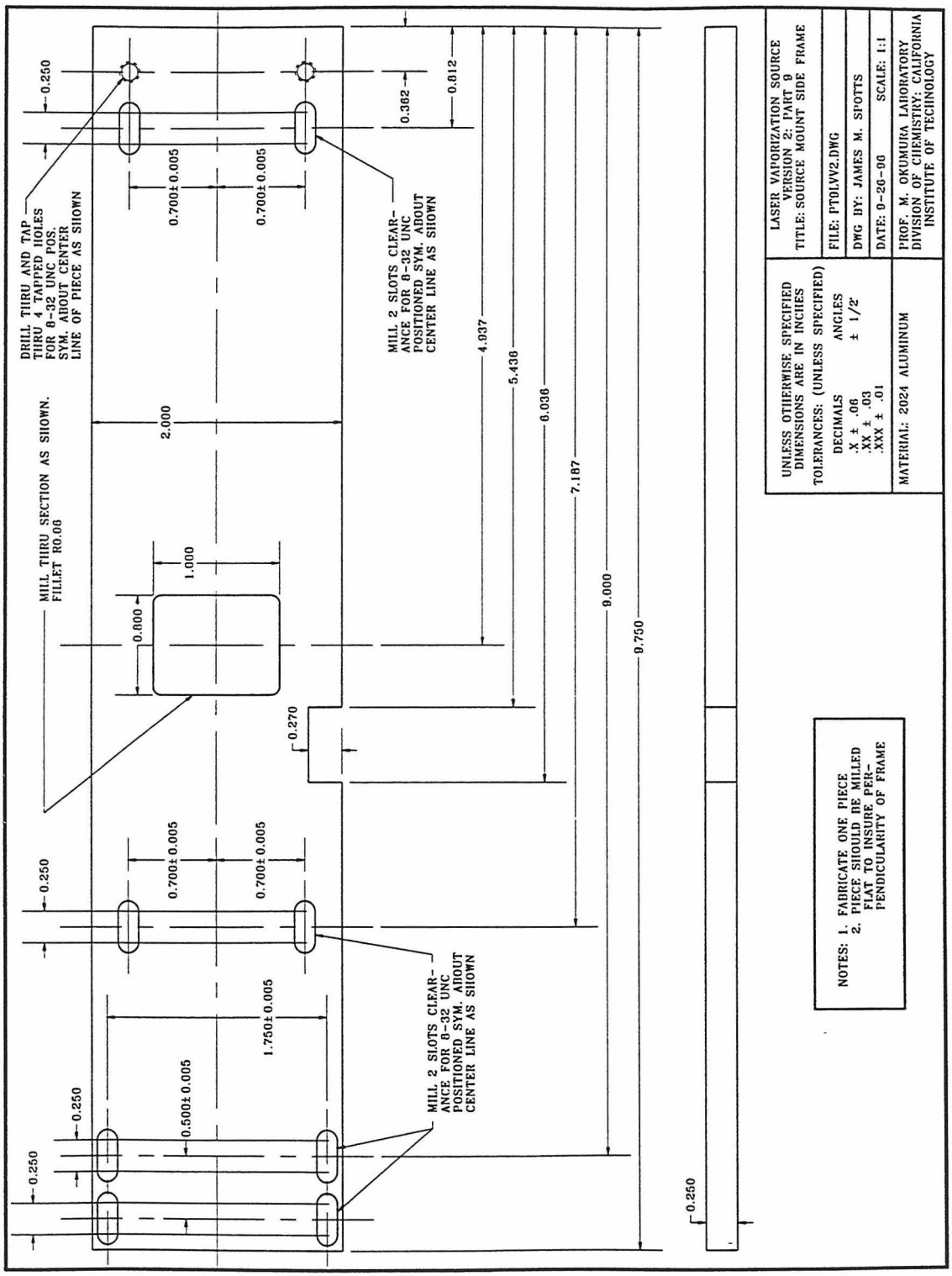

NOTES: 1. FABRICATE ONE PIECE
2. "CRITICAL ALIGNMENT DIMENSIONS" MUST BE THE SAME IN EACH OF THE RELEVANT PARTS OF ASSEMBLY
3. 4 X 0.250 O.D./0.125 I.D./0.250 LONG AND 2 X 0.375 O.D./0.250 I.D./ 0.750 LONG DRILL BUSHINGS PROVIDED AT SUBMISSION OF JOB
4. DRAWING SHOWS DRILL BUSHINGS PRESSED INTO PLACE
CRITICAL ALIGNMENT DIMENSIONS
-A- = 0.2200 ± 0.0005
-B- = 0.4050 ± 0.0005
-V-
-B-
0.100
0.530
PRESS FIT 0.375 O.D./0.250 I.D. /0.750 LONG DRILL BUSHING INTO EACH CHANNEL
ø0.3750 0.0000 -0.0005 BORE 2
CHANNELS POSITIONED AS SHOWN. CHANNELS TO ACCOMIDATE PRESS FIT ø0.375 DRILL BUSHINGS
CHANNELS SHOULD BE BORED AS STRAIGHT AS IS POSSIBLE AND AS PERPENDICULAR AS POSSIBLE TO OTHER TWO CHANNELS
ø0.2500 0.0000 -0.0005 BORE THRU 2
CHANNELS POSITIONED AS SHOWN. CHANNELS TO ACCOMIDATE PRESS FIT ø0.250 DRILL BUSHINGS
CHANNELS SHOULD BE BORED AS STRAIGHT AS IS POSSIBLE
0.940
1.000
1.625± 0.005
0.875
0.313
0.375
0.187 ± 0.002
PRESS FIT 0.250 O.D./0.125 I.D./0.500 LONG DRILL BUSHING AT EACH CHANNEL END
UNLESS OTHERWISE SPECIFIED DIMENSIONS ARE IN INCHES
TOLERANCES: (UNLESS SPECIFIED)
DECIMALS ANGLES
X ± .06 ± 1/2°
.XX ± .03
.XXX ± .01
MATERIAL: 2024 ALUMINUM
LASER VAPORIZATION SOURCE VERSION 2: PART 5
TITLE: HOT. RAIL CART TO MOUNT LV SCREW DRIVE & LV CART RODS
FILE: PT5LVV2.DWG
DWG BY: JAMES M. SPOTTS
DATE: 9-10-96 SCALE: 1:1
PROF. M. OKUMURA LABORATORY
DIVISION OF CHEMISTRY: CALIFORNIA INSTITUTE OF TECHNOLOGY

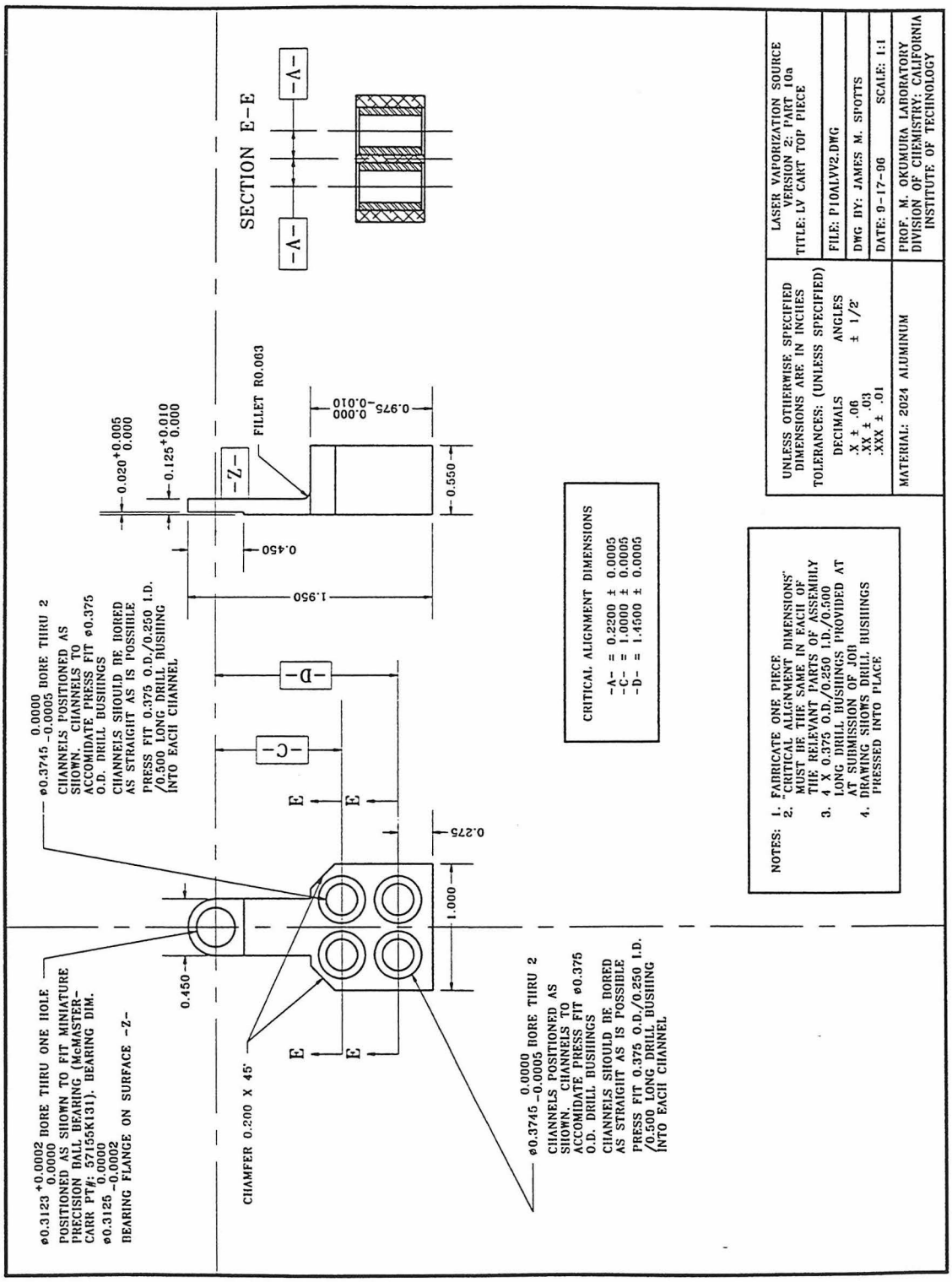

NOTES: 1. FABRICATE TWO PIECES
2. "CRITICAL ALIGNMENT DIMENSIONS" MUST BE THE SAME IN EACH OF THE RELEVANT PARTS OF ASSEMBLY
3. 4 X 0.250 O.D./0.125 I.D./0.500 LONG DRILL BUSHINGS PROVIDED AT SUBMISSION OF JOB
4. DRAWING SHOWS DRILL BUSHINGS PRESSED INTO PLACE
CRITICAL ALIGNMENT DIMENSIONS
-A- = 0.2200 ± 0.0005
-B- = 0.4050 ± 0.0005
UNLESS OTHERWISE SPECIFIED DIMENSIONS ARE IN INCHES
TOLERANCES: (UNLESS SPECIFIED)
DECIMALS
.X ± .06
.XX ± .03
.XXX ± .01
ANGLES ± 1/2°
MATERIAL: 2024 ALUMINUM
LASER VAPORIZATION SOURCE VERSION 2: PART 6
TITLE: BOTTOM RAIL END MOUNTS
FILE: PTGLVV2.DWG
DWG BY: JAMES M. SPOTTS
DATE: 9-16-96
SCALE: 1:1
PROF. M. OKUMURA LABORATORY
DIVISION OF CHEMISTRY: CALIFORNIA INSTITUTE OF TECHNOLOGY
0.375±0.005
0.550+0.010 0.000
0.138±0.005
0.138±0.005
0.187 ± 0.002
1.750+0.005 0.000
SECTION Y-Y
-A-
-A-
-B-
-B-
Y
Y
DRILL THRU 4 HOLES CLOSE CLEARANCE FOR 4-40 POS. AS SHOWN. COUNTERBORE FOR 4-40 SOCKET HEAD CAP SCREW
ø0.2495 0.0000 -0.0005 BORE THRU 2 CHANNELS POSITIONED AS SHOWN. CHANNELS TO ACCOMIDATE PRESS FIT ø0.250 O.D. DRILL BUSHING CHANNELS SHOULD BE BORED AS STRAIGHT AS IS POSSIBLE

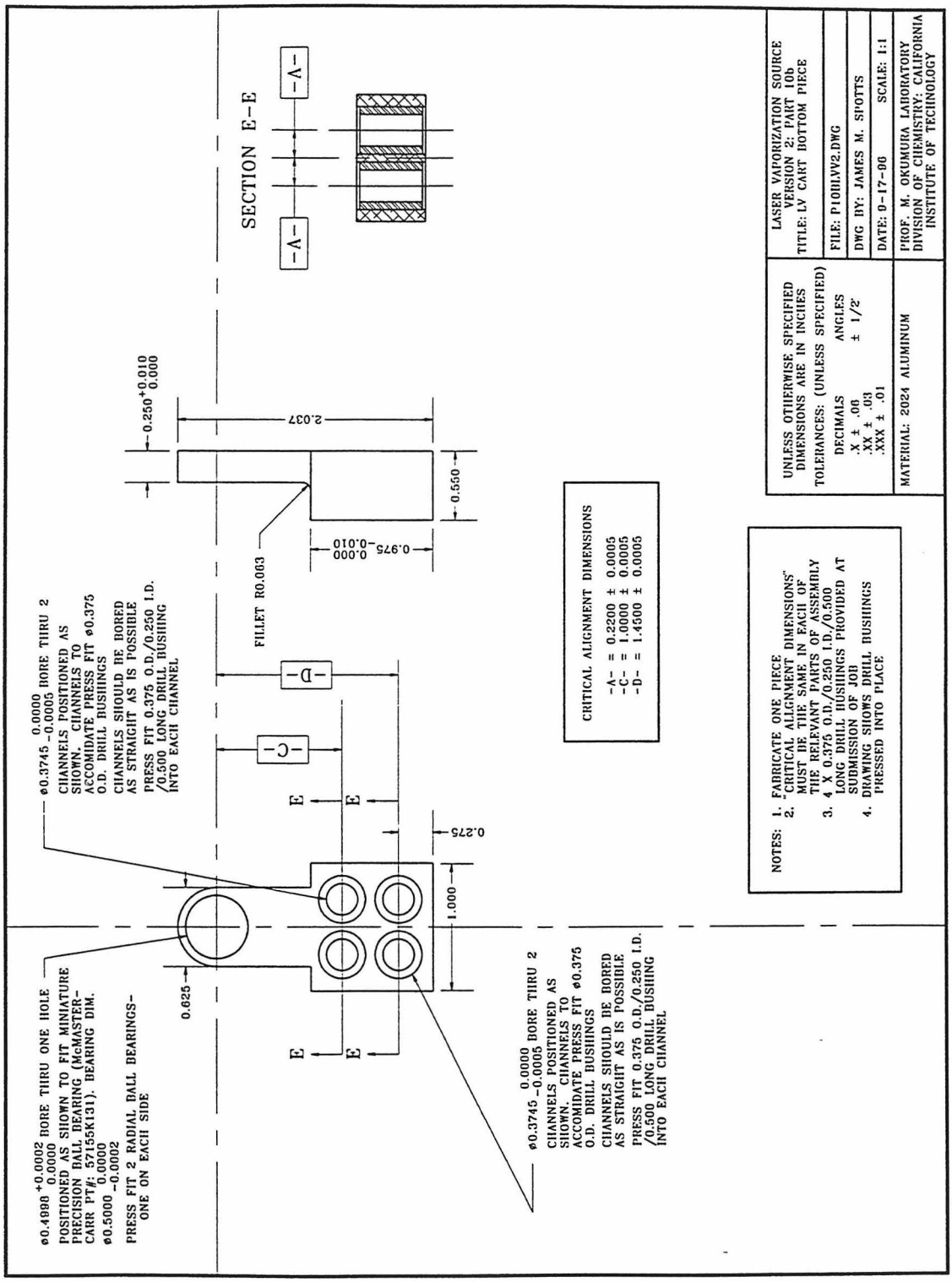

SECTION A-A
0.461
0.200
0.355
0.750
0.300
0.700± 0.005
2.00
DRILL AND TAP FOR 8-32 UNC
2 TAPPED HOLES POSITIONED
AS SHOWN
DRILL X 0.400 DEEP
TAP X 0.350 DEEP
DRILL THRU 2 SLOTS CLEARANCE
FOR 8-32 UNC POSITIONED AS
SHOWN. COUNTERBORE CLEARANCE
FOR 8-32 UNC SOCKET HEAD
CAP SCREW TO DEPTH INDICATED
IN SECTION A-A
DRILL THRU 2 SLOTS CLEARANCE
FOR 8-32 UNC POSITIONED AS
SHOWN. COUNTERBORE CLEARANCE
FOR 8-32 UNC SOCKET HEAD
CAP SCREW TO DEPTH INDICATED
IN SECTION A-A
A
A
1.25
1.25
0.750
0.700± 0.005
0.700± 0.005
NOTE: 1. FABRICATE ONE PIECE
UNLESS OTHERWISE SPECIFIED
DIMENSIONS ARE IN INCHES
TOLERANCES: (UNLESS SPECIFIED)
DECIMALS ANGLES
.X ± .06 ± 1/2°
.XX ± .03
.XXX ± .01
MATERIAL: 2024 ALUMINUM
LASER VAPORIZATION SOURCE
VERSION 2: PART 7
TITLE: BOTTOM/SIDE FRAME CORNER
SUPPORT
FILE: PT7LVV2.DWG
DWG BY: JAMES M. SPOTTS
DATE: 0-17-00 SCALE: 1:1
PROF. M. OKUMURA LABORATORY
DIVISION OF CHEMISTRY: CALIFORNIA
INSTITUTE OF TECHNOLOGY

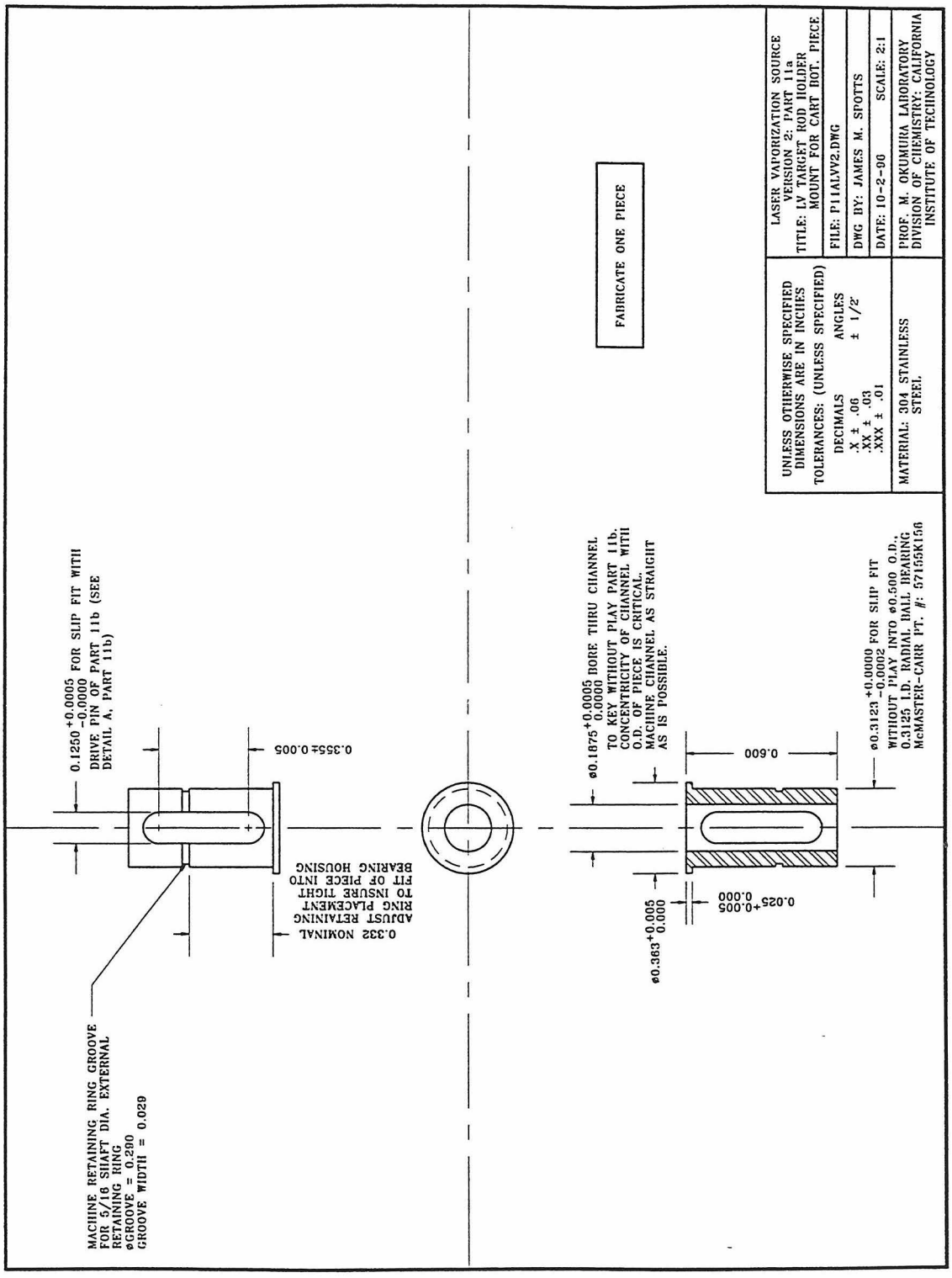

0.587± 0.002
0.500± 0.005
0.500± 0.005
DRILL THRU TO CENTER CHANNEL 2 HOLES VERY CLOSE CLEARANCE FOR 8-32 UNC POSITIONED AS SHOWN.
COUNTERBORE BOTH HOLES VERY CLOSE CLEARANCE FOR 8-32 SOCKET HEAD CAP SCREW TO DEPTH SHOWN IN SECTION B-B
B
B
DRILL THRU AND TAP THRU TO CENTER OF PIECE 2 TAPPED HOLES FOR 8-32 UNC POSITIONED AS SHOWN
0.700± 0.005
0.700± 0.005
2.00
DRILL THRU AND TAP THRU TO CENTER CHANNEL 2 TAPPED HOLES FOR 8-32 UNC POSITIONED AS SHOWN
0.587± 0.002
0.500± 0.005
0.500± 0.005
ø1.0000 +0.0005 0.0000
0.020 +0.010 0.000
0.075± 0.005
ø1.500± 0.005
SECTION B-B
0.250 +0.005 0.000
NOTE: 1. FABRICATE TWO PIECES
UNLESS OTHERWISE SPECIFIED DIMENSIONS ARE IN INCHES
TOLERANCES: (UNLESS SPECIFIED)
DECIMALS ANGLES
.X ± .06 ± 1/2°
.XX ± .03
.XXX ± .01
MATERIAL: 2024 ALUMINUM
LASER VAPORIZATION SOURCE VERSION 2; PART 8a
TITLE: BOTTOM & SIDE FRAME MOUNT
FILE: PT8ALVV2.DWG
DWG BY: JAMES M. SPOTTS
DATE: 8-17-96 SCALE: 1:1
PROF. M. OKUMURA LABORATORY
DIVISION OF CHEMISTRY; CALIFORNIA INSTITUTE OF TECHNOLOGY

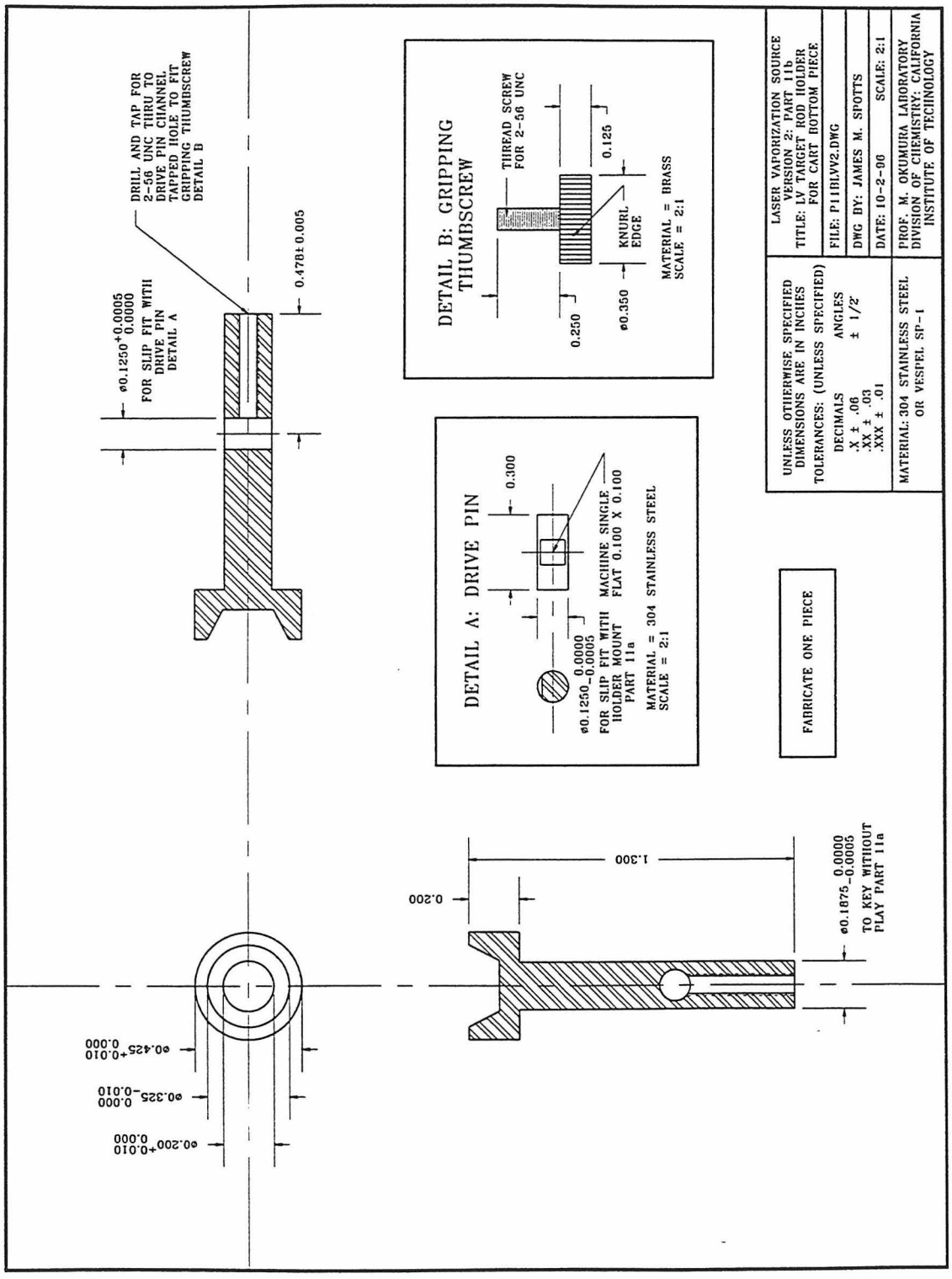

DRILL THRU AND TAP THRU 4 TAPPED HOLES FOR 4-40 UNC POSITIONED AS SHOWN
DRILL THRU AND TAP THRU 2 TAPPED HOLES FOR 8-32 UNC POSITIONED AS SHOWN
DRILL THRU AND TAP THRU 4 TAPPED HOLES FOR 4-40 UNC POSITIONED AS SHOWN
MILL 2 SLOTS CLEARANCE FOR 8-32 UNC POSITIONED AS SHOWN
2.00
0.250
0.700± 0.005
0.450
0.138
0.275± 0.005
1.485
2.085
0.270
1.100 +0.010 0.000
0.700± 0.005
0.700± 0.005
0.750± 0.005
2.727± 0.005
4.938
0.250
0.270
0.275± 0.005
0.138
0.875 +0.002 0.000
0.875 +0.002 0.000
0.450
0.728
1.328
NOTES: 1. FABRICATE ONE PIECE.
2. PIECE SHOULD BE MILLED FLAT TO INSURE PERPENDICULARITY OF FRAME
UNLESS OTHERWISE SPECIFIED DIMENSIONS ARE IN INCHES
TOLERANCES: (UNLESS SPECIFIED)
DECIMALS ANGLES
.X ± .06 ± 1/2°
.XX ± .03
.XXX ± .01
MATERIAL: 2024 ALUMINUM
LASER VAPORIZATION SOURCE VERSION 2: PART 8b
TITLE: BOTTOM RAIL FRAME
FILE: PT8BLVV2.DWG
DWG BY: JAMES M. SPOTTS
DATE: 8-17-96 SCALE: 1:1
PROF. M. OKUMURA LABORATORY
DIVISION OF CHEMISTRY: CALIFORNIA INSTITUTE OF TECHNOLOGY

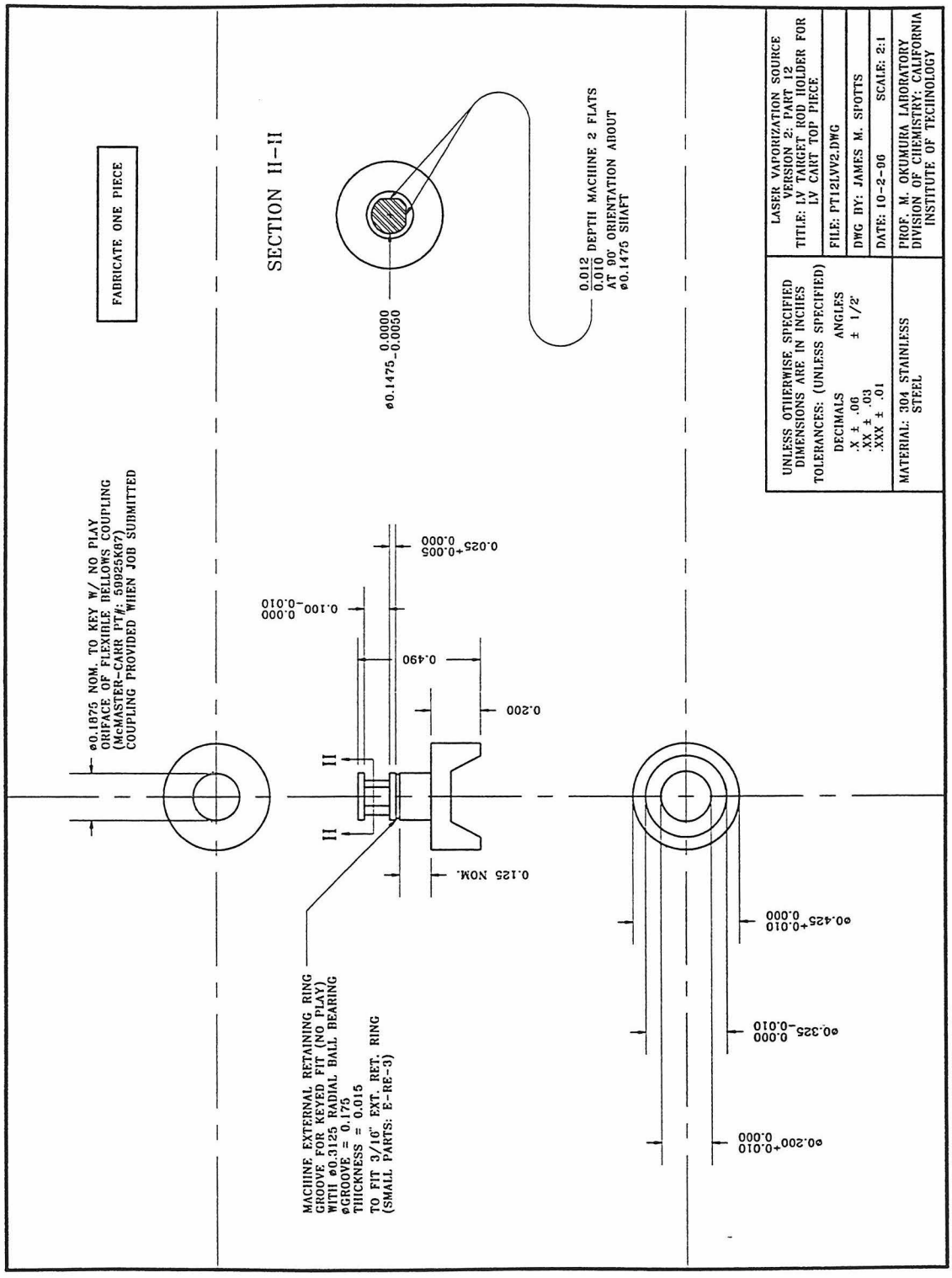

DRILL THRU AND TAP THRU 4 TAPPED HOLES FOR 8-32 UNC POS. SYM. ABOUT CENTER LINE OF PIECE AS SHOWN
MILL THRU SECTION AS SHOWN. FILLET R0.06
MILL 2 SLOTS CLEARANCE FOR 8-32 UNC POSITIONED SYM. ABOUT CENTER LINE AS SHOWN
MILL 2 SLOTS CLEARANCE FOR 8-32 UNC POSITIONED SYM. ABOUT CENTER LINE AS SHOWN
0.250
0.700±0.005
0.500±0.005
1.750±0.005
2.000
1.000
0.000
0.270
0.362
0.812
4.937
5.438
6.038
7.187
9.000
9.750
NOTES: 1. FABRICATE ONE PIECE
2. PIECE SHOULD BE MILLED FLAT TO INSURE PERPENDICULARITY OF FRAME
UNLESS OTHERWISE SPECIFIED DIMENSIONS ARE IN INCHES
TOLERANCES: (UNLESS SPECIFIED)
DECIMALS ANGLES
.X ± .06 ± 1/2°
.XX ± .03
.XXX ± .01
MATERIAL: 2024 ALUMINUM
LASER VAPORIZATION SOURCE VERSION 2: PART 9
TITLE: SOURCE MOUNT SIDE FRAME
FILE: PT0LVV2.DWG
DWG BY: JAMES M. SPOTTS
DATE: 9-26-90
SCALE: 1:1
PROF. M. OKUMURA LABORATORY
DIVISION OF CHEMISTRY: CALIFORNIA INSTITUTE OF TECHNOLOGY

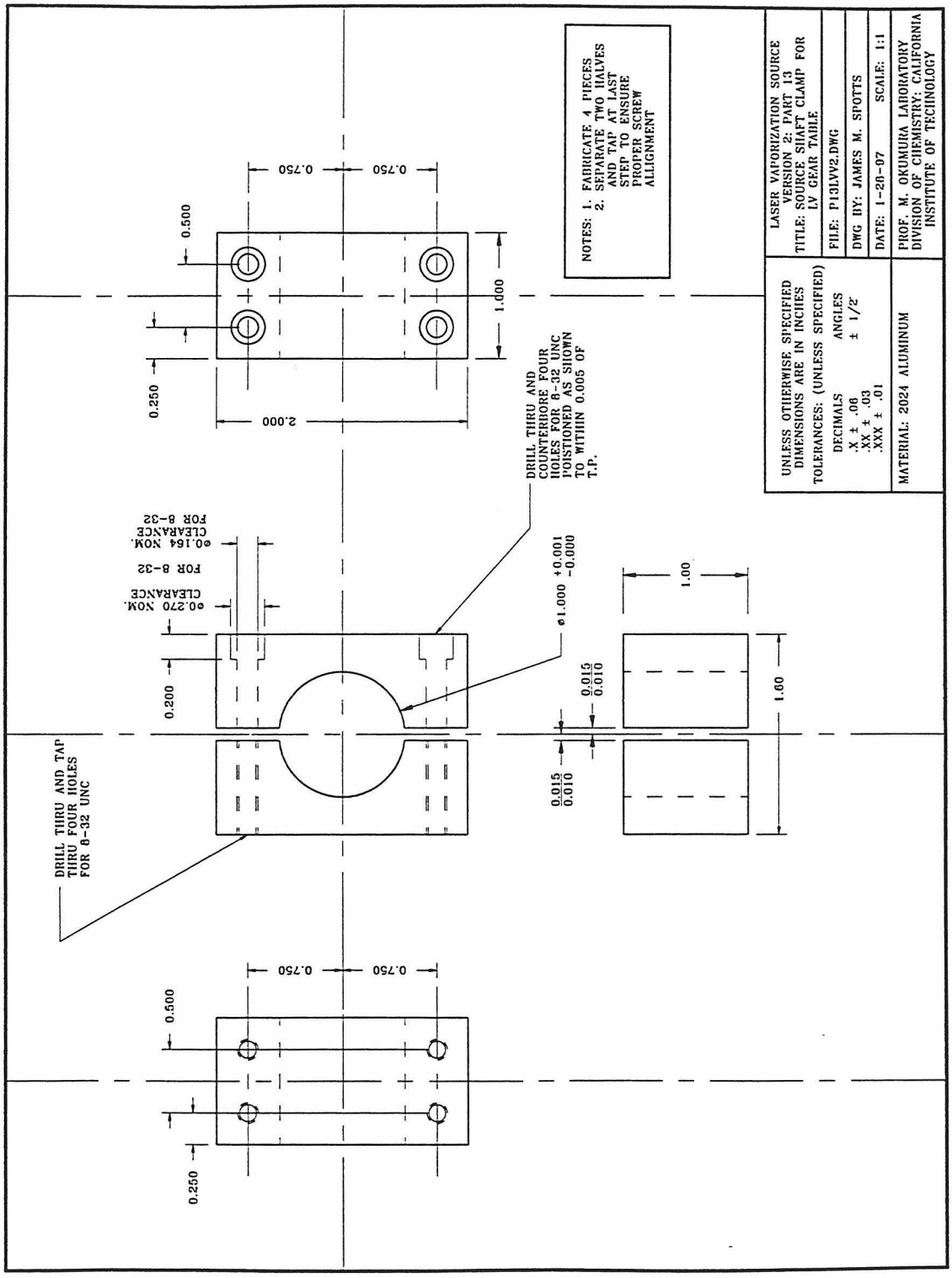

SECTION E-E
-V-
-V-
-Z-
FILLET R0.063
0.020 +0.005 0.000
0.125 +0.010 0.000
0.975 0.000 -0.010
0.550
0.450
1.950
-D-
-C-
E
E
E
E
0.275
1.000
0.450
CHAMFER 0.200 X 45°
ø0.3123 +0.0002 0.0000 BORE THRU ONE HOLE POSITIONED AS SHOWN TO FIT MINIATURE PRECISION BALL BEARING (McMASTER-CARR PT#: 57155K131). BEARING DIM. ø0.3125 0.0000 -0.0002 BEARING FLANGE ON SURFACE -Z-
ø0.3745 0.0000 -0.0005 BORE THRU 2 CHANNELS POSITIONED AS SHOWN. CHANNELS TO ACCOMIDATE PRESS FIT ø0.375 O.D. DRILL BUSHINGS CHANNELS SHOULD BE BORED AS STRAIGHT AS IS POSSIBLE PRESS FIT 0.375 O.D./0.250 I.D. /0.500 LONG DRILL BUSHING INTO EACH CHANNEL
ø0.3745 0.0000 -0.0005 BORE THRU 2 CHANNELS POSITIONED AS SHOWN. CHANNELS TO ACCOMIDATE PRESS FIT ø0.375 O.D. DRILL BUSHINGS CHANNELS SHOULD BE BORED AS STRAIGHT AS IS POSSIBLE PRESS FIT 0.375 O.D./0.250 I.D. /0.500 LONG DRILL BUSHING INTO EACH CHANNEL
CRITICAL ALIGNMENT DIMENSIONS
-A- = 0.2200 ± 0.0005
-C- = 1.0000 ± 0.0005
-D- = 1.4500 ± 0.0005
NOTES:
1. FABRICATE ONE PIECE
2. "CRITICAL ALIGNMENT DIMENSIONS" MUST BE THE SAME IN EACH OF THE RELEVANT PARTS OF ASSEMBLY
3. 4 X 0.375 O.D./0.250 I.D./0.500 LONG DRILL BUSHINGS PROVIDED AT AT SUBMISSION OF JOB
4. DRAWING SHOWS DRILL BUSHINGS PRESSED INTO PLACE
UNLESS OTHERWISE SPECIFIED DIMENSIONS ARE IN INCHES
TOLERANCES: (UNLESS SPECIFIED)
DECIMALS ANGLES
.X ± .06 ± 1/2°
.XX ± .03
.XXX ± .01
MATERIAL: 2024 ALUMINUM
LASER VAPORIZATION SOURCE VERSION 2: PART 10a
TITLE: LV CART TOP PIECE
FILE: P10ALVV2.DWG
DWG BY: JAMES M. SPOTTS
DATE: 9-17-96 SCALE: 1:1
PROF. M. OKUMURA LABORATORY
DIVISION OF CHEMISTRY: CALIFORNIA INSTITUTE OF TECHNOLOGY

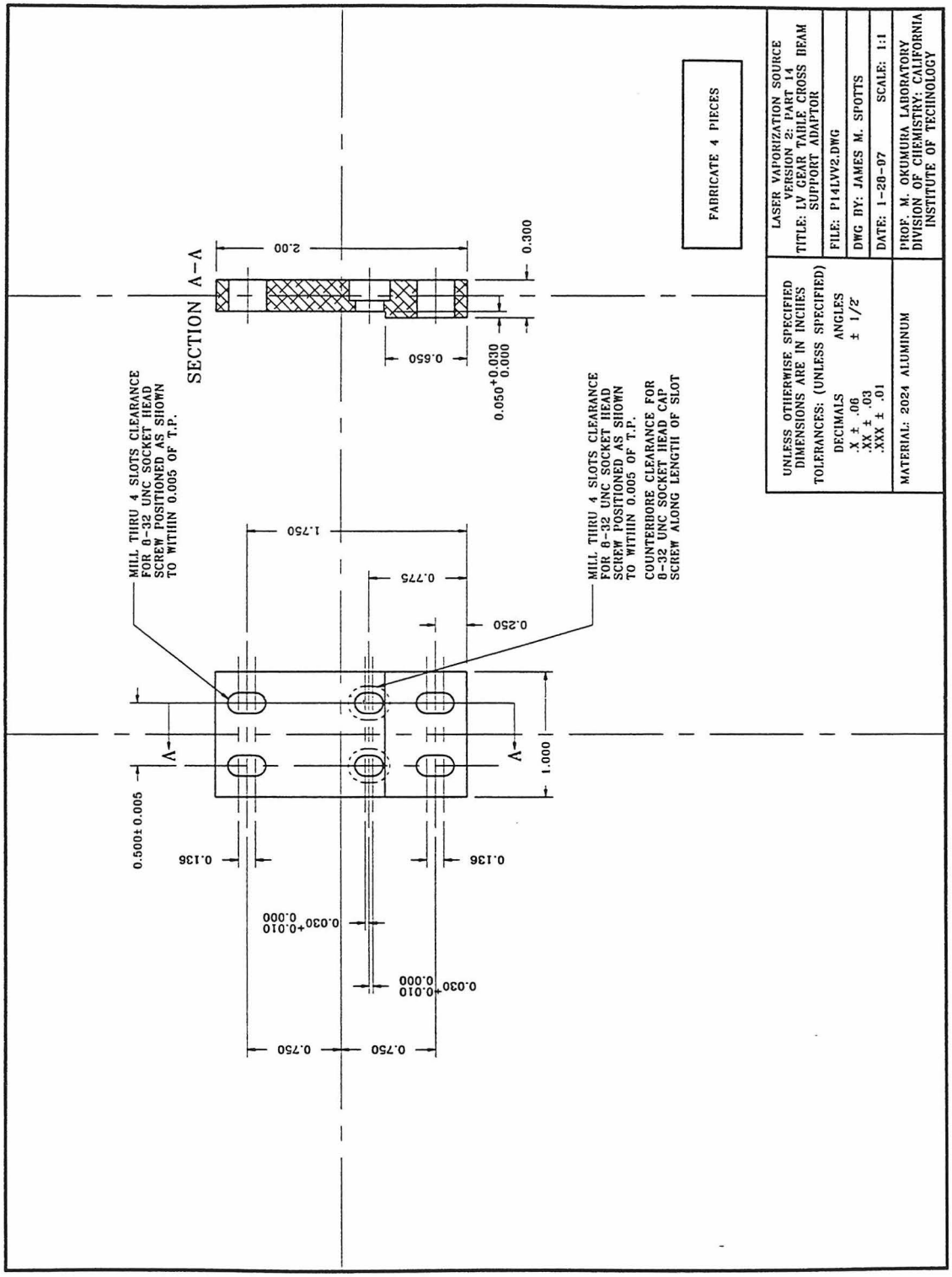

SECTION E-E
-A-
-A-
-A-
-C-
-D-
E
E
E
E
FILLET R0.003
2.037
0.550
0.275
1.000
0.625
0.975 0.000 -0.010
0.250 +0.010 0.000
ø0.3745 -0.0005 0.0000 BORE THRU 2
CHANNELS POSITIONED AS SHOWN. CHANNELS TO ACCOMIDATE PRESS FIT ø0.375 O.D. DRILL BUSHINGS
CHANNELS SHOULD BE BORED AS STRAIGHT AS IS POSSIBLE
PRESS FIT 0.375 O.D./0.250 I.D. /0.500 LONG DRILL BUSHING INTO EACH CHANNEL
ø0.4990 +0.0002 0.0000 BORE THRU ONE HOLE POSITIONED AS SHOWN TO FIT MINIATURE PRECISION BALL BEARING (McMASTER-CARR PT#: 57155K131). BEARING DIM. ø0.5000 0.0000 -0.0002
PRESS FIT 2 RADIAL BALL BEARINGS- ONE ON EACH SIDE
ø0.3745 -0.0005 0.0000 BORE THRU 2
CHANNELS POSITIONED AS SHOWN. CHANNELS TO ACCOMIDATE PRESS FIT ø0.375 O.D. DRILL BUSHINGS
CHANNELS SHOULD BE BORED AS STRAIGHT AS IS POSSIBLE
PRESS FIT 0.375 O.D./0.250 I.D. /0.500 LONG DRILL BUSHING INTO EACH CHANNEL
CRITICAL ALIGNMENT DIMENSIONS
-A- = 0.2200 ± 0.0005
-C- = 1.0000 ± 0.0005
-D- = 1.4500 ± 0.0005
NOTES:
1. FABRICATE ONE PIECE
2. "CRITICAL ALIGNMENT DIMENSIONS" MUST BE TIE SAME IN EACH OF THE RELEVANT PARTS OF ASSEMBLY
3. 4 X 0.375 O.D./0.250 I.D./0.500 LONG DRILL BUSHINGS PROVIDED AT SUBMISSION OF JOB
4. DRAWING SHOWS DRILL BUSHINGS PRESSED INTO PLACE
UNLESS OTHERWISE SPECIFIED DIMENSIONS ARE IN INCHES
TOLERANCES: (UNLESS SPECIFIED)
DECIMALS ANGLES
.X ± .06 ± 1/2°
.XX ± .03
.XXX ± .01
MATERIAL: 2024 ALUMINUM
LASER VAPORIZATION SOURCE VERSION 2: PART 10b
TITLE: LV CART BOTTOM PIECE
FILE: P10BLVV2.DWG
DWG BY: JAMES M. SPOTTS
DATE: 9-17-96 SCALE: 1:1
PROF. M. OKUMURA LABORATORY
DIVISION OF CHEMISTRY: CALIFORNIA INSTITUTE OF TECHNOLOGY

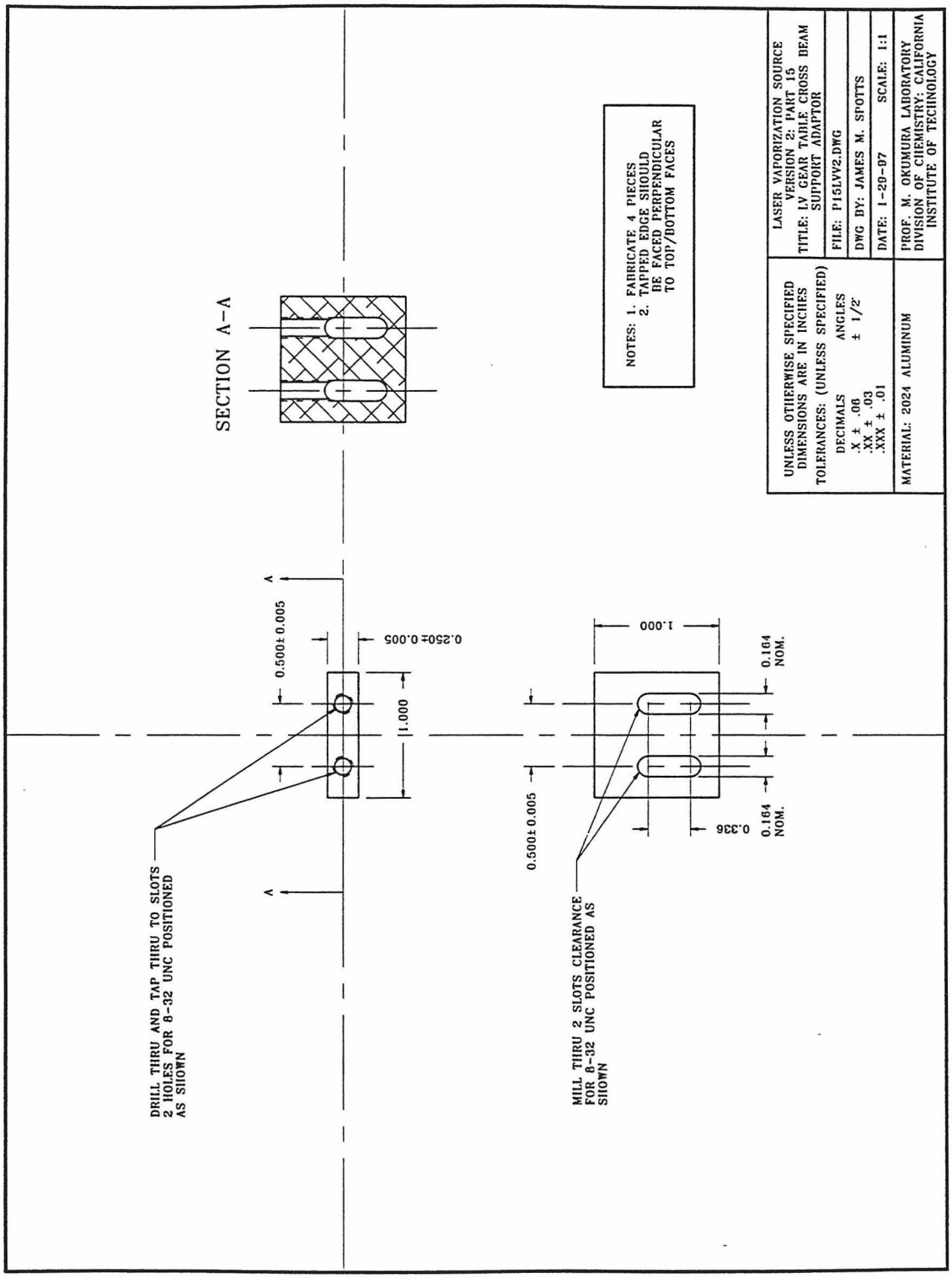

0.1250 +0.0005 -0.0000 FOR SLIP FIT WITH DRIVE PIN OF PART 11b (SEE DETAIL A, PART 11b)
0.354±0.005
0.332 NOMINAL
ADJUST RETAINING RING PLACEMENT TO INSURE TIGHT FIT OF PIECE INTO BEARING HOUSING
MACHINE RETAINING RING GROOVE FOR 5/16 SHAFT DIA. EXTERNAL RETAINING RING
øGROOVE = 0.290
GROOVE WIDTH = 0.029
ø0.1875 +0.0005 0.0000 BORE THRU CHANNEL TO KEY WITHOUT PLAY PART 11b. CONCENTRICITY OF CHANNEL WITH O.D. OF PIECE IS CRITICAL. MACHINE CHANNEL AS STRAIGHT AS IS POSSIBLE.
0.600
ø0.363 +0.005 0.000
0.025 +0.005 0.000
ø0.3123 +0.0000 -0.0002 FOR SLIP FIT WITHOUT PLAY INTO ø0.500 O.D., 0.3125 I.D. RADIAL BALL BEARING McMASTER-CARR PT. #: 57155K156
FABRICATE ONE PIECE
UNLESS OTHERWISE SPECIFIED DIMENSIONS ARE IN INCHES
TOLERANCES: (UNLESS SPECIFIED)
DECIMALS ANGLES
X ± .06 ± 1/2°
.XX ± .03
.XXX ± .01
MATERIAL: 304 STAINLESS STEEL
LASER VAPORIZATION SOURCE VERSION 2: PART 11a
TITLE: LV TARGET ROD HOLDER MOUNT FOR CART BOT. PIECE
FILE: P11ALVV2.DWG
DWG BY: JAMES M. SPOTTS
DATE: 10-2-90 SCALE: 2:1
PROF. M. OKUMURA LABORATORY
DIVISION OF CHEMISTRY: CALIFORNIA INSTITUTE OF TECHNOLOGY

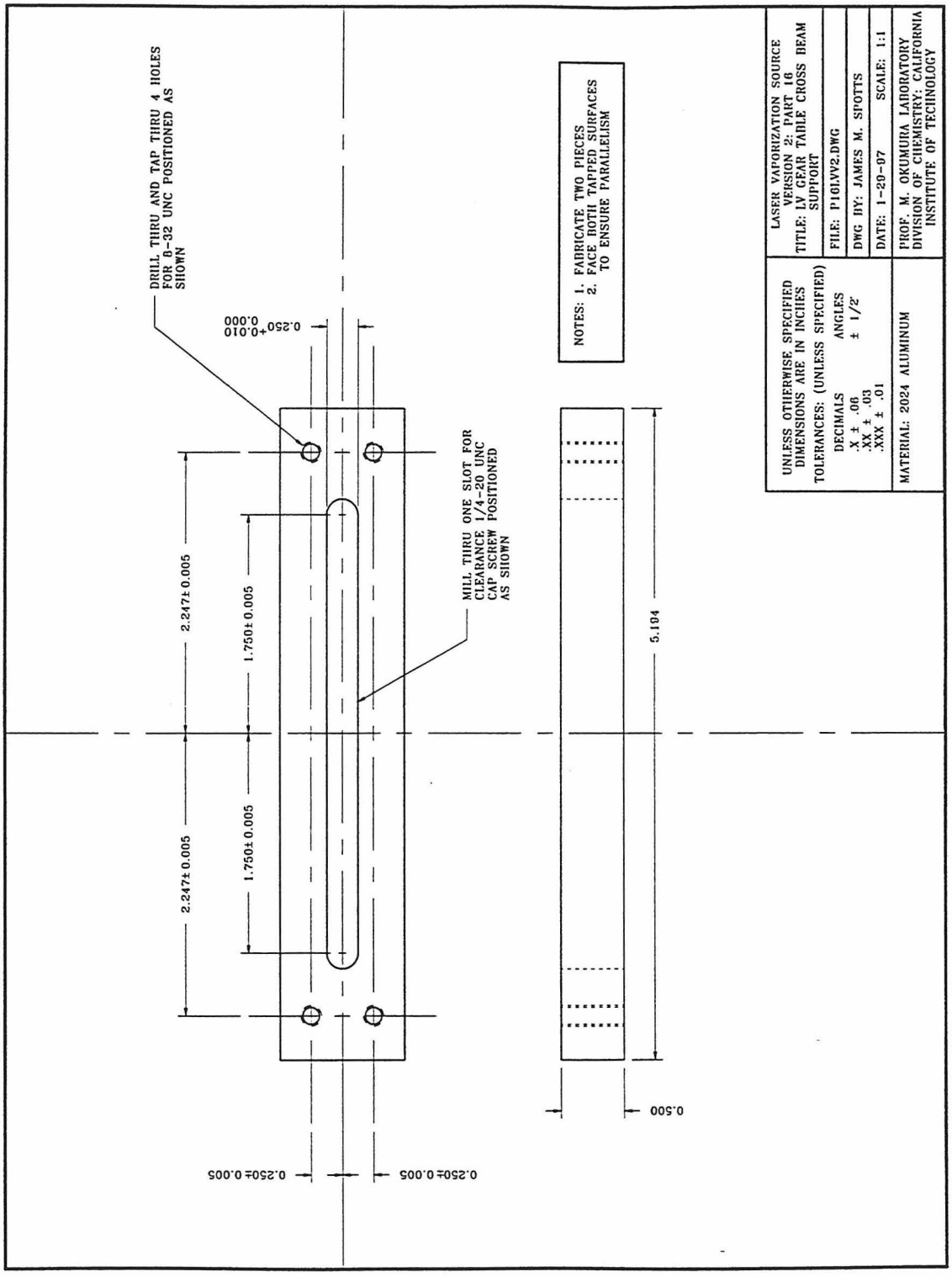

DRILL AND TAP FOR 2-56 UNC THRU TO DRIVE PIN CHANNEL TAPPED HOLE TO FIT GRIPPING THUMBSCREW DETAIL B
ø0.1250 +0.0005 0.0000
FOR SLIP FIT WITH DRIVE PIN DETAIL A
0.478±0.005
DETAIL B: GRIPPING THUMBSCREW
THREAD SCREW FOR 2-56 UNC
0.250
ø0.350
0.125
KNURL EDGE
MATERIAL = BRASS
SCALE = 2:1
DETAIL A: DRIVE PIN
0.300
ø0.1250 0.0000 −0.0005
FOR SLIP FIT WITH HOLDER MOUNT PART 11a
MACHINE SINGLE FLAT 0.100 X 0.100
MATERIAL = 304 STAINLESS STEEL
SCALE = 2:1
FABRICATE ONE PIECE
UNLESS OTHERWISE SPECIFIED DIMENSIONS ARE IN INCHES
TOLERANCES: (UNLESS SPECIFIED)
DECIMALS
.X ± .06
.XX ± .03
.XXX ± .01
ANGLES ± 1/2°
MATERIAL: 304 STAINLESS STEEL OR VESPEL SP-1
LASER VAPORIZATION SOURCE VERSION 2: PART 11b
TITLE: LV TARGET ROD HOLDER FOR CART BOTTOM PIECE
FILE: P11BLVV2.DWG
DWG BY: JAMES M. SPOTTS
DATE: 10-2-96
SCALE: 2:1
PROF. M. OKUMURA LABORATORY DIVISION OF CHEMISTRY: CALIFORNIA INSTITUTE OF TECHNOLOGY
1.300
0.200
ø0.1875 0.0000 −0.0005
TO KEY WITHOUT PLAY PART 11a
ø0.425 +0.010 0.000
ø0.325 −0.010 0.000
ø0.200 +0.010 0.000

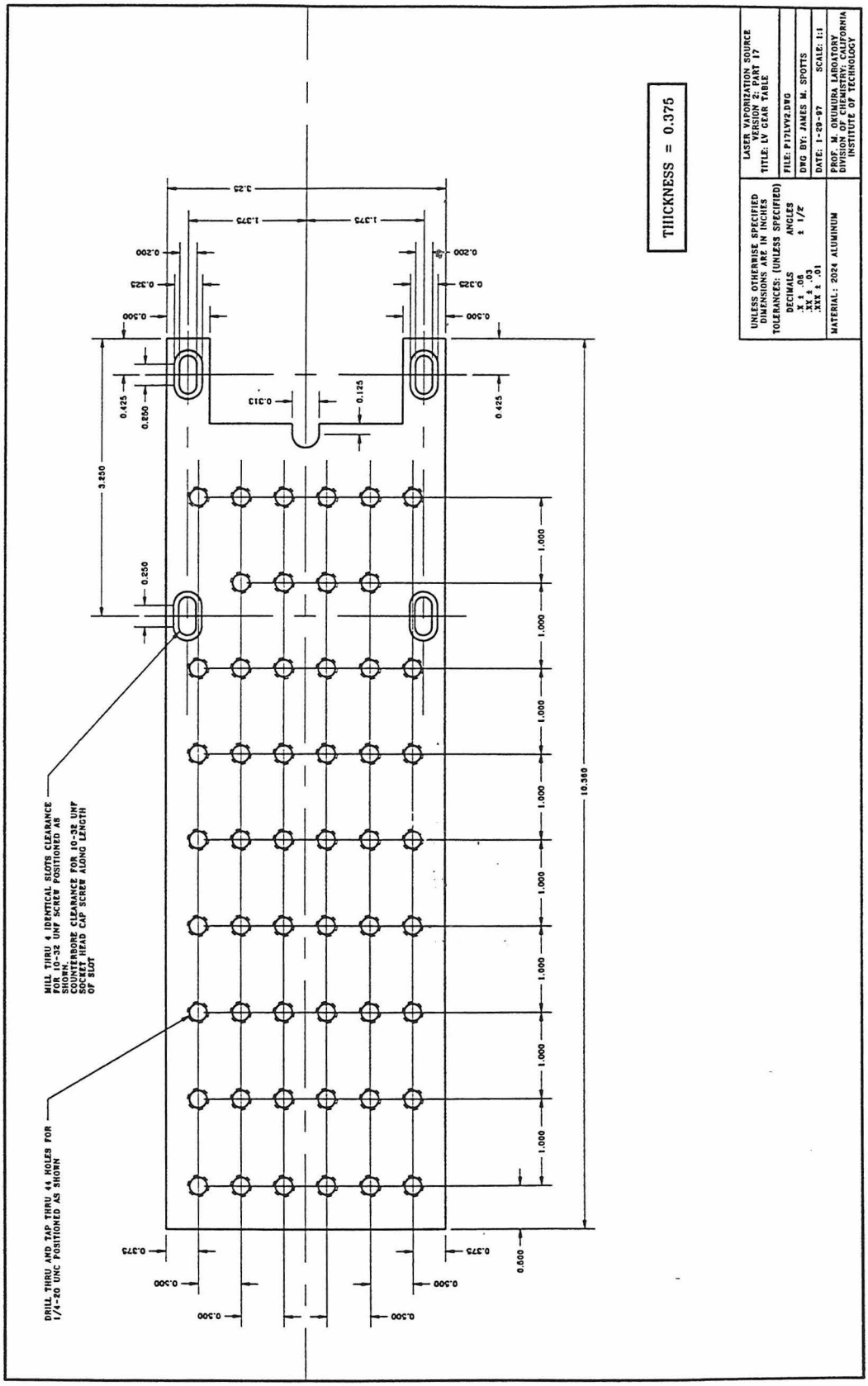

FABRICATE ONE PIECE
SECTION II-II
ø0.1475 0.0000 -0.0050
0.012 0.010 DEPTH MACHINE 2 FLATS AT 90° ORIENTATION ABOUT ø0.1475 SHAFT
ø0.1875 NOM. TO KEY W/ NO PLAY ORIFACE OF FLEXIBLE BELLOWS COUPLING (McMASTER-CARR PT#: 59925K07) COUPLING PROVIDED WHEN JOB SUBMITTED
0.025 +0.005 0.000
0.100 0.000 -0.010
0.490
0.200
0.125 NOM.
II
II
MACHINE EXTERNAL RETAINING RING GROOVE FOR KEYED FIT (NO PLAY) WITH ø0.3125 RADIAL BALL BEARING øGROOVE = 0.175 THICKNESS = 0.015 TO FIT 3/16" EXT. RET. RING (SMALL PARTS: E-RE-3)
ø0.425 +0.010 0.000
ø0.325 0.000 -0.010
ø0.200 +0.010 0.000
UNLESS OTHERWISE SPECIFIED DIMENSIONS ARE IN INCHES TOLERANCES: (UNLESS SPECIFIED)
DECIMALS ANGLES
.X ± .06 ± 1/2°
.XX ± .03
.XXX ± .01
MATERIAL: 304 STAINLESS STEEL
LASER VAPORIZATION SOURCE VERSION 2: PART 12
TITLE: LV TARGET ROD HOLDER FOR LV CART TOP PIECE
FILE: PT12LVV2.DWG
DWG BY: JAMES M. SPOTTS
DATE: 10-2-00
SCALE: 2:1
PROF. M. OKUMURA LABORATORY DIVISION OF CHEMISTRY: CALIFORNIA INSTITUTE OF TECHNOLOGY


NOTES: 1. FABRICATE 4 PIECES
2. SEPARATE TWO HALVES AND TAP AT LAST STEP TO ENSURE PROPER SCREW ALLIGNMENT
LASER VAPORIZATION SOURCE
VERSION 2: PART 13
TITLE: SOURCE SHAFT CLAMP FOR LV GEAR TABLE
FILE: P13LVV2.DWG
DWG BY: JAMES M. SPOTTS
DATE: 1-28-07
SCALE: 1:1
UNLESS OTHERWISE SPECIFIED DIMENSIONS ARE IN INCHES
TOLERANCES: (UNLESS SPECIFIED)
DECIMALS
.X ± .06
.XX ± .03
.XXX ± .01
ANGLES
± 1/2°
MATERIAL: 2024 ALUMINUM
PROF. M. OKUMURA LABORATORY
DIVISION OF CHEMISTRY: CALIFORNIA INSTITUTE OF TECHNOLOGY
DRILL THRU AND TAP THRU FOUR HOLES FOR 8-32 UNC
DRILL THRU AND COUNTERBORE FOUR HOLES FOR 8-32 UNC POSITIONED AS SHOWN TO WITHIN 0.005 OF T.P.
ø0.270 NOM. CLEARANCE FOR 8-32
ø0.164 NOM. CLEARANCE FOR 8-32
ø1.000 +0.001 -0.000
0.750
0.750
0.500
1.000
0.250
2.000
0.200
0.015
0.010
1.00
1.60


FABRICATE 4 PIECES
SECTION A–A
2.00
0.300
0.650
0.050 +0.030 0.000
MILL THRU 4 SLOTS CLEARANCE FOR 0–32 UNC SOCKET HEAD SCREW POSITIONED AS SHOWN TO WITHIN 0.005 OF T.P.
MILL THRU 4 SLOTS CLEARANCE FOR 0–32 UNC SOCKET HEAD SCREW POSITIONED AS SHOWN TO WITHIN 0.005 OF T.P.
COUNTERBORE CLEARANCE FOR 0–32 UNC SOCKET HEAD CAP SCREW ALONG LENGTH OF SLOT
1.750
0.775
0.250
1.000
0.500± 0.005
0.136
0.136
0.030 +0.010 0.000
0.030 +0.010 0.000
0.750
0.750
UNLESS OTHERWISE SPECIFIED DIMENSIONS ARE IN INCHES
TOLERANCES: (UNLESS SPECIFIED)
DECIMALS ANGLES
.X ± .06 ± 1/2°
.XX ± .03
.XXX ± .01
MATERIAL: 2024 ALUMINUM
LASER VAPORIZATION SOURCE
VERSION 2: PART 14
TITLE: LV GEAR TABLE CROSS BEAM SUPPORT ADAPTOR
FILE: P14LVV2.DWG
DWG BY: JAMES M. SPOTTS
DATE: 1-28-97 SCALE: 1:1
PROF. M. OKUMURA LABORATORY
DIVISION OF CHEMISTRY: CALIFORNIA INSTITUTE OF TECHNOLOGY


SECTION A-A
NOTES: 1. FABRICATE 4 PIECES
2. TAPPED EDGE SHOULD BE FACED PERPENDICULAR TO TOP/BOTTOM FACES
DRILL THRU AND TAP THRU TO SLOTS 2 HOLES FOR 8-32 UNC POSITIONED AS SHOWN
MILL THRU 2 SLOTS CLEARANCE FOR 8-32 UNC POSITIONED AS SHOWN
0.500±0.005
0.250±0.005
1.000
0.164 NOM.
0.336
UNLESS OTHERWISE SPECIFIED DIMENSIONS ARE IN INCHES
TOLERANCES: (UNLESS SPECIFIED)
DECIMALS ANGLES
.X ± .06 ± 1/2°
.XX ± .03
.XXX ± .01
MATERIAL: 2024 ALUMINUM
LASER VAPORIZATION SOURCE VERSION 2: PART 15
TITLE: LV GEAR TABLE CROSS BEAM SUPPORT ADAPTOR
FILE: P15LVV2.DWG
DWG BY: JAMES M. SPOTTS
DATE: 1-29-97 SCALE: 1:1
PROF. M. OKUMURA LABORATORY
DIVISION OF CHEMISTRY: CALIFORNIA INSTITUTE OF TECHNOLOGY


DRILL THRU AND TAP THRU 4 HOLES FOR 8-32 UNC POSITIONED AS SHOWN
0.250+0.010 0.000
MILL THRU ONE SLOT FOR CLEARANCE 1/4-20 UNC CAP SCREW POSITIONED AS SHOWN
2.247± 0.005
1.750± 0.005
1.750± 0.005
2.247± 0.005
0.250± 0.005
0.250± 0.005
NOTES: 1. FABRICATE TWO PIECES
2. FACE BOTH TAPPED SURFACES TO ENSURE PARALLELISM
5.104
0.500
UNLESS OTHERWISE SPECIFIED DIMENSIONS ARE IN INCHES
TOLERANCES: (UNLESS SPECIFIED)
DECIMALS ANGLES
.X ± .06 ± 1/2°
.XX ± .03
.XXX ± .01
MATERIAL: 2024 ALUMINUM
LASER VAPORIZATION SOURCE VERSION 2: PART 16
TITLE: LV GEAR TABLE CROSS BEAM SUPPORT
FILE: P16LVV2.DWG
DWG BY: JAMES M. SPOTTS
DATE: 1-20-07 SCALE: 1:1
PROF. M. OKUMURA LABORATORY
DIVISION OF CHEMISTRY: CALIFORNIA INSTITUTE OF TECHNOLOGY


THICKNESS = 0.375
MILL THRU 4 IDENTICAL SLOTS CLEARANCE FOR 1/4-20 UNC SCREW POSITIONED AS SHOWN. COUNTERBORE CLEARANCE FOR 10-32 UNF SOCKET HEAD CAP SCREW ALONG LENGTH OF SLOT
DRILL THRU AND TAP THRU 44 HOLES FOR 1/4-20 UNC POSITIONED AS SHOWN
UNLESS OTHERWISE SPECIFIED DIMENSIONS ARE IN INCHES TOLERANCES: (UNLESS SPECIFIED) DECIMALS .X ± .08 .XX ± .03 .XXX ± .01 ANGLES ± 1/2°
MATERIAL: 2024 ALUMINUM
LASER VAPORIZATION SOURCE VERSION 2: PART 17 TITLE: LV GEAR TABLE
FILE: P17LVV2.DWG
DWG BY: JAMES M. SPOTTS
DATE: 1-20-97 SCALE: 1:1
PROF. M. OKUMURA LABORATORY DIVISION OF CHEMISTRY, CALIFORNIA INSTITUTE OF TECHNOLOGY
3.25
1.375
1.375
0.200
0.323
0.300
0.200
0.323
0.300
0.313
0.125
0.425
0.250
0.425
3.250
0.250
1.000
1.000
1.000
1.000
1.000
1.000
1.000
1.000
10.360
0.373
0.300
0.300
0.300
0.300
0.373
0.600